AWARD NUMBER: W81XWH-16-1-0692

TITLE: Selective AAK1 and GAK inhibitors for combating dengue and other emerging viral infections

PRINCIPAL INVESTIGATOR: Dr. John Dye

CONTRACTING ORGANIZATION: The Geneva Foundation, Tacoma, WA

REPORT DATE: January 2021

TYPE OF REPORT: Final

PREPARED FOR: U.S. Army Medical Research and Materiel Command
                Fort Detrick, Maryland 21702-5012

DISTRIBUTION STATEMENT: Approved for Public Release;
                        Distribution Unlimited

The views, opinions and/or findings contained in this report are those of the author(s) and should not be construed as an official Department of the Army position, policy or decision unless so designated by other documentation.

REPORT DOCUMENTATION PAGE

Form Approved
OMB No. 0704-0188

1. REPORT DATE	2. REPORT TYPE	3. DATES COVERED
January 2021	Final	15Sep2016-14Sep2020

4. TITLE AND SUBTITLE
Selective AAK1 and GAK inhibitors for combating dengue and other emerging viral infections

5a. CONTRACT NUMBER
W81XWH-16-1-0692

5b. GRANT NUMBER PR151090P1

5c. PROGRAM ELEMENT NUMBER

6. AUTHOR(S)
Dr. John Dye, Shirit Einav, Steven De Jonghe, Jennifer Brannan, Raul Andino

E-Mail:seinav@stanford.edu

5d. PROJECT NUMBER

5e. TASK NUMBER

5f. WORK UNIT NUMBER

7. PERFORMING ORGANIZATION NAME(S) AND ADDRESS(ES)
Stanford University School of Medicine, Stanford CA 94305
KU Leuven, 3000 Leuven, Belgium
USAMRIID, Frederick, MD 21702
University of California San Francisco, San Francisco, CA 94143

8. PERFORMING ORGANIZATION REPORT

9. SPONSORING / MONITORING AGENCY NAME(S) AND ADDRESS(ES)

U.S. Army Medical Research and Materiel Command
Fort Detrick, Maryland 21702-5012

10. SPONSOR/MONITOR'S ACRONYM(S)

11. SPONSOR/MONITOR'S REPORT NUMBER(S)

12. DISTRIBUTION / AVAILABILITY STATEMENT

Approved for Public Release; Distribution Unlimited

13. SUPPLEMENTARY NOTES

14. ABSTRACT

Emerging viruses, such as dengue (DENV) and Ebola (EBOV), pose threats to military and global health. There are no approved drugs or vaccines available against these viruses. Our goal is to develop broad-spectrum antivirals with a high genetic barrier to resistance by targeting host proteins that are critical to the life cycle of multiple viruses. The goals of this project are to optimize selective inhibitors of AAK1 and GAK, host kinases we discovered as targets for broad-spectrum antivirals, and advance their development to a pre-IND stage. This approach would also protect against multiple other biothreat agents. During the past year we have optimized the antiviral activity of two distinct series of GAK inhibitors and a series of AAK1 inhibitors, all with excellent broad-spectrum antiviral activity (DENV, CHIKV and EBOV and SARS-CoV-2), including in human primary cells, with a high barrier to resistance. We have also demonstrated target modulation with representative compounds and determined key in vitro ADME parameters. We have submitted a proposal for an expansion award whose goal is to advance these imporved compounds to animal studies.

15. SUBJECT TERMS
Antivirals, kinase inhibitors, dengue virus, Ebola virus, broad-spectrum antivirals, host-targeted antivirals

16. SECURITY CLASSIFICATION OF:

a. REPORT	b. ABSTRACT	c. THIS PAGE	17. LIMITATION OF ABSTRACT	18. NUMBER OF PAGES	19a. NAME OF RESPONSIBLE PERSON USAMRMC
Unclassified	Unclassified	Unclassified	Unclassified	246	19b. TELEPHONE NUMBER *(include area code)*

Standard Form 298 (Rev. 8-98)
Prescribed by ANSI Std. Z39.18

Table of Contents

1. INTRODUCTION:

Emerging viruses, such as dengue (DENV), chikungunya (CHIKV), and Ebola (EBOV), pose major threats to military and global health. There are no approved drugs or vaccines available against these viruses. The current "one drug, one threat" approach to drug development is slow and expensive and is therefore not easily scalable to meet the large unmet clinical need. Our overall goal is to develop broad-spectrum antiviral drugs with a high genetic barrier to resistance by targeting host proteins that are critical to the life cycle of multiple viruses.We discovered an Achilles' heel of multiple unrelated viruses: a requirement for AP2-associated protein kinase 1 (AAK1) and cyclin G-associated kinase (GAK), host kinases that regulate clathrin adaptor proteins-mediated pathways. Our data point to AAK1 and GAK as "master regulators" of viral infection and attractive targets for broad-spectrum antivirals. We discovered that approved anticancer drugs that target these kinases; sunitinib and erlotinib, potently inhibit replication of multiple viruses *in vitro* and reduce mortality in mice infected with DENV and EBOV. This approach is being advanced into clinical trials for both of these indications. Nevertheless, potential toxicity resulting from inhibition of other host cell kinases by these non-selective inhibitors may limit their use. The goals of this project are to optimize novel, chemically distinct, selective lead AAK1 and GAK inhibitors, already demonstrating great promise against DENV, and advance their development to a pre-IND stage. This approach would also protect against biothreat agents from multiple other viral families, including EBOV and CHIKV.

2. KEYWORDS:

Antivirals, kinase inhibitors, dengue virus, Ebola virus, broad-spectrum antivirals, host-targeted antivirals

3. ACCOMPLISHMENTS:
The major goals of the project and the accomplishments under these goals

The major goals of this project were to optimize novel, chemically distinct, selective lead AAK1 and GAK inhibitors and advance their preclinical development as anti-DENV agents that could also protect against other biothreat agents from multiple viral families, including EBOV and chikungunya (CHIKV). Aims: 1. Optimize lead inhibitors of AAK1 and/or GAK and maximize their therapeutic index (TI); 2. Determine the *in vivo* metabolism, activity, and relative barrier to resistance of the above AAK1 and GAK inhibitors in best characterized mouse models; 3. Subject optimized leads to *in vitro* ADME-toxicity and initial preclinical animal safety studies; and 4. Validate the mechanism of action (MOA) of selective AAK1 and GAK inhibitors in DENV infection by studying target binding and modulation.

Accomplished tasks:

1. AAK1 and GAK validated as targets for broad-spectrum antiviral therapy and their role in viral infection established (Figures 1, 2, 4, and 6 in Bekerman et al. JCI 2017 and Figures 1-7 in Xiao et al. mBio 2018).

2. A series of *iso*thiazolo[4,3-b]pyridines-based GAK inhibitors with excellent kinase activity (Figures 1, table 1 in Pu et al. Journal of Med Chem 2018), selectivity (Figure 7 in Pu et al. JMC 2018), improved broad-spectrum antiviral activity (DENV, CHIKV, and EBOV) (Figures 2, 4 Table 2 in Pu et al. JMC 2018) generated.

3. Another series of 4-anilinoquin(az)oline-based analogs with very potent antiviral activity identified and characterized (Figures 1-4 and Tables 1-4 in Saul et al. Bioorganic & Medicinal Chemistry Letter 2020).

4. Novel pyrrolo[2,3-b]pyridines-based AAK1 inhibitors (Schemes 1-6 and Figures 4-5 in Verdonck et. JMC 2019), with excellent broad-spectrum antiviral activity (DENV, CHIKV and EBOV) (Tables 2-6 and Figures 6, 7 in in Verdonck et al. JMC 2019), yet lack of selectivity (Figure 10 and Table 7 in Verdonck et al. JMC 2019) developed. The mode of binding of the most promising compound from this series was studied by crystalography experiments (Fig 5, 11, 12, and Table 8 in Verdonck et. JMC 2019).

5. A chemically distinct series of 3-acylaminoindazole-based analogs with extremely potent activity identified (Figure 4 in Pu et al. AVR 2020; and Wells C et al. *ACS Med Chem Lett* 2020).

6. Potent anti-DENV activity of the above classes of inhibitors demonstrated in human primary MDDCs; an established *ex vivo* model system for DENV (Figure 2 in Pu et al. JMC 2018; Figure 9 in Verdonck et al. JMC 2019; and Figure 6A in Pu et al. AVR 2020).

7. Synergistic antiviral activity (but not toxicity) demonstrated with approved (Figures 3 and 4 in Bekerman et al. JCI 2017) and selective AAK1 and GAK inhibitors (Figure 5 in annual report 2019).

8. Key *in vitro* ADME-Tox parameters determined for representative compounds (Table 3 in Pu et al. JMC 2018 and Figure 1 and Tables 1-5 in Appendix A).

9. The molecular targets of AAK1 and GAK inhibitors validated and functional substrate modulation monitored *in vitro* (Figure 6 in Bekerman et al. JCI 2017; Figures 5 and 6 in Pu et al. JMC 2018; Figure 8 in Verdonck et al. JMC 2019; Figures 3-5 in Pu et al. AVR 2020) and in *vivo* in AG129 mice (Figure 6 Bekerman et al. JCI 2017).

10. No resistance (genotypic/phenotypic) detected in viral-infected cells (Figure 3F in Bekerman et al. JCI 2017, Figure 7 in Pu et al. AVR 2020, and Figure 2 in Appendix B)

11. No resistance (genotypic/phenotypic) detected in viral-infected mice with selected inhibitors (Figure 3 and 4 and Tables 7-8 in Appendix B).

12. PK profiled in mice for representative GAK inhibitors (Figures 5-7 in Appendix C). Various formulations for selected GAK inhibitors somewhat improved the C max, yet the overall half-life and exposure remained suboptimal.

13. We have shown *in vivo* efficacy with sunitinib and erlotinib combinations both in DENV- and EBOV-infected mice (Figure 5 in Bekerman et al. JCI 2017). Our multiple attempts to demonstrate *in vivo* efficacy with selected selective GAK inhibitors in AG129 mice inoculated with DENV did not show a significant effect beyond vehicle, due to the limited PK profile discussed in point 12 (Figures 8-11 in Appendix D). Given this limitation we did not pursue experiments in guinea pigs (task 3.4) or advanced a compound into non-GLP rat toxicology studies (tasks 5.3 and 5.4).

Accomplishments achieved beyond the proposed tasks:

1. We have validated AAK1 and GAK as antiviral targets for SARS-CoV-2 infection and have demonstrated that representative compounds from the AAK1 and GAK series show potent activity against virulent SARS-CoV-2 (undetectable viral replication at non-toxic concentrations) (Figures 12-15 in Appendix E).

2. BIKE, a third member (out of 4) of the NAK (Numb-associated kinase) family that is closely related to AAK1, was identified as a target for broad-spectrum antivirals (Figures 1-3 in Pu et al. in AVR 2020); both repurposed (Figures 5 and 6 in Pu et al. AVR 2020) and novel, selective AAK1/BIKE inhibitors (Figure 4 in Pu et al. AVR 2020) demonstrate broad-spectrum antiviral activity (DENV, EBOV, SARS-CoV-2, alphaviruses) .

3. A series of compounds emerging from our GAK inhibitors with a different MOA (does not target GAK) has a very potent broad-spectrum antiviral activity including against multiple alpha encephalitis viruses, DENV and SARS-CoV-2 and is being advanced with DTRA funding (Figures 17-20 in Appendix F). This series of compounds target the endosomal lipid kinase PIKfyve (Figures 21-22 in Appendix F)

Training opportunities that the project provided
- Students and postdoctoral fellows at the Einav, Herdewijn, Andino and Dye labs have been mentored by the respective PI and benefited from interdisciplinary training provided by this project. The PIs were actively involved in designing experiments, data analysis, overseeing the study strategies and participating in presentations and manuscripts preparation.

- The trainees at Stanford enjoyed the privilege of participating in the Stanford SPARK program; a Stanford-based initiative aimed at translating targets to drugs, directed by Dr. Mochly-Rosen. SPARK consultants have expertise in multiple aspects of the development process including medicinal-chemistry, PK/PD, formulation, toxicology, regulatory process, and successful early drug development. The trainees meet on a weekly basis with this talented group of consultants. In addition, they presented their progress to the SPARK medicinal chemistry group every quarter.

- All the trainees on this project have also benefited from regular conference calls, which enriched their multidisciplinary training opportunities to students and research fellows.

- The Stanford trainees have attended the annual Bay Virology Symposium, the annual retreats of the Microbiolgy Department and the division of infectious diseases, as well as monthly seminars of the NIH U19 (to SE) which was focused on developing host-targeted broad-spectrum antiviral approaches. They also attended monthly seminars of the arboviral working group at Stanford, which is directed by Dr. Einav and integrates members from 16 labs on campus, all dedicated to study mosquito transmitted viruses.

Dissemination of the results to communities of interest
DTRA is funding a follow up project that is built on this award. The DTRA project is focused on developing countermeasures based on a series that emerged from our GAK inhibitors program but targets a different cellular kinase, namely PIKFYVE, to combat the encephalitic alphaviruses (VEEV, EEEV and WEEV). It work expanded the scope of our work to other series of compounds as well as new disease models.

What do you plan to do during the next reporting period to accomplish the goals?
Nothing to report

4. IMPACT:

The impact on the development of the principal discipline(s) of the project

We have generated a set of pharmacological probes that can be used to rapidly screen any emerging virus for its dependence on AAK1, GAK and BIKE, as we have recently done successfully with SARS-CoV-2.

Moreover, we have developed a pipeline for the discovery and preclinical development of host-targeted antivirals, which has recently shown promise in our DTRA-funded project that is now focused on an independent, chemically distinct, host-targeted approach for combating encephalitis alphaviruses.

We will be submitting an Expansion award whose main goal is to enhance the PK profiles of our two lead GAK and new lead AAK1/BIKE inhibitors, while maintaining the delicate balance of potency and activity, and to quickly advance them into animal studies.
 Changing the paradigm for treating viral infections from a "one drug, one threat" approach to a "one drug, multiple threats" approach has the potential to <u>drastically decrease the time and cost associated with developing antivirals against emerging pathogens</u>.

Such a "pandemic pill" <u>will position the military to combat newly emerging</u> pathogens which we have not yet encountered, including new pandemic coronaviruses, <u>thereby providing readiness for future outbreaks</u>.

A therapeutic with broad-spectrum potential could be deployed with troops, providing our military with the means to rapidly treat these devastating illnesses in the field. This ability would have a significant positive impact on military health and troop readiness.

Such a safe broad-spectrum therapeutic <u>could also be administered even before a viral threat has been accurately identified (in an outbreak context) or diagnosed (in an individual), thereby overcoming the time-to-treatment challenge and providing</u> ideal protection from viral threats while <u>preventing spread.</u> This advantage also makes these drugs potential candidates for the treatment of bioterror or biowarfare attacks.

The impact on other disciplines
Excitingly, our lead compounds show very potent activity against SARS-CoV-2 replication. We are currently attempting to secure funding to expand their development to target this indication in parallel to DENV and EBOV.

Our DTRA grant expands the work to encephalitic alphaviruses; currently untreatable biothreat agents highly relevant to military personnel.

Lastly, since NAKs are implicated in other diseases, such as cancer, chronic pain and Parkinson's disease, our compounds may find additional future clinical indications beyond viral infections.

The impact on technology transfer
Nothing to Report.

The impact on society beyond science and technology
Nothing to Report.

5. CHANGES/PROBLEMS:
Changes in approach and reasons for change
There have been no changes in objectives or scope.

Actual or anticipated problems or delays and actions or plans to resolve them

Our primary structure-activity relationship (SAR)'s goal to improve antiviral activity of our original AAK1 and GAK lead inhibitors has been achieved. Yet, the PK profile of these compounds has limited their success in *in vivo* efficacy studies in mice and the advancement of the compounds to other animal models. Nevertheless, we have demonstrated potent activity in human primary monocyte-derived dendritic cells (MDDCs), an established *ex vivo* DENV system that models human physiology and disease better than immortalized cell lines. Our finding that treatment exhibits antiviral efficacy in MDDCs thus more accurately reflects the dependence of DENV on AAK1 and GAK during human infection and supports the biological relevance and therapeutic potential of this approach. Moreover, our collaborator, Dr. Asquith has recently demonstrated *in vivo* activity of 4-anilinoquin(az)oline-based GAK inhibitors by addition of a cytochrome P450 inhibitor(1). While reported in a different disease model, we have since shown that these compounds are extremely potent against DENV(2). This finding provides a proof-of-concept that we should be able to achieve a similar *in vivo* dosing effect in our viral infection models.

A second challenge has been that while the pyrrolo[2,3-*b*]pyridines-based AAK1 inhibitors we developed exhibit potent broad-spectrum antiviral activity, including in human primary cells, they lack kinase selectivity(3). We have thus advanced a back-up series of potent and highly selective inhibitors of AAK1 and BIKE (a third member of the NAK kinase family) based on a 3-acylaminoindazole scaffold from the literature(4, 5) and showed antiviral activity at submicromolar concentrations (the best achieved with AAK1 inhibitors to date)(6).

Changes that had a significant impact on expenditures

None
Significant changes in use or care of human subjects, vertebrate animals, biohazards, and/or select agents
None
Significant changes in use or care of human subjects
N/A
Significant changes in use or care of vertebrate animals.
None
Significant changes in use of biohazards and/or select agents
None

6. PRODUCTS:

Journal publications (the 10 published papers are attached in the appendix):

1. Bekerman E, Neveu G, Shulla A, Brannan J, Pu SZ, Wang S, Xiao F, Barouch-Bentoc R, Bakken RR, Mateo R, Govero J, Nagamine C, Diamond M, De Jonghe S, Herdewijn P, Dye J, Randall G, and Einav S. Anticancer kinase inhibitors impair intracellular viral trafficking and exert broad-spectrum antiviral effects. *Journal of Clinical Investigation*. 2017 Feb 27. pii: 89857. doi: 10.1172/JCI89857. PMID: 28240606

2. Xiao F, Shulla A, Wang S, Pu S, Neveu G, Beer M, Schor S, Barouch-Bentov R, Randall G, and Einav S. Interactions between the nonstructural 2 protein and host adaptor proteins 1 and 4 orchestrate hepatitis C virus release. *mBio*. 2018 Mar 13;9(2). pii: e02233-17. doi: 10.1128/mBio.02233-17.

3. Pu S, Wouters R, Schor S, Barouch-Bentov R, Brannan J, Dye J, Herdewijn P, De Jonghe S and Einav S. Optimization of *iso*thiazolo[4,3-b]pyridines-based inhibitors of cyclin G associated kinase (GAK) with broad-spectrum antiviral activity. *Journal of Medicinal Chemistry*. 2018 June 28. PMID: 29953812.

4. Wouters R, Pu SY, Froeyen M, Lescrinier E, Einav S, Herdewijn P, De Jonghe S. Cyclin G-associated kinase (GAK) affinity and antiviral activity studies of a series of 3-C-substituted *iso*thiazolo[4,3-b]pyridines. *Eur J Med Chem*. 2018 Nov 28;163:256-265. doi: 10.1016/j.ejmech.2018.11.065.PMID: 30529544

5. Verdonck S, Pu S, Sorrell FJ, Elkins JM, Froeyen M, Gao LJ, Prugar LI, Dorosky DE, Brannan JM, Knapp S, Dye JM, Herdewijn P, Einav S, De Jonghe S. Synthesis and structure-activity relationships of 3,5-disubstituted-pyrrolo[2,3-*b*]pyridines as inhibitors of adaptor associated kinase 1 (AAK1) with antiviral activity. *Journal of Medicinal Chemistry*. 2019 Jun 27;62(12):5810-5831. PMID: 31136173

6. Martinez-Gualda, B, Pu S, Froeyen M, Herdewijn P, Einav, S, De Jonghe S. Structure-activity relationship study of the pyridine moiety of *iso*thiazolo[4,3-b]pyridines as antiviral agents targeting cyclin G-associated kinase. *Bioorganic & medicinal chemistry*. 2019 Nov. 115188. PMID: 31757682

7. Randy Wouters, Junjun Tian, Piet Herdewijn, and Steven De Jonghe. A Scaffold-Hopping Strategy toward the Identification of Inhibitors of Cyclin G Associated Kinase. *ChemMedChem.* 2019, 14, 237 – 254. PMID: 30548533

8. Schor S and Einav S. Combating intracellular pathogens with repurposed host-targeted drugs. *American Chemical Society Infectious Diseases.* 2018 Jan 3. PMID: 29298032. (Invited Review)

9. Schor S and Einav S. Repurposing kinase inhibitors as broad-spectrum antiviral drugs. *DNA and Cell Biology.* 2017 Nov 17. doi: 10.1089/dna.2017.4033. PMID: 29148875. (Invited Review)

10. Saul S, Pu S-Y, Zuercher WJ, Einav S & Asquith CRM. Potent antiviral activity of novel multi-substituted 4-anilinoquin(az)olines. *Bioorganic & medicinal chemistry letters*, 127284, doi:https://doi.org/10.1016/j.bmcl.2020.127284 (2020). PMID: 32631507

11. Saul S and Einav S. Old drugs for a new virus: repurposed approaches for combating COVID-19. *ACS Infectious Diseases*. 10.1021/acsinfecdis.0c00343. PMID: 32687696. (Invited Perspective)

12. Pu S, Schor S, Robinson M, Neveu G, Prugar LI, Dorosky DE, Brannan J, Dye JM, and Einav S. BIKE regulates dengue virus infection and is a host target for broad-spectrum antivirals. *AVR 2020*.

Presentations:

1. Brannan JM, Bekerman E, Neveu G, Shulla A, Pu S, Wang S, Xiao F, Barouch-Bentov R, Claude M. Nagamine1, Dye JM, Randall G, and Einav S. "Inhibition of host kinases AAK1 and GAK during Ebola and dengue virus infections." Keystone Symposium on Hemorrhagic Fever Viruses, Santa Fe, New Mexico, December 2016.
2. De Jonghe S, Knapp S, Herdewijn P, and Einav S. "Cyclin G associated kinase (GAK) inhibition as a strategy for the discovery of broad spectrum antivirals." International Conference on Antiviral Research, Atlanta, May 2017.
3. Prugar LI, Brannan JM, Pu S, Dorosky D, O'Brien C, Bakken RR, De Jonghe S, Herdewijn P, Dye JM, and Einav S. "Selective AAK1 and GAK inhibitors demonstrate activity against multiple RNA viruses". 9th International Filovirus Symposium: Filo2017, Sept 2017.
4. Xiao F, Shulla A, Wang S, Pu S, Neveu G, Beer M, Schor S, Barouch-Bentov R, Randall G, and Einav S. "Interactions between the nonstructural 2 protein and host adaptor proteins 1 and 4 orchestrate hepatitis C virus release." The 24th International Symposium on HCV and Related Viruses, USA MA, Sept 2017.
5. Narayanan A and Einav S. "Discovery and Development of Host-Based Kinase Inhibitors Using Medicinal Chemistry Tools As Therapeutic Strategies To Combat Alphavirus Infection." DTRA chemical and biological defense science & technology conference. Oct 2017.
6. Dorosky D, Prugar LI, Pu S, O'Brien C, Bakken RR, De Jonghe S, Herdewijn P, Brannan JM, Dye JM, Einav S. "AAK1 and GAK inhibitors demonstrate activity against filoviruses." American Association of Immunlogists (AAI) Annual Meeting, Austin TX, May 2018.
7. Einav S. "Broad-spectrum host-targeted approaches to combat emerging viral infections." Pharmaceutical & BioScience Society/SPARK conference. Foster City, California, March 2019.
8. Steven De Jonghe, Randy Wouters, Junjun Tian, Piet Herdewijn
Poster : "Inhibitors of cyclin G associated kinase based on novel heterocyclic scaffolds."
XVIII International Conference on Heterocycles in Bioorganic Chemistry (Bioheterocycles 2019)
June 17 to 20, 2019 ; Gent (Belgium)
9. Steen De Jonghe and Shirit Einav. "Inhibitors of GAK based on novel heterocyclic scaffolds".
Bioheterocycles 2019, Belgium, June 2019.
10. Sven Verdonck, Szu-Yuan Pu, Fiona J. Sorrell, Jon M. Elkins, Mathy Froeyen, Ling-Jie Gao, Laura I. Prugar, Danielle E. Dorosky, Jennifer M. Brannan, Rina Barouch-Bentov, Stefan Knapp, John M. Dye, Piet Herdewijn, Shirit Einav, Steven De Jonghe
 "Synthesis and SARs of 3,5-disubstituted-pyrrolo[2,3-*b*]pyridines as antivirals". EFMC Symposium on Advances in Synthetic and Medicinal Chemistry (EFMC-ASMC'19). Poster. Greece, Sept 2019.

7. PARTICIPANTS & OTHER COLLABORATING ORGANIZATIONS

Individuals who have worked on the project throughout the award period:

Name:	**John Dye**
Project Role:	PD/PI
Researcher Identifier (e.g. ORCID ID):	0000-0002-0883-5016
Nearest person month worked:	0.60

Contribution to Project:	Dr. Dye is a Lead Research Scientist at USAMRIID and will be responsible for designing and supervising the in vitro experiments with live virus and the mouse challenge studies. He assisted with experimental procedures, data analysis, and writing reports and publication of results.
Funding Support:	DoD, DTRA, NIAID
Name:	**Courtney Cohen**
Project Role:	Staff Scientist
Researcher Identifier (e.g. ORCID ID):	[0000-0002-4963-2493](0000-0002-4963-2493)
Nearest person month worked:	4.2
Contribution to Project:	Dr. Cohen provided her expertise in the area of microbiology and in mouse models of viral infections. She will be responsible for the design and implementation of experimental
Funding Support:	DoD, DTRA, NIAID
Name:	**Samantha Zak**
Project Role:	Postdoctoral fellow
Researcher Identifier (e.g. ORCID ID):	
Nearest person month worked:	0.60
Contribution to Project:	Helped perform *in vivo* (animal model) experiments testing candidate inhibit inhibitors against authentic viruses.
Funding Support:	DoD, DTRA, NIAID

Active other support of the PD/PI(s) or senior/key personnel:

1R01 AI111516   06/01/2014 – 05/31/2020   0.60 calendar months
NIH/NIAID   total direct costs
Mammalian and Plant-derived Ab-based Therapies against SUDV
The overall goal of the proposed work is to develop an antibody-based therapy for the treatment and management of Sudan virus infection, one of the most common and lethal species of Ebola virus.We will develop a renewable commercial source of Sudan virus-specific antibody therapies and determine the protective efficacy of these therapies using a non-human primate model of Sudan virus disease.
Role: PI

JSTO_CBD   10/01/2015 – 12/31/2020   0.60 calendar months
DTRA   total costs
Development of Human Marburg Virus-Specific and Lassa Virus-Specific Antibodies for Product Development
This proposal will address the portfolio gap of monoclonal antibody therapeutics specific to Sudan Ebolavirus (SUDV). We will create and produce SUDV-specific monoclonal antibodies (mAbs) from B cells of human survivors of SUDV infections. We believe this product will provide the best option for a medical counter measure against future emerging infectious diseases like SUDV. Additionally, we will be assessing whether

antibodies that are generated against SUDV might exhibit cross reactivity against other filovirus species [ie: Zaire ebolavirus (EBOV), Bundibugyo ebolavirus (BDBV), Marburgviruses (MARV)].
Role: PI

1R01 AI126587-01A1   07/01/2016 – 06/30/2021   0.60 calendar months
NIH/Einstein   subaward total costs
Evolution of Anti-filovirus B Cell Responses and Mechanisms of Protection
This proposal is aimed at understanding the mechanisms of antibody mediated protection against filoviruses. Several novel macaque-derived monoclonal antibodies will be identified. The mAbs will be provided to USAMRIID for testing for efficacy in mouse models of EBOV, SUDV, and MARV.
Role: Co-Investigator

1R01 AI125462-01A1   06/01/2017 – 05/31/2021   0.60 calendar months
NIH/NIAID/Einstein   subaward total costs
Engineered, Multispecific Antibodies as Broad Anti-filovirus Therapeutics
The Dye lab will be responsible for testing bispecific antibodies in viral neutralization and mouse challenge experiments under BSL4 conditions. In addition, USAMRIID personnel (Dr. Dye) will provide input into the design of bispecific antibodies, as well as overall project direction, priorities, and manuscript preparation.
Role: Co-Investigator

1R01AI32256-01   07/01/2017 – 06/30/2022   0.60 calendar months
NIH/Einstein   subaward total costs
A 'Trojan Horse' Bispecific Antibody Strategy for Broad Filovirus Therapeutics
This project focuses on the generation and characterization of antibodies that have the potential to be cross-reactive against multiple filovirus species.
Role: Co-Investigator

2R42 AI122403-02   07/01/2017 – 06/30/2020   0.60 calendar months
NIH/IBT   subaward total costs
Broadly Protective Bispecific Antibodies for Treatment of Ebola Virus Disease
Working with Integrated BioTherapeutics, Inc. (IBT), this project is aimed at developing a bispecific antibody as pan-ebolavirus therapeutics.
Role: Co-Investigator

1R01AI132633-01   07/01/2017 – 06/30/2021   0.60 calendar months
NIH/Einstein   subaward total costs
Dissecting the Receptor-mediated Infection Mechanisms of Hantaviruses
The aim of this project is to evaluate and characterize hantavirus entry mechanisms by providing authentic, live-hantavirus experiments, pathology, and immunohistochemistry analysis.
Role: Co-Investigator

HDTRA118C001   12/15/2017 – 12/31/2020   0.60 calendar months
DTRA/Microbiotix   subaward total costs
Optimization of Broad-spectrum Inhibitors of Filovirus Infection that Antagonize the NPC1-GP Interaction
In collaboration with CytoSorbents, Geneva and USAMRIID will conduct paired EBOV infected rhesus macaque monkey experiments to obtain proof-of-concept EBOV non-human primate data for an anti-Ebolavirus pre-Emergency Use Authorization application for use in humans.
Role: PI

R43AI136188   01/15/2018 – 12/31/2020   0.60 calendar months
NIH/Microbiotix   subaward total costs
Inhibitors of Virus Glycoprotein-LAMP1 Receptor Binding for Lassa Virus Therapy
This project aims to develop and optimize a biochemical high throughput screen for inhibitors of the LASV GP1/LAMP1 interaction and to develop and optimize biolayer interferometry (BLI) assays and cell-based secondary assays to confirm initial screening hits. In addition, it aims to identify and confirm inhibitors

targeting the LASV GP1 interaction with LAMP1 by HTS. The team will also work to validate inhibitors against authentic LASV and prioritize by drug-likeness and ADME predictors.
Role: PI

R43AI136229   1/26/2018 – 12/31/2019   0.60 calendar months
NIH/SBIR
Remodeled Glycoprotein for broad protection against ebolaviruses
This project is aimed at developing an engineered pan-ebolavirus vaccine using targeted mutations of GP that expose broadly neutralizing antibody epitopes to the immune system. For active vaccination, animals will be immunized once with the respective VSV-GP vaccine and challenged with virus 4 weeks after immunization. For passive immunization, anti-sera (0.5 ml) will be given intraperitoneally (IP) to IFNAR-/- mice 24 hours before IP challenge.
Role: PI

R43 AI134598   02/08/2018 – 01/31/2020   0.60 calendar months
NIH/SBIR
Synergistic Pan-filoviral Entry Inhibiting Antibody Drug Conjugates
The overall goal of this project is to inhibit viral entry using Antibody Drug Conjugates (ADCs) that synergistically combine small molecule NPC1-binding filovirus entry inhibitors with GP-specific, broadly neutralizing antibodies (bNAbs) to target low-dose pan ebolavirus activity.
Role: PI

PRMRP-IIRA   10/01/2018 – 09/30/2020   0.60 calendar months
CDMRP/GeoVax   subaward total costs
Advanced Preclinical Development and Production of Master Seed Virus of GEO-LM01, a Novel MVA-VLP Vaccine Against Lassa Fever
The objective of this study is the development of a vaccine against LASV that can be used for protection from LASV infection in military service members, and which could furthermore be used by civilians traveling to endemic areas and those residing therein.
Role: PI

PA-16-302   02/16/2018 – 01/31/2023   0.60 calendar months
NIH/SBIR
Development of CM-SV1, a Monoclonal Antibody Treatment for Sudan Virus
This project is aimed at evaluating the efficacy of CM-SV1, a monoclonal antibody treatment for SUDV. Animals will be challenged with SUDV by the intra-peritoneal route and treated with the therapeutic antibody.
Role: PI

PA-16-302   02/16/2018 – 01/31/2023   0.60 calendar months
NIH/SBIR
Development of CM-SV1, a Monoclonal Antibody Treatment for Sudan Virus
This project is aimed at evaluating the efficacy of CM-SV1, a monoclonal antibody treatment for SUDV. Animals will be challenged with SUDV by the intra-peritoneal route and treated with the therapeutic antibody.
Role: PI

BRCWMD-BAA   02/01/2019 – 01/31/2022   0.60 calendar months
DTRA/UW   subaward total costs
Computational Epitope Design for Protective Vaccines
As a proof of concept for vaccine design, we will generate a vaccine expressing the E1 and E2 (glycoproteins) of VEEV. The candidate vaccine will then utilize to immunize 60 BALB/c mice. These mice will be challenged by the standard aerosol route of administration of VEEV (Trinidad strain). This virus and delivery system has been well developed and is recognized as an excellent animal model for early vaccine evaluation against this agent.
Role: PI

U19 RFA-AI-17-042 (CETR) 02/14/2019 – 01/31/2024   2.4 calendar months
NIH

Prometheus: A Platform for Rapid Development of Human Antibody-based Therapeutics and Prophylactics against Emerging Viral Threats

In support of overall Prometheus objectives, Core C will execute in vivo efficacy testing of antibody-based MCMs derived from Projects I, II, and III in rodent and nonhuman primate (NHP) models of filovirus, hantavirus, and nairovirus disease. Rodent models of ebolavirus, hantavirus, and nairovirus disease will serve as the first in vivo screening mechanism to down-select monoclonal antibody (mAb)-based MCMs for further assessment in higher animal models. Hamster models of hantavirus infection and mouse models of CCHFV infection will be utilized to evaluate newly discovered mAbs from Project I and down-select lead mAbs for NHP testing. Core C will evaluate in vivo efficacy of mAbs with altered Fc effector functions from Project II in rodent models of disease to identify mAb modifications with optimal in vivo potency. The prophylactic efficacy of Project III DMAbs expressing ebolavirus, hantavirus, and CCHFV-specific mAbs will be evaluated first in rodent models of disease and lead DMAbs will be tested in NHPs. In vivo efficacy results from all Core C efforts will be funneled into Projects I, II, and III and Cores A and B for identification of lead mAb cocktails and/or DMAb constructs for advanced development discussions.
Role: PI

CBM-02-01-0101   09/01/2019 – 08/31/2024   0.60 calendar months
DTRA
Development of Novel Monoclonal Antibodies to Marburg Virus and Other High Interest Pathogens
The goal of this project to is to generate novel antibodies to multiple high interest pathogens: Marburgvirus (MARV), Venezuelan Equine Encephalitis Virus (VEEV), and Machupo Virus (MACV).
Role: PI

CBM-02-01-0101   09/01/2019 – 08/31/2024   0.60 calendar months
DTRA
Development of Novel Monoclonal Antibodies to Marburg Virus and Other High Interest Pathogens
The goal of this project to is to generate novel antibodies to multiple high interest pathogens: Marburgvirus (MARV), Venezuelan Equine Encephalitis Virus (VEEV), and Machupo Virus (MACV).
Role: PI

Other organizations involved as partners:
We have been collaborating with Stanford, KU Leuven and UCSF as per the original proposal.
Otherwise there is nothing to report.

8. SPECIAL REPORTING REQUIREMENTS
Partnering PI AWARD: Dr. Shirit Einav, our Partnering PI, will be submitting a separate report describing the work conducted in his lab during this award period.

9. APPENDIX:

A. Representative key *in vitro* ADME-Tox parameters determined for prioritized compounds.

B. No resistance (genotypic/phenotypic) detected in DENV-infected cells and mice with select inhibitors

C. In vivo PK analysis with representative GAK inhibitors with multiple formulations.

D. Representative *in vivo* efficacy experiments with selected GAK inhibitors in mice inoculated with DENV.

E. Representative NAK inhibitors have potent activity against virulent SARS-CoV-2.

F. A series of GAK inhibitors with a different MOA that does not target GAK, but rather PIKFYVE, and has a broad-spectrum antiviral activity.

G. References Cited.

H. Our 12 papers published during the award period.

A. **Representative key *in vitro* ADME-Tox parameters determined for priotized compounds**

Name	Binding Affinity (K_D µM)				Antiviral Activity (EC_{50}/CC_{50})			Solubility (µM)			Stability in mouse microsomes		Permeability			Protein binding	Selectivity
	GAK	AAK1	BIKE	STK16	DENV	EBOV	SARS2	PBS	SIF	SGF	% rem at 30 min	Mean $t_{1/2}$ (min)	Mean A-B 10^{6} cm/s	Mean B-A 10^{6} cm/s	Efflux	Plasma (human)	S(35) at 10 µM
2787	0.089	>10	ND	ND	0.82 >25	2 >20	1.02 >20	0.52	3.2	173	26.9	>60	22.6	7	0.58	97%	0.057
CA-93	0.0029	>10	>10	>10	0.078 >10	ND	ND	57.8	ND	ND	ND	5.7	ND	ND	ND	99%	0.005

Table 1. Profile of representative selective GAK inhibitors from the isothiazolo[4,3-b]pyridines (2787) and the 4-anilinoquin(az)oline (CA-93) series.
Selectivity score (S35): # of kinases with % Ctrl<35/# of kinases tested. ND, Not determined; STK16, serine/threonine kinase 16 (the 4th NAK, not required for viral infection(6)); SIF, simulated intestinal fluid; SGF, simulated gastric fluid.
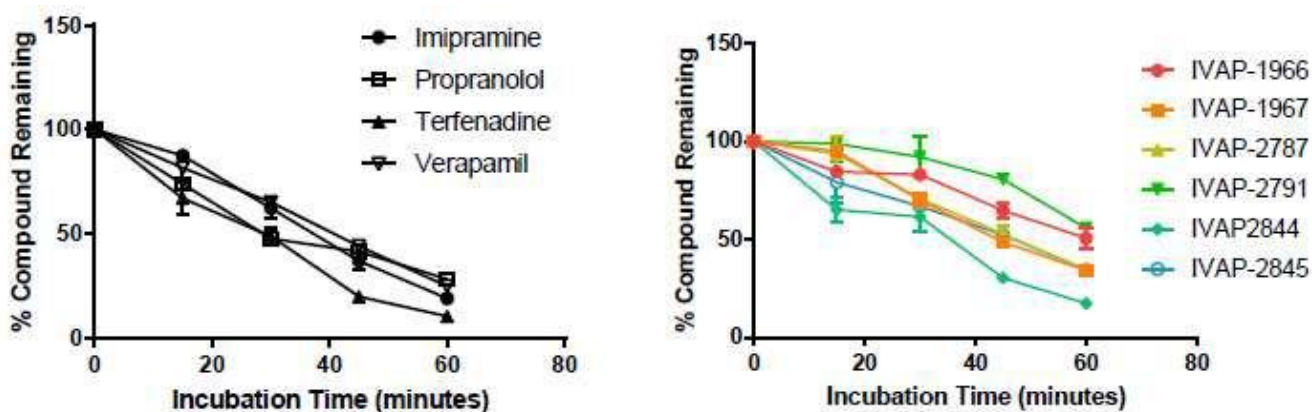

Fig. 1. Microsomal stability assays of selected GAK and AAK1 inhibitors

Table 2: Metabolic stability analysis of optimized GAK inhibitors

Test Article	Species		Percent Remaining (%)	
			0 min	30 min
ketanserin	human	Mean	100,00	**65,45**
		RSD of Area Ratio	0,03	0,02
	mouse	Mean	100,00	**43,86**
		RSD of Area Ratio	0,00	0,01
2787	human	Mean	100,00	**78,47**
		RSD of Area Ratio	0,01	0,08
	mouse	Mean	100,00	**26,94**
		RSD of Area Ratio	0,01	0,01
T-0008	human	Mean	100,00	**76,12**
		RSD of Area Ratio	0,01	0,00
	mouse	Mean	100,00	**25,81**
		RSD of Area Ratio	0,02	0,01

Table 3: ADME properties of an optimized AAK1 inhibitor (RMC-76)

Solubility	PBS	8.4 µM
	SIF	12.3 µM
	SGF	172.8 µM
Stability human	Human (% remained 30 min)	18 min
Stability mouse	Mouse (% remained 30 min)	
	Mean half life	
Permeability	Mean A-B	0.2 10^-6 cm/s*
Caco-2 / MDCK	Mean B-A	0.0 10^-6 cm/s*
Mean protein binding	Plasma human	100%

Table 4. Permeability of selected AAK1 and GAK inhibitors.

Table 1b: Permeability of Reference Compound and Test Articles.

Test Article		Sample - 01	Sample - 02	Mean	RSD	Efflux Ratio
		$P_{app} \times 10^6$ cm/sec		
Metoprolol	A-B	40.33	38.24	39.29	0.04	0.78
	B-A	30.64	30.69	30.66	0.00	
Atenolol	A-B	1.21	1.21	1.21	0.00	1.03
	B-A	1.27	1.23	1.25	0.02	
Quinidine	A-B	12.98	13.07	13.03	0.01	3.22
	B-A	42.41	41.57	41.99	0.01	
1966	A-B	39.13	44.53	41.83	0.09	0.69
	B-A	27.56	29.86	28.71	0.06	
1967	A-B	47.60	43.26	45.43	0.07	0.68
	B-A	32.64	28.96	30.80	0.08	
2608	A-B	45.40	48.04	46.72	0.04	0.73
	B-A	35.55	33.00	34.28	0.05	
2787	A-B	30.69	31.97	31.33	0.03	0.58
	B-A	21.71	14.86	18.28	0.26	
2845	A-B	36.28	26.93	31.61	0.21	0.62
	B-A	20.02	19.20	19.61	0.03	
10769	A-B	27.04	29.70	28.37	0.07	1.21
	B-A	34.42	34.11	34.27	0.01	
Aza	A-B	13.63	15.81	14.72	0.10	3.56
	B-A	53.48	51.35	52.41	0.03	
7745	A-B	19.81	23.22	21.51	0.11	1.26
	B-A	25.36	28.79	27.08	0.09	
82	A-B	41.27	44.03	42.65	0.05	0.71
	B-A	30.31	29.84	30.07	0.01	
93	A-B	28.33	28.23	28.28	0.00	0.67
	B-A	18.92	19.04	18.98	0.00	

*: Papp values were expressed as "<" than the values that were calculated using the minimum concentration of the standards for receiver sides due to the fact that real concentration in the receivers were below quantitation limit (BQL).

N/A: Not Acquired

Table 5. Permeability of selected AAK1 and GAK inhibitors.

Table 1b: Permeability of Reference Compound and Test Articles.

Test Article		P_{app} (10^{-6} cm/sec)		
		Sample - 01	Sample - 02	Mean
Metoprolol	A-B	31.87	33.47	32.67
	B-A	37.98	35.20	36.59
Atenolol	A-B	0.81	0.97	0.89
	B-A	0.57	0.55	0.56
Quinidine	A-B	13.56	15.29	14.42
	B-A	52.43	49.69	51.06
RMC-34	A-B	8.75	9.66	9.21
	B-A	66.45	70.26	68.35
RMC-91	A-B	<14.91*	<13.76*	<14.91
	B-A	<4.66*	<3.73*	<4.66
RMC-92	A-B	18.33	17.80	18.07
	B-A	11.10	10.45	10.78
RMC-96	A-B	37.96	41.29	39.62
	B-A	24.74	26.23	25.48
RMC-108	A-B	33.24	<20.13*	<33.24
	B-A	<7.84*	<8.07*	<8.07
RMC-109	A-B	11.84	<8.86*	<11.84
	B-A	<10.83*	<11.40*	<11.40
RMC-113	A-B	1.56	<2.10*	<2.10
	B-A	0.58	0.59	0.58
RMC-145	A-B	32.72	37.16	34.94
	B-A	35.87	35.44	35.65

*: Papp values were expressed as "<" than the values that were calculated using the minimum concentration of the standards for receiver fact that real concentration in the receivers were below quantitation limit (BQL).

N/A: Not Acquired

Table 6. ADME data for optimized GAK inhibitors.

GAK Inhibitor	Structure	GAK Kd (µM)	DENV Activity			ADME Data							
			EC$_{50}$ (µM)	EC$_{90}$ (µM)	CC$_{50}$ (µM)	Mean Aqueous solubility PBS, pH 7.4 (µm)	Mean Aqueous solubility SIF (µm)	Mean Aqueous solubility SGF (µm)	Mean A-B permeability, Caco-2 (10 ^-6 cm/s)	Mean B-A permeability, Caco-2 (10 ^-6 cm/s)	Ratio (B-A / A-B)	Mean Half-Life (minute)	Mean Protein Binding (plasma, human) % protein bound
12r 2787		0.089	0.87	1.92	>25	33.3	10.5	197.8	22.6	7	0.31	> 60	97
12f 2790		0.21	5.3	>10	>10	7.2	193.3	190.4	34.1	22.2	0.65	> 60	77
12i 10736		0.17	7.115	>10	>10	11.3	16.1	196.8	50.6	16.1	0.32	> 60	77
12t RMC16		1.6	6.38	>10	>10	200	193.7	194	8.4	1.8	0.21	> 60	79
12h RMC17		0.052	4.03	>10	>10	33.8	67.7	174.4	36.9	34.6	0.94	> 60	81

B. No resistance (genotypic/phenotypic) detected in DENV-infected cells and mice with select inhibitors

In collaboration with the Andino lab (UCSF) we have conducted both in vitro and in vivo analysis to determine the genetic barrier to resistance of representative AAK1 and GAK inhibitors alone and in combination.

No phenotypic resistance is detected with AAK1 and/or GAK inhibitors in DENV-infected cultured cells.
To select for viral resistant variants in cultured cells, we serially passaged (N=9 passages) DENV in the presence of the sunitinib (AAK1 inhibitor) and/or erlotinib (GAK inhibitor) at concentrations between their EC$_{50}$ and EC$_{90}$. Virus was titered between each passage. No phenotypic resistance was detected (**Figure 2**).
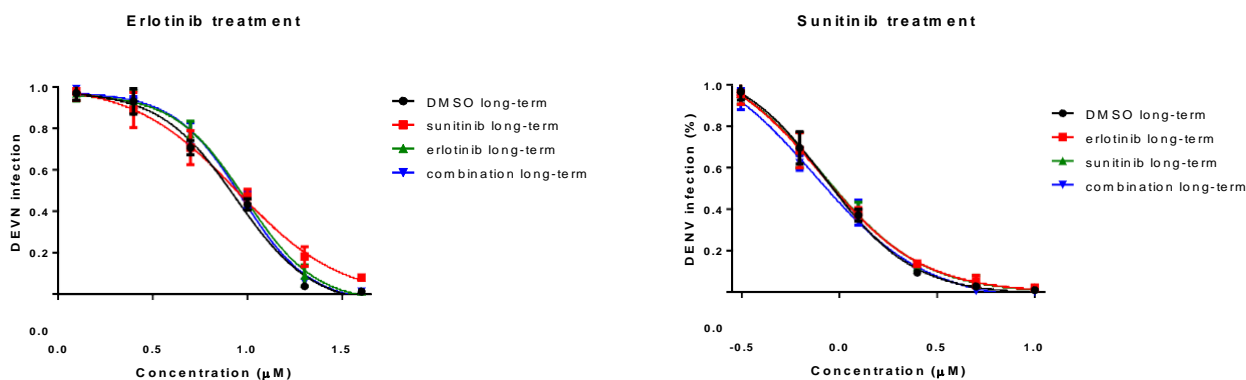
Figure 2. Dose response curves demonstrating the anti-DENV effect of erlotinib (left) and sunitinib (right) in Huh7 cells infected with DENV that was previously passaged for 9 passages in DMSO, sunitinib and/or erlotinib via plaque assays. No shifts in the EC50 or EC90 are shown, indicating absence of phenotypic resistance.

No genotypic resistance is detected with AAK1 and/or GAK inhibitors following serial passaging of DENV in mice.
We analyzed amplicon sequencing data from 12 samples obtained from sunitinib- and erlotinib- or mock-treated mice infected with Dengue 2. Two mutations shown in **Figure 3** are of particular interest in terms of the potential drug resistance effect. Because samples collected here only from the passage 5, we set out to evaluate how frequencies of these two mutations change in previous passages.
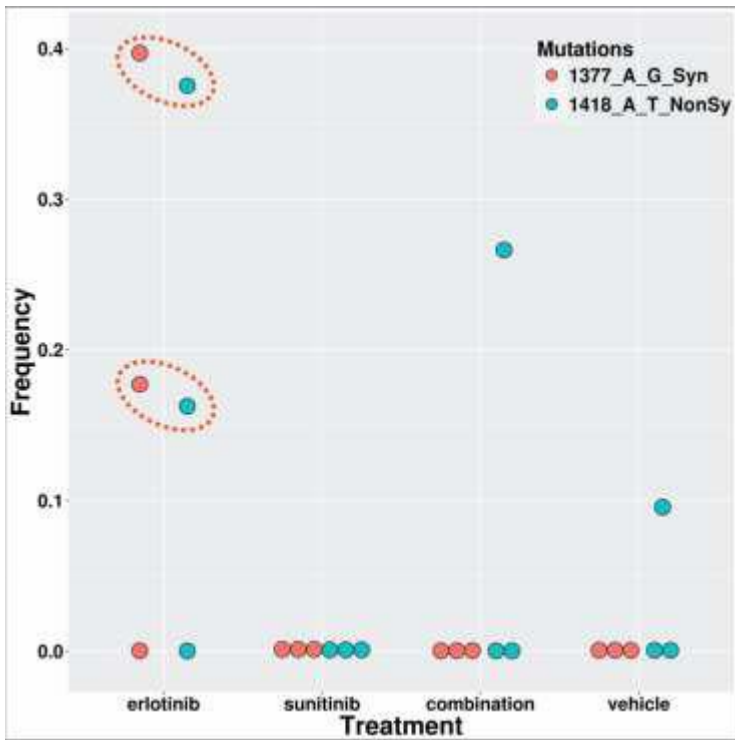
Figure 3. The frequencies of two potential drug resistant mutations. The A-to-G mutation at position 1377 is synonymous. The other A-to-T mutation at 1418 is nonsynonymous. Frequencies were calculated as the number of mutations divided by the coverage at corresponding loci.

In newly generated amplicon sequencing libraries. We focused on erlotinib (2R) treatment and two mice (190 and 191) which carry those two mutations of interest at passage 5. Details on the samples from which amplicon sequencing libraries were made are shown in Table 2.

SampleID	Sample
1	P1-190-2R
2	P1-191-2R
3	P2-190-2R
4	P2-191-2R
5	P3-190-2R
6	P3-191-2R
7	P4-190-2R

Table 7. 6 Samples used to make amplicon sequencing libraries.

Notes: P1-P4 denotes passage 1 to 4; 190, 191 represents each individual mouse; 2R refers to erlotinib treatment.

Data analyses

We firstly mapped reads to DENV2 virus genome (NCBI Accession Number: NC_001474.2) and kept reads that can be uniquely mapped to one locus of the genome. Afterwards, genetic mutations were called and corresponding frequencies were calculated from the sequencing coverage information.

Two goals of analyses are, 1) to evaluate the frequencies of 1377 and 1418 mutations in Passage 1 to 4; 2) to combine data from Passage 1 to 5 and check whether there are novel mutations with potential drug resistance effects.

Results

1) Although we observe relatively high frequencies of 1377 and 1418 mutations at Passage 5, the mutation at locus 1377 is almost not detectable in previous passages while the mutation at locus 1418 can be detected in one mouse sample (Mouse190) (**Figure 4**).
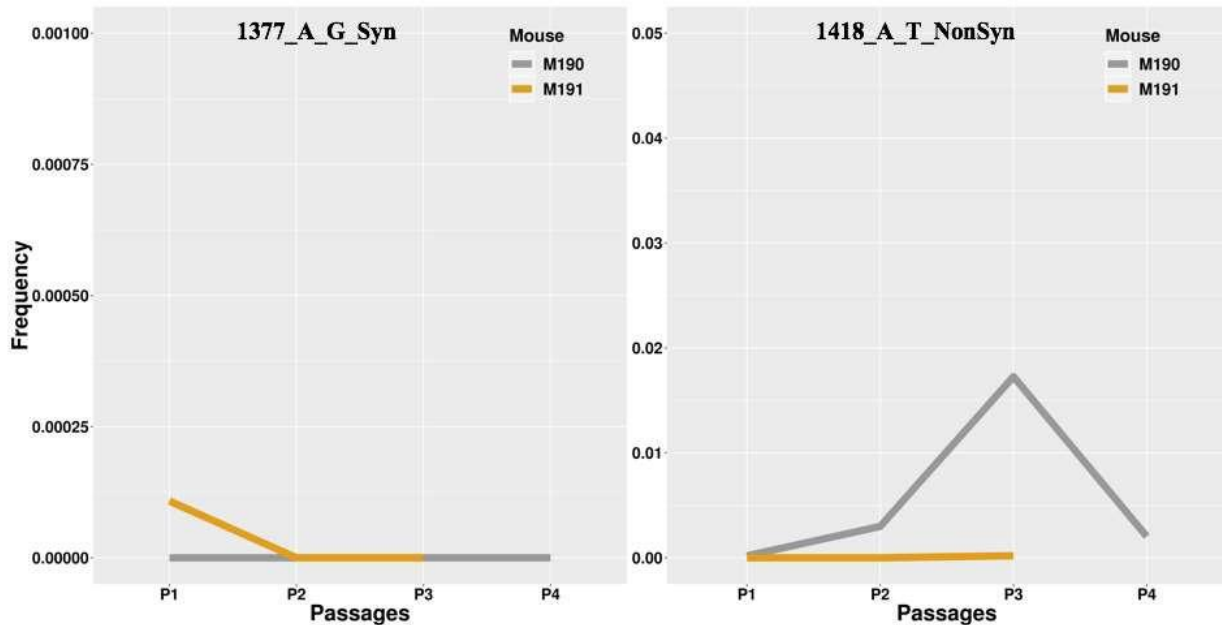
Figure 4. Trajectories of frequencies of 1377 and 1418 mutations in Passage 1 to 4.

2) To exclude false positives from sequencing errors, we set a cutoff of base quality scores at Q20, checked mutations with a frequency higher than 0.01and shared by Mouse190 and Mouse 191 (Table. 2). However, these mutations are not unique and can be detected in other treatments or controls.

Passage	Loci of shared mutations
1	123,248,6513
2	123,124
3	123, 3200

Table 8. Shared mutation at Passage 1 to 3 in erlotinib (2R) treatment groups.

Conclusion: There was no genotypic resistance detected upon passaging DENV2 in mice in the presence of AAK1/GAK inhibitors combination.

C. In vivo PK analysis with representative GAK inhibitors with multiple formulations.
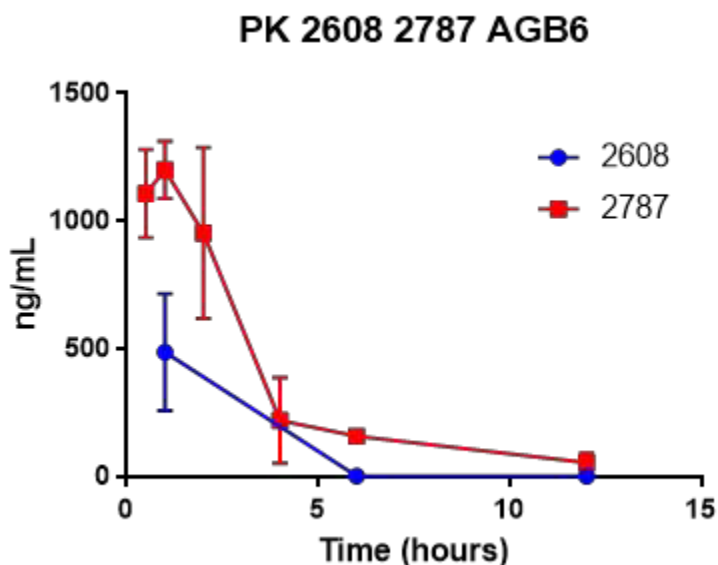
Fig. 5. PK analysis of 2608 and 2787 in AG129 mice.
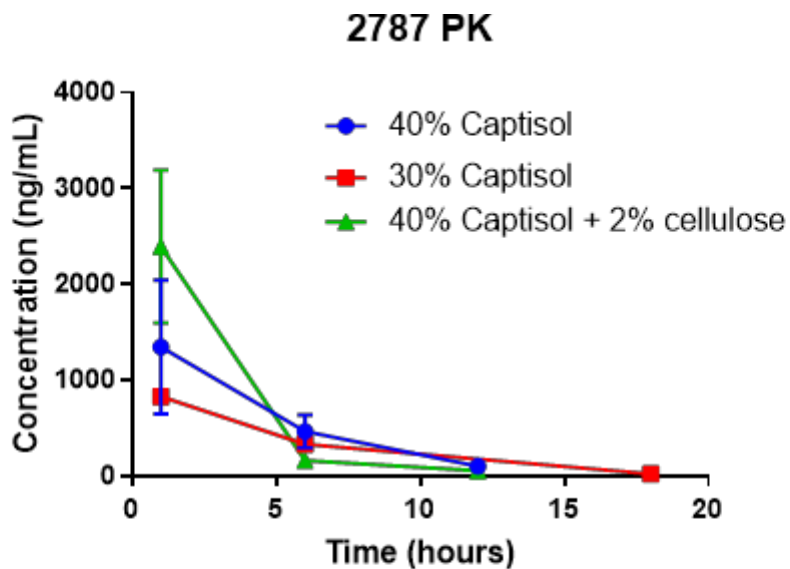
hours	40% Captisol			30% Captisol			40% Captisol + 2% cellulose		
X	Y1	Y2	Y3	Y1	Y2	Y3	Y1	Y2	Y3
1	1090	819	2140	858	805		2050.0	3310.0	1830.0
6	352	668	389	324	349		156.0	158.0	181.0
12	133	143	43				38.6	36.5	98.3
18					25				

Fig. 6. PK analysis of 2787 in the indicated formulations in AG129 mice

Fig. 7. PK analysis of 2787 in the indicated formulations in AG129 mice
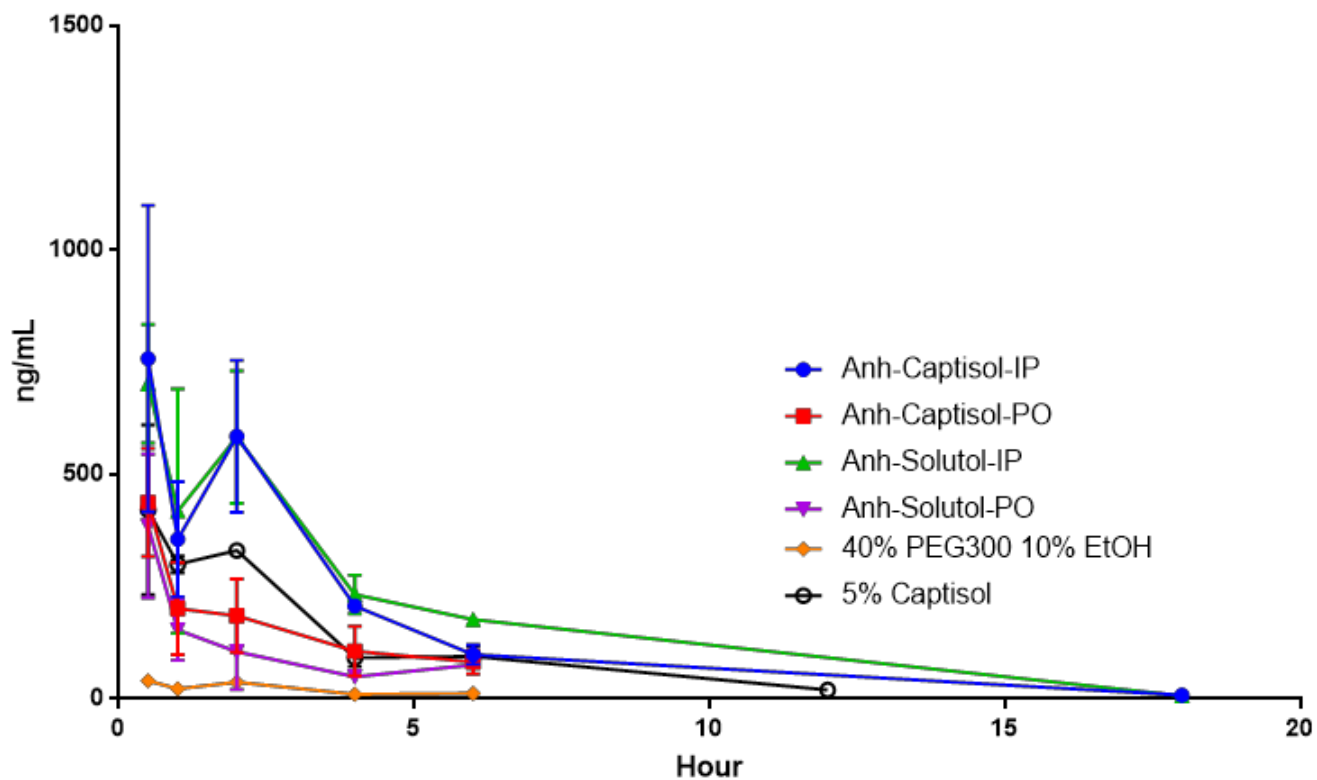
	Anh-Captisol-IP	Anh-Captisol-PO	Anh-Solutol-IP	Anh-Solutol-PO	40% PEG300 10% EtOH	5% Captisol
Baseline	0	0	0	0	0	0
Total Area	2472	828	3096	537.5	109.8	1439
Std. Error	256.9	140	235.3	111.3	9.107	91.09
95% Confidence Interval	1968 to 2975	553.5 to 1102	2634 to 3557	319.4 to 755.6	91.96 to 127.7	1260 to 1617

Fig. 8. The effect of 7 day treatment with 1967 (a GAK inhibitor) on survival (left upper), viral titer in serum (right upper) and weight loss in AG129 mice inoculated with DENV. While a mild reduction in viral titer was measured with 1967 relative to vehicle, the mortality was comparable.
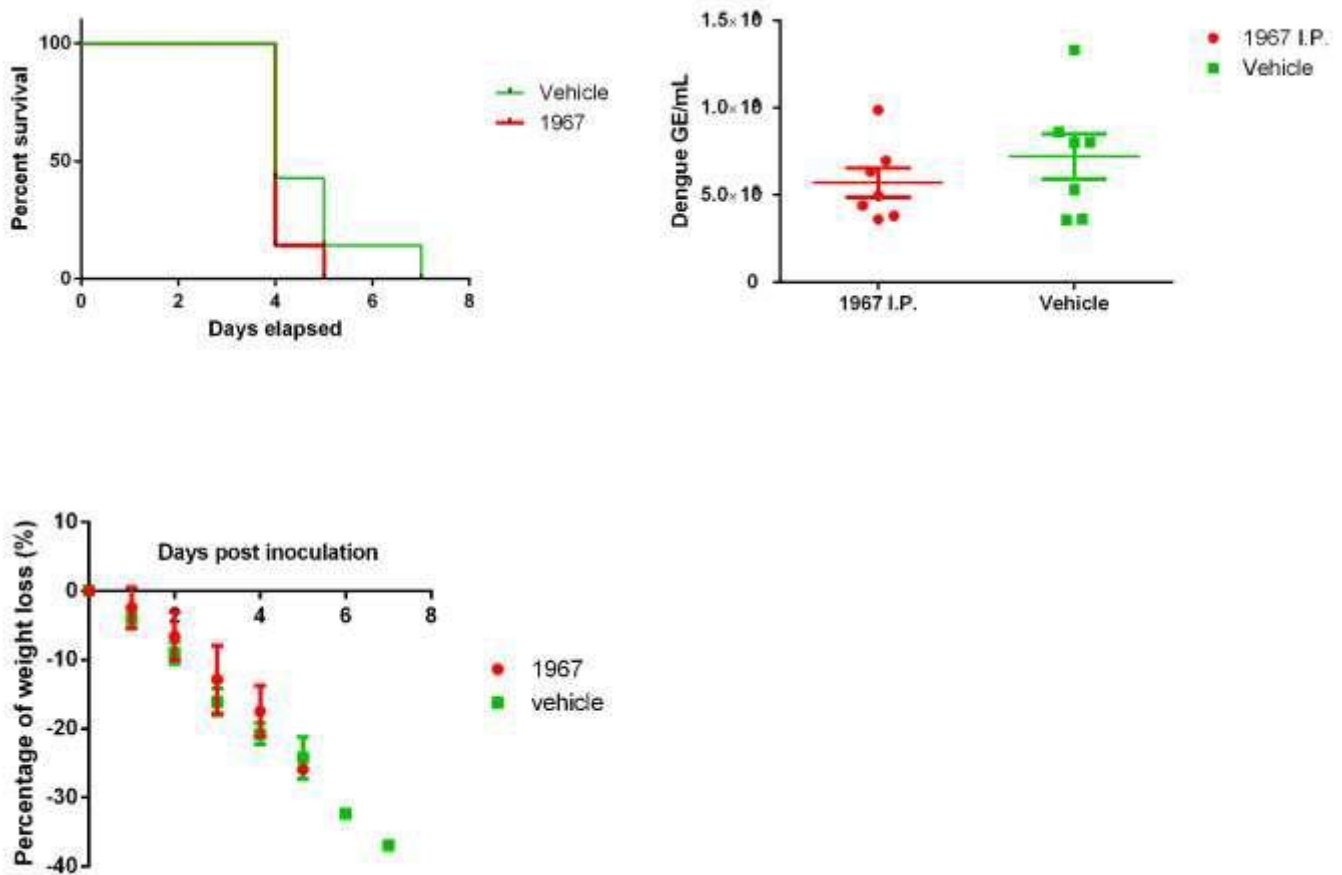
Fig. 9. The effect of 5 day treatment with 2787 (a GAK inhibitor) individually or in combination with sunitinib and sunitinib/erlotinib combinations on survival (left) and weight loss in AGB6 mice inoculated with DENV. 2787 showed some benefit relative to vehicle when used individually at 30 mg/kg or in combination with sunitinib. At 60 mg/kg 2787 increased toxicity suggesting that it is toxic at this dose. Mpk, mg/kg; SM/EL, sunitinib/erlotinib.
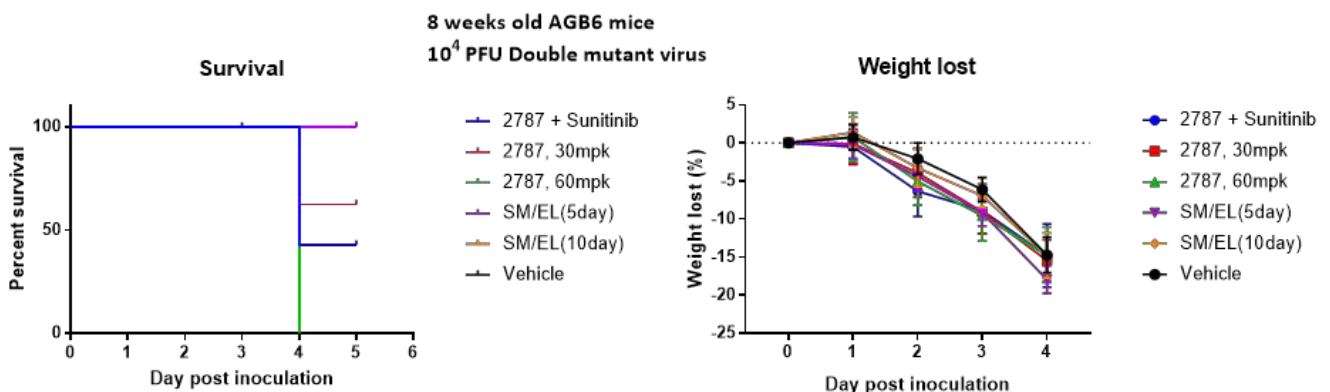
Fig. 10. The effect of 7 day treatment with 2787 (a GAK inhibitor) at the indicated dose three time a day (TID) in combination with sunitinib at 30mg/kg on survival total (left upper), survival by gender (right upper), viral titers in serum (left lower) and weight loss (right lower) are shown. This experiment was limited by the fact that the mice in the vehicle group did not die. TID, three times a day.
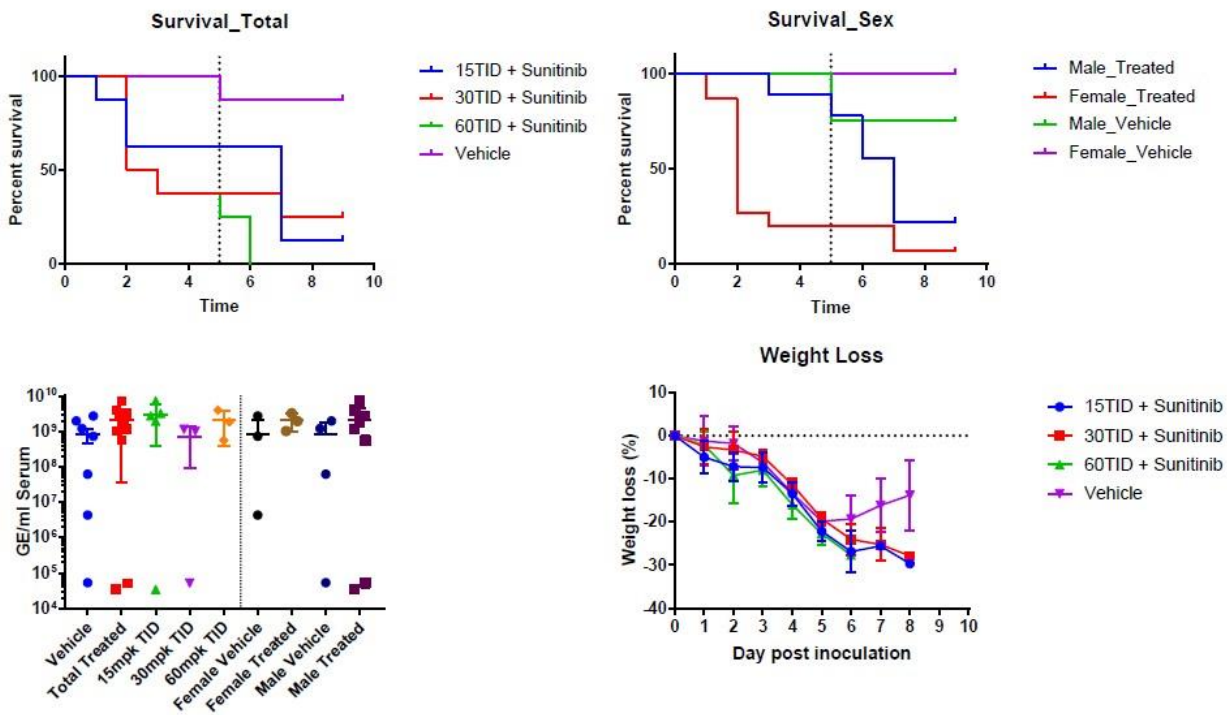
Fig. 11. The effect of 7 day treatment with 2787 (a GAK inhibitor) or sunitinib/erlotinib combination with or without PPI at the indicated dose on weight loss and survival in AGB6 mice infected with DENV2 or uninfected with DENV (2787 only). While sunitinib/erlotinib combination reduced mortality, 2787 was comparable to the vehicle only, yet it did not increase mortality or reduced weight when used by itself in uninfected mice, suggesting it was tolerated well tolerated. MPK, mg/Kg; QD, once daily; S/E, sunitinib/erlotinib; PPI, proton pump inhibitor.
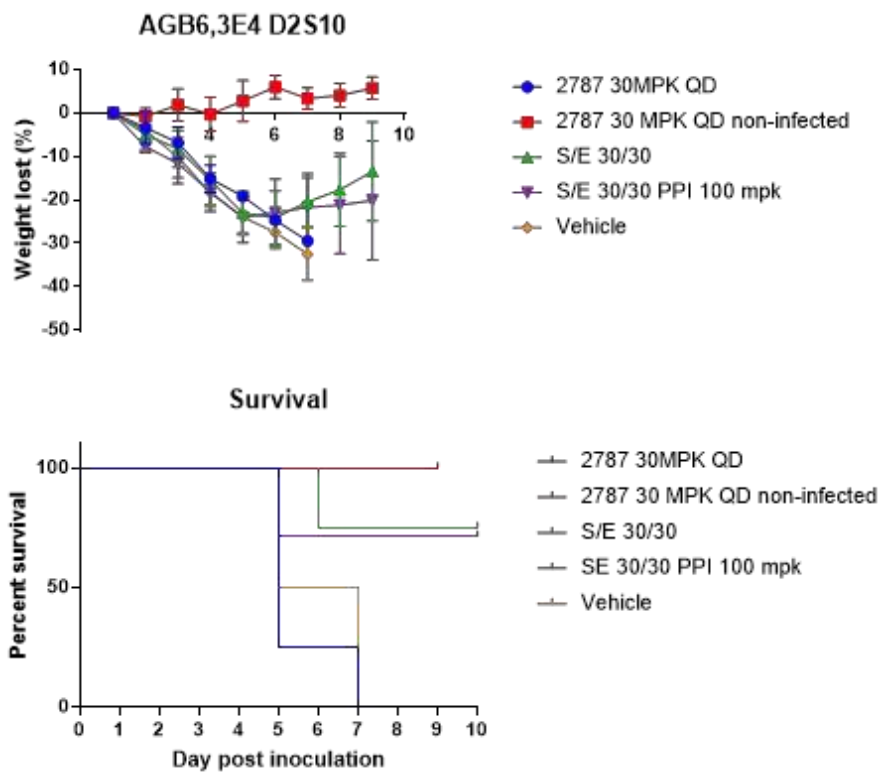
E. **Representative NAK inhibitors have potent activity against virulent SARS-CoV-2.**

NAKs are required for SARS-CoV-2 entry. NAK depletion by siRNAs inhibits infection of vesicular stomatitis virus encapsidated RNA (encoding a luciferase reporter gene) pseudotyped with SARS-CoV-2 spike glycoprotein (GP) (rVSV-GP SARS-CoV-2), suggesting a possible role in SARS-CoV-2 entry (**Fig. 12**).

Fig. 12. NAKs are essential for infection of VSVG spiked with SARS-CoV-2 GP via luciferase assay at 24 hrs postinfection of Vero-E6 cells. Shown is data From 2 experiments. ***p<0.001 relative to non-targeting (NT) controls by student T test. No toxicity was measured (not shown).

Selective NAK inhibitors suppress virulent SARS-CoV-2 infection via two different assays with low toxicity. In a standard plaque assay, Vero E6 cells were infected with SARS-CoV-2 (strain: USA-WA1/2020, MOI=0.05) and treated with the compounds for 24 hrs. Culture supernatants were harvested and used to inoculate naïve cells, and virus was tittered. Several NAK inhibitors, such as STL3-T-0008, an *iso*thiazolo[4,3-b]pyridines-based GAK inhibitor, dose-dependently inhibited SARS-CoV-2 infection with an EC_{50} of 0.46 µM, EC_{90} of 1.14 µM, and undetectable virus at $\geq$ 5 µM (of note, the EC_{50} of remdesivir is 0.77 µM in this cell line(7)) (**Fig. 13**).

Fig. 13. Dose response of virulent SARS-CoV-2 infection (black) and cellular viability (blue) to STL3-T-0008 in Vero E6 cells by plaque and TiterGlo assays at 24 hrs postinfection (MOI= 0.05). Titers are plotted relative to DMSO. Note, undetectable virus at ≥5 µM.

In a stringent reporter assay, 5 day treatment of Vero E6 cells stably expressing GFP with STL3-T-0008 rescued these cells from lethality induced by SARS-CoV-2 (Belgium-GHB-03021) (EC_{50}=3 µM) (**Fig. 14**).

Fig. 14. Dose response of Vero-GFP cell rescue from SARS-CoV-2-induced lethality to STL-T-0008 at 5 days post-infection (MOI= 0.01). Note, comparable effect of 10 µM remdesivir.

GAK inhibitors inhibit infection of SARS-CoV-2 pseudovirus.
In vitro anti-SARS-CoV-2 activity was studied first via our established high-throughput pseudovirus infection assay based on VSV encapsidated RNA (encoding a luciferase reporter gene) pseudotyped with SARS-CoV-2 spike GP (rVSV-GP SARS-CoV-2) (**Fig. 15**). Vero E6 cells were pre-treated with the the compound or DMSO control, infected with rVSV-GP SARS-CoV-2, followed by luciferase assays at 24 hrs. Cellular viability was monitored by alamarBlue-based assay.

Fig. 15. STL3-T-0008 inhibits infection of rVSV-GP SARS-CoV-2. Dose response of infection of VSVG spiked with SARS-CoV-2 GP (black) and cell viability (blue) to STL3-T-0008 via luciferase and alamarBlue assays at 24 hrs postinfection of Vero-E6 cells. Data are representative of 2 experiments plotted relative to

F. **A series of GAK inhibitors with a different MOA that does not target GAK, but rather PIKFYVE, and has a broad-spectrum antiviral activity**

While optimizing more selective inhibitors of GAK, we discovered an unexpected isothiazolo[4,3-b]pyridine compound, RMC-113 (**Fig. 16**), that does NOT inhibit AAK1 or GAK, but rather PIKFYVE, a lipid kinase that regulates endosomal traffic (IC_{50}=8nM), and shows broad-spectrum antiviral activity without toxicity.

Fig. 16. RMC-113 is a novel broad-spectrum inhibitor emerging from our GAK inhibitors that does not bind GAK.
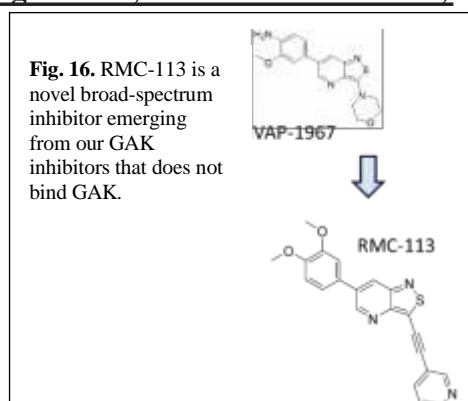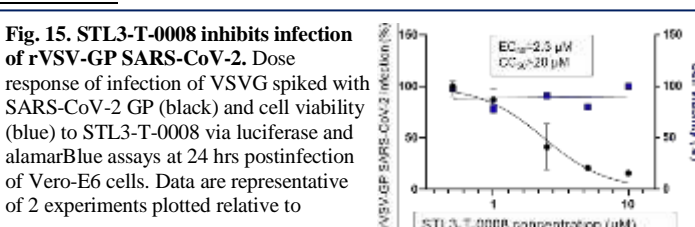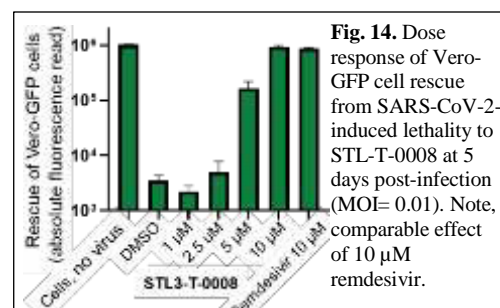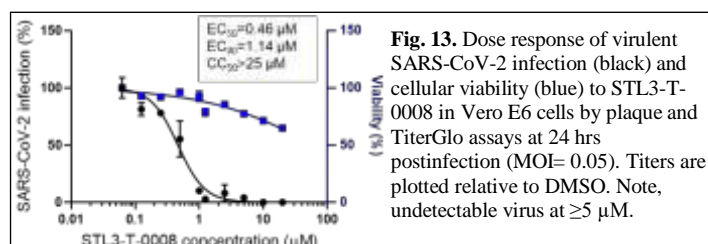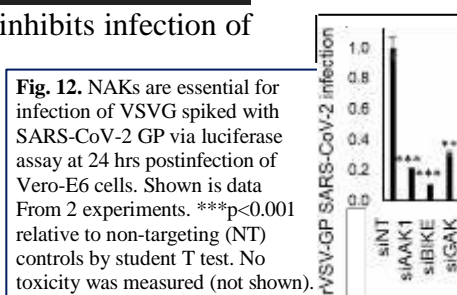
RMC-113 has potent broad-spectrum antiviral activity. It inhibits replication of alphaviruses (VEEV and EEEV) in primary human astrocytes and endothelial cells (EC$_{50}$=0.2-0.5µM) (**Fig. 17**) and of the unrelated flavivirus, dengue (DENV) (EC$_{50}$=1.4 µM) (**Fig. 18**), with CC$_{50}$>30 µM. In a plaque assay, RMC-113 inhibited SARS-CoV-2 infection in Vero E6 at 24 hrs postinfection (US strain) with an EC$_{50}$ of 0.3 µM (remdesivir's EC$_{50}$ is 0.77 µM in this cell line) (**Fig. 19**). In a stringent reporter assay, 5 day treatment with RMC-113 rescued Vero E6 cells stably expressing GFP from SARS-CoV-2's (Belgium strain) lethality (EC$_{50}$=2 µM, CC$_{50}$>30 µM) (**Fig. 20**).
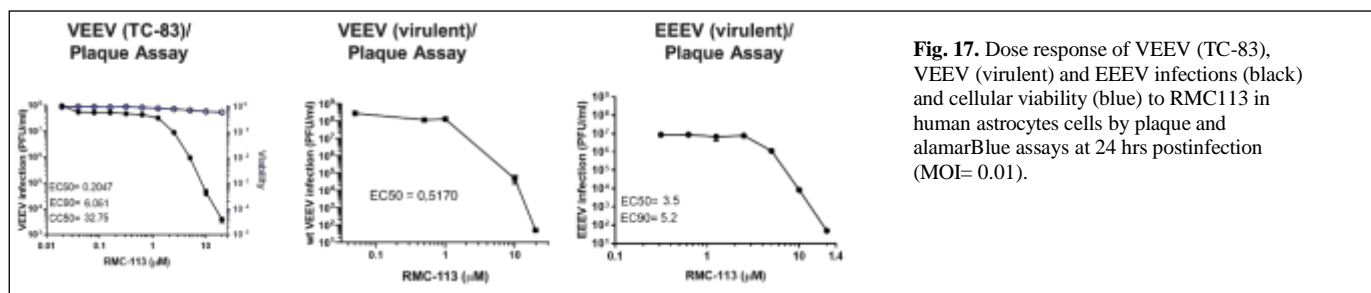
Fig. 17. Dose response of VEEV (TC-83), VEEV (virulent) and EEEV infections (black) and cellular viability (blue) to RMC113 in human astrocytes cells by plaque and alamarBlue assays at 24 hrs postinfection (MOI= 0.01).

Fig. 18. Dose response of DENV infection (black) and cellular viability (blue) to RMC113 in Huh7 cells by plaque and alamarBlue assays at 48 hrs postinfection (MOI= 0.1).

Fig. 19. Dose response of virulent SARS-CoV-2 infection (black) and cellular viability (blue) to STL3-T-0008 in Vero E6 cells by plaque and TiterGlo assays at 24 hrs postinfection (MOI= 0.05). Titers are plotted relative to DMSO. Note, undetectable virus at ≥5 µM.

Fig. 20. Dose response of Vero-GFP cell rescue from SARS-CoV-2-induced lethality to RMC-113 at 5 days postinfection

PIKfyve is the primary target of RMC-113. RMC-113 emerged from our GAK inhibitors, but it does not inhibit GAK (K_D=7.6 µM). Kinome scan (>400 kinases/DiscoverX) revealed that at 10 µM, RMC-113 binds 10 kinases <26% of control, with most potent binding to PIKfyve (0% of control). Among the other 9 targets were 3 additional lipid kinases: PI4KB (16%), PIP4K2C (11%), and PIK3C3 (26%). Enzyme activity assay (335 kinases/ ProQinase) showed an excellent selectivity score (0.003) and no activity against any kinase including 6 of the targets bound by RMC-113 (yet the 4 lipid kinases are absent from this panel). RMC-113 indeed binds and inhibits the kinase activity of PIKfyve (K$_D$=370 nM, IC$_{50}$=8nM) (**Fig. 21**).

Fig. 21. RMC-113 inhibits PIKFYVE *in vitro (Nanosyn)*
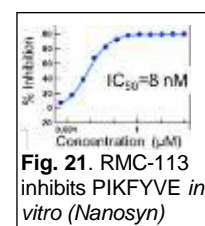
Moreover, preliminary homology modeling supports PIKfyve as a target (**Fig. 22**).

Fig. 22. Interactions of RMC-113 in the ATP-binding site of PIKFYVE by homology model (PDB ID: 60SP).
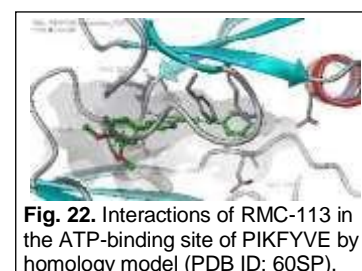
G. References Cited:

1. Asquith CRM, Bennett JM, Su L, Laitinen T, Elkins JM, Pickett JE, Wells CI, Li Z, Willson TM, Zuercher WJ. 2019. Towards the Development of an In vivo Chemical Probe for Cyclin G Associated Kinase (GAK). *Molecules* 24

2. Saul S, Pu S-Y, Zuercher WJ, Einav S, Asquith CRM. 2020. Potent antiviral activity of novel multi-substituted 4-anilinoquin(az)olines. *Bioorganic & Medicinal Chemistry Letters* 30: 127284

3. Verdonck S, Pu SY, Sorrell FJ, Elkins JM, Froeyen M, Gao LJ, Prugar LI, Dorosky DE, Brannan JM, Barouch-Bentov R, Knapp S, Dye JM, Herdewijn P, Einav S, De Jonghe S. 2019. Synthesis and Structure-Activity Relationships of 3,5-Disubstituted-pyrrolo[2,3- b]pyridines as Inhibitors of Adaptor-Associated Kinase 1 with Antiviral Activity. *J Med Chem* 62: 5810-31

4. Wells C, Counago RM, Limas JC, Almeida TL, Cook JG, Drewry DH, Elkins JM, Gileadi O, Kapadia NR, Lorente-Macias A, Pickett JE, Riemen A, Ruela-de-Sousa RR, Willson TM, Zhang C, Zuercher WJ, Zutshi R, Axtman AD. 2020. SGC-AAK1-1: A Chemical Probe Targeting AAK1 and BMP2K. *ACS Med Chem Lett* 11: 340-5

5. Agajanian MJ, Walker MP, Axtman AD, Ruela-de-Sousa RR, Serafin DS, Rabinowitz AD, Graham DM, Ryan MB, Tamir T, Nakamichi Y, Gammons MV, Bennett JM, Couñago RM, Drewry DH, Elkins JM, Gileadi C, Gileadi O, Godoi PH, Kapadia N, Müller S, Santiago AS, Sorrell FJ, Wells CI, Fedorov O, Willson TM, Zuercher WJ, Major MB. 2019. WNT Activates the AAK1 Kinase to Promote Clathrin-Mediated Endocytosis of LRP6 and Establish a Negative Feedback Loop. *Cell reports* 26: 79-93.e8

6. Pu S SS, Karim M, Saul S, Robinson M, and Einav S. . BIKE regulates dengue virus infection via CLINT1 phosphorylation and is a host target for broad-spectrum antivirals. *Antiviral Research (under revision)*

7. Wang M, Cao R, Zhang L, Yang X, Liu J, Xu M, Shi Z, Hu Z, Zhong W, Xiao G. 2020. Remdesivir and chloroquine effectively inhibit the recently emerged novel coronavirus (2019-nCoV) in vitro. *Cell Research* 30: 269-71

Anticancer kinase inhibitors impair intracellular viral trafficking and exert broad-spectrum antiviral effects

Elena Bekerman,[1] Gregory Neveu,[1] Ana Shulla,[2] Jennifer Brannan,[3] Szu-Yuan Pu,[1] Stanley Wang,[1] Fei Xiao,[1] Rina Barouch-Bentov,[1] Russell R. Bakken,[3] Roberto Mateo,[4] Jennifer Govero,[5] Claude M. Nagamine,[6] Michael S. Diamond,[5] Steven De Jonghe,[7] Piet Herdewijn,[7] John M. Dye,[3] Glenn Randall,[2] and Shirit Einav[1]

[1]Department of Medicine, Division of Infectious Diseases and Geographic Medicine, and Department of Microbiology and Immunology, Stanford University School of Medicine, Stanford, California, USA. [2]Department of Microbiology, University of Chicago, Chicago, Illinois, USA. [3]US Army Medical Research Institute of Infectious Diseases, Viral Immunology Branch, Frederick, Fort Detrick, Maryland, USA. [4]Department of Genetics and Department of Microbiology and Immunology, Stanford University School of Medicine, Stanford, California, USA. [5]Departments of Medicine, Molecular Microbiology, and Pathology and Immunology, Washington University School of Medicine, St. Louis, Missouri, USA. [6]Department of Comparative Medicine, Stanford University School of Medicine, Stanford, California, USA. [7]Laboratory of Medicinal Chemistry, Rega Institute for Medical Research, KU Leuven, Leuven, Belgium.

Global health is threatened by emerging viral infections, which largely lack effective vaccines or therapies. Targeting host pathways that are exploited by multiple viruses could offer broad-spectrum solutions. We previously reported that AAK1 and GAK, kinase regulators of the host adaptor proteins AP1 and AP2, are essential for hepatitis C virus (HCV) infection, but the underlying mechanism and relevance to other viruses or in vivo infections remained unknown. Here, we have discovered that AP1 and AP2 cotraffic with HCV particles in live cells. Moreover, we found that multiple viruses, including dengue and Ebola, exploit AAK1 and GAK during entry and infectious virus production. In cultured cells, treatment with sunitinib and erlotinib, approved anticancer drugs that inhibit AAK1 or GAK activity, or with more selective compounds inhibited intracellular trafficking of HCV and multiple unrelated RNA viruses with a high barrier to resistance. In murine models of dengue and Ebola infection, sunitinib/erlotinib combination protected against morbidity and mortality. We validated sunitinib- and erlotinib-mediated inhibition of AAK1 and GAK activity as an important mechanism of antiviral action. Additionally, we revealed potential roles for additional kinase targets. These findings advance our understanding of virus-host interactions and establish a proof of principle for a repurposed, host-targeted approach to combat emerging viruses.

Introduction

A major threat to human health is posed by emerging viruses, such as dengue (DENV) and Ebola (EBOV). Dengue is estimated to infect 390 million people annually in over 100 countries (1). Dengue fever can progress to a life-threatening disease, known as severe dengue, particularly upon a secondary infection with a heterologous DENV strain. Consequently, development of a dengue vaccine has been hampered by the necessity to generate simultaneous protection against 4 distinct DENV serotypes (2). As a further challenge, recent studies have suggested that preexisting DENV immunity may enhance Zika virus (ZIKV) infection and vice versa, and consequently increase disease severity (3–5). While an Ebola vaccine has shown promise recently (6), it is not yet approved. Moreover, no effective antiviral treatment is available against DENV, EBOV, ZIKV, and most other emerging viral pathogens, leaving the global population at risk for significant morbidity and mortality.

Most antiviral therapies approved to date target viral enzymes (e.g., protease or polymerase) via a "one drug, one bug" approach.

This approach has demonstrated measurable success in treating chronic viral infections, such as hepatitis C virus (HCV). However, such an approach to drug development is inefficient, expensive, and, therefore, not easily scalable to address the large unmet clinical need (7). Moreover, targeting virally encoded factors by monotherapy often is associated with rapid emergence of drug resistance (7). One alternative approach to treating viral infections while increasing the barrier to resistance is to target host functions, which the viruses intimately rely on (7). Moreover, focusing on host factors commonly required by multiple viral pathogens could provide broad-spectrum coverage. The host-targeted approach is attractive, particularly for the treatment of emerging viral infections lacking any treatment, given the opportunities to repurpose already existing drugs that are known to modulate specific host functions with tolerable side effect and toxicity profiles.

Intracellular membrane traffic is one of many cellular processes hijacked by viruses. Membrane traffic relies, in part, on the interactions between adaptor protein complexes (AP1 through AP5) and the transmembrane cargo. The well-characterized clathrin-associated APs, AP1 and AP2, are heterotetrameric complexes, which orchestrate the formation of vesicles destined for bidirectional transport in the secretory pathway and for endocytosis from the plasma membrane, respectively (8). The 2 host cell kinases AP2-associated protein kinase 1 (AAK1) and cyclin G–associated kinase (GAK) regulate
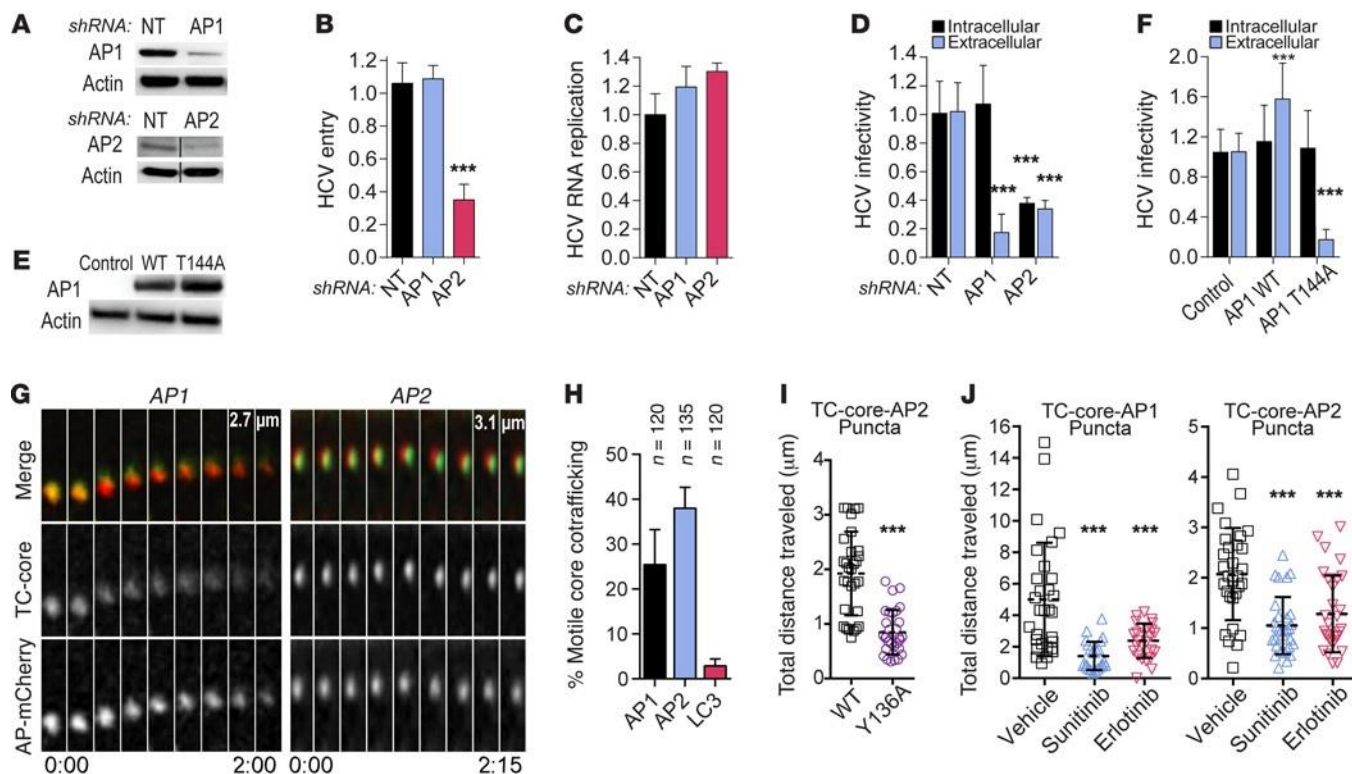
Figure 1. AP1 and AP2 cotraffic with HCV and orchestrate infection. (**A**) Confirmation of gene expression knockdown by Western blot in Huh7.5 cells stably expressing AP shRNA or nontargeting control (NT). (**B**) Entry of HCV pseudoparticles (HCVpp) was measured by luciferase assays at 48 hours after infection. (**C**) HCV RNA replication measured via luciferase assays 72 hours after HCV RNA electroporation. (**D**) HCV infectivity measured via luciferase assays by inoculation of naive cells with lysates (intracellular) and supernatants (extracellular) from electroporated cells. (**E**) AP1 ectopic expression following transfection of Huh7.5 cells with GLuc-tagged WT, T144A AP1, or an empty control; blotted with anti-GLuc antibody. (**F**) HCV intra- and extracellular infectivity in AP1-overexpressing cells versus control. Shown are means ± SD ($n = 3–10$). (**G**) Representative live cell fluorescence microscopy montages of TC-core HCV (green) cotrafficking with AP1- and AP2-mCherry (red). Distance traveled (μm) and time elapsed (min:s) during video acquisition are indicated. (**H**) Quantification of motile TC-core puncta cotrafficking with AP1, AP2, and LC3. (**I**) Quantification of distance traveled per acquisition of WT or Y136A mutant TC-core HCV associated with AP2. (**J**) Quantification of distance traveled per acquisition of TC-core HCV associated with AP1 or AP2 upon treatment with sunitinib (4 μM) and erlotinib (10 μM). Results in **B**–**D** and **F** represent data pooled from at least 2 independent experiments each with 6–10 biological replicates. **H**–**J** are representative experiments out of at least 3 conducted. Shown are means ± SD; ***$P < 0.001$ relative to corresponding NT (**B**–**D**), empty vector control (**F**), WT TC-core (**I**), or vehicle control (**J**) by 1-way ANOVA, followed by Dunnett's (**B**, **D**, and **J**) or Tukey's (**F**) multiple comparisons test or 2-tailed unpaired t test (**I**).

receptor-mediated endocytosis and *trans*-Golgi network (TGN) transport (9–12). Specifically, AAK1 and GAK phosphorylate the μ subunits of AP1 and AP2, thereby enhancing their binding affinity for sorting motifs within the cargo (9, 10, 13–15). Moreover, GAK recruits clathrin-associated APs to the plasma membrane and TGN (16).

Other groups have implicated APs in the life cycle of multiple unrelated viruses (17–26), and we reported roles for AP2 in HCV entry and assembly (22, 23). Our work demonstrated that through AP2 phosphorylation, AAK1 and GAK regulate these temporally distinct steps of the HCV life cycle, thereby, for the first time, uncovering their role as "master regulators" of a viral infection (22, 23). Moreover, we reported that sunitinib and erlotinib, approved anticancer drugs with potent binding to AAK1 and GAK (dissociation constant [K_D] of 11 and 3.1 nM, respectively; ref. 27), or selective, chemically distinct GAK inhibitors, block HCV entry and assembly in tissue culture (22, 23, 28). Although clathrin APs are presumed to mediate intracellular viral trafficking, this hypothesis has not been addressed in live cells. Moreover, the roles of AAK1 and GAK in viral infections beyond HCV and their in

vivo functional relevance remain unknown. In the present study, we demonstrate a role for AAK1- and GAK-regulated AP1 activity in HCV release and document that HCV particles specifically cotraffic with AP1 and AP2 in live cells. We also show a requirement for AAK1 and GAK in the life cycles of DENV and EBOV. Furthermore, we provide support for the feasibility of repurposing sunitinib/erlotinib combination as a broad-spectrum antiviral approach using in vitro models of multiple viral infections and murine models of DENV and EBOV. Lastly, we characterize the mechanism of action of sunitinib and erlotinib by validating AAK1 and GAK as critical mediators of the antiviral effect and revealing additional potential antiviral host targets, which include AXL receptor tyrosine kinase (AXL), KIT proto-oncogene receptor tyrosine kinase (KIT), and the proto-oncogene RET.

Results

APs cotraffic with HCV and orchestrate infection. To determine the differential roles of AP1 and AP2 in HCV infection, we examined the effect of depleting their μ subunits in Huh7.5 human hepatoma
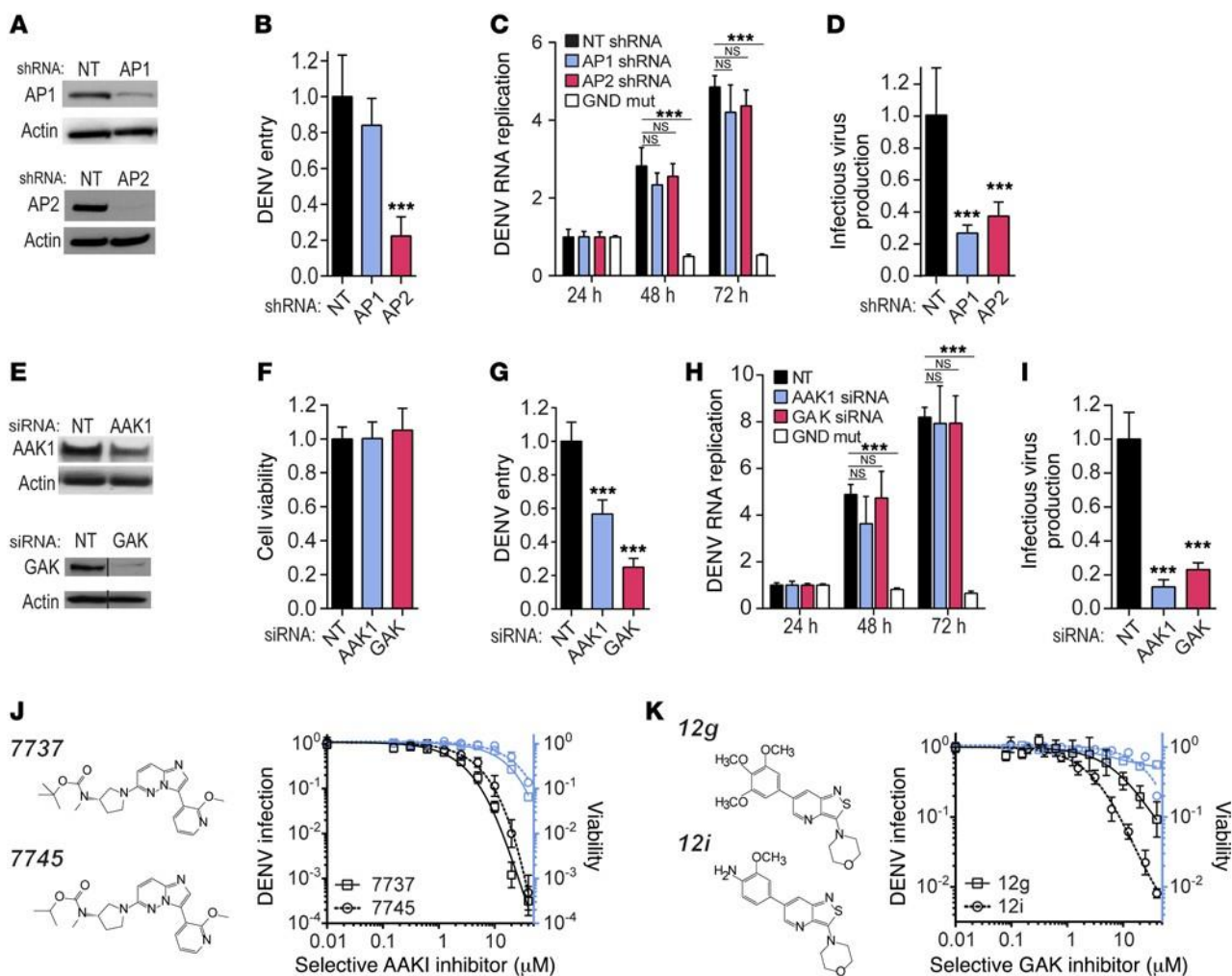
Figure 2. AP1, AP2, and their regulatory kinases, AAK1 and GAK, are essential for DENV infection in vitro. (**A** and **E**) Confirmation of stable shRNA-mediated (**A**) or transient siRNA-mediated (**E**) gene expression silencing by Western blot in Huh7 cells. (**B** and **G**) DENV entry measured via luciferase assay 6 hours after infection. (**C** and **H**) DENV RNA replication monitored by luciferase activity every 24 hours following transfection of Huh7 cells with a Tet-inducible DNA-launched DENV replicon and induction by doxycycline for 6 hours (GND is a replication-incompetent DENV). Data are normalized to signal at 24 hours. (**D** and **I**) Infectious DENV production measured via luciferase assays by inoculation of naive cells with supernatants from stable or siRNA-transfected cells 48 hours after electroporation with DENV RNA. (**F**) Relative cell viability following gene expression knockdown measured by alamarBlue assays. (**J** and **K**) Cell viability (blue) and dose response of DENV infection (black) to more selective AAK1 (**J**) and GAK (**K**) inhibitors (structures shown) measured by luciferase assays 48 hours after infection. Data are plotted relative to vehicle control. Shown are representative experiments from at least 2 conducted. Individual experiments in **B–D** and **F–K** had 8–10 biological replicates; shown are means ± SD; ***$P < 0.001$ relative to corresponding NT control by 1-way ANOVA (**B**, **D**, **F**, **G**, and **I**) or 2-way ANOVA (**C** and **H**), followed by Dunnett's multiple comparisons test.

cells on distinct steps of the viral life cycle. Successful depletion of each targeted AP was confirmed (Figure 1A), with no alteration in the expression of the nontargeted AP (data not shown). AP2 depletion reduced HCV entry, had no effect on HCV RNA replication, and reduced HCV assembly (i.e., reduced intra- and extracellular infectivity in lysates and culture supernatants derived from HCV-transfected cells, respectively), as we previously reported (Figure 1, B–D, and refs. 22, 23). In contrast, AP1 depletion reduced extracellular infectivity only (Figure 1, B–D), consistent with a defect in viral release, in agreement with prior reports (29, 30). To test whether, in addition to AP2 (22), phosphorylation of AP1 by AAK1 and GAK is important for infectious HCV production, we studied the effect of overexpressing phosphorylation site mutant AP1 (T144A) on HCV infectivity (Figure 1E and ref. 31). Intracel-

lular infectivity was not affected by overexpression of either WT or T144A AP1 (Figure 1F). In contrast, extracellular infectivity increased upon ectopic expression of WT AP1 and decreased with ectopic expression of T144A AP1 (Figure 1F). Thus, viral release emerges as yet another step of the HCV life cycle, beyond entry and assembly, which is regulated by AAK1 and GAK.

While APs were postulated to directly mediate intracellular viral trafficking, this has never been addressed experimentally in live cells with any virus. To test the hypothesis that HCV particles shuttle with clathrin APs intracellularly, we used live cell imaging. The cotrafficking of individual, infectious HCV particles harboring a tetracysteine (TC) tag within the core protein (TC-core) with AP1- or AP2-mCherry was monitored (32). We previously have shown that TC-core motility requires HCV virion assembly (32).
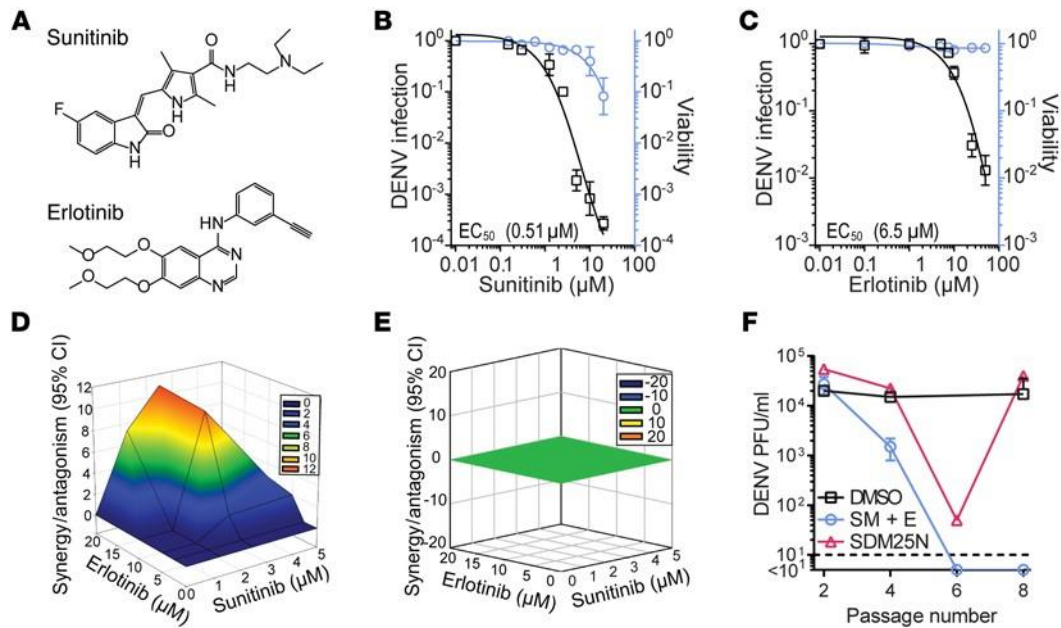
Figure 3. Sunitinib and erlotinib have a synergistic anti-DENV effect and a high genetic barrier to resistance in vitro. (**A**) Chemical structures of the indicated drugs. (**B** and **C**) Cellular viability (blue) and dose response of overall DENV infection (black) to sunitinib and erlotinib measured by luciferase assays at 48 hours after infection. Data are plotted relative to vehicle control. (**D** and **E**) Synergy/antagonism at the 95% CI of sunitinib/erlotinib combination treatment on antiviral effect (**D**) and cellular viability (**E**) computed by MacSynergy II. (**F**) DENV4 was used to infect Huh7 cells and passaged every 72 hours by inoculation of naive cells with equal volumes of viral supernatants under DMSO treatment or selection with sunitinib and erlotinib (SM + E) or SDM25N (DENV NS4B inhibitor) increasing from 0.5 to 2.5 μM over 8 passages. Viral titers were measured by plaque assays at every other passage. Dashed line represents assay detection limit. Results in **B** and **C** represent data pooled from at least 2 independent experiments. Data in **D**–**F** are representative of at least 2 experiments. Shown in **B**, **C**, and **F** are means ± SD. Individual experiments in **B**–**E** and **F** had 5–10 and 2 biological replicates, respectively.

Analysis of TC-core puncta stained with the biarsenical dye FlAsH revealed that a large fraction of motile TC-core cotrafficked with either AP1 (25%) or AP2 (38%), whereas only 3% cotrafficked with the autophagosomal marker LC3 (Figure 1, G and H, Supplemental Figure 1A, and Supplemental Videos 1–3; supplemental material available online with this article; https://doi.org/10.1172/JCI89857DS1). The velocities of the cotrafficking particles were consistent with previous reports on secretory vesicle trafficking as well as TC-core puncta cotrafficking with vesicle-associated membrane protein (VAMP) (refs. 32, 33, and Supplemental Figure 1B). AP2-associated TC-core puncta motility was reduced significantly upon mutation (Y136A) of a YxxΦ motif within core, a motif critical for AP2 binding and HCV assembly (22), as measured by the overall distance traveled (Figure 1I and Supplemental Video 4). These findings provide direct experimental evidence for a role of clathrin-associated APs in mediating intracellular virus trafficking. Specifically, these imaging data combined with our current and previous characterization of the roles of AP1 and AP2 in the life cycle of HCV (22, 23) support the hypothesis that AP1 cotraffics with HCV during viral release, while AP2 cotraffics with HCV during viral entry and subsequently to the sites of assembly.

To understand whether drug modulation of AP phosphorylation by AAK1 and GAK manifests itself in an intracellular trafficking defect, we studied the effect of sunitinib and erlotinib, approved drugs with potent anti-AAK1 and/or anti-GAK activity, on HCV particle trafficking by live cell imaging. Treatment of HCV-infected cells with sunitinib and erlotinib reduced motility of TC-core puncta cotrafficking with AP1 and AP2 (Figure 1J and

Supplemental Videos 5–10). These findings support our hypothesis that the antiviral effect of sunitinib and erlotinib is associated with reduced intracellular viral traffic.

The role of AAK1 and GAK in DENV infection in cells. The requirement for AAK1 and GAK in viral infections beyond HCV is unknown. To investigate whether another, distantly related member of the Flaviviridae family relies on these regulatory kinases and their associated AP targets, we examined the effect of the corresponding gene silencing on DENV infection in human hepatoma (Huh7) cells. We observed a requirement for AP2, but not AP1, in DENV entry using cell lines stably expressing shRNA targeting AP1, AP2, or a nontargeting (NT) sequence (Figure 2, A and B). While depletion of AP1 and AP2 had no effect on DENV RNA replication as measured by subgenomic replicon assays (ref. 34 and Figure 2C), it diminished the production of infectious virus in culture supernatants (Figure 2D). Silencing expression of AAK1 and GAK resulted in no apparent cytotoxic effect (Figure 2, E and F) but, analogously to experiments with HCV, inhibited entry and infectious virus production of DENV, with no effect on RNA replication (Figure 2, G–I). These results implicate AAK1 and GAK in the DENV life cycle via regulation of 2 temporally distinct steps that depend on the clathrin-associated APs: entry and infectious virus production.

To determine whether a comparable effect on DENV infection can be achieved pharmacologically and further validate AAK1 and GAK as antiviral targets, we treated DENV-infected cells with selective AAK1 and GAK inhibitors. The imidazo[1,2-b]pyridazine-based compounds 7737 and 7745 were originally developed

Table 1. Antiviral activity of sunitinib and erlotinib

Family	Virus	Strain	Sunitinib EC$_{50}$/CC$_{50}$ (μM)	Erlotinib EC$_{50}$/CC$_{50}$ (μM)	Cells	Assay
Flaviviridae	HCV	J6/JFH	1.2/>10	0.6/>15	Huh7.5	Luciferase, FFA
	DENV1	276RKI, PRS41393	0.6/>10	1.9/>20	BHK-21	Plaque
	DENV2	TSV01, 429557, New Guinea C	0.51/11.5	2.5/>20–6.5/>50	Huh7, BHK-21	Luciferase, plaque
	DENV3	Philippines/H87/1956	0.3/>10	1.3/>20	BHK-21	Plaque
	DENV4	BC287/97, H241	0.23/>10	3.9/>20	BHK-21	Plaque
	WNV	NY 99 3000.0259	0.55/>20	NE	MEF, Vero	FFA
	ZIKV	MR766	0.51/14.1	6.28/>30	Huh7	Plaque
Filoviridae	EBOV	Zaire	0.47/>10	12.9/>30 2.88/15	Huh7 Vero	Immunostaining
Togaviridae	CHIKV	181/25	4.67/11.9	0.7/>30	Vero	Plaque
Arenaviridae	JUNV	Candid 1	4.8/10.4	1.7/>20	Vero	CPE
Retroviridae	HIV	NL4-3	0.8/>20	2/>20	HeLa/TZM-b1	Luciferase
Paramyxoviridae	RSV	A2	<0.12/12.5	<0.12/>30	Hep2	Immunoplaque

EC$_{50}$, half-maximal effective concentration; CC$_{50}$, half-maximal cellular cytotoxicity; FFA, focus-forming assay; NE, no effect; CPE, cytopathic effect. Virus abbreviations: WNV, West Nile virus; CHIKV, chikungunya virus; JUNV, Junin virus; RSV, respiratory syncytial virus. Each virus was tested as least twice with 3 or more technical replicates.

to modulate AAK1 activity as a potential treatment of neurological disorders (K_D = 1 nM, IC$_{50}$ < 10 nM) (Figure 2J, Supplemental Figure 2, and ref. 35). The isothiazolo[5,4-b]pyridines 12g and 12i (Figure 2K) are potent (K_D = ~8 nM), selective, ATP-competitive GAK inhibitors capable of restricting HCV infection (28). We measured a dose-dependent inhibition of the DENV serotype 2 (DENV2) infection following a 2-day drug treatment with all 4 compounds, with half-maximal effective concentrations (EC$_{50}$s) of 1.5–5.1 μM (Figure 2, J and K). The concentration range yielding at least 1 log reduction in viral infection showed minimal or no toxicity as measured by alamarBlue assays.

Together, these results validate AAK1 and GAK as regulators of DENV infection and point to their pharmacological inhibition as a potential anti-DENV strategy.

Sunitinib and erlotinib have a synergistic anti-DENV effect and a high genetic barrier to resistance in vitro. To determine whether a similar effect on DENV infection can be achieved with approved drugs with potent anti-AAK1 and/or anti-GAK activity, we treated DENV-infected cells with sunitinib and erlotinib (Figure 3A). Consistent with published HCV data (22, 23), we measured a dose-dependent inhibition of DENV2 infection following a 2-day drug treatment with an EC$_{50}$ of 0.51 μM for sunitinib and 6.5 μM for erlotinib by luciferase assays (Figure 3, B and C). The concentration range yielding at least 2 log reduction in viral infection showed minimal or no toxicity as measured by alamarBlue assays with half-maximal cellular

To determine whether DENV can escape treatment with sunitinib and erlotinib, we passaged DENV in the presence of sunitinib/erlotinib combination or the DENV nonstructural (NS) 4B protein inhibitor SDM25N at increasing concentrations (0.5–2.5 μM) corresponding to values between EC$_{50}$ and EC$_{90}$. Infectious virus output was quantified over several passages by plaque assays. By passage 8, DENV4 overcame inhibition by SDM25N with the emergence of a previously characterized resistance mutation in NS4B (P101L, analogous to P104L in DENV2) (36). In contrast, DENV4 was cleared from the culture by passage 6 under the sunitinib/erlotinib treatment without any phenotypic resistance (Figure 3F). These results point to sunitinib/erlotinib combination as a potential anti-DENV strategy with a higher relative barrier to resistance than a direct-acting antiviral.

Broad-spectrum activity of sunitinib and erlotinib. Next, we studied the effect of sunitinib and erlotinib on replication of 2 additional flaviviruses, West Nile virus (WNV) and ZIKV. Sunitinib dose-dependently inhibited both WNV and ZIKV by focus-formation and plaque assays with EC$_{50}$ of 0.51–0.55 μM, whereas erlotinib demonstrated some efficacy only against ZIKV with EC$_{50}$ of 6.28 μM (Supplemental Figure 4, A and B, and Table 1).

We also investigated whether EBOV, a member of an unrelated viral family (Filoviridae), whose entry depends on AP1 and AP2 activity (18, 37–39), may be similarly dependent on AAK1 and GAK. To test this hypothesis, we silenced AAK1 and GAK expression in Vero cells (Figure 4A) and measured infection of vesicular stomati-

cytotoxicities (CC$_{50}$s) of 8.0 μM for sunitinib and >50 μM for erlotinib (Figure 3, B and C, and Table 1). Similar results were demonstrated by standard plaque assays (Supplemental Figure 3A). Notably, treatment with combinations of the 2 drugs revealed synergistic inhibition of DENV2 infection with a synergy volume of 36.7 μM^2% at the 95% CI and no synergistic toxicity (Figure 3, D and E, and Supplemental Figure 3B). Importantly, sunitinib and erlotinib also dose-dependently inhibited infection of DENV1, DENV3, and DENV4 (Table 1).

tis virus encapsidated RNA (encoding a GFP reporter gene) pseudotyped with EBOV glycoproteins (rVSV-GP EBOV). Quantification of GFP-positive cells at the 20-hour time point by flow cytometry revealed that AAK1 and GAK depletion reduced infection relative to NT control (Figure 4C) without impacting cell viability (Figure 4B). A similar level of inhibition was observed upon quantification of viral RNA at 3 hours after infection, highlighting a defect in the entry step (Supplemental Figure 5A). These data further validate AAK1 and GAK as targets for broad-spectrum antiviral therapy. More-

34
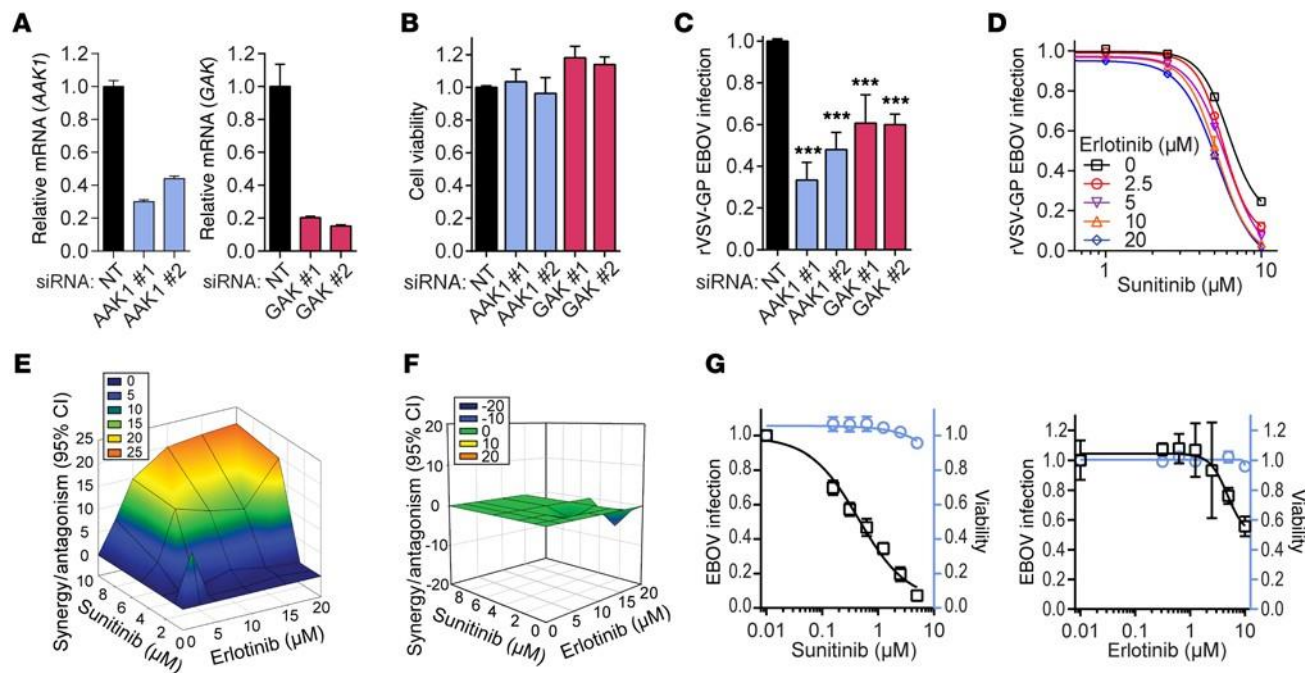
Figure 4. Inhibition of AAK1 and GAK suppresses EBOV infection. (**A**) Confirmation of siRNA-mediated gene expression silencing by quantitative PCR in Vero cells. Shown is normalized gene expression relative to *GAPDH* at 48 hours after transfection. (**B** and **C**) Relative cell viability measured by alamarBlue assays (**B**) and rVSV-GP EBOV infection of Vero cells measured by flow cytometry (**C**) at 20 hours after infection of AAK1- and GAK-depleted cells. ***P < 0.001 relative to NT (1-way ANOVA followed by Dunnett's multiple comparisons test). (**D**) Dose response of rVSV-GP EBOV infection to 4-hour treatment with inhibitors measured by flow cytometry at 20 hours after infection in Vero cells. (**E** and **F**) Synergy/antagonism of sunitinib/erlotinib combination treatment on rVSV-GP EBOV infection (**E**) and cell viability (**F**). (**G**) Dose response to drug treatment in Huh7 cells under biosafety level 4 containment following 48 hours with EBOV infection (black) measured by immunostaining with an anti-GP antibody, and cell viability (blue) measured by Hoechst counterstain and quantified by a high-content imager. Data are plotted relative to vehicle control. All data shown are representative of at least 2 experiments; **B–G** have 3 biological replicates each. Shown in **B–D** and **G** are means ± SD.

over, treatment of Vero cells with sunitinib and erlotinib resulted in a dose-dependent decrease in rVSV-GP EBOV infection measured by flow cytometry 20 hours after infection and entry measured by quantitative reverse transcriptase PCR (qRT-PCR) 3 hours after infection (Figure 4D and Supplemental Figure 5B). Although the effect of erlotinib measured by flow cytometry was modest relative to that of sunitinib, combination treatment displayed measurable synergy in inhibiting entry with a synergy volume of 147.05 μM²% at the 95% CI and zero synergistic toxicity (Figure 4, E and F). Next, we tested the ability of these drugs to inhibit authentic EBOV infection in Huh7 cells. Sunitinib treatment resulted in a dose-dependent

reduction in EBOV infection with EC$_{50}$ value of 0.47 μM and CC$_{50}$ greater than 10 μM, whereas erlotinib showed moderate activity with EC$_{50}$ of 12.9 μM and no appreciable cytotoxicity at the concentrations tested (Figure 4G and Table 1).

To explore more broadly the spectrum of coverage provided by sunitinib and erlotinib, we studied their antiviral effects against additional unrelated viruses. Viral infection was measured in various cell lines following 3-day treatment regimens. We detected antiviral activity of either or both drugs against RNA viruses in 6 families (Table 1), including Togaviridae (e.g., chikungunya virus [CHIKV]), Arenaviridae (e.g., Junin virus [JUNV]), and Paramyxoviridae (e.g., respiratory syncytial virus [RSV]). These data expand the possible indications of sunitinib and/or

Sunitinib/erlotinib combinations are effective in vivo. To address the therapeutic potential of sunitinib and erlotinib as antiviral agents, we tested their application in a murine model of dengue. We measured viral burden and mortality in an IFN- α/β and IFN-γ receptor–deficient murine model of dengue on 129/Sv (AG-129) (40, 41) and C57BL/6 (AG-B6) genetic backgrounds. In a prophylaxis model, we initiated once-daily treatment of AG-B6 mice with 30–60 mg/kg of sunitinib and erlotinib in combination or individually concurrently with DENV inoculation and analyzed viremia at 48 hours. The doses tested for each drug were at or near the equivalent of approved human dose as calculated based on the body surface area per the FDA's guidelines (42). These doses were below the maximum tolerated dose (MTD) in mice and confirmed to be nontoxic in our

erlotinib as antiviral agents beyond Flaviviridae infections, to other established and emerging RNA viruses.

dengue model (42–44). Treatment with erlotinib did not alter viremia, whereas sunitinib alone marginally reduced it (Figure 5A). Consistent with our in vitro synergy results, daily admin- istration of the combination treatment resulted in 11-fold reduction in viral RNA (Figure 5A). In addition, we measured a significant reduction of the infectious virus load by plaque assays in the serum as well as spleen and liver in mice treat- ed with 30 mg/kg doses of sunitinib and erlotinib relative to vehicle controls (Supplemental Figure 6A). Pharmacokinetic analysis revealed that within the first 6 hours of administration each drug concentration in the serum, as measured by liquid chromatography–tandem mass spectrometry, exceeded the
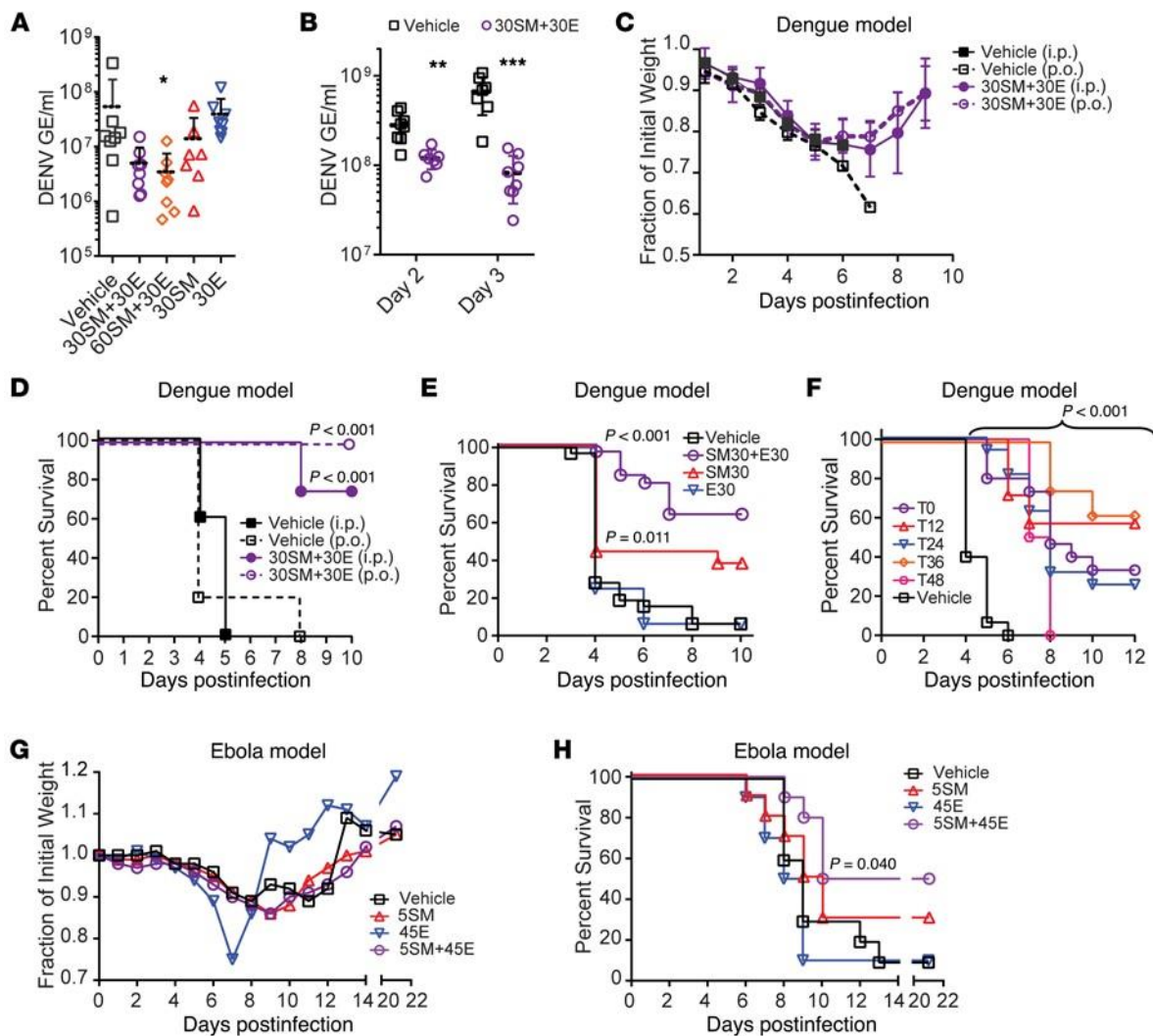
Figure 5. AAK1 and GAK inhibitors are protective in murine models of dengue and Ebola. (**A**) DENV viremia in AG-B6 mice measured by qRT-PCR on day 2 postinfection following once-daily administration of vehicle, sunitinib (SM), and/or erlotinib (E). (**B**) DENV viremia in AG-B6 mice on days 2 and 3 postinfection following twice-daily drug administration. (**C** and **D**) Weight loss (**C**) and mortality (**D**) of DENV-infected AG-B6 mice treated once daily for 5 days with vehicle or sunitinib/erlotinib combination (*n* = 8 per treatment group). (**E**) Mortality of DENV-infected AG-129 mice treated once daily for 5 days with vehicle, sunitinib, and/or erlotinib (data are pooled from 2 independent experiments, *n* = 8–16 per treatment group). (**F**) Mortality of DENV-infected AG-B6 mice treated once daily with vehicle or sunitinib/erlotinib combination beginning at the indicated hour after inoculation, T0–T48 (data are pooled from 2 independent experiments, *n* = 8–16 per treatment group). (**G** and **H**) Weight loss (**G**) and mortality (**H**) of EBOV-infected C57BL/6 mice treated once daily for 10 days with vehicle, sunitinib, and/or erlotinib (*n* = 10 per treatment group). Doses are in mg/kg. Administration was i.p., except when denoted p.o. (**C** and **D**), at inoculation (**A**–**E**, **G**, and **H**) or after inoculation (**F**). **A**–**D**, **G**, and **H** are representative of 2 or more independent experiments. *$P < 0.05$, **$P < 0.01$, ***$P < 0.001$ relative to vehicle control by nonparametric Kruskal-Wallis test with Dunn's multiple comparisons post-test (**A**) or nonparametric Mann-Whitney test (**B**). Survival analysis (**D**–**F** and **H**) was done with log-rank (Mantel-Cox) test; *P* values are relative to vehicle control. GE, genomic equivalents.

corresponding EC_{50} concentration deduced from our in vitro data (Supplemental Figure 6B). Moreover, the synergy between sunitinib and erlotinib predicts even more potency in combination. Although sunitinib and erlotinib were largely cleared from the serum by 18 hours, which is in contrast with the slower clearance rates reported in humans (44, 45), both drugs concentrate severalfold within tissues where DENV replicates, such as liver (46, 47). To maintain higher serum drug concentration, we next administered 30 mg/kg drug combination at 12-hour intervals and measured viremia. The twice-daily drug administration resulted in an even more apparent reduction of viral load rela-

tive to vehicle control (Figure 5B). Notably, drug administration reduced viral load from day 2 to 3 postinfection in contrast to an increase in viral load within the control arm during that time.

To assess whether the reduction in viral load would translate into improved disease outcome, we determined the effect of combination treatment with sunitinib and erlotinib on morbidity and mortality in AG-129 and AG-B6 mice. Following infection with a lethal DENV inoculum, we initiated once-daily drug administration at a dose sufficient to significantly reduce viremia (i.e., 30 mg/kg of each drug). The animals were monitored twice daily and were euthanized when moribund (48). The experiment was
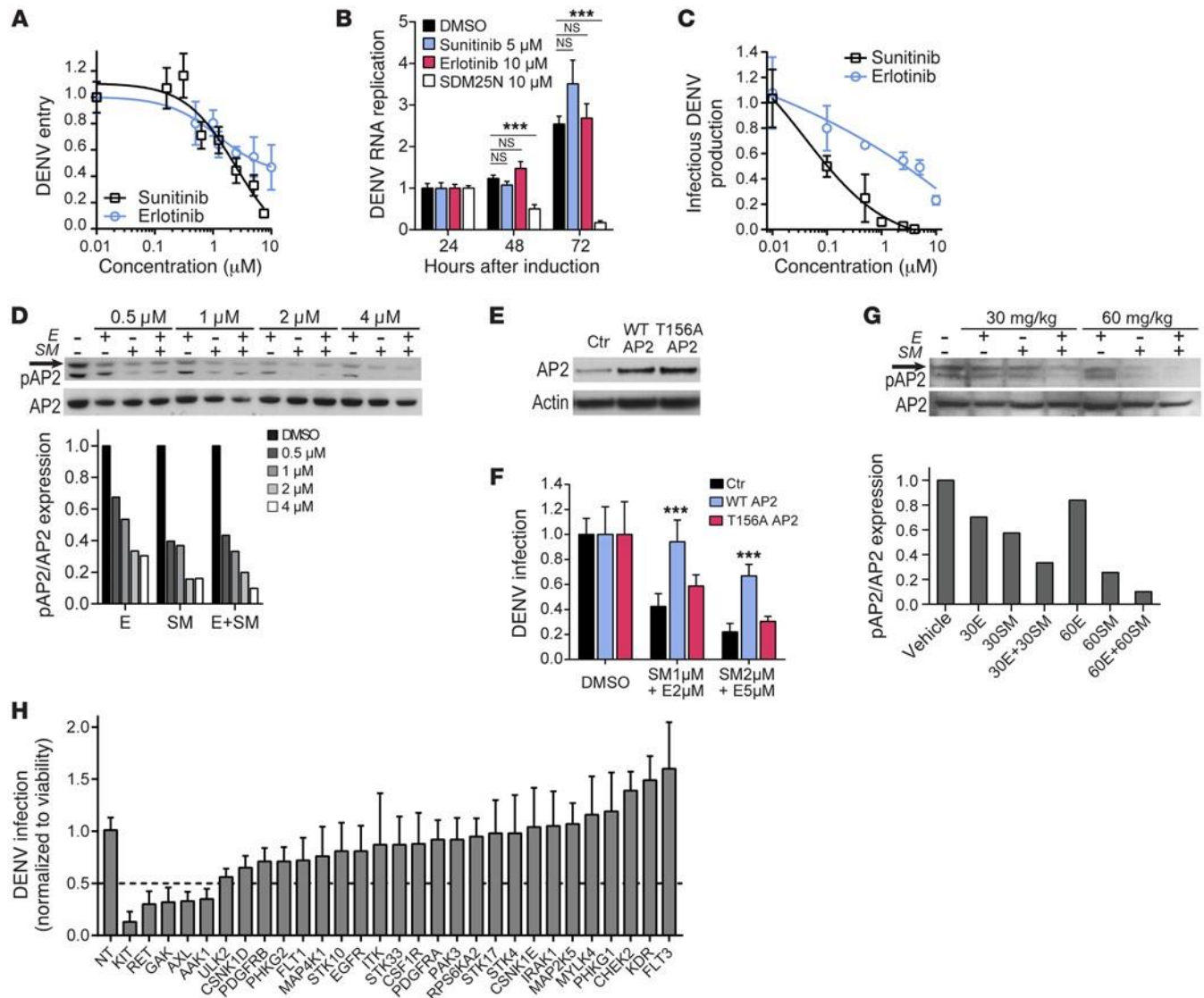
Figure 6. Mechanisms underlying the antiviral effect of sunitinib and erlotinib in vitro and in vivo. (**A**–**C**) Huh7 cells were treated with the inhibitors and monitored for DENV entry (**A**) at 6 hours after infection, DENV RNA replication (**B**) after induction of replication of DNA-launched DENV replicon, and infectious virus production (**C**) at 48 hours after electroporation with DENV RNA. SDM25N is an inhibitor of DENV RNA replication. (**D**) Effect of 1-hour treatment with erlotinib (E) and/or sunitinib (SM) on phosphorylation of AP2 in DENV-infected Huh7 cells measured by Western blotting. Arrow indicates approximately 50 kDa. The ratio of phospho-AP2 (pAP2) to total AP2 was quantified. (**E**) Level of AP2 and actin expression measured by Western blot following lentiviral transduction with control or AP2-expressing constructs. (**F**) Rescue of DENV infection in the presence of inhibitors upon overexpression of WT or T156A AP2 versus vector control measured by luciferase assays 48 hours after infection. Micromolar concentration of each inhibitor is noted on the *x* axis. (**G**) Effect of 3-hour i.p. treatment with erlotinib (E) and/or sunitinib (SM) on phosphorylation of AP2 in liver tissue of AG-B6 mice measured by Western blotting and quantified as the ratio of pAP2 to total AP2. (**H**) DENV infection relative to NT control following siRNA-mediated knockdown of kinases targeted by sunitinib and erlotinib measured by luciferase assays at 48 hours and normalized to cell viability. Data in **A**, **C**, and **I** are pooled from 2 independent experiments with 4–8 replicates each. Data in the other panels are representative of 2 or more independent experiments. **B** and **F** have at least 5 replicates each. ***P < 0.001 relative to DMSO by 2-way ANOVA followed by Dunnett's multiple comparisons test (**B**) or relative to vector control by 1-way ANOVA followed by Dunnett's multiple comparisons test (**F**).

concluded when all the remaining animals regained full mobility and displayed weight gain for at least 2 consecutive days. Upon a 5-day drug treatment regimen given either i.p. or orally, we observed a significant reduction in morbidity and mortality of infected animals relative to vehicle controls (Figure 5, C and D). Specifically, 100% of vehicle-treated mice succumbed to infection on day 4–8 postinfection, whereas sunitinib/erlotinib treatment protected 75%–100% of the mice. This combination

treatment proved efficacious with either i.p. or oral administration, the latter of which is approved for use in humans (Figure 5, C and D). We also compared the effect of daily treatment with the individual drugs with that of the combination. In this trial, 94% of vehicle-treated AG-129 mice succumbed to infection; treatment with erlotinib did not alter survival, whereas sunitinib alone offered partial (37%) protection. Consistent with our in vitro synergy results, we observed the greatest protection (62%) from
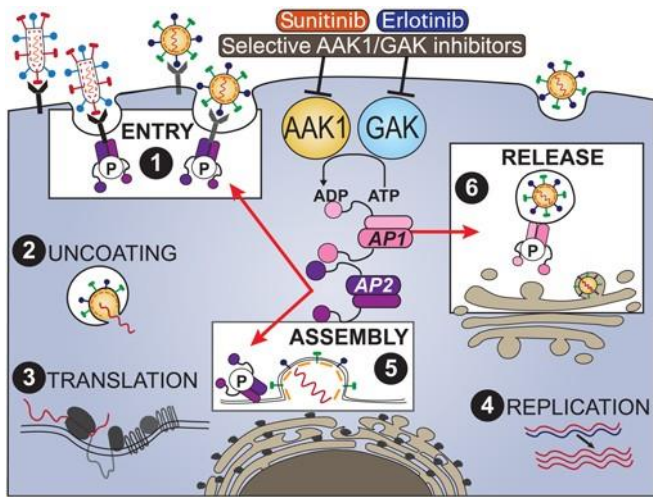
37

Figure 7. Model: AAK1 and GAK in infection and as broad-spectrum antiviral targets. Host kinases AAK1 and GAK regulate entry, assembly, and/or release of multiple RNA viruses through phosphorylation of the membrane trafficking adaptors AP1 (pink) and AP2 (purple). Sunitinib, erlotinib, and selective inhibitors of AAK1 and GAK disrupt these temporally distinct steps of the viral life cycle and act as broad-spectrum antivirals.

mortality with combination drug treatment (Figure 5E). Furthermore, even when the combination drug treatment was initiated at various time points after infection, the mice remained protected relative to vehicle control, albeit mice treated at 48 hours after inoculation eventually succumbed to infection (Figure 5F).

Given the observed potency of sunitinib and sunitinib/erlotinib combination against EBOV infection in vitro, we assessed in vivo efficacy of these drugs in a murine model of Ebola. Drugs were

administered daily i.p. for 10 days beginning at 6 hours before infec-

tion. As with the dengue model, the chosen doses were at or near the equivalent of approved human dose, below the MTD in mice, and confirmed to be nontoxic in our Ebola model. All mice demonstrated signs of morbidity as evident by weight loss during the first 7–10 days after infection (Figure 5G). Ninety percent of vehicle-treated mice succumbed to infection on days 6–13 postinfection; treatment with erlotinib at 45 mg/kg did not alter animal survival, whereas 5 mg/kg sunitinib alone increased survival to 30% (Figure 5H). Consistent with our in vitro synergy results, we observed the greatest weight gain and survival (50%) with a combination drug treatment.

Together, these results demonstrate therapeutic potential of sunitinib/erlotinib combinations against infections with 2 unrelated emerging RNA viruses.

Mechanisms underlying the antiviral effects of sunitinib and erlotinib in vitro and in vivo. To better understand the target(s) and mechanism of action underlying the anti-DENV activity of sunitinib and erlotinib, we first probed the steps of the viral life cycle affected by these compounds. We detected interference precisely with the steps inhibited via siRNAs against AAK1 and GAK (Figure 2, G and I), namely entry and infectious DENV production (Figure 6, A–C). Notably, DENV RNA replication, a step commonly inhibited by direct-acting antivirals (7), was not affected by these drugs. This phenotype supports a hypothesis that inhibition of AAK1 and GAK likely contributes to the anti-DENV effect of these drugs.

To confirm that the antiviral activity is correlated with functional inhibition of AAK1 and GAK activity, we measured levels of phospho-AP2 upon drug treatment. Dose-dependent reduction in the phospho-AP2 to total AP2 ratio was demonstrated in DENV-infected cells (Figure 6D).

Next, we conducted gain-of-function assays to further validate AP2, a substrate for both AAK1 and GAK, as a key mediator of the anti-DENV effect of these drugs. Ectopic expression of WT but not T156A phosphorylation AP2 mutant or vector control either partially or completely rescued the antiviral effect of sunitinib/erlotinib combination (Figure 6, E and F). These results indicate that AAK1- and GAK-mediated phosphorylation of AP2 is a mechanism underlying the antiviral effect of sunitinib and erlotinib against DENV.

Next, we determined whether these drugs exert their antiviral effect in vivo by similarly inhibiting phosphorylation of the AAK1 and GAK ligand AP2. Liver tissue lysates harvested from AG-B6 mice 3 hours after drug administration revealed dose-dependent inhibition of AP2 phosphorylation upon treatment with sunitinib and erlotinib, and most markedly with the combination (Figure 6G). These results provide evidence that drug exposure in animals is associated with modulation of AP2.

These data, combined with the finding that more selective AAK1 and GAK inhibitors lacking affinity to most of sunitinib's and erlotinib's cancer targets (e.g., VEGFR and EGFR) (28, 35) have anti-DENV activity, indicate that AAK1 and GAK are important mediators of the observed antiviral effect. Nevertheless, these data cannot rule out additional potential cellular targets mediating the anti-DENV activity of these compounds. Whereas erlotinib's target selectivity is quite narrowly focused on EGFR and GAK with significantly less affinity for other kinases, sunitinib is a multitarget kinase inhibitor (49, 50). We thus examined the effects of siRNA-mediated depletion of 27 major kinases targeted by these small molecules ($K_D < 20$ nM)

on DENV infection and cellular viability. Using a cutoff of greater than 50% inhibition of viral infection as measured by luciferase assays normalized to cell viability in 2 independent screens, we identified AXL, KIT, and RET as possible antiviral targets of our kinase inhibitors in addition to AAK1 and GAK (Figure 6H). However, silencing of KIT also substantially reduced cellular viability (Supplemental Figure 7).

Taken together, our data indicate that inhibition of AP-mediated intracellular membrane trafficking regulated by AAK1 and GAK represents an important mechanism by which sunitinib and erlotinib inhibit DENV infection in vitro and in vivo and that additional mechanisms, potentially mediated by other kinases, may act in concert.

Discussion

Clathrin-associated AP1 and AP2 complexes have been implicated in orchestrating multiple viral infections; however, their precise mechanistic involvement was not characterized. Moreover, the relevance of AAK1 and GAK, kinase regulators of these APs that we discovered as essential for HCV infection, to other viral infections remained unknown. Here, we addressed this knowledge gap and evaluated the therapeutic potential of inhibiting AAK1 and GAK as a broad-spectrum antiviral strategy. Integrating RNAi, dominant interfering, pharmacological and molecular virology

approaches, we demonstrate roles for AP1 and AP2 complexes as well as AAK1 and GAK in entry and assembly/release of Flaviviridae family members and validate these host factors as attractive targets for broad-spectrum antiviral therapy (Figure 7). We establish that sunitinib and erlotinib inhibit DENV and EBOV infections in vitro and in vivo, and are potent in vitro against WNV, ZIKV, and RNA viruses from 4 additional families: Togaviridae, Arenaviridae, Paramyxoviridae, and Retroviridae. Together, our data illustrate the utility of these 2 clinically approved compounds both as tools to identify host factors important in viral infection and as potential therapies against emerging viral infections.

Using advanced live cell imaging, we provide the first direct evidence, to our knowledge, that viral particles cotraffic intracellularly with AP complexes. Our imaging findings exclude a theory whereby AP complexes contribute to viral infections solely by recruiting or mediating intracellular traffic of host cargo components essential for the viral life cycle.

We show that sunitinib and erlotinib, potent, albeit nonselective, inhibitors of AAK1 and GAK, respectively, restrict DENV and EBOV infections in vitro and their combination reduces viremia, morbidity, and mortality in the relevant murine models. Replication assays demonstrating efficacy against viral species in 6 unrelated families (Table 1) further support our broad-spectrum hypothesis, though in vivo efficacy beyond dengue and Ebola remains to be tested. AAK1 and GAK have partially overlapping functions (12, 23), which may explain moderate antiviral effect in vitro with either sunitinib or erlotinib, yet synergistic activity upon treatment with both. The synergy also may result from inhibition of additional targets by these compounds. Although the observed reduction in DENV load was relatively modest in mice, it correlated with a significant survival benefit, comparable to the report on host α-glucosidase inhibitor celgosivir (51), which yielded 100% protection from mortality with less than 10-fold reduction in viremia. Importantly, the sunitinib/erlotinib combination remained protective in the mouse model of dengue even when administered after established infection, thereby supporting its promise as both prophylaxis and therapy.

We provide multiple lines of evidence to support modulation of AAK1 and GAK activity as an important mode of antiviral action of sunitinib and erlotinib in the dengue model. We demonstrate that these drugs inhibit both DENV entry and infectious virus production, analogous to the phenotype seen with RNAi-mediated suppression of clathrin-associated APs and AAK1 and GAK. Additionally, we demonstrate antiviral effects of more selective AAK1 and GAK inhibitors. Due to lack of affinity to most of sunitinib's and erlotinib's cancer targets (e.g., VEGFR and EGFR) (28, 35), the activity of the selective compounds further confirms that AAK1 and GAK are relevant antiviral targets. While the more selective GAK inhibitors also bind KIT, more work is required to validate whether KIT is an anti-DENV target. Furthermore, we characterized the mechanism by which the pharmacological inhibition of AAK1 and GAK mediates the anti-dengue effect. We establish that antiviral activity of sunitinib and erlotinib correlates with reduced phospho-AP2 levels in vitro. In accordance with this observation, we show that WT but not a phosphorylation AP2 mutant can rescue the anti-dengue effect of these drugs. We provide evidence that this mechanism also plays a role in vivo by demonstrating that

antiviral activity correlates with reduced AP2 phosphorylation in tissues upon drug treatment. These findings reveal that a block in AP2 phosphorylation mechanistically explains at least in part the antiviral effect of AAK1 and GAK inhibitors. These findings also present AP2 phosphorylation as a useful pharmacodynamic biomarker in potential future clinical studies. We further demonstrate that sunitinib and erlotinib reduce HCV-AP1 and -AP2 cotrafficking by live cell imaging, thereby validating this mode of action at the molecular level. While AP-mediated intracellular membrane trafficking likely represents a primary mechanism by which AAK1 and GAK regulate viral infection, additional substrates of these kinases, such as NUMB, also may contribute to this function (23).

We explore the possible involvement of additional targets with K_D's of 20 nM or less reported for sunitinib and erlotinib using a siRNA library against 27 kinases. Our siRNA screen reveals that none of the other major targets of erlotinib beyond GAK, namely EGFR and STK10, affect DENV infection. In contrast, at least 3 additional targets of sunitinib beyond AAK1, namely AXL, KIT, and RET, may facilitate DENV infection and thus potentially also mediate sunitinib's antiviral effect. AXL is an already known attachment factor/signaling receptor for multiple RNA viruses, including DENV, EBOV, and possibly ZIKV (52–55). Although confirmatory studies with AXL-deficient cells are required, inhibition of AXL by sunitinib may contribute to its effect on DENV entry. KIT and RET are paralogs with no reported roles in RNA viral infections and await further investigation. Given our inability to silence expression of KIT without a substantial negative impact on cell viability (likely due to its role in cell survival and proliferation; ref. 56), its specific relevance to DENV infection remains unclear. Overall, our data underscore the utility of using sunitinib and erlotinib as pharmacological probes to identify novel host factors required for viral infection.

We speculate that inhibition of AAK1 and GAK accounts for these drugs' effect against a broad spectrum of viruses, particularly those previously shown to depend on AP1 and AP2 activity, such as EBOV (18, 37–39). Inhibition of additional kinases including AXL, KIT, and RET may play a role. Though most of the EC_{50} values we report fall in the low micromolar range for the 6 viral families tested (Table 1), the relative potency of sunitinib and erlotinib varies between the different viral species. Such differences can be attributed to both variations in the assays used and the likely distinct dependence on the various host factors targeted by these inhibitors in the life cycle of different viruses. Other mechanisms of action, such as modulation of immune responses, also could contribute to the protective phenotype observed in vivo.

Although toxicity is a concern when targeting host functions, finding a safe therapeutic window may be feasible. Sunitinib and erlotinib each are approved as a once-daily oral treatment for multiple cancers at doses comparable to those exhibiting antiviral activity in vivo. A combination therapy already has been evaluated clinically and was tolerated, albeit with an increase in the adverse events primarily related to gastrointestinal disturbances (57, 58). However, a shift from the long-term treatment of cancer to acute infection such as with DENV should improve tolerance and minimize adverse effects. The safety and efficacy of sunitinib and/or erlotinib will be evaluated in dengue patients in the near future and potentially in patients with EBOV disease in future outbreaks (ClinicalTrials.gov NCT02380625).

The vast genetic diversity of viral species and replication strategies challenges the design of broadly effective direct-acting antivirals; however, a host-targeted approach could circumvent this issue. Sunitinib and erlotinib inhibit all 4 DENV serotypes. Moreover, a broad-spectrum therapy, such as with sunitinib/erlotinib combination, could be used to treat DENV-CHIKV (59, 60) or DENV-ZIKV (61) coinfections and infections with newly emerging RNA viruses. It also can be administered even before an accurate diagnosis of a viral threat, thereby increasing protection. Furthermore, although viral resistant mutations can emerge during treatment with host-targeted approaches (62), targeting of host proteins that are not under the genetic control of viruses is more likely to have a higher barrier to resistance than classical direct-acting antivirals. This is exemplified by our data and treatment with cyclophilin inhibitors (63). We recognize, however, that our dengue resistance assay is somewhat limited by the short-term virus passage. Although we predict that the genetic barrier to resistance is high, it may be possible to select for resistance over longer-term passage under different conditions or in a different, chronic infection model. Lastly, viruses use strategies similar to those of cancer cells for overcoming drug-mediated inhibition. Simultaneous inhibition of several kinases or targeting of several pathways by the same drug or drug combination may prove attractive in combating viral pathogens, as previously shown in cancer (64). Such "polypharmacology" by a single drug could increase the effectiveness while minimizing viral resistance.

In summary, our study serves as a proof of concept for the feasibility of identifying novel host-targeted broad-spectrum antiviral therapies via both repurposing and development of novel chemical entities. Such approaches may provide additive and possibly synergistic effects in combination with other strategies being developed to combat emerging viral infections.

Methods

Plasmids and virus constructs. ORFs encoding AP1M1 (AP1) and AP2M1 (AP2) were selected from the Human ORFeome library of cDNA clones (65) (Open Biosystems) and recombined into either pCherry (for mCherry fluorescence protein tagging) or pGLuc (for Gaussia Princeps luciferase fragment [GLuc] tagging) vectors using Gateway technology (Invitrogen). GFP-LC3 construct was previously described (66). pFLJ6/JFH(p7-Rluc2A) was a gift from Charles M. Rice (Rockefeller University, New York, New York, USA) (67). HCV TC-core was previously described (32). Plasmids used in the HCVpp entry assays (pNL4-3.Luc.R-E, pcDM8, and pcDM8-E1E2) were a gift from Shoshana Levy (Stanford Univer- sity, Stanford, California, USA). DENV2 TSV01 Renilla reporter plasmid was a gift from Pei-Yong Shi (University of Texas Medical Branch, Galveston, Texas, USA) (68), and DENV 16681 plasmid (pD2IC-30P-NBX) used to produce virus for the plaque assay was a gift from Claire Huang (Centers for Disease Control and Prevention, Public Health Service, US Department of Health and Human Services, Fort Collins, Colorado, USA) (69). Additional DENV isolates and ZIKV MR766 were from ATCC/BEI Resources. Lentiviral constructs used for AP2 overexpression were cloned into the pRRL-SIN backbone. rVSV-GP EBOV construct was a gift from Kartik Chandran (Albert Einstein College of Medicine, New York, New York, USA) (69, 70). Mouse-adapted N124D/K128E DENV2 PL046

was a gift from Sujan Shresta (70, 71). pCMV-DV2Rep was a gift from Andrew Yueh (Institute of Biotechnology and Pharmaceutical Research, Taipei, Taiwan) (34). Mutations were introduced by site-directed mutagenesis using the QuikChange kit (Stratagene).

Cells. Huh7 (Apath LLC), Huh7.5 (Apath LLC), BHK-21 (ATCC), and Vero (ATCC) cells were grown in DMEM (Mediatech) supplemented with 10% FBS, nonessential amino acids (Gibco), 1% l-glutamine (Gibco), and 1% penicillin-streptomycin (Gibco) and maintained in a humidified incubator with 5% CO_2 at 37°C. C6/36 cells were grown in Leibovitz's L-15 media (CellGro) supplemented with 10% FBS and 1% HEPES in a humidified chamber at 28°C and 0% CO_2

Reagents. The following reagents were used: sunitinib malate (Selleckchem), erlotinib (LC Laboratories), Captisol (Captisol), siImporter (Millipore), and Lipofectamine 2000 (Invitrogen). 12g and 12i were synthesized by the Herdewijn laboratory (28); 7737 and 7745 were synthesized by ACME Bioscience Inc.

Western blotting and antibodies. Cells were lysed in M-Per protein extraction reagent (Thermo Fisher Scientific). For phosphorprotein detection, cells were pretreated with 100 nM calyculin A (Cell Signaling), a PP1 and PP2a phosphatase inhibitor, for 30 minutes prior to lysis. Liver tissue was homogenized in RIPA buffer supplemented with Halt protease and phosphatase inhibitor cocktail (Thermo Fisher Scientific) and 100 nM calyculin A using 0.9- to 2-mm stainless steel beads in a BBX24 Bullet Blender homogenizer (NextAdvance). Clarified protein lysates were run on 4%–12% Bis-Tris gels (Invitrogen), transferred onto PVDF membranes (Bio-Rad). Blots were blocked and blotted with anti-AP1M1 (Abcam, catalog ab111135), anti-AP2M1 (Abcam, catalog ab75995), anti-GLuc (New England BioLabs, catalog E8023S), anti–phospho-AP2M1 (T156) (Cell Signaling, catalog 3843S), anti-AAK1 (Abcam, catalog ab134971), anti-GAK (MBL International, catalog MO573), and anti–β-actin (Sigma-Aldrich, catalog A3854) antibodies. Signal was detected with HRP-conjugated secondary antibodies. Band intensity was quantified with ImageJ software (NIH). See complete unedited blots in the supplemental material.

RNA interference. siRNAs (100–250 nM) were transfected into cells using siIMPORTER (Millipore) 48 hours before infection. Sequences/catalog numbers are as follows: human AAK1 and GAK, Silencer Select predesigned siRNA ID#s22494 and s5529, respec- tively (Thermo Fisher Scientific); *Chlorocebus sabaeus* (green monkey) AAK1 siRNA#1, GGUAUAUGUUGGAACCAGATT; AAK1 siRNA#2, GAAUAUUGUGGGUUACAUUTT; GAK siRNA#1, GCAUUAAAGAG-GCUAUUAATT; GAK siRNA#2, CAGCAUCCAUAGGAAAAGATT; NT, Silencer Select negative control (Thermo Fisher Scientific, catalog 4390844). Infections were performed at 48 hours after transfection. AP1M1 and AP2M1 were silenced via transduction with shRNA-expressing lentivirus (TRCN0000218336, TRCN0000060239, or Mission pLKO.1-puro nonmammalian shRNA control; Sigma-Aldrich) and selection on 1 μg/ml puromycin. Custom Cherry-Pick ON-TARGETplus siRNA library against 27 kinase genes was purchased from Dharmacon (see Supplemental Table 1 for gene and siRNA sequence details).

Virus production. HCV 2a J6/JFH(p7-Rluc2A) was transcribed in vitro using Megascript T7 kit (Ambion), and DENV2 TSV01, 16681 (used for DENV in vitro assays), or N124D/K128E DENV2 PL046 (used for DENV in vivo infections) RNA was transcribed in vitro using mMessage/mMachine (Ambion) kits. HCVcc and HCVpp were produced as previously described (23). DENV was produced by electro-

poration of RNA into BHK-21 cells, harvesting of supernatants at day 10, and titering via standard plaque assays on BHK-21 cells. In parallel, on day 2 after electroporation, DENV-containing supernatant was used to inoculate C6/36 cells to amplify the virus. For in vivo experiments, DENV supernatant was concentrated 100-fold by centrifugation at 50,000 g. rVSV-GP EBOV was propagated and titered on Vero cells via fluorescent-focus assay (69).

Entry assays. Huh7.5 cells were infected with HCVpp (71, 72) and 8 μg/ml Polybrene for 4 hours. Firefly luciferase activity was measured at 48–72 hours after infection. DENV2 entry was measured at 6 hours after infection of Huh7 cells by monitoring of *Renilla* luciferase activity. Luminescence was detected on InfiniteM1000 plate reader (Tecan). Vero cells were infected with rVSV-GP EBOV for 3 hours, total RNA was harvested and reverse transcribed, and EBOV GP transcript was quantified by real-time PCR and normalized to *GAPDH* expression.

Infection assays. Huh7 cells were infected with DENV or ZIKV in replicates ($n = 3$–10) for 4 hours at MOI of 0.01. Overall infection was measured either at 48 hours using a *Renilla* luciferase substrate or at 72 hours by plaque assays. Vero cells were infected with rVSV-GP EBOV for 4 hours and washed. At 20 hours after infection, cells were fixed with 4% formaldehyde and analyzed on an LSR II cytometer (BD Biosciences) using FITC channel. Data were processed using FlowJo software. EBOV infection was carried out under biosafety level 4 conditions. Forty-eight hours after infection, cells were formalin-fixed, and infection was measured by immunofluorescence using KZ52 anti-EBOV antibody in an Operetta HCS using the Harmony software package. Other viral infection assays, conducted by the Diamond lab (WNV), IBT Bioservices (CHIKV, RSV, JUNV), and the NIH/National Institute of Allergy and Infectious Diseases (others), were performed as summarized in Table 1.

RNA replication assays. HCV RNA replication was measured 72 hours after electroporation, as previously described (22). DENV2 replication assays were performed as previously described (34). Briefly, Huh7 cells were transfected with DNA-launched DENV2 replicon, pCMV-DV2Rep along with TET-ON plasmids. Thirty-six hours after transfection, viral RNA transcription was induced by doxycycline and shut down by changing to doxycycline-free medium 6 hours later. Replication was monitored by luciferase activity every day for 3 days. Data were normalized to activity at 24 hours after induction.

Infectious virus production. Infectious HCV or DENV production (i.e., extracellular infectivity) was measured in culture supernatants of cells electroporated with viral RNA for 48–72 hours and used to infect naive cells for 48 hours. Intracellular HCV infectivity was measured by inoculation of naive cells with lysates of electroporated cells subjected to 4 rounds of free-thawing and clarified at 5,000 g, as previously described (22).

Pharmacological inhibition. For entry assays, cells were pretreated with the inhibitors or DMSO for 1 hour before and for the duration of the infection, followed by replacement with drug-free medium. For the overall infection, RNA replication, or infectious virus production assays, inhibitors were left in for the duration of the study.

Gain-of-function assays. WT or T156A AP2 or empty vector control was expressed ectopically in Huh7 cells by lentiviral transduction. Twenty-four hours after transduction, cells were pretreated with sunitinib and erlotinib, infected with luciferase reporter DENV at MOI of 0.01, and incubated for 72 hours prior to luciferase and viability assays.

Live cell imaging. Huh7.5 cells were infected with concentrated HCV TC-core (32) at MOI of 1 for 24 hours, then transfected with either AP1- or AP2-mCherry using Lipofectamine 2000 (Invitrogen) and seeded onto collagen-coated 35-mm fluorodishes (World Precision Instruments). At 72 hours after infection, cells were labeled with biarsenical dye (1.25 μM) in Opti-MEM at 37°C for 30 minutes, then washed 3 times with 1X BAL (2,3-dimercapto-1-propanol) wash buffer (Invitrogen) supplemented with 500 μM 1,2-ethanedithiol in Opti-MEM. The cells were washed and incubated in prewarmed imaging media (DMEM-F12; Invitrogen) supplemented with 10% FBS, 0.1 mM nonessential amino acids, 1% penicillin-streptomycin, and 25 mM HEPES. When specified, TC-core–infected cells were incubated with DMSO, sunitinib (4 μM), or erlotinib (10 μM) beginning at 24 hours after infection. Time-lapse images were taken using a Leica SP5 II AOBS Tandem Scanner Spectral confocal microscope with a ×100 1.46 oil objective and a heated (37°C) chamber. An average of 5 movies representing individual cells with 15–30 trackable puncta each were recorded per sample with sequential frames taken every 2 seconds. Individual core puncta run lengths and transport velocities were calculated using the Manual Tracking plug-in for ImageJ, measuring the distance traveled (in any direction) between frames for a respective TC-core puncta.

Resistance studies. DENV4 (BC287/97; ATCC/BEI Resources, BEI NR-3806) was used to inoculate Huh7 cells at MOI of 0.01 and passaged every 3 days by transferring of an equal volume of viral supernatant to naive cells under increasing drug selection (0.5–1.5 μM, passages 1–6; 2.5 μM, passages 7 and 8). Upon completion of 8 passages, virus from the resulting supernatants was titered by plaque assays. SDM25N resistance mutation in NS4B at passage 8 was confirmed by purification and reverse transcription of viral RNA from supernatants of cells treated with DMSO or SDM25N as described in the RNA extraction and quantification section. NS4B region was amplified with iProof high-fidelity PCR kit (Bio-Rad) using primers NS4B forward GATGTGGAYYTGAGACCAGCYTCAGCATGGAC and NS4B reverse AGTCAANACTTCACAGAAAGCCCATGTTGTTCTCATCAA (N = any base, Y = C or T) and sequenced (Sequetech Corp.).

In vivo dengue studies. AG-129 mice deficient in type I and II IFN receptors were obtained from Harry Greenberg (Stanford University, Stanford, California, USA). Mice were backcrossed to C57B6/6J for $n = 10$ generations to obtain congenic AG-B6 strain. Age-matched, male and female mice at 8–10 weeks of age were used for all experiments. Mouse-adapted N124D/K128E DENV2 (5×10^5 PFU produced in BHK-21 cells or 10^7 PFU produced in C6/36 cells) was inoculated retro-orbitally into mice under general and local anesthesia. Drugs were administered at the indicated doses in a total volume of 100–200 μl per animal using 10% Captisol as vehicle. Drugs or vehicle were administered i.p. or orally once or twice daily starting at the time of inoculation or at various time points after inoculation for a total of 3–5 days. Mice were monitored twice daily until the conclusion of the experiment. Moribund animals were euthanized by carbon dioxide inhalation. Serum was isolated from whole blood harvested retro-orbitally at 48 or 72 hours after DENV inoculation under general and local anesthesia. Tissues were harvested following euthanasia and snap-frozen on dry ice until further analysis.

In vivo Ebola studies. Groups of 10 female C57BL/6 mice (8–12 weeks of age) purchased from Jackson Laboratory were treated with drugs or vehicle 6 hours before viral challenge. Erlotinib and sunitinib

were administered i.p. at the indicated doses in a total volume of 200 μl using 10% Captisol as vehicle. A group of 10 mice was left untreated to allow for interpretation of any survival seen in the vehicle-treated group. Mice were inoculated i.p. with 100 PFU of mouse-adapted EBOV. Mice were then treated once daily for a total of 10 days and observed daily for 28 days for lethality or clinical signs of disease.

RNA extraction and quantification. Total RNA from cells was isolated using an RNA purification kit (Macherey-Nagel). Mouse serum was purified from whole blood using Terumo Capiject Capillary Blood collection tubes (Thermo Fisher Scientific). Tissues were homogenized using 0.9- to 2-mm stainless steel beads in a BBX24 Bullet Blender homogenizer (NextAdvance). Total RNA from serum and tissues was extracted with QIAamp UltraSens Virus kit (Qiagen). cDNA was generated using a high-capacity cDNA reverse transcription kit (Invitrogen). DENV RNA was quantified by qRT-PCR using TaqMan GEX master mix (Thermo Fisher Scientific), and AAK1, GAK, EBOV GP, and housekeeping gene (*GAPDH*) RNA was quantified using iTaq Universal SYBR Green Supermix (Bio-Rad) on a StepOnePlus real-time PCR system (Applied Biosystems). Primer and probe sequences are as follows: DENV2 forward, GAGAGCAGATCTCTGATGAATAA; DENV2 reverse, ACTGTTGCACAGTCGACAC; DENV2 probe, TATGCTGAAACGCGAGAGAAACCGC; *GAPDH* forward, GAAATCCCATCACCATCTTCCAG; *GAPDH* reverse, GAGCCCCAGCCTTCTCCATG.

Viability assays. Viability was assessed using alamarBlue reagent (Invitrogen) according to the manufacturer's protocol. Fluorescence was detected at 560 nm on an InfiniteM1000 plate reader (Tecan).

Data analysis of combination drug treatment. Synergy/antagonism analysis was performed using the MacSynergy II program as previously described (23, 73). Matrix data sets in 4 replicates were assessed at the 95% confidence level for each experiment. Synergy and log volume were calculated. As suggested by Prichard et al. (73), such data sets should be interpreted as follows: volumes of synergy or antagonism at values less than 25 μM²% are insignificant, those of 25–50 μM²% are minor but significant, those of 50–100 μM²% are moderate and probably important in vivo, and those of greater than 100 μM²% are strong and likely to be important in vivo.

Statistics. All data were analyzed with GraphPad Prism software.

Fifty percent effective concentrations (EC$_{50}$) were measured by fitting of data to a 3-parameter logistic curve. *P* values were calculated by 2-tailed unpaired *t* test and 1- or 2-way ANOVA with either Dunnett's or Tukey's multiple comparisons tests for in vitro data sets and by Mann-Whitney test for in vivo data sets as specified in each figure legend. Survival curve *P* values were calculated by log-ranked Mantel-Cox test.

Study approval. Animal research was conducted under a protocol approved by Stanford's IACUC (Administrative Panel on Laboratory Animal Care) and its Institutional Biosafety Committee (Administrative Panel on Biosafety) or by the US Army Medical Research Institute of Infectious Diseases (USAMRIID) IACUC in compliance with the Animal Welfare Act and other federal statutes and regulations relating to animals and experiments involving animals. The Stanford and USAMRIID animal facilities are AAALAC-accredited and adhere to the principles stated in the 2005 *Guide for the Care and Use of Laboratory Animals* (National Academies Press). DENV and EBOV challenge studies were conducted in a biosafety level 2 (BSL-2) and a maximum-containment BSL-4 facility, respectively. Moribund mice were humanely euthanized on the basis of IACUC-approved criteria.

Author contributions

Acknowledgments

Address correspondence to: Shirit Einav, Department of Medicine, Stanford University, 300 Pasteur Drive, Lane Building L127, Stanford, California 94305, USA. Phone: 650.723.8656; E-mail: seinav@stanford.edu.

GN's present address is: International Center for Infectiology Research, Université de Lyon; Inserm, U1111; Ecole Normale Supérieure de Lyon; Université Claude Bernard Lyon 1, Centre International de Recherche en Infectiologie; LabEx Ecofect, Université de Lyon, Lyon, France.

1. Bhatt S, et al. The global distribution and burden of dengue. *Nature.* 2013;496(7446):504–507.

2. Flipse J, Smit JM. The complexity of a Dengue vaccine: a review of the human antibody response. *PLoS Negl Trop Dis.* 2015;9(6):e0003749.

3. Priyamvada L, et al. Human antibody responses after dengue virus infection are highly cross-reactive to Zika virus. *Proc Natl Acad Sci U S A.* 2016;113(28):7852–7857.

4. Dejnirattisai W, et al. Dengue virus sero-cross-reactivity drives antibody-dependent enhance-

ment of infection with Zika virus. *Nat Immunol*. 2016;17(9):1102–1108.

5. Stettler K, et al. Specificity, cross-reactivity, and function of antibodies elicited by Zika virus infection. *Science*. 2016;353(6301):823–826.

6. Henao-Restrepo AM, et al. Efficacy and effectiveness of an rVSV-vectored vaccine expressing Ebola surface glycoprotein: interim results from the Guinea ring vaccination cluster-randomised trial. *Lancet*. 2015;386(9996):857–866.

7. Bekerman E, Einav S. Infectious disease. Combating emerging viral threats. *Science*. 2015;348(6232):282–283.

8. Park SY, Guo X. Adaptor protein complexes and intracellular transport. *Biosci Rep*. 2014;34(4):e00123.

9. Olusanya O, Andrews PD, Swedlow JR, Smythe E. Phosphorylation of threonine 156 of the mu2 subunit of the AP2 complex is essential for endocytosis in vitro and in vivo. *Curr Biol*. 2001;11(11):896–900.

10. Ricotta D, Conner SD, Schmid SL, von Figura K, Honing S. Phosphorylation of the AP2 mu subunit by AAK1 mediates high affinity binding to membrane protein sorting signals. *J Cell Biol*. 2002;156(5):791–795.

11. Umeda A, Meyerholz A, Ungewickell E. Identification of the universal cofactor (auxilin 2) in clathrin coat dissociation. *Eur J Cell Biol*. 2000;79(5):336–342.

12. Zhang CX, Engqvist-Goldstein AE, Carreno S, Owen DJ, Smythe E, Drubin DG. Multiple roles for cyclin G-associated kinase in clathrin-mediated sorting events. *Traffic*. 2005;6(12):1103–1113.

13. Ghosh P, Kornfeld S. AP-1 binding to sorting signals and release from clathrin-coated vesicles is regulated by phosphorylation. *J Cell Biol*. 2003;160(5):699–708.

14. Conner SD, Schmid SL. Identification of an adaptor-associated kinase, AAK1, as a regulator of clathrin-mediated endocytosis. *J Cell Biol*. 2002;156(5):921–929.

15. Fingerhut A, von Figura K, Honing S. Binding of AP2 to sorting signals is modulated by AP2 phosphorylation. *J Biol Chem*. 2001;276(8):5476–5482.

16. Lee DW, Zhao X, Zhang F, Eisenberg E, Greene LE. Depletion of GAK/auxilin 2 inhibits receptor-mediated endocytosis and recruitment of both clathrin and clathrin adaptors. *J Cell Sci*. 2005;118(pt 18):4311–4321.

17. Alconada A, Bauer U, Hoflack B. A tyrosine-based motif and a casein kinase II phosphorylation site regulate the intracellular trafficking of the varicella-zoster virus glycoprotein I, a protein localized in the trans-Golgi network. *EMBO J*. 1996;15(22):6096–6110.

18. Bhattacharyya S, Hope TJ, Young JA. Differential requirements for clathrin endocytic pathway components in cellular entry by Ebola and Marburg glycoprotein pseudovirions. *Virology*. 2011;419(1):1–9.

19. Dutta D, et al. EphrinA2 regulates clathrin mediated KSHV endocytosis in fibroblast cells by coordinating integrin-associated signaling and c-Cbl directed polyubiquitination. *PLoS Pathog*. 2013;9(7):e1003510.

20. Huang HC, Chen CC, Chang WC, Tao MH, Huang C. Entry of hepatitis B virus into immortalized human primary hepatocytes by clathrin-dependent endocytosis. *J Virol*. 2012;86(17):9443–9453.

21. Humphries AC, Dodding MP, Barry DJ, Collinson LM, Durkin CH, Way M. Clathrin potentiates vaccinia-induced actin polymerization to facilitate viral spread. *Cell Host Microbe*. 2012;12(3):346–359.

22. Neveu G, Barouch-Bentov R, Ziv-Av A, Gerber D, Jacob Y, Einav S. Identification and targeting of an interaction between a tyrosine motif within hepatitis C virus core protein and AP2M1 essential for viral assembly. *PLoS Pathog*. 2012;8(8):e1002845.

23. Neveu G, Ziv-Av A, Barouch-Bentov R, Berkerman E, Mulholland J, Einav S. AP-2-associated protein kinase 1 and cyclin G-associated kinase regulate hepatitis C virus entry and are potential drug targets. *J Virol*. 2015;89(8):4387–4404.

24. Ohka S, Ohno H, Tohyama K, Nomoto A. Basolateral sorting of human poliovirus receptor alpha involves an interaction with the mu1B subunit of the clathrin adaptor complex in polarized epithelial cells. *Biochem Biophys Res Commun*. 2001;287(4):941–948.

25. Ohno H, Aguilar RC, Fournier MC, Hennecke S, Cosson P, Bonifacino JS. Interaction of endocytic signals from the HIV-1 envelope glycoprotein complex with members of the adaptor medium chain family. *Virology*. 1997;238(2):305–315.

26. Agrawal T, Schu P, Medigeshi GR. Adaptor protein complexes-1 and 3 are involved at distinct stages of flavivirus life-cycle. *Sci Rep*. 2013;3:1813.

27. Karaman MW, et al. A quantitative analysis of kinase inhibitor selectivity. *Nat Biotechnol*. 2008;26(1):127–132.

28. Kovackova S, et al. Selective inhibitors of cyclin G Associated Kinase (GAK) as anti-hepatitis C agents. *J Med Chem*. 2015;58(8):3393–3410.

29. Benedicto I, et al. Clathrin mediates infectious hepatitis C virus particle egress. *J Virol*. 2015;89(8):4180–4190.

30. Coller KE, Heaton NS, Berger KL, Cooper JD, Saunders JL, Randall G. Molecular determinants and dynamics of hepatitis C virus secretion. *PLoS Pathog*. 2012;8(1):e1002466.

31. Sorensen EB, Conner SD. AAK1 regulates Numb function at an early step in clathrin-mediated endocytosis. *Traffic*. 2008;9(10):1791–1800.

32. Coller KE, Heaton NS, Berger KL, Cooper JD, Saunders JL, Randall G. Molecular determinants and dynamics of hepatitis C virus secretion. *PLoS Pathog*. 2012;8(1):e1002466.

33. Wacker I, Kaether C, Krömer A, Migala A, Almers W, Gerdes HH. Microtubule-dependent transport of secretory vesicles visualized in real time with a GFP-tagged secretory protein. *J Cell Sci*. 1997;110(pt 13):1453–1463.

34. Yang CC, et al. Characterization of an efficient dengue virus replicon for development of assays of discovery of small molecules against dengue virus. *Antiviral Res*. 2013;98(2):228–241.

35. Kostich W et al. Inhibition of AAK1 kinase as a novel therapeutic approach to treat neuropathic pain. *J Pharmacol Exp Ther*. 2016;358(3):371–386.

36. van Cleef KW, et al. Identification of a new dengue virus inhibitor that targets the viral NS4B protein and restricts genomic RNA replication. *Antiviral Res*. 2013;99(2):165–171.

37. Bhattacharyya S, Mulherkar N, Chandran K. Endocytic pathways involved in filovirus entry: advances, implications and future directions. *Viruses*. 2012;4(12):3647–3664.

38. Poirier S, et al. The cytosolic adaptor AP-1A is essential for the trafficking and function of Niemann-Pick type C proteins. *Traffic*. 2013;14(4):458–469.

39. Carette JE, et al. Ebola virus entry requires the cholesterol transporter Niemann-Pick C1. *Nature*. 2011;477(7364):340–343.

40. Johnson AJ, Roehrig JT. New mouse model for dengue virus vaccine testing. *J Virol*. 1999;73(1):783–786.

41. Schul W, Liu W, Xu HY, Flamand M, Vasudevan SG. A dengue fever viremia model in mice shows reduction in viral replication and suppression of the inflammatory response after treatment with antiviral drugs. *J Infect Dis*. 2007;195(5):665–674.

42. Nair AB, Jacob S. A simple practice guide for dose conversion between animals and human. *J Basic Clin Pharm*. 2016;7(2):27–31.

43. Mendel DB, et al. In vivo antitumor activity of SU11248, a novel tyrosine kinase inhibitor targeting vascular endothelial growth factor and platelet-derived growth factor receptors: determination of a pharmacokinetic/pharmacodynamic relationship. *Clin Cancer Res*. 2003;9(1):327–337.

44. Higgins B, et al. Antitumor activity of erlotinib (OSI-774, Tarceva) alone or in combination in human non-small cell lung cancer tumor xenograft models. *Anticancer Drugs*. 2004;15(5):503–512.

45. Haznedar JO, et al. Single- and multiple-dose disposition kinetics of sunitinib malate, a multitargeted receptor tyrosine kinase inhibitor: comparative plasma kinetics in non-clinical species. *Cancer Chemother Pharmacol*. 2009;64(4):691–706.

46. Chee EL, Lim AY, Modamio P, Fernandez-Lastra C, Segarra I. Sunitinib tissue distribution changes after coadministration with ketoconazole in mice. *Eur J Drug Metab Pharmacokinet*. 2016;41(3):309–319.

47. Zerbe LK, et al. Inhibition by erlotinib of primary lung adenocarcinoma at an early stage in male mice. *Cancer Chemother Pharmacol*. 2008;62(4):605–620.

48. Orozco S, et al. Characterization of a model of lethal dengue virus 2 infection in C57BL/6 mice deficient in the alpha/beta interferon receptor. *J Gen Virol*. 2012;93(pt 10):2152–2157.

49. Human Kinome Heat Map. SuperNova Life Science. http://www.supernovalifescience.com/HM/HM%2041.pdf. Accessed January 11, 2017.

50. Davis MI, et al. Comprehensive analysis of kinase inhibitor selectivity. *Nat Biotechnol*. 2011;29(11):1046–1051.

51. Rathore AP, et al. Celgosivir treatment misfolds dengue virus NS1 protein, induces cellular pro-survival genes and protects against lethal challenge mouse model. *Antiviral Res*. 2011;92(3):453–460.

52. Brindley MA, et al. Tyrosine kinase receptor Axl enhances entry of Zaire ebolavirus without direct interactions with the viral glycoprotein. *Virology*.

2011;415(2):83–94.

53. Meertens L, et al. The TIM and TAM families of phosphatidylserine receptors mediate dengue virus entry. *Cell Host Microbe*. 2012;12(4):544–557.

54. Hamel R, et al. Biology of Zika virus infection in human skin cells. *J Virol*. 2015;89(17):8880–8896.

55. Nowakowski TJ, Pollen AA, Di Lullo E, Sandoval-Espinosa C, Bershteyn M, Kriegstein AR. Expression analysis highlights AXL as a candidate Zika virus entry receptor in neural stem cells. *Cell Stem Cell*. 2016;18(5):591–596.

56. Roskoski R. Signaling by Kit protein-tyrosine kinase--the stem cell factor receptor. *Biochem Biophys Res Commun*. 2005;337(1):1–13.

57. Scagliotti GV, et al. Sunitinib plus erlotinib versus placebo plus erlotinib in patients with previously treated advanced non-small-cell lung cancer: a phase III trial. *J Clin Oncol*. 2012;30(17):2070–2078.

58. Blumenschein GR, et al. Sunitinib plus erlotinib for the treatment of advanced/metastatic non-small-cell lung cancer: a lead-in study. *J Thorac Oncol*. 2012;7(9):1406–1416.

59. Chipwaza B, et al. Dengue and Chikungunya fever among viral diseases in outpatient febrile children in Kilosa district hospital, Tanzania. *PLoS Negl Trop Dis*. 2014;8(11):e3335.

60. Karthik R, Vineetha KR, Raut CG. Seroprevalance of dengue and chikungunya co infection and its clinical correlation in bangalore city hospitals. *Int J Curr Res*. 2014;6(12):11040–11044.

61. Dupont-Rouzeyrol M, et al. Co-infection with Zika and dengue viruses in 2 patients, New Caledonia, 2014. *Emerging Infect Dis*. 2015;21(2):381–382.

62. de Wispelaere M, LaCroix AJ, Yang PL. The small molecules AZD0530 and dasatinib inhibit dengue virus RNA replication via Fyn kinase. *J Virol*. 2013;87(13):7367–7381.

63. Lin K, Gallay P. Curing a viral infection by targeting the host: the example of cyclophilin inhibitors. *Antiviral Res*. 2013;99(1):68–77.

64. Knight ZA, Lin H, Shokat KM. Targeting the cancer kinome through polypharmacology. *Nat Rev Cancer*. 2010;10(2):130–137.

65. Rual JF, et al. Human ORFeome version 1.1: a platform for reverse proteomics. *Genome Res*. 2004;14(10B):2128–2135.

66. Heaton NS, Randall G. Dengue virus-induced autophagy regulates lipid metabolism. *Cell Host Microbe*. 2010;8(5):422–432.

67. Tscherne DM, Jones CT, Evans MJ, Lindenbach BD, McKeating JA, Rice CM. Time- and temperature-dependent activation of hepatitis C virus for low-pH-triggered entry. *J Virol*. 2006;80(4):1734–1741.

68. Zou G, Xu HY, Qing M, Wang QY, Shi PY. Development and characterization of a stable luciferase dengue virus for high-throughput screening. *Antiviral Res*. 2011;91(1):11–19.

69. Huang CY, et al. The dengue virus type 2 envelope protein fusion peptide is essential for membrane fusion. *Virology*. 2010;396(2):305–315.

70. Chandran K, Sullivan NJ, Felbor U, Whelan SP, Cunningham JM. Endosomal proteolysis of the Ebola virus glycoprotein is necessary for infection. *Science*. 2005;308(5728):1643–1645.

71. Prestwood TR, Prigozhin DM, Sharar KL, Zellweger RM, Shresta S. A mouse-passaged dengue virus strain with reduced affinity for heparan sulfate causes severe disease in mice by establishing increased systemic viral loads. *J Virol*. 2008;82(17):8411–8421.

72. Bartosch B, Dubuisson J, Cosset FL. Infectious hepatitis C virus pseudo-particles containing functional E1-E2 envelope protein complexes. *J Exp Med*. 2003;197(5):633–642.

73. Prichard MN, Shipman C. Analysis of combinations of antiviral drugs and design of effective multidrug therapies. *Antivir Ther (Lond)*. 1996;1(1):9–20.

Interactions between the Hepatitis C Virus Nonstructural 2 Protein and Host Adaptor Proteins 1 and 4 Orchestrate Virus Release

Fei Xiao,[a] Stanley Wang,[a] Rina Barouch-Bentov,[a] Gregory Neveu,[a] Szuyuan Pu,[a] Melanie Beer,[a] Stanford Schor,[a] Sathish Kumar,[a] Vlad Nicolaescu,[b] Brett D. Lindenbach,[c] Glenn Randall,[b] Shirit Einav[a]

[a]Division of Infectious Diseases and Geographic Medicine, Department of Medicine, and Department of Microbiology and Immunology, Stanford University School of Medicine, Stanford, California, USA
[b]Department of Microbiology, the University of Chicago, Chicago, Illinois, USA
[c]Department of Microbial Pathogenesis, Yale School of Medicine, New Haven, Connecticut, USA

ABSTRACT Hepatitis C virus (HCV) spreads via secreted cell-free particles or direct cell-to-cell transmission. Yet, virus-host determinants governing differential intracellu- lar trafficking of cell-free- and cell-to-cell-transmitted virus remain unknown. The host adaptor proteins (APs) AP-1A, AP-1B, and AP-4 traffic in post-Golgi compart- ments, and the latter two are implicated in basolateral sorting. We reported that AP-1A mediates HCV trafficking during release, whereas the endocytic adaptor AP-2 mediates entry and assembly. We demonstrated that the host kinases AAK1 and GAK regulate HCV infection by controlling these clathrin-associated APs. Here, we sought to define the roles of AP-4, a clathrin-independent adaptor; AP-1A; and AP-1B in HCV infection. We screened for interactions between HCV proteins and the μ subunits of AP-1A, AP-1B, and AP-4 by mammalian cell-based protein fragment complementation assays. The nonstructural 2 (NS2) protein emerged as an interactor of these adaptors in this screening and by coimmunoprecipitations in HCV-infected cells. Two previously unrecognized dileucine-based motifs in the NS2 C terminus mediated AP binding and HCV release. Infectivity and coculture assays demonstrated that while all three adaptors mediate HCV release and cell-free spread, AP-1B and AP-4, but not AP-1A, mediate cell-to-cell spread. Live-cell imaging revealed HCV cotrafficking with AP-1A, AP-1B, and AP-4 and that AP-4 mediates HCV trafficking in a post-Golgi compartment. Lastly, HCV cell-to-cell spread was regulated by AAK1 and GAK and thus susceptible to treatment with AAK1 and GAK inhibitors. These data provide a mechanistic understanding of HCV trafficking in distinct release path- ways and reveal a requirement for APs in cell-to-cell viral spread.

IMPORTANCE HCV spreads via cell-free infection or cell-to-cell contact that shields it from antibody neutralization, thereby facilitating viral persistence. Yet, factors gov- erning this differential sorting remain unknown. By integrating proteomic, RNA inter- ference, genetic, live-cell imaging, and pharmacological approaches, we uncover dif- ferential coopting of host adaptor proteins (APs) to mediate HCV traffic at distinct late steps of the viral life cycle. We reported that AP-1A and AP-2 mediate HCV traf- ficking during release and assembly, respectively. Here, we demonstrate that dileu- cine motifs in the NS2 protein mediate AP-1A, AP-1B, and AP-4 binding and cell-free virus release. Moreover, we reveal that AP-4, an adaptor not previously implicated in viral infections, mediates cell-to-cell spread and HCV trafficking. Lastly, we demon- strate cell-to-cell spread regulation by AAK1 and GAK, host kinases controlling APs, and susceptibility to their inhibitors. This study provides mechanistic insights into virus-host determinants that facilitate HCV trafficking, with potential implications for pathogenesis and antiviral agent design.

Hepatitis C virus (HCV) is a major global health problem; it is estimated to chronically infect 71 million people worldwide (1). HCV persists in the majority (>70%) of infected individuals, resulting in severe liver disease, including cirrhosis, liver failure, and hepatocellular carcinoma (reviewed in reference 2).

HCV is an enveloped, positive single-stranded RNA virus in the *Flaviviridae* family. Its 9.6-kb genome encodes a single polyprotein that is proteolytically cleaved into individual proteins. The HCV core protein and E1 and E2 glycoproteins form new virions; nonstructural (NS) proteins NS3, -4A, -4B, -5A, and -5B form the viral replication machinery, whereas p7 and NS2 are essential for infectious virus production (3–5). The current model of infectious HCV production suggests that viral particles begin to assemble on or near the surface of lipid droplets (LD), where core is concentrated (6). Similar to flaviviruses, HCV is thought to bud into the endoplasmic reticulum (ER), where the envelope glycoproteins are retained. HCV particles, rendered infectious upon budding, exit the cell via the secretory pathway (7), where they cotraffic with various components of the ER, the trans-Golgi network (TGN), and recycling endosomes (8). Upon their release, these cell-free viral particles can infect distant cells. Infectious HCV production requires coordination of all 10 HCV proteins along with multiple host factors (6). NS2, in particular, plays a critical role in early viral assembly, envelopment, maturation, and release (3, 4, 9–11). Nevertheless, a comprehensive understanding of the mechanisms that govern viral particle trafficking during HCV release is still lacking.

In addition to the release of cell-free virus, HCV transmission occurs via cell-to-cell spread, whereby viral particles spread directly to neighboring cells while being protected from antibody neutralization and other extracellular viral clearance mechanisms (12–14). Cell-to-cell spread is therefore implicated in immune evasion, HCV persistence, and antiviral treatment failure (15, 16). It remains unknown, however, how viral particles are differentially directed to cell membrane sites for cell-to-cell versus cell-free spread.

Intracellular membrane traffic relies, to a large extent, on the interactions between adaptor protein (AP) complexes (AP-1 through AP-5) and the transmembrane cargo (17). APs are heterotetrameric complexes composed of two large (γ and α., '', o, or e) subunits (110 to 130 kDa), a medium (μ) subunit (~50 kDa), and a small (σ) subunit (15 to 20 kDa) (17). AP complexes orchestrate the formation of vesicles destined for transport by distinct intracellular pathways. While AP-2 sorts in the endocytic pathway, AP-1 and AP-4 facilitate sorting in post-Golgi compartments (18, 19). Specifically, AP-1A typically mediates sorting from the TGN to recycling endosomes; AP-1B mediates sorting from the TGN to the basolateral membrane, whereas AP-4 is thought to facilitate exiting from the TGN and sorting by both the endosomal and basolateral pathways (17, 20–24). Recognition of either tyrosine-based (YXXØ) or dileucine-based [(D/E)XXXL(L/I) and (LL/LI)] motifs within the cargo protein by subunits of the AP complex mediates these interactions (X is any amino acid, and Ø is a bulky hydrophobic amino acid) (19). The two host cell kinases AP-2-associated protein kinase 1 (AAK1) and cyclin G-associated kinase (GAK) regulate receptor-mediated endocytosis and TGN transport (25, 26). Specifically, AAK1 and GAK phosphorylate the μ subunits of clathrin- associated AP-1 and AP-2, thereby enhancing their binding to sorting motifs within the cargo (25, 27–29). Moreover, GAK recruits clathrin-associated APs to the plasma mem- brane and TGN (30).

The clathrin-associated AP-1 and AP-2 complexes have been implicated in multiple viral infections (31–34). We have previously reported that AP-2 is essential for HCV entry (35) and is also recruited by a tyrosine-based motif within the HCV core protein to LDs, where it plays a critical role in HCV assembly (36). More recently, we and others have demonstrated a role for AP-1A in HCV release (8, 37–40). By using live-cell imaging, we showed that a fraction of HCV particles cotraffics with AP-1A and AP-2 (39). Moreover, we showed that AAK1 and GAK regulate HCV entry and assembly via AP-2 phosphor-

46

ylation and HCV release via AP-1A phosphorylation (35, 36, 39). Compounds with potent anti-AAK1 and/or anti-GAK activity, including the already approved anticancer drugs sunitinib and erlotinib and novel more selective AAK1 and GAK inhibitors, inhibit HCV entry, assembly, and cotrafficking with AP-1A and AP-2 (35, 36, 39, 41). Neverthe- less, the HCV determinant(s) required for binding of APs for steps beyond viral assembly remained unknown. Moreover, the role of AP complexes in viral cell-to-cell spread and the role of AP-4 specifically in any aspect of a viral life cycle have not been reported to date.

We hypothesized that HCV proteins differentially bind AP complexes via tyrosine- or dileucine-based motifs to mediate intracellular traffic of viral particles at temporally distinct late steps of the viral life cycle. To test this hypothesis, we screened for interactions between HCV proteins and the μ subunits of four AP complexes by mammalian cell-based protein fragment complementation assays (PCAs) (36, 42). NS2 emerged as a critical viral protein for binding of the AP-1A, AP-1B, and AP-4 complexes. We demonstrate that two heretofore unrecognized dileucine-based motifs in the C-terminal protease domain of NS2 mediate binding to APs and HCV release. Further- more, we show that while AP-1A, AP-1B, and AP-4 are required for HCV release and cell-free infectivity, AP-1B and AP-4, but not AP-1A, are involved in the mediation of cell-to-cell spread. Importantly, we provide evidence that the majority of HCV particles cotraffic with AP-4, in part via a post-Golgi pathway. Lastly, we demonstrate a role for AAK1- and GAK-regulated AP activity in yet another step of the HCV life cycle beyond entry, assembly, and cell-free virus release, namely, cell-to-cell spread.

RESULTS

Differential binding of AP complexes by HCV proteins. We initially screened for interactions between the AP-1A, AP-1B, AP-2, and AP-4 complexes and the HCV proteome (excluding E1 and E2, which form disulfide-linked misfolded aggregates when ectopically coexpressed in cells [43]) by using PCAs. This PCA format relies on reversible reconstitution of a split luciferase reporter and provides a high-fidelity means to measure weak and transient interactions (36) such as those between APs and cargo (K_ds in the micromolar range) (18, 24). Moreover, it allows detection of interactions involving membrane proteins in mammalian cells and within appropriate subcellular compartments (36, 42). Since the μ subunits of AP complexes interact with both tyrosine and dileucine motifs (31–34), their coding genes were fused to an N-terminal luciferase fragment reporter (GLuc1-A), while individual HCV proteins derived from the J6/JFH genome (44) were fused to an N-terminal complementary luciferase fragment (GLuc2-B). AP and viral genes were transfected pairwise into 293T cells. When screening for NS3-AP interactions, a plasmid encoding FLAG-tagged NS4A was added to allow membrane binding of the NS3 protein (45). Expression of the viral (42) and host APs (see Fig. S1A in the supplemental material) was confirmed by Western blot assays. Luciferase activity was measured at 24 h posttransfection, and results were expressed as normalized luminescence ratios (NLR). We benchmarked the accuracy and sensitivity of this screening by a random reference set (RRS) composed of 53 noninteracting human protein pairs and CHMP2B, which did not interact with the HCV proteome in a recent unrelated screening (42) (Fig. S1B). z scores indicating the number of standard deviations (SDs) above the mean NLR of the control RRS were calculated. A histogram distribution curve of the mean z score values obtained from three independent experiments exhibited a clear separation between the set studied and the RRS ($P =$
6.22×10^{-6}, t test) (Fig. 1A). A cutoff value of >2.2 SDs (corresponding to an NLR of >25) was chosen as the threshold to define positive interactions. Novel prominent interactions between NS2 and several APs were identified in this screening. NS2 bound the μ subunit of AP-4 with the greatest apparent affinity, followed by AP-1A and AP-1B (Fig. 1B). NS5A also bound AP-4, albeit with a lower apparent affinity than NS2. In contrast, HCV core bound AP-2 with the highest apparent affinity, supporting the important role of this interaction in HCV infection (36) (Fig. 1B). P7, NS3, NS4A, NS4B, and NS5B coexpression with APs yielded luciferase signals comparable to the back-
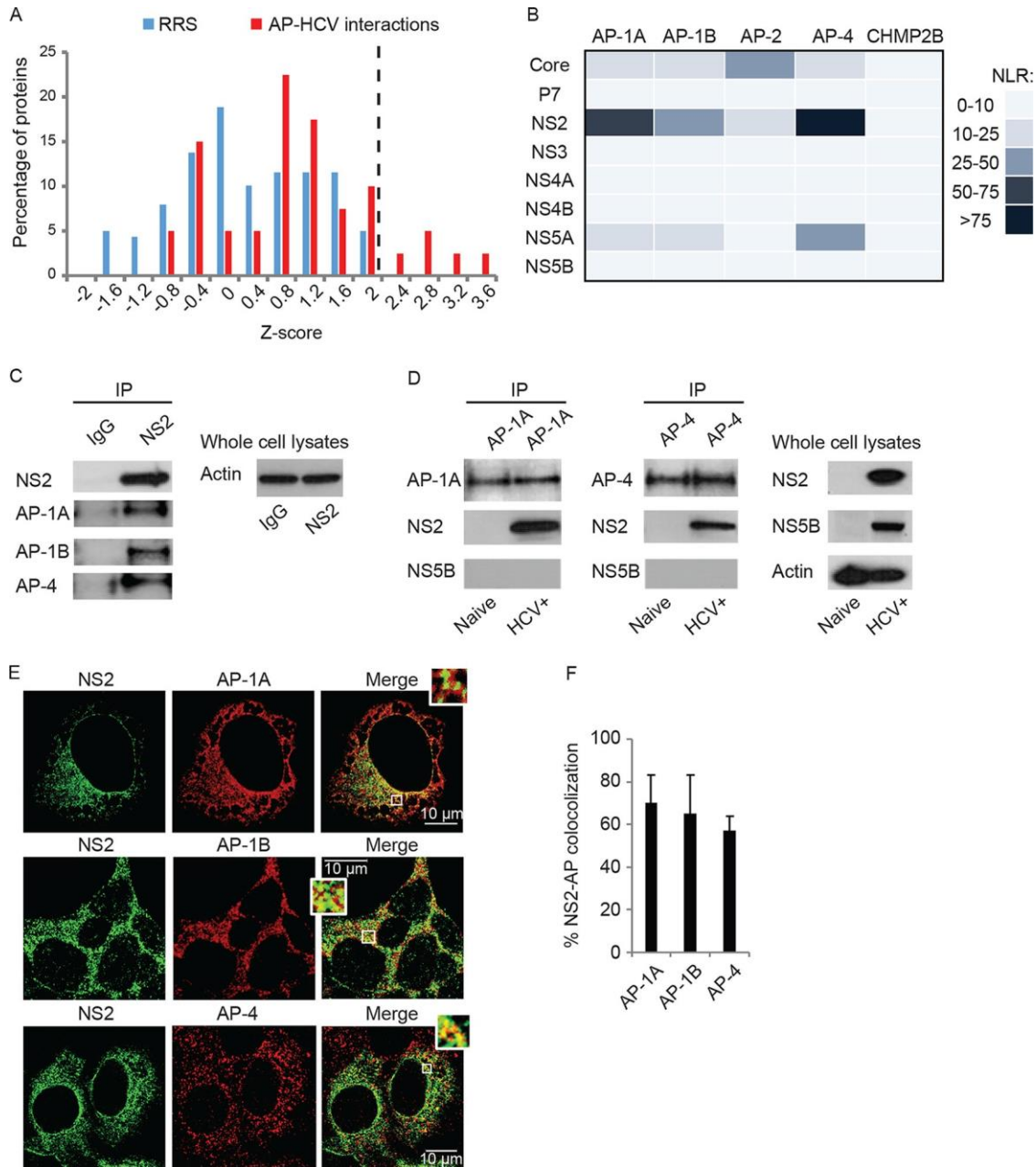
Xiao et al.

FIG 1 Interactions between HCV proteins and host APs. (A) Results of PCA screening for interactions of AP μ subunits with individual HCV proteins. Histogram of the mean z scores of the set studied and RRS of interactions obtained from three independent experiments. The dotted line defines the cutoff used for positive interactions. (B) Heat map of the interactions color coded on the basis of the NLR. (C) NS2 interacts with APs in HCV RNA-transfected cells. Immunoprecipitations (IPs) from membrane fractions of HCV RNA-transfected or naive Huh7.5 cells with anti-NS2 (C), anti-AP-1A, or anti-AP-4 (D) antibodies and IgG controls (C). Antibodies used for immunoblotting are indicated on the left. (E) Representative confocal IF microscopy images at X40 magnification of AP (red) and NS2 (green) in HCV-transfected cells. Scale bars represent 10 μm. (F) Quantitative colocalization analysis of z stacks by using Manders' colocalization coefficients. Mean M2 values are presented as percent colocalization (the fraction of green intensity that coincides with red intensity) ± SD.

ground (Fig. 1B). Moreover, NS2 did not bind the μ subunits of the AP-2, AP-3, and AP-5 complexes, supporting the specificity of its interactions with the AP-1A, AP-1B, and AP-4 complexes (Fig. S1C).

NS2 binds AP-1 and AP-4 in the context of HCV infection. Since NS2 emerged as a key binding partner in the screening, we validated its interactions with AP-1A, AP-1B, and AP-4. Coimmunoprecipitations (co-IPs) were conducted with membrane fractions

48

derived from cells transfected with J6/JFH HCV RNA and untransfected (naive) controls. Because of the weak and transient nature of typical adaptor-cargo interactions (18, 24), a cross-linker was added to allow covalent binding of the already bound interacting proteins, as we previously reported (36, 42). Anti-NS2 antibody effectively pulled down AP-1A, AP-1B, and AP-4, whereas only a background signal was demonstrated with IgG controls (Fig. 1C). Reciprocal co-IPs revealed that anti-AP-1A or -AP-4 antibodies pulled down NS2 but not a control protein, NS5B, from HCV RNA-transfected cells (Fig. 1D). Lack of NS2 signal in IPs from naive cells (Fig. 1D) confirmed the specificity of viral protein detection in the HCV RNA-transfected cells. In addition, significant colocalization of NS2 with AP-1A, AP-1B, and AP-4 was observed by confocal immunofluorescence (IF) analysis of 15 to 20 HCV-infected cells (Manders' colocalization coefficients of 70% ± 13%, 65% ± 18%, and 57% ± 7%, respectively) (Fig. 1E and F).

NS2 harbors dileucine motifs that mediate AP-1 and AP-4 binding and HCV release. Inspection of the primary sequence of NS2 revealed two conserved dileucine motifs (LL) within the cytoplasmic C-terminal protease domain of the protein (Fig. 2A) (10, 46). To study the role of these dileucine motifs in the binding of AP-1A, AP-1B, and AP-4, we first introduced single, double (double mutant [DM]; L202A-L217A), and quadruple (quadruple mutant [QM]; L202A-L203A-L216A-L217A) leucine-to-alanine substitutions into the GLuc-NS2 vector (Fig. 2A). None of these mutations impaired NS2 expression (Fig. 2B), as previously shown with respect to L217 mutations (9). The single mutations reduced AP-4 binding measured via PCAs by ~2-fold relative to wild-type (WT) NS2, whereas the DM and QM reduced AP-4 binding by 3- and 4-fold, respectively (Fig. 2C). These NS2 mutations also reduced AP-1A and AP-1B binding, albeit the magnitude of the effect was smaller (Fig. 2C). Additionally, QM NS2 reduced AP-4 binding relative to WT NS2 via co-IPs from membrane fractions of Huh7.5 cells ectopically expressing WT or QM mutant GLuc-NS2 and AP-4, supporting the PCA data (Fig. S1D).

Dileucine-based sorting motifs often harbor acidic residues in the −4 [(D/E)XXXL(L/I)], −3 (DXXLL) (19, 32–34), or other position (47–49). NS2 has two highly conserved acidic residues adjacent to the first leucine pair: glutamate in position −2 and aspartate in position +4 (Fig. 2A). To determine the roles of these acidic residues, we mutated them individually to alanine. E200A and D207A did not reduce NS2 expression (Fig. 2B). Whereas the E200A mutation had no effect on AP binding, the D207A mutation reduced NS2 binding to AP-1A, AP-1B, and AP-4 (Fig. 2C). No conserved acidic residues are present adjacent to the second leucine pair of NS2. These results suggest that AP-1A, AP-1B, and AP-4 binding is mediated by two dileucine motifs within the C terminus of NS2. Nevertheless, the remaining signal observed with the QM suggests that additional NS2 residues may be involved in the mediation of AP μ subunit binding. To investigate the role of these NS2 residues in the HCV life cycle, we introduced the single, double, and quadruple leucine mutations and single acidic residue mutations into a bicistronic luciferase reporter HCV genome, J6/H77NS2/JFH(NS2-IRES-nsGluc2AUbi) (3), which enables expression of the HCV replicase independently of NS2-3 cleavage. These mutations did not impair HCV RNA replication, as measured by luciferase assays at 8 and 72 h posttransfection (Fig. 2D). Moreover, inoculation of naive cells with clarified cell lysates derived from the HCV RNA-transfected cells demonstrated no effect of the mutations on intracellular infectivity (Fig. 2E). Nevertheless, the single-leucine and D207A mutations, but not the E200A mutation, caused an up to ~2-log reduction in extracellular infectivity measured by inoculation of naive cells with supernatants derived from the HCV RNA-transfected cells, consistent with a defect in viral release (Fig. 2E). The extracellular infectivity of the DM and QM was at the background level (~3.5-log reduction). To determine whether this defect in viral release was associated with accumulation of intracellular particles, we measured infectious virus titers in cell lysates and culture supernatants derived from cells transfected with the WT or NS2 mutant HCV genome. Consistent with our luciferase data, NS2 mutations significantly reduced the extracellular, but not the intracellular, viral titer (Fig. 2F). Moreover, these mutations significantly increased the ratio of intracellular infectivity to
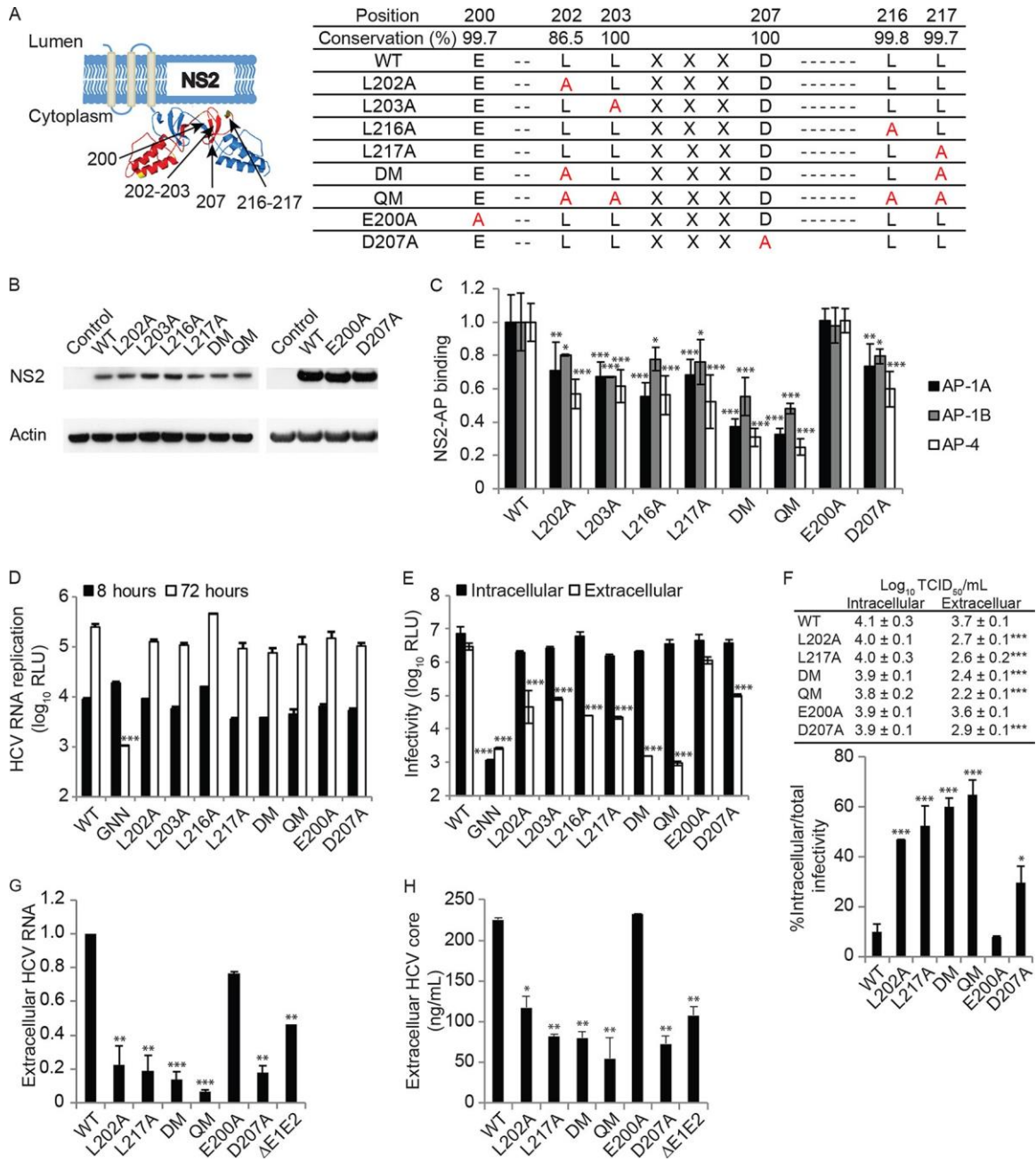
Xiao et al.

FIG 2 NS2 harbors two dileucine motifs that mediate AP binding and HCV release. (A) Dileucine motifs in the C terminus of NS2 and the cloned mutations. The schematic shown was based on data from reference 46. (B) Levels of NS2 in lysates of cells transfected with the plasmids indicated and blotted with anti-GLuc and anti-actin antibodies. (C) Interactions of WT or mutant NS2 with AP-1A, AP-1B, and AP-4 by PCAs. Plotted are NLRs relative to WT NS2-AP binding. (D) Cells were electroporated with WT or mutated NS2 bicistronic J6/H77NS2/JFH HCV RNA. HCV RNA replication measured via luciferase assays 8 and 72 h after HCV RNA electroporation. RLU, relative light units. (E) HCV infectivity measured via luciferase assays by inoculating naive cells with lysates (intracellular) and supernatants (extracellular) from electroporated cells. (F) Intra- and extracellular infectivity titers measured by limiting-dilution assays (top) and percentages of intracellular infectivity per total (intra- and extracellular) infectivity for the dish (bottom). Viral RNA (G) and HCV core protein (H) release into culture supernatant at 72 h postelectroporation measured by qRT-PCR and ELISA, respectively. GNN is a replication-incompetent HCV strain. ΔE1-E2 is an assembly-defective mutant. Results in panels C to H represent data pooled from at least two independent experiments each with 3 to 10 biological replicates. Shown are the mean ± SD. *, $P < 0.05$; **, $P < 0.01$; ***, $P < 0.001$ (relative to the corresponding WT; one-way [C and E to H] or two-way [D] ANOVA with Dunnett's *post hoc* test).

total (intra- plus extracellular) infectivity (Fig. 2F). The magnitude of intracellular particle accumulation correlated with the effect of these mutations on viral release. We also measured the effect of these mutations on the release of noninfectious core protein- and RNA-containing particles. Detectable levels of HCV RNA and core protein release

were measured in culture supernatants by quantitative reverse transcription (qRT)-PCR and enzyme-linked immunosorbent assay (ELISA), respectively (Fig. 2G and H), as previously described (11, 36). Nevertheless, the levels of defective particles released by the various NS2 mutants correlated with the infectious titers and were not higher than those released by the assembly-defective ΔE1-E2 mutant (Fig. 2G and H). Together, these results suggest that NS2 dileucine motifs mediate binding to AP-1A, AP-1B, and AP-4 and consequently HCV release.

AP-1A, AP-1B, and AP-4 mediate HCV release. We and others have previously demonstrated that the μ (AP1M1), u (AP1S3), and $"'$ (AP1G1) subunits of the AP-1A complex are required for HCV release (8, 37–40). Here, we sought to determine whether the AP-1B and AP-4 complexes, which emerged in the PCA screening as binding partners of NS2, are also required for infectious HCV production. To do so, we established Huh7.5 cell lines stably expressing short hairpin RNAs (shRNAs) targeting the various AP genes or a nontargeting (NT) sequence and transfected them with J6/JFH(p7-Rluc2A), a luciferase reporter virus, RNA (50). Effective suppression of APs was achieved (Fig. 3A) without apparent cytotoxic effects (Fig. 3B). AP-1A, AP-1B, AP-4, and AP-2 depletion had no effect on HCV RNA replication, as measured by luciferase assays at 5 and 72 h posttransfection (Fig. 3C). Inoculation of naive cells with clarified cell lysates derived from the HCV RNA-transfected (AP-depleted or NT control) cells resulted in comparable intracellular infectivity (Fig. 3D). Nevertheless, AP-1A, AP-1B, and AP-4 depletion caused a ~1-log reduction in extracellular infectivity upon inoculation of naive cells with supernatants derived from the HCV RNA-transfected cells. This effect on HCV release correlated with the level of AP-1A and AP-4 suppression. In contrast, as we previously reported (36), AP-2 depletion reduced both intra- and extracellular infectivity (Fig. 3D). Moreover, AP-1A, AP-1-B, and AP-4 depletion reduced the extracellular but not intracellular viral titer and significantly increased the accumulation of infectious intracellular viral particles (Fig. 3E to G). Importantly, ectopic expression of shRNA-resistant AP-1A, AP-1B, and AP-4 reversed the effect of the respective shRNAs on HCV release (Fig. 3E to G). Lastly, the observed defect in HCV release was not associated with increased release of noninfectious viral particles, as indicated by the levels of HCV RNA and core protein in supernatants derived from cells depleted of these APs (Fig. 3H and I). These results indicate that while AP-2 mediates HCV assembly, AP-1A, AP-1B, and AP-4 mediate HCV release.

Differential requirement for host APs in distinct modes of HCV spread. To determine whether AP-1A, AP-1B, and AP-4 specifically mediate the release of secreted and/or cell-to-cell-transmitted viruses, we first studied the effect of their depletion on cell-free infectivity. Stable cell lines depleted of AP-1A, AP-1B, or AP-4 and NT control cells (Fig. 3A) were electroporated with J6/JFH(p7-Rluc2A) RNA and incubated for 72 h. The infectivity of cell-free virus was measured in a single cycle, independently of cell-to-cell spread, via luciferase assays 6 h following the inoculation of naive Huh7.5 cells with culture supernatants derived from the electroporated cells. Depletion of AP-1A, AP-1B, and AP-4 significantly reduced cell-free infectivity relative to that of the NT control (Fig. 4A).

Next, we measured the effect of AP-1A, AP-1B, or AP-4 depletion on HCV cell-to-cell spread by coculture assays (14, 16, 51). Cell lines stably expressing shRNAs targeting AP-1A, AP-1B, AP-4, or an NT sequence (Fig. 3A) were electroporated with Jc1 HCV RNA (52). At 72 h posttransfection, these HCV donor cells were cocultured with green fluorescent protein (GFP)-expressing Huh7.5 target cells at a 1:2 ratio for 48 h. This was followed by immunostaining for HCV NS5A protein and quantification of the percentage of newly infected target cells (GFP+ NS5A+) in the target cell population (GFP+) by flow cytometry (Fig. 4B). To block cell-free transmission, as previously shown (14), extracellular infectious virus was neutralized by the addition of anti-E2 antibodies to the culture medium immediately following electroporation, as well as during the coculturing step. Effective blocking of cell-free infectivity was confirmed (Fig. S2A and B). Suppression of AP-1B and AP-4, but not AP-1A, significantly reduced HCV cell-to-cell
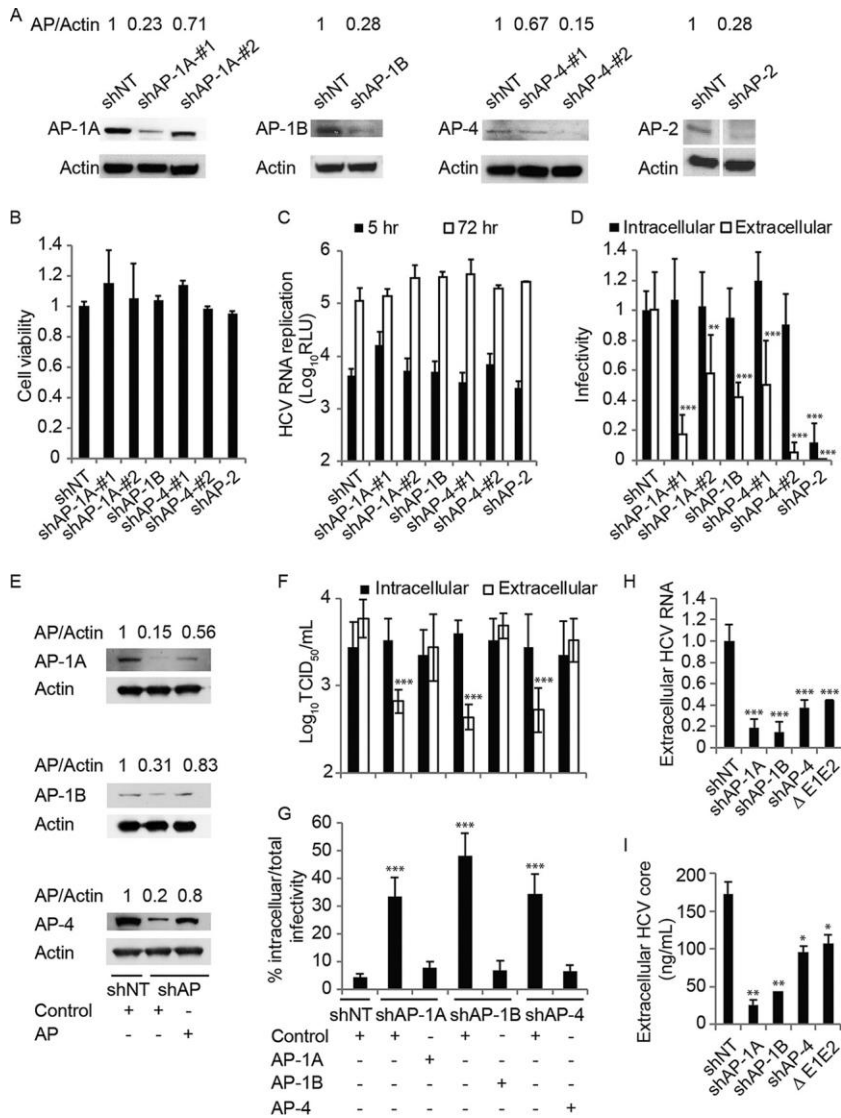
51

mBio®

FIG 3 AP-1A/B and AP-4 mediate HCV release. (A) Confirmation of gene expression knockdown by Western blotting in Huh7.5 cells stably expressing AP shRNA or an NT control (values are AP-to-actin protein ratios relative to the NT control). (B) Relative cell viability in these cell lines measured by alamarBlue assays. (C) HCV RNA replication measured via luciferase assays 5 and 72 h after HCV RNA electroporation. RLU, relative light units. (D) HCV infectivity measured via luciferase assay by inoculating naive cells with lysates (intracellular) and supernatants (extracellular) from electroporated cells. (E to G) Levels of APs by Western blot analysis (E), intra- and extracellular viral titers measured by limiting-dilution assays (F), and intracellular infectivity as a percentage of the total infectivity (G) in cells concurrently transduced with shAP-1A, shAP-1B, and shAP-4 and transfected with the respective shRNA-resistant AP cDNA or an empty control plasmid. (H and I) Viral RNA (H) and core protein (I) release into the culture supernatant at 72 h postelectroporation measured by qRT-PCR and ELISA, respectively. Data are plotted relative to NT control values. Results in panels C, D, and F to I represent data pooled from three independent experiments each with three to six biological replicates. Shown are the mean ± SD. *, $P < 0.05$; **, $P < 0.01$; ***, $P < 0.001$ (relative to the corresponding NT control; one-way [B, D, and F to I] or two-way [C] ANOVA with Dunnett's [C, D, H, and I] or Tukey's [F and G] post hoc test).

spread (Fig. 4C). Overexpression of shRNA-resistant AP-1B and AP-4 (Fig. 3E) reversed the inhibitory effect of AP-1B and AP-4 depletion on cell-to-cell spread, respectively (Fig. 4D and E). Moreover, ectopic expression of AP-1A did not reverse the effect of AP-1B depletion on cell-to-cell spread, suggesting that the two adaptors do not have a redundant role in HCV spread. In contrast, ectopic expression of AP-1B in cells depleted of AP-1A increased cell-to-cell spread relative to the comparable level mea-sured in AP-1A-depleted cells and NT controls expressing a control plasmid (Fig. 4D
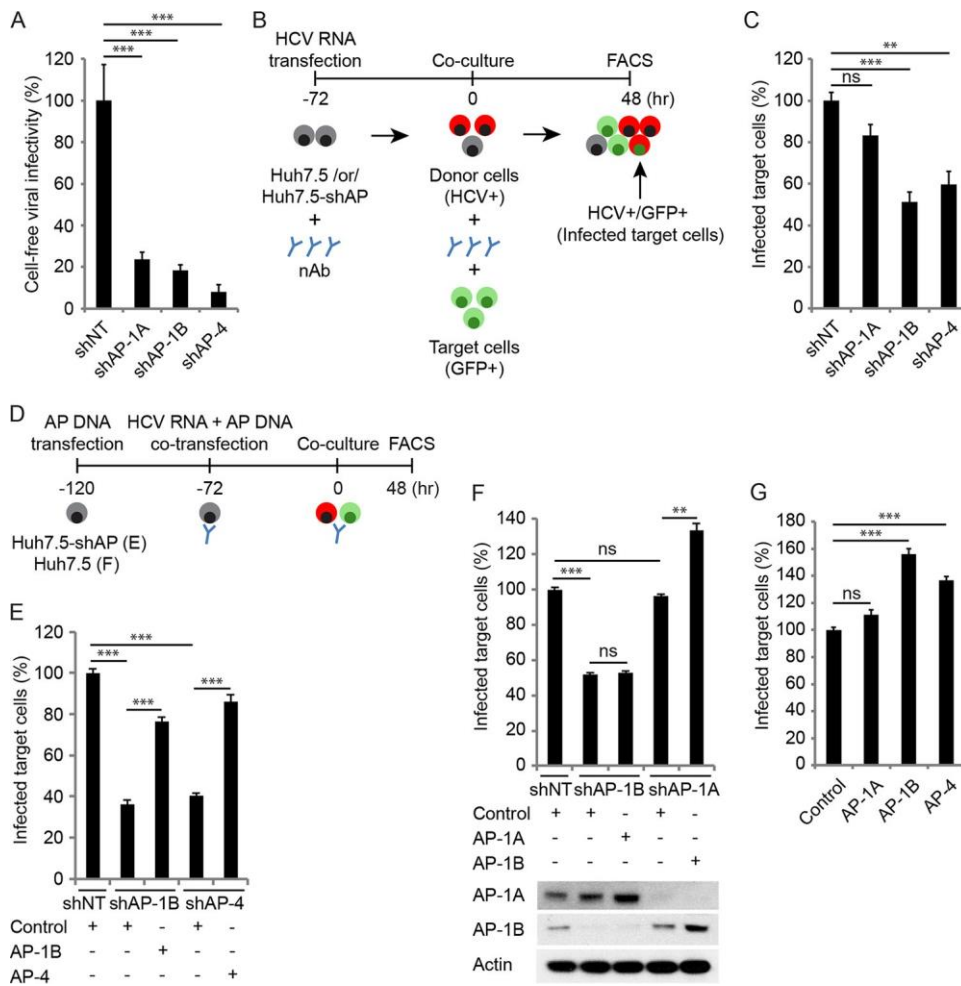
FIG 4 AP-1B and AP-4 mediate HCV cell-to-cell spread. (A) Cell-free infectivity measured via luciferase assays 6 h postinoculation of naive cells with supernatants derived from HCV RNA-transfected Huh7.5 cells stably expressing AP shRNA or an NT control. (B) Schematic of the coculture assay. (C) Cell-to-cell spread 48 h after coculturing of HCV RNA-transfected donor cells depleted of AP or NT controls with GFP-expressing target cells measured via FACS analysis following staining of HCV NS5A. Plotted is the percentage of infected target cells (NS5A$^+$ GFP$^+$) in the target cell population (GFP$^+$) pooled from two independent experiments relative to the NT control. (D) Schematic of the experiments displayed in panels E to G. (E, F) Cell-to-cell spread (E and F, top) and expression (see Fig. 3E and F, bottom) in cells concurrently transduced with lentiviruses expressing the shRNAs indicated and transfected with shRNA-resistant GLuc-tagged AP-1A, AP-1B, or AP-4 or an empty control. (G) Cell-to-cell spread in Huh7.5 cells following transfection with the GLuc-tagged APs indicated or an empty control. ns, nonsignificant. Representative experiments of at least two conducted, each with three biological replicates, are shown. Shown are the mean ± SD. *, $P < 0.05$; **, $P < 0.01$; ***, $P < 0.001$ (relative to the corresponding NT control; one-way ANOVA with Dunnett's [A, C, and G] or Tukey's [E and F] post hoc test).

and F). In agreement with these results, ectopic expression of AP-1B and AP-4, but not AP-1A, in WT Huh7.5 cells increased cell-to-cell spread, further supporting the differential roles of these adaptors in viral spread (Fig. 4D and G). Whereas depletion of AP-1A, AP-1B, and AP-4 suppressed the release of HCV genotype 1a H77S (53), depletion of AP-1B and AP-4, but not AP-1A, suppressed cell-to-cell H77S spread (Fig. S2C to F), indicating that the observed differential adaptor requirement is not specific to genotype 2a.

Together, these data demonstrate a differential coopting of APs in distinct modes of viral spread and are in line with the functions of these AP adaptors in polarized epithelia (17, 20–23).

HCV particles cotraffic with AP-4 in a post-TGN compartment. To define the mechanism by which AP-4 mediates its role in HCV infection, we tested our hypothesis that AP-4 facilitates HCV particle trafficking during viral release. To do so, we used

live-cell imaging to monitor the cotrafficking of individual, infectious HCV particles harboring a tetracysteine (TC) tag within the core protein (TC-core) with AP-4. We have previously shown that while static TC-core associates with LDs, motile TC-core requires HCV virion assembly (8, 54). Motile TC-core cotraffics with RNA, ApoE, microtubules, and components of the secretory pathway (8). Additionally, a fraction of HCV TC-core particles cotraffics with the AP-1A (25%) or AP-2 (38%) complexes (39).

Analysis of TC-core puncta stained with the biarsenical dye FlAsH revealed that the largest fraction of motile TC-core cotrafficked with AP-4 (~60%), followed by AP-1B (~54%), whereas only 3% cotrafficked with the autophagosomal marker LC3 (Fig. 5A). Approximately half of the TC-core/AP-4 puncta move with velocities and distances similar to those of AP-1A, AP-1B, and AP-2 (Fig. 5B and C; Movies S1 to S3). These slower, short-range, AP-4-associated TC-core puncta traffic at velocities that are consistent with previous reports on secretory vesicle trafficking and TC-core punctum cotrafficking with vesicle-associated membrane protein (VAMP), AP-1A, and AP-2 (8, 39, 55) (Fig. 5B and C). The remaining TC-core/AP-4 puncta cotraffic at significantly higher velocities and over longer distances than the other AP-associated puncta, suggesting that they may have a distinct trafficking pattern (Fig. 5B and C).

Next, we determined the role of core and NS2, two AP binding viral proteins required for virion assembly, in HCV particle trafficking with AP-4. To do so, we monitored the cotrafficking of AP-4 with TC-core HCV harboring either a mutation (Y136A) within a YXXØ motif of core, a motif critical for interaction and cotrafficking with AP-2 and for HCV assembly (36, 39), or a deletion of NS2. The Y136A core mutation did not alter AP-4 colocalization with TC-core puncta (Fig. 5D; Movie S4). Moreover, while this mutation reduced the overall percentage of motile TC-core puncta by >60% relative to WT TC-core, it did not alter the proportion or velocity of particles that cotraffic with AP-4 (Fig. 5D and E; Movie S4). TC-core puncta only partially overlapped AP-4 puncta in the context of infection with the NS2 deletion virus, suggesting that they are juxtaposed (Fig. 5D and E). However, AP-4-associated TC-core punctum motility was entirely abolished (0% moving particles) upon the deletion of NS2, as measured by the overall distance traveled (Fig. 5D and E; Movie S5). These results suggest that while another viral protein may be required to recruit AP-4 to the proximity of HCV sites of assembly, NS2 is absolutely essential for full colocalization of HCV particles with AP-4 and their cotrafficking. Since NS2 is essential for virion assembly, we introduced the AP-4 binding dileucine motif double mutation into TC-core (TC-core DM). Cotrafficking of this TC-core DM with AP-4 was significantly reduced relative to that of WT TC-core, although some cotrafficking occurred with the mutant (Fig. 5D and E; Movie S6). This suggests that the dileucine motifs are required for some AP-4 cotrafficking (and functional release) and that either a subset of cotrafficking is independent of the dileucine motifs or, alternatively, the mutation reduces but does not abolish AP-4 interactions (as in Fig. 2C).

Phosphatidylinositol-4 kinase III l is a Golgi compartment lipid kinase that is important in Golgi compartment structure and function, in addition to being involved in HCV egress (8, 56). PIK93 is a kinase inhibitor that at 0.5 μM inhibits phosphatidylinositol-4 kinase III l (57, 58). This concentration of PIK93 inhibits TC-core trafficking to post-Golgi compartments, leading to enhanced accumulation in the TGN (8). To test our hypothesis that cotrafficking of viral particles with AP-4 is via the secretory pathway, we treated HCV-infected cells with 0.5 μM PIK93. PIK93 treatment did not alter colocaliza- tion of AP-4 with TC-core puncta or the traffic of slowly moving TC-core–AP-4 puncta; however, it eliminated the rapidly moving, long-range TC-core–AP-4 puncta (Fig. 5F). PIK93 thus significantly reduced the average velocity of the population of rapidly moving TC-core puncta cotrafficking with AP-4. The rapidly moving particles that cotraffic with AP-4 are therefore indicative of transport at a post-Golgi compartment. Moreover, a 6-h PIK93 treatment of cocultures of HCV RNA-transfected and GFP target cells inhibited cell-to-cell spread (Fig. 5G), suggesting that the cotrafficking of the rapidly moving particles with AP-4 is involved in cell-to-cell spread. To further define the role of NS2 in the observed transport, we studied its localization in post-Golgi
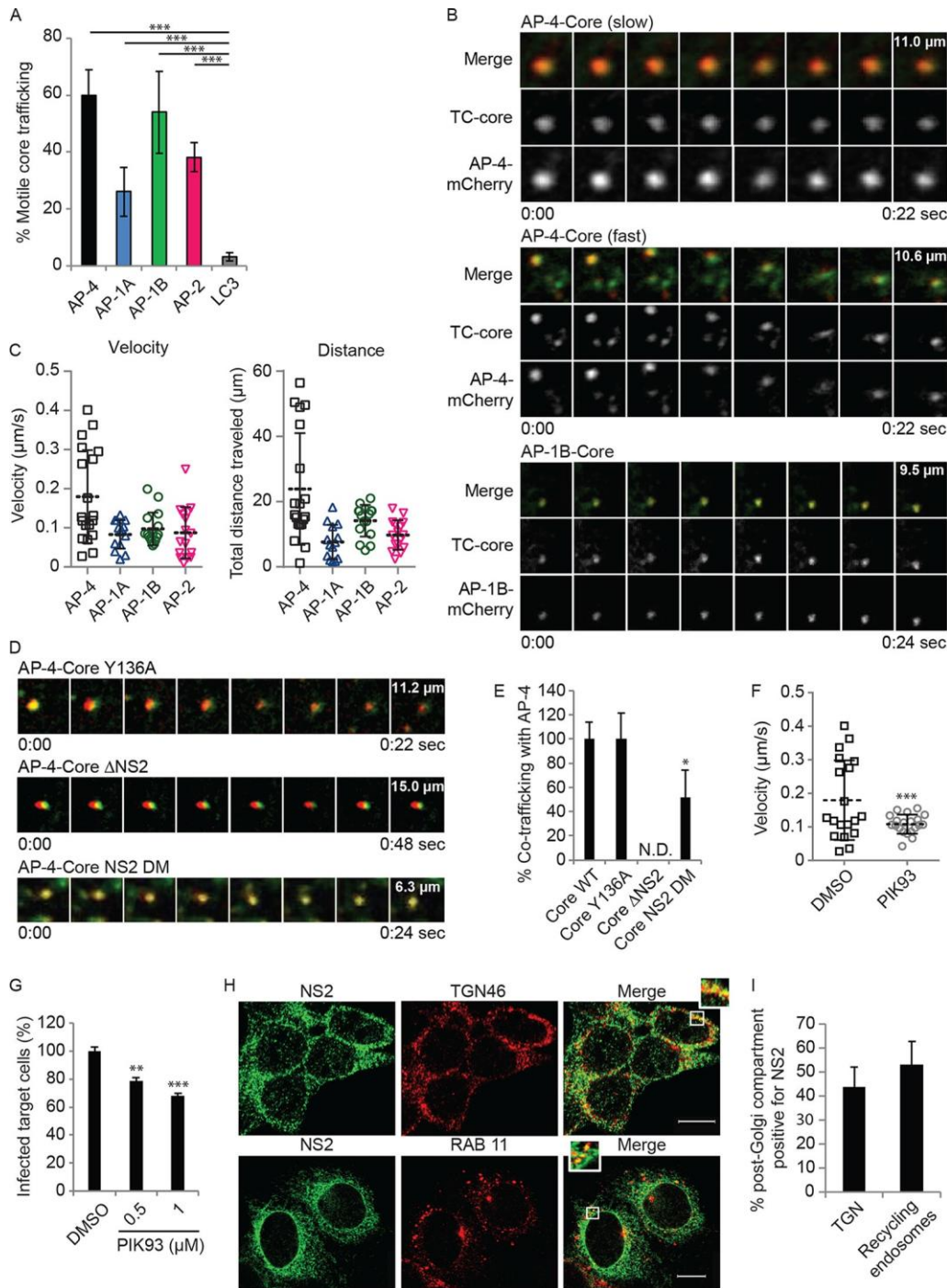
54

FIG 5 HCV particles cotraffic with AP-4 in a post-TGN compartment. (A) Quantification of motile TC-core puncta cotrafficking with AP-4, AP-1A, AP-1B, AP-2, and LC3. (B) Representative live-cell fluorescence microscopy montages of TC-core HCV (green) cotrafficking with AP-4-mCherry (top and panels middle) or AP-1B-meCherry (bottom) (red). The time elapsed (seconds) during video acquisition and the vertical dimension of the crop (micrometers) are indicated. (C) Velocity (left) and total distance traveled (right) of individual TC-core puncta cotrafficking with AP-4, AP-1A, AP-1B, or AP-2. (D and E) Representative montages (D) and quantitative data relative to WT TC-core (E) from live cell fluorescence microscopy of AP-4 cotrafficking with Y136A (top), NS2 deletion (middle), and NS2 double dileucine (DM; bottom) TC-core mutants. (F) Quantification of velocity per acquisition of WT TC-Core associated with AP-4 upon treatment with PIK93. (G) HCV cell-to-cell spread measured by FACS analysis following a 6-h treatment of cocultures of HCV RNA-transfected Huh7.5 donor cells and GFP-expressing target cells with PIK93. (H) Representative confocal IF microscopy images at X40 magnification of NS2 (green) and TGN46 (red) or RAB11 (red) in HCV-transfected cells. $n = >25$. Scale bars represent 10 μm. (I) Quantitative colocalization analysis of z stacks by using Manders' colocalization coefficients. Mean M2 values are represented as percent colocalization (the fraction of green intensity that coincides with red intensity $\pm$ SD). N.D., not detected. Experiments were replicated at least twice. *, $P < 0.05$; **, $P < 0.01$; ***, $P < 0.001$ (one-way ANOVA with Dunnett's *post hoc* test [A, E, and G] or two-tailed unpaired t test [F]).

compartments by a quantitative confocal IF analysis. As shown in Fig. 5H and I, 44% ± 8% of the TG46-labeled TGN and 53% ± 10% of the RAB11-labeled recycling endo- somes stained positive for NS2 in HCV-infected cells (n = 25 to 40 cells), suggesting localization in post-Golgi compartments in addition to the ER and ER-derived struc- tures.

Together, these findings reveal the mechanistic involvement of AP-4 in late steps of the HCV life cycle and provide direct evidence of a role for additional APs in the mediation of intracellular viral trafficking.

AP-1B regulation by AAK1 and GAK modulates NS2 binding and HCV cell-to-cell spread. Next, we tested whether AAK1 and GAK regulate NS2–AP-1 binding by studying the effect of phosphorylation site (T144A) mutant AP-1 (59) on NS2 binding. A T144A mutation in AP-1A or AP-1B did not impair protein expression, yet it reduced NS2 binding by ~2-fold, as measured by PCAs (Fig. 6A and B).

We previously reported that ectopic expression of WT but not T144A mutant AP-1A increased HCV release (39). Here, we studied the role of the T144 residue of AP-1B in the regulation of cell-to-cell spread by using coculture assays as described above. Ectopic expression of WT but not T144A AP-1B mutant increased HCV cell-to-cell spread (Fig. 6C). Moreover, in contrast to WT AP-1B (Fig. 4E), overexpression of T144A mutant AP-1B did not reverse the defect in cell-to-cell spread induced by AP-1B suppression (data not shown).

To test our hypothesis that AAK1 and GAK regulate the NS2–AP-1B interaction, we conducted binding experiments with Huh7.5 cells following the knockout of AAK1 or GAK by CRISPR/Cas9 (Fig. 6D). Knockout of either AAK1 or GAK significantly reduced NS2–AP-1B binding compared to that seen with an NT control, as measured by PCAs (Fig. 6E).

These results suggest that AP-1A and AP-1B phosphorylation by AAK1 and GAK stimulates their binding to NS2 and regulates AP-1B-mediated HCV cell-to-cell spread in addition to cell-free viral release (39).

Pharmacological inhibition of NS2–AP-1B binding and HCV cell-to-cell spread. To determine whether NS2–AP-1B binding and HCV cell-to-cell spread could be inhib- ited pharmacologically and further validate AAK1 and GAK as antiviral targets, we treated cells with selective AAK1 and GAK inhibitors. Compound 7745 is an imidazo[1,2-b]pyridazine-based molecule originally developed to modulate AAK1 activity as a potential treatment of neurological disorders ($K_d = 1$ nM; 50% inhibitory concentration, <10 nM) (Fig. 6F) (39, 60). The isothiazolo[5,4-b]pyridine 12i (Fig. 6F) is a potent ($K_d = $ ~8 nM), selective, ATP-competitive GAK inhibitor capable of restricting HCV and dengue virus (DENV) infections (39, 41). We measured the inhibition of NS2–AP-1B binding following treatment with both compounds (Fig. 6G). Consistent with these findings, we also measured the inhibition of NS2–AP-1B binding by PCAs upon treatment with sunitinib and erlotinib, two approved anticancer drugs with potent, albeit nonselective, anti-AAK1 and/or anti-GAK activity (Fig. 6G).

We previously reported that these compounds inhibit the entry and intra- and extracellular infectivity of HCV and DENV (35, 36, 39, 41). Here, we used these phar- macological tools to probe the role of AAK1 and GAK in HCV cell-free and cell-to-cell spread independently of their roles in viral entry and assembly. To measure the effect of these compounds on cell-free infectivity, HCV RNA-transfected Huh7.5 cells were treated at 72 h posttransfection for 6 h (Fig. 6H). Compounds were then washed, cells were incubated with fresh medium for an additional 6 or 12 h, and supernatants were used to inoculate naive cells, which were then subjected to luciferase assays at 72 h. Treatment with the individual four compounds for 6 h (Fig. S3A) or 12 h (Fig. 6H) significantly reduced cell-free infectivity. The observed defect in HCV cell-free infectivity was not associated with increased release of noninfectious viral particles, as indicated by the levels of HCV RNA and core protein in supernatants derived from cells depleted of these APs (Fig. S3B and C).

To determine an effect on cell-to-cell HCV spread, treatment was initiated upon the coculturing of Huh7.5 HCV donor cells and GFP-expressing target cells for 6 h in the
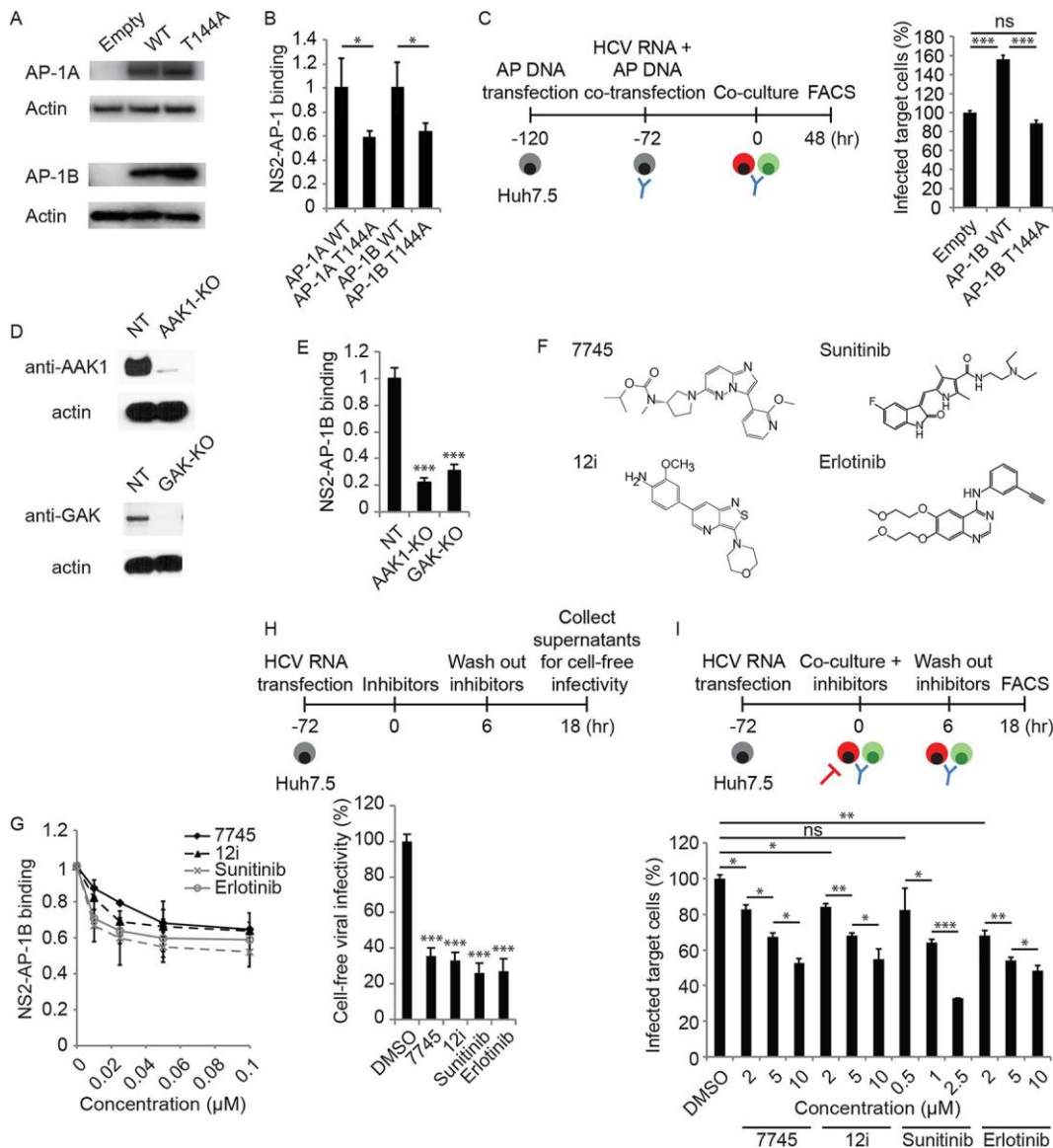
56

FIG 6 AAK1 and GAK regulate NS2–AP-1 binding and HCV cell-free and cell-to-cell spread. (A) AP-1 expression following transfection of Huh7.5 cells with GLuc-tagged WT or T144A mutant AP-1A/B or an empty control and blotting with anti-GLuc and anti-actin antibodies. (B) NS2 binding to WT and T144A mutant AP-1A/B measured by PCA. Data are plotted relative to the respective WT control. (C) HCV cell-to-cell spread in AP-1B-overexpressing cells versus an empty-vector control measured via FACS analysis 48 h following coculturing of HCV RNA-transfected donor Huh7.5 cells with GFP-expressing target cells. (D) Confirmation of gene expression knockout (KO) by Western blotting in Huh7.5 cells transduced with CRISPR subgenomic RNA lentivirus targeting AAK1 or GAK or an NT control. (E) NS2 binding to AP-1B measured in AAK1 and GAK knockout cells by PCAs. Data are plotted relative to the control cells. (F) Chemical structures of the compounds indicated. (G) Effects of the compounds indicated on NS2–AP-1B binding measured by PCA. (H) Cell-free infectivity of culture supernatants collected following a 6-h treatment of HCV RNA-transfected cells with the four individual compounds at a concentration of 10 μM (compound 7745, 12i, and erlotinib) or 2.5 μM (sunitinib), followed by compound removal and a 12-h incubation in fresh medium, measured via luciferase assay at 72 h postinoculation of naive cells. (I) Dose response of HCV cell-to-cell spread to the compounds indicated measured by FACS analysis following a 6-h treatment of cocultures of HCV RNA-transfected Huh7.5 donor cells and GFP-expressing target cells. Shown in panels B, C, E, and G to I are representative results of experiments from at least two conducted, each with three to six biological replicates. Shown are the mean ± SD. ns, not significant; *, $P < 0.05$; **, $P < 0.01$; ***, $P < 0.001$ (relative to WT AP-1 [B] or an empty-vector [C], NT [E], or vehicle [G to I] control; two-tailed unpaired t test [B], one-way ANOVA with Tukey's [C] or Dunnett's [E, H, and I] post hoc test).

presence of neutralizing anti-E2 antibodies (Fig. 6I). Following the removal of residual inhibitors and 12 h of incubation, cocultures were stained with anti-NS5A antibody and analyzed by flow cytometry. Treatment with various concentrations of all four compounds resulted in dose-dependent inhibition of cell-to-cell spread (Fig. 6I), with no

appreciable toxicity at the concentrations used (data not shown). Notably, a 6-h treatment of HCV RNA-transfected cells with the four individual compounds had no effect on the assembly of new viral particles, as measured by intracellular infectivity (Fig. S3D). These findings indicate that the effect of these compounds on HCV cell-free and cell-to-cell spread is independent of their effect on HCV entry and assembly.

Together, these data suggest that, in addition to regulating HCV entry and assembly (35, 36), AAK1 and GAK are involved in the regulation of HCV cell-free and cell-to-cell spread.

DISCUSSION

It has been unknown which viral determinants and cellular adaptors are essential for HCV particle traffic during the release of cell-free- or cell-to-cell-transmitted virus. And while clathrin-associated AP-1 and AP-2 complexes have been implicated in multiple viral infections (31, 32, 61, 62), the involvement of the non-clathrin-associated AP-4 complex in viral infection and its precise mechanistic involvement were not characterized. Moreover, the relevance of AP complexes to viral cell-to-cell spread remained unknown. Here, we set out to address this knowledge gap. By integrating proteomic, RNA interference (RNAi), viral genetic, advanced live-cell imaging, and pharmacological approaches, we provide evidence that two conserved heretofore unrecognized dileucine motifs in NS2 mediate AP-1A, AP-1B, and AP-4 binding and HCV release. Moreover, we demonstrate differential HCV hijacking of these AP complexes to facilitate the trafficking of HCV particles during cell-free and cell-to-cell spread. Lastly, we establish that, in addition to viral entry, assembly, and cell-free virus release, HCV cell-to-cell spread is also regulated by AAK1 and GAK and is susceptible to their pharmacological inhibition.

NS2 was identified in our PCA screening and co-IP experiments as a prominent binding partner of the μ subunits of AP-1A, AP-1B, and AP-4. AP-4 also interacted with NS5A. These data, together with the finding that AP-2 binds HCV core with the highest apparent affinity, indicate differential binding of APs by individual HCV proteins. Moreover, we reveal that two dileucine motifs within NS2 mediate AP-1A, AP-1B, and AP-4 binding. These results are in agreement with prior reports of tyrosine and dileucine motif binding to AP μ subunits (31–34) and display the flexibility of interac-tions for an individual AP binding motif with the μ subunits of several distinct AP complexes (31, 63, 64).

Infectivity assays revealed that, in addition to previously reported N-terminal resi-dues (11), the dileucine motifs in the C terminus of NS2 are also essential for HCV release. Whereas NS2 mutations had no effect on the absolute intracellular infectivity, they significantly increased the ratio of intracellular infectivity to total (intra- plus extracellular) infectivity in line with prior reports (11). The effect of NS2 mutations on HCV release was greater than their effect on AP binding, presumably because of differences in the dynamic range of the assays. Nevertheless, our data indicate that these motifs are required for a functional interaction. It was previously speculated that the L217 residue, which is locked in the active site of the protease domain of NS2, mediates its role in infectious virus production via interactions with host proteins (9). We provide evidence that L217 and additional NS2 C-terminal leucine residues play a role in infectious HCV production in part by binding AP-1A, AP-1B, and AP-4. Some of the leucine residues are within the NS2 dimer interface based on the structure of the catalytic domain of the NS2-3 protease (46). Nevertheless, it is possible that the interaction with APs is via the monomeric and not the dimeric form of NS2, suggesting a potential change in confirmation, as previously shown with other viral (65) and host (66) proteins. While the first leucine motif includes a functional acidic residue (D207), the second motif resembles previously described dileucine-based motifs lacking acidic residues (67, 68). We thereby define the mechanism by which NS2 interacts with host APs and genetically validate the requirement for two dileucine motifs in HCV release.

We previously reported that AP-2 is essential for HCV assembly (36). Moreover, we and others showed that AP-1A is required for HCV release (8, 37–39). In this study, we

extended these observations by demonstrating a role for AP-1B in HCV infection and for AP-4 in any viral infection. Moreover, prior studies have focused on the mechanisms that facilitate HCV entry into the recipient neighboring cell (12, 51, 69), rather than those involved in the sorting of virions toward the sites of cell-cell contact in the plasma membrane within the donor cell. Our data thus provide insight into these mechanisms. Since cell-to-cell spread represents a mechanism by which HCV evades immune clearance and establishes persistence (12–14), our results suggest that host APs may be involved in the facilitation of HCV persistence. Notably, a tyrosine-based motif in the HIV-1 envelope glycoprotein is essential for the mediation of cell-to-cell spread (70), yet a requirement for APs in the cell-to-cell spread of a virus has not been described yet. Our findings may thus encourage future investigations of these mechanisms in other viruses that establish persistent infection.

Our advanced live-cell imaging data provide direct evidence that the majority of HCV particles cotraffic intracellularly with AP-4, followed by AP-1B, AP-1A, and AP-2, thereby indicating the critical roles of AP-4 in intracellular HCV traffic. These results raise the following question: why does HCV utilize three adaptors to traffic during its release? We favor the explanation that AP-1A, AP-1B, and AP-4 mediate viral traffic in distinct pathways. Although all three complexes sort in post-Golgi compartments, multiple studies indicate that they function in physically and functionally distinct membrane domains. AP-1B and AP-4 have been implicated in sorting to the basolateral membrane, while AP-1A and AP-4 have been implicated in sorting between the TGN and recycling endosomes (20, 21). Whereas there is evidence that AP-1A can also be involved in basolateral sorting and that AP-1B can compensate for a lack of AP-1A, this was documented specifically in MDCK cells (71), whose protein trafficking is substantially different from that of hepatocytes (72).

Differences in the μ subunits of the otherwise closely homologous AP-1A and AP-1B complexes (79% amino acid sequence identity [73]) and differential preferences for specific membrane lipids define their distinct functions (20, 22, 74, 75). Our data provide evidence that these two distinct proteins have differential functionality in HCV release, yet their patterns of cotrafficking with TC-core in terms of distance and velocity are similar. This suggests that AP-1A and AP-1B mediate distinct trafficking pathways that operate with similar kinetics. Indeed, our finding that ectopic expression of AP-1A does not reverse the effect of AP-1B depletion on cell-to-cell spread suggests that the two adaptors do not have a redundant role in HCV spread and are in line with prior reports that AP-1A cannot substitute for AP-1B in the basolateral sorting of cellular receptors (76, 77).

We demonstrate that while AP-1A, AP-1B, and AP-2 cotraffic with TC-core particles over short distances, two patterns of movement characterize HCV particles that cotraffic with AP-4: a slow, short-range pattern and a fast, long-range pattern. The short-range moving population that cotraffics with AP-1A, AP-1B, and AP-4 is consistent with the previously reported TC-core particles associated with apolipoprotein E and VAMP1 vesicles (8). On the basis of the functions of these APs in polarized epithelia, we predict that these particles traffic from the TGN to recycling endosomes. Since pharmacological inhibition of trafficking from the Golgi compartment to the plasma membrane disrupts both AP-4-associated long-range movement and HCV cell-to-cell spread and since AP-4 mediates cell-to-cell spread, the long-range pattern likely represents basolateral sorting. Our data also demonstrate that even though both AP-1B and AP-4 mediate cell-to-cell spread, the patterns of their cotrafficking with TC-core are different. This suggests that the two adaptors may either mediate trafficking in distinct pathways or act in two steps in the same pathway. Interestingly, in contrast to the clathrin-associated AP-1A, AP-1B, and AP-2 complexes, AP-4's coat protein has not been identified (19), and this complex mediates cargo transport in a clathrin-independent manner (78), providing a possible explanation for the observed differential phenotype. Together, our imaging findings contribute to our understanding of the complex mechanism by which these APs are involved in infectious HCV production and exclude a theory whereby AP complexes contribute to viral infections solely by recruiting or

59

mediating intracellular traffic of host cargo components essential for the viral life cycle or by mediating other roles (e.g., HCV E2 stabilization [38]). Further investigation is, however, required to understand exactly where in the secretory pathway these APs exert their functions. Although these APs appear to maintain at least some of their distinct sorting properties in our nonpolarized Huh7.5 cell culture model, it will be important to validate these findings in a more biologically relevant polarized cell model that supports authentic apical and basolateral sorting events. It is also possible that by interacting with several complexes, HCV coopts differential functions of these APs beyond post-Golgi traffic, such as exocyst complex recruitment for fusion with the plasma membrane by AP-1B (20). Lastly, utilizing different adaptors could facilitate differential and/or tighter regulation of HCV traffic.

We previously showed that AAK1 and GAK regulate HCV assembly and release by phosphorylating AP-2 and AP-1A, respectively (36, 39). Here, we show that regulation of AP-1B T144 by AAK1 and GAK increases both its apparent affinity for NS2 and cell-to-cell spread. Moreover, using pharmacological inhibitors of AAK1 and GAK, we further establish a novel role for these kinases in the regulation of cell-free and cell-to-cell viral spread. Since treatment with the kinase inhibitors was limited to 6 to 12 h (an incubation time that we show is too short to suppress viral assembly), the observed impairment of viral cell-free and cell-to-cell spread was likely to have resulted not from suppressed viral assembly but rather from suppressed spread of preformed particles. Additionally, collection of supernatants 12 h following compound removal from cell culture and inclusion of neutralizing anti-E2 antibodies enabled measure- ments of these compounds' effect on cell-free and cell-to-cell spread, respectively, independently of their effect on viral entry. These findings underscore the utility of these pharmacological tools in probing distinct steps of the HCV life cycle. Furthermore, they point to the potential of this antiviral approach to suppress the establishment and/or maintenance of viral persistence and possibly reduce viral escape and treatment failure (15, 16). Higher concentrations of the compounds were required to inhibit HCV release and cell-to-cell spread than to inhibit NS2–AP-1 binding. Such differences between biological and biochemical effects are typical for kinase inhibitors and often result from limited permeability and/or efflux (36, 79).

On the basis of these mechanistic data and our former work (35, 36, 39, 41), we propose a model wherein HCV proteins bind AP complexes to mediate intracellular traffic of HCV particles in temporally distinct steps of infectious HCV production (Fig. 7). In addition to playing an essential role in HCV endocytosis, AP-2 is recruited to the surface of LD by a tyrosine motif within core to mediate a role in HCV assembly (36). AP-1A, AP-1B, and AP-4 are recognized by dileucine motifs within NS2, and these interactions mediate HCV release. AP-1B and AP-4 also play a role in HCV cell-to-cell spread. The host cell kinases AAK1 and GAK represent "master regulators" of HCV infection; by stimulating AP-1A, AP-1B, and AP-2 interactions with host and viral proteins (such as core and NS2), they regulate HCV entry, assembly, release of cell-free virus, and cell-to-cell spread. Kinase inhibitors with activity against AAK1 and GAK, including selective inhibitors and already approved nonselective drugs such as sunitinib and erlotinib, inhibit these temporally distinct steps of the viral life cycle, in part by suppressing the cotrafficking of HCV particles with AP-1A and AP-2 (39).

It remains to be investigated precisely how NS2-AP binding facilitates HCV particle traffic. In the case of HIV, the envelope protein is thought to interact with APs to mediate traffic (34, 64). Similarly, HCV E2 was recently reported to bind AP1S3, the u subunit of the AP-1 complex (38). However, it is unclear how this interaction can occur topologically, since in contrast to HIV Env, the HCV E1 and E2 glycoproteins lack a cytosolic domain. NS2 was previously reported to mediate HCV release (11) and to alter the TGN architecture when expressed in the context of the HCV replicase (40), sug- gesting that in addition to the ER, it is localized in post-Golgi compartments. Indeed, our confocal IF analysis demonstrated significant localization of NS2 in both the TGN and recycling endosomes. One model predicts that NS2 may recognize a lipid enriched in HCV-containing vesicles, thereby bridging between the luminal virions and the
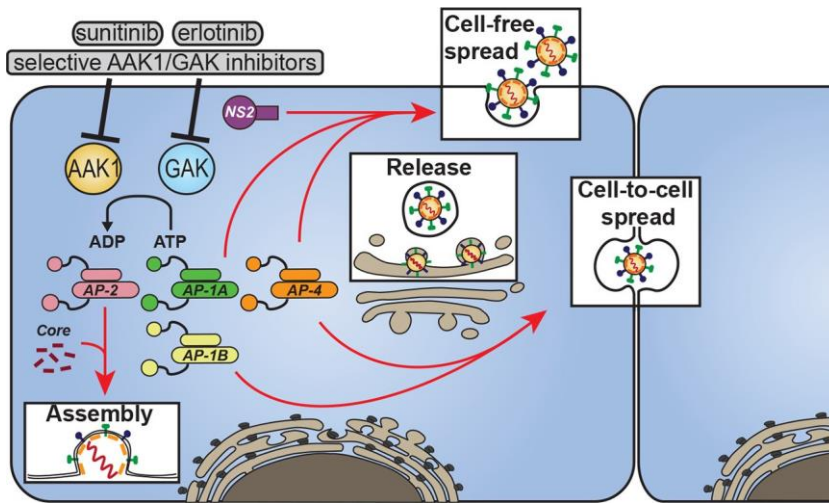
60

FIG 7 Model showing the orchestration of viral trafficking in late steps of the HCV life cycle by AP complexes and their regulators. HCV hijacks the AP-1A, AP-1B, AP-2, and AP-4 complexes to mediate intracellular traffic of viral particles in temporally distinct late steps of its life cycle. Host kinases AAK1 and GAK regulate the assembly and release of cell-free- and cell-to-cell-transmitted virus through phosphorylation of AP-1 (green and yellow) and AP-2 (pink). Sunitinib, erlotinib, and selective inhibitors of AAK1 and GAK disrupt these temporally distinct steps of the viral life cycle.

cytoplasmic APs. Alternatively, a transmembrane protein or protein complex may bind NS2 and a component of the virion. NS2 would then bind the AP complex, which recruits clathrin in the case of AP-1A and AP-1B (and another coat in the case of AP-4). Notably, our cotrafficking data indicate that upon NS2 deletion, TC-core puncta and AP-4 are not fully colocalized but rather juxtaposed, and the motility of TC-core punctum cotrafficking with AP-4 is completely abolished. These data support a critical role for NS2 in facilitating cotraffic with AP-4 but also suggest the existence of another factor(s) for the recruitment of AP-4 to the vicinity of HCV sites of assembly. Intriguingly, NS5A was identified in our PCA screening as another potential partner of AP-1A, AP-1B, and AP-4. We thus speculate that these complexes are first recruited, possibly by NS5A, and subsequently bind NS2. By interacting with the envelope glycoproteins within the secretory vesicle and the cytoplasmic AP complex, the transmembrane NS2 facilitates the traffic of viral particles between various distinct compartments in the secretory pathway.

In summary, our study uncovers novel virus and host determinants, as well as molecular mechanisms, underlying differential HCV trafficking during the release of cell-free- and cell-to-cell-transmitted viral particles with potential implications for pathogenesis of viral persistence and the design of novel antiviral strategies.

MATERIALS AND METHODS

The plasmids, reagents, antibodies, and RNAi used in this study are summarized in Text S1.

Cell cultures. Huh7.5 (Apath LLC) and 293T (ATCC) cells were grown in Dulbecco's modified Eagle's medium supplemented with 10% fetal bovine serum (Omega Scientific), 1X nonessential amino acids, 1% L-glutamine, and 1% penicillin-streptomycin (Gibco).

PCAs. PCAs with mammalian cells were conducted as described previously (36, 42) and in Text S1.

Co-IPs. Co-IPs in membrane fractions derived from HCV RNA-transfected cells or cells ectopically expressing NS2 and AP-4 were carried out as described previously (36, 42) and in Text S1.

***In vitro* transcription of HCV RNA, electroporation, and viral titration.** *In vitro* transcription of HCV RNA, electroporation, and viral titration were performed as previously reported (36).

HCV RNA replication and intra- and extracellular infectivity. As previously described (36, 50), HCV RNA replication was measured by luciferase assays (Promega) in Huh7.5 cell lysates 5 to 8 h and 72 h postelectroporation with J6/JFH(p7-Rluc2A) or pH77S.3/GLuc2A HCV RNA harboring a luciferase reporter. At 72 h, electroporated cells were trypsinized, centrifuged, resuspended in 500 μl of medium, lysed, and pelleted. To measure intra- and extracellular infectivity, these clarified lysates and culture supernatants, respectively, were used to inoculate naive cells in triplicate, followed by luciferase assays and limiting-dilution assays and 50% tissue culture infective dose ($TCID_{50}$) calculation (44) at 72 h. Accumulation of

infectious intracellular viral particles was calculated by dividing the intracellular infectivity by the sum of the intra- and extracellular infectivity for the dish.

Cell-free infectivity. As previously described (16, 51), Huh7.5 cells were electroporated with J6/ JFH(p7-Rluc2A) RNA and incubated for 72 h. Culture supernatants were used to inoculate naive cells in triplicate, followed by luciferase assays at 6 h. When relevant, inhibitors were added at 72 h posttrans- fection for 6 h of incubation. Compounds were then washed, cells were incubated with fresh medium for an additional 6 or 12 h, supernatants were used to inoculate naive cells, and luciferase assays were performed at 72 h.

Cell-to-cell spread assays. As previously described (14, 16, 80), Huh7.5 cells were transfected with Jc1 (52) or H77S (53) RNA and cocultured with naive target Huh7.5-GFP cells at a 1:2 ratio in the presence of 2 μg/ml neutralizing human anti-E2 antibodies (CBH-5) to block the spread of cell-free virus. Samples were fixed and permeabilized by Cytofix/Cytoperm (BD), stained with mouse anti-NS5A antibodies (Virostat), and analyzed by flow cytometry (Stanford shared fluorescence-activated cell sorter [FACS] facility) at different time points following coculture. Cell-to-cell spread was defined as the percentage of newly infected target cells (GFP+ NS5A+) in the target cell population (GFP+).

Viability assays. Viability was assessed by using alamarBlue reagent (Invitrogen) in accordance with the manufacturer's protocol. Fluorescence was detected at 560 nm on a Tecan Infinite M1000 reader.

Core protein ELISA. The concentration of released core protein was measured in clarified cell culture supernatants by ELISA (Cell Biolabs) against standard curves of recombinant core antigen in accordance with the manufacturer's instructions.

IF confocal microscopy. IF confocal microscopy was performed with Huh7.5 cells at 72 h posttrans- fection with HCV RNA. Colocalization was quantified via ImageJ (JACoP) software and M2 Manders' colocalization coefficients as previously described (36).

Live-cell imaging. Huh7.5 cells were infected with concentrated HCV TC-core at a multiplicity of infection of 1 for 24 h, transfected with AP-4–mCherry by using Lipofectamine 2000 (Invitrogen), and then seeded onto collagen-coated 35-mm FluoroDishes (World Precision Instruments, Inc.) (8, 39). When specified, TC-core-infected cells were incubated with dimethyl sulfoxide (DMSO) or PIK93 (0.5 μM) for 3 h beginning at 72 h postinfection. At 72 h postinfection, cells were labeled with biarsenical dye and time-lapse images were taken and analyzed as described in Text S1.

Generation of AAK1 and GAK knockout cell lines was performed as described in Text S1.

Statistical analysis. *P* values were calculated by two-tailed unpaired *t* test or one- or two-way analysis of variance (ANOVA) with either Dunnett's or Tukey's *post hoc* test.

SUPPLEMENTAL MATERIAL

Supplemental material for this article may be found at https://doi.org/10.1128/mBio .02233-17.

TEXT S1, PDF file, 1.7 MB.
FIG S1, TIF file, 0.7 MB.
FIG S2, TIF file, 0.3 MB.
FIG S3, TIF file, 0.1 MB.
MOVIE S1, AVI file, 0.3 MB.
MOVIE S2, AVI file, 0.3 MB.
MOVIE S3, AVI file, 0.01 MB.
MOVIE S4, AVI file, 0.3 MB.
MOVIE S5, AVI file, 1 MB.
MOVIE S6, AVI file, 0.01 MB.

REFERENCES

1. Polaris Observatory HCV Collaborators. 2017. Global prevalence and genotype distribution of hepatitis C virus infection in 2015: a modelling study. Lancet Gastroenterol Hepatol 2:161–176. https://doi.org/10.1016/S2468-1253(16)30181-9.

2. Lemon SM, Walker C, Alter MJ, Yi M. 2007. Hepatitis C viruses, p 1253–1304. In Knipe DM, Howley PM, Griffin DE, Martin MA, Lamb RA, Roizman B, Straus SL (ed), Fields virology, 5th ed. Lippincott, Williams & Wilkins, Philadelphia, PA.

3. Jones CT, Murray CL, Eastman DK, Tassello J, Rice CM. 2007. Hepatitis C virus p7 and NS2 proteins are essential for production of infectious virus. J Virol 81:8374–8383. https://doi.org/10.1128/JVI.00690-07.

4. Jirasko V, Montserret R, Lee JY, Gouttenoire J, Moradpour D, Penin F, Bartenschlager R. 2010. Structural and functional studies of nonstructural protein 2 of the hepatitis C virus reveal its key role as organizer of virion assembly. PLoS Pathog 6:e1001233. https://doi.org/10.1371/journal.ppat.1001233.

5. Gentzsch J, Brohm C, Steinmann E, Friesland M, Menzel N, Vieyres G, Perin PM, Frentzen A, Kaderali L, Pietschmann T. 2013. Hepatitis C virus p7 is critical for capsid assembly and envelopment. PLoS Pathog 9:e1003355. https://doi.org/10.1371/journal.ppat.1003355.

6. Bartenschlager R, Penin F, Lohmann V, André P. 2011. Assembly of infectious hepatitis C virus particles. Trends Microbiol 19:95–103. https://doi.org/10.1016/j.tim.2010.11.005.

7. Jones DM, McLauchlan J. 2010. Hepatitis C virus: assembly and release of virus particles. J Biol Chem 285:22733–22739. https://doi.org/10.1074/jbc.R110.133017.

8. Coller KE, Heaton NS, Berger KL, Cooper JD, Saunders JL, Randall G. 2012. Molecular determinants and dynamics of hepatitis C virus secretion. PLoS Pathog 8:e1002466. https://doi.org/10.1371/journal.ppat.1002466.

9. Dentzer TG, Lorenz IC, Evans MJ, Rice CM. 2009. Determinants of the hepatitis C virus nonstructural protein 2 protease domain required for production of infectious virus. J Virol 83:12702–12713. https://doi.org/10.1128/JVI.01184-09.

10. Popescu CI, Callens N, Trinel D, Roingeard P, Moradpour D, Descamps V, Duverlie G, Penin F, Héliot L, Rouillé Y, Dubuisson J. 2011. NS2 protein of hepatitis C virus interacts with structural and non-structural proteins towards virus assembly. PLoS Pathog 7:e1001278. https://doi.org/10.1371/journal.ppat.1001278.

11. de la Fuente C, Goodman Z, Rice CM. 2013. Genetic and functional characterization of the N-terminal region of the hepatitis C virus NS2 protein. J Virol 87:4130–4145. https://doi.org/10.1128/JVI.03174-12.

12. Timpe JM, Stamataki Z, Jennings A, Hu K, Farquhar MJ, Harris HJ, Schwarz A, Desombere I, Roels GL, Balfe P, McKeating JA. 2008. Hepatitis C virus cell-cell transmission in hepatoma cells in the presence of neutralizing antibodies. Hepatology 47:17–24. https://doi.org/10.1002/hep.21959.

13. Sattentau Q. 2008. Avoiding the void: cell-to-cell spread of human viruses. Nat Rev Microbiol 6:815–826. https://doi.org/10.1038/nrmicro1972.

14. Brimacombe CL, Grove J, Meredith LW, Hu K, Syder AJ, Flores MV, Timpe JM, Krieger SE, Baumert TF, Tellinghuisen TL, Wong-Staal F, Balfe P, McKeating JA. 2011. Neutralizing antibody-resistant hepatitis C virus cell-to-cell transmission. J Virol 85:596–605. https://doi.org/10.1128/JVI.01592-10.

15. Sigal A, Kim JT, Balazs AB, Dekel E, Mayo A, Milo R, Baltimore D. 2011. Cell-to-cell spread of HIV permits ongoing replication despite antiretroviral therapy. Nature 477:95–98. https://doi.org/10.1038/nature10347.

16. Xiao F, Fofana I, Heydmann L, Barth H, Soulier E, Habersetzer F, Doffoël M, Bukh J, Patel AH, Zeisel MB, Baumert TF. 2014. Hepatitis C virus cell-cell transmission and resistance to direct-acting antiviral agents. PLoS Pathog 10:e1004128. https://doi.org/10.1371/journal.ppat.1004128.

17. Owen DJ, Collins BM, Evans PR. 2004. Adaptors for clathrin coats: structure and function. Annu Rev Cell Dev Biol 20:153–191. https://doi.org/10.1146/annurev.cellbio.20.010403.104543.

18. Nakatsu F, Ohno H. 2003. Adaptor protein complexes as the key regulators of protein sorting in the post-Golgi network. Cell Struct Funct 28:419–429. https://doi.org/10.1247/csf.28.419.

19. Park SY, Guo X. 2014. Adaptor protein complexes and intracellular transport. Biosci Rep 34:e00123. https://doi.org/10.1042/BSR20140069.

20. Fölsch H. 2005. The building blocks for basolateral vesicles in polarized epithelial cells. Trends Cell Biol 15:222–228. https://doi.org/10.1016/j.tcb.2005.02.006.

21. Simmen T, Höning S, Icking A, Tikkanen R, Hunziker W. 2002. AP-4 binds basolateral signals and participates in basolateral sorting in epithelial MDCK cells. Nat Cell Biol 4:154–159. https://doi.org/10.1038/ncb745.

22. Fölsch H, Pypaert M, Schu P, Mellman I. 2001. Distribution and function of AP-1 clathrin adaptor complexes in polarized epithelial cells. J Cell Biol 152:595–606. https://doi.org/10.1083/jcb.152.3.595.

23. Gravotta D, Deora A, Perret E, Oyanadel C, Soza A, Schreiner R, Gonzalez A, Rodriguez-Boulan E. 2007. AP1B sorts basolateral proteins in recycling and biosynthetic routes of MDCK cells. Proc Natl Acad Sci U S A 104:1564–1569. https://doi.org/10.1073/pnas.0610700104.

24. Aguilar RC, Boehm M, Gorshkova I, Crouch RJ, Tomita K, Saito T, Ohno H, Bonifacino JS. 2001. Signal-binding specificity of the mu4 Subunit of the adaptor protein complex AP-4. J Biol Chem 276:13145–13152. https://doi.org/10.1074/jbc.M010591200.

25. Ricotta D, Conner SD, Schmid SL, von Figura K, Honing S. 2002. Phosphorylation of the AP2 u subunit by AAK1 mediates high affinity binding to membrane protein sorting signals. J Cell Biol 156:791–795. https://doi.org/10.1083/jcb.200111068.

26. Zhang CX, Engqvist-Goldstein AE, Carreno S, Owen DJ, Smythe E, Drubin DG. 2005. Multiple roles for cyclin G-associated kinase in clathrin-mediated sorting events. Traffic 6:1103–1113. https://doi.org/10.1111/j.1600-0854.2005.00346.x.

27. Ghosh P, Kornfeld S. 2003. AP-1 binding to sorting signals and release from clathrin-coated vesicles is regulated by phosphorylation. J Cell Biol 160:699–708. https://doi.org/10.1083/jcb.200211080.

28. Conner SD, Schmid SL. 2003. Differential requirements for AP-2 in clathrin-mediated endocytosis. J Cell Biol 162:773–779. https://doi.org/10.1083/jcb.200304069.

29. Umeda A, Meyerholz A, Ungewickell E. 2000. Identification of the universal cofactor (auxilin 2) in clathrin coat dissociation. Eur J Cell Biol 79:336–342. https://doi.org/10.1078/S0171-9335(04)70037-0.

30. Lee DW, Zhao X, Zhang F, Eisenberg E, Greene LE. 2005. Depletion of GAK/auxilin 2 inhibits receptor-mediated endocytosis and recruitment of both clathrin and clathrin adaptors. J Cell Sci 118:4311–4321. https://doi.org/10.1242/jcs.02548.

31. Craig HM, Reddy TR, Riggs NL, Dao PP, Guatelli JC. 2000. Interactions of HIV-1 Nef with the μ subunits of adaptor protein complexes 1, 2, and 3: role of the dileucine-based sorting motif. Virology 271:9–17. https://doi.org/10.1006/viro.2000.0277.

32. Greenberg M, DeTulleo L, Rapoport I, Skowronski J, Kirchhausen T. 1998. A dileucine motif in HIV-1 Nef is essential for sorting into clathrin-coated pits and for downregulation of CD4. Curr Biol 8:1239–1242. https://doi.org/10.1016/S0960-9822(07)00518-0.

33. Hofmann MW, Höning S, Rodionov D, Dobberstein B, von Figura K, Bakke O. 1999. The leucine-based sorting motifs in the cytoplasmic domain of the invariant chain are recognized by the clathrin adaptors AP1 and AP2 and their medium chains. J Biol Chem 274:36153–36158. https://doi.org/10.1074/jbc.274.51.36153.

34. Bhakta SJ, Shang L, Prince JL, Claiborne DT, Hunter E. 2011. Mutagenesis of tyrosine and di-leucine motifs in the HIV-1 envelope cytoplasmic domain results in a loss of Env-mediated fusion and infectivity. Retrovirology 8:37. https://doi.org/10.1186/1742-4690-8-37.

35. Neveu G, Ziv-Av A, Barouch-Bentov R, Berkerman E, Mulholland J, Einav S. 2015. AP-2-associated protein kinase 1 and cyclin G-associated kinase regulate hepatitis C virus entry and are potential drug targets. J Virol 89:4387–4404. https://doi.org/10.1128/JVI.02705-14.

36. Neveu G, Barouch-Bentov R, Ziv-Av A, Gerber D, Jacob Y, Einav S. 2012. Identification and targeting of an interaction between a tyrosine motif within hepatitis C virus core protein and AP2M1 essential for viral assembly. PLoS Pathog 8:e1002845. https://doi.org/10.1371/journal.ppat.1002845.

37. Benedicto I, Gondar V, Molina-Jiménez F, García-Buey L, López-Cabrera M, Gastaminza P, Majano PL. 2015. Clathrin mediates infectious hepatitis C virus particle egress. J Virol 89:4180–4190. https://doi.org/10.1128/JVI.03620-14.

38. Li X, Niu Y, Cheng M, Chi X, Liu X, Yang W. 2016. AP1S3 is required for hepatitis C virus infection by stabilizing E2 protein. Antiviral Res 131:26–34. https://doi.org/10.1016/j.antiviral.2016.04.006.

39. Bekerman E, Neveu G, Shulla A, Brannan J, Pu SY, Wang S, Xiao F, Barouch-Bentov R, Bakken RR, Mateo R, Govero J, Nagamine CM, Dia-

63

mond MS, De Jonghe S, Herdewijn P, Dye JM, Randall G, Einav S. 2017. Anticancer kinase inhibitors impair intracellular viral trafficking and exert broad-spectrum antiviral effects. J Clin Invest 127:1338–1352. https://doi.org/10.1172/JCI89857.

40. Mankouri J, Walter C, Stewart H, Bentham M, Park WS, Heo WD, Fukuda M, Griffin S, Harris M. 2016. Release of infectious hepatitis C virus from Huh7 cells occurs via a trans-Golgi network-to-endosome pathway independent of very-low-density lipoprotein secretion. J Virol 90: 7159–7170. https://doi.org/10.1128/JVI.00826-16.

41. Kovackova S, Chang L, Bekerman E, Neveu G, Barouch-Bentov R, Chaikuad A, Heroven C, Šála M, De Jonghe S, Knapp S, Einav S, Herdewijn P. 2015. Selective inhibitors of cyclin G associated kinase (GAK) as antihepatitis C agents. J Med Chem 58:3393–3410. https://doi.org/10.1021/jm501759m.

42. Barouch-Bentov R, Neveu G, Xiao F, Beer M, Bekerman E, Schor S, Campbell J, Boonyaratanakornkit J, Lindenbach B, Lu A, Jacob Y, Einav S. 2016. Hepatitis C virus proteins interact with the endosomal sorting complex required for transport (ESCRT) machinery via ubiquitination to facilitate viral envelopment. mBio 7:e01456-16. https://doi.org/10.1128/mBio.01456-16.

43. Op De Beeck A, Cocquerel L, Dubuisson J. 2001. Biogenesis of hepatitis C virus envelope glycoproteins. J Gen Virol 82:2589–2595. https://doi.org/10.1099/0022-1317-82-11-2589.

44. Lindenbach BD, Evans MJ, Syder AJ, Wölk B, Tellinghuisen TL, Liu CC, Maruyama T, Hynes RO, Burton DR, McKeating JA, Rice CM. 2005. Complete replication of hepatitis C virus in cell culture. Science 309: 623–626. https://doi.org/10.1126/science.1114016.

45. Lin C, Thomson JA, Rice CM. 1995. A central region in the hepatitis C virus NS4A protein allows formation of an active NS3-NS4A serine proteinase complex in vivo and in vitro. J Virol 69:4373–4380.

46. Lorenz IC, Marcotrigiano J, Dentzer TG, Rice CM. 2006. Structure of the catalytic domain of the hepatitis C virus NS2-3 protease. Nature 442: 831–835. https://doi.org/10.1038/nature04975.

47. Gabilondo AM, Hegler J, Krasel C, Boivin-Jahns V, Hein L, Lohse MJ. 1997. A dileucine motif in the C terminus of the l2-adrenergic receptor is involved in receptor internalization. Proc Natl Acad Sci 94:12285–12290. https://doi.org/10.1073/pnas.94.23.12285.

48. Johnson KF, Kornfeld S. 1992. A His-Leu-Leu sequence near the carboxyl terminus of the cytoplasmic domain of the cation-dependent mannose 6-phosphate receptor is necessary for the lysosomal enzyme sorting function. J Biol Chem 267:17110–17115.

49. Dittrich E, Haft CR, Muys L, Heinrich PC, Graeve L. 1996. A di-leucine motif and an upstream serine in the interleukin-6 (IL-6) signal transducer gp130 mediate ligand-induced endocytosis and down-regulation of the IL-6 receptor. J Biol Chem 271:5487–5494. https://doi.org/10.1074/jbc.271.10.5487.

50. Murray CL, Jones CT, Tassello J, Rice CM. 2007. Alanine scanning of the hepatitis C virus core protein reveals numerous residues essential for production of infectious virus. J Virol 81:10220–10231. https://doi.org/10.1128/JVI.00793-07.

51. Catanese MT, Loureiro J, Jones CT, Dorner M, von Hahn T, Rice CM. 2013. Different requirements for scavenger receptor class B type I in hepatitis C virus cell-free versus cell-to-cell transmission. J Virol 87:8282– 8293. https://doi.org/10.1128/JVI.01102-13.

52. Pietschmann T, Kaul A, Koutsoudakis G, Shavinskaya A, Kallis S, Steinmann E, Abid K, Negro F, Dreux M, Cosset FL, Bartenschlager R. 2006. Construction and characterization of infectious intragenotypic and intergenotypic hepatitis C virus chimeras. Proc Natl Acad Sci U S A 103:7408–7413. https://doi.org/10.1073/pnas.0504877103.

53. Shimakami T, Welsch C, Yamane D, McGivern DR, Yi M, Zeuzem S, Lemon SM. 2011. Protease inhibitor-resistant hepatitis C virus mutants with reduced fitness from impaired production of infectious virus. Gastroenterology 140:667–675. https://doi.org/10.1053/j.gastro.2010.10.056.

54. Counihan NA, Rawlinson SM, Lindenbach BD. 2011. Trafficking of hepatitis C virus core protein during virus particle assembly. PLoS Pathog 7:e1002302. https://doi.org/10.1371/journal.ppat.1002302.

55. Wacker I, Kaether C, Krömer A, Migala A, Almers W, Gerdes HH. 1997. Microtubule-dependent transport of secretory vesicles visualized in real time with a GFP-tagged secretory protein. J Cell Sci 110:1453–1463.

56. Godi A, Pertile P, Meyers R, Marra P, Di Tullio G, Iurisci C, Luini A, Corda D, De Matteis MA. 1999. ARF mediates recruitment of PtdIns-4-OH kinase-l and stimulates synthesis of PtdIns(4,5)P2 on the Golgi complex. Nat Cell Biol 1:280–287. https://doi.org/10.1038/12993.

57. Knight ZA, Gonzalez B, Feldman ME, Zunder ER, Goldenberg DD, Wil-

liams O, Loewith R, Stokoe D, Balla A, Toth B, Balla T, Weiss WA, Williams RL, Shokat KM. 2006. A pharmacological map of the PI3-K family defines a role for p110a in insulin signaling. Cell 125:733–747. https://doi.org/10.1016/j.cell.2006.03.035.

58. Tóth B, Balla A, Ma H, Knight ZA, Shokat KM, Balla T. 2006. Phosphatidylinositol 4-kinase IIIl regulates the transport of ceramide between the endoplasmic reticulum and Golgi. J Biol Chem 281:36369 –36377. https://doi.org/10.1074/jbc.M604935200.

59. Sorensen EB, Conner SD. 2008. AAK1 regulates Numb function at an early step in clathrin-mediated endocytosis. Traffic 9:1791–1800. https://doi.org/10.1111/j.1600-0854.2008.00790.x.

60. Bi Y, Carson KG, Cianchetta G, Green MA, Kumi G, Liang Z, Liu YJ, Main A, Zhang Y, Zipp GG. 14 January 2015. Imidazo[1,2-b]pyridazine-based compounds, compositions comprising them, and uses thereof. Patent EP2822559A1.

61. Bhattacharyya S, Warfield KL, Ruthel G, Bavari S, Aman MJ, Hope TJ. 2010. Ebola virus uses clathrin-mediated endocytosis as an entry pathway. Virology 401:18–28. https://doi.org/10.1016/j.virol.2010.02.015.

62. Agrawal T, Schu P, Medigeshi GR. 2013. Adaptor protein complexes-1 and 3 are involved at distinct stages of flavivirus life-cycle. Sci Rep 3:1813. https://doi.org/10.1038/srep01813.

63. Ohno H, Aguilar RC, Yeh D, Taura D, Saito T, Bonifacino JS. 1998. The medium subunits of adaptor complexes recognize distinct but overlapping sets of tyrosine-based sorting signals. J Biol Chem 273: 25915–25921. https://doi.org/10.1074/jbc.273.40.25915.

64. Ohno H, Aguilar RC, Fournier MC, Hennecke S, Cosson P, Bonifacino JS. 1997. Interaction of endocytic signals from the HIV-1 envelope glycoprotein complex with members of the adaptor medium chain family. Virology 238:305–315. https://doi.org/10.1006/viro.1997.8839.

65. Levy Y, Caflisch A, Onuchic JN, Wolynes PG. 2004. The folding and dimerization of HIV-1 protease: evidence for a stable monomer from simulations. J Mol Biol 340:67–79. https://doi.org/10.1016/j.jmb.2004.04.028.

66. Erdtmann L, Franck N, Lerat H, Le Seyec J, Gilot D, Cannie I, Gripon P, Hibner U, Guguen-Guillouzo C. 2003. The hepatitis C virus NS2 protein is an inhibitor of CIDE-B-induced apoptosis. J Biol Chem 278:18256 –18264. https://doi.org/10.1074/jbc.M209732200.

67. Shin J, Dunbrack RL, Lee S, Strominger JL. 1991. Phosphorylation-dependent down-modulation of CD4 requires a specific structure within the cytoplasmic domain of CD4. J Biol Chem 266:10658–10665.

68. Geisler C, Dietrich J, Nielsen BL, Kastrup J, Lauritsen JPH, Ødum N, Christensen MD. 1998. Leucine-based receptor sorting motifs are dependent on the spacing relative to the plasma membrane. J Biol Chem 273:21316–21323. https://doi.org/10.1074/jbc.273.33.21316.

69. Witteveldt J, Evans MJ, Bitzegeio J, Koutsoudakis G, Owsianka AM, Angus AGN, Keck ZY, Foung SKH, Pietschmann T, Rice CM, Patel AH. 2009. CD81 is dispensable for hepatitis C virus cell-to-cell transmission in hepatoma cells. J Gen Virol 90:48–58. https://doi.org/10.1099/vir.0.006700-0.

70. Lodge R, Lalonde JP, Lemay G, Cohen EA. 1997. The membrane-proximal intracytoplasmic tyrosine residue of HIV-1 envelope glycoprotein is critical for basolateral targeting of viral budding in MDCK cells. EMBO J 16:695–705. https://doi.org/10.1093/emboj/16.4.695.

71. Gravotta D, Carvajal-Gonzalez JM, Mattera R, Deborde S, Banfelder JR, Bonifacino JS, Rodriguez-Boulan E. 2012. The clathrin adaptor AP-1A mediates basolateral polarity. Dev Cell 22:811–823. https://doi.org/10.1016/j.devcel.2012.02.004.

72. Treyer A, Müsch A. 2013. Hepatocyte polarity. Compr Physiol 3:243–287. https://doi.org/10.1002/cphy.c120009.

73. Ohno H, Tomemori T, Nakatsu F, Okazaki Y, Aguilar RC, Foelsch H, Mellman I, Saito T, Shirasawa T, Bonifacino JS. 1999. Mu1B, a novel adaptor medium chain expressed in polarized epithelial cells. FEBS Lett 449:215–220. https://doi.org/10.1016/S0014-5793(99)00432-9.

74. Fölsch H, Pypaert M, Maday S, Pelletier L, Mellman I. 2003. The AP-1A and AP-1B clathrin adaptor complexes define biochemically and functionally distinct membrane domains. J Cell Biol 163:351–362. https://doi.org/10.1083/jcb.200309020.

75. Fields IC, King SM, Shteyn E, Kang RS, Fölsch H. 2010. Phosphatidylinositol 3,4,5-trisphosphate localization in recycling endosomes is necessary for AP-1B-dependent sorting in polarized epithelial cells. Mol Biol Cell 21:95–105. https://doi.org/10.1091/mbc.E09-01-0036.

76. Fields IC, Shteyn E, Pypaert M, Proux-Gillardeaux Vr, Kang RS, Galli T, Fölsch H. 2007. v-SNARE cellubrevin is required for basolateral sorting of AP-1B-dependent cargo in polarized epithelial cells. J Cell Biol 177: 477–488. https://doi.org/10.1083/jcb.200610047.

77. Fölsch H, Ohno H, Bonifacino JS, Mellman I. 1999. A novel clathrin

64

adaptor complex mediates basolateral targeting in polarized epithelial cells. Cell 99:189–198. https://doi.org/10.1016/S0092-8674(00)81650-5.

78. Dell'Angelica EC, Mullins C, Bonifacino JS. 1999. AP-4, a novel protein complex related to clathrin adaptors. J Biol Chem 274:7278–7285. https://doi.org/10.1074/jbc.274.11.7278.

79. Knight ZA, Shokat KM. 2005. Features of selective kinase inhibitors. Chem Biol 12:621–637. https://doi.org/10.1016/j.chembiol.2005.04.011.

80. Lupberger J, Zeisel MB, Xiao F, Thumann C, Fofana I, Zona L, Davis C, Mee CJ, Turek M, Gorke S, Royer C, Fischer B, Zahid MN, Lavillette D, Fresquet J, Cosset FL, Rothenberg SM, Pietschmann T, Patel AH, Pessaux P, Doffoël M, Raffelsberger W, Poch O, McKeating JA, Brino L, Baumert TF. 2011. EGFR and EphA2 are host factors for hepatitis C virus entry and possible targets for antiviral therapy. Nat Med 17:589–595. https://doi.org/10.1038/nm.2341.

Optimization of Isothiazolo[4,3-*b*]pyridine-Based Inhibitors of Cyclin G Associated Kinase (GAK) with Broad-Spectrum Antiviral Activity

Szu-Yuan Pu,[†,‖] Randy Wouters,[‡,‖] Stanford Schor,[†] Jef Rozenski,[‡] Rina Barouch-Bentov,[†] Laura I. Prugar,[§] Cecilia M. O'Brien,[§] Jennifer M. Brannan,[§] John M. Dye,[§] Piet Herdewijn,[‡] Steven De Jonghe,*[,‡,‖] and Shirit Einav*[,†,‖]

[†]Department of Medicine, Division of Infectious Diseases and Geographic Medicine, and Department of Microbiology and Immunology, Stanford University School of Medicine, Stanford, California 94305, United States

[‡]Medicinal Chemistry, Rega Institute for Medical Research, KU Leuven, Herestraat 49, Bus 1041, 3000 Leuven, Belgium

[§]U.S. Army Medical Research Institute of Infectious Diseases, Viral Immunology Branch, Fort Detrick, Maryland 21702, United States

* Supporting Information

ABSTRACT: There is an urgent need for strategies to combat dengue and other emerging viral infections. We reported that cyclin G-associated kinase (GAK), a cellular regulator of the clathrin-associated host adaptor proteins AP-1 and AP-2, regulates intracellular trafficking of multiple unrelated RNA viruses during early and late stages of the viral lifecycle. We also reported the discovery of potent, selective GAK inhibitors based on an isothiazolo[4,3-*b*]pyridine scaffold, albeit with moderate antiviral activity. Here, we describe our efforts leading to the discovery of novel isothiazolo[4,3-*b*]pyridines that maintain high GAK affinity and selectivity. These compounds demonstrate improved in vitro activity against dengue virus, including in human primary dendritic cells, and efficacy against the unrelated Ebola and chikungunya viruses. Moreover, inhibition of GAK activity was validated as an important mechanism of antiviral action of these compounds. These findings demonstrate the potential utility of a GAK-targeted broad-spectrum approach for combating currently untreatable emerging viral infections.
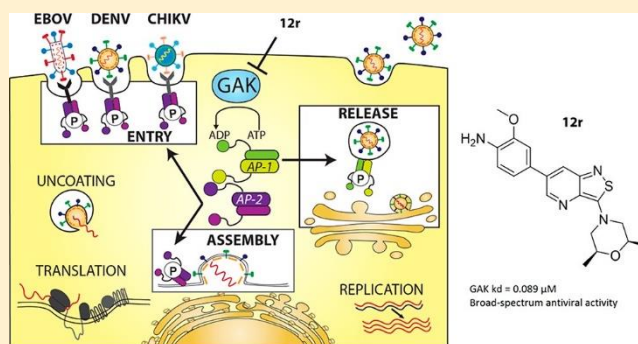
INTRODUCTION

Emerging viral infections, such as those caused by dengue (DENV), Ebola (EBOV), and chikungunya (CHIKV) viruses, represent major threats to global health. DENV is estimated to infect 390 million people annually in over 100 countries.[1] The majority of individuals infected with any of the four DENV serotypes remain asymptomatic or present with acute dengue fever.[2] A fraction (∼5−20%) of dengue patients, particularly those secondarily infected with a heterologous DENV serotype, will progress to severe dengue, manifested by bleeding, plasma leakage, shock, organ failure, and death. The development of an effective vaccine for DENV has been hampered by the need to generate simultaneous protection against the four distinct DENV serotypes to avoid antibody-dependent enhancement (ADE), with recent data indicating an increase in dengue severity requiring hospitalization in vaccinated children.[3] EBOV is the causative agent of a severe and often fatal hemorrhagic disease.[4−6] The unprecedented scope of the 2013−2016 Ebola virus disease (EVD) epidemic in western Africa highlighted the need for effective medical

massive outbreaks in various parts of Africa and Asia and more recently in Central and South America.[8] There are currently no vaccines available for the prevention of CHIKV infection.[9] While an EBOV vaccine has shown promise recently, it is not yet approved. Importantly, no effective antiviral treatment is available against DENV, EBOV, CHIKV, and most other emerging viral pathogens.

The majority of the currently approved antiviral drugs target viral enzymatic functions and thus typically have a narrow spectrum of coverage and a low genetic barrier to resistance. An attractive approach to overcome these limitations is to develop compounds that target host factors broadly required for the effective replication of multiple viral pathogens.[10] Such a host-targeted broad-spectrum approach is more scalable to address the large unmet clinical need and is particularly attractive for the treatment of emerging viral infections lacking any treatment.[10]

Intracellular membrane trafficking is one of multiple cellular processes usurped by viruses. Cyclin G-associated kinase

countermeasures against this emerging infectious disease.[7]
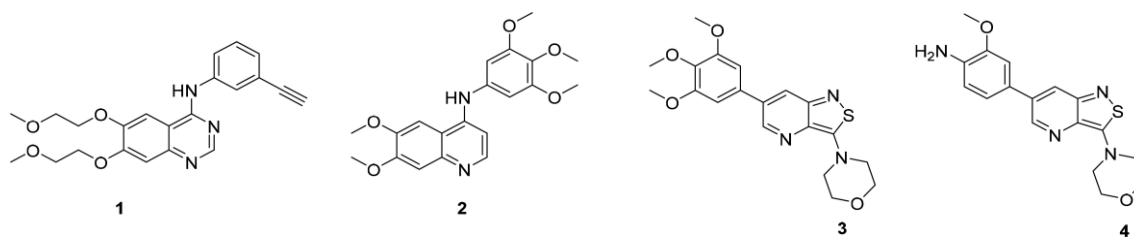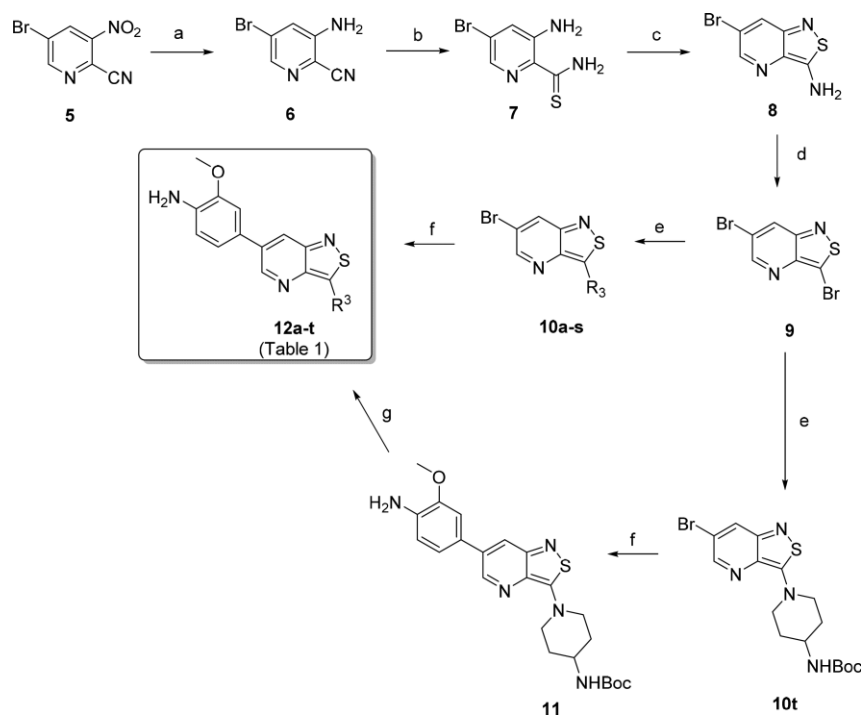CHIKV is a re-emerging alphavirus that has been causing

A

66

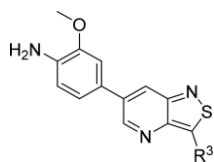Figure 1. Known GAK inhibitors.

Scheme 1[a]

[a]Reagents and conditions: (a) Fe, CH$_3$COOH, rt; (b) Lawesson's reagent, EtOH, reflux; (c) 30% aq H$_2$O$_2$, MeOH, 0 °C; (d) NaNO$_2$, HBr, CuBr, H$_2$O, 0 °C to rt; (e) R$_3$H, EtOH, or n-BuOH, reflux; (f) 4-amino-3-methoxyphenylboronic acid pinacol ester, K$_2$CO$_3$, Pd(PPh$_3$)$_4$, dioxane/water, 100 °C; (g) 37% HCl, dioxane, rt.

(GAK) is a ubiquitously expressed host cell kinase that regulates clathrin-mediated intracellular trafficking of cellular cargo proteins.[11] GAK is a 134 kDa serine/threonine kinase belonging to the numb-associated kinase (NAK) family, which also includes adaptor-associated kinase 1 (AAK1), BMP-2-inducible kinase (BIKE/BMP2K), and myristoylated and palmitoylated serine/threonine kinase 1 (MPSK1/STK16). Clathrin-mediated membrane trafficking is dependent on the action of oligomeric clathrin and adaptor protein complexes (APs) that coordinate the specific recruitment and assembly of clathrin into clathrin-coated vesicles (CCVs) as well as its coupling to endocytic cargo.[12−14] The heterotetrameric AP-1 and AP-2 complexes are major components of CCVs, responsible for vesicle formation in the trans-Golgi network (TGN) and plasma membrane, respectively.[12,15] The μ subunit of these AP complexes recognizes and binds sorting signals in the form of tyrosine- or dileucine-based motifs present on cargo molecules. The efficiency of cargo protein binding to APs is regulated via phosphorylation of a threonine residue within their μ subunit (Thr 144 in AP-1 and Thr 156 in AP-2), which induces a conformational change.[12,16,17] Both GAK and AAK1 phosphorylate these Thr residues, thereby enhancing

cargo recruitment and vesicle assembly.[18−21] Additionally, these kinases regulate the recruitment of clathrin and AP-2 to the plasma membrane, and GAK also controls the uncoating of CCVs, enabling recycling of clathrin back to the cell surface.[12,14]

We have previously demonstrated that depletion of GAK by siRNAs or ectopic expression of phosphorylation mutants of AP-1 and AP-2 is dispensable for RNA replication of hepatitis C virus (HCV) but significantly inhibits four temporally distinct steps of the HCV lifecycle, namely, entry (AP-2), assembly (AP-2), release of cell-free virus (AP-1), and direct cell-to-cell spread (AP-1).[14−16,22] Moreover, we discovered a requirement for GAK in early and late stages of the lifecycle of other viruses, including DENV and EBOV, thereby validating GAK as a potential cellular target for the development of broad-spectrum antiviral agents.[15] Indeed, erlotinib (compound 1, Figure 1), an approved anticancer drug with potent, yet nonselective, anti-GAK activity (dissociation constant (K_d) value of 3.1 nM), inhibits replication of multiple viruses from six unrelated viral families in cell culture.[15] Combinations of erlotinib and sunitinib, an approved anticancer drug with potent anti-AAK1 activity, protected mice from morbidity and

67

Table 1. SAR at Position 3 of Isothiazolo[4,3-*b*]pyridines

Compound#	R³	GAK affinity Kd (μM)[a]	DENV-2 antiviral activity		Cytotox CC$_{50}$ (μM)[d]
			EC$_{50}$ (μM)[b]	EC$_{90}$ (μM)[c]	
4		0.0089	1.844	8.05	17
12a		0.97	5.72	>10	>10
12b		4.3	>10	>10	>10
12t		1.6	6.38	>10	>10
12c		7.2	>10	>10	>10
12d		0.25	0.18	0.56	2.09
12e		0.16	5.28	>10	>10
12f		0.21	5.305	>10	>10
12g		0.08	>20	>20	>20
12h		0.052	4.03	>10	>10
12i		0.19	2	4.15	>10
12j		0.17	7.12	>10	>10
12k		0.061	2.735	>10	>10
12l		0.046	0.76	2.74	21.5
12m		0.026	1.1	2.9	>25
12n		0.019	2.09	6.5	20.68
12o		0.035	0.8416	3.92	4.14
12p		0.018	0.47	1.34	6.32
12q		0.8	>10	>10	>10
12r		0.089	0.82	1.76	>25
12s		0.011	0.70	2.15	>10

[a]K_{d} = dissociation constant. Values represent the average of two independent experiments. [b]EC$_{50}$ = half-maximal effective concentration. [c]EC$_{90}$ = 90% effective concentration. [d]CC$_{50}$ = half-maximal cytotoxic concentration.

mortality associated with DENV and EBOV infections.[15] These data provide a proof-of-concept that small-molecule inhibitors of GAK and AAK1 are useful candidates for broad-spectrum antiviral therapy. The safety and efficacy of erlotinib and/or sunitinib will be evaluated in DENV infected patients in the near future and potentially in patients with EVD in future outbreaks (ClinicalTrials.gov NCT02380625). Nevertheless, erlotinib is a potent, yet nonselective inhibitor whose side effects result not only from on target inhibition of EGFR but also from inhibition of other cellular kinases and non-kinase proteins.[23−25] A particularly relevant side effect that often complicates combination regimens of erlotinib with sunitinib is diarrhea, attributed in part to inhibition erlotinib's cancer target, EGFR.[26] This side effect may limit erlotinib's use in patients with EVD, who often present with diarrhea.[27] To overcome this challenge and avoid other potential toxicity, we have sought to develop novel, chemically distinct, and more selective inhibitors of GAK.

To the best of our knowledge, only two series of potent and selective GAK inhibitors have been reported to date. The first, represented by 4-anilinoquinoline analogue 2 (Figure 1), displays low nM GAK inhibition, has over 50,000 fold greater selectivity to GAK than to other members of the NAK subfamily of kinases, and shows selective GAK inhibition when tested against a large panel of kinases.[28] Nevertheless, this series has not been tested for its antiviral activity. We have previously reported the discovery and synthesis of isothiazolo-[4,3-b]pyridines, a second, structurally distinct class of selective GAK inhibitors.[29] The two most prominent derivatives within this series (compounds 3 and 4, Figure 1) have a high GAK affinity (K_d = 8 nM).[29] We reported that these isothiazolo[4,3-b]pyridines have antiviral activity against both HCV and DENV, yet the measured 50% effective concentration (EC_{50}) values were at a micromolar range.[15,29] Here, we describe our efforts to optimize the antiviral activity of these isothiazolo[4,3-b]pyridines while maintaining their potency and selectivity to GAK.

RESULTS AND DISCUSSION

Synthesis of Isothiazolo[4,3-b]pyridines. To synthesize isothiazolo[4,3-b]pyridine derivatives, a known procedure was followed with minor modifications (Scheme 1).[29,30] First, the nitro group of 3-nitro-5-bromopyridine-2-carbonitrile 5 was reduced by treatment with iron under acidic conditions, generating the desired aniline 6 as the major product. However, due to the acid hydrolysis of the cyano group, a substantial amount (12%) of 3-amino-5-bromopicolinamide was also formed. These two compounds were easily separated by silica gel flash chromatography. Thionation of 6 using phosphorus pentasulfide yielded thioamide 7 in moderate yield. Although this procedure was successful on a small scale (<100 mg), upon upscaling, the starting material 6 was not completely consumed, drastically reducing the reaction yield. Substituting phosphorus pentasulfide by Lawesson's reagent allowed isolation of 3-amino-5-bromopyridine-2-carbothioa-mide 7 in good yield at a larger (gram) scale. The isothiazole moiety was formed by an oxidative ring closure using hydrogen peroxide in methanol, generating 3-amino-6-bromoisothiazolo-[4,3-b]pyridine 8. The subsequent Sandmeyer reaction of the exocyclic amino group with sodium nitrite, hydrogen bromide, and CuBr yielded the key intermediate 3,6-dibromo-isothiazolo[4,3-b]pyridine 9 in moderate yield. Workup of this reaction was initially done by careful addition of solid

K_2CO_3 to the reaction mixture. Since it is time-consuming on a larger scale, this step was substituted with neutralization with a 30% aqueous NaOH solution. Various nitrogen nucleophiles were introduced at position 3 of the isothiazolo[4,3-b]pyridine scaffold, generating compounds 10a−t in yields ranging from 25% to 97%. Subsequently, Suzuki coupling of compounds 10a−s using 4-amino-3-methoxyphenylboronic acid pinacol ester, potassium carbonate as a base, and tetrakis(triphenyl-phosphine)palladium(0) as a catalyst in a mixture of dioxane/water yielded compound 11 and a series of isothiazolo[4,3-b]pyridines 12a−s. Finally, acidic cleavage of the Boc protecting group of compound 11 furnished compound 12t, giving rise to a small library of isothiazolo[4,3-b]pyridines 12a−t (Table 1), which was then evaluated biologically.

GAK Binding Affinity Studies. All compounds were tested for GAK binding affinity using the KINOMEscan platform, which quantitatively measures the ability of a compound to compete with an immobilized active-site-directed ligand.[31] Compound 4 was used as a positive control, as it has a potent GAK affinity (K_d = 8 nM).[29] Prior work revealed that position 3 of the isothiazolo[4,3-b]pyridine scaffold can tolerate structural modifications without impairing GAK affinity. Various amines,[29] alkoxy,[30] and carboxamide[30] groups have thus been inserted at this position. Indeed, many of these molecules demonstrated high affinity to GAK (low μM range), with 3-N-morpholinoisothiazolo[4,3-b]pyridines emerging as the most potent derivatives within this series. In combination with the appropriate aryl substituent (e.g., 3,4,5-trimethoxyphenyl, 3-methoxy-4-aminophenyl) at position 6, these compounds demonstrated K_d values in a low nM range. We therefore focused on the synthesis and biological evaluation of isothiazolo[4,3-b]pyridine analogues bearing substituents at position 3 that closely resemble morpholine. The aryl moiety at position 6 was fixed as a 4-amino-3-methoxyphenyl residue, since this was shown to be optimal for GAK affinity and antiviral activity.

The isosteric replacement of the oxygen atom of the morpholino ring of compound 4 by a carbon gave rise to the 3-N-piperidine analogue 12a. Compound 12a displayed reasonable affinity to GAK (K_d = 0.97 μM), albeit 100-fold lower than that of compound 4 (K_d = 0.0089 μM). A number of substituents at position 4 of the piperidinyl moiety were introduced. Whereas the 4,4-difluoropiperidine (compound 12b), 4-aminopiperidine (compound 12t), and 4-carboxamidepiperidine (compound 12c) derivatives exhibit GAK K_d values exceeding 1 μM, the 4-cyano analog (compound 12d) has a quite potent GAK affinity (K_d = 0.25 μM). Remarkably, the 3-carboxamide congener (compound 12e) demonstrates potent affinity for GAK (K_d = 0.16 μM), yet its 4-substituted congener 12c is much less active. Replacing the morpholino oxygen with a sulfon moiety yielded compound 12f, which is 20-fold less active as a GAK ligand relative to the morpholino containing derivative 4. We have previously demonstrated that the presence of a piperazine ring in place of morpholine reduced GAK affinity, suggesting that a basic nitrogen atom is not tolerated at this position.[29] A lactam containing analogue (compound 12h) was therefore prepared, with potent binding affinity to GAK (K_d = 0.052 μM). Since the morpholine oxygen seems to play a crucial role in mediating GAK affinity, it was kept fixed, whereas the morpholine nitrogen was changed to an externally secondary amine group. The resulting compound 12g bound GAK with a K_d of 80 nM.
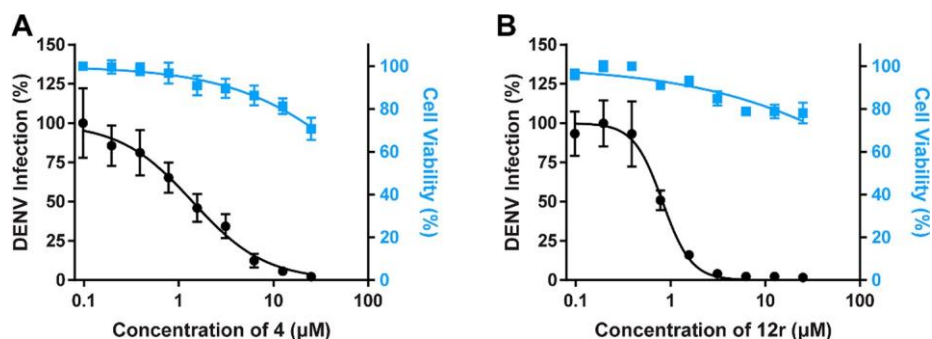
Figure 2. Compound 12r suppresses DENV infection more effectively than compound 4. Shown are cell viability (blue) and dose response of DENV infection (black) to compound 4 (A) and 12r (B) measured by luciferase and alamarBlue assays, respectively, 48 h after infection. Data are plotted relative to vehicle control. Shown are representative experiments from at least two conducted, each with six biological replicates; shown are the mean ± SD.

Expansion of the six-membered morpholino moiety toward a seven-membered homomorpholino derivative yielded compound 12i. This 1,4-oxazepine derivative is 20-fold less potent as a GAK ligand than the morpholine analogue (compound 4). Additionally, using a spirocyclic oxetane, a well-known isoster for morpholine, compound 12j was obtained, with a GAK K_d value of 0.17 μM. Surprisingly, the bridged morpholine derivative 12k (with an 8-oxa-3-aza-bicyclo[3.2.1]octane moiety) displayed potent GAK affinity (K_d = 61 nM). Since this suggested a positive effect of aliphatic substituents, the SAR of the morpholine ring was further explored by introducing methyl groups at various positions of the morpholine moiety. Introducing a single methyl group at position 2 yielded compound 12l as a racemic mixture. This compound demonstrated potent GAK affinity (K_d = 46 nM). The enantiopure compounds 12m and 12n were thus prepared using optically pure building blocks. The two enantiomers demonstrated very similar K_d values (26 nM and 19 nM, respectively). To avoid the racemic mixtures and the high cost of enantiopure building blocks, a geminal dimethyl group was introduced at position 2 of the morpholine ring, yielding compound 12o as a potent GAK ligand (K_d = 35 nM). The stereochemistry of the 3-methyl substituted morpholine analogues demonstrated a strong impact on GAK binding, with the S-3-methylmorpholine derivative (compound 12p) showing a K_d value of 18 nM, and the corresponding R-isomer (compound 12q) demonstrating a 40-fold reduction in GAK affinity. To expand the SAR at position 2 of the morpholine moiety, two 2,6-dimethyl-substituted morpholine derivatives were prepared. Both the *cis* (compound 12r) and *trans* (compound 12s) diastereoisomers demonstrated potent GAK affinity (K_d values of 89 nM and 11 nM, respectively). X-ray crystallography has previously demonstrated that compound 4 bound to the ATP binding site of GAK according to a "type I" binding mode.[29] Given the close structural similarity between the most potent congeners of the current series and compound 4, we predict that their mode of binding to GAK is similar.

Anti-DENV Activity of Isothiazolo[4,3-b]pyridines. All the synthesized derivatives were tested for their activity against DENV, independently of their affinity to GAK. Human hepatoma (Huh7) cells infected with DENV2 (New Guinea C strain) harboring a luciferase reporter[32,33] were treated with the individual compounds for 48 h. Antiviral activity (EC$_{50}$ and EC$_{90}$) was measured via luciferase assays. Cytotoxicity (CC$_{50}$) was measured in the same cell culture wells via alamarBlue assays (Table 1). In general, isothiazolo[4,3-b]pyridines

demonstrating GAK binding displayed a dose-dependent inhibition of DENV infection. The 3-N-piperidinyl isothiazolo-[4,3-b]pyridine analogues, which displayed GAK K_d values in the range of 0.16−1.6 μM (compounds 12a, 12t, 12d, and 12e), inhibited DENV with EC$_{50}$ values ranging from 0.18 to 6.38 μM, albeit compound 12d was more cytotoxic. As predicted, inactive GAK ligands with substitutions at the piperidinyl ring (compounds 12b, 12c) demonstrated no antiviral activity. Nevertheless, the introduction of other saturated heterocycles at position 3, such as a tetrahydro-2H-pyran-4-amine (compound 12g) and a piperazinyl-2-one (compound 12h), yielded analogues with potent GAK affinity (K_d < 100 nM), yet with limited antiviral activity (EC$_{50}$ > 20 μM and 4.03 μM, respectively). Among the series of isothiazolo[4,3-b]pyridines, which bear a closely related analogue of morpholine as substituent at position 3, the homomorpholino (compound 12i) and 2-oxa-6-azaspiro[3.3]-heptane (compound 12j) analogues are the least active GAK binders. Accordingly, these compounds demonstrated a moderate antiviral activity (EC$_{50}$ values of 2 μM and 7.12 μM, respectively). The majority of the 3-N-morpholinyl-isothiazolo[4,3-b]pyridines (compounds 12k−p and 12r,s), which demonstrated potent affinity to GAK, displayed potent antiviral activity, with EC$_{50}$ values of ~1 μM. Notably, these new analogues also displayed significantly lower EC$_{90}$ values (at a low μM range) and reduced cytotoxicity relative to the original lead compound 4. A comparison of the dose−response curves of compound 12r, the most promising compound in this series, and the parental compound 4 reveals the improved antiviral activity and toxicity profiles of 12r (Figure 2). Several derivatives within this series, such as the geminal 2,2-dimethylmorpholino (compound 12o) and the 3-S-methyl-morpholino (compound 12p), demonstrated no antiviral activity beyond toxicity. The 3-R-methylmorpholine analogue 12q, which had poor GAK affinity, also lacked antiviral activity (Table 1).

Compound 12r Inhibits DENV Infection in Human Primary Monocyte-Derived Dendritic Cells. To further determine the therapeutic potential of compound 12r as an anti-DENV compound, we studied its antiviral effect in human primary monocyte-derived dendritic cells (MDDCs), an established ex vivo model system for DENV.[34] We measured a dose-dependent inhibition of DENV infection with minimal cytotoxicity following a 3-day compound treatment with an EC$_{50}$ of 3.537 μM and CC$_{50}$ > 20 μM by plaque assays and alamarBlue assays, respectively (Figure 3). Dendritic cells
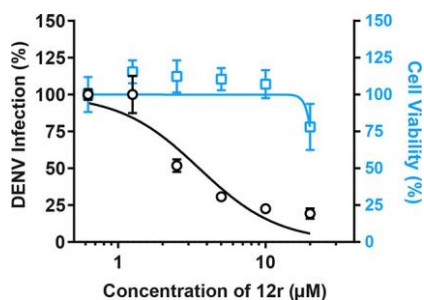
70

E

Figure 3. Ex vivo antiviral activity of 12r in human primary dendritic cells: cell viability (blue) and dose response of DENV infection (black) to 12r measured by plague assays and alamarBlue assays, respectively, 72 h after infection of primary human monocyte-derived dendritic cells (MDDCs). Data are plotted relative to vehicle control. Shown is a representative experiment with cells from a single donor, out of two independent experiments conducted with cells derived from two donors, each with five biological replicates; shown are the mean ± SD.

represent the primary target of DENV in humans.[35] Moreover, primary cells model human physiology and disease better than immortalized cell lines.[35] Our finding that 12r treatment exhibits antiviral efficacy in MDDCs may therefore more accurately reflect the dependence of DENV on GAK during human infection and support the biological relevance of this approach.

Broad-Spectrum Antiviral Activity of 3-*N*-Morpholinylisothiazolo[4,3-*b*]pyridine Analogues. To explore the spectrum of coverage of the new 3-*N*-morpholinyl-isothiazolo[4,3-*b*]pyridine analogues beyond DENV, we studied their antiviral effects against two unrelated viruses: EBOV (*Filoviridae* family), which was previously shown to hijack GAK,[15] and CHIKV (*Togaviridae* family). Huh7 cells were infected with authentic EBOV and treated for 48 h with individual isothiazolo[4,3-*b*]pyridine derivatives. Antiviral activity was measured via an immunofluorescence assay and cytotoxicity via a CellTiter-Glo assay (Table 2). Whereas

Table 2. Activity against EBOV

	GAK affinity	EBOV antiviral activity		cytotoxicity
compd	K_d $(\mu M)^a$	EC_{50} $(\mu M)^b$	EC_{90} $(\mu M)^c$	CC_{50} $(\mu M)^d$
4	0.0089	11.86	21.91	11
12r	0.089	2.436	7.732	>10
12l	0.046	2.001	7.865	9.398
12m	0.026	2.728	8.062	>10
12n	0.019	4.345	>10	>10

$^a K_d$ = dissociation constant. Values represent the average of two independent experiments. $^b EC_{50}$ = half-maximal effective concentration. $^c EC_{90}$ = 90% effective concentration. $^d CC_{50}$ = half-maximal cytotoxic concentration.

treatment with compound 4 showed no anti-EBOV activity beyond cytotoxicity, treatment with 12r and 3-*N*-morpholinyl-isothiazolo[4,3-*b*]pyridine analogues (compounds 12l, 12m, and 12n) resulted in a dose-dependent inhibition of EBOV infection, with EC_{50} values of ~2 μM and CC_{50} > 10 μM (Figure 4A, Table 2). Additionally, treatment of Vero cells with 12r commencing 48 h before infection resulted in a dose-dependent decrease in CHIKV infection measured by plaque assay 48 h following infection (Figure 4B). These data expand the possible future indications of these compounds as antiviral

agents beyond *Flaviviridae* infections to other emerging RNA viral infections.

Antiviral Effect of Compound 12r Correlates with Functional Inhibition of GAK. To confirm that the observed antiviral activity is correlated with functional inhibition of GAK activity, we measured levels of the phosphorylated form of the μ subunit of the AP-2 complex, AP2M1, upon treatment with compound 12r. Since AP2M1 phosphorylation is transient (due to phosphatase PP2A activity),[27] to allow capturing of the phosphorylated state, Huh7 cells were incubated for 30 min in the presence of the PP2A inhibitor calyculin A prior to lysis. Treatment with compound 12r reduced AP2M1 phosphorylation (Figure 5), indicating modulation of AP2M1 phosphorylation via GAK inhibition.

GAK Is a Molecular Target Underlying the Antiviral Effect of Compound 12r. Next, we conducted gain-of-function assays to confirm that inhibition of GAK is a mechanism underlying the anti-DENV effect of compound 12r. A doxycycline-inducible cell line was established to overexpress GAK using the Flp-In recombination system in T-REx 293 cells.[36] Following doxycycline-mediated induction of GAK expression, these cells were infected with a luciferase reporter DENV and treated with compound 12r for 72 h prior to luciferase and viability assays. Doxycycline-induced GAK expression either partially or completely reversed the antiviral effect of compound 12r relative to uninduced cells (Figure 6). These results validate GAK as a key mediator of the anti-DENV effect of compound 12r.

Kinase Selectivity Profile of Compound 12r. Due to its excellent GAK affinity, good antiviral activity, and relatively low cytotoxicity, compound 12r was selected as a lead compound for further analysis. While our data provide evidence that GAK is an important mediator of the observed antiviral effect of compound 12r, additional cellular kinases may mediate its antiviral activity. This is particularly relevant as X-ray crystallography has previously demonstrated targeting of the ATP binding site of GAK by compound 3, thereby classifying it as a classical type I kinase inhibitor.[29] Since the ATP binding site is highly conserved across the kinome, achieving high selectivity of kinase inhibitors is quite challenging.[31] To determine whether the improved antiviral activity of compound 12r resulted from reduced selectivity, we screened it against a diverse panel of 468 kinases (74 mutant and 394 wild-type kinases) using an in vitro ATP-site competition binding assay (DiscoveRX, KinomeScan). This assay measures binding and not functional activity, is conducted in the absence of ATP, and is quite heterogeneous, yet it is commonly used for selectivity assessment. Overall, the selectivity profile of compounds 3 and 12r is comparable, as illustrated by their kinome trees (Figure 7), with selectivity

indices $S(35)$ of 0.033 and 0.057, respectively. Beyond GAK, at

a concentration of 10 μM, compound 12r targets only eight other kinases with greater than 90% inhibition (<10% control): ABL1, AURKC, EPHA7, FLT3, KIT, MAP2K5, MAPK14, and PDGFRB. ABL1 (Abelson proto-oncogene 1), a member of the Abl family of nonreceptor tyrosine kinases, is implicated in the lifecycle of both DENV[37] and EBOV[38] and thus represents another target of 12r that may be contributing to the observed antiviral effect. We previously reported that siRNA-mediated silencing of KIT (KIT proto-oncogene receptor tyrosine kinase) reduced DENV infection.[15] Nevertheless, KIT″s role in DENV infection remained questionable since its suppression substantially reduced cellular viability (likely due to its role in
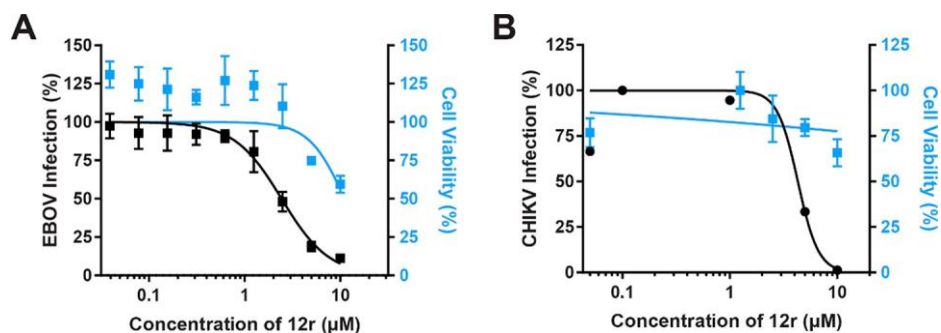
71

F

Figure 4. Compound 12r suppresses EBOV and CHIKV infections. Shown are cell viability (blue) and dose response of EBOV (A) or CHIKV (B) infection (black) to compound 12r measured by immunofluorescence (A) or plaque (B) assays in Huh7 (A) or Vero (B) cells 48 h after infection. Data are plotted relative to vehicle control. Shown are representative experiments from at least two conducted, each with six biological replicates; shown are the mean ± SD.
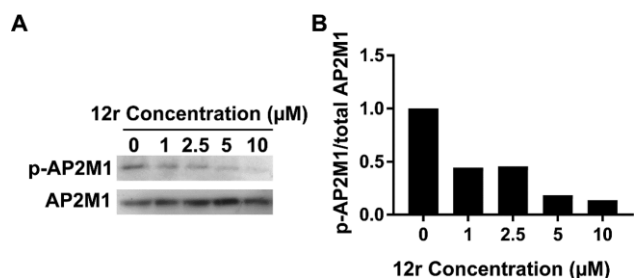

Figure 5. Antiviral effect of compound 12r correlates with functional inhibition of GAK: effect of 12r on AP2M1 phosphorylation by Western analysis in lysates derived from Huh7 cells. Shown are a representative membrane (from two independent experiments) blotted with antiphospho-AP2M1 (p-AP2M1) and anti-AP2M1 antibodies and quantitative data of p-AP2M1/total AP2M1 protein ratio normalized to DMSO controls.
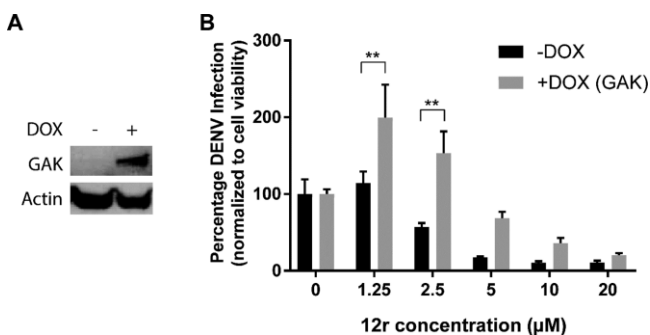

Figure 6. GAK is a molecular target underlying the antiviral effect of compound 12r. (A) Expression of GAK in T-REx 293 cells induced with doxycycline and uninduced control cells. (B) DENV infection normalized to cellular viability in the induced cells (+DOX, gray) or uninduced control cells (−DOX, black) 72 h following infection with a luciferase reporter DENV and 12r treatment, via luciferase and alamarBlue assays, respectively. Shown is a representative experiment out of two conducted, each with five replicates: (∗∗) $P < 0.01$ relative to induced or uninduced cells treated with DMSO by one-way ANOVA with Dunnett's multiple comparisons test. Mean ± SD vlues are shown.

cell survival and proliferation).[39,15] Moreover, the anti-DENV activity of the tested derivatives does not correlate with the binding affinity to KIT. Compound 4 exhibits potent KIT affinity ($K_d = 0.0045$ μM), yet only moderate antiviral activity, whereas compound 12r is 300-fold less potent as a KIT inhibitor ($K_d = 1.3$ μM) but displays an improved antiviral

activity. These data suggest that KIT is unlikely to be an important molecular target underlying the antiviral effect of these compounds.

ADME Profiling. Compounds 4 and 12h exhibit a large (200 fold) or moderate (75-fold) difference between their GAK affinity and anti-DENV cellular activity, respectively (Table 1). In contrast, the antiviral activity of the structurally related isothiazolo[4,3-b]pyridine 12r is only 10-fold lower than its GAK affinity (Table 1). We thus tested our hypothesis that the aqueous solubility and/or cellular permeability of these compounds accounts for these observed differences. We measured the solubility of compounds 4, 12h, and 12r, as well as of three reference compounds (propranolol, ketoconazole, and tamoxifene) in phosphate buffered saline at a pH of 7.4 (Table 3). Compound 12r exhibited very poor aqueous solubility yet potent antiviral activity, compound 4 demonstrated low solubility and intermediate antiviral activity, whereas compound 12h demonstrated high solubility but reduced antiviral activity relative to compounds 4 and 12r (Table 3). The membrane permeability properties of these compounds were then measured via MDR1-MDCK permeability assays. The permeability measured in the apical to basolateral (A-to-B) direction was higher (compound 4) or slightly lower (compounds 12h, 12r) than that of metoprolol (a highly permeable compound) and much higher than that of the low permeable control, atenolol. In the basolateral to apical (B-to-A) direction, the permeability of compound 4 was comparable to that of metoprolol, whereas the permeability of compound 12r was lower than metoprolol's. Notably, compound 12h exhibited permeability in the B−A direction that was higher than that of quinidine's, a compound that is subjected to efflux (Table 3). Accordingly, the calculated efflux ratios ((B-to-A)/(A-to-B)) (Table 3) suggest that compound 12h is likely subjected to efflux, which may explain in part its diminished anti-DENV activity relative to compounds 4 and 12r. In contrast, compound 12r has reduced efflux compared to compounds 4 and 12h, suggesting that it may achieve a higher intracellular concentration, contributing to its enhanced antiviral activity.

Taken together, these data suggest that differences in the efflux ratio of these compounds, but not their aqueous solubility, may in part account for the measured differences between their GAK affinity and antiviral activity. Additionally, GAK binding rather than enzymatic activity was measured. It is therefore possible that the degree of the functional inhibition of GAK activity by these compounds is different from their
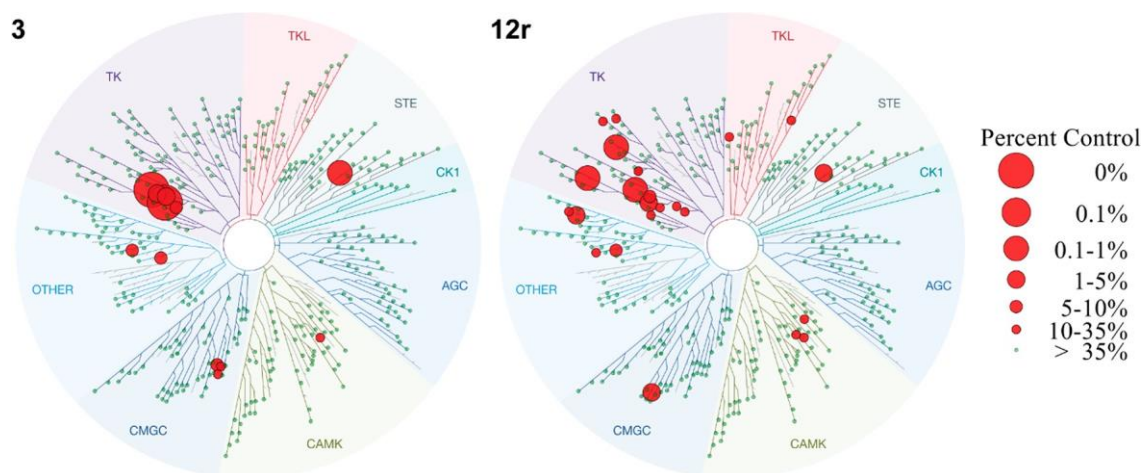
G

Figure 7. Kinase selectivity of compound 12r: kinome tree comparison of 3 (left) and 12r (right). Red circles indicate kinases inhibited by more than 90% at a concentration of 10 μM of the indicated compounds.

Table 3. Solubility (in PBS) and Permeability Values of Compounds 4, 12h, and 12r

compd	solubility (μM)		$P_{app} \times 10^6$ (cm/s)	efflux ratio[c]
4	3.44 ± 0.03	A−B[a]	45.45 ± 0.07	0.68
		B−A[b]	30.80 ± 0.08	
12h	51.30 ± 0.02	A−B[a]	30.32 ± 0.01	1.43
		B−A[b]	43.48 ± 0.02	
12r	0.52 ± 0.23	A−B[a]	31.33 ± 0.03	0.58
		B−A[b]	18.28 ± 0.26	
propanolol	117 ± 0.15		ND[d]	
ketoconazole	32.00 ± 0.03		ND[d]	
tamoxifene	1.32 ± 0.09		ND[d]	
metoprolol	ND[d]	A−B[a]	39.29 ± 0.04	0.78
		B−A[b]	30.66 ± 0.00	
atenolol	ND[d]	A−B[a]	1.21 ± 0.00	1.03
		B−A[b]	1.25 ± 0.00	
quinidine	ND[d]	A−B[a]	13.03 ± 0.01	3.22
		B−A[b]	41.99 ± 0.01	

[a]A−B: apical to basolateral. [b]B-A: basolateral to apical. [c]Efflux ratio: (B−A)/(A−B). [d]ND: not determined.

GAK affinity, particularly in a cellular environment where high ATP concentrations and other cellular proteins are present.

CONCLUSIONS

On the basis of our earlier discovery of isothiazolo[4,3-b]pyridine (compound 4) as a potent and selective GAK inhibitor with moderate antiviral activity, we embarked on an optimization campaign aimed at improving the antiviral activity while maintaining potent and selective GAK inhibition. Synthesis of novel isothiazolo[4,3-b]pyridines with structural variation at position 3 of the scaffold led to the discovery of 3-(cis-2,6-dimethylmorpholino)-6-(4-amino-3-methoxypheny)-isothiazolo[4,3-b]pyridine 12r. Compound 12r maintains potent activity and high selectivity to GAK and displays significantly improved antiviral activity against DENV with reduced cellular toxicity relative to the parental compound 4. Our gain-of-function assays provide evidence that GAK is an important molecular target underlying the antiviral effect of compound 12r. Compound 12r treatment exhibits antiviral efficacy in human primary dendritic cells with minimal toxicity to host cells, further supporting the biological relevance of this

approach. Lastly, our finding that compound 12r also demonstrates antiviral activity against EBOV and CHIKV establishes the broad-spectrum potential of this and related GAK inhibitors.

EXPERIMENTAL SECTION

Chemistry. For all reactions, analytical grade solvents were used. All moisture-sensitive reactions were carried out in oven-dried glassware (125 °C). ^{1}H and ^{13}C NMR spectra were recorded on a Bruker Avance 300 MHz instrument (^{1}H NMR, 300 MHz; ^{13}C NMR, 75 MHz), 500 MHz instrument (^{1}H NMR, 500 MHz; ^{13}C NMR, 125 MHz), or a 600 MHz instrument (^{1}H NMR, 600 MHz; ^{13}C NMR, 150 MHz), using tetramethylsilane as internal standard for ^{1}H NMR spectra and DMSO-d_6 (39.5 ppm) or CDCl$_3$ (77.2 ppm) for ^{13}C NMR spectra. Abbreviations used are s = singlet, d = doublet, t = triplet, q = quartet, m = multiplet, b = broad. Coupling constants are expressed in Hz. High resolution mass spectra were acquired on a quadrupole orthogonal acceleration time-of-flight mass spectrometer (Synapt G2 HDMS, Waters, Milford, MA). Samples were infused at 3 μL/min, and spectra were obtained in positive or negative ionization mode with a resolution of 15 000 (fwhm) using leucine enkephalin as lock mass. Precoated aluminum sheets (Fluka silica gel/TLC-cards, 254 nm) were used for TLC. Column chromatography was performed on silica gel 0.060−0.200 mm, 60 Å (Acros Organics). Purity of final compounds was verified to be >95% by HPLC analysis. HPLC conditions to assess purity were as follows: Shimadzu HPLC equipped with a LC-20AT pump, DGU-20A5 degasser, and a SPD-20A UV−vis detector; Symmetry C18 column (5 μm, 4.6 mm × 150 mm); gradient elution of H$_2$O/CH$_3$CN from 95/5 or 70/30 to 5/95 over 25 min; flow rate 1 mL/min; wavelength, UV 254 nm. Preparative HPLC purifications were performed using a Phenomenex Gemini 110A column (C18, 10 μm, 21.2 mm × 250 mm).

3-Amino-5-bromopyridine-2-carbonitrile (6). To a stirred solution of iron powder (4.900 g, 87.7 mmol) in acetic acid (50 mL) at room temperature was added 5-bromo-3-nitropyridine-2-carbonitrile 5 (10.00 g, 43.9 mmol) in one portion. The resulting reaction mixture was stirred for 3 h. After completion, ethyl acetate was added and the reaction mixture was filtered through a paper filter. The filtered cake was washed thoroughly with ethyl acetate, and the filtrate was evaporated under reduced pressure. The crude residue was purified by silica gel flash column chromatography (using dichloromethane as mobile phase) to yield the title compound (4.845 g, 56%). ^{1}H NMR (300 MHz, DMSO-d_6): δ = 8.08−7.66 (m, 1H), 7.55−7.26 (m, 1H), 6.58 (bs, 2H) ppm. HRMS m/z [M + H]$^+$ calcd for C$_6$H$_4$BrN$_3$: 197.96618, found 197.9656.

3-Amino-5-bromo-2-pyridinecarbothioamide (7). To a solution of 3-amino-5-bromopyridine-2-carbonitrile 6 (5.395 g, 25.00

H

mmol) in absolute ethanol (50 mL) was added Lawesson's reagent (20.22 g, 50.0 mmol). The mixture was refluxed for 24 h. When the starting material was completely consumed according to TLC analysis, the solvent was evaporated under reduced pressure. The residue was redissolved in water and extracted three times with dichloromethane. The combined organic layers were evaporated under reduced pressure. The crude residue was purified by silica gel flash column chromatography (using a mixture of heptane/acetone in a ratio of 60:40 as mobile phase) yielding the title compound (4.513 g, 78%). ^{1}H NMR (300 MHz, DMSO) δ 9.64 (bs, 1H), 9.60 (bs, 1H), 7.83 (d, J = 2.0 Hz, 1H), 7.81 (s, 1H), 7.50 (d, J = 2.0 Hz, 1H) ppm.

3-Amino-6-bromoisothiazolo[4,3-b]pyridine (8). To a solu-tion of 3-amino-5-bromopyridine-2-carbothioamide 7 (2.0 g, 8.62 mmol) in methanol (30 mL) at 0 °C was added dropwise a 30% aqueous H_2O_2 solution (2.22 mL, 21.54 mmol). The mixture was stirred overnight at room temperature. After disappearance of the starting material, the mixture was cooled to 0 °C. The precipitate was filtered off and washed with cold methanol to yield the title compound (1.0 g, 50%). ^{1}H NMR (300 MHz, DMSO) δ 8.29 (d, J = 2.0 Hz, 1H), 8.07 (s, 2H), 8.03 (d, J = 2.0 Hz, 1H) ppm. HRMS m/z [M + H]$^+$ calcd for $C_6H_6BrN_3S$: 229.9383, found 229.9380.

3,6-Dibromoisothiazolo[4,3-b]pyridine (9). A solution of 3-amino-6-bromoisothiazolo[4,3-b]pyridine 8 (1.1 g, 4.78 mmol) in HBr (50 mL) was stirred for 10 min at room temperature, and then CuBr was added in one portion (1.37 g, 9.56 mmol, 2.0 equiv). The resulting mixture was cooled to 0 °C. A solution of sodium nitrite (0.99 g, 14.34 mmol, 3.0 equiv) in H_2O (15 mL) was added dropwise over a period of 30 min. The reaction mixture was stirred for 2 h at 0 °C and overnight at room temperature. The mixture was cooled to 0 °C and carefully neutralized with a 30% aqueous NaOH solution. The formed precipitate was filtered over Celite and thoroughly washed with dichloromethane and methanol. The filtrate was evaporated in vacuo and the crude residue was purified by silica gel flash chromatography (using a mixture of cyclohexane and ethyl acetate in a ratio of 95:5 as mobile phase), yielding the title compound (1.1 g,

78%). ^{1}H NMR (300 MHz, DMSO-d_6): δ 8.92 (d, J = 2.04 Hz, 1H),

8.70 (d, J = 2.01 Hz, 1H) ppm. HRMS m/z [M + H]$^+$ calcd for $C_6H_2Br_2N_2S$: 292.8379, found 292.8373.

Synthesis of 6-Bromo-3-substituted-isothiazolo[4,3-b]-pyridines (10a−t). General Procedure. To a solution of 3,6-dibromoisothiazolo[4,3-b]pyridine 9 in ethanol or as specified was added an appropriate nitrogen nucleophile (3 equiv or specified otherwise). The reaction was stirred at reflux overnight or as specified. When TLC analysis indicated complete disappearance of the starting material, the solvent was evaporated in vacuo and the crude residue was purified either by silica gel flash chromatography or extraction with dichloromethane yielding the 3-substituted-6-bromoisothiazolo-[4,3-b]pyridine derivatives.

The following compounds were made according to this procedure:

6-Bromo-3-(piperidin-1-yl)isothiazolo[4,3-b]pyridine (10a). This compound was prepared from compound 9 (0.68 mmol, 200 mg) and piperidine (2.04 mmol, 174 mg). The product was purified by silica gel flash column chromatography (using a mixture of dichloromethane/ethyl acetate in a ratio of 90:10 as mobile phase) yielding the title compound (180 mg, 60%). ^{1}H NMR (300 MHz, DMSO-d_6): δ = 8.32 (d, J = 2.0 Hz, 1H), 8.07 (d, J = 2.0 Hz, 1H), 4.00−3.70 (m, 4H), 1.74−1.62 (m, 6H) ppm. HRMS m/z [M + H]$^+$ calcd for $C_{11}H_{12}BrN_3S$: 298.0009, found 298.0014.

6-Bromo-3-(4,4-difluoropiperidin-1-yl)isothiazolo[4,3-b]-pyridine (10b). This compound was prepared from compound 9 (0.34 mmol, 100 mg), 4,4-difluoropiperidine hydrochloride (1.02 mmol, 161 mg), and DIPEA (1.70 mmol, 296 μL). The product was purified by silica gel flash column chromatography (using a mixture of heptane/ethyl acetate in a ratio of 60:40 as mobile phase) yielding the

title compound (110 mg, 97%). ^{1}H NMR (300 MHz, DMSO-d_6): δ =

8.40 (d, J = 1.4 Hz, 1H), 8.16 (d, J = 1.4 Hz, 1H), 4.20−3.98 (m,

1-(6-Bromoisothiazolo[4,3-b]pyridin-3-yl)piperidine-4-car-boxamide (10c). This compound was prepared from compound 9 (0.68 mmol, 200 mg) and piperidine-4-carboxamide (1.36 mmol, 174 mg, 2 equiv). The crude product was resuspended in water and washed three times with dichloromethane. The combined organic layers evaporated in vacuo yielding the title compound (160 mg, 69%). The compound was used as such for further reaction.

1-(6-Bromoisothiazolo[4,3-b]pyridin-3-yl)piperidine-4-car-bonitrile (10d). This compound was prepared from compound 9 (0.68 mmol, 200 mg) and piperidine-4-carbonitrile (1.36 mmol, 150 mg, 2 equiv). The crude product was resuspended in water and washed with dichloromethane three times. The combined organic phases were evaporated in vacuo to yield the title compound (190 mg, 86%). ^{1}H NMR (300 MHz, DMSO-d_6): δ = 8.37 (d, J = 2.0 Hz, 1H), 8.13 (d, J = 2.0 Hz, 1H), 4.29−4.02 (m, 2H), 3.86−3.58 (m, 2H), 3.29−3.08 (m, 1H), 2.15−2.00 (m, 2H), 2.00−1.85 (m, 2H) ppm. HRMS m/z [M + H]$^+$ calcd for $C_{12}H_{11}BrN_4S$: 322.9961, found 322.9958.

1-(6-Bromoisothiazolo[4,3-b]pyridin-3-yl)piperidine-3-car-boxamide (10e). This compound was prepared from compound 9 (0.68 mmol, 200 mg) and piperidine-3-carboxamide (1.36 mmol, 174 mg, 2 equiv). The crude product was resuspended in water and washed three times with dichloromethane. The combined organic layers were evaporated in vacuo to yield the title compound (150 mg, 65%). ^{1}H NMR (300 MHz, DMSO-d_6): δ = 8.36 (d, J = 2.0 Hz, 1H), 8.10 (d, J = 2.0 Hz, 1H), 7.44 (bs, 1H), 6.99 (bs, 1H), 4.51 (dd, J = 60.1, 11.6 Hz, 2H), 3.51−3.12 (m, 2H), 2.00−1.79 (m, 2H), 1.77−1.58 (m, 2H) ppm. HRMS m/z [M + H]$^+$ calcd for $C_{12}H_{13}BrN_4OS$: 341.0067, found 341.0064.

4-(6-Bromoisothiazolo[4,3-b]pyridin-3-yl)thiomorpholine 1,1-Dioxide (10f). This compound was prepared from compound 9 (1.02 mmol, 300 mg) and thiomorpholine 1,1-dioxide (3.06 mmol, 414 mg). The product was purified by silica gel flash column chromatography (using a mixture of dichloromethane/acetone in a ratio 95:5 as mobile phase) generating the title compound (90 mg, 25%). ^{1}H NMR (300 MHz, DMSO-d_6): δ = 8.44 (d, J = 2.1 Hz, 1H), 8.21 (d, J = 2.1 Hz, 1H), 4.42 (m, 4H), 3.42 (m, 4H) ppm. HRMS $m/$

z [M + H] calcd for $C_{10}H_{10}BrN_3O_2S_2$: 347.9471, found 347.9480.

6-Bromo-N-(tetrahydro-2H-pyran-4-yl)isothiazolo[4,3-b]-pyridin-3-amine (10g). This compound was prepared from compound 9 (0.68 mmol, 200 mg), 4-aminotetrahydro-2H-pyran hydrochloride (3.4 mmol, 468 mg), and DIPEA (3.4 mmol, 595 μL). The product was purified by silica gel flash column chromatography (using a mixture of dichloromethane/acetone in a ratio 95:5 as mobile phase) yielding the title compound (90 mg, 42%). ^{1}H NMR (300 MHz, DMSO-d_6): δ = 8.81 (d, J = 8.07 Hz, 1H), 8.30 (d, J = 1.98 Hz, 1H), 8.05 (d, J = 1.86 Hz, 1H), 3.92 (dd, J = 1.86 Hz, J = 10.08 Hz, 2H), 3.58 (m, 1H), 3.42 (td, J = 2.1 Hz, J = 11.78 Hz, 2H), 1.96 (dd, J = 12.7 Hz, J = 2.2 Hz, 2H), 1.68 (m, 2H) ppm. HRMS m/z [M + H]$^+$ calcd for $C_{11}H_{12}BrN_3OS$: 313.9958, found 313.9954.

4-(6-Bromoisothiazolo[4,3-b]pyridin-3-yl)piperazin-2-one (10h). This compound was prepared from compound 9 (0.68 mmol, 200 mg) and 2-piperazinone (2.06 mmol, 206 mg) and stirred for 7 days. The crude product was purified by silica gel flash column chromatography (eluting with a mixture of dichloromethane/MeOH in a ratio of 95:5 as mobile phase) yielding the title compound (150 mg, 70%). ^{1}H NMR (300 MHz, DMSO-d_6): δ = 8.40−8.33 (m, 1H), 8.22−8.04 (m, 1H), 4.42−4.29 (m, 2H), 4.24−3.94 (m, 2H), 3.65−3.49 (m, 2H) ppm.

4-(6-Bromoisothiazolo[4,3-b]pyridin-3-yl)-1,4-oxazepane (10i). This compound was prepared from compound 9 (0.34 mmol, 100 mg) and 1,4-oxazepane (1.02 mmol, 103 mg). The product was purified by silica gel flash column chromatography (using a mixture of dichloromethane/acetone in a ratio 95:5 as mobile phase) affording the title compound (100 mg, 96%). ^{1}H NMR (300 MHz, DMSO-d_6): δ = 8.27 (s, 1H), 8.04 (s, 1H), 4.18−4.12 (m, 2H), 4.069−4.0 (m, 2H), 3.87 (d, J = 3.9 Hz, 2H), 3.76−3.68 (m, 2H), 2.08−1.91 (m,

2H) ppm. HRMS m/z [M + H]$^+$ calcd for $C_{11}H_{12}BrN_3OS$: 313.9957,

found 313.9959.

4H), 2.32−2.16 (m, 4H) ppm. HRMS m/z [M + H]$^+$ calcd for $C_{11}H_{12}BrN_3S$: 333.9820, found 333.9823.

6-(6-Bromoisothiazolo[4,3-b]pyridin-3-yl)-2-oxa-6-azaspiro-[3.3]heptane (10j). This compound was prepared from compound 9

(0.34 mmol, 100 mg) and 2-oxa-6-azaspiro[3.3]heptane (1.02 mmol, 206 mg). The crude product was purified by silica gel flash column chromatography (using a mixture of dichloromethane/ethyl acetate in a ratio of 90:10 as mobile phase) yielding the title compound (90 mg, 85%). ^{1}H NMR (300 MHz, CDCl$_3$): δ = 8.29−8.16 (m, 1H), 7.98−7.81 (m, 1H), 4.86 (s, 4H), 4.61−4.47 (m, 4H) ppm. HRMS m/z [M + H]$^+$ calcd for C$_{11}$H$_{10}$BrN$_3$OS: 311.9801, found 311.9815.

3-(6-Bromoisothiazolo[4,3-*b*]pyridin-3-yl)-8-oxa-3-azabicyclo[3.2.1]octane (10k). This compound was prepared from compound 9 (0.68 mmol, 200 mg) and 8-oxa-3-azabicyclo[3.2.1]-octane (1.36 mmol, 154 mg, 2 equiv). The crude product was purified by silica gel flash column chromatography (using a mixture of heptane/acetone in a ratio 8:2 as mobile phase) yielding the title compound (155 mg, 70%). ^{1}H NMR (300 MHz, DMSO-d_6): δ = 8.35 (d, J = 2.1 Hz, 1H), 8.13 (d, 1H), 4.51 (s, 2H), 4.20 (d, J = 12.4 Hz, 2H), 3.43 (dd, J = 12.4, 2.1 Hz, 2H), 2.05−1.78 (m, 4H) ppm. HRMS m/z [M + H]$^+$ calcd for C$_{12}$H$_{12}$BrN$_3$OS: 325.9957, found 325.9964.

4-(6-Bromoisothiazolo[4,3-*b*]pyridin-3-yl)-2-methylmorpholine (10l). This compound was prepared from compound 9 (0.34 mmol, 100 mg) and 2-methylmorpholine (1.02 mmol, 103 μL). The product was purified by silica gel flash column chromatography (eluting with a mixture of dichloromethane/acetone in a ratio 95:5), affording the title compound (93 mg, 87%). ^{1}H NMR (300 MHz, DMSO-d_6): δ = 8.37 (d, 1H), 8.14 (d, J = 2.1 Hz, 1H), 4.47−4.433 (m, 2H), 4.01−3.96 (m, 1H), 3.83−3.68 (m, 2H), 3.36−3.23 (m, 2H), 3.00 (dd, J = 12.4, 10.5 Hz, 1H), 1.18 (d, J = 6.2 Hz, 3H) ppm.

(*S*)-4-(6-Bromoisothiazolo[4,3-*b*]pyridin-3-yl)-2-methylmorpholine (10m). This compound was prepared from compound 9 (0.68 mmol, 200 mg), (*S*)-2-methylmorpholine hydrochloride (2.04 mmol, 281 mg), and DIPEA (2.04 mmol, 264 mg). The crude residue was purified by silica gel flash column chromatography (using a mixture of heptane/ethyl acetate in a ratio 8:2 as mobile phase) yielding the title compound (200 mg, 93%). ^{1}H NMR (300 MHz, DMSO-d_6) δ 8.39 (d, J = 2.1 Hz, 1H), 8.15 (d, J = 2.1 Hz, 1H), 4.53−4.25 (m, J = 29.3, 12.6 Hz, 2H), 4.06−3.92 (m, 1H), 3.88−3.66 (m, 2H), 3.37−3.24 (m, 1H), 3.02 (dd, J = 12.5, 10.5 Hz, 1H), 1.18 (d, J = 6.2 Hz, 3H) ppm. HRMS m/z [M + H]$^+$ calcd for C$_{11}$H$_{12}$BrN$_3$OS: 313.9958, found 313.9961.

(*R*)-4-(6-Bromoisothiazolo[4,3-*b*]pyridin-3-yl)-2-methylmorpholine (10n). This compound was prepared from compound 9 (0.68 mmol, 200 mg) and (*R*)-2-methylmorpholine (2.04 mmol, 206 mg). The crude residue was purified by silica gel flash column chromatography (using a mixture of heptane/ethyl acetate in a ratio 8:2 as mobile phase), yielding the title compound (190 mg, 89%). ^{1}H NMR (300 MHz, DMSO-d_6): δ = 8.36 (d, J = 2.1 Hz, 1H), 8.13 (d, J = 2.1 Hz, 1H), 4.52−4.28 (m, 2H), 4.04−3.92 (m, 1H), 3.83−3.68 (m, 2H), 3.35−3.24 (m, 1H), 3.00 (dd, J = 12.4, 10.5 Hz, 1H), 1.18 (d, J = 6.2 Hz, 3H) ppm. HRMS m/z [M + H]$^+$ calcd for C$_{11}$H$_{12}$BrN$_3$OS: 313.9958, found 313.9954.

4-(6-Bromoisothiazolo[4,3-*b*]pyridin-3-yl)-2,2-dimethylmorpholine (10o). This compound was prepared from compound 9 (0.68 mmol, 200 mg) and 3,3-dimethylmorpholine (2.04 mmol, 235 mg) in EtOH (5 mL). The crude product was purified by silica gel flash column chromatography (using a mixture of heptane/acetone in a ratio 80:20 as mobile phase) affording the title compound (200 mg, 90%). ^{1}H NMR (300 MHz, CDCl$_3$): δ = 8.24 (d, J = 1.9 Hz, 1H), 7.89 (d, J = 2.0 Hz, 1H), 4.02−3.79 (m, 4H), 3.75 (s, 2H), 1.32 (s, 6H) ppm. HRMS m/z [M + H]$^+$ calcd for C$_{12}$H$_{14}$BrN$_3$OS: 328.0114, found 328.0110.

(*S*)-4-(6-Bromoisothiazolo[4,3-*b*]pyridin-3-yl)-3-methylmorpholine (10p). This compound was prepared from compound 9 (0.68 mmol, 200 mg) and (*S*)-3-methylmorpholine (2.04 mmol, 107 mg) in *t*-BuOH (10 mL). The crude residue was washed three times with a mixture of dichloromethane/water to yield the title compound (246 mg, 77%). ^{1}H NMR (300 MHz, DMSO-d_6): δ = 8.37 (d, J = 2.1 Hz, 1H), 8.14 (d, J = 2.1 Hz, 1H), 4.93−4.85 (m, 1H), 4.02−3.95 (m, 2H), 3.85−3.77 (m, 2H), 3.75−3.65 (m, 1H), 3.60−3.49 (m, 1H),

(*R*)-4-(6-Bromoisothiazolo[4,3-*b*]pyridin-3-yl)-3-methylmorpholine (10q). This compound was prepared from compound 9 (1.02 mmol, 300 mg) and (*R*)-3-methylmorpholine (3.06 mmol, 161 mg). The product was purified by silica gel flash column chromatography (using a mixture of heptane/ethyl acetate in a ratio of 60:40 as mobile phase) yielding the title compound (110 mg, 97%). H NMR (300 MHz, DMSO-d_6): δ = 8.36 (d, J = 2.0 Hz, 1H), 8.14 (d, J = 2.0 Hz, 1H), 4.93−4.85 (m, 1H), 4.03−3.94 (m, 2H), 3.85−3.77 (m, 2H), 3.76−3.65 (m, 1H), 3.61−3.49 (m, 1H), 1.30 (d, J = 6.7 Hz, 3H) ppm.

6-Bromo-3-*cis*-2,6-dimethylmorpholinoisothiazolo[4,3-*b*]-pyridine (10r). This compound was prepared from compound 9 (1.02 mmol, 300 mg) and *cis*-2,6-dimethylmorpholine (3.06 mmol, 352 mg). The product was purified by silica gel flash column chromatography (using a mixture of heptane/ethyl acetate in a ratio of 90:10 as mobile phase) yielding the title compound (290 mg, 87%). H NMR (300 MHz, DMSO-d_6) δ = 8.38 (d, J = 2.1 Hz, 1H), 1.30 (d, J = 6.7 Hz, 3H) ppm. HRMS m/z [M + H]$^+$ calcd for C$_{11}$H$_{12}$BrN$_3$OS: 313.9958, found 313.9960.

8.14 (d, J = 2.1 Hz, 1H), 4.50−4.34 (m, 2H), 4.03−3.73 (m, 2H), 2.91 (dd, J = 12.5, 10.8 Hz, 2H), 1.20 (s, 3H), 1.17 (s, 3H) ppm. HRMS m/z [M + H]$^+$ calcd for $C_{12}H_{14}BrN_3OS$: 328.0114, found 328.0105.

trans-4-(6-Bromoisothiazolo[4,3-*b*]pyridin-3-yl)-2,6-dime- thylmorpholine (10s). This compound was prepared from compound 9 (0.51 mmol, 150 mg) and *trans*-2,6-dimethylmorpholine (1.53 mmol, 176 mg). The crude product was resuspended in water
and washed three times with dichloromethane. The combined organic phases were evaporated in vacuo, yielding the title compound (159
mg, 95%). ^{1}H NMR (300 MHz, CDCl$_3$): δ = 8.26 (d, J = 1.9 Hz, 1H), 7.90 (d, J = 1.9 Hz, 1H), 4.32−4.10 (m, 2H), 3.95 (dd, J = 12.6,
3.3 Hz, 2H), 3.70 (dd, J = 12.6, 6.3 Hz, 3H), 1.33 (s, 3H), 1.30 (s, 3H) ppm. HRMS m/z [M + H]$^+$ calcd for $C_{12}H_{14}BrN_3OS$: 328.0114, found 328.0015.

tert-Butyl (1-(6-Bromoisothiazolo[4,3-*b*]pyridin-3-yl)- piperidin-4-yl)carbamate (10t). This compound was prepared from compound 9 (0.34 mmol, 100 mg) and *tert*-butyl piperidin-4- ylcarbamate (1.02 mmol, 206 mg). The crude product was purified by silica gel flash column chromatography (eluting with a mixture of heptane/acetone in a ratio of 80:20 as mobile phase), yielding the title compound (120 mg, 85%). ^{1}H NMR (300 MHz, DMSO-d_6): δ = 8.35 (d, J = 2.1 Hz, 1H), 8.10 (d, J = 2.1 Hz, 1H), 6.95 (bs, 1H), 4.47 (d, J = 13.3 Hz, 2H), 3.67−3.54 (m, 1H), 3.50−3.36 (m, 2H), 2.01− 1.85 (m, 2H), 1.67−1.49 (m, 2H), 1.40 (s, 9H) ppm. HRMS m/z [M + H]$^+$ calcd for $C_{16}H_{21}BrN_4O_2S$: 356.1176, found 356.1172.

Synthesis of 3-Substituted-6-(4-amino-3-methoxyphenyl)-isothiazolo[4,3-*b*]pyridines (11 and 12a−s). General Procedure. To a mixture of dioxane/water (in a ratio of 4:1) were added the appropriate 3-substituted-6-bromoisothiazolo[4,3-*b*]pyridine analogue 10a−t, 4-amino-3-methoxyphenylboronic acid pinacol ester (1.2 equiv), and potassium carbonate (2 equiv). The mixture was degassed and filled with nitrogen. Subsequently, Pd(PPh$_3$)$_4$ (1−10 mol %) was added. The mixture was degassed a second time, filled with nitrogen, and stirred at 100 °C. After completion of the reaction, solvents were evaporated. The crude residue was purified by silica gel flash chromatography and when needed further purified using RP-HPLC yielding the title compounds. All compounds submitted for biological assays had a purity of at least 95%. The following compounds were made according to this procedure:

tert-Butyl (1-(6-(4-Amino-3-methoxyphenyl)isothiazolo[4,3-*b*]pyridin-3-yl)piperidin-4-yl)carbamate (11). This compound was prepared from *tert*-butyl (1-(6-bromoisothiazolo[4,3-*b*]pyridin-3-yl)piperidin-4-yl)carbamate 11 (0.25 mmol, 110 mg). The crude product was purified by silica gel flash column chromatography (using a mixture of dichloromethane/acetone in a ratio of 90:10 as mobile phase), yielding the title compound (90 mg, 79%). ^{1}H NMR (300 MHz, CDCl$_3$): δ = 8.63 (d, J = 2.1 Hz, 1H), 7.81 (d, J = 2.1 Hz, 1H), 7.13 (dd, J = 8.0, 1.9 Hz, 1H), 7.09 (d, J = 1.9 Hz, 1H), 6.81 (bs, 1H), 4.72−4.56 (m, 2H), 4.00−3.96 (m, 1H), 3.93 (s, 3H), 3.42−3.30 (m, 2H), 2.22−2.07 (m, 2H), 1.75−1.64 (m, 2H), 1.47 (s, 9H) ppm. HRMS m/z [M + H]$^+$ calcd for $C_{23}H_{29}N_5O_3S$: 456.2064, found 456.2054.

J

75

2-Methoxy-4-(3-(piperidin-1-yl)isothiazolo[4,3-*b*]pyridin-6-yl)aniline (12a). The title compound was prepared from 6-bromo-3-(piperidin-1-yl)isothiazolo[4,3-*b*]pyridine 10a (0.34 mmol, 100 mg). The crude product was purified by silica gel flash column chromatography (using a mixture of dichloromethane/ethyl acetate in a ratio ranging from 95:5 to 90:10 as mobile phase), yielding the title compound (60 mg, 52%). ^{1}H NMR (300 MHz, DMSO-d_6): δ = 8.70 (d, J = 2.1 Hz, 1H), 7.84 (d, J = 2.1 Hz, 1H), 7.25 (d, J = 1.8 Hz, 1H), 7.20 (dd, J = 8.1, 1.9 Hz, 1H), 6.74 (d, J = 8.1 Hz, 1H), 5.07 (s, 2H), 3.94−3.89 (m, 4H), 3.89 (s, 3H), 1.77−1.66 (m, 6H) ppm. ^{13}C NMR (75 MHz, DMSO-d_6): δ = 172.5, 156.2, 146.8, 143.6, 138.8, 135.3, 132.5, 124.2, 122.1, 120.1, 113.9, 109.4, 55.6, 51.3, 24.9, 23.5 ppm. HRMS m/z [M + H]$^+$ calcd for $C_{18}H_{20}N_4OS$: 341.1431, found 341.1429.

4-(3-(4,4-Difluoropiperidin-1-yl)isothiazolo[4,3-*b*]pyridin-6-yl)-2-methoxyaniline (12b). This compound was prepared from 6-bromo-3-(4,4-difluoropiperidin-1-yl)isothiazolo[4,3-*b*]pyridine 10b (0.24 mmol, 100 mg). The crude residue was purified by silica gel flash column chromatography (using a mixture of dichloromethane/ethyl acetate in a ratio 90:10 as mobile phase) yielding the title compound (49 mg, 54%). ^{1}H NMR (300 MHz, DMSO-d_6): δ = 8.77 (d, J = 2.1 Hz, 1H), 7.90 (d, J = 2.1 Hz, 1H), 7.27 (d, J = 1.7 Hz, 1H), 7.22 (dd, J = 8.1, 1.8 Hz, 1H), 6.75 (d, J = 8.1 Hz, 1H), 5.09 (s, 2H), 4.20−3.98 (m, 4H), 3.89 (s, 3H), 2.42−2.10 (m, 4H) ppm. ^{13}C NMR (75 MHz, DMSO-d_6): δ = 171.6, 156.2, 146.8, 144.6, 138.9, 135.4, 132.7, 124.0, 122.2, 120.2, 113.9, 109.4, 55.6, 47.4, 32.8 ppm. HRMS m/z [M + H]$^+$ calcd for $C_{18}H_{18}F_2N_4OS$: 377.1242, found 377.1260.

1-(6-(4-Amino-3-methoxyphenyl)isothiazolo[4,3-*b*]pyridin-3-yl)piperidine-4-carboxamide (12c). The title compound was prepared from 1-(6-bromoisothiazolo[4,3-*b*]pyridin-3-yl)piperidine-4-carboxamide 10c (0.29 mmol, 100 mg). The crude product was purified by silica gel flash column chromatography (using a mixture of dichloromethane/ethyl acetate in a ratio of 90:10 as mobile phase) yielding the title compound (27 mg, 24%). ^{1}H NMR (300 MHz, DMSO-d_6): δ = 8.72 (d, J = 2.0 Hz, 1H), 7.86 (d, J = 2.0 Hz, 1H), 7.39 (bs, 1H), 7.26 (d, J = 1.6 Hz, 1H), 7.21 (dd, J = 8.1, 1.8 Hz, 1H), 6.89 (bs, 1H), 6.74 (d, J = 8.1 Hz, 1H), 5.09 (bs, 2H), 4.65−4.53 (m, 2H), 3.88 (s, 3H), 3.38−3.22 (m, 3H), 1.95−1.67 (m, 4H) ppm. ^{13}C NMR (75 MHz, DMSO-d_6): δ = 175.9, 172.3, 156.2, 146.8, 143.9, 138.8, 135.3, 132.6, 124.2, 122.1, 120.2, 113.9, 109.4, 55.6, 50.0, 40.9, 27.71 ppm. HRMS m/z [M + H]$^+$ calcd for $C_{19}H_{21}N_5O_2S$: 384.1489, found 384.1483.

1-(6-(4-Amino-3-methoxyphenyl)isothiazolo[4,3-*b*]pyridin-3-yl)piperidine-4-carbonitrile (12d). This compound was pre-pared from 1-(6-bromoisothiazolo[4,3-*b*]pyridin-3-yl)piperidine-4-carbonitrile 10d (0.31 mmol, 100 mg). The crude product was purified by silica gel flash column chromatography (with a mixture of dichloromethane/acetone in a ratio of 95:5 as mobile phase) yielding the title compound (106 mg, 94%). ^{1}H NMR (300 MHz, DMSO-d_6): δ = 8.75 (d, J = 1.8 Hz, 1H), 7.89 (d, J = 1.8 Hz, 1H), 7.29−7.18 (m, 2H), 6.74 (d, J = 8.1 Hz, 1H), 5.10 (bs, 2H), 4.34−4.08 (m, 2H), 3.89 (s, 3H), 3.84−3.70 (m, 2H), 3.32−3.14 (m, 1H), 2.05−1.88 (m, 2H) ppm. ^{13}C NMR (75 MHz, DMSO-d_6): δ = 172.1, 156.2, 146.8, 144.3, 138.9, 135.4, 132.6, 124.0, 122.2, 121.9, 120.2, 113.9, 109.4, 55.6, 48.6, 27.4, 25.0 ppm. HRMS m/z [M + H]$^+$ calcd for $C_{19}H_{19}N_5OS$: 366.1383, found 366.1375.

1-(6-(4-Amino-3-methoxyphenyl)isothiazolo[4,3-*b*]pyridin-3-yl)piperidine-3-carboxamide (12e). This compound was prepared from 1-(6-bromoisothiazolo[4,3-*b*]pyridin-3-yl)piperidine-3-carboxamide 10e (0.29 mmol, 100 mg). The crude product was purified by silica gel flash column chromatography (using a mixture of dichloromethane/ethyl acetate in a ratio of 90:10 as mobile phase), yielding the title compound (63 mg, 57%). ^{1}H NMR (300 MHz, DMSO-d_6): δ = 8.74 (d, J = 1.9 Hz, 1H), 7.86 (d, J = 1.9 Hz, 1H), 7.47 (bs, 1H), 7.29−7.17 (m, 2H), 7.00 (bs, 1H), 6.74 (d, J = 8.0 Hz, 1H), 5.09 (bs, 2H), 4.81−4.64 (m, 1H), 4.47−4.35 (m, 1H), 3.89 (s, 3H), 3.35−3.21 (m, 2H), 2.67−2.54 (m, 1H), 2.10−1.59 (m, 4H) ppm. ^{13}C NMR (75 MHz, DMSO-d_6): δ = 174.67, 172.3, 156.2,

55.6, 52.5, 50.9, 41.4, 27.4, 23.8 ppm. HRMS m/z [M + H]$^+$ calcd for $C_{19}H_{21}N_5O_2S$: 384.1489, found 384.1483.

4-(6-(4-Amino-3-methoxyphenyl)isothiazolo[4,3-*b*]pyridin-3-yl)thiomorpholine 1,1-Dioxide (12f). This compound was prepared from 4-(6-bromoisothiazolo[4,3-*b*]pyridin-3-yl)-thiomorpholine 1,1-dioxide 10f (0.26 mmol, 90 mg). The crude product was purified by silica gel flash column chromatography (using a mixture of dichloromethane/acetone in a ratio of 95:5 as mobile phase), yielding the title compound (53 mg, 51%). ^{1}H NMR (300 MHz, DMSO-d_6): δ = 8.79 (d, J = 2.1 Hz, 1H), 7.93 (d, J = 2.1 Hz, 1H), 7.28 (d, J = 1.8 Hz, 1H), 7.23 (dd, J = 8.1, 1.9 Hz, 1H), 6.75 (d, J = 8.1 Hz, 1H), 5.11 (bs, 2H), 4.48−4.41 (m, 4H), 3.89 (s, 3H), 3.47−3.40 (m, 4H) ppm. ^{13}C NMR (75 MHz, DMSO-d_6): δ = 170.6, 156.3, 146.9, 144.9, 139.0, 135.5, 132.7, 123.9, 122.3, 120.3, 113.9, 109.4, 55.7, 50.1, 49.1 ppm. HRMS m/z [M + H]$^+$ calcd for $C_{17}H_{18}N_4O_3S_2$: 391.0893, found 391.0883.

6-(4-Amino-3-methoxyphenyl)-*N*-(tetrahydro-2*H*-pyran-4-yl)isothiazolo[4,3-*b*]pyridin-3-amine (12g). This compound was prepared from 6-bromo-*N*-(tetrahydro-2*H*-pyran-4-yl)isothiazolo[4,3-*b*]pyridin-3-amine 10g (0.25 mmol, 80 mg). The crude product was purified by silica gel flash column chromatography (using a mixture of

146.8, 143.9, 138.8, 135.3, 132.5, 124.2, 122.1, 120.2, 113.9, 109.4,

puri
dichloromethane/acetone in a ratio 90:10 as mobile phase) yielding the title compound (25 mg, 7%). ^{1}H NMR (300 MHz, DMSO-d_6): δ = 8.63 (d, J = 2.0 Hz, 1H), 8.47 (s, 1H), 7.80 (d, J = 2.0 Hz, 1H), 7.23 (d, J = 1.8 Hz, 1H), 7.20 (dd, J = 8.1, 1.9 Hz, 1H), 6.75 (d, J = 8.0 Hz, 1H), 5.06 (bs, 2H), 3.95 (m, 2H), 3.89 (s, 3H), 3.58 (m, 1H), 3.43 (td, J = 10.9 Hz, 3H), 1.99 (dd, J = 12.7 Hz, J = 2.2 Hz, 2H), 1.72 (m, 2H) ppm. ^{13}C NMR (75 MHz, DMSO-d_6): δ = 170.9, 154.8, 146.9,
143.4, 138.7, 136.3, 132.7, 124.6, 121.8, 120.2, 113.9, 109.5, 66.0, 55.7, 54.4, 31.8 ppm. HRMS m/z [M + H]$^+$ calcd for $C_{18}H_{20}N_4O_2S$: 357.1380, found 357.1379.

4-(6-(4-Amino-3-methoxyphenyl)isothiazolo[4,3-*b*]pyridin- 3-yl)piperazin-2-one (12h). This compound was prepared from 6- (6-bromoisothiazolo[4,3-*b*]pyridin-3-yl)-2-oxa-6-azaspiro[3.3]- heptane 10h (0.19 mmol, 60 mg). The crude product was purified by silica gel flash column chromatography (using a mixture of dichloromethane/acetone in a ratio of 90:10 as mobile phase). The residue was further purified by RP-HPLC (eluting isocratically with a
mixture of acetonitrile/water in a ratio of 4:6) yielding the title compound (30 mg, 45%). ^{1}H NMR (300 MHz, DMSO-d_6): δ = 8.79−8.75 (m, 1H), 8.35 (bs, 1H), 7.92−7.88 (m, 1H), 7.29−7.19
(m, 2H), 6.75 (d, J = 8.1 Hz, 1H), 5.10 (bs, 2H), 4.43−4.37 (m, 2H), 4.21−4.14 (m, 2H), 3.93−3.85 (s, 3H), 3.50−3.42 (m, 2H)

ppm. ^{13}C NMR (75 MHz, DMSO-d_6): δ = 170.5, 165.7, 156.0, 146.9, 144.4,
138.9, 135.6, 124.2, 122.1, 120.2, 114.0, 109.5, 55.7, 52.9, 46.6 ppm. HRMS m/z [M + H]$^+$ calcd for $C_{17}H_{17}N_5O_2S$: 311.9801, found 311.9815.

4-(3-(1,4-Oxazepan-4-yl)isothiazolo[4,3-*b*]pyridin-6-yl)-2-methoxyaniline (12i). This compound was prepared from 4-(6-bromoisothiazolo[4,3-*b*]pyridin-3-yl)-1,4-oxazepane 10i (0.32 mmol, 100 mg). The crude product was purified by silica gel flash column chromatography (using a mixture of dichloromethane/acetone in a ratio 95:5 as mobile phase) yielding the title compound (60 mg, 53%). ^{1}H NMR (300 MHz, DMSO-d_6): δ = 8.68 (d, J = 2.1 Hz, 1H), 7.83 (d, J = 2.1 Hz, 1H), 7.26 (d, J = 1.8 Hz, 1H), 7.21 (dd, J = 8.1, 1.9 Hz, 1H), 6.74 (d, J = 8.1 Hz, 1H), 5.07 (bs, 2H), 4.24−4.18 (m, 2H), 4.08 (t, J = 5.9 Hz, 2H), 3.93−3.86 (m, 4H), 3.77−3.68 (m, 2H), 2.11−1.99 (m, 2H) ppm. ^{13}C NMR (75 MHz, DMSO-d_6): δ = 171.0, 156.0, 146.8, 143.3, 138.8, 135.3, 131.8, 124.3, 122.0, 120.1, 114.0, 109.4, 69.7, 68.6, 55.6, 54.6, 51.9, 29.0 ppm. HRMS m/z [M + H]$^+$ calcd for $C_{18}H_{20}N_4O_2S$: 357.1380, found 357.1379.

4-(3-(2-Oxa-6-azaspiro[3.3]heptan-6-yl)isothiazolo[4,3-*b*]- pyridin-6-yl)-2-methoxyaniline (12j). This compound was pre-pared from 6-(6-bromoisothiazolo[4,3-*b*]pyridin-3-yl)-2-oxa-6-azaspiro[3.3]heptane 10j (0.19 mmol, 60 mg). The crude product was purified by silica gel flash column chromatography (using a mixture of dichloromethane/acetone in a ratio of 9:1 as mobile phase) yielding the title compound (50 mg). This residue was further purified by RP-HPLC (eluting with a mixture of acetonitrile/water in a ratio of 4:6 as mobile phase) yielding the title compound (30 mg,

45%). ^{1}H NMR (300 MHz, CDCl$_3$): δ = 8.6 (d, J = 2.0 Hz, 1H), 7.79 (d, J = 2.0 Hz, 1H), 7.12 (dd, J = 8.0, 1.9 Hz, 1H), 7.07 (d, J = 1.8 Hz, 1H), 6.81 (d, J = 8.0 Hz, 1H), 4.92 (s, 4H), 4.62 (s, 4H), 3.98 (bs, 2H), 3.93 (s, 3H) ppm. ^{13}C NMR (75 MHz, CDCl$_3$): δ = 171.7, 155.9, 147.9, 146.0, 137.2, 136.7, 134.89, 127.9, 123.8, 120.6, 115.3, 109.6, 811, 65.9, 55.9, 42.0 ppm. HRMS m/z [M + H]$^+$ calcd for C$_{18}$H$_{18}$N$_4$O$_2$S: 355.1223, found 355.1220.

4-(3-(8-Oxa-3-azabicyclo[3.2.1]octan-3-yl)isothiazolo[4,3-b]pyridin-6-yl)-2-methoxyaniline (12k). This compound was prepared from 3-(6-bromoisothiazolo[4,3-b]pyridin-3-yl)-8-oxa-3-azabicyclo[3.2.1]octane 10k (0.31 mmol, 100 mg). The crude product was purified by silica gel flash column chromatography (using a mixture of dichloromethane/ethyl acetate in a ratio ranging from 99:1 to 90:10 as mobile phase) yielding the title compound (93 mg, 81%). ^{1}H NMR (300 MHz, CDCl$_3$): δ = 8.61 (d, J = 2.1 Hz, 1H), 7.81 (d, J = 2.1 Hz, 1H), 7.13 (dd, J = 8.0, 1.9 Hz, 1H), 7.08 (d, J = 1.9 Hz, 1H), 6.81 (d, J = 8.0 Hz, 1H), 4.55 (s, 2H), 4.32 (d, J = 12.4 Hz, 2H), 3.98 (bs, 2H), 3.93 (s, 3H), 3.52 (dd, J = 12.3, 2.4 Hz, 2H), 2.15−2.01 (m, 4H) ppm. ^{13}C NMR (75 MHz, CDCl$_3$): δ = 174.0, 156.9, 147.9, 144.7, 137.2, 136.3, 134.0, 127.9, 124.2, 120.5, 115.3, 109.6, 74.1, 56.0, 55.9, 28.4 ppm. HRMS m/z [M + H]$^+$ calcd for C$_{19}$H$_{20}$N$_4$O$_2$S: 369.1380, found 369.1370.

2-Methoxy-4-(3-(2-methylmorpholino)isothiazolo[4,3-b]-pyridin-6-yl)aniline (12l). This compound was prepared from 4-(6-bromoisothiazolo[4,3-b]pyridin-3-yl)-2-methylmorpholine 10l (0.29 mmol, 90 mg). The crude product was purified by silica gel flash column chromatography (using a mixture of dichloromethane/acetone in a ratio of 95:5 as mobile phase) yielding the title compound (53 mg, 51%). ^{1}H NMR (300 MHz, DMSO-d_6): δ = 8.75 (d, J = 2.0 Hz, 1H), 7.89 (d, J = 2.0 Hz, 1H), 7.27 (d, J = 1.6 Hz, 1H), 7.22 (dd, J = 8.1, 1.8 Hz, 1H), 6.75 (d, J = 8.1 Hz, 1H), 5.09 (bs, 2H), 4.45 (d, J = 12.5 Hz, 2H), 4.02−3.71 (m, 6H), 3.32−3.16 (m, 1H), 2.97 (q, J = 12.3, 10.6 Hz, 1H), 1.19 (d, J = 6.2 Hz, 3H) ppm. ^{13}C NMR (75 MHz, DMSO-d_6): δ = 172.3, 156.2, 146.8, 144.4, 138.9, 135.5, 132.8, 124.1, 122.2, 120.2, 113.9, 109.4, 70.8, 65.3, 55.6, 49.3, 18.7 ppm. HRMS m/z [M + H]$^+$ calcd C$_{18}$H$_{20}$N$_4$O$_2$S: for 357.1380, found 357.1385.

(S)-2-Methoxy-4-(3-(2-methylmorpholino)isothiazolo[4,3-b]pyridin-6-yl)aniline (12m). This compound was prepared from (S)-4-(6-bromoisothiazolo[4,3-b]pyridin-3-yl)-2-methylmorpholine 10m (0.32 mmol, 100 mg). The crude product was purified by silica gel flash column chromatography (using a mixture of dichloromethane/acetone in a ratio of 95:5 as mobile phase), yielding the title compound (14 mg, 12%). ^{1}H NMR (300 MHz, DMSO-d_6): δ = 8.75 (d, J = 2.1 Hz, 1H), 7.89 (d, J = 2.1 Hz, 1H), 7.27 (d, J = 1.8 Hz, 1H), 7.22 (dd, J = 8.1, 1.9 Hz, 1H), 6.74 (d, J = 8.1 Hz, 1H), 5.09 (bs, 2H), 4.46 (d, J = 11.8 Hz, 2H), 3.99 (dd, J = 11.7, 2.7 Hz, 1H), 3.89 (s, 3H), 3.86−3.73 (m, 2H), 3.30−3.21 (m, 1H), 2.97 (dd, J = 12.3, 10.6 Hz, 1H), 1.19 (d, J = 6.2 Hz, 3H) ppm. ^{13}C NMR (75 MHz, DMSO-d_6): δ = 172.3, 156.2, 146.9, 144.4, 138.9, 135.5, 132.8, 124.1, 122.2, 120.2, 113.9, 109.4, 70.8, 65.3, 55.7, 55.6, 49.3, 18.7 ppm. HRMS m/z [M + H]$^+$ calcd for C$_{18}$H$_{20}$N$_4$O$_2$S: 357.1380, found 357.1376.

(R)-2-Methoxy-4-(3-(2-methylmorpholino)isothiazolo[4,3-b]pyridin-6-yl)aniline (12n). This compound was prepared from (S)-4-(6-bromoisothiazolo[4,3-b]pyridin-3-yl)-2-methylmorpholine (0.32 mmol, 100 mg). The crude product was purified by silica gel flash column chromatography (using a mixture of dichloromethane/acetone in a ratio of 95:5 as mobile phase) yielding the title compound (23 mg, 20%). ^{1}H NMR (300 MHz, CDCl$_3$): δ = 8.61 (s, 1H), 7.80 (s, 1H), 7.11 (d, J = 8.0 Hz, 1H), 7.06 (s, 1H), 6.78 (d, J = 8.0 Hz, 1H), 4.56−4.36 (m, 2H), 4.06−3.80 (m, 1H), 3.36−3.17 (m, 1H), 3.01−2.85 (m, 1H), 1.28 (d, J = 6.2 Hz, 4H) ppm. ^{13}C NMR (75 MHz, DMSO-d_6): δ = 172.3, 156.2, 146.9, 144.4, 138.9, 135.5, 132.8, 124.1, 122.2, 120.2, 113.9, 109.4, 70.8, 65.3, 55.6, 49.3, 18.7 ppm. HRMS m/z [M + H]$^+$ calcd for C$_{18}$H$_{20}$N$_4$O$_2$S: 357.1380, found 357.1378.

4-(3-(3,3-Dimethylpiperidin-1-yl)isothiazolo[4,3-b]pyridin-6-yl)-2-methoxyaniline (12o). This compound was prepared from 6-bromo-3-(3,3-dimethylpiperidin-1-yl)isothiazolo[4,3-b]pyridine 10o (0.30 mmol, 100 mg). The crude product was purified by silica

gel flash column chromatography (using a mixture of dichloromethane/acetone in a ratio of 9:1 as mobile phase). The residue was further purified using RP-HPLC (eluting with a linear gradient of 30−95% acetonitrile in water) yielding the title compound (23 mg, 21%). ^{1}H NMR (300 MHz, DMSO-d_6): δ = 8.74 (d, J = 1.8 Hz, 1H), 7.87 (d, J = 1.8 Hz, 1H), 7.28−7.18 (m, 2H), 6.74 (d, J = 8.1 Hz, 1H), 5.09 (bs, 2H), 3.89 (s, 3H), 3.88−3.83 (m, 4H), 3.80 (s, 2H), 1.27 (s, 6H) ppm. ^{13}C NMR (75 MHz, DMSO-d_6): δ = 172.6, 156.3, 144.1, 138.9, 135.5, 122.2, 120.2, 114.0, 109.5, 71.2, 59.4, 58.6, 55.7, 49.8, 24.4 ppm. HRMS m/z [M + H]$^+$ calcd for C$_{20}$H$_{24}$N$_4$OS: 371.1536, found 371.1533.

(S)-2-Methoxy-4-(3-(3-methylmorpholino)isothiazolo[4,3-b]pyridin-6-yl)aniline (12p). This compound was prepared from (R)-6-bromo-3-(2-methylpiperidin-1-yl)isothiazolo[4,3-b]pyridine 10p (0.32 mmol, 100 mg). The crude product was purified by silica gel flash column chromatography (using a mixture of dichloromethane/acetone in a ratio 9:1 as mobile phase). The residue was further purified by RP-HPLC (eluting with a gradient of acetonitrile/water in a ratio ranging from 40:60 to 95:5) to yield the title compound (40 mg, 35%). ^{1}H NMR (300 MHz, DMSO-d_6): δ = 8.72 (d, J = 2.0 Hz, 1H), 7.88 (d, J = 2.0 Hz, 1H), 7.26 (d, J = 1.8 Hz, 1H), 7.21 (dd, J = 8.1, 1.8 Hz, 1H), 6.74 (d, J = 8.1 Hz, 1H), 5.09 (s, 2H), 5.03−4.97 (m, 1H), 4.04−3.91 (m, 2H), 3.89 (s, 3H), 3.83−3.67 (m, 3H), 3.58−3.48 (m, 1H), 1.30 (d, J = 6.7 Hz, 3H) ppm. ^{13}C NMR (75 MHz, DMSO-d_6): δ = 171.6, 156.2, 146.8, 144.2, 138.9, 135.5, 132.44, 124.1, 122.2, 120.2, 113.9, 109.4, 70.0, 65.8, 55.6, 52.2, 45.1, 13.1 ppm. HRMS m/z [M + H]$^+$ calcd for C$_{18}$H$_{20}$N$_4$O$_2$S: 357.1380, found 357.1380.

(R)-2-Methoxy-4-(3-(3-methylmorpholino)isothiazolo[4,3-b]pyridin-6-yl)aniline (12q). This compound was prepared from (R)-6-bromo-3-(2-methylpiperidin-1-yl)isothiazolo[4,3-b]pyridine 10q (0.32 mmol, 100 mg). The crude product was purified by silica gel flash column chromatography (using a mixture of dichloromethane/ethyl acetate in a ratio of 9:1 as mobile phase). The residue was then further purified by RP-HPLC (eluting isocratically with a mixture of acetonitrile/water in a ratio of 6:4 as mobile phase), yielding the title compound (22 mg, 20%). ^{1}H NMR (300 MHz, DMSO-d_6): δ = 8.72 (d, J = 2.1 Hz, 1H), 7.88 (d, J = 2.1 Hz, 1H), 7.26 (d, J = 1.9 Hz, 1H), 7.21 (dd, J = 8.1, 2.0 Hz, 1H), 6.74 (d, J = 8.1 Hz, 1H), 5.09 (bs, 2H), 5.04−4.95 (m, 1H), 4.03−3.93 (m, 2H), 3.89 (s, 3H), 3.84−3.67 (m, 3H), 3.59−3.49 (m, 1H), 1.30 (d, J = 6.7 Hz, 3H) ppm. ^{13}C NMR (75 MHz, DMSO-d_6): δ = 171.6, 156.2, 146.8, 144.2, 138.9, 135.5, 132.5, 124.1, 122.2, 120.2, 113.9, 109.4, 70.0, 65.8, 55.6, 52.2, 45.1, 13.0 ppm. HRMS m/z [M + H]$^+$ calcd for C$_{18}$H$_{20}$N$_4$O$_2$S: 357.1380, found 357.1376.

4-(3-(cis-2,6-Dimethylmorpholino)isothiazolo[4,3-b]-pyridin-6-yl)-2-methoxyaniline (12r). This compound was prepared from 6-bromo-3-cis-2,6-dimethylmorpholinoisothiazolo[4,3-b]pyridine 10r (100 mg, 0.30 mmol). The crude product was purified by silica gel flash column chromatography (using a mixture of dichloromethane/acetone in a ratio of 95:5 as mobile phase) yielding the title compound (84 mg, 76%). ^{1}H NMR (300 MHz, DMSO-d_6): δ = 8.76 (d, J = 2.1 Hz, 1H), 7.88 (d, J = 2.1 Hz, 1H), 7.27 (d, J = 1.8 Hz, 1H), 7.22 (dd, J = 8.1, 1.9 Hz, 1H), 6.74 (d, J = 8.1 Hz, 1H), 5.08 (bs, 2H), 4.64−4.37 (m, 2H), 3.89 (s, 3H), 3.88−3.80 (m, 2H), 2.95−2.76 (m, 2H), 1.20 (s, 3H), 1.18 (s, 3H) ppm. ^{13}C NMR (75 MHz, DMSO-d_6): δ = 172.1, 156.2, 146.8, 144.4, 138.9, 135.5, 132.7, 124.1, 122.1, 120.2, 113.9, 109.4, 70.7, 55.6, 54.9, 18.7 ppm. HRMS m/z [M + H]$^+$ calcd for C$_{19}$H$_{22}$N$_4$O$_2$S: 371.1536, found 371.1534.

4-(3-(trans-2,6-Dimethylmorpholino)isothiazolo[4,3-b]-pyridin-6-yl)-2-methoxyaniline (12s). This compound was prepared from trans-4-(6-bromoisothiazolo[4,3-b]pyridin-3-yl)-2,6-dimethylmorpholine 10s (0.30 mmol, 100 mg). The crude product was purified by silica gel flash column chromatography (using a mixture of dichloromethane/acetone in a ratio of 97:3 as mobile phase) yielding the title compound (90 mg, 81%). ^{1}H NMR (300 MHz, CDCl$_3$): δ = 8.62 (d, J = 2.0 Hz, 2H), 7.80 (d, J = 2.0 Hz, 1H), 7.17−7.05 (m, 2H), 6.80 (d, J = 8.0 Hz, 1H), 4.32−4.22 (m, 2H), 4.04−3.96 (m, 4H), 3.92 (s, 3H), 3.71 (dd, J = 12.5, 6.2 Hz, 2H), 1.36 (s, 3H), 1.34 (s, 3H) ppm. ^{13}C NMR (75 MHz, CDCl$_3$): δ =

173.6, 157.0, 147.9, 144.6, 137.2, 136.3, 133.7, 127.9, 124.1, 120.5, 115.3, 109.6, 66.3, 55.9, 55.1, 18.1 ppm. HRMS m/z [M + H]$^+$ calcd for $C_{19}H_{22}N_4O_2S$: 371.1536, found 384.1483.

1-(6-(4-Amino-3-methoxyphenyl)isothiazolo[4,3-b]pyridin-3-yl)piperidin-4-amine (12t). To a solution of *tert*-butyl (1-(6-(4-amino-3-methoxyphenyl)isothiazolo[4,3-b]pyridin-3-yl)piperidin-4-yl)carbamate 11 (0.22 mmol, 80 mg) in dioxane (5 mL) was added a 37% aqueous HCl solution (2.2 mmol, 183 μL). The reaction mixture was stirred at room temperature overnight. The volatiles were evaporated in vacuo. The crude residue was redissolved in water and washed three times with dichloromethane. The organic phases were combined and evaporated in vacuo to yield the title compound (20 mg, 26%). ^{1}H NMR (300 MHz, Pyr-d_5): δ = 8.90 (d, J = 2.1 Hz, 1H), 8.15 (d, J = 2.1 Hz, 1H), 7.37−7.29 (m, 2H), 7.05 (d, J = 7.9 Hz, 1H), 5.54 (bs, 2H), 4.67−4.58 (m, 2H), 4.43 (bs, 2H), 3.79 (s, 3H), 3.38−3.19 (m, 2H), 3.01−2.87 (m, 1H), 1.95−1.81 (m, 2H), 1.70−1.45 (m, 2H) ppm. ^{13}C NMR (75 MHz, DMSO-d_6): δ = 172.3, 156.2, 146.8, 143.7, 138.6, 135.3, 132.5, 124.3, 122.1, 120.2, 114.0, 109.3, 55.6, 49.2, 47.2, 33.7 ppm. HRMS m/z [M + H]$^+$ calcd for $C_{18}H_{21}N_5OS$: 356.1539, found 356.1545.

Plasmids and Virus Constructs. DENV2 (New Guinea C strain)[32,33] *Renilla* reporter plasmid used for in vitro assays was a gift from Pei-Yong Shi (The University of Texas Medical Branch). DENV 16681 plasmid (pD2IC-30P-NBX) used for ex vivo experiments was a gift from Claire Huang (CDC).[40] Plasmids pOG44 for Flp recombinase expression and pG-LAP were from Thermo Fischer Scientific.

Cells. Huh7 (Apath LLC), BHK-21 (ATCC), and T-Rex-293 (ThermoFisher Scientific) cells were grown in DMEM (Mediatech) supplemented with 10% FBS (Omega Scientific), nonessential amino acids, 1% L-glutamine, and 1% penicillin−streptomycin (Thermo-Fisher Scientific) and maintained in a humidified incubator with 5% CO$_2$ at 37 °C. C6/36 cells were grown in Leibovitz's L-15 media (CellGro) supplemented with 10% FBS and 1% HEPES in a humidified chamber at 28 °C and 0% CO$_2$. Vero 76 and Vero E6 cells were grown in EMEM (ThermoFisher Scientific) supplemented with 5% FBS (HyClone) and 1% penicillin−streptomycin (ThermoFisher Scientific) and maintained in a humidified incubator with 5% CO$_2$ at 37 °C.

Virus Production. DENV2 RNA was transcribed in vitro using mMessage/mMachine (Ambion) kits. DENV was produced by electroporating RNA into BHK-21 cells, harvesting supernatants on day 10 and titering via standard plaque assays on BHK-21 cells. In parallel, on day 2 postelectroporation, DENV-containing supernatant was used to inoculate C6/36 cells to amplify the virus. CHIKV (strain AF15561) was grown in Vero 76 cells, and supernatants were collected and clarified and stored at −80 °C until further use. Virus titers were determined via standard plaque assay on Vero 76 cells. EBOV (Kikwit isolate) was grown in Vero E6 cells, and supernatants were collected and clarified and stored at −80 °C until further use. Virus titers were determined via standard plaque assay on Vero E6 cells.

Infection Assays. Huh7 cells were infected with DENV in replicates (n = 3−10) for 4 h at MOI of 0.01. Overall infection was measured at 48 h using a *Renilla* luciferase substrate. MDDCs were infected with DENV2 (16881) at an MOI of 1. Standard plaque assays were conducted following a 72 h incubation. Huh7 cells were infected with EBOV at an MOI of 1 under biosafety level 4 conditions. Forty-eight hours after infection, cells were formalin-fixed for twenty-four hours prior to removal from biosafety level 4. Infected cells were detected using an EBOV glycoprotein specific monoclonal antibody (KZ52) and quantitated by automated fluorescence microscopy using an Operetta High Content Imaging System and the Harmony software package (PerkinElmer). Vero cells were pretreated for 48 prior to infection. Medium was removed, and cells were incubated with CHIKV at an MOI of 1 in compound-free media for 1 h at 37 °C. Cells were then washed and medium containing compound 12r or DMSO was applied. Forty-eight hours following

Viability Assays. Viability was assessed using alamarBlue reagent (Invitrogen) or CellTiter-Glo reagent (Promega) assay according to the manufacturer's protocol. Fluorescence was detected at 560 nm on InfiniteM1000 plate reader and luminescence on InfiniteM1000 plate reader (Tecan) or a Spectramax 340PC.

Generation of MDDCs. MDDCs were prepared as described with[34] slight modifications. Buffy coats were obtained from the Stanford Blood Center. CD14+ cells were purified by EasySep Human Monocyte Enrichment Kit without CD16 Depletion (Stemcell Technologies). Cells were seeded in 6-well plates (2 × 10^6 cells per well), stimulated with 500 U/mL granulocyte-macrophage colony-stimulating and 1000 U/mL interleukin-4 (Pepro tech), and incubated at 37 °C for 6 days prior to DENV infection (MOI 1).

Gain-of-Function Assays. A doxycycline-inducible cell line was established to overexpress GAK using the Flp-In recombination system (ThermoFisher).[41] T-REx 293 cells with a pFRT/lacZeo site and pcDNA6/TR were co-transfected with a puromycin-resistant expression vector encoding a Flp-In recombination target site and a pOG44 plasmid containing the Flp recombinase followed by selection with puromycin. Eight hours after induction with doxycycline, cells were treated with compound 12r, infected with DENV (MOI = 0.01), and incubated for 72 h prior to luciferase and viability assays.

Effect of 12r on AP2M1 Phosphorylation. Huh7 cells were kept in serum free medium for 1 h and then were treated with compound 12r or DMSO in complete medium for 4 h at 37 °C. To allow capturing of phosphorylated AP2M1, 100 nM PP2A inhibitor calyculin A (Cell Signaling) was added 30 min prior to lysis in M-PER lysis buffer (ThermoFisher Scientific) with 1× Halt protease and phosphatase inhibitor cocktail (ThermoFisher Scientific). Samples were then subjected to SDS−PAGE and blotting with antibodies targeting phospho-AP2M1 (Cell Signaling) and total AP2M1 (Santa Cruz Biotechnology). Band intensity was measured with NIH ImageJ.

GAK K_d Assay. K_d values for GAK were determined as previously described.[31] Briefly, the DNA-tagged GAK, an immobilized ligand on

infection, supernatants were collected, pooled, and used to infect naive cells followed by plaque assays.

streptavidin-coated magnetic beads, and the test compound are combined. When binding occurs between GAK and a test compound, no binding can occur between GAK and the immobilized ligand. Upon washing, the compound-bound, DNA-tagged GAK is washed away. The beads carrying the ligands are then resuspended in elution buffer and the remaining kinase concentration measured by qPCR on the eluate. K_d values are determined using dose−response curves.

Kinase Selectivity Assay. Compound 12r was screened against a diverse panel of 468 kinases (DiscoveRX, KinomeScan) using an in vitro ATP-site competition binding assay at a concentration of 10 μM.[31] The results are reported as the percentage of kinase/phage remaining bound to the ligands/beads, relative to a control. High affinity compounds have % of control values close to zero, while weaker binders have higher % control values.

In Vitro ADME Profiling. The solubility and permeability of compounds 4, 12h, and 12r were measured at Chempartner (Shanghai, China). In brief, for solubility assays, 100 μM of the individual compounds were dissolved in 100 mM phosphate buffer (pH 7.4) and incubated at room temperature for 1 h followed by measurement of the solubilized compound fraction in the supernatant via LC−MS/MS. For permeability assay, 5 μM of the compounds were incubated with MDCK-MDR1 cells in either donor or receiver chambers for 90 min at 37 °C. The transport of the compounds via the MDCK-MDR1 monolayer in the apical to basolateral (A-to-B) or basolateral to apical (B-to-A) directions was then measured via LC− MS/MS.

Statistical Analysis. All data were analyzed with GraphPad Prism software. Fifty percent effective concentration (EC_{50}) values were measured by fitting data to a three-parameter logistic curve. P values were calculated by two-tailed unpaired t test and one- or two-way ANOVA with either Dunnett's or Tukey's multiple comparisons tests.

ASSOCIATED CONTENT

* Supporting Information

The Supporting Information is available free of charge on the ACS Publications website at DOI: 10.1021/acs.jmedchem.8b00613.

Molecular formula strings and some data (CSV)

AUTHOR INFORMATION

Corresponding Authors

*S.D.J.: phone, +32 16 32 26 62; e-mail, steven.dejonghe@kuleuven.be.
*S.E.: phone, 650 723 8656; e-mail, seinav@stanford.edu.
ORCID
Piet Herdewijn: 0000-0003-3589-8503
Steven De Jonghe: 0000-0002-3872-6558
Shirit Einav: 0000-0001-6441-4171

Author Contributions

‖S,-Y.P. and R.W. contributed equally to this work, and S.D.J. and S.E. also contributed equally to this work.

Notes

The authors declare no competing financial interest.
The opinions, interpretations, conclusions, and recommendations are those of the authors and are not necessarily endorsed by the U.S. Army or the other funders.

ACKNOWLEDGMENTS

ABBREVIATIONS USED

AAK1, adaptor-associated kinase 1; AP, adaptor protein; CC_{50}, half-maximal cytotoxic concentration; CCV, clathrin-coated vesicle; CHIKV, Chikungunya virus; DENV, Dengue virus; EBOV, Ebola virus; EC_{50}, half-maximal effective concentration; EC_{90}, 90% effective concentration; EGFR, epidermal growth factor receptor; EVD, Ebola virus disease; GAK, cyclin G-associated kinase; K_d, dissociation constant; NAK, numb-associated kinase; TGN, trans-Golgi network.

REFERENCES

(1) Bhatt, S.; Gething, P. W.; Brady, O. J.; Messina, J. P.; Farlow, A. W.; Moyes, C. L.; Drake, J. M.; Brownstein, J. S.; Hoen, A. G.; Sankoh, O.; Myers, M. F.; George, D. B.; Jaenisch, T.; Wint, G. R. W.; Simmons, C. P.; Scott, T. W.; Farrar, J. J.; Hay, S. I. The Global Distribution and Burden of Dengue. *Nature* 2013, *496*, 504−507.
(2) World Health Organization. Dengue: Guidelines for Diagnosis, Treatment, Prevention, and Control. *Special Programme for Research and Training in Tropical Diseases*; WHO: Geneva, Switzerland, 2009; p 147.
(3) Halstead, S. B.; Russell, P. K. Protective and Immunological Behavior of Chimeric Yellow Fever Dengue Vaccine. *Vaccine* 2016, *34* (14), 1643−1647.
(4) Feldmann, H.; Geisbert, T. W. Ebola Haemorrhagic Fever. *Lancet* 2011, *377* (9768), 849−862.
(5) Towner, J. S.; Sealy, T. K.; Khristova, M. L.; Albariño, C. G.; Conlan, S.; Reeder, S. A.; Quan, P.-L.; Lipkin, W. I.; Downing, R.; Tappero, J. W.; Okware, S.; Lutwama, J.; Bakamutumaho, B.; Kayiwa, J.; Comer, J. A.; Rollin, P. E.; Ksiazek, T. G.; Nichol, S. T. Newly Discovered Ebola Virus Associated with Hemorrhagic Fever Outbreak in Uganda. *PLoS Pathog.* 2008, *4* (11), e1000212.
(6) Negredo, A.; Palacios, G.; Vazquez-Moron, S.; Gonzalez, F.; Dopazo, H.; Molero, F.; Juste, J.; Quetglas, J.; Savji, N.; de la Cruz Martínez, M.; Herrera, J. E.; Pizarro, M.; Hutchison, S. K.; Echevarría, J. E.; Lipkin, W. I.; Tenorio, A. Discovery of an Ebolavirus-Like Filovirus in Europe. *PLoS Pathog.* 2011, *7* (10), e1002304.
(7) Wells, C.; Yamin, D.; Ndeffo-Mbah, M. L.; Wenzel, N.; Gaffney, S. G.; Townsend, J. P.; Meyers, L. A.; Fallah, M.; Nyenswah, T. G.; Altice, F. L.; Atkins, K. E.; Galvani, A. P. Harnessing Case Isolation and Ring Vaccination to Control Ebola. *PLoS Neglected Trop. Dis.* 2015, *9* (5), e0003794.
(8) Abdelnabi, R.; Neyts, J.; Delang, L. Chikungunya Virus Infections: Time to Act, Time to Treat. *Curr. Opin. Virol.* 2017, *24*, 25−30.
(9) Henao-Restrepo, A. M.; Longini, I. M.; Egger, M.; Dean, N. E.; Edmunds, W. J.; Camacho, A.; Carroll, M. W.; Doumbia, M.; Draguez, B.; Duraffour, S.; Enwere, G.; Grais, R.; Gunther, S.; Hossmann, S.; Kondé, M. K.; Kone, S.; Kuisma, E.; Levine, M. M.; Mandal, S.; Norheim, G.; Riveros, X.; Soumah, A.; Trelle, S.; Vicari, A. S.; Watson, C. H.; Keïta, S.; Kieny, M. P.; Røttingen, J.-A. Efficacy and Effectiveness of an RVSV-Vectored Vaccine Expressing Ebola Surface Glycoprotein: Interim Results from the Guinea Ring Vaccination Cluster-Randomised Trial. *Lancet* 2015, *386* (9996), 857−866.
(10) Bekerman, E.; Einav, S. Combating Emerging Viral Threats. *Science* 2015, *348* (6232), 282−283.
(11) Edeling, M. A.; Smith, C.; Owen, D. Life of a Clathrin Coat: Insights from Clathrin and AP Structures. *Nat. Rev. Mol. Cell Biol.* 2006, *7* (1), 32−44.
(12) Zhang, C. X.; Engqvist-Goldstein, Å. E. Y.; Carreno, S.; Owen, D. J.; Smythe, E.; Drubin, D. G. Multiple Roles for Cyclin G-Associated Kinase in Clathrin-Mediated Sorting Events. *Traffic* 2005, *6* (12), 1103−1113.
(13) Korolchuk, V. I.; Banting, G. CK2 and GAK/Auxilin2 Are Major Protein Kinases in Clathrin-Coated Vesicles. *Traffic* 2002, *3* (6), 428−439.
(14) Neveu, G.; Ziv-Av, A.; Barouch-Bentov, R.; Berkerman, E.; Mulholland, J.; Einav, S. AP-2-Associated Protein Kinase 1 and Cyclin G-Associated Kinase Regulate Hepatitis C Virus Entry and Are Potential Drug Targets. *J. Virol.* 2015, *89* (8), 4387−4404.
(15) Bekerman, E.; Neveu, G.; Shulla, A.; Brannan, J.; Pu, S. Y.; Wang, S.; Xiao, F.; Barouch-Bentov, R.; Bakken, R. R.; Mateo, R.; Govero, J.; Nagamine, C. M.; Diamond, M. S.; De Jonghe, S.; Herdewijn, P.; Dye, J. M.; Randall, G.; Einav, S. Anticancer Kinase Inhibitors Impair Intracellular Viral Trafficking and Exert Broad-Spectrum Antiviral Effects. *J. Clin. Invest.* 2017, *127* (4), 1338−1352.
(16) Neveu, G.; Barouch-Bentov, R.; Ziv-Av, A.; Gerber, D.; Jacob, Y.; Einav, S. Identification and Targeting of an Interaction between a Tyrosine Motif within Hepatitis C Virus Core Protein and AP2M1 Essential for Viral Assembly. *PLoS Pathog.* 2012, *8* (8), e1002845.
(17) McMahon, H. T.; Boucrot, E. Molecular Mechanism and Physiological Functions of Clathrin-Mediated Endocytosis. *Nat. Rev. Mol. Cell Biol.* 2011, *12* (8), 517−533.
(18) Ricotta, D.; Conner, S. D.; Schmid, S. L.; von Figura, K.; Höning, S. Phosphorylation of the AP2 μ Subunit by AAK1 Mediates High Affinity Binding to Membrane Protein Sorting Signals. *J. Cell Biol.* 2002, *156* (5), 791−795.
(19) Ghosh, P.; Kornfeld, S. AP-1 Binding to Sorting Signals and Release from Clathrin-Coated Vesicles Is Regulated by Phosphorylation. *J. Cell Biol.* 2003, *160* (5), 699−708.
(20) Conner, S. D.; Schmid, S. L. Differential Requirements for AP-2 in Clathrin-Mediated Endocytosis. *J. Cell Biol.* 2003, *162* (5), 773−779.

(21) Umeda, A.; Meyerholz, A.; Ungewickell, E. Identification of the Universal Cofactor (Auxilin 2) in Clathrin Coat Dissociation. *Eur. J. Cell Biol.* 2000, *79* (5), 336−342.

(22) Xiao, F.; Wang, S.; Barouch-Bentov, R.; Neveu, G.; Pu, S.; Beer, M.; Schor, S.; Kumar, S.; Nicolaescu, V.; Lindenbach, B. D.; Randall, G.; Einav, S. Interactions between the Hepatitis C Virus Non-structural 2 Protein and Host Adaptor Proteins 1 and 4 Orchestrate Virus Release. *mBio* 2018, *9* (2), e02233-17.

(23) Fedorov, O.; Marsden, B.; Pogacic, V.; Rellos, P.; Muller, S.; Bullock, A. N.; Schwaller, J.; Sundstrom, M.; Knapp, S. A Systematic Interaction Map of Validated Kinase Inhibitors with Ser/Thr Kinases. *Proc. Natl. Acad. Sci. U. S. A.* 2007, *104* (51), 20523−20528.

(24) Davis, M. I.; Hunt, J. P.; Herrgard, S.; Ciceri, P.; Wodicka, L. M.; Pallares, G.; Hocker, M.; Treiber, D. K.; Zarrinkar, P. P. Comprehensive Analysis of Kinase Inhibitor Selectivity. *Nat. Biotechnol.* 2011, *29* (11), 1046−1051.

(25) Karaman, M. W.; Herrgard, S.; Treiber, D. K.; Gallant, P.; Atteridge, C. E.; Campbell, B. T.; Chan, K. W.; Ciceri, P.; Davis, M. I.; Edeen, P. T.; Faraoni, R.; Floyd, M.; Hunt, J. P.; Lockhart, D. J.; Milanov, Z. V.; Morrison, M. J.; Pallares, G.; Patel, H. K.; Pritchard, S.; Wodicka, L. M.; Zarrinkar, P. P. A Quantitative Analysis of Kinase Inhibitor Selectivity. *Nat. Biotechnol.* 2008, *26* (1), 127−132.

(26) Scagliotti, G. V.; Krzakowski, M.; Szczesna, A.; Strausz, J.; Makhson, A.; Reck, M.; Wierzbicki, R. F.; Albert, I.; Thomas, M.; Miziara, J. E. A.; Papai, Z. S.; Karaseva, N.; Thongprasert, S.; Portulas, E. D.; von Pawel, J.; Zhang, K.; Selaru, P.; Tye, L.; Chao, R. C.; Govindan, R. Sunitinib plus Erlotinib versus Placebo plus Erlotinib in Patients with Previously Treated Advanced Non-Small-Cell Lung Cancer: A Phase III Trial. *J. Clin. Oncol.* 2012, *30* (17), 2070−2078.

(27) Bah, E. I.; Lamah, M.-C.; Fletcher, T.; Jacob, S. T.; Brett-Major, D. M.; Sall, A. A.; Shindo, N.; Fischer, W. A.; Lamontagne, F.; Saliou, S. M.; Bausch, D. G.; Moumié, B.; Jagatic, T.; Sprecher, A.; Lawler, J. V.; Mayet, T.; Jacquerioz, F. A.; Mendez Baggi, M. F.; Vallenas, C.; Clement, C.; Mardel, S.; Faye, O.; Faye, O.; Soropogui, B.; Magassouba, N.; Koivogui, L.; Pinto, R.; Fowler, R. A. Clinical Presentation of Patients with Ebola Virus Disease in Conakry, Guinea. *N. Engl. J. Med.* 2015, *372* (1), 40−47.

(28) Asquith, C. R. M.; Laitinen, T.; Bennett, J. M.; Godoi, P. H.; East, M. P.; Tizzard, G. J.; Graves, L. M.; Johnson, G. L.; Dornsife, R. E.; Wells, C. I.; Elkins, J. M.; Willson, T. M.; Zuercher, W. J. Identification and Optimization of 4-Anilinoquinolines as Inhibitors of Cyclin G Associated Kinase. *ChemMedChem* 2018, *13* (1), 48−66.

(29) Kovackova, S.; Chang, L.; Bekerman, E.; Neveu, G.; Barouch-Bentov, R.; Chaikuad, A.; Heroven, C.; Sala, M.; De Jonghe, S.; Knapp, S.; Einav, S.; Herdewijn, P. Selective Inhibitors of Cyclin G Associated Kinase (GAK) as Anti- Hepatitis C Agents. *J. Med. Chem.* 2015, *58*, 3393−3410.

(30) Li, J.; Kovackova, S.; Pu, S.; Rozenski, J.; De Jonghe, S.; Einav, S.; Herdewijn, P. Isothiazolo[4,3-b]Pyridines as Inhibitors of Cyclin G Associated Kinase: Synthesis, Structure−activity Relationship Studies and Antiviral Activity. *MedChemComm* 2015, *6* (9), 1666−1672.

(31) Fabian, M. A.; Biggs, W. H.; Treiber, D. K.; Atteridge, C. E.; Azimioara, M. D.; Benedetti, M. G.; Carter, T. A.; Ciceri, P.; Edeen, P. T.; Floyd, M.; Ford, J. M.; Galvin, M.; Gerlach, J. L.; Grotzfeld, R. M.; Herrgard, S.; Insko, D. E.; Insko, M. A.; Lai, A. G.; Lelias, J.-M.; Mehta, S. A.; Milanov, Z. V.; Velasco, A. M.; Wodicka, L. M.; Patel, H. K.; Zarrinkar, P. P.; Lockhart, D. J. A Small Molecule−kinase Interaction Map for Clinical Kinase Inhibitors. *Nat. Biotechnol.* 2005, *23* (3), 329−336.

(32) Xie, X.; Gayen, S.; Kang, C.; Yuan, Z.; Shi, P.-Y. Membrane Topology and Function of Dengue Virus NS2A Protein. *J. Virol.* 2013, *87* (8), 4609−4622.

(33) Zou, G.; Xu, H. Y.; Qing, M.; Wang, Q. Y.; Shi, P. Y. Development and Characterization of a Stable Luciferase Dengue Virus for High-Throughput Screening. *Antiviral Res.* 2011, *91* (1), 11−19.

(34) Rodriguez-Madoz, J. R.; Bernal-Rubio, D.; Kaminski, D.; Boyd, K.; Fernandez-Sesma, A. Dengue Virus Inhibits the Production of

Type I Interferon in Primary Human Dendritic Cells. *J. Virol.* 2010, *84* (9), 4845−4850.

(35) Schmid, M. A.; Diamond, M. S.; Harris, E. Dendritic Cells in Dengue Virus Infection: Targets of Virus Replication and Mediators of Immunity. *Front. Immunol.* 2014, *5*, 647.

(36) O'Gorman, S.; Fox, D. T.; Wahl, G. M. Recombinase-Mediated Gene Activation and Site-Specific Integration in Mammalian Cells. *Science* 1991, *251* (4999), 1351−1355.

(37) Clark, M. J.; Miduturu, C.; Schmidt, A. G.; Zhu, X.; Pitts, J. D.; Wang, J.; Potisopon, S.; Zhang, J.; Wojciechowski, A.; Hann Chu, J. J.; Gray, N. S.; Yang, P. L. GNF-2 Inhibits Dengue Virus by Targeting Abl Kinases and the Viral E Protein. *Cell Chem. Biol.* 2016, *23* (4), 443−452.

(38) García, M.; Cooper, A.; Shi, W.; Bornmann, W.; Carrion, R.; Kalman, D.; Nabel, G. J. Productive Replication of Ebola Virus Is Regulated by the C-Abl1 Tyrosine Kinase. *Sci. Transl. Med.* 2012, *4* (123), 123ra24.

(39) Roskoski, R. Signaling by Kit Protein-Tyrosine Kinase⎯The Stem Cell Factor Receptor. *Biochem. Biophys. Res. Commun.* 2005, *337* (1), 1−13.

(40) Huang, C. Y.-H.; Butrapet, S.; Moss, K. J.; Childers, T.; Erb, S. M.; Calvert, A. E.; Silengo, S. J.; Kinney, R. M.; Blair, C. D.; Roehrig, J. T. The Dengue Virus Type 2 Envelope Protein Fusion Peptide Is Essential for Membrane Fusion. *Virology* 2010, *396* (2), 305−315.

(41) Torres, J. Z.; Miller, J. J.; Jackson, P. K. High-Throughput Generation of Tagged Stable Cell Lines for Proteomic Analysis. *Proteomics* 2009, *9* (10), 2888−2891.

O

Research paper

Cyclin G-associated kinase (GAK) affinity and antiviral activity studies of a series of 3-*C*-substituted isothiazolo[4,3-*b*]pyridines

Randy Wouters [a], Szu-Yuan Pu [b], Mathy Froeyen [a], Eveline Lescrinier [a], Shirit Einav [b], Piet Herdewijn [a], Steven De Jonghe [a, *, 1]

[a] *Medicinal Chemistry, Rega Institute for Medical Research, KU Leuven, Herestraat 49, bus 1041, 3000, Leuven, Belgium*
[b] *Department of Medicine, Division of Infectious Diseases and Geographic Medicine, Department of Microbiology and Immunology, Stanford University School of Medicine, Stanford, CA, 94305, USA*

a b s t r a c t

Cyclin G-associated kinase (GAK) is a cellular regulator of the clathrin-associated host adaptor proteins AP-1 and AP-2, which regulates intracellular trafficking of dengue virus during early and late stages of the viral lifecycle. Previously, the discovery of isothiazolo[4,3-*b*]pyridines as potent and selective GAK inhibitors with promising antiviral activity was reported. In this manuscript, the synthesis of isothiazolo [4,3-*b*]pyridines with a carbon-linked substituent at position 3 is described by the application of regioselective Suzuki and Sonogashira coupling reactions. A derivative with a 3,4-dimethoxyphenyl residue at position 3 demonstrates low nanomolar binding affinity for GAK and antiviral activity against dengue virus. These findings reveal that appropriate substitution of a phenyl moiety at position 3 of the scaffold can improve GAK binding affinity.

1. Introduction

Human kinases are a well-established class of drug targets. For more than 30 years, the search for kinase inhibitors has been the focus of significant pharmaceutical research. Today, more than 200 small molecule kinase inhibitors are in clinical trials, and about 30 such drugs have already received marketing approval for use in humans. Because of the central role of kinases in intracellular signal transduction, kinases have mainly been targeted for oncology indications [1]. Deregulation of kinase activity has also been implicated in various other diseases, ranging from inflammatory and autoimmune diseases [2] to neurological disorders [3]. However, indications for kinase-targeted drugs beyond cancer are lagging behind, with a single kinase inhibitor, Tofacitinib, receiving market approval for the treatment of rheumatoid arthritis [4].

Viruses depend on various host cellular kinases for their replication [5]. For example, phosphatidylinositol-4-kinase IIIb (PI4KIIIb), is an essential host factor for many viruses, including

enteroviruses, rhinoviruses and hepatitis C virus (HCV) [6]. The specific inhibition of the Raf/MEK/ERK mitogenic kinase cascade by a small molecule was shown to strongly impair the replication of all influenza virus A and B-types [7]. Phosphatidylinositol 3-kinase class II alpha (PI3KeC2A) likely plays a prominent role in the production of infectious human cytomegalovirus (HCMV) virions [8]. Using a combination of small molecule inhibitors and an RNA interference approach, it has been demonstrated that polo-like-kinase 1 activity is crucial for the replication of the hepatitis virus B (HBV) [9]. As these host kinases are required for the viral life cycle, they represent candidate therapeutic targets for antiviral therapy. Although toxicity might be an issue, the restriction of viral replication by targeting host factors is an attractive strategy, since it may confer a higher genetic barrier for the development of resistance than antiviral agents acting on viral factors. In addition, since many viruses rely on overlapping host factors for their life cycle, broad-spectrum antivirals can be developed by targeting cellular kinases [10].

In the past few years, our group has focused on cyclin G-associated kinase (GAK) as an antiviral drug target. GAK is a cellular serine/threonine kinase that plays a major role in clathrin-mediated membrane trafficking, which is dependent on the action of oligomeric clathrin and adaptor protein complexes (APs)

* Corresponding author.
E-mail address: steven.dejonghe@kuleuven.be (S. De Jonghe).
[1] Present affiliation: Laboratory of Virology and Chemotherapy, Rega Institute for Medical Research, KU Leuven, Herestraat 49 - bus 1043, 3000, Leuven, Belgium.

[11,12]. These APs coordinate the recruitment and assembly of clathrin-coated vesicles (CCVs) as well as their coupling to cargo proteins [12]. GAK phosphorylates the m subunits of AP-1 and AP-2, thereby initiating a conformational change and enhancing their binding to sorting signals (in the form of tyrosine- or dileucine-based motifs) within the cargo [13e15]. Moreover, GAK recruits clathrin and AP-2 to the plasma membrane and AP-1 to the *trans*-Golgi network (TGN) [15,16]. GAK also controls the uncoating of CCVs to recycle clathrin back to the cell surface [11e13,15,17]. GAK-dependent phosphorylation of APs has been implicated in the life cycle of multiple viruses including HCV and dengue virus (DENV) (*Flaviviridae* family) and the Ebola virus (EBOV) (*Filoviridae* family) [18e20].

We have previously reported the discovery of 3,6-disubstituted isothiazolo[4,3-*b*]pyridines as potent and selective GAK inhibitors with antiviral activity against HCV, DENV, EBOV and chikungunya virus (CHIKV) (*Togaviridae* family) [21,22]. Structural modifications revealed that an aromatic moiety, and particularly a 3,4-dimethoxyphenyl (compound 1, Fig. 1), a 3,4,5-trimethoxyphenyl (compound 2, Fig. 1) and a 3-methoxy-4-aminophenyl (compound 3, Fig. 1) at position 6 in combination with morpholine at position 3 is optimal for potent GAK affinity [22]. Recently, the structure-activity relationship (SAR) at position 3 of the isothiazolo [4,3-*b*]pyridine skeleton was studied more exhaustively [21]. The introduction of different amines revealed that methyl substituted morpholine analogues (Fig. 1) are optimal for GAK binding (low nM Kd values) and for antiviral activity (low mM EC$_{50}$ values) [21]. The insertion of other nitrogen containing nucleophiles [21,22] and oxygen nucleophiles (alkoxides) [23] yielded compounds with a greatly diminished GAK affinity. Similarly, introduction of carboxamide side chains reduced activity [23].

In the scheme established for the preparation of a library of 3,6-disubstituted isothiazolo[4,3-*b*]pyridines, 3,6-dibromoisothiazolo [4,3-*b*]pyridine 4 was synthesized as a key intermediate at a large scale [21e23]. Polyhalogenated heteroaromatics are attractive synthons in medicinal chemistry, as they allow for sequential palladium-catalyzed cross-coupling reactions, giving rise to a library of compounds with structural variety. In this manuscript, we describe our efforts to further explore the SAR of the isothiazolo [4,3-*b*]pyridine scaffold with respect to GAK inhibition, by performing hitherto unknown regioselective palladium-catalyzed cross-coupling reactions at the isothiazolo[4,3-*b*]pyridine skeleton.

2. Chemistry

The key intermediate 3,6-dibromoisothiazolo[4,3-*b*]pyridine 4 was resynthesized at a large scale, starting from commercially available 3-nitro-5-bromopyridine-2-carbonitrile in 4 steps, according to a known procedure [21e23].
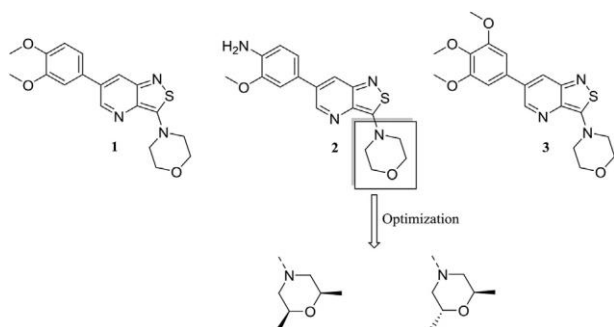

Fig. 1. Optimal substitution pattern of isothiazolo[4,3-b]pyridines as GAK inhibitors.

Aryl and heteroaryl groups were regioselectively introduced at position 3 of compound 4 by a Suzuki coupling using classical reaction conditions: Pd(PPh$_3$)$_4$ as the catalyst, an appropriate aryl-boronic acid (R$_3$B(OH)$_2$) and K$_2$CO$_3$ as the base in a mixture of dioxane and water. This furnished the desired products 5a-e in yields ranging from 37% to 91% (Scheme 1). Moreover, rather than using the classical arylboronic acids, a Suzuki reaction with *(E)*-styrylboronic acid worked equally well, affording compound 5f. Before the addition of the palladium catalyst, the mixture was degassed and air was replaced by a nitrogen atmosphere to prevent reaction of the catalyst with oxygen [24]. For the subsequent Suzuki coupling with 3,4-dimethoxyphenylboronic acid, the same reaction conditions were applied but longer reaction times (up to 24 h) were required to yield compounds 6a-f. To prevent hydrolysis of the ester function of methyl 4-(6-bromoisothiazolo[4,3-*b*]pyridin-3-yl) benzoate 5g, the second Suzuki coupling at position 6 was carried out in anhydrous conditions using potassium phosphate as a base and dioxane as the solvent, furnishing the desired product 6g in moderate yield. The synthesis of the di-substituted-3,4-dimethoxyphenyl congener was done by using an excess of boronic acid (3 eq) and a longer reaction time (3 days) resulting in the formation of the desired product 6h, albeit in a low yield.

The regiochemistry of the first Suzuki reaction was elucidated by a 2D NMR NOESY experiment (Fig. 2), using compound 6b as a representative example. The clear NOE correlations between Ha e H5/H7 and Hb e H5/H7 confirmed that the 3,4-dimethoxyphenyl moiety is attached to position 6 of the isothiazolo[4,3-*b*]pyridine scaffold.

To introduce various aromatic and aliphatic alkyne functionalities, a Sonogashira coupling reaction was applied according to a general protocol (Scheme 2). Compounds 7a-c were isolated in good yields (59e99%) by using an appropriate acetylene derivative, bis(triphenylphosphine)palladium(II) dichloride (Pd(PPh$_3$)$_2$Cl$_2$) and copper iodide as the catalysts, triethylamine (TEA) as the base and THF as the solvent. In contrast to the Suzuki coupling, the reaction mixture was degassed and filled with argon, since using nitrogen gas consistently led to lower yields. In the last step, the Sonogashira coupling products 7a-c were subjected to a Suzuki coupling with 3,4-dimethoxyphenylboronic acid using the classical reaction conditions (as in Scheme 1) yielding compounds 8a-c.

To ensure the selectivity of the Sonogashira coupling at position 3, a NOESY spectrum of compound 8b was recorded (Fig. 3). The observation of NOE contacts between Ha e H5/H7 and Hbe H5/H7 clearly indicated that the 3,4-dimethoxyphenyl ring is present at position 6 of the isothiazolo[4,3-*b*]pyridine scaffold.

The alkyne functionality of compound 8a was reduced by catalytic hydrogenation using palladium on activated carbon yielding the corresponding alkane 9 in low yield (Scheme 3). Despite carrying out this reaction under 50 psi at room temperature, the reduction never fully achieved completion as a significant amount of alkene 6f was present (61%). Interestingly, based on the vicinal coupling constant ^3J of 16.4 Hz, this alkene turned out to be the thermodynamic *trans*-alkene, rather than the expected kinetic *cis*-alkene. In addition, the spectral data of compound 6f, obtained either via the Suzuki reaction (Scheme 1) or the catalytic hydrogenation of alkyne 8a (Scheme 3) were identical. It is possible that upon reduction of the *cis*-alkene to alkane, a rapid isomerisation occurred to the more thermodynamically stable product. Indeed, *cis*-*trans* isomerizations of alkenes during catalytic hydrogenation have been previously reported in literature [25,26].

3. GAK affinity studies

All compounds were tested for GAK binding affinity using the KINOME*scan*™ platform, which quantitatively measures the ability
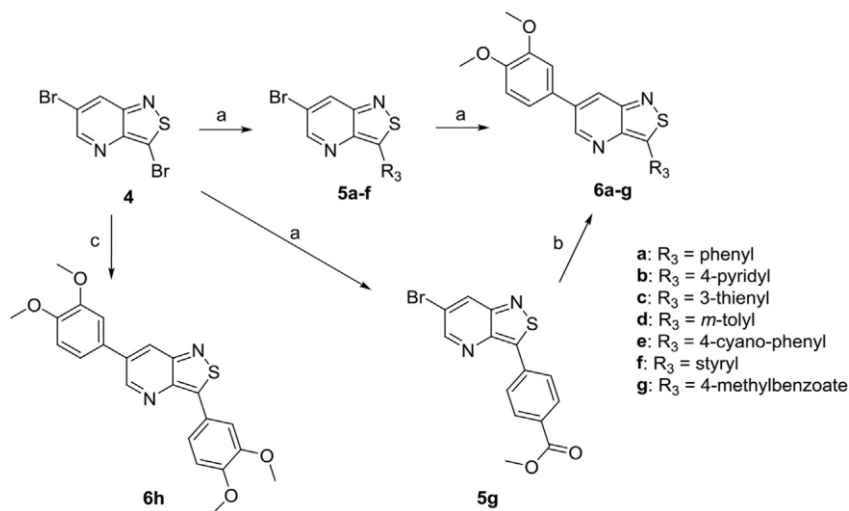
Scheme 1. Suzuki reactions on the isothiazolo[4,3-*b*]pyridine scaffold. *Reagents and conditions:* a) $R_3B(OH)_2$, K_2CO_3, $Pd(PPh_3)_4$, dioxane/water, 100 °C; b) 3,4-dimethoxyphenylboronic acid, K_3PO_4, $Pd(PPh_3)_4$, dioxane, 100 °C; c) 3,4-dimethoxyphenylboronic acid (3 eq), K_2CO_3, $Pd(PPh_3)_4$, dioxane/water, 100 °C, 3 days.
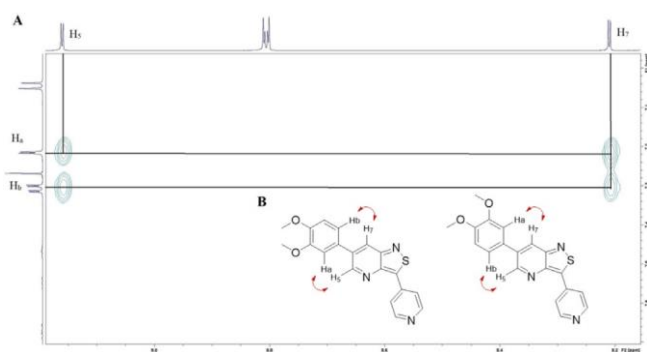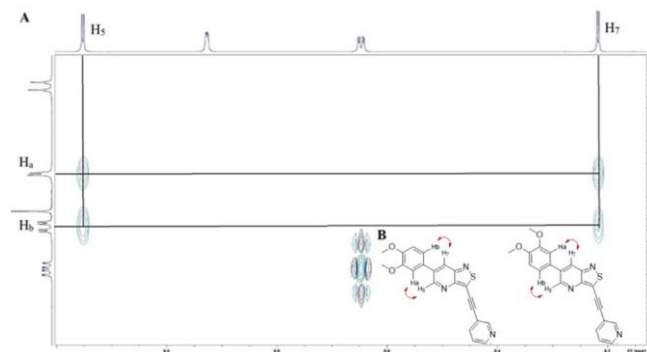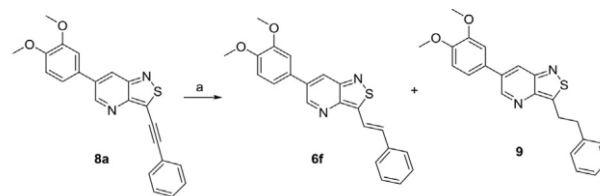

Fig. 2. A) NOESY spectrum of compound **6b**. B) Red arrows showing the spatial interaction between protons of the rotational isomers. (For interpretation of the references to colour in this figure legend, the reader is referred to the Web version of this article.)

Fig. 3. A) NOESY spectrum of compound **8b**. B) Red arrows represent the spatial interaction between protons of the rotational isomers. (For interpretation of the references to colour in this figure legend, the reader is referred to the Web version of this article.)
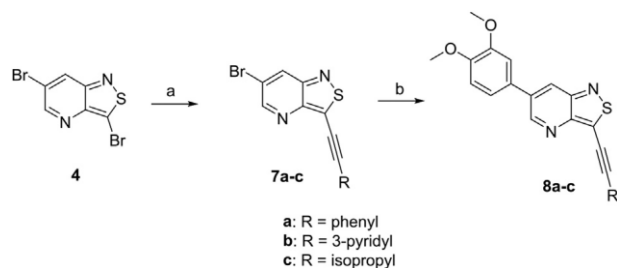
Scheme 2. Sonogashira reactions on the isothiazolo[4,3-*b*]pyridine scaffold. *Reagents and conditions:* a) RCCH, CuI, $Pd(PPh_3)_2Cl_2$, TEA, THF, rt; b) ArB(OH)_2, K_2CO_3, $Pd(PPh_3)_4$, H_2O, dioxane, 100 °C.

Scheme 3. Catalytic reduction of the alkyne moiety. *Reagents and conditions:* a) H_2, Pd/C (10%), 50 psi, rt.

dimethoxyphenyl) congener 1 with a morpholino residue at position 3 as reference compound (Table 1). Substituting the

of a compound to compete with an immobilized active-site-directed ligand [27]. Previous research demonstrated that the presence of electron donating groups (e.g. methoxy, amino) at the phenyl moiety at position 6 of the isothiazolo[4,3-*b*]pyridine scaffold is essential for potent GAK affinity [21e23]. Because of the low cost of commercially available 3,4-dimethoxyphenylboronic acid and its high GAK potency (Kd of 52 nM), we selected the 6-(3,4-
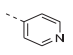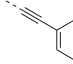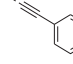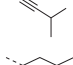
morpholine of compound 1 for different aromatic moieties, such as a phenyl (compound 6a), pyridyl (compound 6b) or thienyl ring (compound 6c) resulted in a 10-fold drop in GAK binding affinity. In an effort to restore the potent GAK affinity, various phenyl substituted analogues were synthesized. The introduction of a methyl ester or a cyano functionality at position 4 of the phenyl ring, afforded compounds 6g and 6e, respectively, both of which completely lacked GAK affinity (Kd > 30 mM). In contrast, introducing an *m*-toluyl (compound 6d) instead of the parent phenyl led to a marginally more active compound (Kd ¼ 0.4 mM). The presence of a 3,4-dimethoxyphenyl residue at position 3 of the isothiazolo [4,3-*b*]pyridine scaffold (compound 6h) resulted in a potent GAK

Table 1
SAR at position 3 of isothiazolo[4,3-b]pyridine.

Cmpd #	R$_3$	Kd (mM)[a]
1	morpholine	0.052
6a	phenyl	0.77
6b	pyridyl	0.52
6c	thienyl	0.86
6d	methylphenyl	0.4
6e	cyanophenyl	>30
6f	styryl	2
6g	methyl benzoate	>30
6h	dimethoxyphenyl	0.041
8a	phenylethynyl	>30
8b	pyridylethynyl	7.6
8c	isopropylethynyl	3.2
9	phenylethyl	3.2

[a] Kd ¼ GAK dissociation constant. Values represent the average of two independent experiments.

ligand, displaying a Kd value of 41 nM.

Different spacers between the phenyl and the central isothiazolo[4,3-b]pyridine scaffold were also evaluated. The 3-styryl-isothiazolo[4,3-b]pyridine derivative (compound **6f**), having an ethenyl linker, was three fold less active as GAK binder than the corresponding 3-phenyl derivative. The presence of an alkyn linker afforded compound **8a**, which was completely devoid of GAK affinity (Kd > 30 mM). Substituting the phenyl moiety of compound **8a** for either a 3-pyridyl moiety (compound **8b**) or isopropyl group (compound **8c**) restored GAK affinity to a limited extent (Kd values of 7.6 mM and 3.2 mM, respectively). In order to increase the conformational flexibility, an analogue with a saturated ethyl linker (compound **9**) was also prepared, displaying a Kd value of 3.2 mM.

4. Molecular modeling

Among the 3-aryl substituted isothiazolo[4,3-b]pyridines, compound **6h** is the only congener endowed with potent GAK

affinity. To explain the improved GAK affinity of compound **6h** compared to the 3-phenyl analogue **6a**, a docking study was performed using Autodock Vina. Docking started from the known co-crystal structure of GAK and compound **2**, displaying a Kd value of 9 nM [22]. The binding mode of both compounds **6a** and **6h** was compared, while compound **2** was used as control. The three compounds (**2**, **6a** and **6h**) are structurally very similar, and hence, they bind in a similar way into the ATP binding site of GAK, with mainly hydrophobic interactions between GAK and the inhibitor. However, compound **6h** prefers an orientation facilitating a hydrogen bond between one of the methoxy groups of the 3,4-dimethoxyphenyl residue at position 3 with the Lys69 side chain. In addition, this orientation creates hydrogen bond opportunities between the two methoxy groups of the 3,4-dimethoxyphenyl moiety at position 6 with the Arg44 side chain thereby anchoring the inhibitor and thus explaining its improved GAK affinity compared to compound **6a**. The resulting top orientation of **6h** superimposed on compound **2** is shown in Fig. 4.

5. Antiviral evaluation

cycle of DENV and GAK inhibitors show activity against DENV [19,21,28]. All compounds arising from the current SAR study were therefore evaluated for their antiviral activity. Huh7 cells infected with DENV2 (New Guinea C strain) harboring a luciferase reporter [29,30] were treated with each compound for 48 h. Fifty percent effective concentration (EC$_{50}$) values were measured via luciferase assays and half-maximal cytotoxic concentration (CC$_{50}$) values were measured in the same cell culture wells via AlamarBlue assays. In line with the poor GAK affinity of most of the congeners, no antiviral activity was detected up to a concentration of 10 mM. Nevertheless, the most potent isothiazolo[4,3-b]pyridine (compound **6h**) displayed modest antiviral activity with an EC$_{50}$ of 3.35 mM, with a minimal effect on cellular viability at the concentrations tested (Fig. 5).

6. Conclusion

In this manuscript, the synthesis of hitherto unknown 3-*C*-linked isothiazolo[4,3-*b*]pyridines by the application of regiose-

lective Suzuki and Sonogashira cross-coupling reactions is described. Evaluation of the compounds as potential GAK ligands clearly demonstrated that appropriate substitution of the phenyl moiety at position 3 improved GAK affinity. The most potent congener in this series was the 3-(3,4-dimethoxyphenyl) derivative (compound **6h**), which had a strong affinity for GAK (Kd ¼ 42 nM). Compound **6h** is also endowed with moderate anti-DENV activity
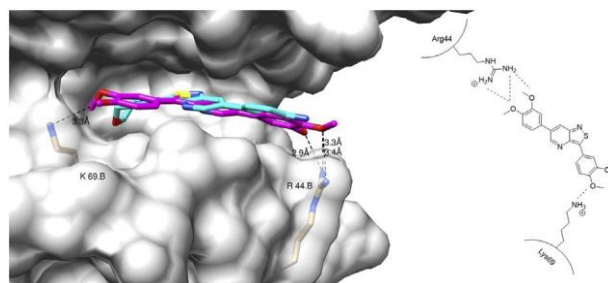

Fig. 4. Autodock Vina docking of inhibitor **6h** (purple carbons) superimposed on the X-ray of compound **2** (cyan carbons). Schematic drawing of interactions of **6h**. (For interpretation of the references to colour in this figure legend, the reader is referred to the Web version of this article.)

Fig. 5. Inhibition of DENV infection by compound **6h**. Cell viability (black) and dose response of DENV infection (red) to compound **6h** measured by luciferase and alamarBlue assays, respectively, 48 h after infection. Data are plotted relative to vehicle control. Shown is a representative experiment from at least 2 conducted, each with 6 biological replicates; shown are means ± SD. (For interpretation of the references to colour in this figure legend, the reader is referred to the Web version of this article.)

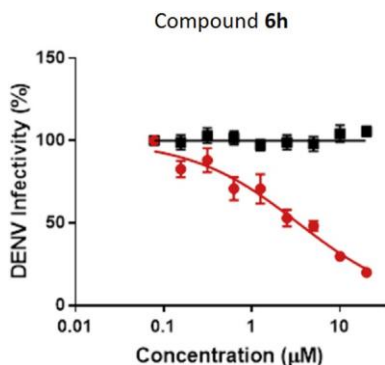with an EC_{50} value of 3.35 mM. Moreover, a docking study showed that the 3,4-dimethoxyphenyl substituent at position 3 of compound **6h** forms a hydrogen bond with Lys44, thereby optimizing its orientation in the ATP-binding site. It allows the formation of additional hydrogen bonds between the 3,4-dimethoxyphenyl moiety at position 6 of the scaffold and GAK, explaining the potent binding affinity of compound **6h**. Since a large number of arylboronic acids are available, this finding paves the way for the synthesis of a library of 3-(hetero)aryl isothiazolo[4,3-*b*]pyridines to further increase GAK affinity and antiviral activity.

7. Experimental section

7.1. Chemistry

For all reactions, analytical grade solvents were used. All moisture-sensitive reactions were carried out in oven-dried glassware (125 °C). ^{1}H and ^{13}C NMR spectra were recorded on a Bruker Avance 300 MHz instrument (^{1}H NMR, 300 MHz; ^{13}C NMR, 75 MHz), 500 MHz instrument (^{1}H NMR, 500 MHz; ^{13}C NMR, 125 MHz) or a 600 MHz instrument (^{1}H NMR, 600 MHz; ^{13}C NMR, 150 MHz), using tetramethylsilane as internal standard for ^{1}H NMR spectra and DMSO-d_6 (39.5 ppm) or CDCl$_3$ (77.2 ppm) for ^{13}C NMR spectra. Abbreviations used are s ¼ singlet, d ¼ doublet, t ¼ triplet, q ¼ quartet, m ¼ multiplet, b ¼ broad. Coupling constants are expressed in Hz. High resolution mass spectra were acquired on a quadrupole orthogonal acceleration time-of-flight mass spectrometer (Synapt G2 HDMS, Waters, Milford, MA). Samples were infused at 3 mL/min and spectra were obtained in positive or negative ionization mode with a resolution of 15000 (FWHM) using leucine enkephalin as lock mass. Precoated aluminum sheets (Fluka silica gel/TLC-cards, 254 nm) were used for TLC. Column chromatography was performed on silica gel 0.060e0.200 mm, 60 Å (Acros Organics). Purity of final compounds was verified to be >95% by HPLC analysis. HPLC conditions to assess purity were as follows: Shimadzu HPLC equipped with a LC-20AT pump, DGU-20A5 degasser, and a SPD-20A UV-VIS detector; Symmetry C18 column (5 mm, 4.6 mm x 150 mm); gradient elution of H$_2$O/CH$_3$CN from 95/5 or 70/30 to 5/95 over 25 min; flow rate 1 mL/min; wavelength, UV 254 nm. Preparative HPLC purifications were performed using a Phenomenex Gemini 110A column (C18, 10 mM, 21.2 mm x 250 mm).

7.1.1. Suzuki coupling at position 3 of the isothiazolo[4,3-b]pyridine scaffold

7.1.1.1. General procedure. To a mixture of dioxane/water (in a ratio of 4:1) were added 3,6-dibromoisothiazolo[4,3-*b*]pyridine 4, an appropriate boronic acid (1.2 equiv) and potassium carbonate (2 equiv). The mixture was degassed and filled with nitrogen. Subsequently, Pd(PPh$_3$)$_4$ (1 mol % - 10 mol%) was added. The mixture was degassed a second time, filled with nitrogen and stirred at 100 °C for the time specified. After completion of the reaction, solvents were evaporated. The following compounds were made according to this procedure.

7.2. 6-Bromo-3-phenylisothiazolo[4,3-b]pyridine (5a)

This product was prepared from 3,6-dibromoisothiazolo[4,3-*b*] pyridine 4 (200 mg, 0.68 mmol), and phenylboronic acid (100 mg, 0.82 mmol) and stirred for 3 h. The crude residue was purified by silica gel flash column chromatography (using a mixture of heptane/ethyl acetate in a ratio of 90:10 as a mobile phase), yielding the title compound (180 mg, 91%).

^{1}H NMR (300 MHz, DMSO) d 8.92 (d, J ¼ 2.1 Hz, 1H), 8.66 (d, J ¼ 2.1 Hz, 1H), 8.24e8.16 (m, 2H), 7.65e7.52 (m, 3H) ppm.

HRMS *m/z* [MþH]^þ calcd for C$_{12}$H$_7$Br$_1$N$_2$S$_1$: 290.95865, found 290.9587.

7.3. 6-Bromo-3-(pyridin-4-yl)isothiazolo[4,3-b]pyridine (5b)

This product was prepared from 3,6-dibromoisothiazolo[4,3-*b*] pyridine 4 (200 mg, 0.68 mmol), and 4-pyridinylboronic acid (101 mg, 0.82 mmol) and stirred for 4 h. The crude residue was purified by silica gel flash column chromatography (using a mixture of dichloromethane/ethyl acetate in a ratio of 90:10 as a mobile phase), yielding the title compound (107 mg, 54%).

^{1}H NMR (300 MHz, CDCl$_3$) d 8.85 (d, J ¼ 2.1 Hz, 1H), 8.81 (dd, J ¼ 4.6, 1.6 Hz, 2H), 8.36 (d, J ¼ 2.1 Hz, 1H), 8.07 (dd, J ¼ 4.6, 1.6 Hz, 2H) ppm.

HRMS *m/z* [MþH]^þ calcd for C$_{11}$H$_6$Br$_1$N$_3$S$_1$: 291.9539, found: 291.9539.

7.4. 6-Bromo-3-(thiophen-3-yl)isothiazolo[4,3-b]pyridine (5c)

This product was prepared from 3,6-dibromoisothiazolo[4,3-*b*] pyridine 4 (200 mg, 0.68 mmol), and 3-thienylboronic acid (105 mg, 0.82 mmol) and stirred for 4 h. The crude residue was purified by silica gel flash column chromatography (using a mixture of dichloromethane/ethyl acetate in a ratio of 90:10 as a mobile phase), yielding the title compound (100 mg, 49%).

^{1}H NMR (300 MHz, DMSO) d 8.90 (d, J ¼ 2.1 Hz, 1H), 8.68e8.58 (m, 2H), 7.93e7.79 (m, 2H) ppm.

^{13}C NMR (75 MHz, DMSO) d 153.31, 151.78, 131.29, 131.01, 129.30, 128.38, 126.77, 126.70, 121.12, 120.46 ppm.

HRMS *m/z* [MþH]^þ calcd for C$_{11}$H$_6$Br$_1$N$_3$S$_1$: 291.9539, found: 291.9539.

7.5. 6-Bromo-3-(m-tolyl)isothiazolo[4,3-b]pyridine (5d)

This product was prepared from 3,6-dibromoisothiazolo[4,3-*b*] pyridine 4 (75 mg, 0.26 mmol), and *m*-tolylboronic acid (42 mg, 1.31 mmol) and stirred overnight. The crude residue was purified by silica gel flash column chromatography (using a mixture of heptane/ethyl acetate in a ratio of 97:3 as a mobile phase), yielding the title compound (37 mg, 47%).

^{1}H NMR (300 MHz, CDCl$_3$) d 8.77 (d, J ¼ 2.0 Hz, 1H), 8.27 (d, J ¼ 2.1 Hz, 1H), 7.98e7.80 (m, 2H), 7.47e7.37 (m, 1H), 7.34e7.26 (m, 1H), 2.46 (s, 3H) ppm.

7.6. 4-(6-Bromoisothiazolo[4,3-b]pyridin-3-yl)benzonitrile (5e)

This product was prepared from 3,6-dibromoisothiazolo[4,3-*b*]pyridine 4 (50 mg, 0.17 mmol), and 4-cyanophenylboronic acid (29 mg, 0.20 mmol) and stirred overnight. The crude residue was purified by silica gel flash column chromatography (using a mixture of heptane/ethyl acetate in a ratio of 90:10 as a mobile phase), yielding the title compound (20 mg, 37%).

^{1}H NMR (300 MHz, CDCl$_3$) ð 8.83 (d, *J* ¼ 2.1 Hz, 1H), 8.35 (d, *J* ¼ 2.1 Hz, 1H), 8.33e8.30 (m, 2H), 7.86e7.78 (m, 2H) ppm.

7.7. (E)-6-Bromo-3-styrylisothiazolo[4,3-b]pyridine (5f)

This product was prepared from 3,6-dibromoisothiazolo[4,3-*b*]pyridine 4 (100 mg, 0.34 mmol), and (*E*)-styrylboronic acid (105 mg, 0.82 mmol) and stirred overnight. The crude residue was purified by silica gel flash column chromatography (using a mixture of heptane/acetone in a ratio of 90:10 as a mobile phase), yielding the title compound (45 mg, 42%).

^{1}H NMR (300 MHz, CDCl$_3$) ð 8.74 (d, *J* ¼ 2.1 Hz, 1H), 8.26 (d, *J* ¼ 2.1 Hz, 1H), 7.82 (d, *J* ¼ 16.4 Hz, 1H), 7.71 (d, *J* ¼ 16.7 Hz, 1H), 7.67e7.64 (m, 2H), 7.48e7.33 (m, 3H) ppm.

^{13}C NMR (151 MHz, CDCl$_3$) ð 160.79, 156.30, 150.57, 149.77, 149.61, 144.20, 136.15, 136.07, 135.26, 129.83, 129.08, 128.87, 127.22, 125.02, 120.09, 115.78, 111.73, 110.41, 56.03 ppm.

HRMS *m/z* [MþH]^þ calcd for C$_{11}$H$_6$Br$_1$N$_3$S$_1$: 316.9743, found: 316.9778.

7.8. Methyl 4-(6-bromoisothiazolo[4,3-b]pyridin-3-yl)benzoate (5g)

This product was prepared from 3,6-dibromoisothiazolo[4,3-*b*]pyridine 4 (100 mg, 0.34 mmol), and 3-methoxycarbonylphenylboronic acid (74 mg, 0.41 mmol) and stirred overnight. The crude residue was purified by silica gel flash column chromatography (using a mixture of heptane/acetone in a ratio of 95:5 as a mobile phase), yielding the title compound (60 mg, 51%).

^{1}H NMR (300 MHz, CDCl$_3$) ð 8.83 (d, *J* ¼ 2.1 Hz, 1H), 8.33 (d, *J* ¼ 2.1 Hz, 1H), 8.27e8.17 (m, 4H), 3.97 (s, 3H) ppm.

HRMS *m/z* [MþH]^þ calcd for C$_{14}$H$_9$Br$_1$N$_2$O$_2$S$_1$: 348.9641, found:348.9637.

7.8.1. Sonogashira coupling at position 3 of the isothiazolo[4,3-b] pyridine scaffold

7.8.1.1. General procedure. To a solution of 3,6-dibromoisothiazolo[4,3-*b*]pyridine 4 in dry THF were added an appropriate acetylene derivative (0.95 eq), triethylamine (3 eq), CuI (1 mol%) and Pd(PPh$_3$)$_2$Cl$_2$ (1 mol%). The mixture was degassed and filled with argon three times, and stirred at room temperature overnight. After disappearance of the starting material, the volatiles were evaporated *in vacuo* and the crude residue was purified by silica gel flash chromatography. The following compounds were made according to this procedure.

7.9. 6-Bromo-3-(phenylethynyl)isothiazolo[4,3-b]pyridine (7a)

This product was prepared from 3,6-dibromoisothiazolo[4,3-*b*]pyridine 4 (100 mg, 0.34 mmol), and phenylacetylene (33 mg, 1.32 mmol) and stirred for 3 h. The crude residue was purified by silica gel flash column chromatography (using a mixture of heptane/ethyl acetate in a ratio of 95:5 as a mobile phase), yielding the title compound (86 mg, 80%).

^{1}H NMR (300 MHz, DMSO) ð 8.94 (d, *J* ¼ 2.0 Hz, 1H), 8.73 (d, *J* ¼ 2.0 Hz, 1H), 7.73e7.44 (m, 5H) ppm.

^{13}C NMR (75 MHz, CDCl$_3$) ð 155.20, 153.54, 152.76, 147.00, 146.22, 132.25, 131.57, 130.18, 128.83, 121.97, 121.11, 109.30 ppm.

HRMS *m/z* [MþH]^þ calcd for C$_{14}$H$_7$Br$_1$N$_2$S$_1$: 314.9587, found: 314.9586.

7.10. 6-Bromo-3-(pyridin-3-ylethynyl)isothiazolo[4,3-b]pyridine (7b)

This product was prepared from 3,6-dibromoisothiazolo[4,3-*b*]pyridine 4 (100 mg, 0.34 mmol), and 3-ethynylpyridine (33 mg, 0.32 mmol) and stirred overnight. The crude residue was purified by silica gel flash column chromatography (using a mixture of heptane/acetone in a ratio of 60:40 as a mobile phase), yielding the title compound (60 mg, 59%).

^{1}H NMR (300 MHz, CDCl$_3$) ð 8.92e8.88 (m, 1H), 8.84 (d, *J* ¼ 2.1 Hz, 1H), 8.67e8.62 (m, 1H), 8.35 (d, *J* ¼ 2.1 Hz, 1H), 7.98e7.93 (m, 1H), 7.39e7.33 (m, 1H) ppm.

^{13}C NMR (75 MHz, CDCl$_3$) ð 155.21, 153.55, 153.18, 152.65, 150.32, 139.03, 131.67, 123.46, 121.26, 119.28, 105.22, 79.79 ppm.

HRMS *m/z* [MþH]^þ calcd for C$_{13}$H$_6$Br$_1$N$_3$S$_1$: 315.9539, found: 315.9536.

7.11. 6-Bromo-3-(3-methylbut-1-yn-1-yl)isothiazolo[4,3-b] pyridine (7c)

This product was prepared from 3,6-dibromoisothiazolo[4,3-*b*]pyridine 4 (100 mg, 0.34 mmol), and 3-methyl-1-butyne (23 mg, 0.32 mmol) and stirred overnight. The crude residue was purified by silica gel flash column chromatography (using a mixture of heptane/ethyl acetate in a ratio of 90:10 as a mobile phase), yielding the title compound (95 mg, 99%).

^{1}H NMR (300 MHz, CDCl$_3$) ð 8.77 (d, *J* ¼ 2.1 Hz, 1H), 8.28 (d, *J* ¼ 2.1 Hz, 1H), 3.04 (hept, *J* ¼ 6.9 Hz, 1H), 1.38 (s, 3H), 1.36 (s, 3H) ppm.

HRMS *m/z* [MþH]^þ calcd for C$_{11}$H$_9$Br$_1$N$_2$S$_1$: 280.9743, found: 280.9743.

7.11.1. Suzuki coupling at position 6 of the isothiazolo[4,3-b] pyridine scaffold

7.11.1.1. General procedure. To a mixture of dioxane/water (in a ratio of 4:1) were added the appropriate 3-substituted-6-bromoisothiazolo[4,3-*b*]pyridine analogue 5a-f, 3,4-dimethoxyphenylboronic acid (1.2 equiv) and potassium carbonate (2 equiv). The mixture was degassed, filled with nitrogen and Pd(PPh$_3$)$_4$ (1 mol % - 10 mol%) was added. The mixture was degassed a second time, filled with nitrogen and stirred at 100 °C. After completion of the reaction, the solvents were evaporated in *vacuo*. The crude residue was purified by silica gel flash chromatography and, when needed, further purified by RP-HPLC yielding the title compounds.

7.12. 6-(3,4-Dimethoxyphenyl)-3-phenylisothiazolo[4,3-b]pyridine (6a)

The title compound was prepared from 6-bromo-3-phenylisothiazolo[4,3-*b*]pyridine 5a (100 mg, 0.34 mmol). The crude residue was purified by silica gel flash column chromatography (using a mixture of heptane/ethyl acetate in a ratio of 90:10 as a mobile phase), yielding the title compound (60 mg, 59%).

^{1}H NMR (300 MHz, DMSO) ð 9.29 (d, *J* ¼ 2.2 Hz, 1H), 8.45 (d, *J* ¼ 2.2 Hz, 1H), 8.35e8.15 (m, 2H), 7.74e7.32 (m, 5H), 7.12 (d, *J* ¼ 8.9 Hz, 1H), 3.91 (s, 3H), 3.84 (s, 3H) ppm.

^{13}C NMR (75 MHz, DMSO) ð 161.23, 156.78, 151.83, 149.80, 149.52, 142.87, 134.99, 130.26, 129.98, 129.47, 128.72, 128.23, 124.51, 120.13, 112.41, 111.12, 55.88, 55.79 ppm.

HRMS m/z [MþH]þ calcd for C$_{20}$H$_{16}$N$_2$O$_2$S$_1$: 349.1005, found: 349.1006.

7.13. 6-(3,4-Dimethoxyphenyl)-3-(pyridin-4-yl)isothiazolo[4,3-b] pyridine (6b)

The title compound was prepared from 6-bromo-3-(pyridin-4-yl)isothiazolo[4,3-*b*]pyridine **5b** (107 mg, 0.37 mmol). The crude residue was purified by silica gel flash column chromatography (using a mixture of dichloromethane/acetone in a ratio of 80:20 as a mobile phase), yielding the title compound (67 mg, 52%).

^{1}H NMR (300 MHz, CDCl$_3$) ð 9.16 (d, J ¼ 2.1 Hz, 1H), 8.83e8.79 (m, 2H), 8.21 (d, J ¼ 2.1 Hz, 1H), 8.14 (dd, J ¼ 4.6, 1.5 Hz, 2H), 7.31 (dd, J ¼ 8.3, 2.1 Hz, 1H), 7.22 (d, J ¼ 2.0 Hz, 1H), 7.05 (d, J ¼ 8.3 Hz, 1H), 4.00 (s, 3H), 3.97 (s, 3H) ppm.

^{13}C NMR (151 MHz, CDCl$_3$) ð 158.43, 157.04, 152.36, 150.77, 149.98, 149.70, 144.09, 137.27, 136.00, 129.37, 125.18, 122.00, 120.17, 111.79, 110.36, 56.05.

HRMS m/z [MþH]þ calcd for C$_{19}$H$_{15}$N$_3$O$_2$S$_1$: 350.0958, found: 350.0955.

7.14. 6-(3,4-Dimethoxyphenyl)-3-(thiophen-3-yl)isothiazolo[4,3-b] pyridine (6c)

The title compound was prepared from 6-bromo-3-(thiophen-3-yl)isothiazolo[4,3-*b*]pyridine **5c** (70 mg, 0.24 mmol). The crude residue was purified by silica gel flash column chromatography (using a mixture of dichloromethane/ethyl acetate in a ratio of 80:20 as a mobile phase), yielding the title compound (50 mg, 59%).

^{1}H NMR (300 MHz, DMSO) ð 9.26 (d, J ¼ 2.0 Hz, 1H), 8.71e8.62 (m, 1H), 8.41 (d, J ¼ 2.0 Hz, 1H), 7.99e7.89 (m, 1H), 7.89e7.79 (m, 1H), 7.56e7.44 (m, 2H), 7.12 (d, J ¼ 8.9 Hz, 1H), 3.91 (s, 3H), 3.84 (s, 3H) ppm.

^{13}C NMR (75 MHz, DMSO) ð 156.38, 156.29, 151.52, 149.77, 149.51, 142.75, 135.16, 129.90, 128.79, 128.16, 126.78, 126.00, 124.39, 120.14, 112.40, 111.13, 55.87, 55.78 ppm.

HRMS m/z [MþH]þ calcd for C$_{18}$H$_{14}$N$_2$O$_2$S$_2$: 355.0569, found: 355.0569.

7.15. 6-(3,4-Dimethoxyphenyl)-3-(m-tolyl)isothiazolo[4,3-b] pyridine (6d)

The title compound was prepared from 6-bromo-3-(*m*-tolyl)isothiazolo[4,3-*b*]pyridine **5d** (35 mg, 0.11 mmol). The crude residue was purified by silica gel flash column chromatography (using a mixture of heptane/acetone in a ratio of 90:10 as a mobile phase), yielding the title compound (17 mg, 43%).

^{1}H NMR (300 MHz, CDCl$_3$) ð 9.11 (d, J ¼ 2.1 Hz, 1H), 8.16 (d, J ¼ 2.1 Hz, 1H), 8.02e7.95 (m, 2H), 7.48e7.41 (m, 1H), 7.30 (dd, J ¼ 8.3, 2.1 Hz, 2H), 7.22 (d, J ¼ 2.1 Hz, 1H), 7.03 (d, J ¼ 8.3 Hz, 1H), 3.99 (s, 3H), 3.96 (s, 3H), 2.49 (s, 3H) ppm.

^{13}C NMR (75 MHz, CDCl$_3$) ð 163.02, 157.10, 151.46, 150.16, 150.02, 143.72, 139.25, 135.73, 131.00, 130.53, 130.18, 129.42, 129.28, 125.92, 125.34, 120.39, 112.20, 110.87, 56.35, 21.78 ppm.

HRMS m/z [MþH]þ calcd for C$_{21}$H$_{18}$N$_2$O$_2$S$_1$: 363.1162, found: 363.1158.

7.16. 4-(6-(3,4-Dimethoxyphenyl)isothiazolo[4,3-b]pyridin-3-yl) benzonitrile (6e)

The title compound was prepared from 4-(6-bromoisothiazolo[4,3-*b*]pyridin-3-yl)benzonitrile **5e** (20 mg, 0.063 mmol). The crude residue was purified by silica gel flash column chromatography (using a mixture of heptane/acetone in a ratio of 97:3 as a mobile phase). The residue was further purified by RP-HPLC

(eluting with a mixture of acetonitrile/water using a gradient from 35/65 to 95/5 over 35 min) yielding the title compound (4 mg, 17%).

^{1}H NMR (600 MHz, CDCl$_3$) ð 9.15 (d, J ¼ 2.1 Hz, 1H), 8.43e8.34 (m, 2H), 8.21 (d, J ¼ 2.1 Hz, 1H), 7.90e7.79 (m, 2H), 7.31 (dd, J ¼ 8.3, 2.2 Hz, 1H), 7.22 (d, J ¼ 2.1 Hz, 1H), 7.05 (d, J ¼ 8.3 Hz, 1H), 4.00 (s, 3H), 3.97 (s, 3H) ppm.

^{13}C NMR (151 MHz, CDCl$_3$) ð 159.19, 157.08, 152.31, 150.02, 149.73, 143.74, 136.02, 134.55, 132.91, 129.39, 128.74, 125.23, 120.19, 118.46, 113.01, 111.82, 110.39, 56.08 ppm.

HRMS m/z [MþH]þ calcd for C$_{21}$H$_{15}$N$_3$O$_2$S$_1$: 374.0958, found: 374.0950.

7.17. (E)-6-(3,4-Dimethoxyphenyl)-3-styrylisothiazolo[4,3-b] pyridine (6f)

The title compound was prepared from (E)-6-bromo-3-styrylisothiazolo[4,3-*b*]pyridine **5f** (45 mg, 0.14 mmol). The crude residue was purified by silica gel flash column chromatography (using a mixture of heptane/acetone in a ratio of 90:10 as a mobile phase), yielding the title compound (28 mg, 53%).

^{1}H NMR (600 MHz, CDCl$_3$) ð 9.03 (d, J ¼ 2.1 Hz, 1H), 8.12 (d, J ¼ 2.1 Hz, 1H), 7.87 (d, J ¼ 16.4 Hz, 1H), 7.71 (d, J ¼ 16.4 Hz, 1H), 7.67e7.64 (m, 2H), 7.43e7.40 (m, 2H), 7.37e7.33 (m, 1H), 7.28 (dd, J ¼ 8.3, 2.2 Hz, 1H), 7.20 (d, J ¼ 2.1 Hz, 1H), 7.02 (d, J ¼ 8.3 Hz, 1H), 3.99 (s, 3H), 3.96 (s, 3H) ppm.

^{13}C NMR (151 MHz, CDCl$_3$) ð 160.79, 156.30, 150.57, 149.77, 149.61, 144.20, 136.15, 136.07, 135.26, 129.83, 129.08, 128.87, 127.22, 125.02, 120.09, 115.78, 111.73, 110.41, 56.03 ppm.

HRMS m/z [MþH]þ calcd for C$_{22}$H$_{18}$N$_2$O$_2$S$_1$: 375.1162, found: 375.1159.

7.18. Methyl 4-(6-(3,4-dimethoxyphenyl)isothiazolo[4,3-b]pyridin-3-yl)benzoate (6g)

To a solution of methyl 4-(6-bromoisothiazolo[4,3-*b*]pyridin-3-yl)benzoate **5g** (60 mg, 0.17 mmol) in dioxane (5 mL) were added 3,4-dimethoxyphenylboronic acid (37 mg, 0.20 mmol) and potassium phosphate tribasic (72 mg, 0.34 mmol). The mixture was degassed, filled with nitrogen and Pd(PPh$_3$)$_4$ (20 mg, 0.017 mmol) was added. The mixture was degassed a second time, filled with nitrogen and stirred at 100 °C overnight. After completion, the solvents were evaporated in *vacuo* and crude residue was purified by silica gel flash column chromatography (using a mixture of heptane/acetone in a ratio of 99:1 as a mobile phase), yielding the title compound (22 mg, 32%).

^{1}H NMR (300 MHz, CDCl$_3$) ð 9.15 (d, J ¼ 2.1 Hz, 1H), 8.34e8.30 (m, 2H), 8.24e8.18 (m, 3H), 7.31 (dd, J ¼ 8.3, 2.1 Hz, 1H), 7.22 (d, J ¼ 2.0 Hz, 1H), 7.04 (d, J ¼ 8.3 Hz, 1H), 4.00 (s, 3H), 3.98e3.96 (m, J ¼ 1.4 Hz, 6H) ppm.

^{13}C NMR (75 MHz, CDCl$_3$) ð 166.79, 160.95, 157.30, 152.19, 150.31, 150.09, 144.02, 136.10, 134.78, 131.27, 130.70, 129.96, 128.51, 125.47, 120.48, 112.25, 110.88, 56.38, 52.58 ppm.

HRMS m/z [MþH]þ calcd for C$_{22}$H$_{18}$N$_2$O$_4$S$_1$: 407.1060, found: 407.1052.

7.19. 6-(3,4-Dimethoxyphenyl)-3-(phenylethynyl)isothiazolo[4,3-b] pyridine (8a)

The title compound was prepared from 6-bromo-3-(phenylethynyl)isothiazolo[4,3-*b*]pyridine **7a** (80 mg, 0.27 mmol). The crude residue was purified by silica gel flash column chromatography (using a mixture of heptane/acetone in a ratio of 90:10 as a mobile phase). The residue was further purified by RP-HPLC (eluting with a mixture of acetonitrile/water using a gradient

from 55/45 tot 95/5 over 15 min) yielding the title compound (60 mg, 60%).

^{1}H NMR (300 MHz, CDCl3) d 9.11 (d, *J* ¼ 2.0 Hz, 1H), 8.18 (d, *J* ¼ 2.0 Hz, 1H), 7.74e7.58 (m, 2H), 7.47e7.31 (m, 3H), 7.27 (dd, *J* ¼ 8.3, 2.1 Hz, 1H), 7.18 (d, *J* ¼ 2.0 Hz, 1H), 7.01 (d, *J* ¼ 8.3 Hz, 1H), 3.97 (s, 3H), 3.95 (s, 4H) ppm.

^{13}C NMR (75 MHz, CDCl3) d 155.59, 152.36, 150.38, 150.12, 147.88, 144.78, 136.48, 132.21, 129.91, 128.77, 127.53, 125.65, 122.34, 120.57, 112.28, 111.00, 108.35, 56.41, 56.38 ppm.

HRMS *m/z* [MþH][þ] calcd for $C_{22}H_{16}N_2O_2S_1$: 373.1005, found: 373.1007.

7.20. 6-(3,4-Dimethoxyphenyl)-3-(pyridin-3-ylethynyl)isothiazolo [4,3-b]pyridine (8b)

The title compound was prepared from 6-bromo-3-(pyridin-3-ylethynyl)isothiazolo[4,3-*b*]pyridine **7b** (60 mg, 0.18 mmol). The crude residue was purified by silica gel flash column chromatography (using a mixture of heptane/acetone in a ratio of 60:40 as a mobile phase), yielding the title compound (40 mg, 60%).

^{1}H NMR (300 MHz, CDCl3) d 9.16 (d, *J* ¼ 2.1 Hz, 1H), 8.95e8.91 (m, 1H), 8.65 (dd, *J* ¼ 4.9, 1.6 Hz, 1H), 8.22 (d, *J* ¼ 2.1 Hz, 1H), 8.01e7.95 (m, 1H), 7.37 (ddd, *J* ¼ 7.9, 4.9, 0.8 Hz, 1H), 7.30 (dd, *J* ¼ 8.3, 2.1 Hz, 1H), 7.20 (d, *J* ¼ 2.0 Hz, 1H), 7.04 (d, *J* ¼ 8.4 Hz, 1H), 4.00 (s, 3H), 3.97 (s, 3H) ppm.

^{13}C NMR (151 MHz, CDCl3) d 155.27, 152.48, 152.34, 150.02, 149.81, 149.72, 147.72, 143.30, 138.69, 136.33, 129.36, 125.40, 123.14, 120.26, 119.26, 111.80, 110.45, 104.05, 56.07 ppm.

HRMS *m/z* [MþH][þ] calcd for $C_{21}H_{15}N_3O_2S_1$: 374.0958, found: 374.0952.

7.21. 6-(3,4-Dimethoxyphenyl)-3-(3-methylbut-1-yn-1-yl)isothiazolo[4,3-b]pyridine (8c)

The title compound was prepared from 6-bromo-3-(pyridin-3-ylethynyl)isothiazolo[4,3-*b*]pyridine **7c** (95 mg, 0.34 mmol). The crude residue was purified by silica gel flash column chromatography (using a mixture of heptane/acetone in a ratio of 90:10 as a mobile phase), yielding the title compound (64 mg, 56%).

^{1}H NMR (300 MHz, CDCl3) d 9.08 (d, *J* ¼ 2.1 Hz, 1H), 8.15 (d, *J* ¼ 2.1 Hz, 1H), 7.26 (dd, *J* ¼ 8.3, 2.1 Hz, 1H), 7.17 (d, *J* ¼ 2.1 Hz, 1H), 7.02 (d, *J* ¼ 8.4 Hz, 1H), 3.98 (s, 3H), 3.95 (s, 3H), 3.05 (hept, *J* ¼ 6.9 Hz, 1H), 1.40 (s, 3H), 1.37 (s, 3H) ppm.

^{13}C NMR (75 MHz, CDCl3) d 155.46, 151.97, 150.28, 150.06, 147.69, 145.86, 136.20, 129.96, 125.59, 120.48, 116.13, 112.24, 110.96, 68.28, 56.34, 22.74, 22.53 ppm.

HRMS *m/z* [MþH][þ] calcd for $C_{19}H_{18}N_2O_2S_1$: 339.1162, found: 339.1164.

7.22. 6-(3,4-Dimethoxyphenyl)-3-phenethylisothiazolo[4,3-b]pyridine (9)

To a solution of 6-(3,4-dimethoxyphenyl)-3-(phenylethynyl)isothiazolo[4,3-*b*]pyridine **8a** (50 mg, 0.13 mmol) in dioxane (10 mL) was added palladium on activated carbon (10% Pd, 50% wet with water, 50 mg). The mixture was degassed, filled with hydrogen gas and stirred at 60 psi at room temperature for 7 h. After disappearance of the starting material, the palladium on carbon residue was filtered off and the filtrate was evaporated *in vacuo*. The crude residue was purified by RP-HPLC (using a gradient mixture of acetonitrile/water in a ratio of 40:60 to 95:5 over 40 min) to yield title compound (10 mg, 20%) and (*E*)-6-(3,4-dimethoxyphenyl)-3-styrylisothiazolo[4,3-*b*]pyridine **6f** (25 mg, 51%).

^{1}H NMR (300 MHz, CDCl3) d 9.02 (d, *J* ¼ 2.0 Hz, 1H), 8.13 (d,

J ¼ 2.1 Hz, 1H), 7.35e7.27 (m, 3H), 7.26e7.21 (m, 3H), 7.19 (d, *J* ¼ 2.1 Hz, 1H), 7.03 (d, *J* ¼ 8.3 Hz, 1H), 3.99 (s, 3H), 3.96 (s, 3H), 3.79 (t, *J* ¼ 7.6 Hz, 2H), 3.23 (t, *J* ¼ 7.6 Hz, 2H) ppm.

^{13}C NMR (75 MHz, CDCl3) d 165.15, 155.87, 150.55, 150.16, 150.06, 147.17, 145.48, 140.44, 135.99, 130.46, 128.87, 126.86, 125.32, 120.44, 112.28, 111.05, 99.66, 56.37, 36.82, 28.27 ppm.

HRMS *m/z* [MþH][þ] calcd for $C_{22}H_{20}N_2O_2S_1$: 377.1318, found: 377.1317.

7.23. 3,6-Bis(3,4-dimethoxyphenyl)isothiazolo[4,3-b]pyridine (6h)

To a mixture of dioxane/water (in a ratio of 4:1) were added 3,6-dibromoisothiazolo[4,3-*b*]pyridine **4** (50 mg, 0.17 mmol), 3,4-dimethoxyphenylboronic acid (62 mg, 0.51 mmol, 3 eq) and potassium carbonate (2 equiv). The mixture was degassed, filled with nitrogen and Pd(PPh3)4 (10 mol%) was added. The mixture was degassed a second time, filled with nitrogen and stirred at 100 °C for 3 days. After completion of the reaction, solvents were evaporated *in vacuo*. The crude residue was purified by silica gel flash chromatography (using a mixture of heptane/acetone in a ratio of 95:5 as a mobile phase), yielding the title compound (12 mg, 17%).

^{1}H NMR (300 MHz, CDCl3) d 9.07 (d, *J* ¼ 2.0 Hz, 1H), 8.13 (d, *J* ¼ 2.0 Hz, 1H), 7.87 (d, *J* ¼ 1.8 Hz, 1H), 7.76 (dd, *J* ¼ 8.4, 1.9 Hz, 1H), 7.29 (dd, *J* ¼ 8.3, 2.0 Hz, 1H), 7.20 (d, *J* ¼ 1.8 Hz, 1H), 7.02 (d, *J* ¼ 8.4 Hz, 2H), 4.02 (s, 3H), 3.98 (s, 3H), 3.96 (s, 3H), 3.95 (s, 3H) ppm.

^{13}C NMR (75 MHz, CDCl3) d 162.79, 157.17, 151.16, 151.08, 150.22, 150.07, 149.87, 143.56, 135.80, 130.30, 125.40, 123.71, 121.84, 120.43, 112.28, 112.06, 111.92, 110.99, 56.45, 56.37 ppm.

HRMS *m/z* [MþH][þ] calcd for $C_{22}H_{20}N_2O_4S_1$: 409.1216, found: 409.1210.

7.24. Molecular modeling

Docking started from the GAK structure available in PDB entry 4y8d, from which all ligands and water molecules were removed. The remaining structure was prepared by AutodockTools as a receptor: polar hydrogens were added, Gasteiger charges were added, the AD4 atom type was assigned and finally everything was saved in a PDBQT file. The original inhibitor 12i (compound **2**) from PDB4y8d was extracted and processed by AutodockTool [31]. Polar hydrogens were added, Gasteiger charges were calculated, autodock4 atom types were assigned and everything was saved in a PDBQT file. Compounds **6a** and **6h** were drawn in Chemdraw and a 3D structure was generated by Chem3D. Then, Autodocktools was used again to prepare the PDBQT files. Autodock vina was used for the docking experiments [32]. A cubic box was defined 50 x 50 x 50 units (0.375 Å/unit) and the box was centred at the B.ALA67.CB atom in the second kinase domain (chain B). During docking, the enzyme was rigid and the ligand flexible around the torsion angles. A control docking was executed using the original inhibitor 12i present in the 4y8d PDB file. The root mean square deviation (RMSD) between docked and crystallized ligand is 0.9 Å, showing that the docking program Vina can reproduce the crystallized conformation quite well. Compounds **6a** and **6h** were then docked using the same protocol.

7.25. GAK binding assay

Kd values for GAK were determined as previously described [27]. Briefly, the DNA-tagged GAK, an immobilized ligand on streptavidin-coated magnetic beads, and the test compound are combined. When binding occurs between GAK and a test compound, no binding can occur between GAK and the immobilized ligand. Upon washing, the compound-bound, DNA-tagged GAK is

washed away. The beads carrying the ligands are then resuspended in elution buffer and the remaining kinase concentration measured by qPCR on the eluate. Kd values are determined using dose-response curves.

7.26. Antiviral assays

Virus construct. DENV2 (New Guinea C strain) [29,30] *Renilla* reporter plasmid used for *in vitro* assays was a gift from Pei-Yong Shi (The University of Texas Medical Branch).

Cells. Huh7 (Apath LLC) cells were grown in DMEM (Mediatech) supplemented with 10% FBS (Omega Scientific), nonessential amino acids, 1% L-glutamine, and 1% penicillin-streptomycin (Thermo-Fisher Scientific) and maintained in a humidified incubator with 5% CO_2 at 37 °C.

Virus Production. DENV2 RNA was transcribed *in vitro* using mMessage/mMachine (Ambion) kits. DENV was produced by electroporating RNA into BHK-21 cells, harvesting supernatants on day 10 and titering via standard plaque assays on BHK-21 cells. Virus titers were determined via standard plaque assay on Vero 76 cells.

Infection assays. Huh7 cells were infected with DENV in replicates ($n ¼ 3e10$) for 4 h at MOI of 0.05. Overall infection was measured at 48 h using a *Renilla* luciferase substrate.

Viability assays. Viability was assessed using AlamarBlue® reagent (Invitrogen) or Cell-Titer-Glo® reagent (Promega) assay according to manufacturer's protocol. Fluorescence was detected at 560 nm on InfiniteM1000 plate reader and luminescence on InfiniteM1000 plate reader (Tecan) or a Spectramax 340 PC.

Acknowledgements

Abbreviations

AP	adaptor protein complex
CCV	clathrin-coated vesicle
CHIKV	chikungunya virus
DENV	dengue virus
EBOV	ebola virus
GAK	cyclin G-associated kinase
HBV	hepatitis B virus
HCMV	human cytomegalovirus
HCV	hepatitis C virus
PI3KeC2A	phosphatidylinositol 3-kinase class II alpha
PI4KIIIb	phosphatidylinositol-4-kinase IIIb
SAR	structure activity relationship
TEA	triethylamine
TGN	*trans*-golgi network

Appendix A. Supplementary data

Supplementary data to this article can be found online at https://doi.org/10.1016/j.ejmech.2018.11.065.

References

[1] D. Fabbro, S.W. Cowan-Jacob, H. Möbitz, G. Martiny-Baron, Targeting cancer with small-molecular-weight kinase inhibitors, Methods Mol. Biol. 795 (2012) 1e34, https://doi.org/10.1007/978-1-62703-239-1_1.

[2] M.C. Bryan, N.S. Rajapaksa, Kinase inhibitors for the treatment of immunological disorders: recent advances, J. Med. Chem. (2018), https://doi.org/10.1021/acs.jmedchem.8b00667 acs.jmedchem.8b00667.

[3] Y. Shi, M. Mader, Brain penetrant kinase inhibitors: learning from kinase neuroscience discovery, Bioorg. Med. Chem. Lett 28 (2018) 1981e1991, https://doi.org/10.1016/j.bmcl.2018.05.007.

[4] Y. Tanaka, Recent progress and perspective in JAK inhibitors for rheumatoid arthritis: from bench to bedside, J. Biochem. 158 (2015) 173e179, https://doi.org/10.1093/jb/mvv069.

[5] S. Schor, S. Einav, Repurposing of kinase inhibitors as broad-spectrum antiviral drugs, DNA Cell Biol. 37 (2018) 63e69, https://doi.org/10.1089/dna.2017.4033.

[6] H.M. van der Schaar, P. Leyssen, H.J. Thibaut, A. de Palma, L. van der Linden, K.H.W. Lanke, C. Lacroix, E. Verbeken, K. Conrath, A.M. Macleod, D.R. Mitchell, N.J. Palmer, H. van de Poël, M. Andrews, J. Neyts, F.J.M. van Kuppeveld, A novel, broad-spectrum inhibitor of enterovirus replication that targets host cell factor phosphatidylinositol 4-kinase IIIb, Antimicrob. Agents Chemother. 57 (2013) 4971e4981, https://doi.org/10.1128/AAC.01175-13.

[7] E. Haasbach, C. Müller, C. Ehrhardt, A. Schreiber, S. Pleschka, S. Ludwig, O. Planz, The MEK-inhibitor CI-1040 displays a broad anti-influenza virus activity in vitro and provides a prolonged treatment window compared to standard of care in vivo, Antivir. Res. 142 (2017) 178e184, https://doi.org/10.1016/J.ANTIVIRAL.2017.03.024.

[8] W.S. Polachek, H.F. Moshrif, M. Franti, D.M. Coen, V.B. Sreenu, B.L. Strang, High-Throughput small interfering RNA screening identifies phosphatidylinositol 3-kinase class II alpha as important for production of human cytomegalovirus virions, J. Virol. 90 (2016) 8360e8371, https://doi.org/10.1128/JVI.01134-16.

[9] A. Diab, A. Foca, F. Fusil, T. Lahlali, P. Jalaguier, F. Amirache, L. N'Guyen, N. Isorce, F.-L. Cosset, F. Zoulim, O. Andrisani, D. Durantel, Polo-like-kinase 1 is a proviral host factor for hepatitis B virus replication, Hepatology 66 (2017) 1750e1765, https://doi.org/10.1002/hep.29236.

[10] M. Robinson, S. Schor, R. Barouch-Bentov, S. Einav, Viral journeys on the intracellular highways, Cell. Mol. Life Sci. 75 (2018) 3693e3714, https://doi.org/10.1007/s00018-018-2882-0.

[11] H.T. McMahon, E. Boucrot, Molecular mechanism and physiological functions of clathrin-mediated endocytosis, Nat. Rev. Mol. Cell Biol. 12 (2011) 517e533, https://doi.org/10.1038/nrm3151.

[12] M.A. Edeling, C. Smith, D. Owen, Life of a clathrin coat: insights from clathrin and AP structures, Nat. Rev. Mol. Cell Biol. 7 (2006) 32e44, https://doi.org/10.1038/nrm1786.

[13] D. Ricotta, S.D. Conner, S.L. Schmid, K. Von Figura, S. Höning, Phosphorylation of the AP2 m subunit by AAK1 mediates high affinity binding to membrane protein sorting signals, J. Cell Biol. 156 (2002) 21e9525, https://doi.org/10.1083/jcb.200111068.

[14] L. Zhang, O. Gjoerup, T.M. Roberts, The serine/threonine kinase cyclin G-associated kinase regulates epidermal growth factor receptor signaling, Proc. Natl. Acad. Sci. Unit. States Am. 101 (2004) 10296e10301, https://doi.org/10.1073/pnas.0403175101.

[15] P. Ghosh, S. Kornfeld, AP-1 binding to sorting signals and release from clathrin-coated vesicles is regulated by phosphorylation, J. Cell Biol. 160 (2003) 699e708, https://doi.org/10.1083/jcb.200211080.

[16] D.-W. Lee, X. Zhao, F. Zhang, E. Eisenberg, L.E. Greene, Depletion of GAK/auxilin 2 inhibits receptor-mediated endocytosis and recruitment of both clathrin and clathrin adaptors, J. Cell Sci. 118 (2005) 4311e4321, https://doi.org/10.1242/jcs.02548.

[17] S.K. Lemmon, Clathrin uncoating: auxilin comes to life, Curr. Biol. 11 (2001) R49eR52, https://doi.org/10.1016/S0960-9822(01)00010-0.

[18] G. Neveu, A. Ziv-Av, R. Barouch-Bentov, E. Berkerman, J. Mulholland, S. Einav, AP-2-Associated protein kinase 1 and cyclin G-associated kinase regulate hepatitis C virus entry and are potential drug targets, J. Virol. 89 (2015) 4387e4404, https://doi.org/10.1128/JVI.02705-14.

[19] E. Bekerman, G. Neveu, A. Shulla, J. Brannan, S.Y. Pu, S. Wang, F. Xiao, R. Barouch-Bentov, R.R. Bakken, R. Mateo, J. Govero, C.M. Nagamine, M.S. Diamond, S. De Jonghe, P. Herdewijn, J.M. Dye, G. Randall, S. Einav, Anticancer kinase inhibitors impair intracellular viral trafficking and exert broad-spectrum antiviral effects, J. Clin. Invest. 127 (2017) 1338e1352, https://doi.org/10.1172/JCI89857.

[20] F. Xiao, S. Wang, R. Barouch-Bentov, G. Neveu, S. Pu, M. Beer, S. Schor, S. Kumar, V. Nicolaescu, B.D. Lindenbach, G. Randall, S. Einav, Interactions between the hepatitis C virus nonstructural 2 protein and host adaptor proteins 1 and 4 orchestrate virus release, mBio 9 (2018), https://doi.org/10.1128/mBio.02233-17 e02233-17.

[21] S.-Y. Pu, R. Wouters, S. Schor, J. Rozenski, R. Barouch-Bentov, L.I. Prugar, C.M. O'Brien, J.M. Brannan, J.M. Dye, P. Herdewijn, S. De Jonghe, S. Einav, Optimization of isothiazolo[4,3-b]pyridine-based inhibitors of cyclin G associated kinase (GAK) with broad-spectrum antiviral activity, J. Med. Chem. 61 (2018) 6178e6192, https://doi.org/10.1021/acs.jmedchem.8b00613.

[22] S. Kovackova, L. Chang, E. Bekerman, G. Neveu, R. Barouch-Bentov, A. Chaikuad, C. Heroven, M. Sàla, S. De Jonghe, S. Knapp, S. Einav, P. Herdewijn, Selective inhibitors of cyclin G associated kinase (GAK) as anti-hepatitis C agents, J. Med. Chem. 58 (2015) 3393e3410.

[23] J. Li, S. Kovackova, S. Pu, J. Rozenski, S. De Jonghe, S. Einav, P. Herdewijn, Isothiazolo[4,3-b]pyridines as inhibitors of cyclin G associated kinase:

synthesis, structure–activity relationship studies and antiviral activity, Med-chemcomm 6 (2015) 1666e1672, https://doi.org/10.1039/C5MD00229J.

[24] C.J. Nyman, C.E. Wymore, G. Wilkinson, Reactions of tris(triphenylphosphine) platinum(o) and tetrakis(triphenylphosphine)palladium(o) with oxygen and carbon dioxide, J. Chem. Soc. A Inorganic, Phys. Theor. 0 (1968) 561, https://doi.org/10.1039/j19680000561.

[25] B. Brandt, J.-H. Fischer, W. Ludwig, J. Libuda, F. Zaera, S. Schauermann, H.-J. Freund, Isomerization and hydrogenation of *cis* -2-Butene on Pd model catalyst, J. Phys. Chem. C 112 (2008) 11408e11420, https://doi.org/10.1021/jp800205j.

[26] I. Heertje, G.K. Koch, W.J. Wösten, Mechanism of heterogeneous catalytic cis-trans isomerization and double-bond migration of octadecenoates, J. Catal. 32 (1974) 337e342, https://doi.org/10.1016/0021-9517(74)90085-2.

[27] M.A. Fabian, W.H. Biggs, D.K. Treiber, C.E. Atteridge, M.D. Azimioara, M.G. Benedetti, T.A. Carter, P. Ciceri, P.T. Edeen, M. Floyd, J.M. Ford, M. Galvin, J.L. Gerlach, R.M. Grotzfeld, S. Herrgard, D.E. Insko, M.A. Insko, A.G. Lai, J.-M. Lélias, S.A. Mehta, Z. V Milanov, A.M. Velasco, L.M. Wodicka, H.K. Patel, P.P. Zarrinkar, D.J. Lockhart, A small molecule–kinase interaction map for clinical kinase inhibitors, Nat. Biotechnol. 23 (2005) 329e336, https://doi.org/10.1038/nbt1068.

[28] S.-Y. Pu, F. Xiao, S. Schor, E. Bekerman, F. Zanini, R. Barouch-Bentov, C.M. Nagamine, S. Einav, Feasibility and biological rationale of repurposing sunitinib and erlotinib for dengue treatment, Antivir. Res. 155 (2018) 67e75, https://doi.org/10.1016/J.ANTIVIRAL.2018.05.001.

[29] X. Xie, S. Gayen, C. Kang, Z. Yuan, P.-Y. Shi, Membrane topology and function of dengue virus NS2A protein, J. Virol. 87 (2013) 4609e4622, https://doi.org/10.1128/JVI.02424-12.

[30] G. Zou, H.Y. Xu, M. Qing, Q.Y. Wang, P.Y. Shi, Development and character-ization of a stable luciferase dengue virus for high-throughput screening, Antivir. Res. 91 (2011) 11e19, https://doi.org/10.1016/j.antiviral.2011.05.001.

[31] G.M. Morris, R. Huey, W. Lindstrom, M.F. Sanner, R.K. Belew, D.S. Goodsell, A.J. Olson, AutoDock4 and AutoDockTools4: automated docking with selective receptor flexibility, J. Comput. Chem. 30 (2009) 2785e2791, https://doi.org/10.1002/jcc.21256.

[32] O. Trott, A.J. Olson, AutoDock Vina, Improving the speed and accuracy of docking with a new scoring function, efficient optimization, and multi-threading, J. Comput. Chem. 31 (2010) 455e461, https://doi.org/10.1002/jcc.21334.

Synthesis and Structure−Activity Relationships of 3,5-Disubstituted-pyrrolo[2,3-*b*]pyridines as Inhibitors of Adaptor-Associated Kinase 1 with Antiviral Activity

Sven Verdonck,[†] Szu-Yuan Pu,[‡] Fiona J. Sorrell,[§] Jon M. Elkins,[§,∥] Mathy Froeyen,[ID] Ling-Jie Gao,[†] Laura I. Prugar,[#] Danielle E. Dorosky,[#] Jennifer M. Brannan,[#] Rina Barouch-Bentov,[‡] Stefan Knapp,[§,⊥ID] John M. Dye,[#] Piet Herdewijn,[†ID] Shirit Einav,*[,‡ID] and Steven De Jonghe*[,†ID]

[†]Medicinal Chemistry, Rega Institute for Medical Research, KU Leuven, Herestraat 49□bus 1041, 3000 Leuven, Belgium

[‡]Department of Medicine, Division of Infectious Diseases and Geographic Medicine, and Department of Microbiology and Immunology, Stanford University School of Medicine, Stanford, California 94305, United States

[§]Nuffield Department of Clinical Medicine, Target Discovery Institute (TDI) and Structural Genomics Consortium (SGC), University of Oxford, Old Road Campus, Roosevelt Drive, Oxford OX3 7DQ, U.K.

[∥]Structural Genomics Consortium, Universidade Estadual de Campinas, Cidade Universitaria Zeferino Vaz, Av. Dr. André Tosello, 550, Barão Geraldo, Campinas, São Paulo 13083-886, Brazil

[⊥]Institute for Pharmaceutical Chemistry, Buchmann Institute for Life Sciences Campus Riedbeerg, Goethe-University Frankfurt, 60438 Frankfurt am Main, Germany

[#]US Army Medical Research Institute of Infectious Diseases, Viral Immunology Branch, Fort Detrick, Maryland 21702, United States

***** Supporting Information**

AAK1 Kd = 0.12 μM
DENV (Huh7): EC$_{50}$ = 8 μM; CC$_{50}$ > 50 μM
EBOV EC$_{50}$ > 10 μM ; CC$_{50}$ > 10 μM

AAK1 IC$_{50}$ = 0.00402 μM
DENV (Huh7): EC$_{50}$ = 0.72 μM; CC$_{50}$ = 17.0 μM
DENV (MDCCs): EC$_{50}$ = 0.043 μM; CC$_{50}$ > 20 μM
EBOV: EC$_{50}$ = 1.59 μM; CC$_{50}$ > 10 μM
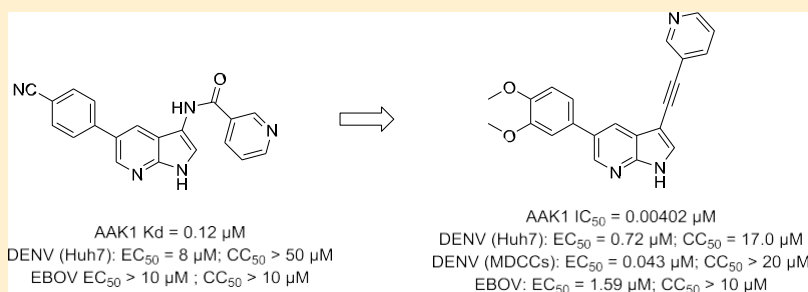
ABSTRACT: There are currently no approved drugs for the treatment of emerging viral infections, such as dengue and Ebola. Adaptor-associated kinase 1 (AAK1) is a cellular serine−threonine protein kinase that functions as a key regulator of the clathrin-associated host adaptor proteins and regulates the intracellular trafficking of multiple unrelated RNA viruses. Moreover, AAK1 is overexpressed specifically in dengue virus-infected but not bystander cells. Because AAK1 is a promising antiviral drug target, we have embarked on an optimization campaign of a previously identified 7-azaindole analogue, yielding novel pyrrolo[2,3-*b*]pyridines with high AAK1 affinity. The optimized compounds demonstrate improved activity against dengue virus both in vitro and in human primary dendritic cells and the unrelated Ebola virus. These findings demonstrate that targeting cellular AAK1 may represent a promising broad-spectrum antiviral strategy.

INTRODUCTION

Dengue virus (DENV) is an enveloped, positive-sense, single-stranded RNA virus belonging to the Flaviviridae family. DENV is transmitted by the mosquitoes *Aedes aegypti* and *Aedes albopictus*, which mainly reside in (sub)tropical climates. Hence, dengue outbreaks are mainly confined to equatorial areas, where more than 100 countries have been declared dengue-endemic.[1] The World Health Organization (WHO) estimates that up to 3.9 billion people are at risk of dengue infection at any given time.[2] In 2013, the WHO reported 3.2

related deaths worldwide.[3] Up to 80% of DENV-infected patients remain asymptomatic. Symptomatic patients usually experience an acute febrile illness, characterized by high fever, muscle and joint pain, and sometimes rash.[1] The likelihood of progression to severe dengue, manifesting by shock, hemorrhage, and organ failure, is greater upon secondary infection with a heterologous dengue serotype (of four that circulate) due to antibody-dependent enhancement.[4]

million cases of severe dengue and more than 9000 dengue-

5810

IC$_{50}$ = 0.2 nM
WO2017/059080

IC$_{50}$ = 0.3 nM
WO2017/059085

IC$_{50}$ = 0.62 nM
WO2016/164295

IC$_{50}$ = 6 nM
WO2016/053794

IC$_{50}$= 4 nM
WO2016/022312
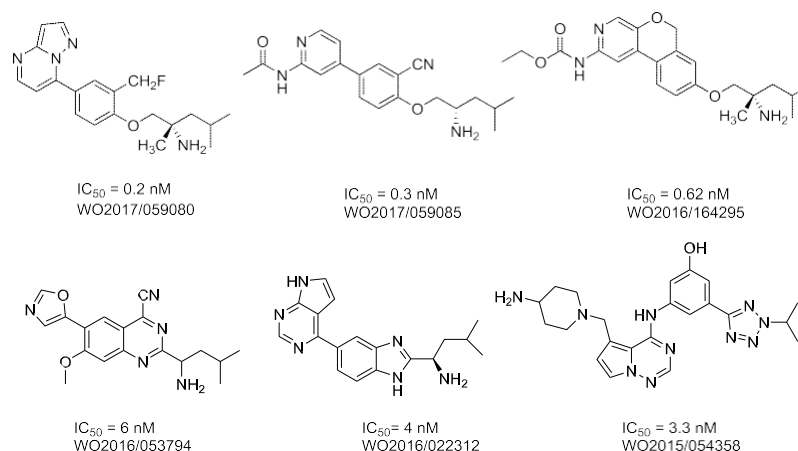
IC$_{50}$ = 3.3 nM
WO2015/054358

Figure 1. Known AAK1 inhibitors.

Ebola virus (EBOV) is a member of the Filoviridae family. Four of the five known EBOV species have been responsible for over 20 outbreaks and over 10,000 deaths since their identification in 1976.[5]

Current efforts in search for drugs active against DENV focus primarily on viral targets, such as the NS3 helicase, NS2B-NS3 protease, NS4B, NS5 methyltransferase, NS5 polymerase, and the viral envelope.[6] In search for anti-EBOV drugs, the RNA-dependent RNA polymerase L, the viral surface glycoprotein GP, and viral proteins VP24 and VP35 have been explored as candidate targets.[6] However, targeting viral functions is often associated with the rapid emergence of drug resistance and usually provides a "one drug, one bug" approach. DENV and EBOV rely extensively on host factors for their replication and survival. These cellular factors represent attractive candidate targets for antiviral agents, potentially with a higher barrier to resistance. In addition, when targeting a host function required for the replication of several unrelated viruses, such compounds are more likely to exhibit broad-spectrum antiviral activity.[7,8]

Intracellular membrane trafficking is an example of a cellular process that is hijacked by various viruses.[9] Intracellular membrane trafficking depends on the function of tyrosine- and dileucine-based signals in host cargo proteins, which are recognized by μ1−5 subunits of the clathrin adaptor protein (AP) complexes AP1−5. Adaptor complexes mediate the sorting of cargo proteins to specific membrane compartments within the cell. While AP2 sorts in the endocytic pathway, AP1 and AP4 sort in the secretory pathway.[10]

The activity of AP2M1 and AP1M1, the μ subunits of AP2 and AP1, respectively, is regulated by two host cell kinases, adaptor-associated kinase 1 (AAK1) and cyclin G-associated kinase (GAK). Phosphorylation of specific threonine residues in AP2M1 and AP1M1 by these kinases is known to stimulate their binding to tyrosine signals in cargo proteins and enhance vesicle assembly and internalization. Both AAK1 and GAK regulate clathrin-mediated endocytosis by recruiting clathrin and AP2 to the plasma membrane. AAK1 also regulates clathrin-mediated endocytosis of cellular receptors via alternative sorting adaptors that collaborate with AP-2, for example, by phosphorylation of NUMB.[10] Additionally, AAK1 has been implicated in the regulation of epidermal growth factor receptor (EGFR) internalization and recycling to the plasma membrane via its effects on and interactions with alternate endocytic adaptors. We have demonstrated that

AAK1 and GAK regulate hepatitis C virus (HCV) entry and assembly by modulating AP2 activity[10,11] and viral release and cell-to-cell spread via regulation of AP1.[7,12] AAK1 and GAK are also required in the life cycles of DENV and EBOV.[7]

We have reported that the approved anticancer drugs sunitinib and erlotinib that potently inhibit AAK1 and GAK, respectively, demonstrate broad-spectrum in vitro antiviral activity against different members of the Flaviviridae family (HCV, DENV, Zika virus, West Nile virus), as well as against various unrelated families of RNA viruses.[7] We have also demonstrated that the combination of these two drugs effectively reduces viral load, morbidity, and mortality in mice infected with DENV and EBOV.[7,13] These data provide a proof of concept that small-molecule inhibition of AAK1 and GAK can yield broad-spectrum antiviral agents.[7,13] Moreover, using single-cell transcriptomic analysis, AAK1 has been validated as a particularly attractive target because it is overexpressed specifically in DENV-infected and not bystander cells (uninfected cells from the same cell culture), and its expression level increases with cellular virus abundance.[13]

AAK1 has been studied primarily as a drug target for the treatment of neurological disorders, such as schizophrenia, Parkinson's disease, neuropathic pain,[14] bipolar disorders, and Alzheimer's disease.[15,16] Consequently, very potent AAK1 inhibitors based on different chemotypes have been disclosed in the patent literature. Figure 1 shows representative examples of these AAK1 inhibitors and their enzymatic inhibition data.

Despite the fact that AAK1 has emerged as a promising antiviral target, none of these compound classes have been evaluated and/or optimized for antiviral activity, the only exception being a series of imidazo[1,2-b]pyridazines, which were originally developed by Lexicon Pharmaceuticals (Figure 2).[14] We have previously resynthesized these molecules, confirmed their potent AAK1 affinity, and demonstrated their antiviral activity against HCV and DENV.[7]
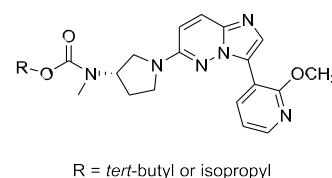

R = tert-butyl or isopropyl

Figure 2. AAK1 inhibitors with documented antiviral activity.

Here, rather than starting from a potent AAK1 inhibitor, we started from a structurally simple compound with reasonable AAK1 activity from which easy structural variation could be introduced. A screening campaign of 577 structurally diverse compounds (representing kinase inhibitor chemical space) across a panel of 203 protein kinases using the DiscoverX binding assay format previously identified a pyrrolo[2,3-b]pyridine or 7-aza-indole derivative (compound 1, Figure 3) as a potent AAK1 inhibitor ($K_D = 53$ nM).[17] In this manuscript, we describe our efforts to optimize the AAK1 affinity and antiviral activity of compound 1.
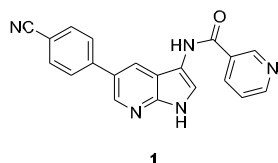
Figure 3. Pyrrolo[2,3-b]pyridine (7-aza-indole) based AAK1 inhibitor.

RESULTS AND DISCUSSION

Chemistry. *Synthesis of 3-Substituted-5-aryl Pyrrolo[2,3-b]pyridines.* A regioselective Sonogashira coupling of trimethylsilylacetylene with commercially available 5-bromo-3-iodo-2-aminopyridine 2 afforded the alkynyl derivative 3 (Scheme 1).[18] Compound 3 was then reductively ring-closed with a strong base yielding pyrrolo[2,3-b]pyridine 4. Initially, NaH was used as base,[18] but later on potassium *tert*-butoxide[19] was applied as this gave a cleaner reaction outcome and an improved yield. Initial attempts to nitrate position 3 of the 7-azaindole scaffold employed a mixture of a 65% HNO3 solution and sulfuric acid.[20] However, the desired product was difficult to isolate from this reaction mixture, and

therefore, the nitration was performed by treatment of compound 4 with fuming nitric acid.[21] The 3-nitro derivative 5 precipitated from the reaction mixture and was conveniently isolated by filtration. Suzuki coupling of compound 5 with a number of arylboronic acids yielded the 3-nitro-5-aryl-pyrrolo[2,3-b]pyridines 6a−h in yields ranging from 65 to 85%.[22] Catalytic hydrogenation of the nitro moiety yielded the corresponding amino derivatives 7a−h. Because of the instability of the 3-amino-pyrrolo[2,3-b]pyridines, these were not purified and used as such for further reaction. Coupling with an acid chloride in a mixture of pyridine and dichloromethane (DCM)[23] or alternatively, reaction with a carboxylic acid using (benzotriazol-1-yloxy)tris-(dimethylamino)phosphonium hexafluorophosphate (BOP) as a coupling reagent[24] yielded a small library of pyrrolo[2,3-b]pyridines 8a−o. A sulfonamide derivative 8p was prepared via reaction of 7g with phenylsulfonyl chloride in pyridine.

Synthesis of 3-Benzoyl-5-(3,4-dimethoxyphenyl)-pyrrolo-[2,3-b]pyridine. Formylation of compound 4 by a Duff reaction[25] yielded 3-formyl-5-bromo-azaindole 9 (Scheme 2). The pyrrole nitrogen was protected[26] using NaH and tosylchloride yielding compound 10. Suzuki coupling reaction with 3,4-dimethoxyphenylboronic acid furnished compound 11. Nucleophilic addition[27] of phenylmagnesium bromide to the aldehyde furnished the secondary alcohol 12. Oxidation[28] of the benzylic alcohol using MnO2 afforded ketone 13. Finally, alkaline deprotection[29] of the tosyl group yielded the desired compound 14.
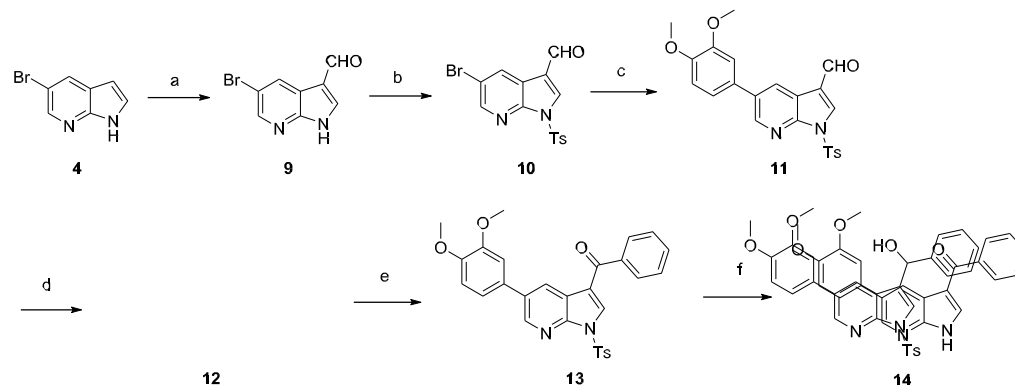
Synthesis of 3-Phenyl-5-(3,4-dimethoxyphenyl)-pyrrolo-[2,3-b]pyridine. Iodination of compound 4 with *N*-iodosuccinimide[30] afforded compound 15 (Scheme 3). Reaction of compound 15 with phenylboronic acid led only to recovery of unreacted starting material. Therefore, the pyrrole nitrogen of the 7-azaindole scaffold was protected as a tosyl group,[26] affording compound 16. A regioselective Suzuki coupling

**Scheme 1. Synthesis of 3-Substituted-5-aryl Pyrrolo[2,3-b]pyridines 8a−p**[a]

8a: R1 = Ph; R2 = 3-pyridyl
8b: R1 = 4-F-Ph; R2 = 3-pyridyl
8c: R1 = 4-CF3-Ph; R2 = 3-pyridyl
8d: R1 = 4-OCH3-Ph; R2 = 3-pyridyl
8e: R1 = 4-CH3-Ph; R2 = 3-pyridyl
8f: R1 = 3-CH3-Ph; R2 = 3-pyridyl
8g: R1 = 3,4-di-OCH3-Ph; R2 = 3-pyridyl
8h: R1 = 3-thienyl; R2 = 3-pyridyl
8i: R1 = 3,4-di-OCH3-Ph; R2 = Ph
8j: R1 = 3,4-di-OCH3-Ph; R2 = 4-F-Ph
8k: R1 = 3,4-di-OCH3-Ph; R2 = 4-OCH3-Ph
8l: R1 = 3,4-di-OCH3-Ph; R2 = 4-pyridyl
8m: R1 = 3,4-di-OCH3-Ph; R2 = benzyl
8n: R1 = 3,4-di-OCH3-Ph; R2 = cyclopentyl
8o: R1 = 3,4-di-OCH3-Ph; R2 = cyclohexyl

6a: R1 = Ph
6b: R1 = 4-F-Ph
6c: R1 = 4-CF3-Ph
6d: R1 = 4-OCH3-Ph
6e: R1 = 4-CH3-Ph
6f: R1 = 3-CH3-Ph
6g: R1 = 3,4-di-OCH3-Ph
6h: R1 = 3-thienyl

7a: R1 = Ph
7b: R1 = 4-F-Ph
7c: R1 = 4-CF3-Ph
7d: R1 = 4-OCH3-Ph
7e: R1 = 4-CH3-Ph
7f: R1 = 3-CH3-Ph
7g: R1 = 3,4-di-OCH3-Ph
7h: R1 = 3-thienyl

8p: R1 = 3,4-di-OCH3-Ph

[a]Reagents and conditions. (a) TMSA, Pd(PPh3)2Cl2, CuI, Et3N, THF, rt; (b) KOtBu, NMP, 80 °C; (c) HNO3, 0 °C to rt; (d) Pd(PPh3)4, K2CO3, ArB(OH)2, H2O, dioxane, 105 °C; (e) H2, Pd/C, THF, rt; (f) RCOCl, pyridine, THF, 1 M NaOH, rt; (g) RCOOH, BOP, Et3N, DMF, rt; (h)

PhSO$_2$Cl, pyridine, rt.

Scheme 2. Synthesis of 3-Benzoyl-5-(3,4-dimethoxyphenyl)-pyrrolo[2,3-*b*]pyridine 14[a]

[a]Reagents and conditions. (a) Hexamine, H_2O, CH_3COOH, 120 °C; (b) NaH, TsCl, 0 °C to rt; (c) 3,4-dimethoxyphenylboronic acid, Pd(PPh3)4, 2 M K_2CO_3, toluene, EtOH, 105 °C; (d) 3 M PhMgBr, THF, rt; (e) MnO_2, THF, rt; (f) KOH, EtOH, 80 °C.

Scheme 3. Synthesis of 3-Phenyl-5-(3,4-dimethoxyphenyl)-pyrrolo[2,3-*b*]pyridine 19[a]
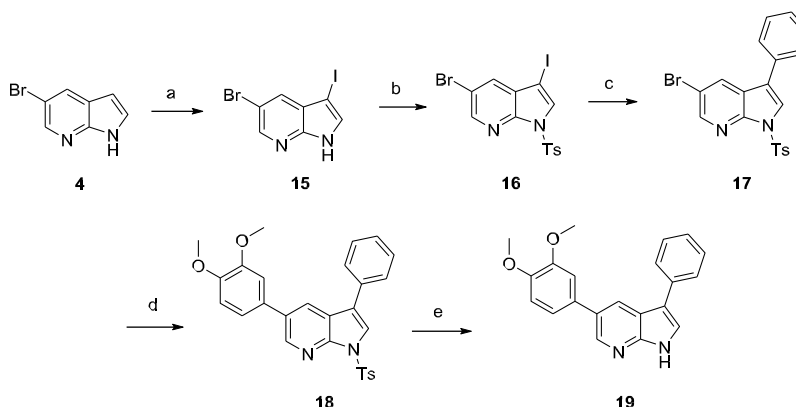
[a]Reagents and conditions. (a) NIS, acetone, rt; (b) NaH, TsCl, THF, 0 °C to rt; (c) PhB(OH)2, Pd(PPh3)4, K_2CO_3, toluene, EtOH, H_2O, 90 °C; (d) 3,4-dimethoxyphenylboronic acid, Pd(PPh3)4, K_2CO_3, toluene, EtOH, H_2O, 105 °C; (e) KOH, EtOH, 80 °C.

reaction using phenylboronic acid furnished the 3-phenyl-pyrrolo[2,3-*b*]pyridine analogue 17. A subsequent Suzuki reaction[22] with 3,4-dimethoxyphenylboronic acid yielded compound 18. Finally, alkaline cleavage of the tosyl protecting group afforded the desired target compound 19.[29]

Synthesis of 3-Alkynyl-5-(3,4-dimethoxyphenyl)-pyrrolo-[2,3-b]pyridines. Sonogashira reaction of compound 15 with a number of (hetero)arylacetylenes yielded regioselectively compounds 20a−f in yields varying from 20 to 70% (Scheme 4).[18] In contrast to Suzuki couplings (Scheme 3), protection of
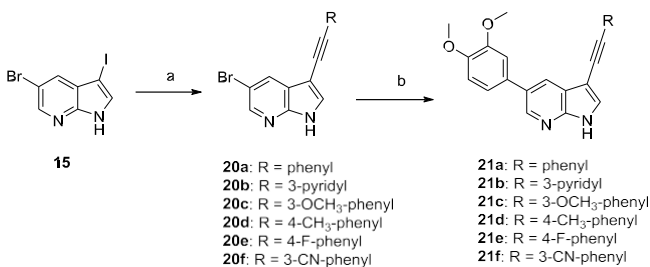
the pyrrole nitrogen was not necessary. Subsequent Suzuki coupling[22] with 3,4-dimethoxyphenylboronic acid gave access to final compounds 21a−f.

Synthesis of 1-Methyl-1H-pyrrolo[2,3-b]pyridine. Methylation[31] of compound 4 using NaH and MeI furnished compound 22 (Scheme 5). Nitration,[21] followed by Suzuki coupling,[22] gave access to compound 24. Finally, catalytic reduction of the nitro group, followed by condensation[23] of the exocyclic amino group of compound 25 with nicotinoyl chloride, yielded target compound 26.
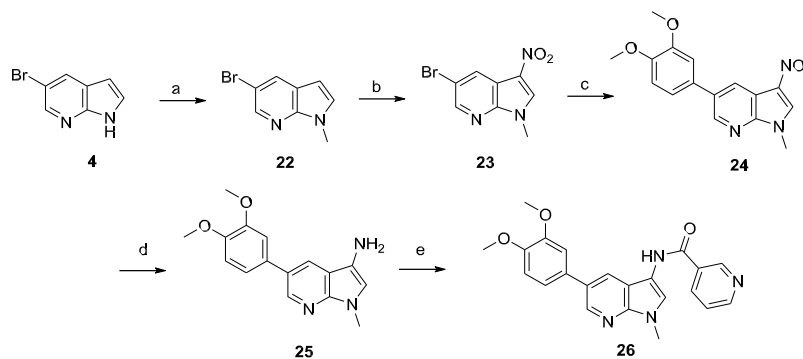
Synthesis of Pyrazolo[3,4-b]pyridine. Suzuki coupling[22] between commercially available 5-bromo-2-chloronicotinonitrile 27 and 3,4-dimethoxyphenylboronic acid yielded regioselectively compound 28. Nucleophilic displacement of the chlorine by hydrazine, with a concomitant nucleophilic addition at the cyano group,[32] allowed to construct the pyrazole moiety, yielding compound 29. Finally, amide formation[33] using nicotinoyl chloride yielded the final compound 30 (Scheme 6).

Synthesis of Pyrrolo[2,3-b]pyrazine. Treatment of 2-aminopyrazine 31 with N-bromosuccinimide yielded the 3,5-dibromopyrazine intermediate 32 (Scheme 7).[34] A regioselective Sonogashira coupling with trimethylsilylacetylene, followed by a reductive ring closure with potassium *tert*-butoxide, furnished pyrrolo[2,3-b]pyrazine 34.[35] Iodination[36]

Scheme 4. Synthesis of 3-Alkynyl-5-(3,4-dimethoxyphenyl)-pyrrolo[2,3-*b*]pyridines 21a−f[a]

20a: R = phenyl
20b: R = 3-pyridyl
20c: R = 3-OCH3-phenyl
20d: R = 4-CH3-phenyl
20e: R = 4-F-phenyl
20f: R = 3-CN-phenyl

21a: R = phenyl
21b: R = 3-pyridyl
21c: R = 3-OCH3-phenyl
21d: R = 4-CH3-phenyl
21e: R = 4-F-phenyl
21f: R = 3-CN-phenyl

[a]Reagents and conditions. (a) RC☐CH, Pd(PPh3)2Cl2, CuI, THF, EtN, rt; (b) 3,4-dimethoxyphenylboronic acid, Pd(PPh), K_2CO_3,
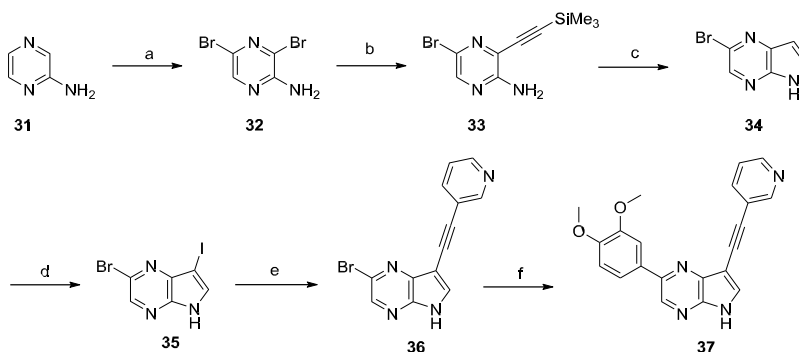
H$_2$O, dioxane, 105 °C.

with *N*-iodosuccinimide yielded the dihalogenated intermedi-

Scheme 5. Synthesis of 1-Methyl-1*H*-pyrrolo[2,3-*b*]pyridine 26[a]

[a]Reagents and conditions. (a) NaH, MeI, THF, 0 °C to rt; (b) HNO₃, 0 °C to rt; (c) 3,4-dimethoxyphenylboronic acid, Pd(PPh₃)₄, K₂CO₃, H₂O, dioxane, 105 °C; (d) H₂, THF, rt; (e) nicotinoyl chloride, pyridine, THF, 1 M NaOH, rt.

Scheme 6. Synthesis of Pyrazolo[3,4-*b*]pyridine 30[a]
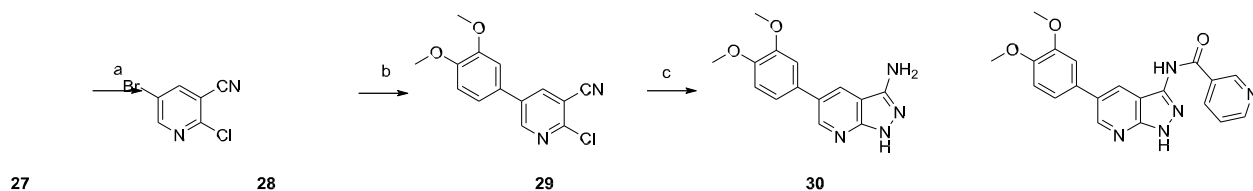
[a]Reagents and conditions (a) 3,4-dimethoxyphenylboronic acid, Pd(PPh₃)₄, K₂CO₃, H₂O, dioxane, 105 °C; (b) 35% hydrazine hydrate, EtOH, 80 °C; (c) nicotinoyl chloride, pyridine, rt.

Scheme 7. Synthesis of Pyrrolo[2,3-*b*]pyrazine 37[a]

[a]Reagents and conditions (a) NBS, DMSO, rt; (b) Me₃SiC≡CH, Pd(PPh₃)₂Cl₂, CuI, THF, Et₃N, rt; (c) KOtBu, NMP, 100 °C; (d) NIS, acetone, rt; (e) 3-ethynylpyridine, Pd(PPh₃)₂Cl₂, CuI, THF, Et₃N, rt; (f) 3,4-dimethoxyphenylboronic acid, Pd(PPh₃)₄, K₂CO₃, H₂O, dioxane, 105 °C.

ate 35 that was subsequently treated with 3-ethynylpyridine[18] and 3,4-dimethoxyphenylboronic acid[22] leading to the desired pyrrolo[2,3-*b*]pyrazine 37.

Kinase Profiling and X-ray Crystallography of Compound 1. AAK1 is a serine−threonine kinase that belongs to the family of NUMB-associated kinases (NAKs). Other members of this kinase family include BIKE/BMP2K (BMP-2 inducible kinase), GAK (cyclin G-associated kinase), and MPSK1 (myristoylated and palmitoylated serine−threonine kinase 1, also known as STK16). As part of an early profiling of hit compound 1, we assessed its selectivity by a binding-displacement assay against each of the four NAK family kinases (Figure 4). Conversion of the experimentally determined IC₅₀ values to K_i values to allow estimation of the selectivity showed that compound 1 was 3-fold more selective for AAK1 over GAK, and 8-fold and 22-fold more selective for AAK1 over BMP2K and STK16, respectively (Table 1).
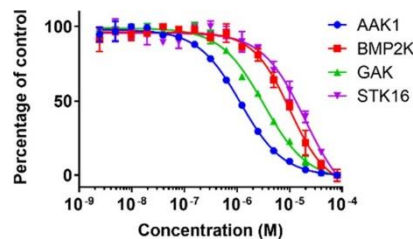

Figure 4. Binding displacement assay of compound 1 against the NAK family members.

To analyze the binding mode of compound 1, the crystal structure of compound 1 bound to AAK1 to 2.0 Å resolution was determined (Figure 5). Data collection and refinement statistics are provided in Table S1 (see Supporting Information), and PDB coordinates are deposited under PDB ID 5L4Q. Compound 1 binds in the ATP-binding site of AAK1 in a relatively planar manner (Figure 5), with the

Table 1. Selectivity of Compound 1 for AAK1 against the NAK Family Kinases

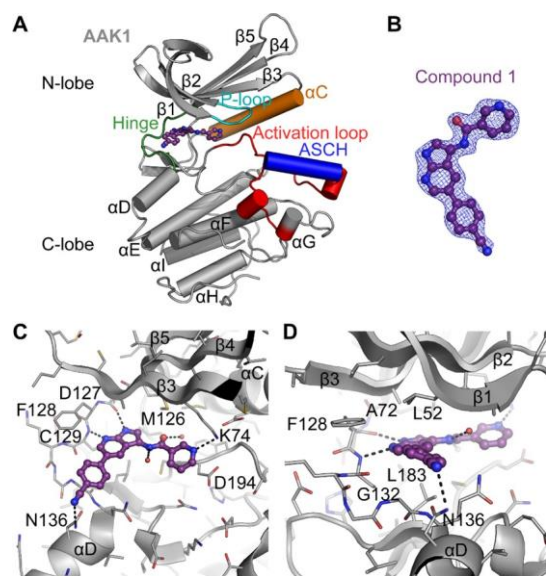| | binding displacement assay | | |
NAK	IC$_{50}$ (μM)	K_i (μM)	K_i/K_i (AAK1)
AAK1	1.17	0.541	1.0
BMP2K	10.1	4.40	8.13
GAK	3.25	1.75	3.23
STK16	20.0	11.9	22.0

Figure 5. Crystal structure of AAK1 (gray) in complex with compound 1 (purple), PDB ID 5L4Q. (A) Overview of the crystal structure of AAK1. Highlighted are areas that are important for kinase function. Compound 1 bound at the hinge is shown. ASCH = activation segment C-terminal Helix, a feature unique to kinases of the NAK family. (B) 2F_o − F_c electron density map contoured at 1σ around compound 1, showing the fit of the model to the map. (C,D) Detailed views of the interactions of compound 1 in the ATP-binding site from two orientations. Black dotted lines indicate polar interactions, and red spheres indicate water molecules. Note that residues 48−63 from β1 and β2 are removed from (C) for clarity.

pyrrolo[2,3-b]pyridine moiety bound directly between the side chains of two highly conserved residues: Ala72 from β2 in the kinase N-lobe and Leu183 of the C-lobe, the location where the adenine ring of ATP would bind. The nitrogen atoms of the pyrrolo[2,3-b]pyridine moiety form two hydrogen bonds to the peptide backbone of residues Asp127 and Cys129 at the kinase hinge region (Figure 5). The 4-cyanophenyl moiety is oriented toward the solvent, with the phenyl ring directly sandwiched between the backbone of Gly132 of the hinge and Leu52 of β1 in the N-lobe, and the nitrogen of the cyano moiety forming a polar interaction with the side chain of Asn136. The nicotinamide moiety is bound against the "gatekeeper" residue Met126 and forms a hydrogen bond to the side chain of Lys74, another highly conserved residue that normally links the phosphate of ATP to the αC-helix and is required for correct positioning of the N-lobe for efficient catalysis. Compound 1 also interacts with two water molecules, one situated at the back of the ATP pocket that bridges between the oxygen of the amide moiety and the backbone nitrogen of Asp194, and a second at the front of the adenosine binding site directly below Val60 in the β1 strand that interacts with the amide nitrogen and surrounding solvent. The DFG motif (Asp194) is in the conformation expected of active AAK1 (Figure 5), with the activation loop of AAK1 in the same conformation as seen in previous AAK1 and BMP2K crystal structures, including the activation-segment C-terminal helix (ASCH), a structural element that is rare among other protein kinases, but conserved across the NAK family.[37]

Structure−Activity Relationship Study. All compounds synthesized in this study were evaluated for AAK1 affinity using two different, commercially available AAK1 binding assays. In the early stage of the program, the proprietary KINOMEscan screening platform of DiscoverX was used. In this assay, compounds that bind the kinase active site prevent kinase binding to an immobilized ligand and reduce the amount of kinase captured on the solid support. Hits are then identified by measuring the amount of kinase captured in test versus control samples via quantitative polymerase chain reaction (qPCR) that detects an associated DNA label.[38] Later on in the project, compounds were evaluated by the LanthaScreen Eu kinase binding assay (ThermoFisher Scientific), in which binding of an Alexa Fluor conjugate or

Table 2. SAR at Position 5 of the 7-Aza-indole Scaffold

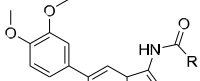|		AAK1 enzymatic data		DENV antiviral activity		cytotoxicity
Cmpd#	R$_5$	AAK1 K_D (μM) (DiscoverX)	AAK1 IC$_{50}$ (μM) LanthaScreen	EC$_{50}$ (μM)	EC$_{90}$ (μM)	CC$_{50}$ (μM)
1	4-cyanophenyl	0.120	ND^a	8.37	46.8	>50
8a	phenyl	0.0822	ND^a	5.29	87.1	NE^b
8b	4-F-phenyl	0.141	ND^a	6.43	25.2	NE^b
8c	4-CF$_3$-phenyl	ND^a	0.23	2.94	12.0	57.0
8d	4-OCH$_3$-phenyl	0.0194	ND^a	4.39	25.8	NE^b
8e	4-Me-phenyl	0.0532	ND^a	2.60	33.6	>100
8f	3-Me-phenyl	ND^a	0.0186	4.86	10.8	16.0
8g	3,4-di-OCH$_3$-phenyl	0.00673	0.00432	1.64	7.46	39.7
8h	3-thienyl	0.0161	ND^a	3.01	66.8	NE^b
sunitinib		0.0110	0.0474	1.35	2.71	246

[a]ND: not determined. [b]NE: No effect (no apparent effect on cellular viability up to a concentration of 10 μM).

"tracer" to a kinase is detected by addition of a Eu-labeled anti-tag antibody. Binding of the tracer and antibody to a kinase results in a high degree of fluorescence resonance energy transfer (FRET), whereas displacement of the tracer with a kinase inhibitor results in loss of FRET.

The compounds were also assessed for antiviral activity in human hepatoma (Huh7) cells infected with DENV2. Their effect on overall infection was measured at 48 h postinfection with DENV2 via luciferase assays and the half-maximal effective concentration and the 90% effective concentrations (EC_{50} and EC_{90} values, respectively) were calculated. In parallel, the cytotoxicity of the compounds (expressed as the half-maximal cytotoxic concentration or CC_{50} value) was measured via an alamarBlue assay in the DENV-infected Huh7 cells (Tables 2−6).

Table 3. SAR of the N-Acyl Moiety
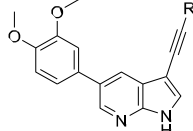
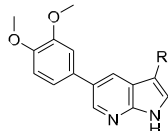| Cmpd#	R	AAK1 enzymatic data AAK1 IC$_{50}$ (µM) LanthaScreen	DENV antiviral activity EC$_{50}$ (µM)	DENV antiviral activity EC$_{90}$ (µM)	Cytotoxicity CC$_{50}$ (µM)
8g	3-pyridyl	0.00432	1.64	7.46	39.7
8i	phenyl	0.108	4.07	50.5	17.3
8j	4-F-phenyl	0.161	8.34	30.2	15.9
8k	4-OCH$_3$-phenyl	0.0721	NE^a	NE^a	23.6
8l	4-pyridyl	0.381	12.6	26.8	NE^a
8m	benzyl	0.612	142	NE^a	NE^a
8n	cyclopentyl	0.398	3.42	8.34	15.2
8o	cyclohexyl	0.319	4.27	10.8	14.7

^{a}NE: no effect (no apparent antiviral effect or effect on cellular viability up to a concentration of 10 µM).

In all these enzymatic and antiviral assays, sunitinib was included as a positive control (Table 2). Sunitinib has potent

Table 5. SAR of Phenylacetylene Moiety

Cmpd#	R	AAK1 enzymatic data AAK1 IC$_{50}$ (µM) LanthaScreen	DENV antiviral activity EC$_{50}$ (µM)	DENV antiviral activity EC$_{90}$ (µM)	cytotoxicity CC$_{50}$ (µM)
21a	phenyl	0.209	5.64	10.58	20.1
21b	3-pyridyl	0.00402	0.72	4.16	17.0
21c	3-OCH$_3$-phenyl	0.149	NE^a	NE^a	19.6
21d	4-CH$_3$-phenyl	0.420	7.45	20.5	NE^a
21e	4-F-phenyl	0.387	4.21	8.57	19.9
21f	3-CN-phenyl	0.381	10.2	41.2	NE^a

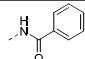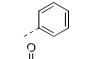^{a}NE: no effect (no apparent antiviral effect or effect on cellular viability up to a concentration of 10 µM).
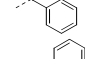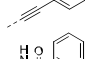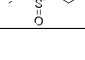
AAK1 affinity as measured by the KinomeScan format (K_D = 11 nM) and LanthaScreen assay (IC_{50} = 47 nM) and displayed potent activity against DENV with an EC_{50} value of 1.35 µM.

Structure−Activity Relationship at Position 5 of the 7-Aza-indole Scaffold. We confirmed the AAK1 binding affinity of hit compound 1, yet in our hands, a K_D value of 120 nM was measured (vs the reported K_D = 53 nM).[17] This hit demonstrated antiviral activity, although it was rather weak (EC_{50} = 8.37 µM). Substitution of the 5-(4-cyanophenyl) moiety of compound 1 by phenyl (compound 8a), thienyl (compound 8h), and substituted phenyl rings with electron-withdrawing groups (compound 8c), electron-donating substituents (compounds 8d−g), and a halogen (compound 8b) gave rise to a series of analogues with structural variety that were at least equipotent to compound 1, suggesting that structural modification at this position is tolerated for AAK1 binding (Table 2). The synthesis of this limited number of analogues allowed us to quickly identify the 5-(3,4-dimethoxyphenyl) congener (compound 8g) with low nM AAK1

Table 4. SAR of the Linker Moiety at Position 3

Cmpd#	R	AAK1 enzymatic data AAK1 IC$_{50}$ (µM) LanthaScreen	DENV antiviral activity EC$_{50}$ (µM)	DENV antiviral activity EC$_{90}$ (µM)	Cytotoxicity CC$_{50}$ (µM)
	(amide)	0.108	4.07	50.5	17.3
	(ether)	0.0236	3.02	8.34	990
	(ketone)	0.184	1.07	3.73	35.3
	(alkyne)	0.209	5.64	10.58	20.1
	(sulfonamide)	4.44	8.14	106	NE^a

[a]NE: no effect (no apparent effect on cellular viability up to a concentration of 10 μM).

Table 6. Scaffold Modifications

| Cmpd# | Structure | AAK1 enzymatic data | DENV antiviral activity | | Cytotoxicity |
		AAK1 IC$_{50}$ (μM) LanthaScreen	EC$_{50}$ (μM)	EC$_{90}$ (μM)	CC$_{50}$ (μM)
26		3.39	NE[a]	NE[a]	NE[a]
30		0.462	2.09	19.0	16.0
37		0.00927	3.28	7.68	4.81

[a]NE: no effect (no apparent antiviral effect or effect on cellular viability up to a concentration of 10 μM).
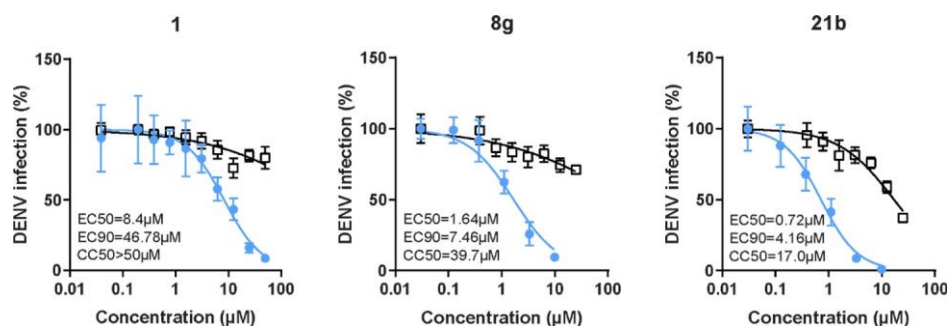
Figure 6. Compounds 8g and 21b suppress DENV infection more effectively than compound 1. Dose response of DENV infection (blue) and cell viability (black) to compounds 1, 8g, and 21b measured by luciferase and alamarBlue assays, respectively, 48 h after infection. Data are plotted relative to vehicle control. At least two representative experiments conducted are shown, each with 5 biological replicates, and the values are expressed as means ± SD.

binding affinity in both the KinomeScan and LanthaScreen assay, indicating an excellent correlation between the two assays. As compound 8g showed stronger AAK1 affinity than the positive control sunitinib, no additional efforts were done to further explore the structure–activity relationship (SAR) at this position of the 7-aza-indole scaffold.

All analogues within this series had an improved antiviral activity against DENV, relative to the original hit 1. The compound with the highest binding affinity for AAK1 (compound 8g) also demonstrated the most effective anti-DENV activity, with EC$_{50}$ and EC$_{90}$ values of 1.64 and 7.46 μM, respectively (Figure 6).

SAR of the N-Acyl Moiety. Given the improved AAK1 affinity and antiviral activity of compound 8g, the SAR of this compound was further examined through the replacement of the 3-pyridyl group by a number of (hetero)aromatics and cycloaliphatic groups, while the 3,4-dimethoxyphenyl residue was kept fixed (Table 3). Our findings indicate that the 3-pyridyl moiety is critical for AAK1 binding as all analogues showed a 100-fold decreased AAK1 affinity, when compared to compound 8g, giving rise to AAK1 IC$_{50}$ values in the 0.1−0.6 μM range. Only the congener with a 4-methoxyphenyl residue (compound 8k) was endowed with an enhanced AAK1 affinity with an IC$_{50}$ value of 0.072 μM. In correlation with their weaker affinity for AAK1, these compounds had a diminished antiviral activity relative to compound 8g.

SAR of the Linker Moiety at Position 3. To evaluate the importance of the amide linker, a number of surrogates were prepared (Table 4). For synthetic feasibility reasons, compound 8i, having a phenyl residue instead of a 3-pyridyl ring, and endowed with quite potent AAK1 affinity and moderate antiviral activity, was selected as a reference compound. Removing the amide linker furnished the 3-phenyl substituted analogue 19, which was 4-fold more potent as AAK1 ligand than compound 8i, and showed a slightly improved antiviral activity against DENV (EC$_{50}$ and EC$_{90}$ values of 3.02 and 8.34 μM, respectively). When the amide linker of compound 8i was replaced by a ketone (compound 14) or alkyne (compound 21a) functionality, AAK1 affinity was retained. Compound 14 exhibited an improved antiviral activity in comparison with compound 8i. Finally, replacement of the amide moiety by a sulfonamide linker was not well-tolerated, as compound 8p showed close to 200-fold drop in AAK1 affinity.

SAR of Phenylacetylene. The data in Table 4 suggest that the amide moiety is not essential for AAK1 binding and can be replaced. Although the 3-phenyl derivative 19 displayed potent AAK1 affinity, 3,5-diaryl pyrrolo[2,3-b]pyridines are well known in the literature as kinase inhibitors. In contrast, 3-alkynyl-7-aza-indoles are studied to a much less extent. We, therefore, selected the acetylene derivate 21a to decipher if it was possible to improve AAK1 affinity and antiviral activity by further modifying the substitution pattern. A number of
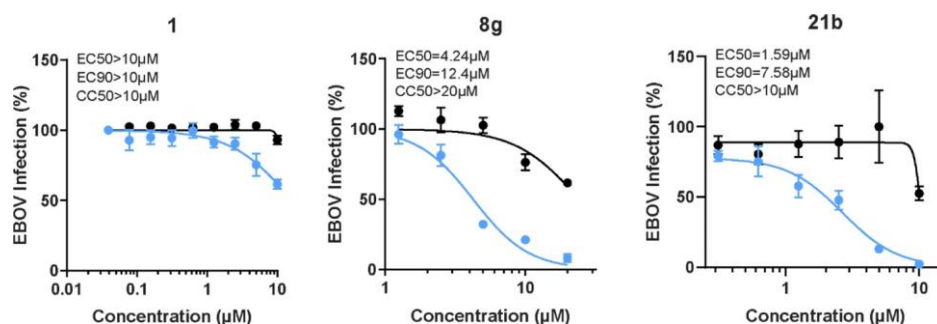
Figure 7. Compounds 1, 8g, and 21b suppress EBOV infection. Dose response of EBOV infection (blue) and cell viability (black) to compounds 1, 8g, and 21b measured by plaque assay (for compound 1) or immunofluorescence assays (for compounds 8g and 21b) and CellTiter-Glo luminescent cell viability assay in Huh7 cells 48 h after infection. Data are plotted relative to vehicle control. A representative experiment, out of at least two conducted, is shown and the values are shown as means ± SD.

substituted phenylacetylene derivatives were prepared (compounds 21b−f). The SAR in this series was quite flat, as all compounds displayed very similar AAK1 affinity with IC_{50} values in the 0.1−0.4 μM range (Table 5). In contrast, the

introduction of a 3-pyridylacetylene (compound 21b) led to a substantial improvement in AAK1 affinity (IC_{50} = 0.0042 μM) with a concomitant improvement in antiviral activity (EC_{50} = 0.72 μM) and only a moderate cytotoxic effect (CC_{50} = 17 μM, Figure 6).

Scaffold Modifications. Lastly, our SAR exploration focused on the 7-aza-indole scaffold itself (Table 6). Methylation of the pyrrole nitrogen afforded compound 26, displaying a greatly decreased AAK1 affinity (>800-fold loss in activity relative to compound 8g) and antiviral activity (EC_{50} > 10 μM). Insertion of an additional nitrogen atom in the pyrrole moiety yielded the pyrazolo[3,4-*b*]pyridine analogue 30 that is 100-fold less active as an AAK1 ligand relative to the parent compound 8g. When the pyridine moiety of compound 21b was replaced by a pyrazine ring, the pyrrolo[2,3-*b*]pyrazine analogue 37 was obtained. This compound was endowed with very potent AAK1 affinity (IC_{50} = 0.00927 μM), comparable to its 7-aza-indole counterpart 21b. Unfortunately, compound 37 demonstrated greater cytotoxicity than compound 21b in Huh7 cells with CC_{50}'s of 4.81 versus 17.0 μM, respectively.

Broad-Spectrum Antiviral Activity. AAK1 has been demonstrated to be important for the regulation of intracellular viral trafficking of multiple unrelated viruses.[7] Sunitinib, an approved anticancer drug with potent anti-AAK1 activity, displayed antiviral activity against RNA viruses from six different families.[7] To evaluate for potential broad-spectrum antiviral coverage of our molecules beyond DENV infection, hit compound 1 and the optimized congeners (compounds 8g and 21b) were tested for their activity against the unrelated EBOV. Huh7 cells were infected with EBOV and treated for 48 h with each compound (Figure 7). Whereas compound 1 did not show effective activity against EBOV, the more potent AAK1 inhibitors 8g and 21b displayed anti-EBOV activity with EC_{50} values in the low μM range and CC_{50} > 10−20 μM.

Correlation of the Antiviral Effect of Compounds 1, 8g, and 21b with Functional AAK1 Inhibition. To confirm that the observed antiviral activity is correlated with functional inhibition of AAK1 activity, we measured levels of the phosphorylated form of the μ subunit of the AP2 complex, AP2M1, upon treatment with compounds 1, 21b, and 8g. Because AP2M1 phosphorylation is transient (due to phosphatase PP2A activity),[27] to allow capturing of the phosphorylated state, Huh7 cells were incubated for 30 min

in the presence of the PP2A inhibitor calyculin A prior to lysis. Treatment with compounds 1, 21b, and 8g reduced AP2M1 phosphorylation (Figure 8), indicating modulation of AP2M1 phosphorylation via AAK1 inhibition.
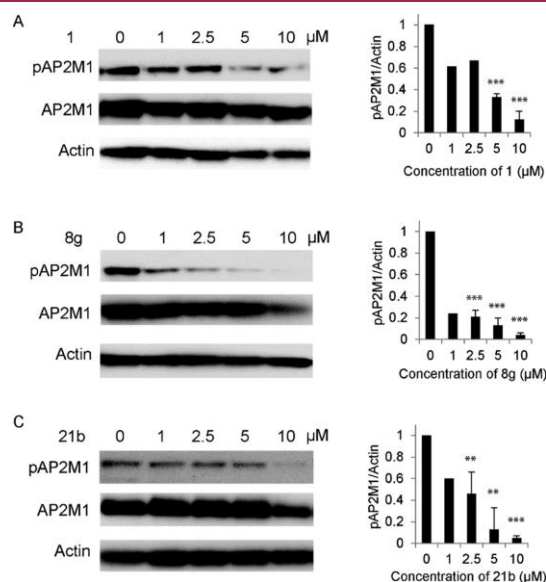

Figure 8. Antiviral effect of compounds 1, 8g, and 21b correlates with functional inhibition of AAK1. Dose response of AP2M1 phosphorylation to treatment with 1 (A), 8g (B), and 21b (C) by western analysis in lysates derived from Huh7 cells. Representative membranes (from two independent experiments) blotted with anti-phospho-AP2M1 (pAP2M1), anti-AP2M1 (AP2M1), and anti-actin (actin) antibodies and quantified data of pAP2M1/actin protein ratio normalized to dimethyl sulfoxide (DMSO) controls are shown. **p < 0.01, ***p < 0.001 by 2-tailed unpaired *t*-test.

Inhibition of DENV Infection in Human Primary Monocyte-Derived Dendritic Cells. To determine the therapeutic potential of the AAK1 inhibitors, their antiviral activity was studied in human primary dendritic cells. Primary cells are a physiologically more relevant model for DENV infection than immortalized cell lines and are considered an ex vivo model for DENV infection.[39] Compounds 21b and 8g showed a dose-dependent inhibition of DENV infection with EC_{50} and EC_{90} values of 0.0428 and 1.49 μM and 0.739 and 3.32 μM, respectively (Figure 9). This very potent activity in monocyte-derived dendritic cells (MDDCs) associated with minimal cytotoxicity (CC_{50} > 20 μM), particularly of
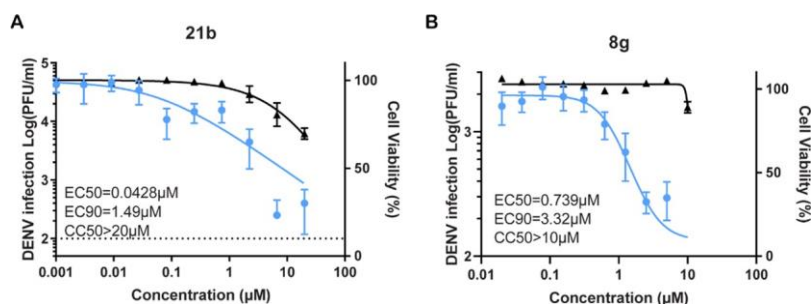
Figure 9. Ex vivo antiviral activity of 21b and 8g in human primary dendritic cells. Dose response of DENV infection (blue) and cell viability (black) to compounds 21b (A) and 8g (B) measured by plaque assays and alamarBlue assays, respectively, 72 h after infection of primary human MDDCs. A representative experiment with cells from a single donor is shown, out of 2 independent experiments conducted with cells derived from 2 donors, each with 6 biological replicates; the values are shown as means ± SD.

compound 21b demonstrates the potential of AAK1 inhibitors as antiviral agents.

Kinase Selectivity. To assess the kinase selectivity of the optimized AAK1 inhibitors, compound 21b was screened against 468 kinases via the KINOMEScan assay (DiscoverX) at a single concentration of 10 μM. As can be derived from the kinase interaction map (Figure 10), compound 21b cannot be
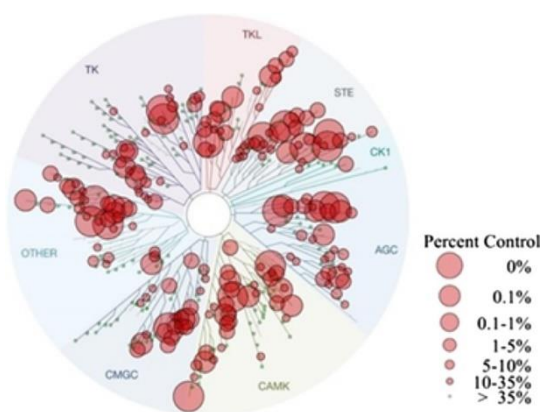

Figure 10. Kinome tree of compound 21b. Kinases that bind compound 21b are marked with red circles. The larger the circle, the

stronger the binding affinity.

considered as a selective AAK1 inhibitor. Beyond AAK1, compound 21b targets multiple other kinases (including the other members of the NAK family), which might contribute to its antiviral effect.

To quantitatively characterize the selectivity of compound 21b, selectivity scores (S-scores) were calculated at a concentration of 10 μM[40] (Table 7). The S(10) score of

Table 7. Selectivity Scores (S Scores) for Compound 21b at 10 μM

S-score type	number of hits	number of nonmutant kinases	selectivity score
S(35)[a]	212	403	0.526
S(10)[b]	138	403	0.342
S(1)[c]	49	403	0.122

[a]S(35) = (number of nonmutant kinases with % ctrl <35)/(number of non-mutant kinases tested). [b]S(10) = (number of nonmutant kinases with % ctrl <10)/(number of non-mutant kinases tested).

21b was calculated by dividing the number of kinases that showed binding at 10% of control or less upon drug treatment by the total number of kinases tested, excluding mutant variants and was found to be 0.342. In comparison, the S(3 μM) score of sunitinib, which is the number of kinases found to bind with a dissociation constant of less than 3 μM divided by the total number of non-mutant kinases tested, is 0.57.[40] Based on these data it can be deduced that, while 21b is not a highly selective AAK1 inhibitor, its selectivity profile is improved relative to that of sunitinib, and it may therefore represent a better pharmacological tool to probe the role of AAK1 in viral infection.

Molecular Modeling. To rationalize the improved AAK1 affinity of compounds 8g and 21b, when compared to the original hit 1, a docking study was performed using AutoDock Vina.[41] A control docking experiment with the original inhibitor lkb (compound 1), present in the 5L4Q PDB file, allowed to reproduce the original X-ray position very well. The best Vina docking scores are reported in Table 8. Despite the

Table 8. Vina Docking and MM/PBSA Results Calculated on Last 4 ns

compound	Vina score (kcal/mol)	MM[a]/GBSA[b] in kcal/mol (SD[d])	MM[a]/PBSA[c] in kcal/mol (SD[d])
1	−10.7	−31.5 (1.6)	−0.7 (2.3)
8g	−10.3	−38.6 (2.2)	−3.0 (2.9)
21b	−10.1	−40.6 (2.2)	−3.1 (2.8)

[a]MM: molecular mechanics. [b]GB: generalized born surface area. [c]PBSA: Poisson−Boltzmann surface area. [d]SD: standard deviation.

higher AAK1 affinity of compounds 8g and 21b, their Vina docking scores are worse than reference compound 1. This might be due to the fact that a rigid enzyme in the docking process that blocks induced-fit effects is used.

Therefore, for the three docked systems with the best Vina docking score, a molecular dynamics (MD) simulation using the Amber 18 software[42] was performed. Figure 11 shows an overlap of representative structures of compounds 1, 8g, and 21b, as extracted from the MD simulations. The three inhibitors form a hydrogen bond between the NH of the pyrrole ring and the backbone carbonyl group of D127. The nitrogen at position 3 of the pyridine ring seems to be essential

[c]S(1) = (number of nonmutant kinases with % ctrl <1)/(number of non-mutant kinases tested).

for strong AAK1 affinity. In the X-ray of AAK1 with compound 1, this nitrogen of the nicotinamide moiety makes a hydrogen bond with K74 side chain. However, this hydrogen/ionic bond is not maintained in the MD simulations of AAK1 with compound 1, and neither with compounds 8g and 21b. On the
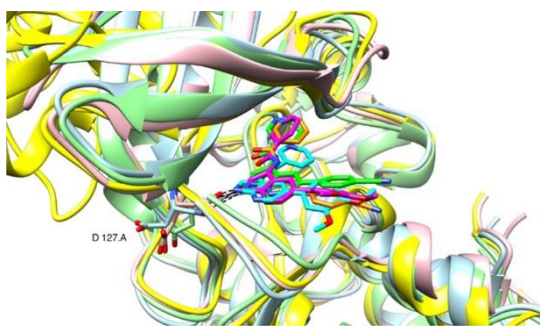
Figure 11. AAK1 snapshot structures with 3 ligands, compound 1 (green, lightgreen), compound 8g (magenta, rose), and compound 21b (cyan; lightblue), extracted from the last 4 ns of the MD trajectory as a representative structure from the biggest cluster using the average linkage clustering method available in cpptraj. The AAK1 and lkb X-ray structures are also shown (orange, yellow). Image made by the Chimera software.[44]

other hand, for the three compounds, frequent van der Waals contacts between this nitrogen and the charged nitrogen in the side chain of K74 (distances < 4 Å) are observed.

For the last 4 ns of the trajectories, MM/GBSA and MM/PBSA (molecular mechanics energies with a generalized Born surface area continuum solvation model and molecular mechanics energies combined with the Poisson−Boltzmann surface area continuum solvation model, respectively)[43] binding affinity calculations were conducted. No entropy contributions were calculated (Table 8). From the data in Table 8, it is clear (more from the general born model than from the Poisson−Boltzmann model) that compounds 8g and 21b are stronger AAK1 binders than reference compound 1. Both methoxy groups of compounds 8g and 21b contribute to the binding energy via van der Waals interactions with specific amino acids of AAK1. Residues L52, L62, F128, C129, R130, G131, G132, Q133, V135, and N136 are involved in binding to compound 21b. The same residues plus E50 make contact with compound 8g. On the other hand, the nitrile function of compound 1 shows clearly less van der Waals contacts with surrounding residues (L52, G132, Q133, and N136, Figure 12).
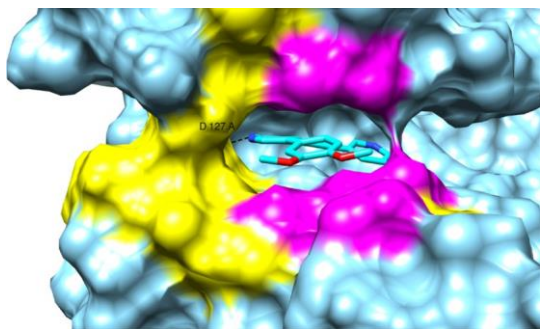

Figure 12. AAK1 enzyme with compound 21b (same snapshot as in Figure 11). Amino acids making contact with the two methoxy groups (heavy atom distances < 4 Å) are colored in yellow and magenta. The magenta color represents also the residues having van der Waals contacts with the nitrile group of compound 1. Image made by the Chimera software.[44]

CONCLUSIONS

AAK1 is a promising host target for the development of broad-spectrum antiviral agents. In this article, the first systematic SAR study of AAK1 inhibitors as antiviral agents is presented. Starting from a known ligand with moderate AAK1 binding affinity and anti-DENV activity, a systematic SAR study was carried out. It led to the discovery of AAK1 ligands with low nM AAK1 binding affinity that display improved antiviral activity against DENV. Moreover, the optimized AAK1 inhibitors exhibit very potent activity in DENV-infected primary dendritic cells and anti-EBOV activity, supporting the potential to develop broad-spectrum antiviral agents based on AAK1 inhibition. Kinase profiling revealed that these compounds have an improved selectivity profile relative to sunitinib, yet further research is necessary to improve their kinase selectivity.

EXPERIMENTAL SECTION

All commercial reagents were obtained via Acros Organics, Sigma-Aldrich, AK Scientific and Fluorochem at least 99% purity unless indicated otherwise. Furthermore, all dry solvents were obtained via Acros Organics with an AcroSeal system, and regular solvents were obtained via Fisher Scientific at technical grade. Thin layer chromatography (TLC) of the reactions was performed on silica gel on aluminum foils (60 Å pore diameter) obtained from Sigma-Aldrich and visualized using ultraviolet light. Recording of the NMR spectra was performed using a Bruker 300, 500, or 600 MHz spectrometer. The chemical shifts are reported in ppm with Me_4Si as the reference and coupling constants (J) are reported in hertz. Mass spectra were acquired on a quadrupole orthogonal acceleration time-of-flight mass spectrometer (Synapt G2 HDMS, Waters, Milford, MA). Samples were infused at 3 μL/min and spectra were obtained in positive or negative ionization mode with a resolution of 15 000 (full width at half-maximum) using leucine enkephalin as lock mass. Purity of the compounds was analyzed on a Waters 600 HPLC system equipped with a Waters 2487 dual λ absorbance detector set at 256 nm using a 5 μm 4.6 × 150 mm XBridge reversed phase (C_{18}) column. The mobile phase was a gradient over 30 min starting from 95% A and 5% B and finishing at 5% A and 95% B with a flow rate of 1 mL per minute (solvent A: Milli-Q water; solvent B: acetonitrile). All synthesized final compounds had a purity of at least 95%. Compound 8o was synthesized according to literature procedure.[22]

5-Bromo-3-((trimethylsilyl)ethynyl)pyridin-2-amine (3). To a stirring suspension of 5-bromo-3-iodopyridin-2-amine 2 (520 mg, 1.74 mmol) in degassed triethylamine (10 mL) were added copper iodide (6.63 mg, 0.034 mmol) and Pd(PPh₃)₂Cl₂ (12 mg, 0.017 mmol). The system was flushed with nitrogen, and trimethylsilyla-cetylene (188 mg, 265 μL, 1.91 mmol) was added dropwise over 5 min. The reaction was allowed to stir for 3 h at room temperature. After reaction completion, the solvent was evaporated and water was added. The resulting suspension was extracted three times using ethyl acetate. The combined organic phases were washed with water and brine, dried over MgSO₄, and evaporated in vacuo. The crude residue was purified by silica gel flash column chromatography using a mixture of heptane and ethylacetate (in a ratio of 80:20) as a mobile phase, yielding the title compound as a yellow-beige solid (420 mg, 90%). ¹H NMR (300 MHz, DMSO-d_6): δ (ppm) 8.03 (s, 1H, ArH), 7.69 (s, 1H, ArH), 6.37 (s, 2H, NH₂), 0.24 (s, 9H, Si(CH₃)₃).

5-Bromo-1H-pyrrolo[2,3-b]pyridine (4). To a solution of 5-bromo-3-((trimethylsilyl)ethynyl)pyridin-2-amine 3 (200 mg, 0.743 mmol) in dry NMP (5 mL) was added portionwise KOtBu (100 mg, 0.891 mmol). The reaction mixture was heated to 80 °C and stirred for 1 h. After reaction completion, the mixture was extracted with water and ethyl acetate three times. The combined organic phases were washed twice with water and once with brine, dried over MgSO₄, and evaporated in vacuo. The crude residue was then purified using silica gel flash column chromatography (using a mixture of heptane

and ethyl acetate in a ratio of 5:1 as mobile phase), yielding the title compound as a white solid (103 mg, 70%). ^{1}H NMR (300 MHz, DMSO-d_6): δ (ppm) 10.33 (br s, 1H, NH), 8.37 (d, J = 2.1 Hz, 1H, ArH), 8.09 (d, J = 2.1 Hz, 1H, ArH), 7.37 (m, 1H, ArH), 6.47 (m, 1H, ArH).

5-Bromo-3-nitro-1H-pyrrolo[2,3-b]pyridine (5). 5-Bromo-1H-pyrrolo[2,3-b]pyridine 4 (730 mg, 3.7 mmol) was added portionwise to a stirring solution of fuming nitric acid (2 mL) at 0 °C over 10 min. The reaction was allowed to stir for 30 min at 0 °C. The mixture was poured into ice water and the formed precipitate was collected via vacuum filtration. The filter cake was washed generously with water and heptane yielding the title compound as a yellow solid (853 mg, 95%). ^{1}H NMR (300 MHz, DMSO-d_6): δ (ppm) 13.48 (br s, 1H, NH), 8.87 (s, 1H, ArH), 8.51 (s, 2H, ArH). ^{13}C NMR (75 MHz, DMSO-d_6): δ (ppm) 145.98, 145.26, 132.13, 129.96, 126.32, 115.17, 114.32.

Synthesis of 3-Nitro-5-aryl-pyrrolo[2,3-b]pyridines (6a−h). General Procedure. To a solution of 5-bromo-3-nitro-1H-pyrrolo-[2,3-b]pyridine 5 (1 equiv) in dioxane (8 mL) were added the appropriate boronic acid (1.2 equiv) and 2 mL of a K$_2$CO$_3$ (3 equiv) solution. The system was purged three times with argon and heated to 105 °C. After stirring for 10 min, Pd(PPh$_3$)$_4$ (0.1 equiv) was added and the reaction was purged once more with argon. The reaction mixture was stirred at 105 °C overnight. After completion, the reaction mixture was cooled to room temperature and filtered through Celite. The filtrate was extracted with water and ethyl acetate. The combined organic phases were washed with brine, dried over MgSO$_4$, and evaporated in vacuo. Purification of the crude residue was achieved by silica gel flash column chromatography using the appropriate solvent mixture.

The following compounds were made according to this procedure.

3-Nitro-5-phenyl-1H-pyrrolo[2,3-b]pyridine (6a). The title compound was synthesized according to the general procedure using 5-bromo-3-nitro-1H-pyrrolo[2,3-b]pyridine 5 (100 mg, 0.413 mmol), phenylboronic acid (61 mg, 0.496 mmol), and K$_2$CO$_3$ (171 mg, 1.24 mmol). Purification by silica gel flash column chromatography using a mixture of DCM and ethyl acetate (in a ratio of 90:10) as the mobile phase, yielded the desired compound as a white solid (83 mg, 84%). ^{1}H NMR (300 MHz, DMSO-d_6): δ (ppm) 13.39 (br s, 1H, NH), 8.89 (s, 1H, HetH), 8.76 (d, J = 2.1 Hz, 1H, HetH), 8.60 (d, J = 2.2 Hz, 1H, HetH), 7.79 (d, J = 7.2 Hz, 2H, o-PhH), 7.54 (t, J = 7.4 Hz, 2H, m-PhH), 7.45 (t, J = 7.3 Hz, 1H, p-PhH).

5-(4-Fluorophenyl)-3-nitro-1H-pyrrolo[2,3-b]pyridine (6b). The title compound was synthesized according to the general procedure using 5-bromo-3-nitro-1H-pyrrolo[2,3-b]pyridine 5 (100 mg, 0.413 mmol), 4-fluorophenylboronic acid (69 mg, 0.496 mmol), and K$_2$CO$_3$ (171 mg, 1.24 mmol). Purification by silica gel flash column chromatography using a mixture of DCM and ethyl acetate (in a ratio of 90:10) as the mobile phase yielded the desired compound as a light brown solid (98 mg, 92%). ^{1}H NMR (300 MHz, DMSO-d_6): δ (ppm) 13.37 (br s, 1H, NH), 8.90 (s, 1H, HetH), 8.82 (d, J = 2.9 Hz, 1H, HetH), 8.68 (d, J = 3.0 Hz, 1H, HetH), 8.01 (m, 4H, PhH).

5-(4-(Trifluoromethyl)phenyl)-3-nitro-1H-pyrrolo[2,3-b]pyridine (6c). The title compound was synthesized according to the general procedure using 5-bromo-3-nitro-1H-pyrrolo[2,3-b]pyridine 5 (100 mg, 0.413 mmol), 4-trifluoromethylphenylboronic acid (94 mg, 0.496 mmol), and K$_2$CO$_3$ (171 mg, 1.24 mmol). Purification by silica gel flash column chromatography using a mixture of DCM and ethyl acetate (in a ratio of 90:10) as the mobile phase yielded the desired compound as a white solid (110 mg, 87%). ^{1}H NMR (300 MHz, DMSO-d_6): δ (ppm) 13.45 (br s, 1H, NH), 8.93 (s, 1H, HetH), 8.84 (d, J = 3.2 Hz, 1H, HetH), 8.70 (d, J = 3.1 Hz, 1H, HetH), 8.45 (m, 1H, PhH), 8.05 (d, J = 8.8 Hz, 2H, PhH), 7.89 (d, J = 8.9 Hz, 1H, PhH).

5-(4-Methoxyphenyl)-3-nitro-1H-pyrrolo[2,3-b]pyridine (6d). The title compound was synthesized according to the general procedure using 5-bromo-3-nitro-1H-pyrrolo[2,3-b]pyridine 5 (100 mg, 0.413 mmol), 4-methoxyphenylboronic acid (75 mg, 0.496 mmol), and K$_2$CO$_3$ (171 mg, 1.24 mmol). Purification by silica gel flash column chromatography using a mixture of DCM and ethyl

acetate (in a ratio of 90:10) as the mobile phase yielded the desired compound as a yellow solid (104 mg, 94%). ^{1}H NMR (300 MHz, DMSO-d_6): δ (ppm) 13.32 (br s, 1H, NH), 8.86 (s, 1H, HetH), 8.72 (d, J = 2.8 Hz, 1H, HetH), 8.55 (d, J = 3.0 Hz, 1H, HetH), 7.73 (d, J = 8.5 Hz, 2H, PhH), 7.10 (d, J = 8.5 Hz, 2H, PhH), 3.83 (s, 3H, OCH$_3$).

3-Nitro-5-(p-tolyl)-1H-pyrrolo[2,3-b]pyridine (6e). The title compound was synthesized according to the general procedure using 5-bromo-3-nitro-1H-pyrrolo[2,3-b]pyridine 5 (100 mg, 0.413 mmol), p-tolylboronic acid (67 mg, 0.496 mmol), and K$_2$CO$_3$ (171 mg, 1.24 mmol). Purification by silica gel flash column chromatography using a mixture of DCM and ethyl acetate (in a ratio of 90:10) as the mobile phase yielded the desired compound as a white solid (83 mg, 74%). ^{1}H NMR (300 MHz, DMSO-d_6): δ (ppm) 13.35 (br s, 1H, NH), 8.88 (s, 1H, HetH), 8.74 (d, J = 3.2 Hz, 1H, HetH), 8.58 (d, J = 3.1 Hz, 1H, HetH), 7.68 (d, J = 7.8 Hz, 2H, PhH), 7.35 (d, J = 7.8 Hz, 2H, PhH), 2.38 (s, 3H, CH$_3$).

3-Nitro-5-(m-tolyl)-1H-pyrrolo[2,3-b]pyridine (6f). The title compound was synthesized according to the general procedure using 5-bromo-3-nitro-1H-pyrrolo[2,3-b]pyridine 5 (100 mg, 0.413 mmol), m-tolylboronic acid (67 mg, 0.496 mmol), and K$_2$CO$_3$ (171 mg, 1.24 mmol). Purification by silica gel flash column chromatography using a mixture of DCM and ethyl acetate (in a ratio of 90:10) as the mobile phase yielded the desired compound as a white solid (83 mg, 74%). ^{1}H NMR (300 MHz, DMSO-d_6): δ (ppm) 13.35 (br s, 1H, NH), 8.88 (s, 1H, HetH), 8.74 (d, J = 3.1 Hz, 1H, HetH), 8.59 (d, J = 3.1 Hz, 1H, HetH), 7.58 (t, J = 7.2 Hz, 2H, PhH), 7.42 (t, J = 7.3 Hz, 1H, PhH), 7.26 (d, J = 3.3 Hz, 1H, PhH), 2.42 (s, 3H, CH$_3$).

5-(3,4-Dimethoxyphenyl)-3-nitro-1H-pyrrolo[2,3-b]pyridine (6g). The title compound was synthesized according to the general procedure using 5-bromo-3-nitro-1H-pyrrolo[2,3-b]pyridine 5 (100 mg, 0.413 mmol), 3,4-dimethoxyphenylboronic acid (63 mg, 0.496 mmol), and K$_2$CO$_3$ (171 mg, 1.24 mmol). The compound precipitated as a yellow solid that was washed twice with dioxane, followed by washing with water yielding the pure title compound (88 mg, 89%). ^{1}H NMR (300 MHz, DMSO-d_6): δ (ppm) 8.82 (s, 1H, HetH), 8.72 (d, J = 2.1 Hz, 1H, HetH), 8.54 (d, J = 2.2 Hz, 1H, HetH), 7.30 (m, 2H, PhH), 7.10 (d, J = 8.3 Hz, 1H, PhH), 3.88 (s, 3H, OCH$_3$), 3.82 (s, 3H, OCH$_3$).

3-Nitro-5-(3-thienyl)-1H-pyrrolo[2,3-b]pyridine (6h). The title compound was synthesized according to the general procedure using 5-bromo-3-nitro-1H-pyrrolo[2,3-b]pyridine 5 (100 mg, 0.413 mmol), 3-thienylboronic acid (69 mg, 0.496 mmol), and K$_2$CO$_3$ (171 mg, 1.24 mmol). Purification by silica gel flash column chromatography using a mixture of DCM and ethyl acetate (in a ratio of 90:10) as the mobile phase yielded the title compound as a brown solid (97 mg, 96%). ^{1}H NMR (300 MHz, DMSO-d_6): δ (ppm) 13.41 (br s, 1H, NH), 8.89 (d, J = 3.0 Hz, 1H, HetH), 8.83 (d, J = 3.1 Hz, 1H, HetH), 8.57 (d, J = 3.0 Hz, 1H, HetH), 7.69 (m, 2H, ThH) ppm, 7.22 (t, J = 4.4 Hz, 1H, ThH).

Synthesis of 5-Aryl-3-amino- and 5-Aryl-3-N-acylamino Pyrrolo[2,3-b]pyridines (7a−f and 8a−o). General Procedure. To a solution of a 5-aryl-3-nitro-pyrrolo[2,3-b]pyridine 6a−h (100 mg) in tetrahydrofuran (THF) (5 mL) was added a slurry of Raney nickel in water in catalytic amounts. The reaction vessel was flushed three times with hydrogen gas and was stirred under a hydrogen atmosphere for 3−4 h. Upon completion of the reaction, the catalyst was removed and the solvent evaporated in vacuo. The crude residue was used in the next reaction without any purification because of the rapid decomposition of the 3-amino-pyrrolo[2,3-b]pyridine intermediates 7a−h. To a solution of compounds 7a−h (1 equiv) in dry pyridine (3 mL) was added a solution of nicotinoyl chloride hydrochloride (1.2 equiv) in CH$_2$Cl$_2$ (2 mL). The reaction was allowed to stir at room temperature for 3 h. The solvent was evaporated in vacuo. THF (5 mL) was added and the resulting solution was stirred for 5 min, followed by the addition of a 1 M NaOH solution in water (5 mL). The resulting suspension was stirred for an additional 10 min. The precipitate was collected via vacuum filtration and purified using flash column chromatography with the

appropriate solvent mixture as mobile phase. Compounds 8a−h were synthesized according to this procedure.

N-(5-Phenyl-1H-pyrrolo[2,3-b]pyridin-3-yl)nicotinamide (8a). The title compound was synthesized according to the general procedure using 3-nitro-5-phenyl-1*H*-pyrrolo[2,3-*b*]pyridine 6a (84 mg, 0.351 mmol). Purification by silica gel flash column chromatography (eluting with a mixture of DCM and methanol in a gradient gradually ranging from 98:2 to 90:10) afforded the title compound as a dark brown solid (47 mg, 36%). Purity of 99%. ^{1}H NMR (300 MHz, DMSO-d_6): δ 11.62 (br s, 1H, NH), 10.58 (br s, 1H, NH), 9.19 (s, 1H, HetH), 8.79 (d, J = 3.0 Hz, 1H, HetH), 8.66 (s, 1H, ArH), 8.58 (s, 1H, ArH), 8.36 (d, J = 6.1 Hz, 1H, ArH), 7.98 (s, 1H, ArH), 7.75 (d, J = 8.8 Hz, 2H, ArH), 7.60 (t, J = 6.0 Hz, 1H, ArH), 7.51 (t, J = 7.3 Hz, 2H, ArH), 7.38 (t, J = 7.4 Hz, 1H, ArH)

ppm. ^{13}C NMR (75 MHz, DMSO-d_6): δ 163.46, 152.01, 148.87, 145.52, 142.23, 139.16, 135.60, 131.63, 130.52, 129.13, 127.06,

126.93, 125.49, 123.61, 117.52, 114.10, 113.45 ppm. HRMS *m/z*: [M + H]$^+$ calcd for $C_{19}H_{14}N_4O$, 315.12403; found, 315.1237.

N-[5-(4-Fluorophenyl)-1H-pyrrolo[2,3-b]pyridin-3-yl]-nicotinamide (8b). The title compound was synthesized according to the general procedure using 3-nitro-5-(4-fluorophenyl)-1*H*-pyrrolo-[2,3-*b*]pyridine 6b (98 mg, 0.381 mmol). Purification by silica gel flash column chromatography (using a mixture of DCM/methanol in a ratio gradually ranging from 98:2 to 90:10 as mobile phase) afforded the title compound as a brown solid (44 mg, 34%). Purity of 99%. ^{1}H NMR (300 MHz, DMSO-d_6): δ 11.63 (br s, 1H, NH), 10.57 (br s, 1H, NH), 9.17 (s, 1H, HetH), 8.78 (d, J = 5.8 Hz, 1H, ArH), 8.62 (s, 1H, HetH), 8.56 (s, 1H, ArH), 8.36 (d, J = 8.9 Hz, 1H, ArH), 7.98 (d, J = 3.2 Hz, 1H, ArH), 7.77 (t, J = 7.6 Hz, 2H, ArH), 7.61 (d, J = 9.0 Hz, 1H, ArH), 7.35 (t, J = 7.5 Hz, 2H, ArH) ppm. ^{13}C NMR (75

MHz, DMSO-d_6): δ 162.24, 161.77 (d, J_{CF} = 242 Hz), 150.23, 148.62, 148.62, 145.58, 142.05, 138.10, 135.66, 128.86 (d, J_{CF} = 8.0 Hz),

126.77, 126.72, 125.74, 122.38, 117.74, 116.00, 115.85 (d, J_{CF} = 20.4), 113.75, 113.47 ppm. HRMS *m/z*: [M + H]$^+$ calcd for $C_{19}H_{13}N_4OF$, 333.11460; found, 333.1145. HRMS *m/z*: [M + Na]$^+$ calcd for $C_{19}H_{13}N_4OF$, 355.09658; found, 355.0950.

N-[5-(4-Trifluoromethylphenyl)-1H-pyrrolo[2,3-b]pyridin-3-yl]-nicotinamide (8c). The title compound was synthesized according to the general procedure using 3-nitro-5-(4-trifluoromethylphenyl)-1*H*-pyrrolo[2,3-*b*]pyridine 6c (116 mg, 377.56 μmol). Purification by silica gel flash column chromatography using a mixture of DCM and methanol (in a ratio gradually ranging from 98:2 to 90:10) as the mobile phase afforded the title compound as a white solid (49 mg, 36%). Purity of 99%. ^{1}H NMR (300 MHz, DMSO-d_6): δ 11.73 (br s,

1H, NH), 10.62 (br s, 1H, NH), 9.19 (d, J = 3.2 Hz, 1H, HetH), 8.78

(t, J = 6.1 Hz, 2H, ArH), 8.67 (d, J = 3.1 Hz, 1H, HetH), 8.36 (d, J = 3.0 Hz, 1H, ArH), 7.99 (d, J = 8.9 Hz, 3H, PhH), 7.87 (d, J = 9.0 Hz, 2H, PhH), 7.61 (q, J = 5.9 Hz, 1H, ArH) ppm. ^{13}C NMR (75 MHz,

DMSO-d_6): δ 163.52, 152.05, 148.85, 145.88, 143.25, 142.35, 135.58, 130.46, 127.48, 126.09, 123.61, 122.80, 117.84, 114.28, 113.52 ppm; missing peaks were observed in an APT spectrum. HRMS *m/z*: [M + H]$^+$ calcd for $C_{20}H_{13}N_4F_3O$, 383.11141; found, 383.1114.

N-[5-(4-Methoxyphenyl)-1H-pyrrolo[2,3-b]pyridin-3-yl]-nicotinamide (8d). The title compound was synthesized according to the general procedure using 3-nitro-5-(4-methoxyphenyl)-1*H*-pyrrolo[2,3-*b*]pyridine 6d (105 mg, 0.390 mmol). Purification by silica gel flash column chromatography using a mixture of DCM and methanol (in a ratio gradually ranging from 98:2 to 90:10) as the mobile phase afforded the title compound as a pink solid (43 mg, 34%). Purity of 99% ^{1}H NMR (300 MHz, DMSO-d_6): δ 11.56 (br s, 1H, NH), 10.56 (br s, 1H, NH), 9.18 (s, 1H, ArH), 8.78 (d, J = 6.1 Hz, 1H, ArH), 8.58 (s, 1H, ArH), 8.52 (s, 1H, ArH), 8.36 (d, J = 9.0

N-(5-(p-Tolyl)-1H-pyrrolo[2,3-b]pyridin-3-yl)nicotinamide (8e). The title compound was synthesized according to the general procedure using 3-nitro-5-(*p*-tolyl)-1*H*-pyrrolo[2,3-*b*]pyridine 6e (96 mg, 0.379 mmol). Purification by silica gel flash column chromatography using a mixture of DCM and methanol (in a ratio gradually ranging from 98:2 to 90:10) as the mobile phase afforded the title compound as a beige solid (48 mg, 37%). Purity of 98%. ^{1}H NMR (300 MHz, DMSO-d_6): δ 11.60 (br s, 1H, NH), 10.59 (br s, 1H, NH), 9.19 (s, 1H, ArH), 8.78 (d, J = 2.9 Hz, 1H, ArH), 8.63 (s, 1H, ArH), 8.56 (s, 1H, ArH), 8.36 (d, J = 6.0 Hz, 1H, ArH), 7.99 (s, 1H, ArH), 7.59 (m, 3H, ArH), 7.31 (d, J = 9.3 Hz, 2H, ArH), 2.35 (s, 3H, CH$_3$) ppm. ^{13}C NMR (75 MHz, DMSO-d_6): δ 163.49, 151.99, 148.85, 145.41, 142.10, 136.28, 136.22, 135.59, 130.51, 129.73, 127.68, 126.73, 125.12, 123.60, 117.50, 114.03, 113.47, 20.77 ppm.

HRMS *m/z*: [M + H]$^+$ calcd for $C_{20}H_{16}N_4O$, 329.13967; found, 329.1398.

N-[5-(m-Tolyl)-1H-pyrrolo[2,3-b]pyridin-3-yl]nicotinamide (8f). The title compound was synthesized according to the general procedure using 3-nitro-5-(*m*-tolyl)-1*H*-pyrrolo[2,3-*b*]pyridine 6f (77 mg, 0.304 mmol). Purification by silica gel flash column chromatography using a mixture of DCM and methanol (in a ratio gradually ranging from 98:2 to 90:10) as the mobile phase afforded the title compound as a beige solid (22 mg, 25% yield). Purity of 98%. ^{1}H NMR (300 MHz, DMSO-d_6): δ 11.61 (br s, 1H, NH), 10.59 (br s, 1H, NH), 9.19 (s, 1H, ArH), 8.79 (d, J = 2.8 Hz, 1H, ArH), 8.64 (s, 1H, ArH), 8.57 (s, 1H, ArH), 8.37 (d, J = 9.0 Hz, 1H, ArH), 7.99 (s, 1H, ArH), 7.59 (m, 3H, CH$_3$), 7.39 (t, J = 7.4 Hz, 1H), 7.19 (d, J = 6.1 Hz, 1H), 2.41 (s, 3H) ppm. ^{13}C NMR (75 MHz, DMSO-d_6): δ 163.49, 151.99, 148.84, 145.47, 142.25, 139.08, 138.27, 135.59, 130.50, 129.02, 127.84, 127.71, 127.53, 125.39, 124.06, 123.60,

117.47, 114.07, 113.42, 21.28 ppm. HRMS *m/z*: [M + H]$^+$ calcd for $C_{20}H_{16}N_4O$, 329.13967; found, 329.1397.

N-[5-(3,4-Dimethoxyphenyl)-1H-pyrrolo[2,3-b]pyridin-3-yl]-nicotinamide (8g). The title compound was synthesized according to the general procedure using 3-nitro-5-(3,4-dimethoxyphenyl)-1*H*-pyrrolo[2,3-*b*]pyridine 6g (80 mg, 0.297 mmol). Purification by silica gel flash column chromatography using a mixture of DCM and methanol (in a ratio gradually ranging from 98:2 to 90:10) as the mobile phase afforded the title compound as a beige solid (56 mg, 50%). Purity of 97%. ^{1}H NMR (300 MHz, DMSO-d_6): δ 11.57 (br s, 1H, NH), 10.56 (br s, 1H, NH), 9.20 (s, 1H, ArH), 8.78 (d, J = 6.1 Hz, 1H, ArH), 8.58 (d, J = 3.2 Hz, 2H, ArH), 8.37 (d, J = 9.1 Hz, 1H, ArH), 7.97 (s, 1H, ArH), 7.60 (t, J = 6.0 Hz, 1H, ArH), 7.27 (t, J = 7.4 Hz, 2H, ArH), 7.09 (d, J_3 = 9.0 Hz, 1H, ArH), 3.88 (s, 3H, OCH$_3$),

3.81 (s, 3H, OCH$_3$) ppm. C NMR (75 MHz, DMSO-d_6): δ 163.45,

152.00, 149.40, 148.88, 148.43, 145.28, 142.26, 135.61, 132.04, 130.51, 127.84, 124.96, 123.61, 119.23, 117.47, 113.93, 113.39,

112.70, 111.09, 55.92, 55.82 ppm. HRMS *m/z*: [M + H]$^+$ calcd for

Hz, 1H, PhH), 7.96 (s, 1H, ArH), 7.62 (m, 3H, ArH), 7.08 (d, J = 8.9

$C_{21}H_{18}N_4O_3$, 375.14515; found, 375.1447, HRMS m/z: [M + Na]$^+$ calcd for $C_{21}H_{18}N_4O_3$, 397.12713; found, 397.1264.

N-[5-(3-Thienyl)-1H-pyrrolo[2,3-b]pyridin-3-yl]nicotinamide (8h). The title compound was synthesized according to the general procedure using 3-nitro-5-(3-thienyl)-1H-pyrrolo[2,3-b]pyridine 6h (97 mg, 0.395 mmol). Purification by silica gel flash column chromatography using a mixture of DCM and methanol (in a ratio gradually ranging from 98:2 to 90:10) as

Hz, 2H, PhH), 3.82 (s, 3H, OCH$_3$) ppm. ^{13}C NMR (75 MHz,

DMSO-d_6): δ 163.45, 158.74, 151.99, 148.85, 145.22, 141.99, 135.59,

131.54, 130.50, 128.00, 127.55, 124.87, 123.60, 117.43, 114.64, 113.94, 113.45, 55.34 ppm. HRMS m/z: [M + H]$^+$ calcd for $C_{20}H_{16}N_4O_2$, 345.13459; found, 345.1343. HRMS m/z: [M + Na]$^+$ calcd for $C_{20}H_{16}N_4O_2$, 367.11656; found, 367.1153.

the mobile phase, afforded the title compound as a brown solid (48 mg, 37%). Purity of 99%. ^{1}H NMR (300 MHz, DMSO-d_6): δ 11.58 (br s, 1H, NH), 10.54 (br s, 1H, NH), 9.20 (d, J = 2.8 Hz, 1H, ArH), 8.79 (d, J = 2.9 Hz, 1H, ArH), 8.67 (d, J = 2.9 Hz, 1H, ArH), 8.64 (d, J = 3.0 Hz, 1H, ArH), 8.36 (m, 1H, ArH), 7.93 (s, 1H, ArH), 7.84 (s, 1H, ArH), 7.71 (m, 1H, ArH), 7.60 (t, J = 5.9 Hz, 2H, ArH) ppm. ^{13}C NMR (75 MHz, DMSO-d_6): δ 163.48, 152.02, 148.86, 145.30, 142.03, 140.21, 135.58, 130.49, 127.30, 126.37, 124.61, 123.60, 123.18, 119.78, 117.63, 113.94, 113.49 ppm. HRMS m/z: [M + H]$^+$ calcd for $C_{17}H_{12}N_4OS$, 321.08045; found, 321.0804.

N-(5-(3,4-Dimethoxyphenyl)-1H-pyrrolo[2,3-b]pyridin-3-yl)-benzamide (8i). To a solution of 3-nitro-5-(3,4-dimethoxyphenyl)-1H-pyrrolo[2,3-b]pyridine 6g (100 mg, 0.334 mmol) in THF (4 mL) was added a catalytic amount of a slurry of Raney nickel in water. The

vessel was flushed three times with hydrogen gas and kept under a hydrogen atmosphere for 4 h. After complete conversion, the catalyst was removed, and the solvent was evaporated in vacuo. The crude product was immediately used for further reaction without purification. To a solution of the crude residue from the previous reaction in pyridine (5 mL) was added a solution of benzoyl chloride (47 μL, 0.401 mmol) in DCM (0.5 mL). The reaction was stirred overnight at room temperature. After reaction completion, the solvent was evaporated in vacuo, and the crude residue was extracted three times with water and ethyl acetate. The combined organic layers were dried over MgSO$_4$ and evaporated to dryness. Purification was achieved by silica gel flash column chromatography (using a mixture of DCM and methanol in a ratio of 97:3 as mobile phase), followed by precipitation of the residue from acetone. The precipitate was collected via filtration yielding the title compound as a white solid (27 mg, 22%). Purity of 98%. ^{1}H NMR (300 MHz, DMSO-d_6): δ 11.52 (br s, 1H, NH), 10.37 (br s, 1H, NH), 8.56 (d, J = 6.52, 2H, ArH), 8.00 (m, 3H, ArH), 7.56 (d, J = 7.6 Hz, 3H, ArH), 7.25 (m, 2H, ArH), 7.08 (d, J = 8.2 Hz, 1H, ArH), 3.87 (s, 3H, OCH$_3$), 3.80 (s, 3H, OCH$_3$) ppm. ^{13}C NMR (75 MHz, DMSO-d_6): δ 165.07, 149.30, 148.30, 145.25, 142.12, 134.88, 132.01, 131.42, 128.48, 127.87, 127.70, 125.04, 119.14, 117.27, 114.22, 113.44, 112.52, 110.87, 55.83, 55.74 ppm. HRMS m/z: [M + H]$^+$ calcd for C$_{22}$H$_{19}$N$_3$O$_3$, 374.14990; found, 374.1493.

Synthesis of 5-(3,4-Dimethoxyphenyl)-3-N-acylamino Pyrrolo[2,3-b]pyridines. *General Procedure.* 3-Nitro-5-(3,4-dimethoxyphenyl)-1H-pyrrolo[2,3-b]pyridine **6g** (100 mg, 0.334 mmol) was hydrogenated with a catalytic amount of Raney nickel as a slurry in water (slurry in water? x mg/mL) in THF (5 mL) for 3 h. The solvents were evaporated in vacuo yielding crude 3-amino-5-(3,4-dimethoxyphenyl)-1H-pyrrolo[2,3-b]pyridine which was used in the next reaction without further purification (90 mg, 99%). To a solution of 3-amino-5-(3,4-dimethoxyphenyl)-1H-pyrrolo[2,3-b]pyridine (90 mg, 0.334 mmol) in dimethylformamide (DMF) (3 mL) was added the appropriate carboxylic acid (1 equiv), BOP (177 mg, 0.401 mmol), and triethylamine (140 μL, 1 mmol). The mixture was stirred overnight. When the reaction reached completion, water was added and the mixture was extracted three times with ethyl acetate. The combined organic layers were washed with brine, dried over Na$_2$SO$_4$, and evaporated in vacuo. The crude residue was purified by silica gel flash chromatography using an appropriate solvent system as the mobile phase. An additional purification was performed by preparative TLC using a mixture of DCM and acetone (in a ratio of 8:2) as eluent. The following compounds were prepared according to this procedure.

N-(5-(3,4-Dimethoxyphenyl)-1H-pyrrolo[2,3-b]pyridin-3-yl)-4-fluorobenzamide (8j). The title compound was synthesized according to the general procedure using 4-fluorobenzoic acid (47 mg, 0.334 mmol). Purification by silica gel flash column chromatography (using a mixture of DCM and methanol as mobile phase in a ratio of 99:1) yielded the desired compound as a white solid (56 mg, 43%). Purity of 99%. ^{1}H NMR (300 MHz, DMSO-d_6): δ 11.53 (br s, 1H, NH), 10.39 (br s, 1H, NH), 8.56 (d, J = 8.5 Hz, 2H, ArH), 8.12 (m, 2H, ArH), 7.93 (s, 1H, ArH), 7.38 (t, J = 8.7 Hz, 2H, ArH), 7.26 (m, 2H, ArH), 7.08 (d, J = 8.3 Hz, 1H, ArH), 3.87 (s, 3H, OCH$_3$), 3.81 (s, 3H, OCH$_3$) ppm. ^{13}C NMR (75 MHz, DMSO-d_6): δ 164.07 (J_{CF} = 245 Hz), 163.93, 149.30, 148.30, 145.25, 142.12, 131.99, 131.27, 130.57 (J_{CF} = 8.97 Hz), 127.69, 125.05, 119.12, 117.35, 115.39 (J_{CF} = 22 Hz), 114.11, 113.46, 112.53, 110.88, 55.84, 55.75 ppm. HRMS m/z: [M + H]$^+$ calcd for C$_{22}$H$_{18}$FN$_3$O$_3$, 392.14048; found, 392.1399.

N-(5-(3,4-Dimethoxyphenyl)-1H-pyrrolo[2,3-b]pyridin-3-yl)-4-methoxybenzamide (8k). The title compound was synthesized according to the general procedure using 4-methoxybenzoic acid (51 mg, 0.334 mmol). Purification by silica gel flash column chromatography (using a mixture of DCM and methanol as mobile phase in a ratio of 99:1) yielded the desired compound as a white solid (64 mg, 47%). Purity of 97%. ^{1}H NMR (600 MHz, DMSO-d_6):

2.16 Hz, ArH), 7.08 (m, 3H, ArH), 3.87 (s, 3H, OCH$_3$), 3.85 (s,3H, OCH$_3$), 3.80 (s, 3H, OCH$_3$) ppm. ^{13}C NMR (150 MHz, DMSO-d_6): δ 164.43, 161.77, 149.25, 148.24, 145.21, 142.00, 131.99, 129.69, 127.58, 126.92, 124.98, 119.08, 117.14, 114.27, 113.65, 113.48, 112.48, 110.82, 55.78, 55.70, 55.50 ppm. HRMS m/z: [M + H]$^+$ calcd for C$_{23}$H$_{21}$N$_3$O$_4$, 404.16047; found, 404.1603.

N-(5-(3,4-Dimethoxyphenyl)-1H-pyrrolo[2,3-b]pyridin-3-yl)-2-phenylacetamide (8m). The title compound was synthesized according to the general procedure using phenylacetic acid (45 mg, 0.334 mmol). Purification by silica gel flash column chromatography (using a mixture of DCM and methanol as mobile phase in a ratio of 99:1) yielded the desired compound as a white solid (49 mg, 54%). Purity of 99%. ^{1}H NMR (300 MHz, DMSO-d_6): δ 11.36 (s, 1H, NH), 10.45 (s, 1H, NH), 8.53 (m, 2H, ArH), 7.79 (d, J = 2.3 Hz, 1H, ArH), 7.31 (m, 7H, ArH), 7.09 (d, J = 8.4 Hz, 1H, ArH), 3.88 (s, 3H, OCH$_3$), 3.81 (s, 3H, OCH$_3$), 3.76 (s, 2H, CH$_2$) ppm. ^{13}C NMR (75 MHz, DMSO-d_6): δ 168.21, 157.37, 149.33, 148.30, 145.01, 142.09, 136.54, 131.94, 129.28, 128.38, 127.55, 126.56, 124.40, 119.00, 115.78, 114.37, 112.78, 112.55, 110.80, 55.83, 55.76, 42.41 ppm.

HRMS m/z: [M + H]$^+$ calcd for C$_{23}$H$_{21}$N$_3$O$_3$, 388.16555; found, 388.1660.

δ 11.46 (s, 1H, NH), 10.16 (s, 1H, NH), 8.55 (d, J = 1.92 Hz, 1H, ArH), 8.53 (d, J = 2.22 Hz, 1H, ArH), 8.01 (m, 2H, ArH), 7.90 (d, J = 2.46 Hz, 1H, ArH), 7.28 (d, J = 2.16 Hz, 1H, ArH), 7.22 (dd, J = 8.22,

N-(5-(3,4-Dimethoxyphenyl)-1H-pyrrolo[2,3-b]pyridin-3-yl)- cyclopentanecarboxamide (8n). To a solution of 3-nitro-5-(3,4- dimethoxyphenyl)-1*H*-pyrrolo[2,3-*b*]pyridine 6g (100 mg, 0.334 mmol) in THF (5 mL) was added a catalytic amount of a slurry of Raney nickel in water. The vessel was flushed three times with hydrogen gas and kept under a hydrogen atmosphere for 4 h. After complete conversion, the catalyst was removed, and the solvent was evaporated in vacuo. The crude product was immediately used for further reaction without purification. To a solution of the crude residue in pyridine (5 mL) was added a solution of cyclo-pentylcarbonyl chloride (46 μL, 0.401 mmol) in DCM (2 mL). The reaction was stirred overnight at room temperature. After reaction completion, the solvent was evaporated in vacuo, and the crude residue was extracted three times with water and ethyl acetate. The combined organic layers were dried over $MgSO_4$ and evaporated to dryness. Purification by silica gel flash column chromatography (using a mixture of DCM and methanol in a ratio of 97:3 as mobile phase) yielded the title compound as a white solid (39 mg, 32%). Purity of 99%. ^{1}H NMR (300 MHz, DMSO-d_6): δ 11.33 (br s, 1H, NH), 9.96 (br s, 1H, NH), 8.51 (s, 1H, ArH), 8.44 (s, 1H, ArH), 7.82 (d, J = 2.2 Hz, 1H, ArH), 7.23 (m, 2H, ArH), 7.08 (d, J = 8.3 Hz, 1H, ArH), 3.88 (s, 3H, OCH_3), 3.81 (s, 3H, OCH_3), 2.90 (m, 1H, CH_2), 1.77 (m, 8H, CH_2) ppm. ^{13}C NMR (75 MHz, DMSO-d_6): δ 173.48, 149.31, 148.30, 145.00, 142.05, 132.01, 127.51, 124.19, 119.05, 115.69, 114.50, 112.71, 112.55, 110.80, 55.82, 55.75, 44.55, 30.46, 25.85. HRMS m/z: [M + H]$^+$ calcd for $C_{21}H_{23}N_3O_3$, 366.18120; found, 366.1808.

N-(5-(3,4-Dimethoxyphenyl)-1H-pyrrolo[2,3-b]pyridin-3-yl)- benzenesulfonamide (8p). To a solution of 3-nitro-5-(3,4-dimethox- yphenyl)-1*H*-pyrrolo[2,3-*b*]pyridine (100 mg, 0.334 mmol) in THF (5 mL) was added a catalytic amount of a slurry of Raney nickel in water. The vessel was flushed with hydrogen gas three times and kept under a hydrogen atmosphere for 4 h. After complete conversion, the catalyst was removed and the solvent was evaporated. The crude was immediately used in the next reaction without further purification because of the rapid decomposition of the amine. To a solution of the crude from the previous reaction in pyridine (5 mL) was added a solution of benzensulfonyl chloride (47 μL, 0.368 mmol) in DCM (1 mL). The reaction was stirred overnight at room temperature. After reaction completion, the solvent was evaporated and the crude was extracted with water and ethyl acetate three times. The collected organics were dried with $MgSO_4$ and evaporated to dryness. Flash column chromatography (using a mixture of DCM and methanol as mobile phase in a ratio of 97:3) yielded the desired compound as an off-white solid (34 mg, 25%). Purity of 98%. ^{1}H NMR (600 MHz, DMSO-d_6): δ 11.64 (br s, 1H, NH), 9.87 (br s, 1H, NH), 8.42 (d, J = 1.92 Hz, 1H, ArH), 7.73 (s, 1H, ArH), 7.72 (s, 2H, ArH), 7.55 (t, J = 7.5 Hz, 1H, ArH), 7.51 (t, J = 7.74 Hz, 2H, ArH), 7.20 (d, J = 2.52 Hz, 1H, ArH), 7.05 (m, 2H, ArH), 6.99 (d, J = 1.74 Hz, 1H, ArH),

3.85 (s, 3H, OCH$_3$), 3.80 (s, 3H, OCH$_3$) ppm. ^{13}C NMR (150 MHz, DMSO-d_6): δ 149.18, 148.27, 145.66, 142.15, 140.05, 132.66, 131.55, 129.03, 128.23, 126.96, 123.76, 121.94, 118.96, 115.65, 113.91, 112.46, 111.06, 110.50, 55.70, 55.68 ppm. HRMS m/z: [M + H]$^+$ calcd for C$_{21}$H$_{19}$N$_3$O$_4$S, 408.10234; found, 408.1024.

5-Bromo-1H-pyrrolo[2,3-b]pyridine-3-carbaldehyde (9). To a solution of 5-bromo-1H-pyrrolo[2,3-b]pyridine 4 (500 mg, 2.54 mmol) in a mixture of water and acetic acid (in a ratio of 3:1, 10 mL) was added hexamine (712 mg, 5.08 mmol). The reaction was heated to 120 °C and refluxed overnight. The formed precipitate was filtered off, affording the title compound (380 mg, 67%). ^{1}H NMR (300 MHz, DMSO-d_6): δ 12.93 (br s, 1H, NH), 9.93 (s, 1H, CHO), 8.55 (s, 1H, HetH), 8.53 (d, J = 2.3 Hz, 1H, HetH), 8.46 (d, J = 2.3 Hz, 1H, HetH) ppm. ^{13}C NMR (75 MHz, DMSO-d_6): δ 185.58, 147.92, 145.09, 139.90, 131.01, 118.32, 116.04, 113.86 ppm.

5-Bromo-1-tosyl-pyrrolo[2,3-b]pyridine-3-carbaldehyde (10). To a suspension of 60% NaH on mineral oil (80 mg, 2 mmol) in dry THF (6 mL) was added 5-bromo-1H-pyrrolo[2,3-b]pyridine-3-carbaldehyde 9 (300 mg, 1.33 mmol) at 0 °C. After stirring for 20 min at room temperature, tosyl chloride (381 mg, 2 mmol) was added and the resulting solution was stirred for another 3 h at room temperature. After reaction completion, the solvent was evaporated in vacuo and the crude residue was extracted with water and DCM. The combined organic layers were dried over MgSO$_4$ and evaporated in vacuo, affording the title compound (460 mg, 91%). ^{1}H NMR (300 MHz, DMSO-d_6): δ 10.03 (s, 1H, CHO), 9.02 (s, 1H, HetH), 8.59 (d, J = 2.2 Hz, 1H, HetH), 8.55 (d, J = 2.2 Hz, 1H, HetH), 8.07 (d, J = 8.4 Hz, 2H, TsH), 7.48 (d, J = 8.2 Hz, 2H, TsH), 2.37 (s, 3H, CH$_3$) ppm.

5-(3,4-Dimethoxyphenyl)-1-tosyl-1H-pyrrolo[2,3-b]pyridine-3-carbaldehyde (11). To a solution of 5-bromo-1-tosyl-pyrrolo[2,3-b]pyridine-3-carbaldehyde 10 (240 mg, 0.633 mmol) in a mixture of toluene and ethanol (in a ratio of 3:1, 4 mL) was added 3,4-dimethoxyphenylboronic acid (138 mg, 0.759 mmol) and a 2 M solution of K$_2$CO$_3$ (950 μL, 1.90 mmol). The system was purged with argon and Pd(PPh$_3$)$_4$ (2 mol %) was added. The reaction was heated to 105 °C and was stirred for 4 h. After completion, the solvent was evaporated in vacuo and the residue was extracted with water and ethyl acetate. Purification by silica gel flash chromatography using a mixture of heptane and ethyl acetate (in a ratio of 7:3) as the mobile phase afforded the title compound (160 mg, 58%). ^{1}H NMR (300 MHz, DMSO-d_6): δ 10.09 (s, 1H, CHO), 9.00 (s, 1H, HetH), 8.76 (s, 1H, HetH), 8.55 (s, 1H, HetH), 8.11 (d, J = 7.7 Hz, 2H, TsH), 7.49 (d, J = 7.4 Hz, 2H, TsH), 7.24 (m, 2H, PhH), 7.07 (d, J = 8.2 Hz, 1H, PhH), 3.85 (s, 3H, OCH$_3$), 3.79 (s, 3H, OCH$_3$), 2.37 (s, 3H, CH$_3$) ppm.

(5-(3,4-Dimethoxyphenyl)-1-tosyl-pyrrolo[2,3-b]pyridin-3-yl)(phenyl)methanol (12). To a solution of 5-(3,4-dimethoxyphenyl)-1-tosyl-1H-pyrrolo[2,3-b]pyridine-3-carbaldehyde 11 (160 mg, 0.367 mmol) in dry THF (5 mL) at 0 °C was added a 3 M solution of phenylmagnesium bromide in diethylether (159 μL, 0.477 mmol). The reaction mixture was stirred for 1 h at 0 °C. After reaction completion, the mixture was quenched with a saturated NH$_4$Cl solution and extracted with water and ethyl acetate. The combined organic layers were dried over Na$_2$SO$_4$ and evaporated to dryness yielding the title compound (130 mg, 69%). ^{1}H NMR (300 MHz, DMSO-d_6): δ 8.62 (s, 1H, ArH), 7.99 (d, J = 8.8 Hz, 3H, ArH), 7.70 (s, 1H, ArH), 7.59□6.99 (m, 10H, ArH), 6.13 (d, J = 4.4 Hz, 1H, ArH), 6.02 (s, 1H, ArH), 3.82 (s, 3H, OCH$_3$), 3.78 (s, 3H, OCH$_3$), 2.34 (s, 3H, CH$_3$) ppm.

(5-(3,4-Dimethoxyphenyl)-1-tosyl-pyrrolo[2,3-b]pyridin-3-yl)(phenyl)methanone (13). To a solution of (5-(3,4-dimethoxyphenyl)-1-tosyl-pyrrolo[2,3-b]pyridin-3-yl) (phenyl)methanol 12 (130 mg, 0.253 mmol) in DCM (8 mL) was added manganese dioxide (220 mg, 2.53 mmol), and the reaction was stirred overnight at room temperature. After completion, the mixture was filtered through Celite, and the filtrate was evaporated to dryness. The crude residue was purified by silica gel flash column chromatography using a mixture of heptane and ethyl acetate (in a ratio of 6:4) as the mobile phase yielding the title compound (64 mg, 49%). ^{1}H NMR (300

Hz, 1H, HetH), 8.33 (s, 1H), 8.16 (d, J = 8.3 Hz, 2H, ArH), 7.96 (d, J = 7.2 Hz, 2H, ArH), 7.70 (m, 3H, ArH), 7.47 (d, J = 8.2 Hz, 2H, ArH), 7.25 (m, 2H, ArH), 7.08 (d, J = 8.4 Hz, 1H, ArH), 3.86 (s, 3H, OCH$_3$), 3.81 (s, 3H, OCH$_3$), 2.37 (s, 3H, CH$_3$) ppm.

(5-(3,4-Dimethoxyphenyl)-1H-pyrrolo[2,3-b]pyridin-3-yl)-(phenyl)methanone (14). To a solution of (5-(3,4-dimethoxyphenyl)-1-tosyl-pyrrolo[2,3-b]pyridin-3-yl) (phenyl)methanone 13 (64 mg, 0.124 mmol) in ethanol (10 mL) was added KOH (35 mg, 0.624 mmol), and the mixture was heated to 80 °C. The reaction was stirred for 3 h. After reaction completion, the solvent was evaporated in vacuo and the crude residue was partitioned between water and ethyl acetate. The combined organic layers were dried over MgSO$_4$ and evaporated to dryness, yielding the title compound as a white

solid (34 mg, 76%). Purity of 95%. H NMR (300 MHz, DMSO-d_6):

MHz, DMSO-d_6): δ 8.78 (d, J = 2.1 Hz, 1H, HetH), 8.64 (d, J = 2.1

δ 12.74 (br s, 1H, NH), 8.67 (s, 2H, ArH), 8.12 (s, 1H, ArH), 7.84 (d, J = 6.8 Hz, 2H, ArH), 7.61 (m, 3H, ArH), 7.25 (m, 2H, ArH), 7.10 (d, J = 8.3 Hz, 1H, ArH), 3.88 (s, 3H, OCH$_3$), 3.82 (s, 3H, OCH$_3$) ppm. ^{13}C NMR (75 MHz, DMSO-d_6): δ 190.00, 149.38, 148.64, 148.45, 143.66, 139.77, 136.58, 131.13, 127.30, 119.42, 118.86, 113.88, 112.59, 110.91, 55.77, 55.75 ppm. HRMS m/z: [M + H]$^+$ calcd for C$_{22}$H$_{18}$N$_2$O$_3$, 359.1390; found, 359.1393.

5-Bromo-3-iodo-1H-pyrrolo[2,3-b]pyridine (15). To a solution of 5-bromo-1H-pyrrolo[2,3-b]pyridine 4 (1.00 g, 5.08 mmol) in acetone (16 mL) was added portionwise N-iodosuccinimide (1.26 g, 5.58 mmol). The reaction mixture was stirred for 2 h at room temperature. The formed precipitate was collected via filtration, yielding the title compound as an off-white solid (1.50 g, 92%). ^{1}H NMR (300 MHz, DMSO-d_6): δ 12.36 (s, 1H, NH), 8.32 (d, J = 2.0 Hz, 1H, HetH), 7.87 (d, J = 1.7 Hz, 1H, HetH), 7.81 (d, J = 2.4 Hz, 1H, HetH) ppm.

5-Bromo-3-iodo-1-tosyl-1H-pyrrolo[2,3-b]pyridine (16). To a solution of 5-bromo-3-iodo-1H-pyrrolo[2,3-b]pyridine 15 (300 mg, 0.929 mmol) in dry THF (10 mL) was added portionwise NaH (41 mg, 1.02 mmol) at 0 °C. After stirring for 20 min at room temperature, tosyl chloride (230 mg, 1.21 mmol) was added, and the reaction was allowed to stir for another 2 h at room temperature. After reaction completion, the reaction was quenched with water and partitioned between water and ethyl acetate. The combined organic phases were dried over MgSO$_4$ and concentrated in vacuo, yielding the title compound as a white solid (420 mg, 95%). ^{1}H NMR (300 MHz, DMSO-d_6): δ 8.51 (d, J = 2.1 Hz, 1H, HetH), 8.22 (s, 1H, HetH), 8.00 (m, 3H, HetH/TsH), 7.43 (d, J = 8.5 Hz, 2H, TsH), 2.34 (s, 3H, CH$_3$) ppm.

5-Bromo-3-phenyl-1-tosyl-1H-pyrrolo[2,3-b]pyridine (17). To a solution of 5-bromo-3-iodo-1-tosyl-1H-pyrrolo[2,3-b]pyridine 16 (200 mg, 0.419 mmol) in a mixture of toluene and ethanol (in a ratio of 3:1) were added phenylboronic acid (51 mg, 0.419 mmol) and a 2 M solution of K$_2$CO$_3$ (420 µL, 0.838 mmol). The reaction was flushed with argon three times, followed by the addition of Pd(PPh$_3$)$_4$ (10 mg, 0.008 mmol). The reaction was stirred at 90 °C for 3 h. After reaction completion, the reaction was filtered through Celite and the filtrate was washed with water and ethyl acetate. The combined organic phases were dried over MgSO$_4$ and evaporated in vacuo. Purification by silica gel flash column chromatography using a mixture of heptane and ethyl acetate (in a ratio of 8:2) as the mobile phase yielded the title compound as a white solid (150 mg, 84%). ^{1}H NMR (300 MHz, DMSO-d_6): δ 8.54 (d, J = 2.1 Hz, 1H, HetH), 8.50 (d, J = 2.1 Hz, 1H, HetH), 8.29 (s, 1H, HetH), 8.04 (d, J = 8.4 Hz, 2H, TsH), 7.79 (d, J = 7.2 Hz, 2H, TsH), 7.45 (m, 5H, PhH), 2.35 (s, 3H, CH$_3$) ppm.

5-(3,4-Dimethoxyphenyl)-3-phenyl-1-tosyl-1H-pyrrolo[2,3- b]pyridine (18). To a solution of 5-bromo-3-phenyl-1-tosyl-1H- pyrrolo[2,3-b]pyridine (150 mg, 0.351 mmol) in a mixture of toluene and ethanol (in a ratio of 3:1) was added 3,4-dimethoxyphenylboronic acid (77 mg, 0.421 mmol) and a 2 M solution of K$_2$CO$_3$ in water (351 µL, 0.702 mmol). The system was flushed with argon and Pd(PPh$_3$)$_4$ (2 mol %) was added. The reaction was stirred for 4 h at 105 °C. Upon reaction completion, the solvents were evaporated in vacuo, and the crude residue was extracted with water and ethyl acetate. Purification by silica gel flash chromatography using a mixture

of heptane and ethyl acetate (in a ratio of 8:2) as the mobile phase yielded the desired compound (100 mg, 59%). ^{1}H NMR (300 MHz, DMSO-d_6): δ 8.71 (d, J = 2.0 Hz, 1H, HetH), 8.37 (d, J = 2.0 Hz, 1H, HetH), 8.23 (s, 1H, HetH), 8.08 (d, J = 8.4 Hz, 2H, ArH), 7.85 (d, J = 7.2 Hz, 2H, ArH), 7.46 (m, 5H, ArH), 7.29 (m, 2H, ArH), 7.06 (d, J = 8.3 Hz, 1H, ArH), 3.84 (s, 3H, OCH$_3$), 3.80 (s, 3H, OCH$_3$), 2.35 (s, 3H, CH$_3$) ppm.

5-(3,4-Dimethoxyphenyl)-3-phenyl-1H-pyrrolo[2,3-b]-pyridine (19). To a solution of 5-(3,4-dimethoxyphenyl)-3-phenyl-1-tosyl-1H-pyrrolo[2,3-b]pyridine 18 (100 mg, 0.309 mmol) in ethanol (5 mL) was added KOH (87 mg, 1.55 mmol). The reaction was allowed to stir for 2 h at 80 °C. After completion, the solvent was evaporated in vacuo and the crude residue was purified by silica gel flash chromatography using a mixture of heptane and ethyl acetate (in a ratio of 7:3) as the mobile phase, affording the title compound (49 mg, 72%). Purity of 97% ^{1}H NMR (300 MHz, DMSO-d_6): δ 11.98 (s, 1H, NH), 8.56 (s, 1H, ArH), 8.39 (s, 1H, ArH), 7.90 (d, J = 2.3 Hz, 1H, ArH), 7.79 (d, J = 7.5 Hz, 2H, ArH), 7.45 (t, J = 7.6 Hz, 2H, ArH), 7.28 (m, 3H, ArH), 7.06 (d, J = 8.3 Hz, 1H, ArH), 3.87 (s, 3H, OCH$_3$), 3.80 (s, 3H, OCH$_3$) ppm. ^{13}C NMR (75 MHz, DMSO-d_6): δ 149.32, 148.56, 148.37, 142.16, 135.18, 132.07, 129.15, 129.06, 126.57, 125.83, 124.63, 119.50, 117.37, 114.73, 112.54, 111.27, 55.84, 55.76 ppm. HRMS m/z: [M + H]$^+$ calcd for C$_{21}$H$_{18}$N$_2$O$_2$, 331.1440; found, 331.1437.

Synthesis of 3-Alkynyl-5-bromo-pyrrolo[2,3-b]pyridines (20a−f). General Procedure. To a degassed solution of 5-bromo-3-iodo-1H-pyrrolo[2,3-b]pyridine 15 (1 equiv) in THF and triethylamine (3 equiv) were added CuI (0.02 equiv) and Pd(PPh$_3$)$_2$Cl$_2$ (0.01 equiv). The resulting mixture was stirred under an inert atmosphere for 10 min at room temperature. A solution of the appropriate alkyne (0.95 equiv) in THF was added to the mixture. The reaction mixture was stirred for an additional 4 h at room temperature. After completion, the reaction was filtered through Celite. The filtrate was extracted with water and ethyl acetate, washed with brine, and dried over MgSO$_4$. The crude residue was purified by silica gel flash column chromatography with an appropriate mobile phase. Compounds 20a−f were made according to this procedure.

5-Bromo-3-(phenylethynyl)-1H-pyrrolo[2,3-b]pyridine (20a). The title compound was synthesized according to the general procedure using 5-bromo-3-iodo-1H-pyrrolo[2,3-b]pyridine 15 (200 mg, 0.619 mmol) and phenylacetylene (60 mg, 0.588 mmol). The crude residue was purified by silica gel flash column chromatography using a mixture of heptane and ethyl acetate (in a ratio of 8:2) as the mobile phase yielding the title compound as a white solid (85 mg, 51%). ^{1}H NMR (300 MHz, DMSO-d_6) 12.40 (br s, 1H, NH), 8.39 (d, J = 2.2 Hz, 1H, HetH), 8.32 (d, J = 2.1 Hz, 1H, HetH), 8.01 (s, 1H, HetH), 7.60 (m, 2H, PhH), 7.42 (m, 3H, PhH) ppm.

5-Bromo-3-(pyridin-3-ylethynyl)-1H-pyrrolo[2,3-b]pyridine (20b). The title compound was synthesized according to the general procedure using 5-bromo-3-iodo-1H-pyrrolo[2,3-b]pyridine 15 (200 mg, 0.619 mmol) and 3-ethynylpyridine (61 mg, 0.588 mmol). The crude residue was purified by silica gel flash column chromatography using a mixture of heptane and ethyl acetate (in a ratio of 7:3) as the mobile phase yielding the title compound as a white solid (140 mg, 75%). ^{1}H NMR (300 MHz, DMSO-d_6) 12.49 (br s, 1H, NH), 8.81 (s, 1H, ArH), 8.56 (d, J = 4.8 Hz, 1H, ArH), 8.40 (s, 2H, ArH), 8.04 (m, 2H, ArH), 7.46 (m, 1H, ArH) ppm.

5-Bromo-3-((3-methoxyphenyl)ethynyl)-1H-pyrrolo[2,3-b]-pyridine (20c). The title compound was synthesized according to the general procedure using 5-bromo-3-iodo-1H-pyrrolo[2,3-b]pyridine 15 (200 mg, 0.619 mmol) and 3-methoxyphenylacetylene (60 mg, 0.588 mmol). The crude residue was purified by silica gel flash column chromatography using a mixture of heptane and ethyl acetate (in a ratio of 7:3) as the mobile phase, yielding the title compound as a white solid (105 mg, 51%). ^{1}H NMR (300 MHz, DMSO-d_6): δ 12.41 (br s, 1H, NH), 8.39 (d, J = 2.2 Hz, 1H, HetH), 8.34 (d, J = 2.1 Hz, 1H, HetH), 8.00 (s, 1H, HetH), 7.33 (t, J = 8.1 Hz, 1H, PhH), 7.16 (m, 2H, PhH), 6.96 (m, 1H, PhH), 3.81 (s, 3H, OCH$_3$) ppm.

5-Bromo-3-(p-tolylethynyl)-1H-pyrrolo[2,3-b]pyridine (20d). The title compound was synthesized according to the general procedure

using 5-bromo-3-iodo-1H-pyrrolo[2,3-b]pyridine 15 (200 mg, 0.619 mmol) and p-tolylacetylene (68 mg, 0.588 mmol). The crude residue was purified by silica gel flash column chromatography using a mixture of heptane and ethyl acetate (in a ratio of 7:3) as the mobile phase, yielding the title compound as a white solid (130 mg, 67%). ^{1}H NMR (300 MHz, DMSO-d_6): δ 12.36 (br s, 1H, NH), 8.38 (d, J = 2.2 Hz, 1H, HetH), 8.30 (d, J = 2.2 Hz, 1H, HetH), 7.98 (s, 1H, HetH), 7.48 (d, J = 8.1 Hz, 2H, PhH), 7.23 (d, J = 7.9 Hz, 2H, PhH), 2.34 (s, 3H, CH$_3$).

5-Bromo-3-((4-fluorophenyl)ethynyl)-1H-pyrrolo[2,3-b]pyridine (20e). The title compound was synthesized according to the general procedure using 5-bromo-3-iodo-1H-pyrrolo[2,3-b]pyridine 15 (200 mg, 0.619 mmol) and 4-fluorophenylacetylene (60 mg, 0.588 mmol). The crude residue was purified by silica gel flash column chromatography using a mixture of heptane and ethyl acetate (in a ratio of 8:2) as the mobile phase yielding the title compound as a white solid (110 mg, 56%). ^{1}H NMR (300 MHz, DMSO-d_6): δ 12.41 (br s, 1H, NH), 8.38 (d, J = 2.1 Hz, 1H, HetH), 8.34 (d, J = 2.1 Hz, 1H, HetH), 8.00 (s, 1H, HetH), 7.66 (dd, J = 8.7, 5.6 Hz, 2H, PhH), 7.27 (t, J = 8.9 Hz, 2H, PhH) ppm.

3-((5-Bromo-1H-pyrrolo[2,3-b]pyridin-3-yl)ethynyl)benzonitrile (20f). The title compound was synthesized according to the general procedure using 5-bromo-3-iodo-1H-pyrrolo[2,3-b]pyridine 15 (200 mg, 0.619 mmol) and 3-cyanophenylacetylene (75 mg, 0.588 mmol). The crude residue was purified by silica gel flash column chromatography using a mixture of heptane and ethyl acetate (in a ratio of 7:3) as the mobile phase, yielding the title compound as a white solid (90 mg, 45%). ^{1}H NMR (300 MHz, DMSO-d_6): δ 8.45 (d, J = 2.2 Hz, 1H, HetH), 8.40 (d, J = 2.1 Hz, 1H, HetH), 8.14 (s, 1H, HetH), 8.05 (s, 1H, PhH), 7.91 (d, J = 8.0 Hz, 1H, PhH), 7.84 (d, J = 7.5 Hz, 1H, PhH), 7.63 (t, J = 7.9 Hz, 1H, PhH) ppm.

Synthesis of 3-Alkynyl-5-(3,4-dimethoxyphenyl)-pyrrolo-[2,3-b]pyridines (21a−f). General Procedure. To a solution of a 5-bromo-3-arylethynyl-1H-pyrrolo[2,3-b]pyridine derivatrive (1 equiv) in dioxane (4 mL) were added 3,4-dimethoxyphenylboronic acid (1.2 equiv) and 1 mL of a K$_2$CO$_3$ (3 equiv) solution. The system was purged three times with argon and heated to 105 °C. After stirring for 10 min, Pd(PPh$_3$)$_4$ (0.1 equiv) was added and the reaction was purged once more with argon. The reaction mixture was stirred at 105 °C for 3 h. After completion, the reaction mixture was cooled to room temperature and filtered through Celite. The filtrate was extracted with water and ethyl acetate. The combined organic layers were washed with brine, dried over MgSO$_4$, and evaporated in vacuo. The crude residue was purified by silica gel flash column chromatography with an appropriate mobile phase. Compounds 21a−f were made according to this procedure.

5-(3,4-Dimethoxyphenyl)-3-(phenylethynyl)-1H-pyrrolo[2,3-b]-pyridine (21a). The title compound was synthesized according to the general procedure using 3-(phenylethynyl)-1H-pyrrolo[2,3-b]pyridine 20a (80 mg, 0.269 mmol). The crude residue was purified by silica gel flash column chromatography using a mixture of DCM and ethyl acetate (in a ratio of 9:1) as the mobile phase yielding the title compound as a brown solid (36 mg, 38%). Purity of 99%. ^{1}H NMR (300 MHz, DMSO-d_6): δ 12.21 (br s, 1H, NH), 8.61 (s, 1H, ArH), 8.25 (s, 1H, ArH), 7.96 (d, J = 2.2 Hz, 1H, ArH), 7.60 (d, J = 6.5 Hz, 1H, ArH), 8.01 (m, 2H, ArH), 7.35 (m, 6H, ArH), 7.06 (d, J = 8.3 Hz, 1H, ArH), 3.88 (s, 3H, OCH$_3$), 3.81 (s, 3H, OCH$_3$) ppm. ^{13}C NMR (75 MHz, DMSO-d_6): δ 149.33, 148.49, 147.24, 143.12, 131.42, 131.27, 131.17, 129.60, 128.80, 128.13, 124.93, 123.48, 120.29, 119.44, 112.48, 111.11, 95.31, 90.75, 83.53, 55.82, 55.73 ppm. HRMS m/z: [M + H]$^+$ calcd for C$_{23}$H$_{18}$N$_2$O$_2$, 355.14409; found, 355.1435.

5-(3,4-Dimethoxyphenyl)-3-(pyridin-3-ylethynyl)-1H-pyrrolo[2,3-b]pyridine (21b). The title compound was synthesized according to the general procedure using 5-bromo-3-(pyridin-3-ylethynyl)-1H-pyrrolo[2,3-b]pyridine 20b (140 mg, 0.470 mmol). The crude residue was purified by silica gel flash column chromatography using a mixture of DCM and ethyl acetate (in a ratio of 9:1) as the mobile phase, yielding the title compound as a white solid (75 mg, 44%). Purity of 98% ^{1}H NMR (300 MHz, DMSO-d_6): δ 12.30 (s, 1H,

NH), 8.81 (s, 1H, ArH) 8.63 (d, J = 2.0 Hz, 1H, ArH), 8.55 (d, J = 4.9 Hz, 1H, ArH), 8.30 (d, J = 1.9 Hz, 1H, ArH), 8.01 (m, 2H, ArH), 7.46 (m, 1H, ArH), 7.31 (m, 2H, ArH), 7.07 (d, J = 8.3 Hz, 1H), 3.89 (s, 3H, OCH$_3$), 3.81 (s, 3H, OCH$_3$) ppm. ^{13}C NMR (75 MHz, DMSO-d_6): δ 151.46, 149.33, 148.52, 148.34, 147.24, 143.24, 138.19, 131.78, 131.33, 129.73, 125.03, 123.68, 120.59, 120.28, 119.46, 112.47, 111.13, 94.77, 87.69, 86.87, 55.83, 55.74 ppm. HRMS m/z: [M + H]$^+$ calcd for C$_{22}$H$_{17}$N$_3$O$_2$, 356.13934; found, 356.1393.

5-(3,4-Dimethoxyphenyl)-3-(3-methoxyphenylethynyl)-1H-pyrrolo[2,3-b]pyridine (21c). The title compound was synthesized according to the general procedure using 3-(3-methoxyphenylethyn-yl)-1H-pyrrolo[2,3-b]pyridine 20c (110 mg, 0.353 mmol). The crude residue was purified by silica gel flash column chromatography using a mixture of DCM and ethyl acetate (in a ratio of 9:1). Further purification by preparative TLC (the mobile phase being a mixture of nitromethane/toluene in a ratio of 6:4) yielded the title compound as a white solid (25 mg, 20%). Purity of 97%. ^{1}H NMR (300 MHz, DMSO-d_6): δ 12.21 (s, 1H, NH), 8.61 (d, J = 1.9 Hz, 1H, ArH), 8.25 (d, J = 1.9 Hz, 1H, ArH), 7.96 (d, J = 2.6 Hz, 1H, ArH), 7.32 (m, 3H, ArH), 7.16 (m, 2H, ArH), 7.07 (d, J = 8.3 Hz, 1H, ArH), 6.96 (m, 1H, ArH), 3.89 (s, 3H, OCH$_3$), 3.81 (s, 3H, OCH$_3$), 3.80 (s, 3H, OCH$_3$) ppm. ^{13}C NMR (75 MHz, DMSO-d_6): δ 159.33, 149.33,

148.50, 147.24, 143.12, 131.41, 131.34, 129.91, 129.60, 124.97,

124.56, 123.61, 120.28, 119.44, 115.95, 114.58, 112.49, 111.12, 95.24, 90.74, 83.43, 55.82, 55.75, 55.34 ppm. HRMS m/z: [M + H]$^+$ calcd for C$_{24}$H$_{20}$N$_2$O$_3$, 385.15465; found, 385.1541.

5-(3,4-Dimethoxyphenyl)-3-(p-tolylethynyl)-1H-pyrrolo[2,3-b]-pyridine (21d). The title compound was synthesized according to the general procedure using 3-(p-tolylethynyl)-1H-pyrrolo[2,3-b]pyridine 20d (110 mg, 0.353 mmol). The crude residue was purified by silica gel flash column chromatography using a mixture of DCM and ethyl acetate (in a ratio of 9:1) as the mobile phase, yielding the title compound as a white solid (25 mg, 20%). Purity of 95%. ^{1}H NMR (300 MHz, DMSO-d_6): δ 12.18 (br s, 1H, NH), 8.60 (d, J = 2.0 Hz, 1H, ArH), 8.22 (d, J = 1.8 Hz, 1H, ArH), 7.93 (d, J = 2.6 Hz, 1H, ArH), 7.49 (d, J = 8.0 Hz, 2H, ArH), 7.27 (m, 4H, ArH), 7.03 (m, 2H, ArH), 3.88 (s, 3H, OCH$_3$), 3.81 (s, 3H, OCH$_3$), 2.34 (s, 3H, CH$_3$). ^{13}C NMR (75 MHz, DMSO-d_6): δ 149.33, 148.48, 147.23, 143.07, 137.78, 131.45, 131.11, 131.04, 129.54, 129.42, 124.91, 120.46, 120.27, 119.43, 112.49, 111.11, 95.49, 90.81, 82.77, 55.83, 55.74, 21.14. HRMS m/z: [M + H]$^+$ calcd for C$_{24}$H$_{20}$N$_2$O$_2$, 369.15974; found, 369.1593.

5-(3,4-Dimethoxyphenyl)-3-(4-fluorophenylethynyl)-1H-pyrrolo-[2,3-b]pyridine (21e). The title compound was synthesized according to the general procedure using 3-(4-fluorophenylethynyl)-1H-pyrrolo-[2,3-b]pyridine 20e (80 mg, 0.269 mmol). The crude residue was purified by silica gel flash column chromatography using a mixture of DCM and ethyl acetate (in a ratio of 9:1), yielding the desired compound as a brown solid (34 mg, 36%). Purity of 98%. ^{1}H NMR (300 MHz, DMSO-d_6): δ 12.21 (br s, 1H, NH), 8.61 (s, 1H, ArH), 8.25 (s, 1H, ArH), 7.95 (d, J = 2.4 Hz, 1H, ArH), 7.65 (m, 2H, ArH), 7.28 (m, 4H, ArH), 7.06 (d, J = 8.5 Hz, 1H, ArH), 3.88 (s, 3H), 3.81 (s, 3H, OCH$_3$) ppm. ^{13}C NMR (150 MHz, DMSO-d_6): δ 161.68 (d, J_{CF} = 247 Hz) 149.27, 148.44, 147.17, 143.07, 133.36 (d, J_{CF} = 8.3 Hz), 131.35, 131.20, 129.54, 124.91, 120.23, 119.90, 119.89, 119.38, 115.95 (d, J_{CF} = 22 Hz), 112.42, 111.05, 95.11, 89.60, 83.20, 55.76, 55.68 ppm. HRMS m/z: [M + H]$^+$ calcd for C$_{23}$H$_{17}$FN$_2$O$_2$, 373.13467; found, 373.1333.

3-((5-(3,4-Dimethoxyphenyl)-1H-pyrrolo[2,3-b]pyridin-3-yl)-ethynyl)benzonitrile (21f). The title compound was synthesized according to the general procedure using 3-(3-cyanophenylethynyl)-1H-pyrrolo[2,3-b]pyridine 20f (100 mg, 0.310 mmol). The crude residue was purified by silica gel flash column chromatography using a mixture of DCM and ethyl acetate (in a ratio of 9:1) as the mobile phase, yielding the title compound as a brown solid (44 mg, 37%). Purity of 98%. ^{1}H NMR (300 MHz, DMSO-d_6): δ 12.31 (br s, 1H, NH), 8.62 (d, J = 2.0 Hz, 1H, ArH), 8.32 (d, J = 1.9 Hz, 1H, ArH), 8.11 (s, 1H, ArH), 8.00 (d, J = 2.5 Hz, 1H, ArH), 7.91 (d, J = 7.9 Hz, 1H, ArH), 7.82 (d, J = 7.9 Hz, 1H, ArH), 7.62 (t, J = 7.9 Hz, 2H,

OCH$_3$), 3.81 (s, 3H, OCH$_3$). ^{13}C NMR (75 MHz, DMSO-d_6): δ 149.33, 148.54, 147.25, 143.28, 135.52, 134.37, 131.91, 131.43, 131.35, 130.10, 129.81, 125.11, 124.93, 120.34, 119.51, 118.33, 112.48, 112.17, 111.17, 94.64, 89.01, 86.05, 55.84, 55.75. HRMS m/z: [M + H]$^+$ calcd for C$_{24}$H$_{17}$N$_3$O$_2$, 380.13934; found, 380.1390.

5-Bromo-1-methyl-1H-pyrrolo[2,3-b]pyridine (22). To a solution of 5-bromo-1H-pyrrolo[2,3-b]pyridine 4 (200 mg, 1.02 mmol) in THF (5 mL) at 0 °C was added 60% NaH on mineral oil (49 mg, 1.22 mmol). The reaction was stirred at 0 °C for 1.5 h. Methyl iodide (70 μL, 1.12 mmol) was added, and the mixture was allowed to warm at ambient temperature and then stirred at room temperature for 3 h. After completion, the mixture was quenched with water and extracted three times with ethyl acetate. The combined organic layers were washed with brine, dried over MgSO$_4$, filtered, and evaporated. The crude residue was purified by silica gel flash column chromatography using a mixture of heptane and ethyl acetate (in a ratio of 8:2) as the mobile phase, yielding the title compound as an oil that subsequently crystallized to an off-white solid (160 mg, 75%). ^{1}H NMR (300 MHz, DMSO-d_6): δ 8.31 (d, J = 2.07 Hz, 1H, HetH), 8.20 (d, J = 2.07 Hz, 1H, HetH), 7.59 (d, J = 3.39 Hz, 1H, HetH), 6.46 (d, J = 3.42 Hz, 1H, HetH), 3.81 (s, 3H, CH$_3$) ppm. HRMS m/z: [M + H]$^+$ calcd for C$_8$H$_7$N$_2$Br, 210.98658; found,

210.9866.

ArH), 7.31 (m, 2H, ArH), 7.07 (d, J = 8.3 Hz, 1H, ArH), 3.89 (s, 3H,

5-Bromo-1-methyl-3-nitro-1*H***-pyrrolo[2,3-***b***]pyridine (23).**
5-Bromo-1*H*-pyrrolo[2,3-*b*]pyridine 22 (130 mg, 0.615 mmol) was added portionwise to a stirring solution of fuming nitric acid (1 mL) at 0 °C over 10 min. The reaction was allowed to stir for 30 min at 0 °C. The mixture was poured out in ice water and the formed precipitate was collected via vacuum filtration. The filter cake was washed generously with water and heptane, yielding the title compound as a pink solid (155 mg, 98%). ^{1}H NMR (300 MHz, DMSO-d_6): δ 8.99 (s, 1H, HetH), 8.61 (s, 1H, HetH), 8.57 (m, 1H, HetH), 3.92 (s, 3H, CH$_3$) ppm.

5-(3,4-Dimethoxyphenyl)-1-methyl-3-nitro-1*H***-pyrrolo[2,3-***b***]pyridine (24).** To a solution of 5-bromo-1-methyl-3-nitro-1*H*- pyrrolo[2,3-*b*]pyridine 23 (100 mg, 0.391 mmol) in dioxane (4 mL) were added 3,4-dimethoxyphenylboronic acid (69 mg, 0.469 mmol) and 1 mL of a K$_2$CO$_3$ solution (161 mg, 1.17 mmol). The system was purged three times with argon and heated to 105 °C. After stirring for 10 min, Pd(PPh$_3$)$_4$ (10 mol %) was added and the reaction was purged once more with argon. The reaction mixture was stirred at 105 °C overnight. After completion, the reaction mixture was cooled to room temperature and filtered through Celite. Extraction was performed with water and ethyl acetate. The combined organic layers were washed with brine, dried over MgSO$_4$, and evaporated. Purification by silica gel flash chromatography using a mixture of DCM and ethyl acetate (in a ratio of 9:1) as the mobile phase yielded the title compound as a yellow solid (90 mg, 83%). ^{1}H NMR (300 MHz, DMSO-d_6): δ 8.96 (s, 1H, HetH), 8.79 (d, J = 2.07 Hz, 1H, HetH), 8.56 (d, J = 2.01 Hz, 1H, HetH), 7.30 (m, 2H, PhH), 7.10 (d, J = 8.22 Hz, 1H, PhH), 3.96 (s, 3H), 3.88 (s, 3H, OCH$_3$), 3.82 (s, 3H) ppm.

N-(5-(3,4-Dimethoxyphenyl)-1-methyl-1*H***-pyrrolo[2,3-***b***]-pyridin-3-yl)nicotinamide (26).** The title compound was synthe- sized according to the general procedure described for the synthesis of compounds 8a−h, starting from 5-(3,4-dimethoxyphenyl)-1-methyl-3-nitro-1*H*-pyrrolo[2,3-*b*]pyridine 24 (90 mg, 0.287 mmol). Purifica- tion by silica gel flash column chromatography using a mixture of DCM and methanol (in a ratio gradually ranging from 98:2 to 95:5) yielded the title compound as a red solid (22 mg, 20%). Purity of 98%. ^{1}H NMR (300 MHz, DMSO-d_6): δ 10.60 (br s, 1H, NH), 9.19 (br s, 1H, NH), 8.77 (d, J = 2.6 Hz, 1H, ArH), 8.60 (s, 2H, ArH), 8.36 (d, J = 8.0 Hz, 1H, ArH), 8.07 (s, 1H, ArH), 7.59 (m, 1H, ArH), 7.26 (m, 2H, ArH), 7.08 (d, J = 8.3 Hz, 1H, ArH), 3.87 (s, 6H, OCH$_3$/CH$_3$), 3.80 (s, 3H, OCH$_3$/CH$_3$). ^{13}C NMR (75 MHz, DMSO-d_6): δ 163.33, 152.03, 149.33, 148.87, 148.39, 144.19, 142.14, 135.65, 131.81, 130.43, 127.77, 125.22, 123.63, 121.31, 119.21, 113.40, 113.14, 112.54, 110.93, 55.83, 55.75, 30.91 ppm. HRMS m/z: [M + H]$^+$ calcd for C$_{22}$H$_{20}$N$_4$O$_3$, 389.16080; found, 389.1604.

2-Chloro-5-(3,4-dimethoxyphenyl)nicotinonitrile (28). To a solution of 3,4-dimethoxyphenylboronic acid (460 mg, 2.53 mmol) and 5-bromo-2-chloronicotinonitrile 27 (500 mg, 2.3 mmol) in isopropanol (12 mL) was added a solution of K_2CO_3 (953 mg, 6.9 mmol) in water (4 mL). The reaction mixture was flushed three times with argon and heated to 90 °C. Then, Pd(PPh$_3$)$_4$ (10 mol %) was added and the system was flushed once more with argon. After stirring at 90 °C for 2.5 h, the reaction was concentrated under reduced pressure. The crude residue was partitioned between ethyl acetate and water and extracted three times. The combined organic phases were washed with brine and dried over MgSO$_4$. The solvent was removed under reduced pressure and the crude residue was purified by silica gel flash column chromatography using a mixture of heptane and ethylacetate (in a ratio of 7:3) as the mobile phase. This was followed by a second purification by silica gel flash column chromatography using a mixture of DCM, heptane, and ethylacetate (in a ratio of 70:25:5) as the mobile phase, yielding the title compound as a white solid (320 mg, 50%). ^{1}H NMR (300 MHz, DMSO-d_6): δ 9.06 (d, J = 2.5 Hz, 1H, HetH), 8.85 (d, J = 2.5 Hz, 1H, HetH), 7.41 (m, 2H, PhH), 7.10 (m, 1H, PhH), 3.87 (s, 3H, OCH$_3$), 3.82 (s, 3H, OCH$_3$).

5-(3,4-Dimethoxyphenyl)-1H-pyrazolo[3,4-b]pyridin-3-amine (29). To a solution of 2-chloro-5-(3,4-dimethoxyphenyl)-nicotinonitrile 28 (100 mg, 0.364 mmol) in pyridine (3 mL) was added a hydrazine monohydrate solution (65% in water, 103 μL, 0.728 mmol). The reaction was refluxed overnight, and after completion, the solvent was evaporated. The crude residue was purified by silica gel flash column chromatography using a mixture of DCM and methanol (in a ratio of 95:5), yielding the title compound as a yellow solid (90 mg, 91%). ^{1}H NMR (300 MHz, DMSO-d_6): δ 11.97 (br s, 1H, NH), 8.66 (d, J = 2.1 Hz, 1H, HetH), 8.36 (d, J = 2.0 Hz, 1H, HetH), 7.21 (m, 2H, PhH), 7.07 (d, J = 8.4 Hz, 1H, PhH), 3.86 (s, 3H, OCH$_3$), 3.80 (s, 3H, OCH$_3$).

N-(5-(3,4-Dimethoxyphenyl)-1H-pyrazolo[3,4-b]pyridin-3-yl)nicotinamide (30). To a solution of 5-(3,4-dimethoxyphenyl)-1H-pyrazolo[3,4-b]pyridin-3-amine 29 (90 mg, 0.332 mmol) in pyridine (3 mL) at 0 °C was added nicotinoyl chloride hydrochloride (71 mg, 0.400 mmol). The reaction was stirred at 0 °C for 1 h and then stirred at room temperature overnight. After reaction completion, water was added and the mixture was extracted three times with ethyl acetate. The combined organic phases were washed with brine, dried over MgSO$_4$, and evaporated to dryness. The crude residue was purified by silica gel flash chromatography using a mixture of DCM and methanol (in a ratio gradually ranging from 98:2 to 96:4), yielding the title compound as a beige solid (76 mg, 61%). Purity of 99%. ^{1}H NMR (300 MHz, DMSO-d_6): δ 13.47 (s, 1H), 11.33 (s, 1H), 9.24 (s, 1H), 8.85 (d, J = 2.1 Hz, 1H), 8.79 (d, J = 3.4 Hz, 1H), 8.50 (d, J = 2.0 Hz, 1H), 8.42 (d, J = 8.1 Hz, 1H), 7.59 (dd, J = 7.7, 4.8 Hz, 1H), 7.28 (s, 1H), 7.23 (d, J = 8.4 Hz, 1H), 7.07 (d, J = 8.4 Hz, 1H), 3.86 (s, 3H), 3.80 (s, 3H). ^{13}C NMR (75 MHz, DMSO-d_6): δ 164.30, 152.57, 151.36, 149.35, 149.22, 148.89, 148.67, 139.54, 135.92, 130.86, 129.45, 129.25, 129.13, 123.66, 119.50, 112.54, 111.08, 108.70, 55.84, 55.74. HRMS m/z: [M + H]$^+$ calcd for C$_{20}$H$_{17}$N$_5$O$_3$, 376.14040; found, 376.1400.

2-Amino-3,5-dibromopyrazine (32). To a solution of amino-pyrazine 31 (1 g, 10.52 mmol) in DMSO (10 mL) was added N-bromosuccinimide (3.94 g, 22.08 mmol) portionwise over 45 min. The resulting mixture was stirred for 3 h at room temperature. The reaction was poured in ice water and extracted five times with ethyl acetate. The combined organic phases were washed with brine, dried over MgSO$_4$, and evaporated to dryness. The crude residue was purified by silica gel flash column chromatography using a mixture of heptane and ethyl acetate (in a ratio of 7:3) as the mobile phase, yielding the desired compound as a fluffy white solid (1.94 g, 73%). ^{1}H NMR (300 MHz, DMSO-d_6): δ 8.13 (s, 1H, ArH), 6.99 (br s, 2H, NH$_2$) ppm. HRMS m/z: [M + H]$^+$ calcd for C$_4$H$_3$N$_3$Br$_2$, 251.87675; found, 251.8765.

5-Bromo-3-((trimethylsilyl)ethynyl)pyrazin-2-amine (33). To a solution of 2-amino-3,5-dibromopyrazine 32 (1 g, 3.95 mmol) in degassed THF (15 mL) was added copper iodide (7.53 mg, 0.040 mmol), Pd(PPh$_3$)$_2$Cl$_2$ (45 mg, 0.040 mmol), and triethylamine (1.65

mL, 11.86 mmol). The system was flushed with nitrogen, and trimethylsilylacetylene (534 μL, 1.91 mmol) was added dropwise over 5 min. The reaction was stirred overnight at room temperature. After reaction completion, the solvent was evaporated and water was added. The resulting suspension was extracted three times with ethyl acetate. The combined organic phases were washed with water and brine, dried over MgSO$_4$, and evaporated to dryness. The crude residue was purified by silica gel flash column chromatography using a mixture of heptane and ethylacetate (in a ratio of 80:20) as the mobile phase, yielding the title compound as a bright yellow solid (769 mg, 72%). ^{1}H NMR (300 MHz, DMSO-d_6): δ 8.12 (s, 1H, ArH), 6.82 (s, 2H, NH$_2$), 0.27 (s, 9H, Si(CH$_3$)$_3$) ppm.

2-Bromo-5H-pyrrolo[2,3-b]pyrazine (34). To a solution of 5-bromo-3-((trimethylsilyl)ethynyl)pyridin-2-amine 33 (1 g, 3.7 mmol) in dry NMP (10 mL) was added portionwise KOtBu (498 mg, 4.44 mmol). The reaction mixture was flushed with nitrogen and stirred for 3 h at 80 °C. After reaction completion, the mixture was extracted three times with water and ethyl acetate. The combined organic layers were washed twice with water and once with brine, dried over MgSO$_4$, and evaporated in vacuo. The crude residue was then purified by silica gel flash column chromatography using a mixture of heptane/ethyl acetate (in a ratio of 7:3) as the mobile phase, yielding the title compound as a yellow solid (502 mg, 69%). ^{1}H NMR (300 MHz, DMSO-d_6): δ 12.42 (br s, 1H, NH), 8.35 (s, 1H, ArH), 7.97 (d, J = 3.48 Hz, 1H, ArH), 6.63 (d, J = 3.48 Hz, 1H, ArH) ppm.

5-Bromo-3-iodo-1H-pyrrolo[2,3-b]pyrazine (35). To a solution of 5-bromo-1H-pyrrolo[2,3-b]pyrazine 34 (500 mg, 2.52 mmol) in a minimal volume of acetone was added portionwise N-iodosuccinimide (625 g, 2.78 mmol). The reaction mixture was stirred for 2 h at room temperature. The formed precipitate was collected via filtration, yielding the title product as an off-white solid (408 mg, 50%).. ^{1}H NMR (300 MHz, DMSO-d_6): δ 12.82 (br s, 1H, NH), 8.40 (d, J = 1.77 Hz, 1H, ArH), 8.19 (s, 1H, ArH) ppm.

2-Bromo-7-(pyridin-3-ylethynyl)-5H-pyrrolo[2,3-b]pyrazine (36). To a solution of 5-bromo-3-iodo-1H-pyrrolo[2,3-b]pyrazine 35 (200 mg, 0.617 mmol) in THF (10 mL) were added triethylamine (238 μL, 1.85 mmol), Pd(PPh$_3$)$_2$Cl$_2$ (4.33 mg, 1 mol %), and CuI (2.35 mg, 2 mol %). The resulting mixture was stirred under inert atmosphere for 10 min at room temperature. Then, a solution of 3-ethynylpyridine (61 mg, 0.586 mmol) in THF (1 mL) was added to the reaction mixture. The reaction was stirred for 4 h at room temperature. After completion, the reaction was filtered through Celite, extracted with water and ethyl acetate, washed with brine, dried over MgSO$_4$, and evaporated in vacuo. The crude residue was purified by silica gel flash column chromatography using a mixture of heptane and ethyl acetate (in a ratio of 6:4) as the mobile phase, yielding the title compound as a white solid (130 mg, 71%). ^{1}H NMR (300 MHz, DMSO-d_6): δ 12.94 (br s, 1H, NH), 8.76 (s, 1H), 8.59 (d, J = 3.2 Hz, 1H, ArH), 8.51 (s, 1H, ArH), 8.45 (s, 1H, ArH), 7.99 (dt, J = 7.9, 1.8 Hz, 1H, ArH), 7.47 (dd, J = 7.8, 4.8 Hz, 1H, ArH). HRMS m/z: [M + H]$^+$ calcd for C$_{13}$H$_7$N$_4$Br, 298.99273; found, 298.9930.

2-(3,4-Dimethoxyphenyl)-7-(pyridin-3-ylethynyl)-5H-pyrrolo[2,3-b]pyrazine (37). To a solution of 2-bromo-7-(pyridin-3-ylethynyl)-5H-pyrrolo[2,3-b]pyrazine 36 (110 mg, 0.368 mmol) in dioxane (4 mL) was added 3,4-dimethoxyphenylboronic acid (80 mg, 0.441 mmol) and 1 mL of a K$_2$CO$_3$ solution (152 mg, 1.1 mmol). The system was purged three times with argon and heated to 105 °C. After stirring for 10 min, Pd(PPh$_3$)$_4$ (10 mol %) was added and the reaction was purged once more with argon. The reaction mixture was stirred at 105 °C for 3 h. After completion, the reaction mixture was cooled to room temperature and filtered through Celite. The filtrate was extracted with water and ethyl acetate. The combined organic layers were washed with brine, dried over MgSO$_4$, and evaporated in vacuo. Purification by silica gel flash column chromatography using a mixture of DCM and ethylcetate (in a ratio of 1:1) as the mobile phase yielded the title compound as a white solid (37 mg, 28%). Purity of 98%. ^{1}H NMR (300 MHz, DMSO-d_6): δ 12.63 (br s, 1H, NH), 8.96 (s, 1H, ArH), 8.78 (s, 1H, ArH), 8.58 (d, J = 3.3 Hz, 1H, ArH), 8.35 (s, 1H, ArH), 8.00 (d, J = 7.8 Hz, 1H, ArH), 7.76 (m, 2H, ArH), 7.48 (m, 1H, ArH), 7.11 (d, J = 9.0 Hz, 1H, ArH), 3.90 (s, 3H,

OCH$_3$), 3.83 (s, 3H, OCH$_3$) ppm. ^{13}C NMR (75 MHz, DMSO-d_6): δ 151.44, 149.97, 149.32, 148.57, 146.70, 139.95, 138.27, 137.69, 136.06, 135.59, 130.21, 123.77, 120.46, 119.60, 112.33, 110.46, 95.69, 88.10, 85.92, 55.88, 55.81 ppm. HRMS m/z: [M + H]$^+$ calcd for C$_{21}$H$_{16}$N$_4$O$_2$, 357.13459; found, 357.1346.

Binding-Displacement Assay for NAK Family Selectivity. Inhibitor binding to NAK family kinase domain proteins was determined using a binding-displacement assay which tests the ability of the inhibitors to displace a fluorescent tracer compound from the ATP binding site of the kinase domain. Inhibitors were dissolved in DMSO and dispensed as 16-point, 2× serial dilutions in duplicate into black multiwell plates (Greiner) using an Echo dispenser (Labcyte Inc). Each well contained 1 nM biotinylated AAK1, BMP2K, GAK or STK16 kinase domain protein ligated to streptavidin-Tb-cryptate (Cisbio), either 12.5 nM (for AAK1 or BMP2K) or 25 nM (for GAK or STK16) Kinase Tracer 236 (Thermo Fisher Scientific), 10 mM 4-(2-hydroxyethyl)-1-piperazineethanesulfonic acid (HEPES) pH 7.5, 150 mM NaCl, 2 mM dithiothreitol, 0.01% bovine serum albumin, 0.01% Tween-20. Final assay volume for each data point was 5 μL, and final DMSO concentration was 1%. The plate was incubated at room temperature for 1.5 h and then read using a TR-FRET protocol on a PheraStarFS plate reader (BMG Labtech). The data were normalized to 0 and 100% inhibition control values and fitted to a four parameter dose−response binding curve in GraphPad Software. For the purpose of estimating the selectivity between each kinase domain, the determined IC$_{50}$ values were converted to K_i values using the Cheng−Prusoff equation and the concentration and K_D values for the tracer (previously determined).

AAK1 Expression, Purification, and Crystallization. AAK1 (UniProtKB: Q2M2I8) residues T27-A365 were cloned, expressed, and purified as described,[37] except that the protein was expressed in a cell line together with lambda phosphatase to produce the unphosphorylated protein. The purified protein was concentrated to 12 mg/mL, and compound 1 dissolved in 100% DMSO was added to a final concentration of 1.5 mM (3% final DMSO concentration). The protein−ligand solution was incubated on ice for 30 min, then centrifuged at 14 000 rpm for 10 min, 4 °C, immediately prior to setting up sitting-drop vapour diffusion crystallization plates. The best-diffracting crystals of the AAK1−compound 1 complex were obtained using a reservoir solution containing 26% PEG 3350, 0.1 M bis−Tris pH 5.5 by spiking drops with 20 nL of seed-stock solution immediately prior to incubation at 18 °C. Seed stock was prepared from poorly formed crystals of AAK1-compound 1 grown during previous rounds of crystal optimization, which were diluted in 50−100 μL reservoir solution and vortexed for 2 min in an Eppendorf containing a seed bead. A 1:1 dilution series of seeds was prepared in order to find the optimal seed concentration. Prior to mounting, crystals were cryo-protected in situ by addition of reservoir solution containing an additional 25% ethylene glycol. Crystals were then flash-frozen in liquid nitrogen.

Data Collection, Structure Solution, and Refinement. Data were collected at Diamond beamline I02 using monochromatic radiation at wavelength 0.9795 Å. Diffraction data were processed using XDS[45] as part of the xia2 pipeline[46] and scaled using AIMLESS,[47] and molecular replacement was carried out in Phaser[48] with PDB ID 4WSQ as a search model. Data processing and refinement statistics are given in Table S1 from the Supporting Information. REFMAC5,[49] PHENIX,[50] and Coot[51] were used for model building and refinement. Coordinates were submitted to the PDB under accession code 5L4Q.

Virus Construct. DENV2 (New Guinea C strain)[52,53] *Renilla* reporter plasmid used for in vitro assays was a gift from Pei-Yong Shi (The University of Texas Medical Branch). DENV 16681 plasmid (pD2IC-30P-NBX) used for ex vivo experiments was a gift from Claire Huang (CDC).[54]

Cells. Huh7 (Apath LLC) cells were grown in Dulbecco's modified Eagle medium (Mediatech) supplemented with 10% fetal bovine serum (FBS; Omega Scientific), nonessential amino acids, 1% L-glutamine, and 1% penicillin−streptomycin (Thermo Fisher Scientific) and maintained in a humidified incubator with 5% CO$_2$ at 37

°C. MDDCs were prepared as described with slight modifications.[55] Buffy coats were obtained from the Stanford Blood Center. CD14+ cells were purified by EasySep Human Monocyte Enrichment Kit without CD16 Depletion (Stemcell Technologies). Cells were seeded in 6-well plates (2 × 10^6 cells per well), stimulated with 500 U/mL granulocyte-macrophage colony-stimulating and 1000 U/mL inter-leukin-4 (PeproTech), and incubated at 37 °C for 6 days prior to DENV infection [multiplicity of infection (MOI) 1].

Virus Production. DENV2 RNA was transcribed in vitro using mMESSAGE/mMACHINE (Ambion) kits. DENV was produced by electroporating RNA into BHK-21 cells, harvesting supernatants on day 10 and titering via standard plaque assays on BHK-21 cells. In parallel, on day 2 post-electroporation, a DENV-containing super-natant was used to inoculate C6/36 cells to amplify the virus. EBOV (Kikwit isolate) was grown in Vero E6 cells, and supernatants were collected and clarified and stored at −80 °C until further use. Virus titers were determined via standard plaque assay on Vero E6 cells.

Infection Assays. Huh7 cells were infected with DENV in replicates ($n = 5$) at a MOI of 0.05. Overall infection was measured at 48 h using a *Renilla* luciferase substrate. MDDCs were infected with DENV2 (16881) at an MOI of 1. Standard plaque assays were conducted following a 72 h incubation. Huh7 cells were infected with EBOV at an MOI of 1 or 0.1 under biosafety level 4 conditions. Forty-eight hours after infection, supernatants were collected and stored at −80 °C until further use. Cells were formalin-fixed for 24 h prior to removal from biosafety level 4. Infected cells were detected using an EBOV glycoprotein-specific monoclonal antibody (KZ52) and quantitated by automated fluorescence microscopy using an Operetta High Content Imaging System and the Harmony software package (PerkinElmer). For select experiments, supernatants were assayed by standard plaque assay, as described previously. Briefly, supernatants were thawed, serially diluted in growth media, added to VeroE6 cells, and incubated for 1 h at 37 °C in a humidified 5% CO$_2$ incubator, prior to being overlaid with agarose. Infected cells were incubated for 7 days and then stained with neutral red vital dye (Gibco). Plaques were counted, and titers were calculated.

Viability Assays. Viability was assessed using alamarBlue reagent (Invitrogen) or CellTiter-Glo reagent (Promega) assay according to manufacturer's protocol. Fluorescence was detected at 560 nm on an InfiniteM1000 plate reader and luminescence on an InfiniteM1000 plate reader (Tecan) or a SpectraMax 340PC.

Effect of Compounds 1, 8g, and 21b on AP-2 Phosphorylation. Huh7 cells were kept in serum-free medium for 1 h and then treated with the compounds or DMSO in complete medium for 4 h at 37 °C. To allow capturing of phosphorylated AP2M1, 100 nM of the PP2A inhibitor calyculin A (Cell Signalling) was added 30 min prior to lysis in M-PER lysis buffer (Thermo Fisher Scientific) with 1× Halt Protease & phosphatase inhibitor cocktail (Thermo Fisher Scientific). Samples were then subjected to sodium dodecyl sulfate-polyacryla-mide gel electrophoresis and blotting with antibodies targeting phospho-AP2M1 (Cell Signaling), total AP2M1 (Santa Cruz Biotechnology), and actin (Sigma-Aldrich). Band intensity was measured with NIH ImageJ.

AAK1 LanthaScreen Eu binding Assay. The compounds were subjected to a LanthaScreen binding assay in which 10 titrations of dissolved test compound in DMSO are transferred to a 384-well plate. Sequential addition of the kinase buffer (50 mM HEPES pH 7.5, 0.01% BRIJ-35, 10 mM MgCl and 1 mM EGTA), the 2× kinase antibody (Eu Anti GST) mixture, and the 4× Tracer 222 solution was performed. After shaking for 30 s and a 1 h incubation period at room temperature, the plate was read on a fluorescence plate reader. When the bound tracer in the active site was displaced by the test compound, fluorescence was not observed. The collected data were then compared to a 0% displacement control with pure DMSO and a 100% displacement control with sunitinib, a known inhibitor of AAK1, and plotted against the logarithmic concentration parameter. The IC$_{50}$ was subsequently extracted.

AAK1 K_D Assay. K_D values for AAK1 were determined as previously described.[38] Briefly, the DNA-tagged AAK1, an immobilized ligand on streptavidin-coated magnetic beads, and the test

compound were combined. When binding occurred between AAK1 and a test compound, no binding can occur between AAK1 and the immobilized ligand. Upon washing, the compound-bound, DNA-tagged AAK1 was washed away. The beads carrying the ligands were then resuspended in elution buffer and the remaining kinase concentration was measured by qPCR on the eluate. K_D values were determined using dose−response curves.

Kinase Selectivity Assay. Compound 21b was screened against a diverse panel of 468 kinases (DiscoverX, KINOMEscan) using an in vitro ATP-site competition binding assay at a concentration of 10 μM. The results are reported as the percentage of kinase/phage remaining bound to the ligands/beads, relative to a control. High affinity compounds have % of control values close to zero, while weaker binders have higher % control values.

Statistical Analysis. All data were analyzed with GraphPad Prism software. Fifty percent effective concentration (EC_{50}, EC_{90} and CC_{50}) values were measured by fitting data to a three-parameter logistic curve. P values were calculated by two-way ANOVA with Bonferroni's multiple comparisons tests or by 2-tailed unpaired t-test.

Molecular Modeling. Docking was initiated from the AAK1 PDB structure 5L4Q, from which first all ligands and water molecules were removed. The remaining structure was prepared by AutodockTools[56] as a receptor: polar hydrogens were added, Gasteiger charges were defined, the AD4 atom type was assigned, and finally everything was saved in a pdbqt file. The original inhibitor lkb (identical to compound 1) from the PDB file 5L4Q was extracted, processed by AutodockTools, and saved in the pdbqt format. Compounds 8g and 21b were drawn in ChemDraw and a 3D structure was generated by Chem3D.[57] The amide conformation in compound 8g was initially chosen having an anti-orientation. Autodocktools was used again to prepare the corresponding pdbqt files. Autodock Vina was used for the docking experiments.[41] A cubic box was defined 60 × 60 × 60 units (0.375 Å/unit) and the box was centred at the ALA72:CB atom in the first kinase domain (chain A). The docking process used variable dihedral angles in the ligand while the receptor was defined as rigid. Amide bonds in the ligands were not allowed to rotate.

A control docking was executed using the original inhibitor lkb present in the 5L4Q PDB file. Vina reproduced the original X-ray position very well. For the three docked systems with the best Vina docking score, a MD simulation using the Amber 18 software was performed.[42] Enzyme parameters and charges were taken from the default amber ff14sb force field. Parameters and atomic charges were calculated by antechamber (gaff2). The barrier of the dihedral torsion parameters for the amide bond was increased from 2.6 (from antechamber) to 10.0 (in line with a peptide bond amide in the standard amber force field).

Three molecular systems (AAK1/compound 1, AAK1/compound 8g, and AAK1/compound 21b) were solvated with TIP3P and neutralized in charge. Standard NPT simulations of 40 ns were started (300 K, periodic conditions with PME, cutoff 10.0 Å, shake for H bonds constraints, 2 fs time step).

ASSOCIATED CONTENT

* Supporting Information

The Supporting Information is available free of charge on the ACS Publications website at DOI: 10.1021/acs.jmedchem.9b00136.

Copies of ^{1}H and ^{13}C NMR spectra of intermediates and final compounds; details of the kinase selectivity profiling of compound 21b; and data collection and refinement statistics for cocrystallography of compound 1 with AAK1 (PDF)

Molecular formula strings (CSV)

Accession Codes

AUTHOR INFORMATION

Corresponding Authors
*E-mail: seinav@stanford.edu. Phone: 650 723 8656 (S.E.).
*E-mail: steven.dejonghe@kuleuven.be. Phone: +32 16 32 26 62 (S.D.J.).

ORCID
Mathy Froeyen: 0000-0002-8675-6540
Stefan Knapp: 0000-0001-5995-6494
Piet Herdewijn: 0000-0003-3589-8503
Shirit Einav: 0000-0001-6441-4171
Steven De Jonghe: 0000-0002-3872-6558

Author Contributions
S.V. and S-Y.P. contributed equally to this work. S.E. and S.D.J. also contributed equally to this work.

Notes
The authors declare no competing financial interest.
Authors will release the atomic coordinates and experimental data upon article publication.

The coordinates have been deposited in the PDB with accession code 5L4Q.

ABBREVIATIONS

AAK1, adaptor-associated kinase 1; AP, adaptor protein; BOP, (benzotriazol-1-yloxy)tris(dimethylamino)phosphonium hexafluorophosphate; CC_{50}, half-maximal cytotoxic concentration; CCV, clathrin-coated vesicle; DENV, Dengue virus; EBOV, Ebola virus; EC_{50}, half-maximal effective concentration; EC_{90}, 90% effective concentration; EGFR, epidermal growth factor receptor; GAK, cyclin G-associated kinase; HCV, hepatitis C virus; K_D, dissociation constant; MM/GBSA, molecular mechanics with a generalized Born surface area continuum solvation model; MM/PBSA, molecular mechanics energies combined with the Poisson–Boltzmann surface area continuum solvation model; NAK, numb-associated kinase; PDB, protein data bank; rmsd, root mean square deviation; TGN, *trans*-Golgi network; WHO, World Health Organization

REFERENCES

(1) Murray, N. A. E.; Quam, M. B.; Wilder-Smith, A. Epidemiology of Dengue: Past, Present and Future Prospects. *Clin. Epidemiol.* 2013, *5*, 299–309.

(2) WHO. Epidemiology. http://www.who.int/denguecontrol/epidemiology/en/ (accessed Nov 15, 2018).

(3) *Weekly Epidemiological Record*; World Health Organization, 2016; Vol. *91* (30), pp 349−364.

(4) Sanyal, S.; Sinha, S.; Halder, K. K. Pathogenesis of Dengue Haemorrhagic Fever. *J. Indian Med. Assoc.* 2013, *89*, 152−153.

(5) WHO. Ebola virus disease http://www.who.int/news-room/fact-sheets/detail/ebola-virus-disease (accessed Aug 7, 2018).

(6) Behnam, M. A. M.; Nitsche, C.; Boldescu, V.; Klein, C. D. The Medicinal Chemistry of Dengue Virus. *J. Med. Chem.* 2016, *59*, 5622−5649.

(7) Bekerman, E.; Neveu, G.; Shulla, A.; Brannan, J.; Pu, S.-Y.; Wang, S.; Xiao, F.; Barouch-Bentov, R.; Bakken, R. R.; Mateo, R.; Govero, J.; Nagamine, C. M.; Diamond, M. S.; De Jonghe, S.; Herdewijn, P.; Dye, J. M.; Randall, G.; Einav, S. Anticancer Kinase Inhibitors Impair Intracellular Viral Trafficking and Exert Broad-Spectrum Antiviral Effects. *J. Clin. Invest.* 2017, *127*, 1338−1352.

(8) Bekerman, E.; Einav, S. Combating Emerging Viral Threats. *Science* 2015, *348*, 282−283.

(9) Grove, J.; Marsh, M. The Cell Biology of Receptor-Mediated Virus Entry. *J. Cell Biol.* 2011, *195*, 1071−1082.

(10) Neveu, G.; Ziv-Av, A.; Barouch-Bentov, R.; Berkerman, E.; Mulholland, J.; Einav, S. AP-2-Associated Protein Kinase 1 and Cyclin G-Associated Kinase Regulate Hepatitis C Virus Entry and Are Potential Drug Targets. *J. Virol.* 2015, *89*, 4387−4404.

(11) Neveu, G.; Barouch-Bentov, R.; Ziv-Av, A.; Gerber, D.; Jacob, Y.; Einav, S. Identification and Targeting of an Interaction between a Tyrosine Motif within Hepatitis C Virus Core Protein and AP2M1 Essential for Viral Assembly. *PLoS Pathog.* 2012, *8*, No. e1002845.

(12) Xiao, F.; Wang, S.; Barouch-Bentov, R.; Neveu, G.; Pu, S.; Beer, M.; Schor, S.; Kumar, S.; Nicolaescu, V.; Lindenbach, B. D.; Randall, G.; Einav, S. Interactions between the Hepatitis C Virus Nonstructural 2 Protein and Host Adaptor Proteins 1 and 4 Orchestrate Virus Release. *mBio* 2018, *9*, 1−21.

(13) Pu, S.-Y.; Xiao, F.; Schor, S.; Bekerman, E.; Zanini, F.; Barouch-Bentov, R.; Nagamine, C. M.; Einav, S. Feasibility and Biological Rationale of Repurposing Sunitinib and Erlotinib for Dengue Treatment. *Antiviral Res.* 2018, *155*, 67−75.

(14) Kostich, W.; Hamman, B. D.; Li, Y.-W.; Naidu, S.; Dandapani, K.; Feng, J.; Easton, A.; Bourin, C.; Baker, K.; Allen, J.; Savelieva, K.; Louis, J. V.; Dokania, M.; Elavazhagan, S.; Vattikundala, P.; Sharma, V.; Das, M. L.; Shankar, G.; Kumar, A.; Holenarsipur, V. K.; Gulianello, M.; Molski, T.; Brown, J. M.; Lewis, M.; Huang, Y.; Lu, Y.; Pieschl, R.; OMalley, K.; Lippy, J.; Nouraldeen, A.; Lanthorn, T. H.; Ye, G.; Wilson, A.; Balakrishnan, A.; Denton, R.; Grace, J. E.; Lentz, K. A.; Santone, K. S.; Bi, Y.; Main, A.; Swaffield, J.; Carson, K.; Mandlekar, S.; Vikramadithyan, R. K.; Nara, S. J.; Dzierba, C.; Bronson, J.; Macor, J. E.; Zaczek, R.; Westphal, R.; Kiss, L.; Bristow, L.; Conway, C. M.; Zambrowicz, B.; Albright, C. F. Inhibition of AAK1 Kinase as a Novel Therapeutic Approach to Treat Neuropathic Pain. *J. Pharmacol. Exp. Ther.* 2016, *358*, 371−386.

(15) Bronson, J.; Chen, L.; Ditta, J.; Dzierba, C. D.; Jalagam, P. R.; Luo, G.; Macor, J.; Maishal, T. K.; Nara, S. J.; Rajamani, R.; Sistla, R. K.; Thangavel, S. Biaryl Kinase Inhibitors. WO 2017/059085, 2017.

(16) Kuai, L.; Ong, S.-E.; Madison, J. M.; Wang, X.; Duvall, J. R.; Lewis, T. A.; Luce, C. J.; Conner, S. D.; Pearlman, D. A.; Wood, J. L.; Schreiber, S. L.; Carr, S. A.; Scolnick, E. M.; Haggarty, S. J. AAK1 Identified as an Inhibitor of Neuregulin-1/ErbB4-Dependent Neurotrophic Factor Signaling Using Integrative Chemical Genomics and Proteomics. *Chem. Biol.* 2011, *18*, 891−906.

(17) Bamborough, P.; Drewry, D.; Harper, G.; Smith, G. K.; Schneider, K. Assessment of Chemical Coverage of Kinome Space and Its Implications for Kinase Drug Discovery. *J. Med. Chem.* 2008, *51*, 7898−7914.

(18) Barl, N. M.; Sansiaume-Dagousset, E.; Karaghiosoff, K.; Knochel, P. Full Functionalization of the 7-Azaindole Scaffold by Selective Metalation and Sulfoxide/Magnesium Exchange. *Angew. Chem., Int. Ed.* 2013, *52*, 10093−10096.

(19) Brumsted, C. J.; Moorlag, H.; Radinov, R. N.; Ren, Y.; Waldmeier, P. Method for Preparation of N-{3-[5-(4-Chlorophenyl)-1H-Pyrrolo[2,3-b]Pyridine-3-Carbonyl]-2,4-Difluorophenyl} Propane-1-Sulfonamide. WO 2012/010538 A2, 2012.

(20) Han, C.; Green, K.; Pfeifer, E.; Gosselin, F. Highly Regioselective and Practical Synthesis of 5-Bromo-4-Chloro-3-Nitro-7-Azaindole. *Org. Process Res. Dev.* 2017, *21*, 664−668.

(21) Stokes, S.; Graham, C. J.; Ray, S. C.; Stefaniak, E. J. 1H-Pyrrolo[2,3-b]Pyridine Derivatives and Their Use as Kinase Inhibitors. WO 2013/114113 A1, 2013.

(22) Gao, L.-J.; Kovackova, S.; Sala, M.; Ramadori, A. T.; De Jonghe, S.; Herdewijn, P. Discovery of Dual Death-Associated Protein Related Apoptosis Inducing Protein Kinase 1 and 2 Inhibitors by a Scaffold Hopping Approach. *J. Med. Chem.* 2014, *57*, 7624−7643.

(23) Le Huerou, Y.; Blake, J.; Gunwardana, I.; Mohr, P.; Wallace, E.; Wang, B.; Chicarelli, M.; Lyon, M. Pyrrolopyridines as Kinase Inhibitors. WO 2009/140320, 2009.

(24) Stavenger, R.; Witherington, J.; Rawlings, D.; Holt, D.; Chan, G. CHK1 Kinase Inhibitors. WO 03/028724, 2003.

(25) Bahekar, R. H.; Jain, M. R.; Jadav, P. A.; Prajapati, V. M.; Patel, D. N.; Gupta, A. A.; Sharma, A.; Tom, R.; Bandyopadhya, D.; Modi, H.; Patel, P. R. Synthesis and antidiabetic activity of 2,5-disubstituted-3-imidazol-2-yl-pyrrolo[2,3-b]pyridines and thieno[2,3-b]pyridines. *Bioorg. Med. Chem.* 2007, *15*, 6782−6795.

(26) Chavan, N. L.; Nayak, S. K.; Kusurkar, R. S. A rapid method toward the synthesis of new substituted tetrahydro α-carbolines and α-carbolines. *Tetrahedron* 2010, *66*, 1827−1831.

(27) Chinta, B. S.; Baire, B. Reactivity of indole-3-alkoxides in the absence of acids: Rapid synthesis of homo- bisindolylmethanes. *Tetrahedron* 2016, *72*, 8106−8116.

(28) McCoull, W.; Hennessy, E. J.; Blades, K.; Box, M. R.; Chuaqui, C.; Dowling, J. E.; Davies, C. D.; Ferguson, A. D.; Goldberg, F. W.; Howe, N. J.; Kemmitt, P. D.; Lamont, G. M.; Madden, K.; McWhirter, C.; Varnes, J. G.; Ward, R. A.; Williams, J. D.; Yang, B. Identification and Optimisation of 7-Azaindole PAK1 Inhibitors with Improved Potency and Kinase Selectivity. *MedChemComm* 2014, *5*, 1533−1539.

(29) Gourdain, S.; Dairou, J.; Denhez, C.; Bui, L. C.; Rodrigues-Lima, F.; Janel, N.; Delabar, J. M.; Cariou, K.; Dodd, R. H. Development of DANDYs, New 3,5-Diaryl-7-Azaindoles Demonstrating Potent DYRK1A Kinase Inhibitory Activity. *J. Med. Chem.* 2013, *56*, 9569−9585.

(30) Gelbard, H.; Dewhurst, S.; Goodfellow, V.; Wiemann, T.; Ravula, S.; Loweth, C.. Bicyclic Heteroaryl Kinase Inhibitors and Methods of Use. WO 2011/149950, 2011.

(31) Knauber, T.; Tucker, J. Palladium Catalyzed Monoselective α-Arylation of Sulfones and Sulfonamides with 2,2,6,6-Tetramethylpiperidine ·ZnCl ·LiCl Base and Aryl Bromides. *J. Org. Chem.* 2016, *81*, 5636−5648.

(32) Zhao, B.; Li, Y.; Xu, P.; Dai, Y.; Luo, C.; Sun, Y.; Ai, J.; Geng, M.; Duan, W. Discovery of Substituted 1H-Pyrazolo[3,4-b]pyridine Derivatives as Potent and Selective FGFR Kinase Inhibitors. *ACS Med. Chem. Lett.* 2016, *7*, 629−634.

(33) Shi, J.; Xu, G.; Zhu, W.; Ye, H.; Yang, S.; Luo, Y.; Han, J.; Yang, J.; Li, R.; Wei, Y.; Chen, L. Design and Synthesis of 1,4,5,6-Tetrahydropyrrolo[3,4-c]Pyrazoles and Pyrazolo[3,4-b]Pyridines for Aurora-A Kinase Inhibitors. *Bioorg. Med. Chem. Lett.* 2010, *20*, 4273−4278.

(34) Van Mileghem, S.; Egle, B.; Gilles, P.; Veryser, C.; Van Meervelt, L.; De Borggraeve, W. M. Carbonylation as a Novel Method for the Assembly of Pyrazine Based Oligoamide Alpha-Helix Mimetics. *Org. Biomol. Chem.* 2017, *15*, 373−378.

(35) Maccormick, S.; Storck, P.-H.; Mertimore, M.; Charrier, J.-D.; Knegtel, R.; Young, S.; Pinder, J.; Durrant, S. Compounds Useful as Inhibitors of ATR Kinase. WO 2012/178123, 2012.

(36) Gelbard, H.; Dewhurst, S.; Goodfellow, V.; Wiemann, T.; Bennet, D. MLK Inhibitors and Methods of Use. WO 2010/068483, 2010.

(37) Sorrell, F. J.; Szklarz, M.; Abdul Azeez, K. R.; Elkins, J. M.; Knapp, S.; Szklarz, M.; Azeez, K. R. A.; Elkins, J. M.; Knapp, S. Family-wide Structural Analysis of Human Numb-Associated Protein Kinases. *Struct. Des.* 2016, *24*, 401−411.

(38) Fabian, M. A.; Biggs, W. H.; Treiber, D. K.; Atteridge, C. E.; Azimioara, M. D.; Benedetti, M. G.; Carter, T. A.; Ciceri, P.; Edeen, P. T.; Floyd, M.; Ford, J. M.; Galvin, M.; Gerlach, J. L.; Grotzfeld, R. M.; Herrgard, S.; Insko, D. E.; Insko, M. A.; Lai, A. G.; Lelias, J.-M.; Mehta, S. A.; Milanov, Z. V.; Velasco, A. M.; Wodicka, L. M.; Patel, H. K.; Zarrinkar, P. P.; Lockhart, D. J. A small molecule-kinase interaction map for clinical kinase inhibitors. *Nat. Biotechnol.* 2005, *23*, 329−336.

(39) Rodriguez-Madoz, J. R.; Bernal-Rubio, D.; Kaminski, D.; Boyd, K.; Fernandez-Sesma, A. Dengue Virus Inhibits the Production of Type I Interferon in Primary Human Dendritic Cells. *J. Virol.* 2010, *84*, 4845−4850.

(40) Karaman, M. W.; Herrgard, S.; Treiber, D. K.; Gallant, P.; Atteridge, C. E.; Campbell, B. T.; Chan, K. W.; Ciceri, P.; Davis, M. I.; Edeen, P. T.; Faraoni, R.; Floyd, M.; Hunt, J. P.; Lockhart, D. J.; Milanov, Z. V.; Morrison, M. J.; Pallares, G.; Patel, H. K.; Pritchard, S.; Wodicka, L. M.; Zarrinkar, P. P. A Quantitative Analysis of Kinase Inhibitor Selectivity. *Nat. Biotechnol.* 2008, *26*, 127−132.

(41) Trott, O.; Olson, A. J. AutoDock Vina: improving the speed and accuracy of docking with a new scoring function, efficient optimization, and multithreading. *J. Comput. Chem.* 2010, *31*, 455−461.

(42) Case, D. A.; Ben-Shalom, I.; Brozell, S. R.; Cerutti, D. S.; Cheatham, T.; Cruzeiro, V. W. D.; Darden, T. A.; Duke, R. A.; Ghoreishi, D.; Gilson, M. K.; Gohlke, H.; Goetz, A. W.; Greene, D.; Harris, R.; Homeyer, N.; Huang, Y.; Izadi, S.; Kovalenko, A.; Kurtzman, T.; Lee, T. S.; LeGrand, S.; Li, P.; Lin, C.; Liu, J.; Luchko, T.; Luo, R.; Mermelstein, D. J.; Merz, K. M.; Miao, Y.; Monard, G.; Nguyen, C.; Nguyen, H.; Omelyan, I.; Onufriev, A.; Pan, F.; Qi, R.; Roe, D. R.; Roitberg, A.; Sagui, C.; Schott-Verdugo, S.; Shen, J.; Simmerling, C. L.; Smith, J.; SalomonFerrer, R.; Swails, J.; Walker, R. C.; Wang, J.; Wei, H.; Wolf, R. M.; Wu, X.; Xiao, L.; York, D. M.; Kollman, P. A. *AMBER 2018*; San Francisco, 2018.

(43) Genheden, S.; Ryde, U. The MM/PBSA and MM/GBSA Methods to Estimate Ligand-Binding Affinities. *Expert Opin. Drug Discovery* 2015, *10*, 449−461.

(44) Pettersen, E. F.; Goddard, T. D.; Huang, C. C.; Couch, G. S.; Greenblatt, D. M.; Meng, E. C.; Ferrin, T. E. UCSF Chimera?A Visualization System for Exploratory Research and Analysis. *J. Comput. Chem.* 2004, *25*, 1605−1612.

(45) Kabsch, W. XDS. *Acta Crystallogr. Sect. D Biol. Crystallogr.* 2010, *66*, 125−132.

(46) Winter, G. xia2: an expert system for macromolecular crystallography data reduction. *J. Appl. Crystallogr.* 2010, *43*, 186−190.

(47) Winn, M. D.; Ballard, C. C.; Cowtan, K. D.; Dodson, E. J.; Emsley, P.; Evans, P. R.; Keegan, R. M.; Krissinel, E. B.; Leslie, A. G. W.; McCoy, A.; McNicholas, S. J.; Murshudov, G. N.; Pannu, N. S.; Potterton, E. A.; Powell, H. R.; Read, R. J.; Vagin, A.; Wilson, K. S. Overview of the CCP4 suite and current developments. *Acta Crystallogr., Sect. D: Biol. Crystallogr.* 2011, *67*, 235−242.

(48) Mccoy, A. J.; Grosse-kunstleve, R. W.; Adams, P. D.; Winn, M. D.; Storoni, L. C.; Read, R. J. Phaser Crystallographic Software Research Papers. *J. Appl. Crystallogr.* 2007, *40*, 658−674.

(49) Murshudov, G. N.; Vagin, A. A.; Dodson, E. J. Refinement of Macromolecular Structures by the Maximum-Likelihood Method. *Acta Crystallogr. Sect. D Biol. Crystallogr.* 1997, *53*, 240−255.

(50) Adams, P. D.; Afonine, P. V.; Bunkoczi, G.; Chen, V. B.; Davis, I. W.; Echols, N.; Headd, J. J.; Hung, L.-W.; Kapral, G. J.; Grosse-Kunstleve, R. W.; McCoy, A. J.; Moriarty, N. W.; Oeffner, R.; Read, R. J.; Richardson, D. C.; Richardson, J. S.; Terwilliger, T. C.; Zwart, P. H. PHENIX: a comprehensive Python-based system for macro-molecular structure solution. *Acta Crystallogr. Sect. D Biol. Crystallogr.* 2010, *66*, 213−221.

(51) Emsley, P.; Lohkamp, B.; Scott, W. G.; Cowtan, K. Features and development ofCoot. *Acta Crystallogr. Sect. D Biol. Crystallogr.* 2010, *66*, 486−501.

(52) Perera, R.; Khaliq, M.; Kuhn, R. J. Closing the Door on Flaviviruses: Entry as a Target for Antiviral Drug Design. *Antiviral Res.* 2008, *80*, 11−22.

(53) Xie, X.; Gayen, S.; Kang, C.; Yuan, Z.; Shi, P.-Y. Membrane Topology and Function of Dengue Virus NS2A Protein. *J. Virol.* 2013, *87*, 4609−4622.

(54) Huang, C. Y.-H.; Butrapet, S.; Moss, K. J.; Childers, T.; Erb, S. M.; Calvert, A. E.; Silengo, S. J.; Kinney, R. M.; Blair, C. D.; Roehrig, J. T. The Dengue Virus Type 2 Envelope Protein Fusion Peptide Is Essential for Membrane Fusion. *Virology* 2010, *396*, 305−315.

(55) Rodriguez-Madoz, J. R.; Bernal-Rubio, D.; Kaminski, D.; Boyd, K.; Fernandez-Sesma, A. Dengue Virus Inhibits the Production of Type I Interferon in Primary Human Dendritic Cells. *J. Virol.* 2010, *84*, 4845−4850.

(56) Morris, G. M.; Huey, R.; Lindstrom, W.; Sanner, M. F.; Belew, R. K.; Goodsell, D. S.; Olson, A. J. AutoDock4 and AutoDockTools4: Automated Docking with Selective Receptor Flexibility. *J. Comput. Chem.* 2009, *30*, 2785−2791.

(57) Evans, D. A. History of the Harvard ChemDraw Project. *Angew. Chem., Int. Ed.* 2014, *53*, 11140−11145.
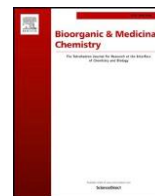
Structure-activity relationship study of the pyridine moiety of isothiazolo[4,3-b]pyridines as antiviral agents targeting cyclin G-associated kinase

Belén Martinez-Gualda[a], Szu-Yuan Pu[b], Mathy Froeyen[a], Piet Herdewijn[a], Shirit Einav[b], Steven De Jonghe[c,*]

[a] KU Leuven, Rega Institute for Medical Research, Laboratory of Medicinal Chemistry, Herestraat 49, 3000 Leuven, Belgium
[b] Department of Medicine, Division of Infectious Diseases and Geographic Medicine, and Department of Microbiology and Immunology, Stanford University School of Medicine, Stanford, CA 94305, USA
[c] KU Leuven, Department of Microbiology, Immunology and Transplantation, Rega Institute for Medical Research, Laboratory of Virology and Chemotherapy, Herestraat 49, 3000 Leuven, Belgium

ARTICLE INFO

ABSTRACT

Previously, we reported the discovery of 3,6-disubstituted isothiazolo[4,3-b]pyridines as potent and selective cyclin G-associated kinase (GAK) inhibitors with promising antiviral activity. In this manuscript, the structure-activity relationship study was expanded to synthesis of isothiazolo[4,3-b]pyridines with modifications of the pyridine moiety. This effort led to the discovery of an isothiazolo[4,3-b]pyridine derivative with a 3,4-di-methoxyphenyl residue at position 5 that displayed low nanomolar GAK binding affinity and antiviral activity against dengue virus.

1. Introduction

Cyclin G-associated kinase (GAK), also known as auxilin 2, is a cellular serine/threonine kinase that belongs to the numb-associated kinases (NAK). This family also includes adaptor-associated kinase 1 (AAK1), BMP-2 inducible kinase (BIKE/BMP2K) and myristoylated and palmitoylated serine/threonine kinase 1 (MPSK1, also known as serine/threonine kinase 16 or STK16).[1] GAK, ubiquitously expressed within the cell in the Golgi apparatus, cytoplasm and nucleus, regulates the clathrin-mediated intracellular trafficking of cellular cargo proteins.[2] Interactions between clathrin- associated adaptor protein (AP) complexes and transmembrane cargo play an important role in membrane trafficking, as these AP complexes orchestrate the formation of vesicles destined for transport in distinct intracellular pathways.[3,4] Phosphorylation of the μ subunits of AP1 and AP2 by GAK leads to a conformational change that enhances their binding to sorting motifs within cargo proteins.[5,6] GAK regulates the recruitment of clathrin and AP-2 to the plasma membrane and of AP-1 to the *trans*-Golgi network (TGN).[3,7,8] GAK also controls the uncoating of clathrin coated vesicles (CCVs) for recycling clathrin back to the cell surface.[3,5]

Viruses hijack these intracellular membrane trafficking machineries, as indicated by the important roles played by various AP complexes in the life cycle of multiple unrelated viruses.[7,9,10] It has been demonstrated that GAK regulates early and late stages of the viral lifecycle and

hence, functions as a master regulator of viral infection. GAK is therefore a promising target for the discovery of novel antiviral agents. Such a host-targeted approach offers advantages, including a high barrier to resistance and an opportunity to develop broad-spectrum antiviral agents when focusing on host factors, such as GAK, that are essential for the life cycle of multiple viruses[11].

Erlotinib (Fig. 1), an approved anticancer drug with potent GAK affinity (dissociation constant value or $K_D = 3.1$ nM), has shown antiviral activity against an array of unrelated viruses including hepatitis C virus (HCV), dengue virus (DENV), and Zika virus (ZIKV) from the Flaviviridae family, the filovirus Ebola (EBOV) and the alpha virus Chikungunya (CHIKV).[9] However, since erlotinib targets EGFR with a comparable affinity to GAK and several other kinases at a lower affinity, it is not an ideal chemical tool to study the role of GAK in viral infection. Several medicinal chemists were thus inspired to develop potent, drug-like and selective GAK inhibitors. Exploring the chemistry of 4-anilino-quinazolines and –quinolines[12] led to the discovery of SGC-GAK-1 (Fig. 1) that was endowed with very strong GAK affinity ($K_D = 1.9$ nM) and displayed an excellent kinase selectivity profile. This compound was not investigated for its antiviral activity, yet it showed cytotoxic activity against selected prostate cancer cell lines.[13]

Our group reported the discovery of 3,6-disubstituted isothiazolo [4,3-b]pyridines as potent and selective GAK inhibitors. The original series of compounds, as represented by compound **2** (Fig. 1), carried a
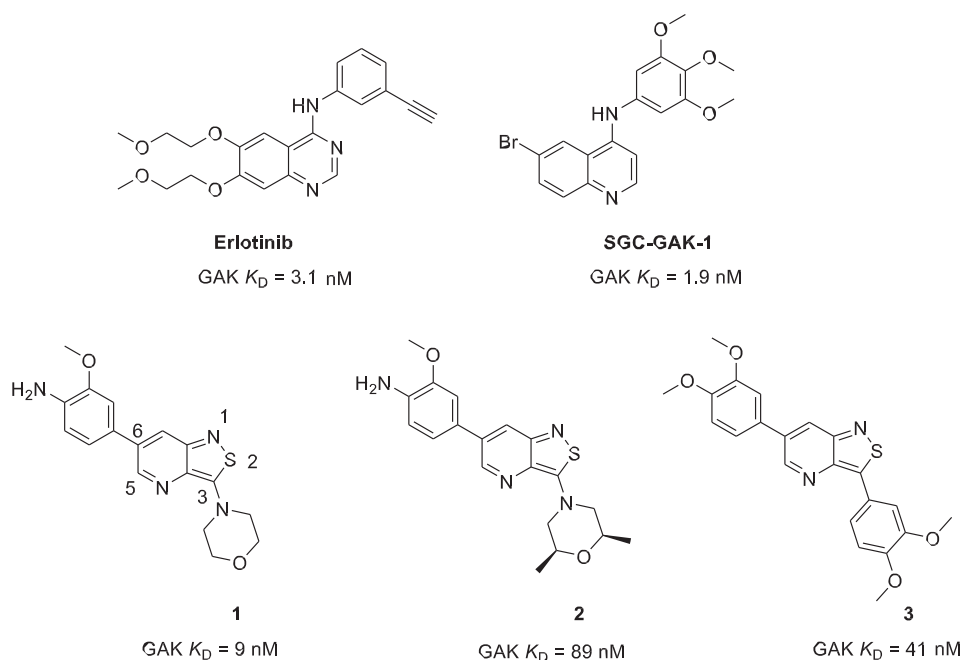

Fig. 1. Previously studied GAK inhibitors.

morpholino residue at position 3 and was endowed with high affinity for GAK ($K_D = 9$ nM), but displayed only low µM antiviral activity against HCV and DENV.[14] Subsequent optimization revealed that a *cis*-2,6-dimethylmorpholine residue at this position (compound **2**, Fig. 1) had a detrimental effect on the GAK affinity ($K_D = 89$ nM), but a favourable effect on the activity against DENV, EBOV and CHIKV.[15] The incorporation of other amines, alkoxides, and carboxamides at position 3 yielded compounds that were much less active as GAK ligands and/or showed weaker antiviral activity.[16] To increase the structural variety at this position, palladium-catalyzed cross couplings (such as Suzuki and Sonogashira reactions) have been performed, leading to the discovery of a congener (compound **3**, Fig. 1) with high GAK affinity

($K_D = 41$ nM) and a moderate antiviral activity against DENV. More recently, the importance of the isothiazolo[4,3-*b*]pyridine core has been evaluated by a scaffold hopping approach, yielding a series of novel scaffolds that displayed a reduced GAK affinity relative to the original scaffold.[18]

Although a broad structural variety has been introduced at position 3 of the isothiazolo[4,3-*b*]pyridine scaffold, and a wide range of heterocyclic core structures have been prepared, the substitution pattern on the pyridine moiety of the isothiazolo[4,3-*b*]pyridine scaffold has not been previously studied in detail. In our prior medicinal chemistry optimization campaigns,[14–18] an aryl group was always present at position 6 of the isothiazolo[4,3-*b*]pyridine scaffold, with a 3,4-dimethoxyphenyl, 3,4,6-trimethoxyphenyl and 3-methoxy-4-aminophenyl being optimal for GAK affinity (Fig. 2). In the present work, we describe our efforts to introduce structural modifications on the

pyridine ring of the isothiazolo[4,3-*b*]pyridine core, keeping the *cis*-2,6-dimethylmorpholine substituent fixed. Several variations were introduced. Besides additional Suzuki couplings, several linkers (amino, alkenyl and alkynyl) were inserted between the phenyl ring at position 6 and the isothiazolo[4,3-*b*]pyridine scaffold. In addition, a number of previously unknown 5-aryl-isothiazolo[4,3-*b*]pyridines were prepared. All compounds were evaluated for their GAK affinity and the most potent GAK ligands were also assessed for anti-DENV activity.

2. Chemistry

For the synthesis of the 6-substituted isothiazolo[4,3-*b*]pyridines,

the known 6-bromo-3-(*cis*-2,6-dimethylmorpholino)isothiazolo[4,3-*b*]

pyridine **4** was selected as the key intermediate (Scheme 1).[15] Aryl groups were conveniently introduced by Suzuki cross-couplings using classical reaction circumstances: an appropriate arylboronic acid, Pd(PPh$_3$)$_4$ as catalyst and potassium carbonate as base in a mixture of dioxane/water. This procedure allowed to assemble a focused library of 6-aryl-isothiazolo[4,3-*b*]pyridines **5a-f** in yields ranging from 78% to 91%. The insertion of an ethenyl linker between the central core structure and the phenyl ring was performed by a palladium-catalyzed cross-coupling between styrene and isothiazolo[4,3-*b*]pyridine **4** applying Heck reaction conditions, using Pd(OAc)$_2$ as catalyst, *N*-phenylurea as ligand and potassium carbonate as base (step b, Scheme 1).[19] This allowed the isolation of the desired compound **5 g** in high yield (88%). Coupling of different anilines at position 6 of the isothiazolo[4,3-*b*]pyridine scaffold was achieved via a Buchwald reaction using Pd
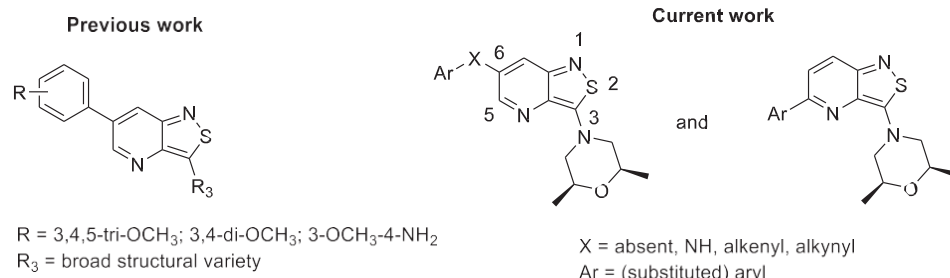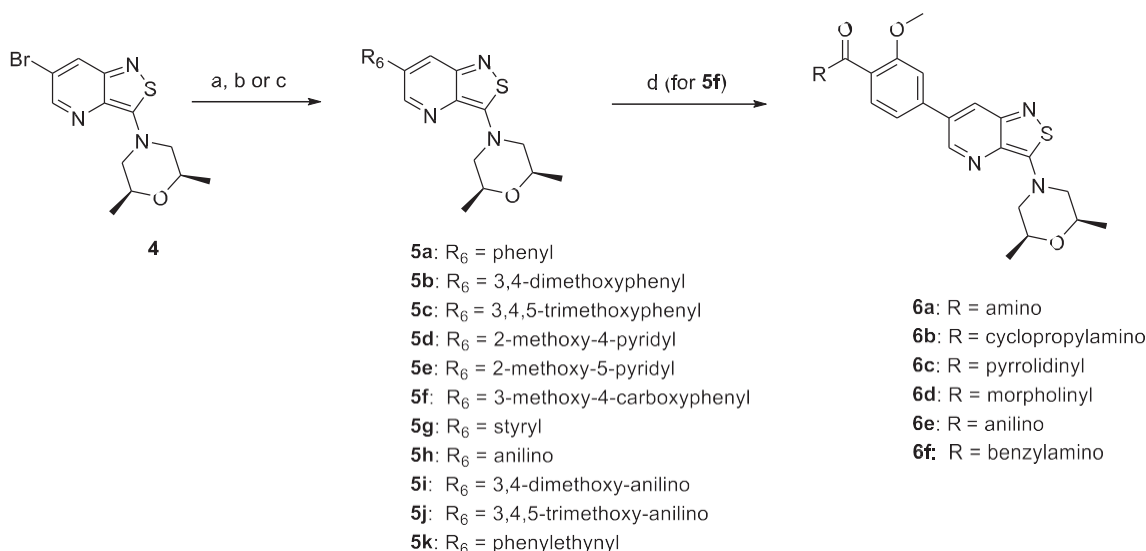

Previous work

R = 3,4,5-tri-OCH$_3$; 3,4-di-OCH$_3$; 3-OCH$_3$-4-NH$_2$
R$_3$ = broad structural variety

Current work

X = absent, NH, alkenyl, alkynyl
Ar = (substituted) aryl

Fig. 2. Medicinal chemistry strategy.

Scheme 1. *Reagents and conditions.* (a) $R_6B(OH)_2$, Pd(PPh$_3$)$_4$, K$_2$CO$_3$, dioxane/water, 90 °C; (b) styrene, *N*-phenylurea, Pd(OAc)$_2$, K$_2$CO$_3$, DMF, 120 °C, overnight; (c) aniline or phenylacetylene, Pd(dba)$_2$, SPhos, *t*BuOK, toluene, 90 °C; (d) (i) SOCl$_2$, DCM, 40 °C, 3 h; (ii) amine, Et$_3$N, rt, 3 h.

(dba)$_2$ as catalyst, SPhos as ligand, potassium *tert*-butoxide as base and toluene as solvent, yielding compounds **5 h-j** in good yields ranging from 73% to 85%.[20] For the insertion of a phenylethynyl residue at position 6 of isothiazolo[4,3-*b*]pyridine scaffold, classical Sonogashira reaction conditions (using ethynylbenzene, Pd(PPh$_3$)$_2$Cl$_2$ and copper(I) iodide) were initially applied, but failed. However, when the same Buchwald conditions, previously employed for the coupling of anilines, were used for the coupling of phenylacetylene (step c, Scheme 1), compound **5k** was obtained in good yield (87%). Prior to the addition of the catalyst, it was necessary to pass a continuous flow of argon for 5–10 min through the reaction mixture, as this led to increased reaction yields in all these palladium-catalyzed cross-couplings.

The carboxylic acid moiety of compound **5f** was converted to several amides.[21] The acid chloride was generated *in situ* by reaction with thionyl chloride, followed by reaction with a number of amines generating target compounds **6a-f** in yields varying from 68% to 85%. Similarly, the amino group of compound **2** was also used to prepare a number of amides (Scheme 2). The formylamino congener **7a** was prepared using MnO$_2$ as catalyst and formamide as solvent.[22] The reaction of compound **2** with acetic anhydride, cyclopropanecarbonyl chloride and benzoyl chloride provided compounds **7b**, **7c** and **7d**, respectively.

For the synthesis of 5-substituted isothiazolo[4,3-*b*]pyridines, an alternative synthetic pathway was followed. Initial attempts were focused on the synthesis of an intermediate (i.e. 3-bromo-5-chloro-isothiazolo[4,3-*b*]pyridine) that could serve as key synthon from which structural variety at two different positions of the scaffold could be

easily introduced. Commercially available 6-chloro-2-cyano-3-nitropyridine **8** was selected as starting material. Reduction of the nitro group to the corresponding amino group led to a concomitant complete hydrolysis of the cyano moiety affording 3-amino-6-chloropicolinic acid as the sole product. As an alternative, we introduced the corresponding aryl group via a Suzuki cross-coupling reaction in the first step of the synthesis (Scheme 3). These reactions were carried out in toluene as solvent (except for compound **9 h** bearing a 3,4,5-trimethoxyphenyl group) instead of the dioxane/water mixture that was commonly applied for the preparation of 6-substituted derivatives. Thus, several aryl groups were introduced at position 6 of compound **8** generating derivatives **9a-i** in yields ranging from 76% to 96%. The nitro group of compounds **9a-i** was reduced by treatment with iron under acidic conditions (acetic acid at 60 °C) affording 3-amino-6-aryl-picolinonitriles **10a-i**. Inevitably, small amounts of the corresponding 3-amino-6-phenylpicolinamides were formed, resulting from hydrolysis of the cyano group. These mixtures were used as such for the next step. Thionation of the nitrile functionality using phosphorus pentasulfide yielded thioamides **11a-i**. The isothiazole moiety was then constructed by an oxidative ring closure using hydrogen peroxide in methanol. As this reaction proceeded smoothly and cleanly, purification of the crude residue was not necessary, and the corresponding 5-aryl-3-amino-iso-thiazolo[4,3-*b*]pyridines **12a-i** were isolated in excellent yields. The conversion of the amino group to a bromine was achieved via a Sandmeyer reaction. Applying the classical reaction conditions (NaNO$_2$, HBr, CuBr, water) was successful for compounds **13a-d** and **13 h**. However, for the analogues (compounds **12e-g**), in which the 5-phenyl moiety carried one or two electron-donating substituents (methyl or methoxy groups), none to very low yields the most were obtained. This result was attributed to multiple brominations at different positions of the 5-phenyl ring. To minimise these aromatic bromination side reactions, milder conditions (*t*BuONO, CuBr$_2$ and dry acetonitrile) were used.[23] This slightly improved the yields of compounds **13e-g** (34–51%), but not of compound **13i**. Finally, *cis*-2,6-dimethylmorpho- line was introduced at position 3 of the isothiazolo[4,3-*b*]pyridine scaffold, affording the desired compounds **14a-h** in yields ranging from 55% to 91%.

To circumvent the Sandmeyer reaction, a 3-*N*-morpholinyl moiety was directly synthesized from the corresponding 3-amino congeners. Reaction of compounds **12f**, **12 g** and **12i** with 2-bromoethyl ether and potassium carbonate as a base generated the desired compounds **15f**, **15 g** and **15i** in decent yields (71–77%).
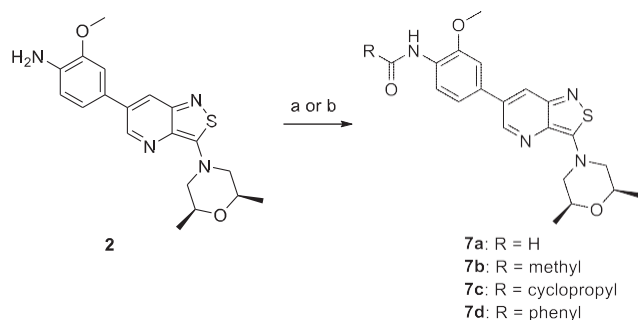
Scheme 2. *Reagents and conditions.* (a) formamide, MnO$_2$, 150 °C, 5 h; (b) acetic anhydride or RCOCl, Et$_3$N, DCM, rt, overnight.
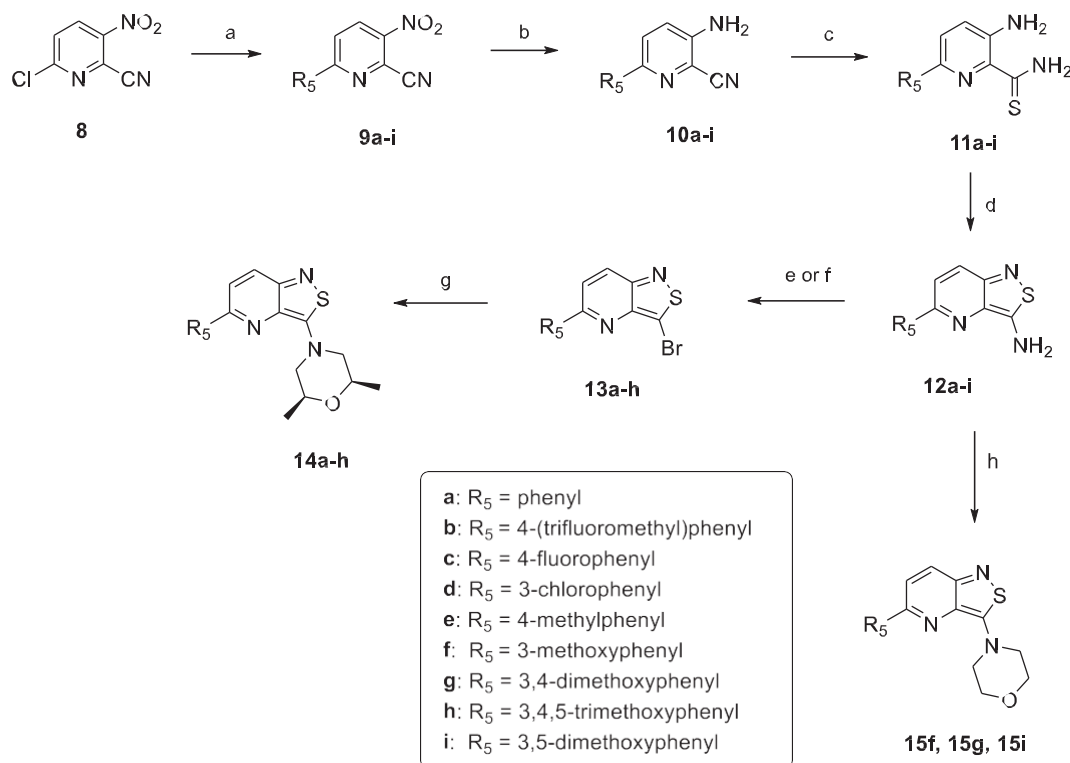
Scheme 3. *Reagents and conditions*. (a) $R_3B(OH)_2$, $Pd(PPh_3)_4$, K_2CO_3, toluene or dioxane/H_2O, 95 °C; (b) Fe, CH_3COOH, 60 °C; (c) P_2S_5, EtOH, 75 °C; (d) 35% aq·H_2O_2, MeOH, rt; (e) $NaNO_2$, HBr, CuBr, H_2O, 0 °C to rt; (f) tBuONO, $CuBr_2$, dry CH_3CN, −10 °C to rt; (g) 2,6-dimethylmorpholine, EtOH, reflux, overnight; (h) 2-bromoethyl ether, K_2CO_3, DMF, 100 °C, 4–5 h.
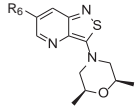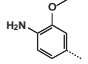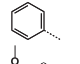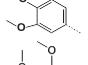
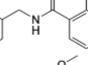## 3. GAK binding affinity
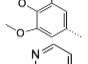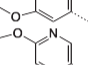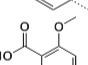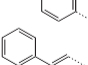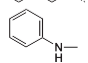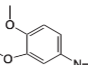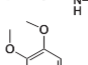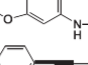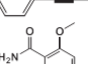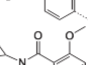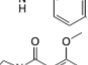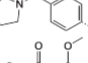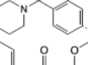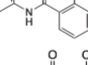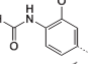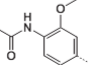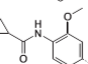
The binding affinity of compounds **5a-k**, **6a-f**, **7a-d**, **14a-h, 15f, 15 g** and **15i** for GAK was evaluated via a commercially available LanthaScreen® Europium kinase binding assay.[24] In this assay format, an Alexa Fluor 647-labeled conjugate or tracer competes with the GAK ligand for the ATP binding site. Signal detection is dependent on the time-resolved fluorescence resonance energy transfer (TR-FRET) signal resulting from the antibody and tracer binding. When the ATP site is occupied by the tracer, there is a high TR-FRET signal. When the tracer is displaced by the GAK inhibitor, a reduction in TR-FRET signal is observed. The GAK binding affinity of reference compound **2** was measured via a LanthaScreen assay with an IC_{50} value of 0.0394 μM, which is in agreement with the K_D of 0.089 μM previously measured via the DiscoverX screening assay.[15] To drive the subsequent structure-activity relationship (SAR) study, the GAK binding affinity of all compounds was evaluated in the Lanthascreen assay (Tables 1 and 2).

Prior SAR studies of 3-*N*-morpholino-isothiazolo[4,3-*b*]pyridines demonstrated that electron-donating substituents (e.g. methoxy, amino) at the 6-phenyl moiety are optimal for GAK binding. Yet, combination of a *cis*-2,6-dimethylmorpholinyl substituent at position 3, which is known to confer potent antiviral activity,[15] with structural variation of the 6-phenyl moiety has not been previously explored. Based on the beneficial effect of methoxy groups on GAK binding,[14] the 6-(3,4-dimethoxy)- and 6-(3,4,5-trimethoxyphenyl) derivatives were synthesized (Table 1). The presence of a 3,4-dimethoxyphenyl residue (compound **5b**) caused a 3-fold drop in GAK affinity ($IC_{50} = 0.136$ μM) relative to compound **2**. Conversely, the 3,4,5-trimethoxyphenyl congener (compound **5c**) showed a slightly improved GAK affinity ($IC_{50} = 0.071$ μM). Removal of the methoxy groups furnished com- pound **5a** which shows an IC_{50} of 0.661 μM, which is about 10-fold less potent than the trimethoxyphenyl congener **5c**. Replacement of one of the methoxy groups by an endocyclic pyridine nitrogen gave rise to compounds **5d** and **5e** that display IC_{50} values of 0.545 μM and >

3.33 μM, respectively. This indicated that the methoxy group at position 3 is more important for GAK binding than the one at position 4. Therefore, keeping the 3-methoxy group fixed, a number of derivatives were prepared with alternative functional groups at position 4 of the aromatic ring. The presence of a 4-carboxylic acid resulted in compound **5f** that showed very potent GAK inhibition ($IC_{50} = 0.042$ μM). The carboxylic acid was used as a chemical handle to make a small set of amides, including a simple carboxamide analogue (compound **6a**), cycloaliphatic amides (compounds **6b-d**) and aromatic amides (**6e-f**). Based on the X-ray crystallographic data that we previously reported,[14] this region (i.e. the 6-phenyl moiety) is oriented towards the solvent and therefore tolerates structural variety. This is in agreement with the experimentally determined IC_{50} values, as several of these compounds, and particularly the carboxamide congener **6a** ($IC_{50} = 0.022$ μM), show good GAK affinity. Because of the good affinity of these amides, a number of reverse amides (compounds **7a-d**) with aliphatic and aromatic side chains were prepared, displaying GAK IC_{50} values in the range of 0.1 to 0.4 μM. To further explore the SAR, the effect of various linkers between the isothiazolo[4,3-*b*]pyridine scaffold and the 6-phenyl moiety on GAK affinity were investigated. An alkenyl (compound **5 g**) or alkynyl (compound **5 k**) spacer gave compounds that were completely devoid of GAK affinity. Albeit weak, an anilino sub-stituent at position 6 (compound **5 h**) gave rise to GAK affinity with an IC_{50} of 1.63 μM. In an effort to restore GAK affinity of the 6-anilino congener, the 3,4-dimethoxy- (compound **5i**) and 3,4,5-trimethoxy-anilino (compound **5j**) congeners were prepared. Consistent with the 6-phenyl series, the 3,4,5-trimethoxyanilino derivative **5j** showed the most potent GAK affinity, with an IC_{50} of 0.458 μM.
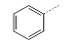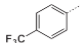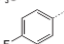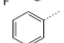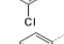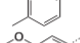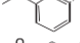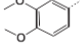
To expand the SAR, a series of regioisomeric 5-aryl-isothiazolo[4,3-*b*]pyridines (compounds **14a-i**) was synthesized (Table 2). Because of synthetic difficulties (*vide supra*), a number of derivatives (compounds **15f**, **15 g** and **15i**) carrying a morpholine instead of a *cis*-2,6-di-methylmorpholino residue were synthesized. An unsubstituted phenyl (compound **14a**), halogen substituted phenyls (compounds **14c-d**) and

Table 1

GAK binding affinity of 6-substituted isothiazolo[4,3-b]pyridines.

Cmpd	R$_6$	GAK IC$_{50}$ (μM)
2		0.0394
5a		0.661
5b		0.136
5c		0.071
5d		0.545
5e		> 3.33
5f		0.042
5g		> 3.33
5h		1.63
5i		1.29
5j		0.458
5k		> 10
6a		0.022
6b		0.118
6c		0.083
6d		0.101
6e		> 0.37
6f		0.073
7a		0.113
7b		0.132
7c		0.173
7d		0.37

Table 2

GAK binding affinity of 5-aryl-isothiazolo[4,3-b]pyridines.

Cmpd	R	R$_5$	GAK IC$_{50}$ (μM)
14a	CH$_3$		0.364
14b	CH$_3$		> 0.37
14c	CH$_3$		0.11
14d	CH$_3$		0.262
14e	CH$_3$		0.214
14f	CH$_3$		0.099
14g	CH$_3$		0.024
14h	CH$_3$		0.422
15f	H		0.136
15g	H		0.124
15i	H		0.126

the 6-phenyl ring is known to be advantageous for GAK affinity,[14] the phenyl at position 5 was also substituted with one, two or three

displayed GAK IC$_{50}$ values in the 0.1–0.5 μM range, with compound **14 g** (carrying a 3,4-dimethoxyphenyl at position 5 and a *cis*-2,6-dimethylmorpholinyl group at position 3) having the most potent GAK affinity (IC$_{50}$ = 0.024 μM). In contras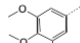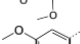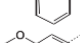t, the corresponding 3-*N*-morpholinyl derivative (compound **15 g**) is 5-fold less active as a GAK ligand (IC$_{50}$ = 0.124 μM).

4. Antiviral activity against DENV
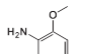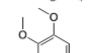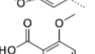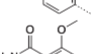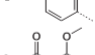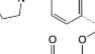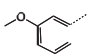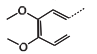
The compounds with the strongest GAK binding affinity (IC$_{50}$ < 0.1 μM) were assessed for antiviral activity in human hepa-

(Table 3). Their effect on DENV2 infection was measured at 48 h post-infection via luciferase assays, and the half-maximal effective concentration (EC$_{50}$ value) was calculated. In parallel, the cytotoxicity of the compounds in the infected cells (expressed as the half-maximal cytotoxic concentration or CC$_{50}$ value) was measured via an Alamar-Blue assay. Compound **2** was included as a reference compound, as it was previously shown to have a promising anti-DENV2 activity, with an

methoxyphenyl) derivative **5c** reduces the anti-DENV activity by 3 folds relative to compound **2**. This is in line with its slightly reduced GAK affinity. Although compound **5f** is a very potent GAK ligand (IC$_{50}$ = 0.042 μM), it lacks antiviral activity. This might be due to impaired cellular permeability resulting from the presence of a polar carboxylic acid group. The corresponding amides (compounds **6a** and **6c**) and particularly compound **6f** (EC$_{50}$ = 5.83 μM) show an improved antiviral activity when compared to the carboxylic acid derivative **5f**. These findings suggest that this site of the molecule tolerates some structural variation with respect to GAK affinity, and that this position can therefore be used to tune physicochemical properties, such as

p-tolyl (compound **14e**) at position 5 of the isothiazolo[4,3-b]pyridine scaffold yielded compounds that displayed GAK IC$_{50}$ values in the 0.1–0.3 μM range. Only the 4-trifluoromethylphenyl analogue (compound **14b**) was less active as GAK ligand. As methoxy substitution of
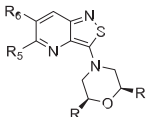
Table 3
Antiviral activity against DENV2.

Cmpd	R	R_5	R_6	DENV EC_{50} (μM)[a]	DENV CC_{50} (μM)[b]
2	CH_3	H		0.82	> 25
5c	CH_3	H		2.79	> 10
5f	CH_3	H		> 10	> 10
6a	CH_3	H		10.05	> 10
6c	CH_3	H		8.85	> 10
6f	CH_3	H		5.83	> 10
14f	CH_3		H	> 10	> 10
14g	CH_3		H	1.049	> 10
Erlotinib	–	–	–	1.22	> 10

[a] EC_{50} = half-maximal effective concentration.
[b] CC_{50} = half-maximal cytotoxic concentration.

Fig. 3. Autodock Vina docking of compound **14 g** (cyan carbons) superimposed on compound **1** (magenta carbons). Amino acids having van der Waals interactions are coloured as green surface.

During this docking process, a rigid enzyme conformation and a flexible ligand by variable torsion angles was applied. Taking into account induced fit effects, the observed interactions may in fact be more favourable. For instance, the Lys69.B side chain is within interaction distance with the oxygen atom of the morpholino ring, possibly forming a hydrogen bond, that is currently not detected.

6. Conclusion

Isothiazolo[4,3-*b*]pyridines are well known as potent and selective GAK inhibitors with antiviral activity. Prior research has focused on structural modifications of the scaffold and the substituent at position 3. In this manuscript, the SAR of the pyridine moiety of the isothiazolo [4,3-*b*]pyridine core structure was studied in detail. The insertion of various linkers between the 6-phenyl ring and the central scaffold generated compounds with decreased GAK affinity. However, position 4 of the 6-phenyl moiety tolerates some structural variety with respect to GAK affinity, and structural variation at this site can be used to modulate the antiviral activity. Furthermore, a novel class of 5-substituted isothiazolo[4,3-*b*]pyridines was synthesized, yielding selected congeners with potent GAK affinity and anti-DENV activity.

7. Experimental section

7.1. Chemistry

For all reactions, analytical grade solvents were used. Argon was used to carry out reactions under an inert atmosphere. Melting points were recorded with a Stuart SMP20 melting point apparatus. ^{1}H and ^{13}C NMR spectra were recorded on a Bruker Avance 300 MHz instrument (^{1}H NMR, 300 MHz; ^{13}C NMR, 75 MHz), 500 MHz instrument (^{1}H NMR, 500 MHz; ^{13}C NMR, 125 MHz) or a 600 MHz instrument (^{1}H NMR, 600 MHz; ^{13}C NMR, 150 MHz, ^{19}F NMR, 471 MHz), using tetramethylsilane as internal standard for ^{1}H NMR spectra and DMSO-d_6 (39.5 ppm) or CDCl$_3$ (77.2 ppm) for ^{13}C NMR spectra. Abbreviations used are s = singlet, d = doublet, t = triplet, q = quartet, m = multiplet, b = broad. Coupling constants are expressed in Hz. High resolution mass spectra were acquired on a quadrupole orthogonal acceleration time-of-flight mass spectrometer (Synapt G2 HDMS, Waters, Milford, MA). Samples were infused at 3 mL/min and spectra were obtained in positive or negative ionization mode with a resolution of 15,000 (FWHM) using leucine enkephalin as lock mass. Precoated aluminum sheets (Fluka silica gel/TLC-cards, 254 nm) were used for TLC. Column chromatography was performed on silica gel 0.060–0.200 mm, 60 (Acros Organics). Purity of final compounds was

aqueous solubility and cellular permeability. Within the 5-aryl-isothiazolo[4,3-*b*]pyridines, two compounds were investigated for antiviral activity. Whereas compound **14f** did not show antiviral activity, the 5-(3,4-dimethoxyphenyl) derivative **14g** was a potent GAK inhibitor (IC$_{50}$ = 0.024 μM) demonstrating potent antiviral activity (EC$_{50}$ and CC$_{50}$ values of 1.049 μM and > 10 μM, respectively). Despite the fact that compound **14g** is less active as GAK ligand when compared to erlotinib (K_D = 3.1 nM), both compounds are equally active as anti-DENV agents. As erlotinib is known to affect multiple other kinases besides GAK, compound **14g** might be a better lead for the discovery of GAK inhibitors as antiviral drugs.

5. Molecular docking of compound 14g into GAK

To rationalize the potent GAK affinity of compound **14g**, molecular docking was initiated starting from the co-crystal X-ray structure of GAK and compound **1** (PDB 4Y8D),[14] with a docking protocol as described before,[17] using the software packages Autodocktools and Autodock vina.[25,26] Compound **14g** has a slightly different substituent at position 3 of the isothiazolo[4,3-*b*]pyridine scaffold from the original crystallized GAK inhibitor **1**. More specifically, compound **14g** bears a *cis*-2,6-dimethylmorpholino ring of which the intrinsic torsion angles are not flexible during docking. However, since the choice of the ring conformation might be important for the final docking orientation and since morpholine can exist in different conformations in crystallized structures,[27] we used different conformations of the morpholino ring of compound **14g** for docking. This analysis revealed that a chair conformation with both methyl groups in an equatorial orientation was optimal. The nitrogen has more a sp^2 character and lays in the same plane as the aromatic ring system. Compound **14g** docked in a favourable way in the ATP binding site. Primarily hydrophobic interactions were observed between GAK and compound **14g,** similarly to compound **1** (Fig. 3). One hydrogen bond with Thr123.B was observed.
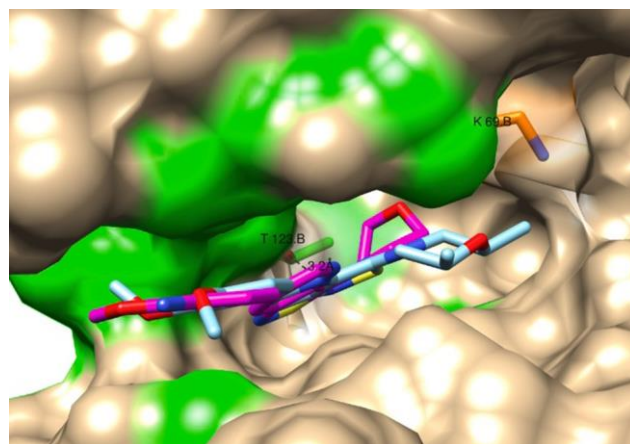
verified to be > 95% by HPLC analysis. HPLC conditions to assess purity were as follows: Shimadzu HPLC equipped with a LC-20AT pump, DGU-20A5 degasser, and a SPD-20A UV–VIS detector; Symmetry C18 column (5 µm, 4.6 mm × 150 mm); gradient elution of H_2O/ CH_3CN from 95/5 or 70/30 to 5/95 over 25 min; flow rate 1 mL/min; wavelength, UV 254 nm. Preparative HPLC purifications were performed using a Phenomenex Gemini 110A column (C18, 10 µM, 21.2 mm × 250 mm).

7.1.1. Synthesis of 6-aryl-3-(cis-2,6-dimethylmorpholino)isothiazolo[4,3-b]pyridines

General procedure. A solution of 6-bromo-3-(*cis*-2,6-dimethylmorpholino) isothiazolo[4,3-*b*]pyridine (1 equiv) in a mixture of dioxane/ water (ratio 4:1) was degassed with argon and subsequently, were added the corresponding boronic acid (1.2 equiv), Pd(PPh$_3$)$_4$ (0.02 equiv) and K_2CO_3 (2 equiv). The mixture was degassed a second time, filled with argon and stirred at 90 °C overnight. After completion of the reaction as monitored by TLC, the volatiles were evaporated to dryness and the crude residue was diluted with EtOAc (20 mL) and washed with water (2 × 20 mL). The organic layer was dried over anhydrous Na_2SO_4 and concentrated *in vacuo*. The resulting residue was purified by silica gel flash chromatography, yielding the corresponding 6-substituted-3-(*cis*-2,6-dimethylmorpholino)isothiazolo[4,3-*b*]pyridines. The following compounds were made according to this general procedure.

7.1.1.1. 3-(cis-2,6-Dimethylmorpholino)-6-(phenyl)isothiazolo[4,3-b] pyridine (5a).
This compound was obtained using phenylboronic acid. The crude residue was purified by silica gel flash chromatography using a mixture of hexane and ethyl acetate (in a ratio of 4:1) as mobile phase, affording the title compound as an amorphous yellow solid in 89% yield (88.3 mg, 0.27 mmol). Mp 141.5–142.3 °C. ^1H NMR (500 MHz, CDCl$_3$) δ: 1.31 (d, $J = 6.2$, Hz, 6H, 2 × CH$_3$), 2.91 (dd, $J = 12.6$, 10.7 Hz, 2H, 2 × NCH), 3.91–3.99 (m, 2H, 2 × OCH), 4.50–4.54 (m, 2H, 2 × NCH), 7.41–7.45 (m, 1H, arom H), 7.48–7.52 (m, 2H, arom H), 7.62–7.68 (m, 2H, arom H), 7.90 (d, $J = 2.1$ Hz, 1H, arom H), 8.63 (d, $J = 2.1$ Hz, 1H, arom H) ppm. ^{13}C NMR (126 MHz, CDCl$_3$) δ: 18.8 (CH$_3$), 55.4 (CH$_2$), 71.2 (CH), 125.6 (CH), 127.4 (CH), 128.4 (CH), 129.1 (CH), 134.2 (C), 135.8 (C), 137.6 (C), 144.3 (CH), 156.3 (C), 172.9 (C) ppm. HR-MS *m/z* [M+H]$^+$ calcd for C$_{18}$H$_{19}$N$_3$OS: 326.1322, found 326.1319.

7.1.1.2. 6-(3,4-Dimethoxyphenyl)-3-(cis-2,6-dimethylmorpholino) isothiazolo[4,3-b]pyridine (5b).
This compound was obtained using 3,4-dimethoxyphenylboronic acid. The crude residue was purified by silica gel flash chromatography using a mixture of hexane and ethyl acetate (in a ratio of 7:3) as mobile phase, affording the title compound as an amorphous yellow solid in 90% yield (52.7 mg, 0.13 mmol). Mp 156.2–157.9 °C. ^1H NMR (600 MHz, CDCl$_3$) δ: 1.32 (d, $J = 6.3$ Hz, 6H, 2 × CH$_3$), 2.91 (dd, $J = 12.5$, 10.7 Hz, 2H, 2 × NCH), 3.92–3.96 (m, 5H, OCH$_3$, 2 × OCH), 3.96 (s, 3H, OCH$_3$), 4.51 (dd, $J = 12.7$, 1.9 Hz, 2H, 2 × NCH), 7.00 (d, $J = 8.3$ Hz, 1H, arom H), 7.16 (d, $J = 2.1$ Hz, 1H, arom H), 7.24 (dd, $J = 8.3$, 2.1 Hz, 1H, arom H), 7.85 (d, $J = 2.1$ Hz, 1H, arom H), 8.63 (d, $J = 2.1$ Hz, 1H, arom H) ppm. ^{13}C NMR (151 MHz, CDCl$_3$) δ: 18.8 (CH$_3$), 55.4 (CH$_2$), 56.0 (OCH$_3$), 56.0 (OCH$_3$), 71.2 (CH), 110.3 (CH), 111.6 (CH), 119.8 (CH), 124.8 (CH), 130.3 (C), 133.9 (C), 135.5 (C), 144.3 (CH), 149.5 (C), 149.5 (C), 156.4 (C), 172.9 (C) ppm. HR-MS *m/z* [M + H]$^+$ calcd for C$_{20}$H$_{23}$N$_3$O$_3$S: 386.1532, found 386.1527.

7.1.1.3. 6-(3,4,5-Trimethoxyphenyl)-3-(cis-2,6-dimethylmorpholino) isothiazolo[4,3-b]pyridine (5c).
This compound was obtained using 3,4,5-trimethoxyphenylboronic acid. The crude residue was purified by silica gel flash chromatography using a mixture of hexane and ethyl acetate (in a ratio of 7:3) as mobile phase, affording the title compound as an amorphous yellow solid in 91% yield (57.7 mg, 0.14 mmol). Mp 154.1–155.5 °C. ^1H NMR (500 MHz, CDCl$_3$) δ: 1.32 (d, $J = 6.3$ Hz, 6H,

2 × CH$_3$), 2.92 (dd, $J = 12.5$, 10.7 Hz, 2H, 2 × NCH), 3.91 (s, 3H, OCH$_3$), 3.93–3.97 (m, 8H, 2 × OCH, 2 × OCH$_3$), 4.52 (dd, $J = 12.7$, 1.9 Hz, 2H, 2 × NCH), 6.85 (s, 2H, arom H), 7.87 (d, $J = 2.1$ Hz, 1H, arom H), 8.62 (d, $J = 2.1$ Hz, 1H, arom H) ppm. ^{13}C NMR (126 MHz, CDCl$_3$) δ: 18.8 (CH$_3$), 55.4 (CH$_2$), 56.2 (OCH$_3$), 61.0 (OCH$_3$), 71.2 (CH), 104.6 (CH), 125.3 (CH), 133.3 (C), 134.1 (C), 135.8 (C), 138.5 (C), 144.1 (CH), 153.7 (C), 156.2 (C), 172.9 (C) ppm. HR-MS *m/z* [M+H]$^+$ calcd for C$_{21}$H$_{25}$N$_3$O$_4$S: 416.1638, found 416.1629.

7.1.1.4. 6-(2-Methoxy-4-pyridyl)-3-(cis-2,6-dimethylmorpholino) isothiazolo[4,3-b]pyridine (5d).
This compound was obtained using 2-methoxypyridine-4-boronic acid. The crude residue was purified by silica gel flash chromatography using a mixture of hexane and ethyl acetate (in a ratio of 7:3) as mobile phase, affording the title compound as an amorphous yellow solid in 87% yield (47.2 mg, 0.13 mmol). Mp 160.5–162.1 °C. ^1H NMR (600 MHz, CDCl$_3$) δ: 1.32 (d, $J = 6.3$ Hz, 6H, 2 × CH$_3$), 2.93 (dd, $J = 12.6$, 10.7 Hz, 2H, 2 × NCH), 3.91–3.97 (m, 2H, 2 × OCH), 4.01 (s, 3H, OCH$_3$), 4.52 (dd, $J = 12.7$, 1.9 Hz, 2H, 2 × NCH), 7.01–7.02 (m, 1H, arom H), 7.15 (dd, $J = 5.3$, 1.5 Hz, 1H, arom H), 7.94 (d, $J = 2.1$ Hz, 1H, arom H), 8.27–8.29 (m, 1H, arom H), 8.59 (d, $J = 2.1$ Hz, 1H, arom H) ppm. ^{13}C NMR (151 MHz, CDCl$_3$) δ: 18.8 (CH$_3$), 53.6 (CH), 55.4 (CH$_2$), 71.2 (OCH$_3$), 108.9 (CH), 115.2 (CH), 126.4 (CH), 133.0 (C), 135.0 (C), 142.9 (CH), 147.7 (CH), 147.8 (C), 155.7 (C), 164.9 (C), 173.2 (C) ppm. HR-MS *m/z* [M+H]$^+$ calcd for C$_{18}$H$_{20}$N$_4$O$_2$S: 357.1380, found 357.1374.

7.1.1.5. 6-(2-Methoxy-5-pyridyl)-3-(cis-2,6-dimethylmorpholino) isothiazolo[4,3-b]pyridine (5e).
This compound was obtained using 2-methoxy-5-pyridineboronic acid. The crude residue was purified by silica gel flash chromatography using a mixture of hexane and ethyl acetate (in a ratio of 7:3) as mobile phase, affording the title compound as an amorphous yellow solid in 88% yield (47.7 mg, 0.13 mmol). Mp 160.2–162.1 °C. ^1H NMR (600 MHz, CDCl$_3$) δ: 1.32 (d, $J = 6.3$ Hz, 6H, 2 × CH$_3$), 2.92 (dd, $J = 12.5$, 10.7 Hz, 2H, 2 × NCH), 3.91–3.97 (m, 2H, 2 × OCH), 4.00 (s, 3H, OCH$_3$), 4.51 (dd, $J = 12.7$, 1.9 Hz, 2H, 2 × NCH), 6.88 (dd, $J = 8.6$, 0.6 Hz, 1H, arom H), 7.82–7.87 (m, 2H, arom H), 8.47 (dd, $J = 2.5$, 0.6 Hz, 1H, arom H), 8.57 (d, $J = 2.1$ Hz, 1H, arom H) ppm. ^{13}C NMR (151 MHz, CDCl$_3$) δ: 18.8 (CH$_3$), 53.7 (OCH$_3$), 55.4 (CH$_2$), 71.2 (CH), 111.4 (CH), 125.0 (CH), 126.5 (C), 132.6 (C), 134.1 (C), 137.4 (CH), 143.4 (CH), 145.4 (CH), 156.0 (C), 164.2 (C), 173.0 (C) ppm. HR-MS *m/z* [M+H]$^+$ calcd for C$_{18}$H$_{20}$N$_4$O$_2$S: 357.1380, found 357.1374.

7.1.1.6. 6-(3-Methoxy-4-carboxyphenyl)-3-(cis-2,6-dimethylmorpholino) isothiazolo[4,3-b]pyridine (5f).
This compound was obtained using 3-methoxy-4-carboxyphenylboronic acid. After completion of the reaction, a solution of HCl (1 M) was added until reach pH acid. The crude residue was purified by silica gel flash chromatography using a mixture of dichloromethane and methanol (in a ratio of 20:1) as mobile phase, affording the title compound as an amorphous yellow solid in 78% yield (47.4 mg, 0.12 mmol). Mp 251.3–253.1 °C. ^1H NMR (600 MHz, DMSO) δ: 1.20 (d, $J = 6.2$ Hz, 6H, 2 × CH$_3$), 2.91 (dd, $J = 12.1$, 11.0 Hz, 2H, 2 × NCH), 3.83–3.89 (m, 2H, 2 × OCH), 3.94 (s, 3H, OCH$_3$), 4.52 (d, $J = 12.0$ Hz, 2H, 2 × NCH), 7.45 (dd, $J = 8.0$, 1.4 Hz, 1H, arom H), 7.52 (d, $J = 1.2$ Hz, 1H, arom H), 7.75 (d, $J = 7.9$ Hz, 1H, arom H), 8.15 (d, $J = 2.0$ Hz, 1H, arom H), 8.81 (d, $J = 2.0$ Hz, 1H, arom H) ppm. ^{13}C NMR (151 MHz, DMSO) δ: 18.6 (CH$_3$), 54.8 (CH$_2$), 56.1 (OCH$_3$), 70.6 (CH), 111.5 (CH), 118.9 (CH), 121.1 (C), 125.7 (CH), 131.5 (CH), 133.8 (C), 134.0 (C), 141.4 (C), 143.8 (CH), 155.4 (C), 158.7 (C), 167.1 (C), 172.5 (C) ppm. HR-MS *m/z* [M + H]$^+$ calcd for C$_{20}$H$_{21}$N$_3$O$_4$S: 400.1325, found 400.1324.

7.1.1.7. 6-(trans-Styryl)-3-(cis-2,6-dimethylmorpholino)isothiazolo[4,3-b] pyridine (5g).
A solution of 6-bromo-3-(*cis*-2,6-dimethylmorpholino) isothiazolo[4,3-*b*]pyridine (1 equiv) in DMF was degassed with argon. Styrene (1.5 equiv), *N*-phenylurea (0.02 equiv), Pd(OAc)$_2$ (0.01 equiv)

and K₂CO₃ (2 equiv) were added. The resulting mixture was degassed a second time, filled with argon and stirred at 120 °C overnight. After completion of the reaction as monitored by TLC, the volatiles were evaporated to dryness and the crude residue was diluted with EtOAc (20 mL) and washed with a 0.5 M HCl solution (2 × 10 mL) and water (20 mL). The organic layer was dried over anhydrous Na_2SO_4 and concentrated *in vacuo*. The resulting residue was purified by silica gel flash chromatography using a mixture of hexane and ethyl acetate (in a ratio of 4:1) as mobile phase, affording the title compound as an amorphous yellow solid in 88% yield (47 mg, 0.13 mmol). Mp 177.4–178.5 °C. ¹H NMR (600 MHz, CDCl₃) δ: 1.31 (d, J = 6.3 Hz, 6H, 2 × CH₃), 2.89 (dd, J = 12.2, 10.9 Hz, 2H, 2 × NCH), 3.90–3.97 (m, 2H, 2 × OCH), 4.48 (dd, J = 12.7, 1.6 Hz, 2H, NCH), 7.12 (d, J = 16.4 Hz, 1H, double bond CH), 7.28 (d, J = 16.4 Hz, 1H, double bond CH), 7.32 (t, J = 7.3 Hz, 1H, arom H), 7.40 (t, J = 7.7 Hz, 2H, arom H), 7.56 (d, J = 7.5 Hz, 2H, arom H), 7.74 (d, J = 1.8 Hz, 1H, arom H), 8.61 (d, J = 1.9 Hz, 1H, arom H) ppm. ¹³C NMR (151 MHz, CDCl₃) δ: 18.8 (CH₃), 55.4 (CH₂), 71.2 (CH), 124.9 (CH), 125.3 (CH), 126.8 (CH), 128.4 (CH), 128.8 (CH), 131.7 (CH), 132.2 (C), 134.0 (C), 136.5 (C), 143.4 (CH), 156.4 (C), 172.7 (C) ppm. HR-MS *m/z* [M+H]⁺ calcd for C₂₀H₂₁N₃OS: 352.1478, found 352.1473.

7.1.2. Synthesis of 6-anilino-3-(cis-2,6-dimethylmorpholino)isothiazolo [4,3-b]pyridines

General procedure. Pd(dba)₂ (0.03 equiv) and SPhos (0.06 equiv) were added to a degassed solution of toluene (15 mL). The resulting mixture was stirred under argon for 5–10 min. Subsequently, 6-bromo-3-(*cis*-2,6-dimethylmorpholino)isothiazolo[4,3-*b*]pyridine (1 equiv), the appropriate aniline or ethynylbenzene (1.5 equiv) and *t*-BuOK (1.5 equiv) were added and the mixture was degassed a second time. The reaction was filled with argon and stirred at 90 °C for 4–5 h. After completion of the reaction as monitored by TLC, the volatiles were evaporated to dryness. The crude residue was diluted with EtOAc (20 mL) and washed twice with a 0.5 M HCl solution (2 × 10 mL) and brine (20 mL). The organic layer was dried over anhydrous Na_2SO_4 and concentrated *in vacuo*. The resulting residue was purified by silica gel flash chromatography, yielding the corresponding 6-substituted-3-(*cis*-2,6-dimethylmorpholino)isothiazolo[4,3-*b*]pyridines. The following compounds were made according to this procedure.

7.1.2.1. 3-(cis-2,6-Dimethylmorpholino)-6-(phenylamino)isothiazolo[4,3-b]pyridine (5h). This compound was obtained using aniline. The crude residue was purified by silica gel flash chromatography using a mixture of hexane and ethyl acetate (in a ratio of 7:3) as mobile phase, affording the title compound as an amorphous yellow solid in 85% yield (44 mg, 0.13 mmol). Mp 186.1–187.5 °C. ¹H NMR (600 MHz, CDCl₃) δ: 1.29 (d, J = 6.3 Hz, 6H, 2 × CH₃), 2.83–2.89 (m, 2H, 2 × NCH), 3.87–3.95 (m, 2H, 2 × OCH), 4.41 (d, J = 12.3 Hz, 2H, 2 × NCH), 6.04 (bs, 1H, NH), 7.04 (t, J = 7.3 Hz, 1H, arom H), 7.17 (d, J = 7.7 Hz, 2H, arom H), 7.26 (s, 1H, arom H), 7.32 (t, J = 7.8 Hz, 2H, arom H), 8.10 (d, J = 2.4 Hz, 1H, arom H) ppm. ¹³C NMR (151 MHz, CDCl₃) δ: 18.8 (CH₃), 55.3 (CH₂), 71.2 (CH), 106.7 (CH), 119.6 (CH), 122.9 (CH), 129.5 (CH), 129.9 (C), 139.2 (C), 140.1 (CH), 140.8 (C), 157.2 (C), 172.0 (C) ppm. HR-MS *m/z* [M+H]⁺ calcd for C₁₈H₂₀N₄OS: 341.1431, found 341.1431.

7.1.2.2. 6-(3,4-Dimethoxyphenylamino)-3-(cis-2,6-dimethylmorpholino)isothiazolo[4,3-b]pyridine (5i). This compound was obtained using 3,4-dimethoxyaniline. The crude residue was purified by silica gel flash chromatography using a mixture of hexane and ethyl acetate (in a ratio of 3:2) as mobile phase, affording the title compound as an amorphous yellow solid in 79% yield (48 mg, 0.12 mmol). Mp 207.1–208.9 °C. ¹H NMR (600 MHz, CDCl₃) δ: 1.29 (d, J = 6.3 Hz, 6H, 2 × CH₃), 2.86 (dd, J = 12.5, 10.7 Hz, 2H, 2 × NCH), 3.86 (s, 3H, OCH₃), 3.89 (s, 3H, OCH₃), 3.90–3.94 (m, 2H, 2 × OCH), 4.40 (dd, J = 12.6, 1.6 Hz, 2H, 2 × NCH), 5.78 (bs, 1H, NH), 6.75–6.79 (m, 2H, arom H), 6.85 (d,

J = 8.2 Hz, 1H, arom H), 7.06 (d, J = 2.4 Hz, 1H, arom H), 8.05 (d, J = 2.5 Hz, 1H, arom H) ppm. ¹³C NMR (151 MHz, CDCl₃) δ: 18.9 (CH₃), 55.5 (CH₂), 56.1 (OCH₃), 56.4 (OCH₃), 71.4 (CH), 105.1, (CH), 106.5 (CH), 112.2 (CH), 113.9 (CH), 129.7 (C), 133.9 (C), 139.8 (CH), 140.9 (C), 146.1 (C), 149.9 (C), 157.5 (C), 172.1 (C) ppm. HR-MS *m/z* [M+H]⁺ calcd for C₂₀H₂₄N₄O₃S: 401,1642, found 401,1638.

7.1.2.3. 6-(3,4,5-Trimethoxyanilino)-3-(cis-2,6-dimethylmorpholino) isothiazolo[4,3-b]pyridine (5j). This compound was obtained using 3,4,5-trimethoxyaniline. The crude residue was purified by silica gel flash chromatography using a mixture of hexane and ethyl acetate (in a ratio of 3:2) as mobile phase, affording the title compound as an amorphous yellow solid in 73% yield (47.8 mg, 0.11 mmol). Mp 252.2–253.5 °C. ¹H NMR (300 MHz, CDCl₃) δ: 1.29 (d, J = 6.3 Hz, 6H, 2 × CH₃), 2.86 (dd, J = 12.5, 10.7 Hz, 2H, 2x NCH), 3.83 (s, 6H, 2 × OCH₃), 3.83 (s, 3H, OCH₃), 3.86–3.98 (m, 2H, 2 × OCH), 4.41 (dd, J = 12.8, 2.0 Hz, 2H, 2 × NCH), 5.88 (bs, 1H, NH), 6.42 (s, 2H, arom H), 7.18 (d, J = 2.5 Hz, 1H, arom H), 8.08 (d, J = 2.5 Hz, 1H, arom H) ppm. ¹³C NMR (151 MHz, CDCl₃) δ: 18.8 (CH₃), 55.3 (CH₂), 56.2 (OCH₃), 61.0 (OCH₃), 71.2 (CH), 98.2 (CH), 106.4 (CH), 129.8 (C), 134.3 (C), 136.8 (C), 139.7 (C), 139.8 (CH), 154.0 (C), 157.2 (C), 172.1 (C) ppm. HR-MS *m/z* [M+H]⁺ calcd for C₂₁H₂₆N₄O₄S: 431.1747, found 431.1745.

7.1.2.4. 3-(cis-2,6-Dimethylmorpholino)-6-(phenylethynyl)isothiazolo [4,3-b]pyridine (5k). This compound was obtained using ethynylbenzene. The crude residue was purifi by silica gel fl chromatography using a mixture of hexane and ethyl acetate (in a ratio of 4:1) as mobile phase, aff the title compound as an amorphous yellow solid in 87% yield (46.3 mg, 0.13 mmol). Mp 162.4–163.8 °C. ¹H NMR (500 MHz, CDCl₃) δ: 1.31 (d, J = 6.1 Hz, 6H, 2 × CH₃), 2.90 (t, J = 11.5 Hz, 2H, 2 × NCH), 3.90–3.98 (m, 2H, 2 × OCH), 4.47 (d, J = 12.5 Hz, 2H, 2 × NCH), 7.35–7.41 (m, 3H, arom H), 7.56–7.61 (m, 2H, arom H), 7.89 (s, 1H, arom H), 8.39 (s, 1H, arom H) ppm. ¹³C NMR (126 MHz, CDCl₃) δ: 18.8 (CH₃), 55.4 (CH₂), 71.2 (CH), 86.6 (C), 93.4 (C), 119.4 (C), 122.5 (C), 128.5 (CH), 128.9 (CH), 130.9 (CH), 131.8 (CH), 133.6 (C), 145.5 (CH), 155.0 (C), 173.0 (C) ppm. HR-MS *m/z* [M+H]⁺ calcd for C₂₀H₁₉N₃OS: 350.1322, found 350.1315.

7.1.3. Synthesis of 6-(benzamide-4-yl)-3-(cis-2,6-dimethylmorpholino) isothiazolo[4,3-b]pyridines

General procedure. To a solution of compound **5f** (6-(3-methoxy-4-carboxyphenyl)-3-(*cis*-2,6-dimethylmorpholino)isothiazolo[4,3-*b*]pyridine) (1 equiv) in dry dichloromethane (15 mL) was added thionyl chloride (SOCl₂) (2 equiv). The mixture was stirred at 40 °C for 3 h. Then, triethylamine (2 equiv) and the appropriate amine (2 equiv) were added and the resulting mixture was stirred at room temperature overnight. After completion of the reaction as monitored by TLC, the residue was diluted with dichloromethane (20 mL) and washed with 0.5 M HCl solution (2 × 10 mL) and water (20 mL). The organic layer was dried over anhydrous Na_2SO_4 and concentrated *in vacuo*. The resulting residue was purified by silica gel flash chromatography, yielding the title compound. The following compounds were made according to this procedure.

7.1.3.1. 6-(2-Methoxybenzamide-4-yl)-3-(cis-2,6-dimethylmorpholino) isothiazolo[4,3-b]pyridine (6a). This compound was obtained using aqueous ammonia (25%) (2 mL). After completion of the reaction as monitored by TLC, water (15 mL) was added, followed by extraction with dichloromethane (2 × 20 mL). The organic layer was dried over anhydrous Na_2SO_4 and concentrated *in vacuo*. The resulting residue was purified by silica gel flash chromatography, using a mixture of dichloromethane and methanol (20:0.5) as mobile phase, yielding the title compound as an amorphous yellow solid in 67% yield (33.4 mg, 0.08 mmol). Mp 270.6–272.2 °C. ¹H NMR (300 MHz, DMSO) δ: 1.20 (d, J = 6.2 Hz, 6H, 2 × CH₃), 2.90 (dd, J = 12.2, 11.0 Hz, 2H, 2 × NCH),

3.87 (dd, *J* = 12.3, 4.3 Hz, 2H, 2 × OCH), 4.03 (s, 3H, OCH₃), 4.51 (d, *J* = 12.3 Hz, 2H, 2 × NCH), 7.48 (dd, *J* = 8.1, 1.5 Hz, 1H, arom H), 7.53 (s, 1H, arom H), 7.62 (bs, 1H, NH), 7.70 (bs, 1H, NH), 7.91 (d, *J* = 8.0 Hz, 1H, arom H), 8.15 (d, *J* = 2.1 Hz, 1H, arom H), 8.81 (d, *J* = 2.1 Hz, 1H, arom H) ppm. ^{13}C NMR (75 MHz, DMSO) *δ*: 18.7 (CH₃), 55.0 (CH₂), 56.3 (OCH₃), 70.7 (CH), 111.1 (CH), 119.4 (CH), 122.7 (C), 125.6 (CH), 131.6 (CH), 133.8 (C), 134.1 (C), 140.9 (C), 143.9 (CH), 155.5 (C), 157.9 (C), 166.0 (C), 172.5 (C) ppm. HR-MS *m/z* [M+H]⁺ calcd for C₂₀H₂₂N₄O₃S: 399.1485, found 399.1483.

7.1.3.2. 6-(N-Cyclopropyl-2-methoxybenzamide-4-yl)-3-(cis-2,6-dimethylmorpholino) isothiazolo[4,3-b]pyridine (6b).

This compound was obtained using cyclopropylamine. The crude residue was purified by silica gel flash chromatography using a mixture of hexane and ethyl acetate (in a ratio of 3:7) as mobile phase, affording the title compound as an amorphous yellow solid in 70% yield (38 mg, 0.09 mmol). Mp 195.1–196.8 °C. ^{1}H NMR (600 MHz, CDCl₃) *δ*: 0.61–0.64 (m, 2H, CH₂), 0.86–0.91 (m, 2H, CH₂), 1.33 (d, *J* = 6.3 Hz, 6H, 2 × CH₃), 2.91–2.99 (m, 3H, CH, 2 × NCH), 3.92–3.99 (m, 2H, 2 × OCH), 4.03 (s, 3H, OCH₃), 4.53 (dd, *J* = 12.7, 1.8 Hz, 2H, 2 × NCH), 7.20 (d, *J* = 1.6 Hz, 1H, arom H), 7.38 (dd, *J* = 8.1, 1.6 Hz, 1H, arom H), 7.91 (d, *J* = 2.8 Hz, 1H, NH), 7.93 (d, *J* = 2.1 Hz, 1H, arom H), 8.35 (d, *J* = 8.1 Hz, 1H, arom H), 8.63 (d, *J* = 2.1 Hz, 1H, arom H) ppm. ^{13}C NMR (151 MHz, CDCl₃) *δ*: 6.9 (CH₂), 18.8 (CH₃), 22.9 (CH), 55.4 (CH₂), 56.1 (OCH₃), 71.2 (CH), 110.3 (CH), 120.3 (CH), 121.3 (C), 126.1 (CH), 133.1 (CH), 134.5 (C), 134.8 (C), 142.1 (C), 143.6 (CH), 155.9 (C), 157.8 (C), 166.1 (C), 173.1 (C) ppm. HR-MS *m/z* [M+H]⁺ calcd for C₂₃H₂₆N₄O₃S: 439.1798, found 439.1798.

7.1.3.3. (4-(3-(cis-2,6-Dimethylmorpholino)isothiazolo[4,3-b]pyridin-6-yl)-2-methoxyphenyl)(pyrrolidin-1-yl)methanone (6c).

This compound was obtained using pyrrolidine. The crude residue was purified by silica gel flash chromatography using a mixture of dichloromethane and methanol (in a ratio of 10:0.1) as mobile phase, affording the title compound as an amorphous yellow solid in 65% yield (36.6 mg, 0.08 mmol). Mp 173.1–174.9 °C. ^{1}H NMR (600 MHz, CDCl₃) *δ*: 1.32 (d, *J* = 6.3 Hz, 6H, 2 × CH₃), 1.86–1.92 (m, 2H, CH₂), 1.94–2.01 (m, 2H, CH₂), 2.93 (dd, *J* = 12.5, 10.7 Hz, 2H, 2 × NCH), 3.30 (t, *J* = 6.7 Hz, 2H, CH₂), 3.68 (t, *J* = 7.0 Hz, 2H, CH₂), 3.92 (s, 3H, OCH₃), 3.93–3.98 (m, 2H, 2 × NCH), 4.53 (dd, *J* = 12.7, 1.8 Hz, 2H, 2 × NCH), 7.16 (d, *J* = 1.4 Hz, 1H, arom H), 7.27 (dd, *J* = 7.7, 1.5 Hz, 1H, arom H), 7.40 (d, *J* = 7.7 Hz, 1H, arom H), 7.90 (d, *J* = 2.1 Hz, 1H, arom H), 8.61 (d, *J* = 2.1 Hz, 1H, arom H) ppm. ^{13}C NMR (151 MHz, CDCl₃) *δ*: 18.8 (CH₃), 24.6 (CH₂), 25.8 (CH₂), 45.6 (CH₂), 47.7 (CH₂), 55.4 (CH₂), 55.7 (OCH₃), 71.2 (CH), 110.2 (CH), 119.9 (CH), 125.8 (CH), 127.5 (C), 128.6 (CH), 134.3 (C), 135.3 (C), 139.9 (C), 143.9 (CH), 155.8 (C), 156.0 (C), 167.2 (C), 173.0 (C) ppm. HR-MS *m/z* [M+H]⁺ calcd for C₂₄H₂₈N₄O₃S: 453.1955, found 453.1945.

7.1.3.4. (4-(3-cis-2,6-Dimethylmorpholino)isothiazolo[4,3-b]pyridin-6-yl)-2-methoxyphenyl)(morpholino)methanone (6d).

This compound was obtained using morpholine. The crude residue was purified by silica gel flash chromatography using a mixture of hexane and ethyl acetate (in a ratio of 3:7) as mobile phase, affording the title compound as an amorphous yellow solid in 68% yield (39 mg, 0.08 mmol). Mp 134.2–135.9 °C. ^{1}H NMR (600 MHz, CDCl₃) *δ*: 1.32 (d, *J* = 6.3 Hz, 6H, 2 × CH₃), 2.90–2.97 (m, 2H, 2 × NCH), 3.27–3.40 (m, 2H, CH₂), 3.58–3.71 (m, 2H, CH₂), 3.76–3.89 (m, 4H, 2 × CH₂), 3.93 (s, 3H, OCH₃), 3.93–3.98 (m, 2H, 2 × OCH), 4.53 (d, *J* = 11.3 Hz, 2H, 2 × NCH), 7.15 (d, *J* = 1.2 Hz, 1H, arom H), 7.29 (dd, *J* = 7.7, 1.4 Hz, 1H, arom H), 7.39 (d, *J* = 7.7 Hz, 1H, arom H), 7.90 (d, *J* = 1.7 Hz, 1H, arom H), 8.60 (d, *J* = 1.9 Hz, 1H, arom H) ppm. ^{13}C NMR (151 MHz, CDCl₃) *δ*: 18.8 (CH₃), 42.2 (CH₂), 47.4 (CH₂), 55.4 (CH₂), 55.7 (OCH₃), 66.8 (CH₂), 67.0 (CH₂), 71.2 (CH), 110.0 (CH), 120.2 (CH), 125.3 (C), 125.9 (CH), 128.9 (CH), 135.1 (C), 140.3 (C), 143.7 (CH), 155.8 (C), 167.3 (C), 173.1 (C) ppm. HR-MS *m/z* [M+H]⁺

calcd for C₂₄H₂₈N₄O₄S: 469.1904, found 469.1898.

7.1.3.5. 3-(cis-2,6-Dimethylmorpholino)-6-(N-phenyl-2-methoxybenzamide-4-yl)isothiazolo[4,3-b]pyridine (6e).

This compound was obtained using aniline. The crude residue was purified by silica gel flash chromatography using a mixture of hexane and ethyl acetate (in a ratio of 3:2) as mobile phase, affording the title compound as an amorphous yellow solid in 76% yield (45 mg, 0.09 mmol). Mp 251.1–252.5 °C. ^{1}H NMR (600 MHz, CDCl₃) *δ*: 1.33 (d, *J* = 6.3, 6H, 2 × CH₃), 2.94 (dd, *J* = 12.6, 10.7 Hz, 2H, 2 × NCH), 3.92–3.98 (m, 2H, 2 × OCH), 4.14 (s, 3H, OCH₃), 4.53 (dd, *J* = 12.6, 1.7 Hz, 2H, 2 × NCH), 7.13–7.16 (m, 1H, arom H), 7.27 (d, *J* = 1.5 Hz, 1H, arom H), 7.36–7.40 (m, 2H, arom H), 7.42 (dd, *J* = 8.1, 1.6 Hz, 1H, arom H), 7.69–7.71 (dd, *J* = 8.5, 1.0 Hz, 2H, arom H), 7.95 (d, *J* = 2.1 Hz, 1H, arom H), 8.40 (d, *J* = 8.1 Hz, 1H, arom H), 8.64 (d, *J* = 2.1 Hz, 1H, arom H), 9.79 (s, 1H, NH) ppm. ^{13}C NMR (151 MHz, CDCl₃) *δ*: 18.8 (CH₃), 55.4 (CH₂), 56.4 (OCH₃), 71.2 (CH), 110.5 (CH), 120.4 (CH), 120.6 (CH), 121.6 (C), 124.3 (CH), 126.1 (CH), 129.0 (CH), 133.4 (CH), 134.5 (C), 138.3 (C), 142.6 (C), 143.5 (CH), 155.8 (C), 157.6 (C), 162.7 (C), 173.1 (C) ppm. HR-MS *m/z* [M+H]⁺ calcd for C₂₆H₂₆N₄O₃S 475.1798, found 475.1799.

7.1.3.6. 6-(N-Benzyl-2-methoxybenzamide-4-yl)-3-(cis-2,6-dimethylmorpholino) isothiazolo[4,3-b]pyridine (6f).

This compound was obtained using benzylamine. The crude residue was purified by silica gel flash chromatography using a mixture of hexane and ethyl acetate (in a ratio of 1:1) as mobile phase, affording the title compound as an amorphous yellow solid in 85% yield (51.2 mg, 0.11 mmol). Mp 172.2–173.4 °C. ^{1}H NMR (600 MHz, CDCl₃) *δ*: 1.32 (d, *J* = 6.2 Hz, 6H, 2 × CH₃), 2.93 (dd, *J* = 12.2, 11.0 Hz, 2H, 2 × NCH), 3.91–3.98 (m, 2H, 2 × OCH), 4.00 (s, 3H, OCH₃), 4.53 (d, *J* = 11.6 Hz, 2H, 2 × NCH), 4.72 (d, *J* = 5.6 Hz, 2H, CH₂), 7.21 (d, *J* = 0.8 Hz, 1H, arom H), 7.27–7.31 (m, 1H, arom H), 7.33–7.42 (m, 5H, arom H), 7.93 (d, *J* = 1.9 Hz, 1H, arom H), 8.20 (m, 1H, NH), 8.38 (d, *J* = 8.1 Hz, 1H, arom H), 8.63 (d, *J* = 1.9 Hz, 1H, arom H) ppm. ^{13}C NMR (151 MHz, CDCl₃) *δ*: 18.8 (CH₃), 43.8 (CH₂), 55.4 (CH₂), 56.1 (OCH₃), 71.2 (CH), 110.3 (CH), 120.3 (CH), 121.3 (C), 126.1 (CH), 127.3 (CH), 127.5 (CH), 128.7 (CH), 133.3 (CH), 134.5 (C), 134.7 (C), 138.7 (C), 142.2 (C), 143.6 (CH), 155.9 (C), 157.9 (C), 164.8 (C), 173.1 (C) ppm. HR-MS *m/z* [M+H]⁺ calcd for C₂₇H₂₈N₄O₃S: 489.1955, found 489.1946.

7.1.3.7. 6-(3-Methoxy-4-formamidophenyl)-3-(cis-2,6-dimethylmorpholino)isothiazolo[4,3-b]pyridine (7a).

To a solution of 6-(4-amino-3-methoxyphenyl)-3-(cis-2,6-dimethylmorpholino)isothiazolo[4,3-b]pyridine (1 equiv) in formamide (10 mL) was added MnO₂ (5% mol) in one portion. The reaction mixture was stirred at 150 °C for 5 h. After completion of the reaction as monitored by TLC, the volatiles were evaporated to dryness and the residue was purified by silica gel flash chromatography, using a mixture of hexane and acetyl acetate, yielding the title compound as an amorphous yellow solid in 73% yield (39.2 mg, 0.10 mmol). Mp 234.3–235.7 °C. Doubling of signals for the protons of the amine and the formyl group in the ^{1}H NMR spectrum at 25 °C was observed, due to restricted rotation around the C∈N amide bond. Based on the integration of the signals in ^{1}H NMR spectrum, the ratio of the isomers was determined to be 95:5 (*cis:trans*).[28] When running the ^{1}H NMR spectrum at 50 °C, coalescence of both signals is observed (see Supporting Information). ^{1}H NMR (600 MHz, DMSO) *δ*: 1.19 (d, *J* = 6.2 Hz, 6H, 2 × CH₃), 2.89 (t, *J* = 11.5 Hz, 2H, 2 × NCH), 3.83–3.89 (m, 2H, 2 × OCH), 3.98 (s, 3H, OCH₃), 4.51 (d, *J* = 12.0 Hz, 1H, 2 × NCH), 7.42 (dd, *J* = 8.3, 1.3 Hz, 1H, arom H), 7.50 (d, *J* = 1.4 Hz, 1H, arom H), 8.06 (d, *J* = 1.8 Hz, 1H, arom H), 8.31 (d, *J* = 8.3 Hz, 1H, arom H), 8.35 (d, *J* = 1.3 Hz, 1H, HCO), 8.80 (d, *J* = 1.8 Hz, 1H, arom H), 9.80 (s, 1H, NH) ppm. ^{13}C NMR (151 MHz, DMSO) *δ*: 18.6 (CH₃), 54.8 (CH₂), 56.2 (OCH₃), 70.6 (CH), 110.0 (CH), 119.5 (CH), 120.5 (CH), 124.3 (CH), 127.5 (C), 132.3 (C), 133.3 (C), 134.5 (C), 144.0 (CH), 149.0 (C), 155.7 (C), 160.3 (HCO), 172.3 (C)

ppm. HR-MS *m/z* [M+H]$^+$ calcd for C$_{20}$H$_{22}$N$_4$O$_3$S: 399.1485, found 399.1485.

7.1.4. Synthesis of 6-(4-aminyl-3-methoxyphenyl)-3-(cis-2,6-dimethyl-morpholino) isothiazolo[4,3-b]pyridine

General procedure. To a solution of the precursor (6-(4-amino-3-methoxyphenyl)-3-(*cis*-2,6-dimethylmorpholino)isothiazolo[4,3-*b*]pyridine) (1 equiv) in dry dichloromethane (15 mL), was added trimethylamine (2 equiv). The reaction mixture was stirred under argon for 10 min and cooled to 0 °C. Then, the appropriate acid chloride (1.5 equiv) or acetic anhydride (2 equiv) was added and the resulting mixture was stirred at room temperature overnight. After completion of the reaction as monitored by TLC, dichloromethane was added (10 mL) and the reaction mixture was washed with 0.5 M HCl solution (2 × 10 mL) and water (20 mL). The organic layer was dried over anhydrous Na$_2$SO$_4$ and concentrated *in vacuo*. The resulting residue was purified by silica gel flash chromatography, yielding the title compound. The following compounds were made according to this procedure.

7.1.4.1. 6-(3-Methoxy-4-acetamidophenyl)-3-(cis-2,6-dimethylmorpholino) isothiazolo[4,3-b]pyridine (7b).

This compound was obtained using acetic anhydride. The crude residue was purifi   by silica gel fl chromatography using a mixture of dichloromethane and acetone (in a ratio of 95:5) as mobile phase, affording the title compound as an amorphous yellow solid in 73% yield (32.5 mg, 0.08 mmol). Mp 255.1–256–4 °C. ^{1}H NMR (600 MHz, CDCl$_3$) δ: 1.32 (d, *J* = 6.3 Hz, 6H, 2 × CH$_3$), 2.24 (s, 3H, CH$_3$), 2.92 (dd, *J* = 12.6, 10.7 Hz, 2H, 2 × NCH), 3.92–3.98 (m, 5H, 2 × OCH, OCH$_3$), 4.52 (dd, *J* = 12.8, 1.9 Hz, 2H, 2 × NCH), 7.14 (d, *J* = 1.9 Hz, 1H, arom H), 7.28 (dd, *J* = 8.3, 1.9 Hz, 1H, arom H), 7.82 (s, 1H, NH), 7.86 (d, *J* = 2.1 Hz, 1H, arom H), 8.49 (d, *J* = 8.4 Hz, 1H, arom H), 8.63 (d, *J* = 2.1 Hz, 1H, arom H) ppm. ^{13}C NMR (151 MHz, CDCl$_3$) δ: 18.8 (CH$_3$), 25.0 (CH$_3$), 55.4 (CH$_2$), 55.8 (OCH$_3$), 71.2 (CH), 108.7 (CH), 120.1 (CH), 120.2 (CH), 125.0 (CH), 128.1 (C), 132.9 (C), 134.0 (C), 135.4 (C), 144.1 (CH), 148.1 (C), 156.3 (C), 168.2 (C), 172.9 (C) ppm. HR-MS *m/z* [M+H]$^+$ calcd for C$_{21}$H$_{24}$N$_4$O$_3$S: 413.1642, found 413.1638.

7.1.4.2. 6-(3-Methoxy-4-cyclopropylamidophenyl)-3-(cis-2,6-dimethyl-morpholino) isothiazolo[4,3-b]pyridine (7c).

This compound was obtained using cyclopropanecarbonyl chloride. The crude residue was purified by silica gel flash chromatography using a mixture of hexane and ethyl acetate (in a ratio of 6:4) as mobile phase, affording the title compound as an amorphous yellow solid in 79% yield (37 mg, 0.08 mmol). Mp 256.4–257.8 °C. ^{1}H NMR (500 MHz, CDCl$_3$) δ: 0.85–0.91 (m, 2H, CH$_2$), 1.10–1.14 (m, 2H, CH$_2$), 1.32 (d, *J* = 6.3 Hz, 6H, 2 × CH$_3$), 1.57–1.64 (m, 1H, CH), 2.92 (dd, *J* = 12.5, 10.7 Hz, 2H, 2 × NCH), 3.94 (m, 2H, 2 × OCH), 3.98 (s, 3H, OCH$_3$), 4.51 (dd, *J* = 12.6, 1.7 Hz, 2H, 2 × NCH), 7.15 (d, *J* = 1.9 Hz, 1H, arom H), 7.26–7.28 (m, 1H, arom H), 7.86 (d, *J* = 2.1 Hz, 1H, arom H), 8.05 (bs, 1H, NH), 8.48 (d, *J* = 8.2 Hz, 1H, arom H), 8.64 (d, *J* = 2.1 Hz, 1H, arom H) ppm. ^{13}C NMR (126 MHz, CDCl$_3$) δ: 8.1 (CH$_2$), 18.8 (CH$_3$), 55.4 (CH$_2$), 55.8 (CH$_3$), 71.2 (CH), 108.8 (CH), 120.0 (CH), 120.2 (CH), 124.9 (CH), 128.4 (C), 132.6 (C), 134.0 (C), 135.5 (C), 144.2 (CH), 148.0 (C), 156.3 (C), 171.8 (C), 172.9 (C) ppm. HR-MS *m/z* [M+H]$^+$ calcd for C$_{23}$H$_{26}$N$_4$O$_3$S: 439.1798, found 439.1794.

7.1.4.3. 6-(3-Methoxy-4-phenylamidophenyl)-3-(cis-2,6-dimethylmopholino) isothiazolo[4,3-b]pyridine (7d).

This compound was obtained using benzoyl chloride. The crude residue was purifi   by silica gel fl chromatography using a mixture of dichloromethane and acetone (in a ratio of 95:5) as mobile phase, aff   the title compound as an amorphous yellow solid in 81% yield (41.1 mg, 0.09 mmol). Mp 195.4–196.3 °C. ^{1}H NMR (600 MHz, CDCl$_3$) δ: 1.32 (d, *J* = 6.3 Hz, 6H, 2 × CH$_3$), 2.93 (dd, *J* = 12.5, 10.7 Hz, 2H, 2 × NCH), 3.93–3.98 (m, 2H, 2 × OCH), 4.02 (s, 3H, OCH$_3$), 4.53 (dd, *J* = 12.7, 1.8 Hz, 2H, 2 × NCH),

7.20 (d, *J* = 1.9 Hz, 1H, arom H), 7.35 (dd, *J* = 8.3, 1.9 Hz, 1H, arom H), 7.50–7.55 (m, 2H, arom H), 7.56–7.60 (m, 1H, arom H), 7.90 (d, *J* = 2.1 Hz, 1H, arom H), 7.91–7.95 (m, 2H, arom H), 8.62 (bs, *J* = 8.2 Hz, 1H, NH), 8.66–8.69 (m, 2H, arom H) ppm. ^{13}C NMR (151 MHz, CDCl$_3$) δ: 18.8 (CH$_3$), 55.4 (CH$_2$), 56.0 (OCH$_3$), 71.2 (CH), 108.8 (CH), 120.2 (CH), 120.3 (CH), 125.0 (CH), 127.1 (CH), 128.2 (C), 128.8 (CH), 131.9 (CH), 133.2 (C), 134.1 (C), 135.1 (C), 135.4 (C), 144.2 (CH), 148.6 (C), 156.3 (C), 165.3 (C), 172.9 (C) ppm. HR-MS *m/z* [M+H]$^+$ calcd for C$_{26}$H$_{26}$N$_4$O$_3$S: 475.1798, found 475.1794.

7.1.4.4. Synthesis of 6-aryl-3-nitropyridine-2-carbonitriles (9a-i). General procedure.

A solution of 6-chloro-2-cyano-3-nitropyridine (1 equiv) in toluene or dioxane/water (see compound description) was degassed with argon and subsequently, the corresponding aryl boronic acid (1.2 equiv), Pd(PPh$_3$)$_4$ (0.02 equiv) and K$_2$CO$_3$ (2 equiv) were added. The mixture was degassed a second time, filled with argon and stirred at 95 °C overnight. After completion of the reaction as monitored by TLC, the volatiles were evaporated to dryness and the crude residue was diluted with EtOAc (20 mL) and washed with water (2 × 20 mL). The organic layer was dried over anhydrous Na$_2$SO$_4$ and concentrated *in vacuo*. The resulting residue was purified by silica gel flash chromatography, yielding the corresponding 6-aryl-3-nitropyridine-2-carbonitrile. The following compounds were made according to this procedure.

7.1.4.5. 3-Nitro-6-phenylpyridine-2-carbonitrile (9a).

This compound was obtained using phenyl boronic acid and toluene as solvent. The crude residue was purified by silica gel flash chromatography using a mixture of hexane and ethyl acetate (in a ratio of 8:2) as mobile phase, affording the title compound as an amorphous light yellow solid in 81% yield (397.6 mg, 1.8 mmol). ^{1}H NMR (300 MHz, CDCl$_3$) δ: 8.65 (d, *J* = 8.9 Hz, 1H, arom H), 8.11–8.19 (m, 3H, arom H), 7.53–7.62 (m, 3H, arom H) ppm. HR-MS *m/z* [M+H]$^+$ calcd for C$_{12}$H$_7$N$_3$O$_2$: 226.0611, found 226.0611.

7.1.4.6. 6-(4-(Trifluoromethyl)phenyl)-3-nitropyridine-2-carbonitrile (9b).

This compound was obtained using 4-(trifluoromethyl)phenyl boronic acid and toluene as solvent. The crude residue was purified by silica gel flash chromatography using a mixture of hexane and dichloromethane (in a ratio of 4:6) as mobile phase, affording the title compound as an amorphous light yellow solid in 85% yield (543.3 mg, 1.85 mmol). ^{1}H NMR (600 MHz, CDCl$_3$) δ: 7.84 (dd, *J* = 8.7, 0.5 Hz, 2H, arom H), 8.22 (d, *J* = 8.8 Hz, 1H, arom H), 8.27 (dd, *J* = 8.8, 0.7 Hz, 2H, arom H), 8.72 (d, *J* = 8.8 Hz, 1H, arom H) ppm. HR-MS *m/z* [M+Na]$^+$ calcd for C$_{13}$H$_6$F$_3$N$_3$O$_2$: 316.0305, found 316.0312.

7.1.4.7. 6-(4-Fluorophenyl)-3-nitropyridine-2-carbonitrile (9c).

This compound was obtained using 4-fl   acid and toluene as solvent. The crude residue was purified by silica gel flash chromatography using a mixture of hexane and dichloromethane (in a ratio of 4:6) as mobile phase, aff   the title compound as an amorphous light yellow solid in 94% yield (498.3 mg, 2.05 mmol). ^{1}H NMR (300 MHz, CDCl$_3$) δ: 7.21–7.29 (m, 2H, arom H), 8.11 (d, *J* = 8.9 Hz, 1H, arom H), 8.14–8.20 (m, 2H, arom H), 8.65 (d, *J* = 8.9 Hz, 1H, arom H) ppm. HR-MS *m/z* [M+H]$^+$ calcd for C$_{12}$H$_6$FN$_3$O$_2$: 244.0517, found 244.0521.

7.1.4.8. 6-(3-Chlorophenyl)-3-nitropyridine-2-carbonitrile (9d).

This compound was obtained using 3-chlorophenylboronic acid and toluene as solvent. The crude residue was purified by silica gel flash chromatography using a mixture of hexane and dichloromethane (in a ratio of 4:6) as mobile phase, aff   the title compound as an amorphous white solid in 98% yield (545.2 mg, 2.1 mmol). ^{1}H NMR (300 MHz, CDCl$_3$) δ: 7.47–7.60 (m, 2H, arom H), 8.01 (dt, *J* = 7.3, 1.6 Hz, 1H, arom H), 8.12–8.17 (m, 2H, arom H), 8.67 (d, *J* = 8.8 Hz,

1H, arom H) ppm. HR-MS *m/z* [M+Na]⁺ calcd for $C_{12}H_6ClN_3O_2$: 282.0041 found 282.0044.

7.1.4.9. 6-(4-Methylphenyl)-3-nitropyridine-2-carbonitrile (9e). This compound was obtained using 4-methylphenylboronic acid and toluene as solvent. The crude residue was purified by silica gel flash chromatography using a mixture of hexane and ethyl acetate (in a ratio of 7:3) as mobile phase, affording the title compound as an amorphous light yellow solid in 93% yield (485 mg, 2.03 mmol). ¹H NMR (300 MHz, CDCl₃) δ: 2.46 (s, 3H, CH₃), 7.36 (d, *J* = 8.1 Hz, 2H, arom H), 8.04 (d, *J* = 8.3 Hz, 2H, arom H), 8.10 (d, *J* = 8.9 Hz, 1H, arom H), 8.60 (d, *J* = 8.9 Hz, 1H, arom H) ppm. HR-MS *m/z* [M+H]⁺ calcd for $C_{13}H_9N_3O_2$: 240.0767, found 240.0775.

7.1.4.10. 6-(3-Methoxyphenyl)-3-nitropyridine-2-carbonitrile (9f). This compound was obtained using 3-methoxyphenylboronic acid and toluene as solvent. The crude residue was purified by silica gel flash chromatography using a mixture of hexane and ethyl acetate (in a ratio of 7:3) as mobile phase, affording the title compound as an amorphous yellow solid in 94% yield (523 mg, 2.05 mmol). ¹H NMR (300 MHz, CDCl₃) δ: 3.92 (s, 3H, OCH₃), 7.09–7.15 (m, 1H, arom H), 7.47 (t, *J* = 8.0 Hz, 1H, arom H), 7.63–7.68 (m, 1H, arom H), 7.68–7.72 (m, 1H, arom H), 8.13 (d, *J* = 8.9 Hz, 1H, arom H), 8.63 (d, *J* = 8.9 Hz, 1H, arom H) ppm. HR-MS *m/z* [M+H]⁺ calcd for $C_{13}H_9N_3O_3$: 256.0717, found 256.0715.

7.1.4.11. 6-(3,4-Dimethoxyphenyl)-3-nitropyridine-2-carbonitrile (9g). This compound was obtained using 3,4-dimethoxyphenylboronic acid and toluene as solvent. The crude residue was purified by silica gel flash chromatography using a mixture of hexane and acetone (in a ratio of 7:3) as mobile phase, affording the title compound as an amorphous orange solid in 78% yield (485.1 mg, 1.7 mmol). ¹H NMR (300 MHz, DMSO) δ: 3.87 (s, 3H, OCH₃), 3.90 (s, 3H, OCH₃), 7.17 (d, *J* = 8.6 Hz, 1H, arom H), 7.77 (d, *J* = 2.0 Hz, 1H, arom H), 7.87 (dd, *J* = 8.5, 2.1 Hz, 1H, arom H), 8.54 (d, *J* = 9.0 Hz, 1H, arom H), 8.75 (d, *J* = 9.0 Hz, 1H, arom H) ppm. HR-MS *m/z* [M+H]⁺ calcd for $C_{14}H_{11}N_3O_4$: 286.0822, found 286.0822.

7.1.4.12. 6-(3,4,5-Trimethoxyphenyl)-3-nitropyridine-2-carbonitrile (9h). This compound was obtained using 3,4,5-trimethoxyphenylboronic acid and dioxane/water (in ratio 4:1) as solvent. The crude residue was purifi by silica gel fl chromatography using a mixture of hexane and acetone (in a ratio of 7:3) as mobile phase, aff the title compound as an amorphous orange solid in 96% yield (659.8 mg, 2.1 mmol). ¹H NMR (300 MHz, CDCl₃) δ: 3.94 (s, 3H, OCH₃), 4.00 (s, 6H, 2 × OCH₃), 7.37 (s, 2H, arom H), 8.09 (d, *J* = 8.9 Hz, 1H, arom H), 8.61 (d, *J* = 8.9 Hz, 1H, arom H) ppm. HR-MS *m/z* [M+H]⁺ calcd for $C_{15}H_{13}N_3O_5$: 316.0928, found 316.0931.

7.1.4.13. 6-(3,5-Dimethoxyphenyl)-3-nitropyridine-2-carbonitrile (9i). This compound was obtained using 3,5-dimethoxyphenylboronic acid and toluene as solvent. The crude residue was purified by silica gel flash chromatography using a mixture of hexane and acetone (in a ratio of 7:3) as mobile phase, affording the title compound as an amorphous orange solid in 81% yield (503.5 mg, 2.1 mmol). ¹H NMR (300 MHz, CDCl₃) δ: 3.91 (s, 6H, 2 × OCH₃), 6.66 (t, *J* = 2.2 Hz, 1H, arom H), 7.25 (d, *J* = 2.2 Hz, 2H, arom H), 8.10 (d, *J* = 8.9 Hz, 1H, arom H), 8.62 (d, *J* = 8.9 Hz, 1H, arom H) ppm. HR-MS *m/z* [M+H]⁺ calcd for $C_{14}H_{11}N_3O_4$: 286.0822, found 286.0818.

7.1.4.14. Synthesis of 3-amino-6-aryl-pyridine-2-carbonitriles (10a-i). General procedure. To a stirred suspension of iron powder (3 equiv) in acetic acid (40 mL) at 60 °C, the corresponding 6-aryl-3- nitropyridine-2-carbonitrile (1 equiv) was added. The reaction mixture was stirred at 60 °C until disappearance of the starting material as monitored by TLC (3–6 h). After cooling, the volatiles were evaporated

to dryness and the crude was diluted with EtOAc (50 mL) and filtered through a paper filter. The filter cake was washed repeated times with ethyl acetate. The organic phase was washed with aqueous solution 1 N NaOH (3 × 30 mL), dried over anhydrous Na₂SO₄ and evaporated to dryness. This mixture of two compounds (3-amino-6-aryl-pyridine-2-carbonitrile as the major and 3-amino-6-aryl-pyridine-2-carboxamide as the minor compound) was used as such in the next reaction.

7.1.4.15. Synthesis of 3-amino-6-aryl-pyridine-2-carbothioamides (11a-i). General procedure. To a solution of the crude mixture of 3-amino-6-aryl-pyridine-2-carbonitrile and 3-amino-6-aryl-pyridine-2-carboxamide in absolute ethanol (40 mL), was added phosphorus pentasulfi (1.2 equiv). The corresponding solution was then heated overnight at 75 °C overnight. After the completion of the reaction as monitored by TLC, the solvent was evaporated to dryness and the residue was washed with an aqueous 1 N NaOH (2 × 30 mL) solution, dried over anhydrous Na₂SO₄ and evaporated to dryness. The residue was purifi by silica gel fl chromatography yielding the 3-amino-6-aryl-pyridine-2-carbothioamide. The following compounds were made according to this procedure.

7.1.4.15.1. 3-Amino-6-phenylpyridine-2-carbothioamide (11a). This compound was obtained from a crude mixture of 3-amino-6-phenylpyridine-2-carbonitrile and 3-amino-6-phenylpyridine-2-carboxamide. The residue was purifi by silica gel fl chromatography using a mixture of hexane and ethyl acetate (in a ratio of 8:2) as mobile phase, affording the title compound as an amorphous yellow solid in 71% yield (166.8 mg, 0.73 mmol). ¹H NMR (300 MHz, DMSO) δ: 7.35 (m, 2H, arom H), 7.43 (m, 2H, arom H), 7.84 (bs, 2H, NH₂), 7.90 (d, *J* = 8.7 Hz, 1H, arom H), 8.08 (d, *J* = 7.4 Hz, 2H, arom H), 9.66 (bs, 1H, NH), 9.74 (bs, 1H, NH) ppm. HR-MS *m/z* [M+H]⁺ calcd for $C_{12}H_{11}N_3S$: 230.0746, found 230.0743.

7.1.4.15.2. 3-Amino-6-(4-trifluoromethylphenyl)pyridine-2-carbothioamide (11b). This compound was obtained from a crude mixture of 3-amino-6-(4-trifluoromethylphenyl)pyridine-2-carbonitrile and 3-amino-6-(4-trifluoromethylphenyl)pyridine-2-carboxamide. The residue was purified by silica gel flash chromatography using a mixture of hexane and ethyl acetate (in a ratio of 7:3) as mobile phase, affording the title compound as an amorphous yellow solid in 81% yield (183 mg, 0.62 mmol). ¹H NMR (300 MHz, DMSO) δ: 7.37 (d, *J* = 8.8 Hz, 1H, arom H), 7.75 (d, *J* = 8.4 Hz, 2H, arom H), 7.99 (d, *J* = 8.8 Hz, 1H, arom H), 7.93 (bs, 2H, NH₂), 8.32 (d, *J* = 8.2 Hz, 2H, arom H), 9.74 (s, 1H, NH), 9.78 (s, 1H, NH) ppm. HR-MS *m/z* [M+H]⁺ calcd for $C_{13}H_{10}F_3N_3S$: 298.0620, found 298.0614.

7.1.4.15.3. 3-Amino-6-(4-fluorophenyl)pyridine-2-carbothioamide (11c). This compound was obtained from a crude mixture of 3-amino-6-(4-fluorophenyl)pyridine-2-carbonitrile and 3-amino-6-(4-fluorophenyl)pyridine-2-carboxamide. The residue was purified by flash chromatography using a mixture of hexane and ethyl acetate (in a ratio of 8:2) as mobile phase, affording the title compound as an amorphous yellow solid in 79% yield (160.4 mg, 0.65 mmol). ¹H NMR (300 MHz, DMSO) δ: 7.23 (t, *J* = 8.8 Hz, 2H, arom H), 7.34 (d, *J* = 8.8 Hz, 1H, arom H), 7.83 (s, 2H, NH₂), 7.88 (d, *J* = 8.8 Hz, 1H, arom H), 8.15 (dd, *J* = 8.7, 5.6 Hz, 2H, arom H), 9.75 (bs, 1H, NH), 9.66 (bs, 1H, NH) ppm. HR-MS *m/z* [M+H]⁺ calcd for $C_{12}H_{10}FN_3S$: 248.0652, found 248.0651.

7.1.4.15.4. 3-Amino-6-(3-chlorophenyl)pyridine-2-carbothioamide (11d). This compound was obtained from a crude mixture of 3-amino-6-(3-chlorophenyl)pyridine-2-carbonitrile and 3-amino-6-(3-chlorophenyl) pyridine-2-carboxamide. The residue was purifi by silica gel fl chromatography using a mixture of hexane and ethyl acetate (in a ratio of 8:2) as mobile phase, affording the title compound as an amorphous yellow solid in 71% yield (173 mg, 0.62 mmol). ¹H NMR (300 MHz, DMSO) δ: 7.31–7.48 (m, 3H, arom H), 7.86 (bs, 2H, NH₂), 7.94 (d, *J* = 8.8 Hz, 1H, arom H), 8.04 (d, *J* = 7.6 Hz, 1H, arom H), 8.19 (t, *J* = 1.6 Hz 1H, arom H), 9.68 (bs, 1H, NH), 9.79 (bs, 1H, NH) ppm. HR-MS *m/z* [M+H]⁺ calcd for $C_{12}H_{10}ClN_3S$: 264.0357, found 264.0353.

7.1.4.15.5. 3-Amino-6-(4-methylphenyl)pyridine-2-carbothioamide

(11e). This compound was obtained from a crude mixture of 3-amino-6-(4-methylphenyl)pyridine-2-carbonitrile and 3-amino-6-(4-methylphenyl)pyridine-2-carboxamide. The residue was purifi   by silica gel fl chromatography using a mixture of hexane and ethyl acetate (in a ratio of 8:2) as mobile phase, aff   the title compound as an amorphous yellow solid in 83% yield (242.3 mg, 1.0 mmol). ^{1}H NMR (300 MHz, DMSO) δ: 2.34 (s, 3H, CH$_3$), 7.23 (d, $J = 8.0$ Hz, 2H, arom H), 7.32 (d, $J = 8.8$ Hz, 1H, arom H), 7.80 (bs, 2H, NH$_2$), 7.86 (d, $J = 8.8$ Hz, 1H, arom H), 7.97 (d, $J = 8.2$ Hz, 2H, arom H), 9.63 (bs, 1H, NH), 9.72 (bs, 1H, NH) ppm. HR-MS *m/z* [M+H]$^+$ calcd for C$_{13}$H$_{13}$N$_3$S: 244.0903, found 244.0916.

7.1.4.15.6. 3-Amino-6-(3-methoxyphenyl)pyridine-2-carbothioamide (11f). This compound was obtained from a crude mixture of 3-amino-6-(3-methoxyphenyl)pyridine-2-carbonitrile and 3-amino-6-(4-methoxyphenyl)pyridine-2-carboxamide. The residue was purifi   by silica gel fl chromatography using a mixture of hexane and ethyl acetate (in a ratio of 8:2) as mobile phase, aff   the title compound as an amorphous yellow solid in 72% yield (261.4 mg, 1.0 mmol). ^{1}H NMR (300 MHz, DMSO) δ: 3.83 (s, 3H, OCH$_3$), 6.91 (dd, $J = 8.1$, 2.5 Hz, 1H, arom H), 7.30–7.38 (m, 2H, arom H), 7.57–7.66 (m, 2H, arom H), 7.89 (d, $J = 8.8$ Hz, 1H, arom H), 9.66 (bs, 1H, NH), 9.72 (bs, 1H, NH) ppm. HR-MS *m/z* [M+H]$^+$ calcd for C$_{13}$H$_{13}$N$_3$OS: 260.0852, found 260.0848.

7.1.4.15.7. 3-Amino-6-(3,4-dimethylphenyl)pyridine-2-carbothioamide (11g). This compound was obtained from a crude mixture of 3-amino-6-(3,4-dimethylphenyl)pyridine-2-carbonitrile and 3-amino-6-(3,4-dimethylphenyl)pyridine-2-carboxamide. The residue was purified by silica gel flash chromatography using a mixture of hexane and ethyl acetate (in a ratio of 7:3) as mobile phase, affording the title compound as an amorphous yellow solid in 73% yield (165.4 mg, 0.57 mmol). ^{1}H NMR (300 MHz, DMSO) δ: 3.79 (s, 3H, OCH$_3$), 3.86 (s, 3H, OCH$_3$), 6.99 (d, $J = 8.4$ Hz, 1H, arom H), 7.32 (d, $J = 8.8$ Hz, 1H, arom H), 7.55–7.60 (m, 1H, arom H), 7.62 (d, $J = 1.9$ Hz, 1H, arom H), 7.76 (bs, 2H, NH$_2$), 7.86 (d, $J = 8.8$ Hz, 1H, arom H), 9.62 (bs, 1H, NH), 9.71 (bs, 1H, NH) ppm. HR-MS *m/z* [M+H]$^+$ calcd for C$_{14}$H$_{15}$N$_3$O$_2$S: 290.0958, found 290.0941.

7.1.4.15.8. 3-Amino-6-(3,4,5-trimethoxyphenyl)pyridine-2-carbothioamide (11h). This compound was obtained from a crude mixture of 3-amino-6-(3,4,5-trimethoxyphenyl)pyridine-2-carbonitrile and 3-amino-6-(3,4,5-trimethoxyphenyl)pyridine-carboxamide. The residue was purified by silica gel flash chromatography using a mixture of hexane and ethyl acetate (in a ratio of 6:4) as mobile phase, affording the title compound as an amorphous yellow solid in 76% yield (170.1 mg, 0.53 mmol). ^{1}H NMR (600 MHz, CDCl$_3$) δ: 3.90 (s, 3H, OCH$_3$), 3.95 (s, 6H, 2 × OCH$_3$), 6.94 (bs, 2H, NH$_2$), 7.05 (s, 2H, arom H), 7.15–7.18 (m, 1H, arom H), 7.30 (bs, 1H, NH), 7.62–7.64 (m, 1H, arom H), 9.64 (bs, 1H, NH) ppm. HR-MS *m/z* [M+H]$^+$ calcd for C$_{15}$H$_{17}$N$_3$O$_3$S: 320.1063, found 320.1072.

7.1.4.15.9. 3-Amino-6-(3,5-dimethylphenyl)pyridine-2-carbothioamide (11i). This compound was obtained from a crude mixture of 3-amino-6-(3,5-dimethylphenyl)pyridine-2-carbonitrile and 3-amino-6-(3,5-dimethylphenyl)pyridine-2-carboxamide. The residue was purified by silica gel flash chromatography using a mixture of hexane and ethyl acetate (in a ratio of 7:3) as mobile phase, affording the title compound as an amorphous yellow solid in 76% yield (258.3 mg, 1.17 mmol). ^{1}H NMR (300 MHz, DMSO) δ: 3.81 (s, 6H, 2 × OCH$_3$), 6.48 (t, $J = 2.1$ Hz, 1H, arom H), 7.18 (d, $J = 2.2$ Hz, 2H, arom H), 7.32 (d, $J = 8.8$ Hz, 1H, arom H), 7.81 (bs, 2H, NH$_2$), 7.88 (d, $J = 8.8$ Hz, 1H, arom H), 9.65 (bs, 1H, NH), 9.70 (bs, 1H, NH) ppm. HR-MS *m/z* [M+H]$^+$ calcd for C$_{14}$H$_{15}$N$_3$O$_2$S: 290.0958, found 290.0963.

7.1.5. Synthesis of 3-amino-5-(aryl)isothiazolo[4,3-b]pyridines (12a-i)
General procedure. To a solution of a 3-amino-6-(aryl)pyridine-2-carbothioamides (1 equiv) in methanol (50 mL) was added dropwise a 35% H$_2$O$_2$ (2.5 equiv) solution in water at 0 °C. The reaction mixture was stirred overnight at room temperature. After disappearance of the

starting material as monitored by TLC, the solvent was evaporated to dryness affording the desired 3-amino-5-aryl-isothiazolo[4,3-*b*]pyridine, that was used as such in the next reaction without any further purification. The following compounds were made according to this procedure.

7.1.5.1. 3-Amino-5-(phenyl)isothiazolo[4,3-b]pyridine (12a). This compound was prepared from 3-amino-6-phenylpyridine-2-carbothioamide aff   the title compound as an amorphous yellow solid in 95% yield (89.4 mg, 0.39 mmol). ^{1}H NMR (600 MHz, DMSO) δ: 7.41–7.46 (m, 1H, arom H), 7.48–7.53 (m, 2H, arom H), 7.81 (d, $J = 9.2$, 1H, arom H), 7.96 (d, $J = 9.3$ Hz, 1H, arom H), 8.20–8.24 (m, 2H, arom H) ppm. HR-MS *m/z* [M+H]$^+$ calcd for C$_{12}$H$_9$N$_3$S: 228.0590, found 228.0583.

7.1.5.2. 3-Amino-5-(4-trifluoromethylphenyl)isothiazolo[4,3-b]pyridine (12b). This compound was prepared from 3-amino-6-(4-fluorophenyl)pyridine-2-carbothioamide affording the title compound as an amorphous yellow solid in 97% yield (120.3 mg, 0.41 mmol). ^{1}H NMR (300 MHz, DMSO) δ: 7.79–7.89 (m, 3H, arom H), 8.01 (d, $J = 9.4$ Hz, 1H, arom H), 8.10 (bs, 2H, NH$_2$), 8.44 (d, $J = 8.1$ Hz, 2H, arom H) ppm. HR-MS *m/z* [M+H]$^+$ calcd for C$_{13}$H$_8$F$_3$N$_3$S: 296.0464, found 296.0471.

7.1.5.3. 3-Amino-5-(4-fluorophenyl)isothiazolo[4,3-b]pyridine (12c). This compound was prepared from 3-amino-6-(4-fluorophenyl)pyridine-2-carbothioamide affording the title compound as an amorphous yellow solid in 98% yield (106.9 mg, 0.44 mmol). ^{1}H NMR (600 MHz, DMSO) δ: 7.30–7.36 (m, 2H, arom H), 7.79 (d, $J = 9.3$ Hz, 1H, arom H), 7.90 (bs, 2H, NH$_2$), 7.91 (d, $J = 9.4$ Hz, 1H, arom H), 8.25–8.30 (m, 2H, arom H) ppm. HR-MS *m/z* [M+H]$^+$ calcd for C$_{12}$H$_8$FN$_3$S: 246.0496, found 246.0506.

7.1.5.4. 3-Amino-5-(3-chlorophenyl)isothiazolo[4,3-b]pyridine (12d). This compound was prepared from 3-amino-6-(3-chlorophenyl)pyridine-2-carbothioamide affording the title compound as an amorphous yellow solid in 97% yield (192.9 mg, 0.74 mmol). ^{1}H NMR (300 MHz, DMSO) δ: 7.45–7.57 (m, 2H, arom H), 7.79 (d, $J = 9.4$ Hz, 1H, arom H), 7.97 (d, $J = 9.4$ Hz, 1H, arom H), 8.07 (bs, 2H, NH$_2$), 8.15 (d, $J = 7.4$ Hz, 1H, arom H), 8.36 (s, 1H, arom H) ppm. HR-MS *m/z* [M+H]$^+$ calcd for C$_{12}$H$_8$ClN$_3$S: 262.0200, found 262.0196.

7.1.5.5. 3-Amino-5-(4-methylphenyl)isothiazolo[4,3-b]pyridine (12e). This compound was prepared from 3-amino-6-(4-methylphenyl)pyridine-2-carbothioamide affording the title compound as an amorphous yellow solid in 98% yield (194.0 mg, 0.8 mmol). ^{1}H NMR (300 MHz, DMSO) δ: 2.37 (s, 3H, CH$_3$), 7.31 (d, $J = 8.1$ Hz, 2H, arom H), 7.78 (d, $J = 9.4$ Hz, 1H, arom H), 7.93 (d, $J = 9.3$ Hz, 1H, arom H), 7.96 (bs, 2H, NH$_2$), 8.13 (d, $J = 8.1$ Hz, 2H, arom H) ppm. HR-MS *m/z* [M+H]$^+$ calcd for C$_{13}$H$_{11}$N$_3$S: 242.0746, found 242.0750.

7.1.5.6. 3-Amino-5-(3-methoxyphenyl)isothiazolo[4,3-b]pyridine (12f). This compound was prepared from 3-amino-6-(3-methoxyphenyl)pyridine-2-carbothioamide affording the title compound as an amorphous yellow solid in 91% yield (117.4 mg, 0.46 mmol). ^{1}H NMR (600 MHz, DMSO) δ: 3.86 (s, OCH$_3$), 7.02 (dd, $J = 8.1$, 2.2 Hz, 1H, arom H), 7.41 (t, $J = 7.9$ Hz, 1H, arom H), 7.78 (d, $J = 7.7$ Hz, 1H, arom H), 7.81–7.85 (m, 2H, arom H), 8.01 (d, $J = 9.0$ Hz, 2H, arom H) ppm. HR-MS *m/z* [M+H]$^+$ calcd for C$_{13}$H$_{11}$N$_3$OS: 258.0696, found 258.0688.

7.1.5.7. 3-Amino-5-(3,4-dimethoxyphenyl)isothiazolo[4,3-b]pyridine (12g). This compound was prepared from 3-amino-6-(3,4-dimethylphenyl)pyridine-2-carbothioamide aff   the title compound as an amorphous yellow solid in 92% yield (79.3 mg, 0.28 mmol). ^{1}H NMR (600 MHz, DMSO) δ: 3.83 (s, 3H, OCH$_3$), 3.90 (s, 3H, OCH$_3$), 7.05

(d, *J* = 8.5 Hz, 1H, arom H), 7.72 (dd, *J* = 8.4, 2.1 Hz, 1H, arom H), 7.76 (d, *J* = 9.4 Hz, 1H, arom H), 7.91 (d, *J* = 2.0 Hz, 1H, arom H), 7.94 (d, *J* = 9.4 Hz, 1H, arom H) ppm. HR-MS *m/z* [M+H]$^+$ calcd for $C_{14}H_{13}N_3O_2S$: 288.0801, found 288.0798.

7.1.5.8. 3-Amino-5-(3,4,5-trimethoxyphenyl)isothiazolo[4,3-b]pyridine (12h).

This compound was prepared from 3-amino-6-(3,4,5-trimethylphenyl)pyridine-2-carbothioamide affording the title compound as an amorphous orange solid in 94% yield (112.1 mg, 0.35 mmol). ^{1}H NMR (300 MHz, DMSO) *δ*: 3.73 (s, 3H, OCH$_3$), 3.92 (s, 6H, 2 × OCH$_3$), 7.54 (s, 2H, arom H), 7.78 (d, *J* = 9.4 Hz, 1H, arom H), 8.02 (d, *J* = 9.4 Hz, 1H, arom H) ppm. HR-MS *m/z* [M+H]$^+$ calcd for $C_{15}H_{15}N_3O_3S$: 318.0907, found 318.0904.

7.1.5.9. 3-Amino-5-(3,5-dimethoxyphenyl)isothiazolo[4,3-b]pyridine (12i).

This compound was prepared from 3-amino-6-(3,5-dimethylphenyl)pyridine-2-carbothioamide aff   the title compound as an amorphous yellow solid in 93% yield (92.2 mg, 0.35 mmol). ^{1}H NMR (300 MHz, DMSO) *δ*: 3.85 (s, 6H, 2 × OCH$_3$), 6.57 (bs, 1H, arom H), 7.40 (s, 2H, arom H), 7.77 (d, *J* = 9.4 Hz, 1H, arom H), 7.95 (d, *J* = 9.4 Hz, 1H, arom H), 8.05 (bs, 2H, NH$_2$) ppm. HR-MS *m/z* [M+H]$^+$ calcd for $C_{14}H_{13}N_3O_2S$: 288.0801, found 288.0803.

7.1.6. Synthesis of 5-aryl-3-bromoisothiazolo[4,3-b]pyridines (13a-h)

General procedure A. A solution of 5-aryl-3-aminoisothiazolo[4,3-b] pyridine (1 equiv) in HBr (30 mL) was stirred for 10 min at room temperature, and then CuBr was added (2 equiv). The resulting mixture was cooled at 0 °C. A solution of sodium nitrite (3 equiv) in H$_2$O (15 mL) was added dropwise over a period of 30 min. The reaction mixture was stirred for 2 h at 0 °C and overnight at room temperature. The mixture was cooled at 0 °C and carefully neutralized with a 2 N NaOH solution. The mixture was extracted with ethyl acetate (3 × 30 mL) and the combined organic layers were dried over anhydrous Na$_2$SO$_4$ and evaporated to dryness. The crude residue was purified by silica gel flash chromatography (using a mixture of hexane/ethyl acetate as mobile phase), yielding the corresponding 5-aryl-3-bromoisothiazolo[4,3-b]pyridine.

General procedure B. To a stirred solution of CuBr$_2$ (1.2 equiv) and 5-aryl-3-aminoisothiazolo[4,3-b]pyridine (1 equiv) in dry acetonitrile (15 mL) under argon atmosphere at −10 °C, was slowly added *tert*-butylnitrite (1.3 equiv). The resulting mixture was stirred at 0 °C for 2 h and additional 3 h at room temperature. After disappearance of the starting material as monitored by TLC, the volatiles were evaporated and the crude residue was purified by silica gel flash column chromatography (using a mixture of hexane/ethyl acetate as eluent) yielding the corresponding 5-aryl-3-bromoisothiazolo[4,3-b]pyridine.

The following compounds were made according to the general procedure A:

7.1.6.1. 3-Bromo-5-(phenyl)isothiazolo[4,3-b]pyridine (13a).

This compound was prepared from 3-amino-5-phenylisothiazolo[4,3-b]pyridine and the residue was purified by flash chromatography using a mixture of hexane and ethyl acetate (in a ratio of 9:1) as mobile phase, affording the title compound as an amorphous white solid in 61% yield (39 mg, 0.13 mmol). ^{1}H NMR (300 MHz, CDCl$_3$) *δ*: 7.48–7.58 (m, 3H, arom H), 7.90 (d, *J* = 9.3 Hz, 1H, arom H), 8.11–8.22 (m, 3H, arom H) ppm. HR-MS *m/z* [M+H]$^+$ calcd for $C_{12}H_7BrN_2S$: 290.9587, found 290.9590.

7.1.6.2. 3-Bromo-5-(4-trifluoromethylphenyl)isothiazolo[4,3-b]pyridine (13b).

This compound was prepared from 3-amino-5-(4-trifl   b]pyridine and the residue was purifi   by fl chromatography using a mixture of hexane and ethyl acetate (in a ratio of 9:1) as mobile phase, aff   the title compound as an amorphous white solid in 57% yield (48.3 mg, 0.13 mmol). ^{1}H NMR (300 MHz, CDCl$_3$) *δ*: 7.79 (d, *J* = 8.4 Hz, 2H, arom H), 7.91 (d, *J* = 9.3 Hz,

1H, arom H), 8.20 (d, *J* = 9.3 Hz, 1H, arom H), 8.30 (d, *J* = 8.4 Hz, 2H, arom H) ppm. HR-MS *m/z* [M+H]$^+$ calcd for $C_{13}H_6BrF_3N_2S$: 358.9460, found 358.9464.

7.1.6.3. 3-Bromo-5-(4-fluorophenyl)isothiazolo[4,3-b]pyridine (13c).

This compound was prepared from 3-amino-5-(4-fluorophenyl)isothiazolo[4,3-b]pyridine and the residue was purified by flash chromatography using a mixture of hexane and ethyl acetate (in a ratio of 9:1) as mobile phase, affording the title compound as an amorphous white solid in 60% yield (105 mg, 0.34 mmol). ^{1}H NMR (300 MHz, CDCl$_3$) *δ*: 7.21 (m, 2H, arom H), 7.86 (d, *J* = 9.4 Hz, 1H, arom H), 8.14 (d, *J* = 9.4 Hz, 1H, arom H), 8.17–8.23 (m, 2H, arom H) ppm. HR-MS *m/z* [M+H]$^+$ calcd for $C_{12}H_6BrFN_2S$: 308.9492, found 308.9503.

7.1.6.4. 3-Bromo-5-(3-chlorophenyl)isothiazolo[4,3-b]pyridine (13d).

This compound was prepared from 3-amino-5-(3-chlorophenyl)isothiazolo[4,3-b]pyridine and the residue was purified by flash chromatography using a mixture of hexane and ethyl acetate (in a ratio of 8:2) as mobile phase, affording the title compound as an amorphous white solid in 51% yield (25.4 mg, 0.08 mmol). ^{1}H NMR (300 MHz, CDCl$_3$) *δ*: 7.41–7.45 (m, 2H, arom H), 7.87 (d, *J* = 9.4 Hz, 1H, arom H), 8.02–8.09 (m, 1H, arom H), 8.17 (d, *J* = 9.4 Hz, 1H, arom H), 8.21 (s, 1H, arom H) ppm. HR-MS *m/z* [M+H]$^+$ calcd for $C_{12}H_6BrClN_2S$: 324.9197, found 324.9191.

The following compounds were made according to the general procedure B:

7.1.6.5. 3-Bromo-5-(4-methylphenyl)isothiazolo[4,3-b]pyridine (13e).

This compound was prepared from 3-amino-5-(4-methylphenyl)isothiazolo[4,3-b]pyridine and the residue was purified by silica gel flash chromatography using a mixture of hexane and ethyl acetate (in a ratio of 9:1) as mobile phase, affording the title compound as an amorphous white solid in 51% yield (25.5 mg, 0.08 mmol). ^{1}H NMR (300 MHz, CDCl$_3$) *δ*: 2.44 (s, 3H, CH$_3$), 7.34 (d, *J* = 8.1 Hz, 2H, arom H), 7.89 (d, *J* = 9.4 Hz, 1H, arom H), 8.07–8.15 (m, 3H, arom H) ppm. HR-MS *m/z* [M+H]$^+$ calcd for $C_{13}H_9BrN_2S$: 304.9743, found 304.9748.

7.1.6.6. 3-Bromo-5-(3-methoxyphenyl)isothiazolo[4,3-b]pyridine (13f).

This compound was prepared from 3-amino-5-(3-methoxyphenyl)isothiazolo[4,3-b]pyridine and the residue was purifi   by silica gel fl chromatography using a mixture of hexane and ethyl acetate (in a ratio of 9:1) as mobile phase, affording the title compound as an amorphous light yellow solid in 34% yield (62 mg, 0.19 mmol). ^{1}H NMR (300 MHz, CDCl$_3$) *δ*: 3.93 (s, 3H, OCH$_3$), 7.06 (dd, *J* = 8.0, 2.3 Hz, 1H, arom H), 7.44 (t, *J* = 8.0 Hz, 1H, arom H), 7.72 (d, *J* = 7.8 Hz, 1H, arom H), 7.77–7.81 (m, 1H, arom H), 7.89 (d, *J* = 9.4 Hz, 1H, arom H), 8.14 (d, *J* = 9.4 Hz, 1H, arom H) ppm. HR-MS *m/z* [M+H]$^+$ calcd for $C_{13}H_9BrN_2S$: 320.9692, found 320.9693.

7.1.6.7. 3-Bromo-5-(3,4-dimethoxyphenyl)isothiazolo[4,3-b]pyridine (13g).

This compound was prepared from 3-amino-5-(3,4-dimethoxyphenyl)isothiazolo[4,3-b]pyridine and the residue was purified by silica gel flash chromatography using a mixture of hexane and ethyl acetate (in a ratio of 8:2) as mobile phase, affording the title compound as an amorphous light yellow solid in 56% yield (58.2 mg, 0.17 mmol). ^{1}H NMR (300 MHz, CDCl$_3$) *δ*: 3.97 (s, 3H, OCH$_3$), 4.04 (s, 3H, OCH$_3$), 6.98 (d, *J* = 8.4 Hz, 1H, arom H), 7.68 (dd, *J* = 8.4, 2.1 Hz, 1H, arom H), 7.89 (dd, *J* = 6.6, 6.0 Hz, 2H, arom H), 8.09 (d, *J* = 9.4 Hz, 1H, arom H) ppm. HR-MS *m/z* [M+H]$^+$ calcd for $C_{14}H_{11}BrN_2O_2S$: 350.9798, found 350.9796.

7.1.6.8. 3-Bromo-5-(3,4,5-trimethoxyphenyl)isothiazolo[4,3-b]pyridine (13h).

This compound was prepared from 3-amino-5-(3,4,5-trimethoxyphenyl)isothiazolo[4,3-b]pyridine and the residue was

purified by silica gel flash chromatography using a mixture of hexane and ethyl acetate (in a ratio of 7:3) as mobile phase, affording the title compound as an amorphous light yellow solid in 35% yield (19.7 mg, 0.05 mmol). ^{1}H NMR (300 MHz, CDCl$_3$) δ: 3.93 (s, 3H, OCH$_3$), 4.01 (s, 6H, 2 × OCH$_3$), 7.42 (s, 2H, arom H), 7.87 (d, $J = 9.4$ Hz, 1H, arom H), 8.14 (d, $J = 9.3$ Hz, 1H, arom H) ppm. HR-MS m/z [M+H]$^+$ calcd for C$_{15}$H$_{13}$BrN$_2$O$_3$S: 380.9903, found 380.9888.

7.1.7. *Synthesis of 5-aryl-3-(cis-2,6-dimethylmorpholino)isothiazolo[4,3-b]pyridines (14a-h)*

General procedure. To a solution of a 5-substituted-3-bromoisothiazolo[4,3-b]pyridine (1 equiv) in absolute ethanol (20 mL) was added *cis*-2,6-dimethylmorpholine (3 equiv) and the mixture was stirred at reflux overnight. After disappearance of the starting material as monitored by TLC, the volatiles were evaporated to dryness and the residue was purified by silica gel flash column chromatography yielding the 5-substituted-3-(*cis*-2,6-dimethylmorpholino)isothiazolo[4,3-b]pyridine. The following compounds were made according to this procedure:

7.1.7.1. *3-(cis-2,6-Dimethylmorpholino)-5-phenylisothiazolo[4,3-b]pyridine (14a).* This compound was prepared from 3-bromo-5-phenylisothiazolo[4,3-b]pyridine. The residue was purified by silica gel flash chromatography using a mixture of hexane and ethyl acetate (in a ratio of 4:1) as mobile phase, affording the title compound as an amorphous yellow solid in 91% yield (40.5 mg, 0.12 mmol). Mp 154.1–155.8 °C. ^{1}H NMR (600 MHz, CDCl$_3$) δ: 1.32 (d, $J = 6.3$ Hz, 6H, 2 × CH$_3$), 2.96 (dd, $J = 12.5$, 10.8 Hz, 2H, 2 × NCH), 3.92–4.00 (m, 2H, 2 × OCH), 4.66 (d, $J = 11.6$ Hz, 2H, 2 × NCH), 7.40–7.44 (m, 1H, arom H), 7.47–7.50 (m, 2H, arom H), 7.72 (d, $J = 9.4$ Hz, 1H, arom H), 7.83 (d, $J = 9.4$ Hz, 1H, arom H), 7.97–8.01 (m, 2H, arom H) ppm. ^{13}C NMR (151 MHz, CDCl$_3$) δ: 18.8 (CH$_3$), 55.6 (CH$_2$), 71.2 (CH), 121.2 (CH), 126.7 (CH), 128.8 (CH), 128.9 (CH), 129.5 (CH), 134.8 (C), 139.1, (C), 150.6 (C), 155.5 (C), 172.5 (C) ppm. HR-MS m/z [M+H]$^+$ calcd for C$_{18}$H$_{19}$N$_3$OS: 326.1322, found 326.1321.

7.1.7.2. *5-(4-Trifluoromethylphenyl)-3-(cis-2,6-dimethylmorpholino)isothiazolo[4,3-b]pyridine (14b).* This compound was prepared from 3-bromo-5-(4-trifluoromethylphenyl)isothiazolo[4,3-b]pyridine. The residue was purified by silica gel flash chromatography using a mixture of hexane and ethyl acetate (in a ratio of 7:3) as mobile phase, affording the title compound as an amorphous yellow solid in 85% yield (37 mg, 0.09 mmol). Mp 238.2–239.7 °C. ^{1}H NMR (600 MHz, CDCl$_3$) δ: 1.33 (d, $J = 6.3$ Hz, 6H, 2 × CH$_3$), 2.99 (dd, $J = 12.6$, 10.7 Hz, 2H, 2 × NCH), 3.93–3.99 (m, 2H, 2 × OCH), 4.64 (d, $J = 11.8$ Hz, 2H, 2 × NCH), 7.72 (d, $J = 9.4$ Hz, 1H, arom H), 7.74 (d, $J = 8.2$ Hz, 2H, arom H), 7.87 (d, $J = 9.4$ Hz, 1H, arom H), 8.09 (d, $J = 8.1$ Hz, 2H, arom H) ppm. ^{13}C NMR (151 MHz, CDCl$_3$) δ: 18.9 (CH$_3$), 55.6 (CH$_2$), 71.2 (CH), 121.0 (CH), 124.2 (q, $J = 272.0$ Hz, C), 125.7 (bq, $J = 3.2$ Hz, CH), 126.9 (CH), 129.8 (CH), 130.6 (q, $J = 32.4$ Hz, C), 135.0 (C), 142.5 (C), 148.9 (C), 155.3 (C), 173.0 (C) ppm. ^{19}F NMR (471 MHz, CDCl$_3$) δ: −62.23 ppm. HR-MS m/z [M+H]$^+$ calcd for C$_{19}$H$_{18}$F$_3$N$_3$OS: 394.1195, found 394.1200.

7.1.7.3. *5-(4-Fluorophenyl)-3-(cis-2,6-dimethylmorpholino)isothiazolo[4,3-b]pyridine (14c).* This compound was prepared from 3-bromo-5-(4-fluorophenyl)isothiazolo[4,3-b]pyridine. The residue was purified by silica gel flash chromatography using a mixture of hexane and ethyl acetate (in a ratio of 7:3) as mobile phase, affording the title compound as an amorphous yellow solid in 91% yield (40 mg, 0.12 mmol). Mp 165.5–166.9 °C. ^{1}H NMR (600 MHz, CDCl$_3$) δ: 1.32 (d, $J = 6.3$ Hz, 6H, 2 × CH$_3$), 2.95 (dd, $J = 12.5$, 10.7 Hz, 2H, 2 × NCH), 3.92–3.99 (m, 2H, 2 × OCH), 4.62 (dd, $J = 12.5$, 1.3 Hz, 1H, 2 × NCH), 7.13–7.20 (m, 2H, arom H), 7.66 (d, $J = 9.4$ Hz, 1H, arom H), 7.83 (d, $J = 9.4$ Hz, 1H, arom H), 7.94–7.98 (m, 2H, arom H) ppm. ^{13}C NMR (151 MHz, CDCl$_3$) δ: 18.8 (CH$_3$), 55.6 (CH$_2$), 71.2 (C), 115.70 (d, $J = 21.6$ Hz, CH), 120.9 (CH), 128.43 (d, $J = 8.2$ Hz, CH), 129.7 (C), 134.7 (C), 135.3 (C),

149.6 (C), 155.3 (C), 163.4 (d, $J = 248.9$ Hz, C), 172.50 (C) ppm. ^{19}F NMR (471 MHz, CDCl$_3$) δ: −111.93 ppm. HR-MS m/z [M+H]$^+$ calcd for C$_{18}$H$_{18}$FN$_3$OS: 344.1227, found 344.1235.

7.1.7.4. *5-(3-Chlorophenyl)-3-(cis-2,6-dimethylmorpholino)isothiazolo[4,3-b]pyridine (14d).* This compound was prepared from 3-bromo-5-(3-chlorophenyl)isothiazolo[4,3-b]pyridine and the residue was purified by silica gel flash chromatography using a mixture of hexane and ethyl acetate (in a ratio of 4:1) as mobile phase, affording the title compound as an amorphous yellow solid in 78% yield (34.5 mg, 0.09 mmol). Mp 160.3–161.9 °C. ^{1}H NMR (600 MHz, CDCl$_3$) δ: 1.33 (d, $J = 6.3$ Hz, 6H, 2 × CH$_3$), 2.95–3.01 (m, 2H, 2 × NCH), 3.93–4.00 (m, 2H, 2 × OCH), 4.65 (d, $J = 12.5$ Hz, 2H, 2 × NCH), 7.36–7.43 (m, 2H, arom H), 7.67 (d, $J = 9.4$ Hz, 1H, arom H), 7.82–7.85 (m, 2H, arom H), 8.00–8.02 (m, 1H, arom H) ppm. ^{13}C NMR (151 MHz, CDCl$_3$) δ: 18.8 (CH$_3$), 55.6 (CH$_2$), 71.3 (CH), 120.7 (CH), 124.6 (CH), 126.9 (CH), 128.8 (CH), 129.7 (CH), 130.0 (CH), 134.8 (C), 134.9 (C), 140.8 (C), 148.8 (C), 155.4 (C), 172.7 (C) ppm. HR-MS m/z [M+H]$^+$ calcd for C$_{18}$H$_{18}$ClN$_3$OS: 360.0932, found 360.0932.

7.1.7.5. *3-(cis-2,6-Dimethylmorpholino)-5-(4-methylphenyl)isothiazolo[4,3-b]pyridine (14e).* This compound was prepared from 3-bromo-5-(4-methylphenyl)isothiazolo[4,3-b]pyridine. The residue was purified by silica gel flash chromatography using a mixture of hexane and ethyl acetate (in a ratio of 4:1) as mobile phase, affording the title compound as an amorphous orange solid in 88% yield (39.1 mg, 0.12 mmol). Mp 198.1–199.8 °C. ^{1}H NMR (600 MHz, CDCl$_3$) δ: 1.32 (d, $J = 6.3$ Hz, 6H, 2 × CH$_3$), 2.42 (s, 3H, CH$_3$), 2.95 (dd, $J = 12.6$, 10.7 Hz, 2H, 2 × NCH), 3.93–4.00 (m, 2H, 2 × OCH), 4.66 (d, $J = 11.2$ Hz, 2H, 2 × NCH), 7.30 (d, $J = 7.9$ Hz, 2H, arom H), 7.70 (d, $J = 9.4$ Hz, 1H, arom H), 7.82 (d, $J = 9.4$ Hz, 1H, arom H), 7.89 (d, $J = 8.2$ Hz, 2H, arom H) ppm. ^{13}C NMR (151 MHz, CDCl$_3$) δ: 18.8 (CH$_3$), 21.3 (CH$_3$), 55.6 (CH$_2$), 71.2 (CH), 121.1 (CH), 126.6 (CH), 129.4 (CH), 129.5 (CH), 134.7 (C), 136.4 (C), 139.0 (C), 150.7 (C), 155.5 (C), 172.3 (C) ppm. HR-MS m/z [M+H]$^+$ calcd for C$_{19}$H$_{21}$N$_3$OS: 340.1478, found 340.1473.

7.1.7.6. *3-(cis-2,6-Dimethylmorpholino)-5-(3-methoxyphenyl)isothiazolo[4,3-b]pyridine (14f).* This compound was prepared from 3-bromo-5-(3-methoxyphenyl)isothiazolo[4,3-b]pyridine and the residue was purified by silica gel flash chromatography using a mixture of hexane and ethyl acetate (in a ratio of 7:3) as mobile phase, affording the title compound as an amorphous yellow solid in 91% yield (40 mg, 0.11 mmol). Mp 146.2–147.9 °C. ^{1}H NMR (600 MHz, CDCl$_3$) δ: 1.32 (d, $J = 6.3$ Hz, 6H, 2 × CH$_3$), 2.97 (dd, $J = 12.5$, 10.8 Hz, 2H, 2 × NCH), 3.89 (s, 3H, OCH$_3$), 3.93–4.00 (m, 2H, 2 × OCH), 4.67 (d, $J = 11.6$ Hz, 2H, 2 × NCH), 6.98 (ddd, $J = 8.2$, 2.6, 0.7 Hz, 1H, arom H), 7.40 (t, $J = 7.9$ Hz, 1H, arom H), 7.55–7.57 (m, 1H, arom H), 7.58–7.61 (m, 1H, arom H), 7.71 (d, $J = 9.4$ Hz, 1H, arom H), 7.83 (d, $J = 9.4$ Hz, 1H, arom H) ppm. ^{13}C NMR (151 MHz, CDCl$_3$) δ: 18.8 (CH$_3$), 55.2 (OCH$_3$), 55.5 (CH$_2$), 71.2 (CH), 111.9 (CH), 114.8 (CH), 119.2 (CH), 121.2 (CH), 129.5 (CH), 129.8 (CH), 134.7 (C), 140.5 (C), 150.3 (C), 155.5 (C), 160.0 (C), 172.5 (C) ppm. HR-MS m/z [M+H]$^+$ calcd for C$_{19}$H$_{21}$N$_3$O$_2$S: 356.1427, found 356.1427.

7.1.7.7. *3-(cis-2,6-Dimethylmorpholino)-5-(3,4-dimethoxyphenyl)isothiazolo[4,3-b]pyridine (14g).* This compound was prepared from 3-bromo-5-(3,4-dimethoxyphenyl)isothiazolo[4,3-b]pyridine. The residue was purified by silica gel flash chromatography using a mixture of hexane and ethyl acetate (in a ratio of 7:3) as mobile phase, affording the title compound as an amorphous yellow solid in 55% yield (24 mg, 0.06 mmol). Mp 200.4–201.7 °C. ^{1}H NMR (600 MHz, CDCl$_3$) δ: 1.31 (d, $J = 6.3$ Hz, 6H, 2 × CH$_3$), 2.95 (dd, $J = 12.3$, 10.8 Hz, 2H, 2 × NCH), 3.93–4.00 (m, 8H, 2 × OCH$_3$, 2 × OCH), 4.64 (d, $J = 11.4$ Hz, 2H, 2 × NCH), 6.96 (d, $J = 8.3$, 1H, arom H), 7.52 (dd, $J = 8.4$, 2.0 Hz, 1H, arom H), 7.68 (d, $J = 2.0$ Hz, 1H, arom H), 7.69–7.72 (m, 1H, arom H),

7.81 (d, $J = 9.4$ Hz, 1H, arom H) ppm. ^{13}C NMR (151 MHz, CDCl$_3$) δ: 18.8 (CH$_3$), 55.5 (CH$_2$), 55.6 (OCH$_3$), 56.0 (OCH$_3$), 71.2 (CH), 109.4 (CH), 111.0 (CH), 119.4 (CH), 120.8 (CH), 129.5 (CH), 131.9 (C), 149.2 (C), 150.1 (C), 150.2 (C), 155.5 (C), 172.1 (C) ppm. HR-MS m/z [M+H]$^+$ calcd for C$_{20}$H$_{23}$N$_3$O$_3$S: 386.1533, found 386.1526.

7.1.7.8. 3-(cis-2,6-Dimethylmorpholino)-5-(3,4,5-trimethoxyphenyl) isothiazolo[4,3-b]pyridine (14h).

This compound was prepared from 3-bromo-5-(3,4,5-trimethoxyphenyl)isothiazolo[4,3-b]pyridine. The residue was purified by silica gel flash chromatography using a mixture of hexane and ethyl acetate (in a ratio of 3:2) as mobile phase, affording the title compound as an amorphous yellow solid in 80% yield (34.8 mg, 0.08 mmol). Mp 196.3–198.1 °C. ^{1}H NMR (600 MHz, CDCl$_3$) δ: 1.31 (d, $J = 6.3$ Hz, 6H, 2 × CH$_3$), 2.94–3.00 (m, 2H, 2 × NCH), 3.92 (s, $J = 2.5$ Hz, 3H, OCH$_3$), 3.95–3.99 (m, 9H, 2 × OCH, 2 × OCH$_3$), 4.64–4.68 (m, 2H, 2 × NCH), 7.27 (s, 2H, arom H), 7.69 (d, $J = 9.4$ Hz, 1H, arom H), 7.84 (d, $J = 9.4$ Hz, 1H, arom H) ppm. ^{13}C NMR (151 MHz, CDCl$_3$) δ: 18.8 (CH$_3$), 55.5 (CH$_2$), 56.1 (OCH$_3$), 61.0 (OCH$_3$), 71.2 (CH), 104.0 (CH), 121.0 (CH), 129.6 (CH), 134.7 (C), 139.2 (C), 150.2 (C), 153.5 (C), 155.4 (C), 172.3 (C) ppm. HR-MS m/z [M+H]$^+$ calcd for C$_{21}$H$_{25}$N$_3$O$_4$S: 416.16384, found 416.1636.

7.1.8. Synthesis of 5-aryl-3-(N-morpholino)isothiazolo[4,3-b]pyridines

General procedure. To a solution of 3-amino-5-arylisothiazolo[4,3-b] pyridine (1 equiv) in DMF (15 mL), was added K$_2$CO$_3$ (2 equiv) and 2-bromoethyl ether (0.7 equiv). The reaction mixture was stirred at 100 °C for 4–5 h. After disappearance of the starting material as mon- itored by TLC, the volatiles were evaporated to dryness and the residue was purified by silica gel flash chromatography, yielding the corresponding 5-aryl-3-(N-morpholino)isothiazolo[4,3-b]pyridines. The following compounds were made according to this procedure:

7.1.8.1. 5-(3-Methoxyphenyl)-3-(N-morpholino)isothiazolo[4,3-b] pyridine (15f).

This compound was prepared from 3-amino-5-(3-methoxyphenyl)isothiazolo[4,3-b]pyridine. The residue was purified by silica gel flash chromatography using a mixture of hexane and ethyl acetate (in a ratio of 7:3) as mobile phase, affording the title compound as an amorphous yellow solid in 77% yield (24.5 mg, 0.08 mmol). Mp 169.1–170.6 °C. ^{1}H NMR (600 MHz, CDCl$_3$) δ: 3.89 (s, 3H, OCH$_3$), 3.97–4.00 (m, 4H, 2 × OCH$_2$), 4.02–4.04 (m, 4H, 2 × NCH$_2$), 6.98 (ddd, $J = 8.2$, 2.5, 0.9 Hz, 1H, arom H), 7.40 (t, $J = 7.9$ Hz, 1H, arom H), 7.55–7.58 (m, 2H, arom H), 7.71 (d, $J = 9.4$ Hz, 1H, arom H), 7.85 (d, $J = 9.4$ Hz, 1H, arom H) ppm. ^{13}C NMR (151 MHz, CDCl$_3$) δ: 50.5 (CH$_2$) 55.3 (OCH$_3$), 66.2 (CH$_2$), 112.6 (CH), 114.3 (CH), 119.4 (CH), 121.4 (CH), 129.6 (CH), 129.8 (CH), 135.0 (C), 140.6 (C), 150.8 (C), 155.5 (C), 160.0 (C), 173.0 (C) ppm. HR-MS m/z [M+H]$^+$ calcd for C$_{17}$H$_{17}$N$_3$O$_2$S: 328.1114, found 328.1111.

7.1.8.2. 5-(3,4-Dimethoxyphenyl)-3-(N-morpholino)isothiazolo[4,3-b] pyridine (15g).

This compound was prepared from 3-amino-5-(3,4-dimethoxyphenyl)isothiazolo[4,3-b]pyridine. The residue was purified by silica gel flash chromatography using a mixture of hexane and ethyl acetate (in a ratio of 3:2) as mobile phase, affording the title compound as an amorphous yellow solid in 73% yield (18.1 mg, 0.05 mmol). Mp 151.2–152.9 °C. ^{1}H NMR (600 MHz, CDCl$_3$) δ: 3.95 (s, 3H, OCH$_3$), 3.97–4.00 (m, 7H, OCH$_3$, 2 × OCH$_2$), 4.01–4.04 (m, 4H, 2 × NCH$_2$), 6.98 (d, $J = 8.3$ Hz, 1H, arom H), 7.55 (dd, $J = 8.3$, 2.1 Hz, 1H, arom H), 7.62 (d, $J = 2.1$ Hz, 1H, arom H), 7.70 (d, $J = 9.4$ Hz, 1H, arom H), 7.84 (d, $J = 9.4$ Hz, 1H, arom H) ppm. ^{13}C NMR (151 MHz, CDCl$_3$) δ: 50.6 (CH$_2$), 55.8 (OCH$_3$), 56.0 (OCH$_3$), 66.2 (CH$_2$), 109.8 (CH), 111.1 (CH), 119.7 (CH), 121.1 (CH), 129.6 (CH), 132.1 (C), 135.0 (C), 149.2 (C), 150.2 (C), 150.8 (C), 155.4 (C), 172.6 (C) ppm. HR-MS m/z [M+H]$^+$ calcd for C$_{18}$H$_{19}$N$_3$O$_3$S: 358.1220, found 358.1220.

7.1.8.3. 5-(3,5-Dimethoxyphenyl)-3-(N-morpholino)isothiazolo[4,3-b] pyridine (15i).

This compound was prepared from 3-amino-5-(3,5-dimethoxyphenyl)isothiazolo[4,3-b]pyridine. The residue was purified by silica gel flash chromatography using a mixture of hexane and ethyl acetate (in a ratio of 3:2) as mobile phase, affording the title compound as an amorphous yellow solid in 71% yield (17.5 mg, 0.05 mmol). Mp 149.2–150.8 °C. ^{1}H NMR (600 MHz, CDCl$_3$) δ: 3.87 (s, 6H, 2 × OCH$_3$), 3.96–3.99 (m, 4H, 2 × OCH$_2$), 4.01–4.04 (m, 4H, 2 × NCH$_2$), 6.54 (t, $J = 2.3$ Hz, 1H, arom H), 7.14 (d, $J = 2.3$ Hz, 2H, arom H), 7.67 (d, $J = 9.4$ Hz, 1H, arom H), 7.84 (d, $J = 9.4$ Hz, 1H, arom H) ppm. ^{13}C NMR (151 MHz, CDCl$_3$) δ: 50.5 (CH$_2$), 55.4 (OCH$_3$), 66.2 (CH$_2$), 100.7 (CH), 105.2 (CH), 121.5 (CH), 129.5 (CH), 134.9 (C), 141.3 (C), 150.7 (C), 155.5 (C), 161.1 (C), 173.0 (C) ppm. HR-MS m/z [M+H]$^+$ calcd for C$_{18}$H$_{19}$N$_3$O$_3$S: 358.1220, found 358.1221.

7.2. GAK LanthaScreen™ Eu binding assay

The compounds were subjected to a LanthaScreen™ binding assay in which 10 titrations of dissolved test compound in DMSO are transferred to a 384-well plate. Sequential addition of the kinase buffer (50 mM HEPES pH 7.5, 0.01% BRIJ-35, 10 mM MgCl and 1 mM EGTA), the 2X kinase antibody (Eu Anti GST) mixture and the 4X Tracer 222 solution was performed. After shaking for 30 s and a one hour incubation period at room temperature, the plate was read on a fluorescence plate reader. When the bound tracer in the active site was displaced by the test compound, fluorescence was not observed. The collected data were then compared to a 0% displacement control with pure DMSO and a 100% displacement control with staurosporine, a known inhibitor of GAK and plotted against the logarithmic concentration parameter. The IC$_{50}$ was subsequently extracted.

7.3. Antiviral assays

Virus construct. DENV2 (New Guinea C strain)[29,30] Renilla reporter plasmid used for the antiviral assays was a gift from Pei-Yong Shi (The University of Texas Medical Branch).

Cells. Huh7 (Apath LLC) cells were grown in DMEM (Mediatech) supplemented with 10% FBS (Omega Scientific), nonessential aminoacids, 1% L-glutamine, and 1% penicillin-streptomycin (Thermo-Fisher Scientific) and maintained in a humidified incubator with 5% CO$_2$ at 37 °C.

Virus Production. DENV2 RNA was transcribed in vitro using mMessage/mMachine (Ambion) kits. DENV was produced by electroporating RNA into BHK-21 cells, harvesting supernatants on day 10 and titering via standard plaque assays on BHK-21 cells. Virus titers were determined via standard plaque assay on Vero76 cells.

Infection assays. Huh7 cells were infected with DENV in replicates (n = 3–10) for 4 h at MOI of 0.05. Overall infection was measured at 48 h by standard luciferase assays.

Viability assays. Viability was assessed using AlamarBlue® reagent (Invitrogen) according to manufacturer's protocol. Fluorescence was detected at 560 nm on InfiniteM1000 plate reader.

Declaration of Competing Interest

None.

Acknowledgments

Appendix A. Supplementary material

Supplementary data to this article can be found online at https://doi.org/10.1016/j.bmc.2019.115188.

References

1. Sorrell FJ, Szklarz M, Abdul Azeez KR, Elkins JM, Knapp S. Family-wide structural analysis of human Numb-associated protein kinases. *Structure.* 2016;24:401–411.
2. Edeling MA, Smith C, Owen D. Life of a clathrin coat: insights from clathrin and AP structures. *Nat Rev Mol Cell Biol.* 2006;7:32–44.
3. Zhang CX, Engqvist-Goldstein AEY, Carreno S, Owen DJ, Smythe E, Drubin DG. Multiple roles for cyclin G-associated kinase in clathrin-mediated sorting events. *Traffic.* 2005;6:1103–1113.
4. Korolchuk VI, Banting G. CK2 and GAK/auxilin2 are major protein kinases in cla-thrin-coated vesicles. *Traffic.* 2002;3:428–439.
5. Ghosh P, Kornfeld S. AP-1 binding to sorting signals and release from clathrin-coated vesicles is regulated by phosphorylation. *J Cell Biol.* 2003;160:699–708.
6. Umeda A, Meyerholz A, Ungewickell E. Identification of the universal cofactor (auxilin 2) in clathrin coat dissociation. *Eur J Cell Biol.* 2000;79:336–342.
7. Neveu G, Barouch-Bentov R, Ziv-Av A, Gerber D, Jacob Y, Einav S. Identification and targeting of an interaction between a tyrosine motif within hepatitis C virus core protein and AP2M1 essential for viral assembly. *PLoS Pathog.* 2012;8:e1002845.
8. McMahon HT, Boucrot E. Molecular mechanism and physiological functions of cla-thrin-mediated endocytosis. *Nat Rev Mol Cell Biol.* 2011;12:517–533.
9. Bekerman E, Neveu G, Shulla A, et al. Anticancer kinase inhibitors impair in-tracellular viral trafficking and exert broad-spectrum antiviral effects. *J Clin Invest.* 2017;127:1338–1352.
10. Neveu G, Ziv-Av A, Barouch-Bentov R, Berkerman E, Mulholland J, Einav S. AP-2-associated protein kinase 1 and cyclin G-associated kinase regulate hepatitis C virus entry and are potential drug targets. *J Virol.* 2015;8:4387–4404.
11. Bekerman E, Einav S. Infectious disease. Combating emerging viral threats. *Science.* 2015;348:282–283.
12. Asquith CRM, Laitinen T, Bennett JM, et al. Identification and optimization of 4-anilinoquinolines as inhibitors of cyclin G associated kinase. *ChemMedChem.* 2018;13:48–66.
13. Asquith CRM, Berger BT, Wan J, et al. SGC-GAK-1: a chemical probe for cyclin G associated kinase (GAK). *J Med Chem.* 2019;62:2830–2836.
14. Kovackova S, Chang L, Bekerman E, et al. Selective inhibitors of cyclin G associated kinase (GAK) as anti-hepatitis C agents. *J Med Chem.* 2015;58:3393–3410.
15. Pu SY, Wouters R, Schor S, Rozenski J, Barouch-Bentov R, Prugar LI, O'Brien CM,

Brannan JM, et al. *J Med Chem.* 2018;61:6178–6192.
16. Li J, Kovackova S, Pu SY, et al. Isothiazolo[4,3-b]pyridines as inhibitors of cyclin G associated kinase: synthesis, structure–activity relationship studies and antiviral ac-tivity. *Med Chem Comm.* 2015;6:1666–1672.
17. Wouters R, Pu SY, Froeyen M, et al. Cyclin G-associated kinase (GAK) affinity and antiviral activity studies of a series of 3-C-substituted isothiazolo[4,3-b]pyridines. *Eur J Med Chem.* 2019;163:256–265.
18. Wouters R, Tian J, Herdewijn P, De Jonghe S. A scaffold-hopping strategy toward the identification of inhibitors of cyclin G associated kinase. *ChemMedChem.* 2018;13:1–19.
19. Cui X, Zhou Y, Wang N, Liu L, Guo QX. *N*-Phenylurea as an inexpensive and efficient ligand for Pd-catalyzed Heck and room-temperature Suzuki reactions. *Tetrahedron Lett.* 2007;48:163–167.
20. Hanthorn JJ, Valgimigli L, Pratt DA. Preparation of highly reactive pyridine- and pyrimidine-containing diarylamine antioxidants. *J Org Chem.* 2012;77:6908–6916.
21. Zhongzhong Y, Aiping L, Mingzhi H, et al. Design, synthesis, DFT study and anti-fungal activity of the derivatives of pyrazolecarboxamide containing thiazole or oxazole ring. *Eur J Med Chem.* 2018;149:170–181.
22. Subhash LY, Denvert SD, Bhalchandra MB. MnO$_2$ catalyzed formylation of amines and transamidation of amides under solvent-free conditions. *RSC Adv.* 2015;5:80441–80449.
23. Striela R, Urbelis G, Sudzius J, Stoncius S, Sadzeviciene R, Labanauskas L. Synthesis of bromocyclopropylpyridines via the Sandmeyer reaction. *Tetrahedron Lett.* 2017;58:1681–1683.
24. Lebakken CS, Riddle SM, Singh U, Frazee WJ, Eliason HC, et al. Development and applications of a broad-coverage, TR-FRET-based kinase binding assay platform. *J Biomol Screening.* 2009;14:924–935.
25. Morris GM, Huey R, Lindstrom W, et al. Autodock4 and AutoDockTools4: automated docking with selective receptor flexibility. *J Comput Chem.* 2009;16:2785–2791.
26. Trott O, Olson AJ. AutoDock Vina: improving the speed and accuracy of docking with a new scoring function, efficient optimization and multithreading. *J Comput Chem.* 2010;31:455–461.
27. Bandaru SSM, Kapdi AR, Schulzkea C. Crystal structure of 4-(pyrazin-2-yl)morpho-line. *Acta Crystallogr E Crystallogr Commun.* 2018;74:137–140.
28. Quintanilla-Licea R, Colunga-Valladares JF, Caballero-Quintero A, et al. NMR Detection of isomers arising from restricted rotation of the C-N amide bond of N-formyl-o-toluidine and N,N'-bis-formyl-o-tolidine. *Molecules.* 2002;7:662–673.
29. Xie X, Gayen S, Kang C, Yuan Z, Shi P-Y. Membrane topology and function of dengue virus NS2A protein. *J Virol.* 2013;87:4609–4622.
30. Zou G, Xu HY, Qing M, Wang QY, Shi PY. Development and characterization of a stable luciferase dengue virus for high-throughput screening. *Antivir Res.* 2011;91:11–19.

A Scaffold-Hopping Strategy toward the Identification of Inhibitors of Cyclin G Associated Kinase

Randy Wouters,[a] Junjun Tian,[a] Piet Herdewijn,[a] and Steven De Jonghe*[a, b]

We recently reported the discovery of isothiazolo[4,3-b]pyridine-based inhibitors of cyclin G associated kinase (GAK) displaying low nanomolar binding affinity for GAK and demonstrating broad-spectrum antiviral activity. To come up with novel core structures that act as GAK inhibitors, a scaffold-hopping approach was applied starting from two different isothiazolo[4,3-b]pyridines. In total, 13 novel 5,6- and 6,6-fused bicyclic heteroaromatic scaffolds were synthesized. Four of them displayed GAK affinity with K_d values in the low micromolar range that can serve as chemical starting points for the discovery of GAK inhibitors based on a different scaffold.

Introduction

Cyclin G associated kinase (GAK), also known as auxilin II, is a cellular serine/threonine protein kinase first identified in 1997.[1] It is highly homologous to auxilin I, with the notable exception of the presence of an N-terminal kinase domain on GAK.[2] In contrast to auxilin I, GAK is ubiquitously expressed, whereas auxilin I is solely expressed in neurons. Many biological effects have been attributed to GAK as a result of its abundance. It has been demonstrated that siRNA-mediated GAK knockdown results in mitotic arrest during metaphase and multipolar spindle formation.[3] Due to this mitotic involvement, GAK is a potential drug target for the treatment of BXW7-deficient tumors, such as cholangiocarcinoma.[4] GAK was also identified as a potential target for the inhibition of prostate cancer growth in cells expressing androgen receptor splice variants.[5] Furthermore, GAK was found to be involved in osteosarcoma, which is the most frequent primary malignant bone tumor among children. In both osteosarcoma cell lines and tissue samples, overexpression of GAK is observed, relative to healthy osteoblasts. Its knockdown by siRNA decreased cell proliferation in both drug-sensitive and multidrug-resistant osteosarcoma cell lines, suggesting osteosarcoma growth and proliferation to be GAK dependent.[6]

In Parkinson's disease, the leucine-rich repeat kinase 2 (LRRK2) is a major contributor to the illness. It is implicated in vesicle trafficking and was found to interact with GAK, where it plays a role in the dysfunction of LRRK2.[7]

GAK is a key regulator of clathrin-mediated endocytosis (CME), as it is one of the kinases known to phosphorylate Thr144 and Thr156 of the m-subunits of adaptor protein complex (AP) 1 and AP2, respectively. While GAK-dependent phosphorylation of AP2 is important for its endocytic activity, GAK's phosphorylation of AP1 is implicated in trans-Golgi network (TGN)-to-lysosome trafficking. This phosphorylation of APs enhances their binding to cargo proteins and helps the recruitment of clathrin to the membrane to form a clathrin-coated vesicle (CCV).[2, 8–11] In analogy to auxilin I, GAK contains a C-terminal J-domain that acts as a co-chaperone with the heat shock cognate 71 kDa protein (HSC70) to uncoat CCVs in order to recycle clathrin back to the cell surface.[2] Depletion of GAK inhibits CME by inhibiting the recruitment of clathrin and clathrin adaptors.[2, 12] Furthermore, we previously discovered that GAK's involvement in CME is required in both early and late stages of the life cycle of distinct viruses, such as Dengue virus (DENV), Ebola virus (EBOV), Chikungunya virus (CHIKV), and hepatitis C virus (HCV).[10, 13, 14]

Recently, we reported the discovery of potent GAK inhibitors based on an isothiazolo[4,3-b]pyridine scaffold, of which compounds 1, 2, and 3 are the most promising representatives (Figure 1). These compounds display potent GAK affinity (K_d values in the range of 8–80 nm), are selective, and are also endowed with broad-spectrum in vitro antiviral activity against HCV, DENV, EBOV, and CHIKV.[15,16]

Previous explorations of the structure–activity relationship (SAR) of isothiazolo[4,3-b]pyridines as GAK inhibitors focused on modifications of the functional groups at positions 3 and 6 of the scaffold.[15–17] In this study, an alternative approach based on scaffold hopping was followed. Scaffold hopping is a widely applied medicinal chemistry strategy in which the core skeleton (the scaffold) of lead molecules is subjected to bioisosteric replacements, leading to the discovery of structurally novel compounds. There are different reasons to search for biologically active compounds based on alternative scaffolds. Examples include the development of analogues with im-

[a] R. Wouters, Dr. J. Tian, Prof. P. Herdewijn, Dr. S. De Jonghe
Medicinal Chemistry, Rega Institute for Medical Research, KU Leuven, Herestraat 49, Box 1041, 3000 Leuven (Belgium)
E-mail: steven.dejonghe@kuleuven.be

[b] Dr. S. De Jonghe
Present affiliation: Laboratory of Virology and Chemotherapy, Rega Institute for Medical Research, KU Leuven, Herestraat 49, Box 1043, 3000 Leuven (Belgium)

The ORCID identification number(s) for the author(s) of this article can be found under:
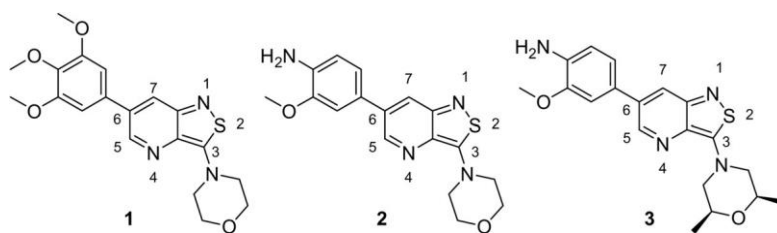https://doi.org/10.1002/cmdc.201800690.

Figure 1. Previously reported isothiazolo[4,3-*b*]pyridines as GAK inhibitors.

proved activity and/or selectivity, altered physicochemical and ADMET properties, as well as obtaining molecules with a favorable intellectual property situation.[18]

A scaffold-hopping exercise starts with an active compound and ends up with a novel chemotype by solely modifying the central core structure of the molecule. Two isothiazolo[4,3-*b*]pyridines with a different substitution pattern were selected as the starting point for the scaffold-hopping exercise (Figure 2). Compound 4[16] bears a 3,4-dimethoxyphenyl resi-
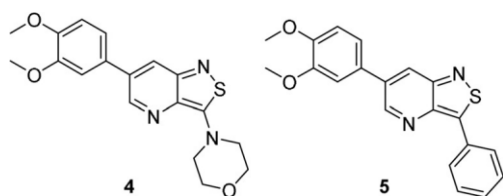

Figure 2. Reference GAK inhibitors for scaffold hopping.

due at position 6, instead of its 3,4,5-trimethoxy (compound 2) or 3-methoxy-4-amino (compound 2) counterparts, and displays a K_d value of 52 nm for GAK. Despite the 5-fold lower GAK affinity of compound 4 relative to compounds 1 and 2, it was selected as a reference compound because of the easy access and low cost of large amounts of 3,4-dimethoxyphenyl- boronic acid. For some of the scaffolds (such as the pyrazo- lo[1,5-*a*]pyrimidine, pyrrolo[3,2-*b*]pyridine, pyrazolo[4,3-*b*]pyri-

dine, and thieno[3,2-*b*]pyridine), the insertion of a morpholine residue via either a nucleophilic aromatic substitution, a palladium-catalyzed Buchwald reaction or a CuI/l-proline mediated amination was cumbersome. In contrast, the introduction of an aryl group via palladium-catalyzed Suzuki cross-coupling reaction proceeded smoothly. Therefore, compound 5, characterized by the presence of a phenyl moiety at position 3 (instead of the morpholine residue of compound 4) was used for comparison purposes.[19] Although, GAK affinity of compound 5 (K_d: 0.77 mm) is 15-fold lower than the corresponding 3-morpholino analogue 4, the straightforward synthesis of various phenyl-substituted scaffold analogues justifies its use as a reference compound. As the substitution pattern is kept intact, the influence of scaffold modification on GAK affinity can be easily studied.

Results and Discussion

Chemistry

*Synthesis of isothiazolo[3,4-*b*]pyridine*

A palladium-catalyzed Suzuki coupling between 2,6-dichloronicotinonitrile 6 and 3,4-dimethoxyphenylboronic acid yielded compound 7 regioselectively (Scheme 1).[20] Nucleophilic displacement of the remaining chlorine at position 2 by ammonia in either water or methanol only led to the recovery of starting material. In contrast, the reaction with sodium azide proceeded smoothly, affording compound 8 in high yield. Staudinger re-
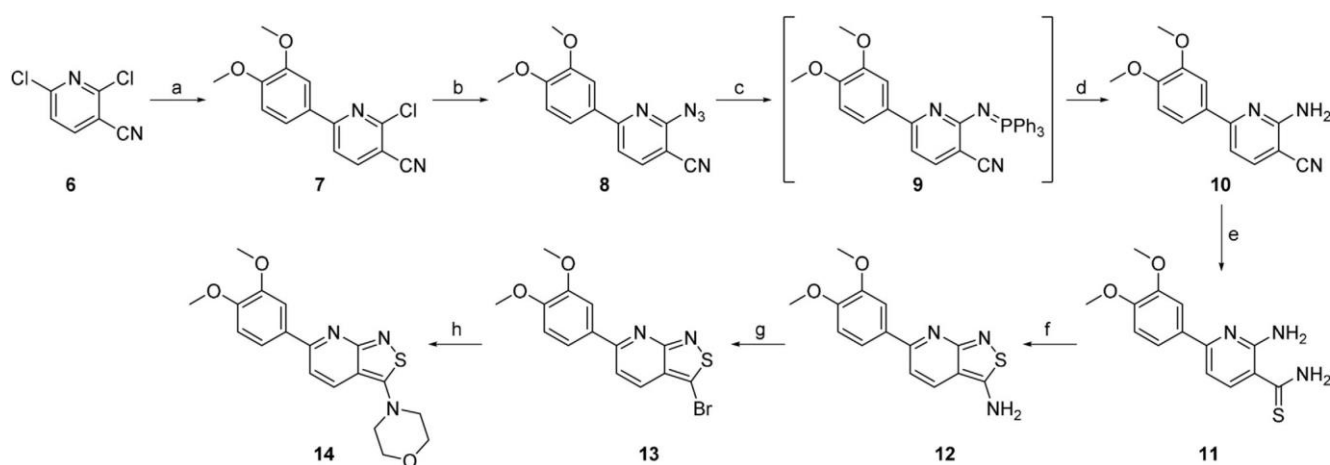
Scheme 1. Synthesis of isothiazolo[3,4-*b*]pyridine: a) 3,4-dimethoxyphenyl B(OH)$_2$, K$_2$CO$_3$, Pd(PPh$_3$)$_4$, H$_2$O, dioxane, 90 °C (63%); b) NaN$_3$, DMF, 70 °C (83%); c) PPh$_3$, pyridine, RT; d) 80% aq. CH$_3$COOH, reflux (95%); e) P$_2$S$_5$, ethanol, reflux (71%); f) 30% aq. H$_2$O$_2$, MeOH, 0 °C (83%); g) NaNO$_2$, HBr, CuBr, H$_2$O, 0 °C→RT (25%); h) morpholine, EtOH, reflux (40%).

130

duction by treatment of compound 8 with triphenylphosphine formed the iminophosphorane intermediate 9, which was subsequently submitted to an acidic hydrolysis yielding the 2-amino pyridine derivative 10.[21] The cyano group of compound 10 was converted into its corresponding thioamide 11 using phosphorus pentasulfide. An oxidative ring closure using hydrogen peroxide in methanol allowed to construct the isothiazole moiety, furnishing isothiazolo[3,4-*b*]pyridine 12. A Sandmeyer reaction using sodium nitrite, hydrogen bromide, and copper(I) bromide yielded 3-bromo-6-(3,4-dimethoxyphenyl)isothiazolo[3,4-*b*]pyridine 13. Finally, a nucleophilic aromatic substitution with morpholine afforded the desired isothiazolo[3,4-*b*]pyridine 14.

Synthesis of isothiazolo[3,4-b]pyrazine

Applying the same aqueous Suzuki conditions that successfully yielded compound 7 (Scheme 1) to the synthesis of compound 16 resulted merely in the formation of different unidentified products. However, the regioselective introduction of a 3,4-dimethoxyphenyl residue on 3,5-dichloropyrazine-2-carbonitrile 15 was possible via an anhydrous Suzuki reaction using tripo- tassium phosphate as a base, affording compound 16 (Scheme 2). The chlorine at position 3 was then exchanged by azide to afford compound 17. The azido moiety was subse- quently converted into an amino group via Staudinger reduc- tion with concomitant acidic hydrolysis of the iminophosphor- ane intermediate 18 to yield pyrazine 19. Thionation of its cyano moiety yielding thioamide 20 was achieved with Lawes- son's reagent (LR) rather than P2S5, as the workup with LR was less labor intensive and consistently led to higher yields. The thioamide 20 was then submitted to an oxidative ring closure furnishing the isothiazolo[3,4-*b*]pyrazine 21. Applying the typi- cal Sandmeyer reaction conditions (as in Scheme 1) to convert the amino group into a bromine was unsuccessful, as a com- plex mixture of unidentified products was formed. An alterna- tive Sandmeyer procedure using *tert*-butyl nitrite (*t*BuONO) and copper(II) bromide in dry acetonitrile yielded the desired

product 22.[22] Finally, nucleophilic substitution with morpholine yielded the title compound 23 in good yield.

Synthesis of isothiazolo[3,4-d]pyrimidine

A Suzuki coupling on 4-amino-2-chloropyrimidine-5-carbonitrile 24 using the aforementioned reaction conditions (Schemes 1 and 2) only resulted in the formation of side products. The presence of a free amino group is known to hamper Suzuki reactions and a common practice to circumvent this is[23] by protecting the amino group. However, additional protecting and deprotecting sequences are time consuming and lead to overall lower reaction yields. Therefore, alternative reaction conditions were explored. Performing the Suzuki reaction using tripotassium phosphate as a base, Pd(OAc)2 as a catalyst and 1,1'-bis(di-*tert*-butylphosphino)ferrocene (D-t-BPF) as a[23] ligand provided compound 25 efficiently (Scheme 3). The subsequent steps are similar as in Schemes 1 and 2. Briefly, thioamide 26 was accessible via thionation of the cyano group of compound 25. The isothiazolo moiety was then constructed via an oxidative ring closure yielding 3-aminoisothiazolo[3,4-*d*]pyrimidine 27. Conversion of the amino group to a bromine 28, followed by the introduction of a morpholine moiety, gave access to isothiazolo[3,4-*d*]pyrimidine 29.

Synthesis of pyrazolo[1,5-a]pyrimidine

Condensation of 4-bromo-1*H*-pyrazol-3-amine 30 and 2-chloromalonaldehyde under acidic conditions afforded 3-bromo-6-chloropyrazolo[1,5-*a*]pyrimidine 31 (Scheme 4).[24] Two consecutive Suzuki reactions allowed to introduce both aromatic substituents regioselectively, as bromine is favored over chlorine during the oxidative addition step.[25] The first Suzuki coupling yielded selectively the 3-phenylpyrazolo[1,5-*a*]pyrimidine 32. A subsequent Suzuki coupling under identical reaction conditions, except for using 3,4-dimethoxyphenylboronic acid, yielded the desired pyrazolo[1,5-*a*]pyrimidine 33 in good yield.

131
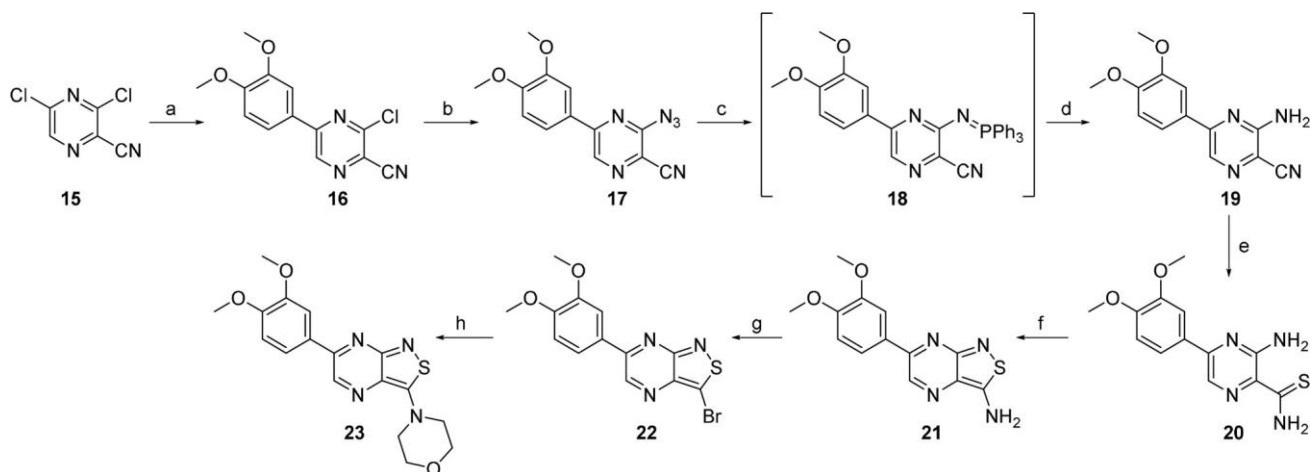
Scheme 2. Synthesis of isothiazolo[3,4-*b*]pyrazine: a) 3,4-dimethoxyphenyl-B(OH)₂, K₃PO₄, Pd(PPh₃)₄, dioxane, 90 °C (74 %); b) NaN₃, DMF, 70 °C (83 %); c) PPh₃, pyridine, RT; d) 80 % aq. CH₃COOH, reflux (95 %); e) LR, ethanol, reflux (83 %); f) 30 % aq. H₂O₂, MeOH, 0 °C (67 %); g) *t*BuONO, CuBr₂, CH₃CN, RT (32 %); h) morpholine, EtOH, reflux (64 %).

131
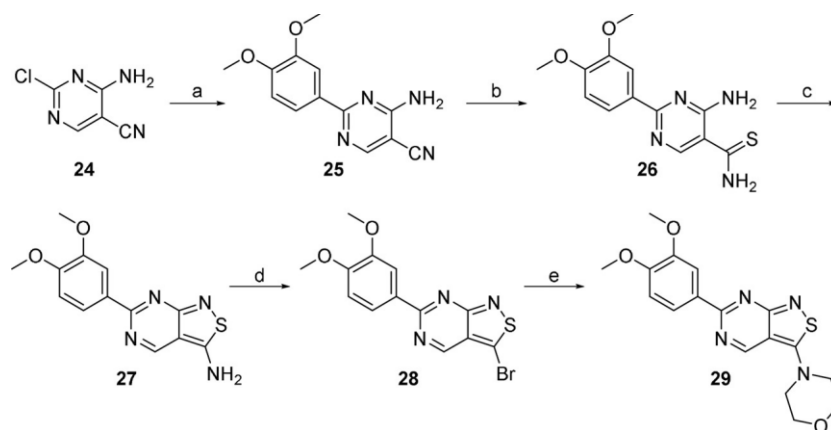
Scheme 3. Synthesis of isothiazolo[3,4-d]pyrimidine: a) 3,4-dimethoxyphenyl-B(OH)₂, K₃PO₄, Pd(OAc)₂, D-t-BPF, dioxane (53 %); b) LR, ethanol, reflux (60 %); c) 30 % aq. H₂O₂, MeOH, 0 8C (84 %); d) tBuONO, CuBr₂, CH₃CN, RT (49 %); e) morpholine, EtOH, reflux (65 %).
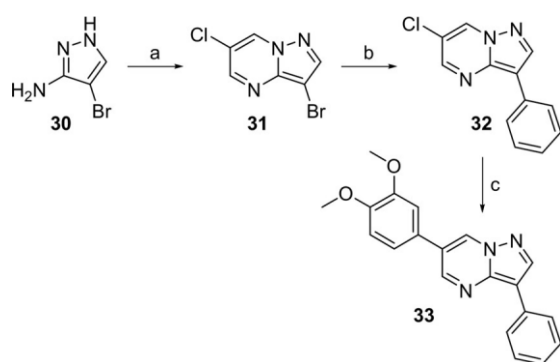
Scheme 4. Synthesis of pyrazolo[1,5-a]pyrimidine: a) 2-chloromalonaldehyde, MeOH, CH₃COOH, 70 8C (57 %); b) phenyl-B(OH)₂, K₂CO₃, Pd(PPh₃)₄, H₂O, dioxane (56 %); c) 3,4-dimethoxyphenyl-B(OH)₂, K₂CO₃, Pd(PPh₃)₄, H₂O, dioxane (27 %).

Synthesis of pyrrolo[3,2-b]pyridine

In analogy to the Lemgruber–Batcho synthesis of indoles, the synthesis of this scaffold started by reacting 5-bromo-2-methyl-3-nitropyridine 34 with N,N-dimethylformamide di-methyl acetal (DMF-DMA) to give enamine 35 (Scheme 5).[26] Reductive cyclization of enamine 35 using iron in acetic acid led to the formation of pyrrolo[3,2-b]pyridine 36. Electrophilic

iodination using N-iodosuccinimide (NIS) in THF yielded the 3-iodo congener 37 in low yield. Suzuki reaction using 37 as sub-strate, with the classical reaction conditions (Scheme 1) did not yield the desired product and only starting material was recov-ered. Protection of the pyrrole nitrogen prior to the palladium-catalyzed cross-coupling reaction turned out to be necessary. The pyrrole nitrogen was protected by reaction of 37 with di-tert-butyl carbonate (Boc₂O), yielding the Boc-protected deriva-tive 38. Suzuki coupling of 38 with phenylboronic acid pro-ceeded with concomitant cleavage of the Boc group, yielding compound 39. Reprotection with Boc (compound 40) and sub-sequent Suzuki coupling furnished compound 41. Remarkably, during this last Suzuki reaction, no Boc deprotection was ob-served, despite using the same reaction conditions as in step (e). Finally, acidic hydrolysis using a 4 n HCl solution in dioxane yielded pyrrolo[3,2-b]pyridine 42 in moderate yield.

Synthesis of pyrazolo[4,3-b]pyridine

Suzuki coupling between 5-bromo-3-fluoropicolinonitrile 43 and 3,4-dimethoxyphenylboronic acid proceeded smoothly yielding compound 44 in excellent yield (Scheme 6). An aro-matic nucleophilic substitution with hydrazine and consecutive ring closure gave access to the pyrazolo[4,3-b]pyridine scaffold 45.[27] Several attempts to convert the amino group into a bro-
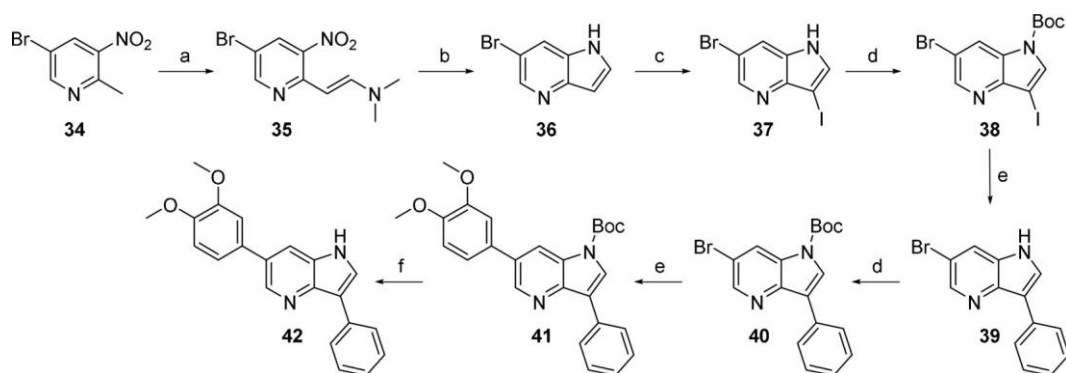
Scheme 5. Synthesis of pyrrolo[3,2-b]pyridine: a) DMF-DMA, DMF, 90 8C (98 %); b) Fe, CH₃COOH, RT (36 %); c) NIS, THF, RT (37 %); d) Boc₂O, TEA, DMAP, THF, RT (95 %); e) phenyl-B(OH)₂ (70 %) or 3,4-dimethoxyphenyl-B(OH)₂ (15 %), K₂CO₃, Pd(PPh₃)₄, H₂O, dioxane; f) 4 n HCl in dioxane, reflux (47 %).

132
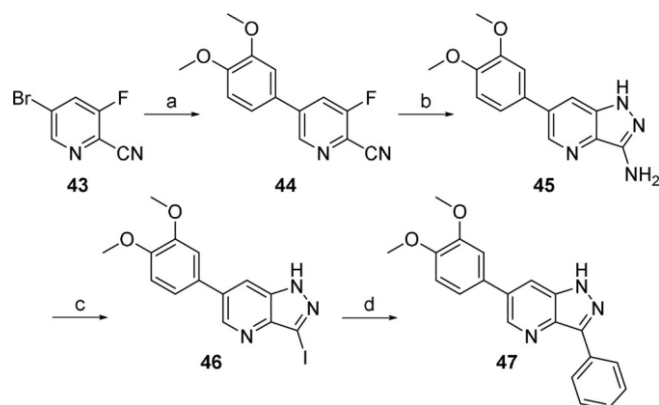
Scheme 6. Synthesis of pyrazolo[4,3-b]pyridine: a) 3,4-dimethoxyphenyl-B(OH)$_2$, K$_2$CO$_3$, Pd(PPh$_3$)$_4$, H$_2$O, dioxane (86%); b) NH$_2$NH$_2$·H$_2$O, nBuOH, 121 °C (83%); c) p-TsOH, KI, NaNO$_2$, CH$_3$CN, RT (28%); d) phenyl-B(OH)$_2$, K$_2$CO$_3$, Pd(PPh$_3$)$_4$, H$_2$O, dioxane, microwave, 120 °C (23%).

Scheme 7. Attempted synthesis of thieno[3,2-b]pyridine: a) DPPA, DIPEA, DMF, RT; b) tBuOH, reflux (61%); c) 4 n HCl in dioxane, reflux (100%); d) 2-chloromalonaldehyde, CH$_3$COOH/MeOH (2:3), 70 °C.

mine via Sandmeyer reactions (using the conditions from Schemes 1 or 2) resulted in unidentified side products. Instead, a diazotation reaction using sodium nitrite, para-toluenesulfon- ic acid (p-TsOH) and potassium iodide was used,[28] yielding the 3-iodopyrazolo[4,3-b]pyridine analogue 46 in low yield. Finally, introduction of a phenyl moiety via a Suzuki coupling yielded the title compound 47 in moderate yield. Notably, unlike in Scheme 5, the Suzuki coupling of pyrazolo[4,3-b]pyridine 46 did not require Boc protection of its pyrrole-like nitrogen for the reaction to be successful.
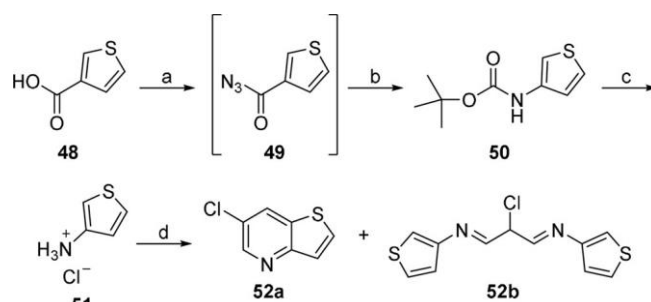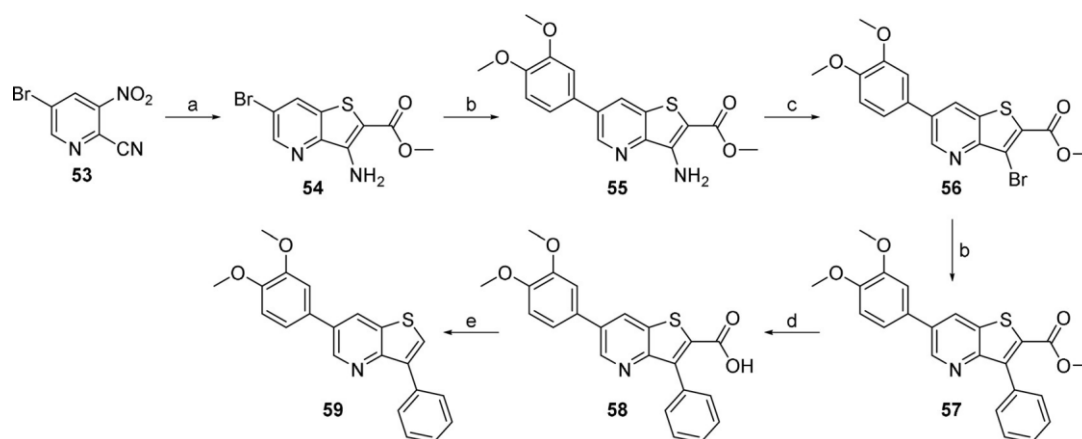
Synthesis of thieno[3,2-b]pyridine

The synthesis started from 3-aminothiophene 51, that was formed by reaction of thiophene-3-carboxylic acid 48 with di-phenyl phosphoryl azide (DPPA) resulting in the acyl azide in-termediate 49 (Scheme 7). This was subsequently submitted to a Curtius rearrangement by addition of dry tBuOH yielding a Boc-protected 3-aminothiophene 50.[24] The use of dry tBuOH was essential to prevent the formation of thiophene-3-carba-moylic acid. Deprotection of Boc using a 4 n HCl solution in di-

oxane yielded 3-aminothiophene hydrochloride 51, which turned out to be UV-sensitive and needed to be protected from light. Reaction of 51 with 2-chloromalonaldehyde did not result in the formation of the desired thieno[3,2-b]pyridine scaffold 52 a, as mass spectrometric analysis showed 2-chloro- N1,N3-di(thiophen-3-yl)propane-1,3-diimine 52 b to be the main product. To avoid this side reaction, a different synthetic route was chosen starting from the pyridine analogue 53 (Scheme 8).

Reaction of pyridine 53 with ethyl 2-mercaptoacetate and potassium tert-butoxide (KOtBu) as a strong base afforded thieno[3,2-b]pyridine 54.[29] Introduction of a 3,4-dimethoxy-phenyl residue at position 6 of the scaffold required harsher re-action conditions than for previous scaffolds. Higher tempera- ture (110 °C) and a longer reaction time (± 3 days) allowed iso- lation of the desired compound 55 in moderate yield. A classi- cal Sandmeyer reaction using conditions from Scheme 2 fol- lowed by Suzuki coupling yielded product 57. Hydrolysis of the ester using NaOH in EtOH yielded the carboxylic acid 58 as a pink precipitate. Holding compound 58 at reflux in a concen- trated HCl solution did not achieve decarboxylation of the car- boxylic acid group. Instead, only harsh conditions of metallic copper in quinoline at 200 °C yielded the title compound 59, albeit in low yield.[30]

Scheme 8. Synthesis of thieno[3,2-b]pyridine: a) ethyl 2-mercaptoacetate, KOtBu, DMF (54%); b) 3,4-dimethoxyphenyl-B(OH)$_2$ (76%) or phenyl-B(OH)$_2$ (42%), K$_3$PO$_4$, Pd(PPh$_3$)$_4$, dioxane, 110 °C; c) tBuONO, CuBr$_2$, CH$_3$CN (47%); d) NaOH, EtOH, RT (89%); e) Cu, quinoline, 200 °C (48%).

133

Synthesis of [1,2,3]triazolo[4,5-b]pyridine

Nucleophilic displacement of the chlorine at position 2 of 2,5-dichloro-3-nitropyridine 60 by aniline furnished substitution product 61 (Scheme 9).[31] Catalytic reduction of the nitro group with Raney nickel under a hydrogen atmosphere yielded the 3-aminopyridine 62. Formation of the triazole ring was achieved by a diazotation reaction using sodium nitrite in acetic acid with concomitant cyclization yielding the [1,2,3]tria- zolo[4,5-b]pyridine scaffold 63. Finally, a Suzuki coupling af- forded the target compound 64.
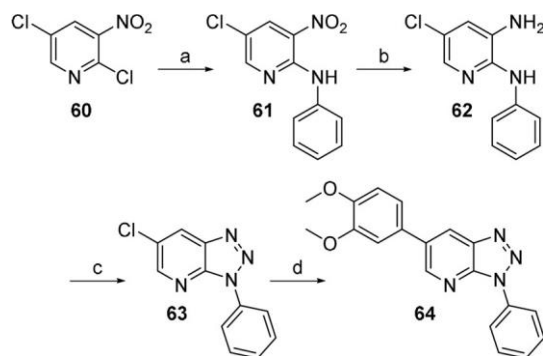
Scheme 9. Synthesis of [1,2,3]triazolo[4,5-b]pyridine: a) aniline, DIPEA, diox-ane, 80 8C (85 %8); b) Raney nickel, H_2, THF, RT; c) $NaNO_2$, acetic acid, CH_2Cl_2, water (62 %); d) 3,4-dimethoxyphenyl-B(OH)$_2$, Cs_2CO_3, Pd(PPh$_3$)$_4$, H_2O, DMF (78 %).

Synthesis of imidazo[4,5-b]pyridine

Initial attempts for the synthesis of the imidazo[4,5-b]pyridine scaffold followed a similar procedure as in Scheme 9. Reaction of compound 62 with triethyl orthoformate allowed to build up the imidazole ring and afforded 6-chloro-3-phenylimida- zo[4,5-b]pyridine. Unfortunately, despite exploring different re- action conditions, the subsequent Suzuki coupling never yield- ed the desired compound. Therefore, an alternative synthetic route was developed in which the 3,4-dimethoxyphenyl resi- due was introduced early on in the synthetic sequence.[32] As the Suzuki coupling on the brominated pyridine analogue was consistently higher yielding, 5-bromo-2-chloro-3-nitropyridine 65 was selected as starting material. Introduction of an anilino moiety at position 2 by nucleophilic aromatic substitution af- forded compound 66 (Scheme 10). Suzuki coupling formed the addition product 67 in good yield. For the reduction of the nitro group, we opted for zinc in acetic acid as this proceeded faster and cleaner than catalytic hydrogenation. The amino in- termediate 68 was used as such without further purification for the formation of the imidazole moiety. Reaction of 68 with triethyl orthoformate afforded imidazo[4,5-b]pyridine 69 in low yield.

Synthesis of quinazoline

Condensation of methyl 2-amino-4-bromobenzoate 70 with triethyl orthoformate as a one-carbon fragment and ammoni-um acetate as nitrogen source allowed the isolation of 7-bro-
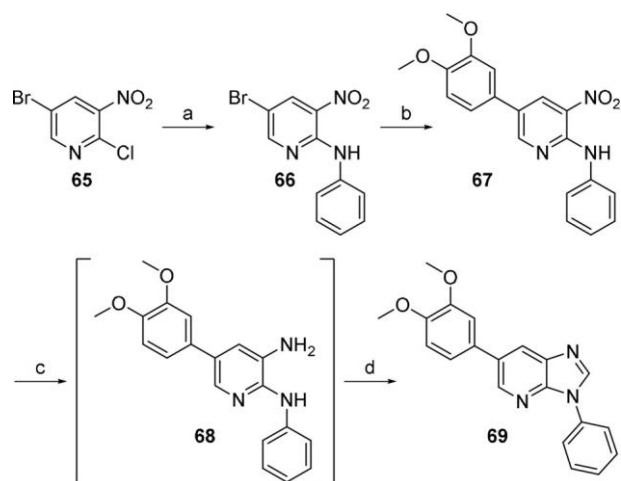
Scheme 10. Synthesis of imidazo[4,5-b]pyridine: a) aniline, DIPEA, NMP, 120 8C (78 %); b) 3,4-dimethoxyphenyl-B(OH)$_2$, K_2CO_3, Pd(PPh$_3$)$_4$, H_2O, dioxane (78 %); c) Zn, CH_3COOH; d) CH(OEt)$_3$, 130 8C (35 %).
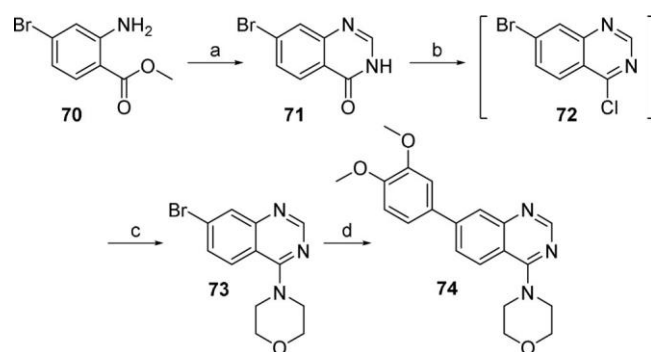
Scheme 11. Synthesis of quinazoline: a) NH_4OAc, CH(OEt)$_3$, reflux (60 %); b) POCl$_3$, reflux; c) morpholine, RT (57 %); d) 3,4-dimethoxyphenyl-B(OH)$_2$, K_2CO_3, Pd(PPh$_3$)$_4$, H_2O, dioxane, 90 8C (75 %).

moquinazolin-4(3H)-one 71 (Scheme 11).[33] The tautomeric hy-droxy group of the lactam moiety was converted into a chlor-ine by treatment with phosphorus oxychloride, yielding a 4-chloro-quinazoline analogue 72.[34] A nucleophilic aromatic substitution with morpholine yielded the 4-morpholino-quina-zoline 73. Coupling of 73 with 3,4-dimethoxyphenylboronic acid using the aforementioned conditions for the Suzuki reac- tion furnished quinazoline 74 in good yield.

Synthesis of pyrido[3,2-d]pyrimidine

First, the nitro group of commercially available 3-nitro-5-bro-mopyridine-2-carbonitrile 53 was reduced by treatment with iron under acidic conditions, generating the desired aniline 75 as the major product (Scheme 12). However, due to the acid hydrolysis of the cyano group, a substantial amount (12 %) of 3-amino-5-bromopicolinamide was also formed. These two compounds were easily separated by silica gel flash chroma-tography. Introduction of a 3,4-dimethoxyphenyl moiety on 75 via a Suzuki coupling yielded compound 76. Construction of the pyrimidine moiety using triethyl orthoformate, as per-

134
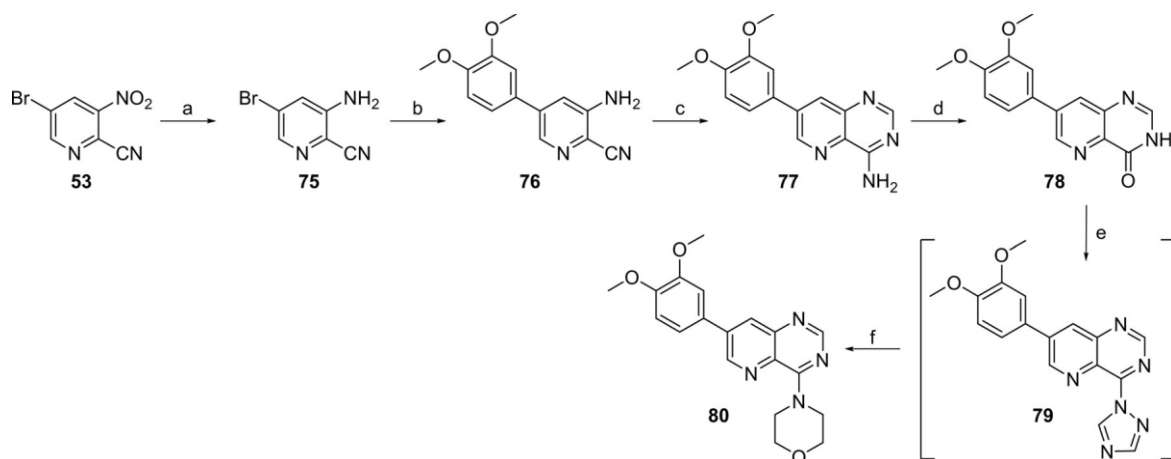
Scheme 12. Synthesis of pyrido[3,2-*d*]pyrimidine: a) Fe, CH$_3$COOH, RT (56%); b) 3,4-dimethoxyphenyl-B(OH)$_2$, K$_2$CO$_3$, Pd(PPh$_3$)$_4$, H$_2$O, dioxane, 90 8C (98%); c) formamide, 160 8C, microwave (74%); d) 6 n HCl, reflux (66%); e) POCl$_3$, 1,2,4-triazole, DIPEA, CH$_3$CN; f) morpholine, dioxane, reflux (25%).

formed before for the synthesis of the quinazoline analogue, did not result in the isolation of the desired product. In contrast, heating of compound 76 in formamide (which functions both as a reagent and solvent) under microwave conditions furnished pyrido[3,2-*d*]pyrimidine 77 as a brown precipitate in excellent yield and the product was used as such without further purification.[35] Acid hydrolysis of the 4-amino group of 77 afforded pyrido[3,2-*d*]pyrimi-din-4(3*H*)-one 78. Phosphorus oxychloride mediated chlorination of compound 78 turned out to be cumbersome as no product was retrieved, even though starting material appeared to be fully consumed. Instead of chloride, 1,2,4-triazole was introduced as a leaving group successfully yielding intermediate 79. Subsequent substitution with morpholine yielded the title compound 80 in moderate yield.

*Synthesis of pyrido[2,3-*d]pyrimidine*

Starting from pyridine analogue 10 (synthesized in Scheme 1), the construction of the pyrimidine moiety and the introduction of morpholine was performed in analogy to Scheme 12, yielding the title compound 84 in moderate yield (Scheme 13).

Synthesis of pteridine

Heating of compound 19 (available from Scheme 3) in forma- mide (as in Schemes 12 and 13) did not allow formation of the pyrimidine moiety, and only starting material was recovered. Alternatively, attempts to build up the pyrimidine ring using concentrated formic acid and concentrated sulfuric acid under microwave irradiation,[22, 36] solely led to the hydrolysis of the cyano group affording carboxamide 85 as a bright-yellow pre-cipitate (Scheme 14). Subsequent ring closure by treatment with formamide afforded pteridin-4(3*H*)-one 86. Chlorination with phosphorus oxychloride yielded 4-chloropteridine 87, which was

Scheme 13. Synthesis of pyrido[2,3-*d*]pyrimidine: a) formamide, 160 8C, microwave (46%); b) HCl 6 n, reflux (60%); c) POCl$_3$, 1,2,4-triazole, DIPEA, CH$_3$CN; d) morpholine, di-oxane, 60 8C (19%).

chromatography. Finally, introduction of morpholine yielded the target compound 88.

Biological evaluation and SAR

All compounds were tested for GAK binding affinity using the KINOME*scan*Q platform, that quantitatively measures the ability of a compound to compete with an immobilized active-site-directed ligand.[37] In an initial series of compounds, the focus

sufficiently stable to be purified by silica gel flash

was on structural modification of the pyridine moiety of the isothiazolo[4,3-*b*]pyridine scaffold (Table 1). Shuffling the posi- tion of the nitrogen yielded isothiazolo[3,4-*b*]pyridine **14**, dis- playing a 75-fold drop in GAK affinity relative to the parent iso- thiazolo[4,3-*b*]pyridine scaffold. Insertion of an additional nitro- gen atom in the pyridine moiety of compound **14** yielded a pyrazine and pyrimidine analogue. The isothiazolo[3,4-*d*]pyri-

midine **29** ($K_d = 3.2$ mM) is equally active a GAK ligand as iso- thiazolo[3,4-*b*]pyridine **14** ($K_d = 3.9$ mM), whereas isothiazo- lo[3,4-*b*]pyrazine **23** ($K_d = 0.36$ mM) is 10-fold more potent than

isothiazolo[3,4-*b*]pyridine **14**, but still shows a 10-fold de- creased GAK affinity relative to the original isothiazolo[4,3-

136
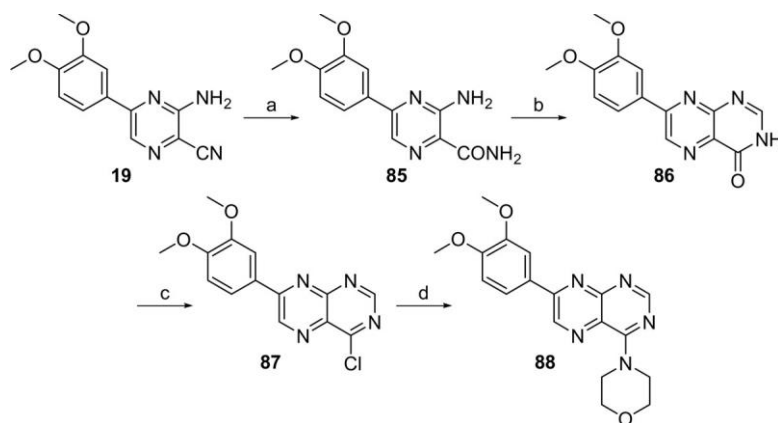
Scheme 14. Synthesis of pteridine: a) HCOOH, H_2SO_4, 120 °C, microwave (78 %); b) formamide, 160 °C, microwave (71 %); c) $POCl_3$, toluene, reflux, RT (55 %); d) morpholine, dioxane, reflux (97 %).

Table 1. SAR of the pyridine moiety of the isothiazolo[4,3-*b*]pyridine scaffold.			
Compd	Scaffold name	Scaffold	GAK K_d [mm][a]
4	isothiazolo[4,3-*b*]pyridine		0.052
14	isothiazolo[3,4-*b*]pyridine		3.9
23	isothiazolo[3,4-*b*]pyrazine		0.36
29	isothiazolo[3,4-*d*]pyrimidine		3.2
[a] Values are the average of two independent experiments.			

b]pyridine skeleton. Overall, the SAR of the pyridine moiety points toward an essential role of the nitrogen at position 4 of the scaffold.

To further evaluate the SAR with respect to GAK binding, the pyridine moiety was kept intact, and the isothiazolo moiety was replaced by a number of five-membered heteroaromatic rings (Table 2). As mentioned above in the introduction, introducing morpholine turned out to be problematic, and therefore the 3-phenylisothiazolo[4,3-*b*]pyridine 5 (K_d: 0.77 mm) was selected as a reference compound. Neither pyrrolo[3,2-*b*]pyridine 42, pyrazolo[4,3-*b*]pyridine 47, thieno[3,2-*b*]pyridine 59 nor [1,2,3]triazolo[4,5-*b*]pyridine 64 were able to reach the GAK affinity value of the reference compound 5. In contrast, pyrazolo[1,5-*a*]pyrimidine 33 and imidazo[4,5-*b*]pyridine 69

were the only scaffolds with a similar GAK affinity as isothiazolo[4,3-*b*]pyridine 5.

Finally, the 6,5-bicyclic isothiazolo[4,3-*b*]pyridine core was replaced by a number of 6,6-bicyclic structures (Table 3). Keeping the pyridine moiety of isothiazolo[4,3-*b*]pyridine intact and re-

Table 2. SAR of the isothiazolo moiety of the isothiazolo[4,3-*b*]pyridine scaffold.			
Compd	Scaffold name	Scaffold	GAK K_d [mm][a]
5	isothiazolo[4,3-*b*]pyridine		0.77
33	pyrazolo[1,5-*a*]pyrimidine		0.69
42	pyrrolo[3,2-*b*]pyridine		4
47	pyrazolo[4,3-*b*]pyridine		1.7
59	thieno[3,2-*b*]pyridine		26
64	[1,2,3]triazolo[4,5-*b*]pyridine		> 30
69	imidazo[4,5-*b*]pyridine		0.14
[a] Values are the average of two independent experiments.			

136

Table 3. SAR of 6,6-bicyclic scaffolds.			

Compd	Scaffold name	Scaffold	GAK K_d [mm][a]
4	isothiazolo[4,3-*b*]pyridine		0.052
74	quinazoline		0.62
78	pyrido[3,2-*d*]pyrimidine		7.3
84	pyrido[2,3-*d*]pyrimidine		20
88	pteridine		25

[a] Values are the average of two independent experiments.

placing the isothiazole moiety with pyrimidine afforded the pyrido[3,2-*d*]pyrimidine 78, which is endowed with a K_d value of 7.3 mm, and hence displays a 140-fold drop in GAK affinity relative to the original isothiazolo[4,3-*b*]pyridine skeleton. Switching the position of the nitrogen in the pyridine ring (yielding pyrido[2,3-*d*]pyrimidine 84) or insertion of an addi- tional nitrogen (affording pteridine 88) afforded scaffolds that were completely lacking GAK affinity (K_d: 20 mm or more). On the other hand, quinazoline 74 shows only a 10-fold drop in GAK affinity ($K_d = 0.62$ mm).

Conclusions

A number of 5,6- and 6,6-fused bicyclic heteroaromatic scaf- folds that bear essential structural features for GAK affinity and that are based on the original isothiazolo[4,3-*b*]pyridine scaf- folds 4 and 5 were synthesized. Four of the 13 novel scaffolds (isothiazolo[3,4-*b*]pyrazine 23, pyrazolo[1,5-*a*]pyrimidine 33, imidazo[4,5-*b*]pyridine 69, and quinazoline 74) displayed GAK affinity with K_d values < 1 mm. Although these compounds are not potent enough to serve as chemical tools to decipher GAK biology in a cellular context, they can serve as starting points for medicinal chemists to further improve the GAK binding af- finity by modification of the decoration pattern.

Moreover, this report also describes the synthesis of new scaffolds that are underrepresented in organic/medicinal chemistry. Examples include the isothiazolo[3,4-*b*]pyridine (206 known compounds according to SciFinder), isothiazolo[3,4-

b]pyrazine (25 known derivatives according to SciFinder), and isothiazolo[3,4-*d*]pyrimidine (80 known analogues in SciFinder).

Experimental Section

For all reactions, analytical-grade solvents were used. All moisture-sensitive reactions were carried out in oven-dried glassware (125 8C). All microwave irradiation experiments were carried out in a dedicated CEM-Discover monomode microwave apparatus, oper- ating at a frequency of 2.45 GHz with continuous irradiation power from 0 to 300 W using the standard absorbance level (300 W maxi- mum power). The reactions were carried out in 10 mL glass tubes, sealed with an aluminum/Teflon crimp top, which can be exposed to 250 8C and 20 bar internal pressure. The temperature was mea- sured with an IR sensor on the outer surface of the process vial. After the irradiation period, the reaction vessel was cooled rapidly (60–120 s) to ambient temperature by gas jet cooling. ^{1}H and ^{13}C NMR spectra were recorded on a Bruker Avance 300 MHz in- strument (^{1}H NMR, 300 MHz; ^{13}C NMR, 75 MHz), 500 MHz instru- ment (^{1}H NMR, 500 MHz; ^{13}C NMR, 125 MHz) or a 600 MHz instru- ment (^{1}H NMR, 600 MHz; ^{13}C NMR, 150 MHz), using tetramethylsi- lane as internal standard for ^{1}H NMR spectra and [D$_6$]DMSO (39.5 ppm) or CDCl$_3$ (77.2 ppm) for ^{13}C NMR spectra. Abbreviations used are s = singlet, d = doublet, t = triplet, q = quartet, m = multip- let, b = broad. Coupling constants are expressed in Hz. High-resolu- tion mass spectra were acquired on a quadrupole orthogonal ac- celeration time-of-flight mass spectrometer (Synapt G2 HDMS, Waters, Milford, MA). Samples were infused at 3 mLmin[@1] and spec- tra were obtained in positive or negative ionization mode with a resolution of 15000 (FWHM) using leucine enkephalin as lock mass. Precoated aluminum sheets (Fluka silica gel/TLC-cards, 254 nm) were used for TLC. Column chromatography was per- formed on silica gel 0.060–0.200 mm, 60 a (Acros Organics). Purity of final compounds was verified to be > 95 % by HPLC analysis. HPLC conditions to asses purity were as follows: Shimadzu HPLC equipped with a LC-20AT pump, DGU-20A5 degasser, and a SPD- 20A UV-VIS detector; Symmetry C$_{18}$ column (5 mm, 4.6 mm V 150 mm); gradient elution of H$_2$O/CH$_3$CN from 95:5 or 70:30 to 5:95 over 25 min; flow rate: 1 mLmin[@1]; wavelength: UV 254 nm. Preparative HPLC purifications were performed using a Phenomen- ex Gemini 110A column (C$_{18}$, 10 mm, 21.2 mm V 250 mm).

Chemistry

2-Chloro-6-(3,4-dimethoxyphenyl)nicotinonitrile (7): To a solution of 2,6-dichloronicotinonitrile 6 (2.0 g, 11.56 mmol) in dioxane (40 mL) and water (10 mL) were added 3,4-dimethoxyphenyl bor- onic acid (2.5 g, 13.87 mmol), potassium carbonate (3.2 g, 23.12 mmol), and Pd(PPh$_3$)$_4$ (134 mg, 0.12 mmol). The reaction mix- ture was stirred at 90 8C for 3 h. The volatiles were evaporated and the crude residue was purified by silica gel flash column chroma- tography (using a mixture of dichloromethane/methanol 99:1) yielding the title compound (2.7 g, 63 %). ^{1}H NMR (300 MHz, DMSO): d = 8.46 (d, J = 8.2 Hz, 1 H), 8.21 (d, J = 8.3 Hz, 1 H), 7.79 (dd, J = 8.5, 2.1 Hz, 1 H), 7.69 (d, J = 2.0 Hz, 1 H), 7.12 (d, J = 8.6 Hz, 1 H), 3.87 (s, 3 H), 3.85 ppm (s, 3 H); ^{13}C NMR (75 MHz, DMSO): d = 159.71, 151.89, 150.95, 149.21, 144.37, 127.95, 121.18, 118.56, 115.65, 111.93, 110.33, 106.55, 55.79 ppm; HRMS m/z [$M + H$]$^+$ calcd for C$_{14}$H$_{11}$Cl$_1$N$_2$O$_2$: 275.0582, found: 275.0589.

2-Azido-6-(3,4-dimethoxyphenyl)nicotinonitrile (8): To a solution of 2-chloro-6-(3,4-dimethoxyphenyl)nicotinonitrile 7 (2.0 g, 7.80 mmol) in DMF (25 mL) was added NaN$_3$ (812 mg, 12.48 mmol).

The mixture was stirred at 70 °C for 4 h upon which a bright yellow precipitate formed. The mixture was allowed to cool to room temperature, the precipitate was filtered off and carefully washed with water to yield the title compound (1.8 g, 83%). ^{1}H NMR (300 MHz, DMSO): d = 8.78–8.55 (m, 1 H), 7.96–7.65 (m, 3 H), 7.47–7.19 (m, 1 H), 3.91 (s, 3 H), 3.88 ppm (s, 3 H); HRMS m/z [M+H]$^+$ calcd for $C_{14}H_{11}N_5O$: 282.0985, found: 282.0985.

2-Amino-6-(3,4-dimethoxyphenyl)nicotinonitrile (10): To a solution of 2-azido-6-(3,4-dimethoxyphenyl)nicotinonitrile 8 (1.5 g, 5.33 mmol) in pyridine was added triphenyl phosphine (2.2 g, 8.53 mmol) and the mixture was stirred at room temperature overnight. After disappearance of the starting material the volatiles were evaporated and the crude residue was dissolved in an 80% solution of acetic acid in water and held at reflux for 1 h. The vola- tiles were evaporated in vacuo and the crude residue was purified by silica gel flash column chromatography (eluting with a gradient of dichloromethane/ethyl acetate in a ratio of 99:1 to 95:5) to yield the title compound (1.92 g, 95%). ^{1}H NMR (300 MHz, DMSO): d = 7.87 (d, J = 8.1 Hz, 1 H), 7.67 (d, J = 1.8 Hz, 1 H), 7.62 (dd, J = 8.5, 1.8 Hz, 1 H), 7.19 (d, J = 8.1 Hz, 1 H), 7.01 (d, J = 8.5 Hz, 1 H), 6.89 (bs, 2 H), 3.84 (s, 3 H), 3.81 ppm (s, 3 H); ^{13}C NMR (75 MHz, DMSO): d = 170.11, 159.71, 158.91, 150.82, 148.89, 142.83, 130.25, 120.31, 117.67, 111.55, 110.41, 108.16, 87.08, 55.65 ppm; HRMS m/z [M+H]$^+$ calcd for $C_{14}H_{13}N_3O_2$: 256.1080, found: 256.1085.

2-Amino-6-(3,4-dimethoxyphenyl)pyridine-3-carbothioamide (11): To a solution of 2-amino-6-(3,4-dimethoxyphenyl)nicotinonitrile 10 (500 mg, 1.96 mmol) in ethanol (25 mL) was added P_2S_5 (1.74 g, 7.84 mmol) and the mixture was stirred at reflux overnight. After disappearance of the starting material, the volatiles were evaporated and the crude residue was purified by silica gel flash column chromatography (eluting with a mixture of dichloromethane/acetone in a ratio of 90:10) to yield the title compound (400 mg, 71%). ^{1}H NMR (300 MHz, DMSO): d = 9.70 (bs, 1 H), 9.43 (bs, 1 H), 7.75–7.57 (m, 3 H), 7.22–7.12 (m, 3 H), 7.04 (d, J = 8.4 Hz, 1 H), 3.85 (s, 3 H), 3.82 ppm (s, 3 H); ^{13}C NMR (75 MHz, DMSO): d = 198.24, 157.11, 156.33, 150.28, 148.87, 136.13, 130.94, 119.72, 115.66, 111.70, 110.22, 107.65, 55.69 ppm; HRMS m/z [M+H]$^+$ calcd for $C_{14}H_{15}N_3O_2S_1$: 290.0958, found: 290.0959.

6-(3,4-Dimethoxyphenyl)isothiazolo[3,4-b]pyridin-3-amine (12): To a solution of 2-amino-6-(3,4-dimethoxyphenyl)pyridine-3-carbo- thioamide 11 (300 mg, 1.04 mmol) in methanol (5 mL) at 0 °C was added dropwise a 30% aqueous H_2O_2 solution (354 mL, 4.15 mmol) and the mixture was stirred overnight at room temperature. After disappearance of the starting material, the mixture was cooled to 0 °C and the precipitate was filtered off and washed with cold methanol to yield the title compound (250 mg, 83%). ^{1}H NMR (300 MHz, DMSO): d = 8.29 (d, J = 8.6 Hz, 1 H), 8.13 (bs, 2 H), 7.80 (s, 1 H), 7.75 (d, J = 8.3 Hz, 1 H), 7.50 (d, J = 8.8 Hz, 1 H), 7.08 (d, J = 8.3 Hz, 1 H), 3.88 (s, 3 H), 3.84 ppm (s, 3 H); ^{13}C NMR (75 MHz, DMSO): d = 173.76, 164.69, 159.85, 150.93, 149.03, 131.91, 131.03, 120.78, 111.65, 110.94, 110.50, 109.72, 55.73, 55.68 ppm; HRMS m/z [M+H]$^+$ calcd for $C_{14}H_{13}N_3O_2S_1$: 288.0801, found: 288.0802.

3-Bromo-6-(3,4-dimethoxyphenyl)isothiazolo[3,4-b]pyridine (13): A solution of 6-(3,4-dimethoxyphenyl)isothiazolo[3,4-b]pyridin-3- amine 12 (200 mg, 0.70 mmol) in HBr (5 mL) was stirred for 10 min at room temperature, then CuBr was added at once (200 mg, 1.40 mmol). The resulting mixture was cooled to 0 °C and solution of sodium nitrite (146 g, 2.10 mmol) in H_2O (5 mL) was added drop- wise over a period of 15 min. The reaction mixture was stirred for 4 h at 0 °C followed by overnight at room temperature. After disap- pearance of the starting material, the mixture was cooled to 0 °C

and carefully neutralized using Na_2CO_3. The neutralized mixture was washed with ethyl acetate 3 times, organic phases were col- lected and concentrated in vacuo. The crude residue was purified by silica gel flash column chromatography (eluting with a mixture of hexane/acetone in a ratio of 80:20) yielding the title compound (60 mg, 25%). HRMS m/z [M+H]$^+$ calcd for $C_{14}H_{11}Br_1N_2O_2S_1$: 350.9798, found: 350.9801

4-(6-(3,4-Dimethoxyphenyl)isothiazolo[3,4-b]pyridin-3-yl)mor- pholine (14): To a solution of 3-bromo-6-(3,4-dimethoxyphenyl)iso- thiazolo[3,4-b]pyridine 13 (50 mg, 0.14 mmol) in ethanol (5 mL) was added morpholine (37 mg, 0.43 mmol). The reaction was stirred at reflux for 4 days. After disappearance of the starting ma- terial volatiles were evaporated in vacuo and the crude residue was purified by silica gel flash column chromatography (eluting with a mixture of dichloromethane/methanol in a ratio of 97:3) to yield the title compound (20 mg, 40%). ^{1}H NMR (300 MHz, DMSO): d = 8.41 (d, J = 9.1 Hz, 1 H), 7.84 (d, J = 1.9 Hz, 1 H), 7.79 (dd, J = 8.4, 2.0 Hz, 1 H), 7.58 (d, J = 9.2 Hz, 1 H), 7.09 (d, J = 8.5 Hz, 1 H), 3.98– 3.81 (m, 10 H), 3.54 ppm (m, 4 H); ^{13}C NMR (75 MHz, DMSO): d = 175.75, 166.13, 159.37, 151.12, 149.11, 132.68, 130.71, 120.92, 112.38, 111.68, 110.37, 109.96, 65.38, 55.76, 55.71, 50.66 ppm; HRMS m/z [M + H]$^+$ calcd for $C_{18}H_{19}N_3O_3S_1$: 358.1220, found: 358.1219.

3-Chloro-5-(3,4-dimethoxyphenyl)pyrazine-2-carbonitrile (16): To a solution 3,5-dichloropyrazine-2-carbonitrile 15 (2.0 g, 11.50 mmol) in dioxane (50 mL) were added 3,4-dimethoxyphenylboronic acid (2.51 g, 13.80 mmol), tripotassium phosphate (4.88 g, 22.99 mmol), and Pd(PPh$_3$)$_4$ (132 mg, 0.12 mmol). The reaction mixture was stirred at 90 °C overnight. The volatiles were evaporated and the crude residue was purified by silica gel flash column chromatogra- phy (eluting with a mixture of dichloromethane/ethyl acetate in a ratio of 99:1) yielding the title compound (2.34 g, 74%). ^{1}H NMR (300 MHz, DMSO): d = 9.48 (s, 1 H), 7.91 (dd, J = 8.5, 2.1 Hz, 1 H), 7.75 (d, J = 2.1 Hz, 1 H), 7.18 (d, J = 8.6 Hz, 1 H), 3.88 (s, 3 H), 3.88 ppm (s, 3 H); HRMS m/z [M+H]$^+$ calcd for $C_{13}H_{10}Cl_1N_3O_2$: 276.0534, found: 276.0528.

3-Azido-5-(3,4-dimethoxyphenyl)pyrazine-2-carbonitrile (17): To a solution of 3-chloro-5-(3,4-dimethoxyphenyl)pyrazine-2-carboni- trile 16 (2.34 g, 8.45 mmol) in DMSO (50 mL) was added NaN$_3$ (604 mg, 9.30 mmol). The mixture was stirred at 70 °C overnight. After disappearance of the starting material the mixture was al- lowed to cool and water was added. The formed precipitate was filtered off and washed with water to yield the title compound (2.10 g, 83%). HRMS m/z [M + Na]$^+$ calcd for $C_{13}H_{10}N_6O_2Na$: 305.0758, found: 305.0755.

3-Amino-5-(3,4-dimethoxyphenyl)pyrazine-2-carbonitrile (19): To a solution of 3-azido-5-(3,4-dimethoxyphenyl)pyrazine-2-carboni- trile 17 (2.07 g, 7.00 mmol) in pyridine (30 mL) was added triphenyl phosphine (2.99 g, 11.40 mmol) and the mixture was stirred at room temperature overnight. After disappearance of the starting material, the volatiles were evaporated and the crude residue was dissolved in an 80% solution of acetic acid in water (20 mL) and held at reflux for 1 h. The volatiles were evaporated and the crude residue was purified by silica gel flash column chromatography (eluting with a gradient of dichloromethane/acetone in a ratio of 95:5) to yield the title compound (1.72 g, 95%). ^{1}H NMR (300 MHz, CDCl$_3$): d = 8.47 (s, 1 H), 7.63–7.56 (m, 2 H), 7.01–6.93 (m, 1 H), 5.27 (bs, 2 H), 3.99 (s, 3 H), 3.97 ppm (s, 3 H); ^{13}C NMR (126 MHz, DMSO): d = 156.66, 153.39, 151.90, 149.48, 131.23, 127.86, 121.35, 117.03, 112.21, 110.74, 108.93, 56.11 ppm; HRMS m/z [M+H]$^+$ calcd for $C_{13}H_{12}N_4O_2$: 257.1033, found: 257.1032.

3-Amino-5-(3,4-dimethoxyphenyl)pyrazine-2-carbothioamide (20): To a solution of 3-amino-5-(3,4-dimethoxyphenyl)pyrazine-2-carbonitrile 19 (700 mg, 2.73 mmol) in ethanol (20 mL) was added Lawesson's reagent (2.21 g, 5.46 mmol) and the mixture was held at reflux overnight. After disappearance of the starting material the volatiles were evaporated in vacuo. The residue was dissolved in water and extracted three times with dichloromethane. The combined organic layers were evaporated under reduced pressure and the crude residue was purified by silica gel silica gel flash column chromatography (using a mixture of dichloromethane/ethyl acetate in a ratio of 99:1 as mobile phase) yielding the title compound (660 mg, 83%). ^{1}H NMR (300 MHz, CDCl$_3$): d = 8.47 (s, 1H), 7.65–7.55 (m, 2H), 7.02–6.93 (m, 1H), 3.99 (s, 3H), 3.97 ppm (s, 3H); ^{13}C NMR (126 MHz, DMSO): d = 192.85, 155.01, 153.30, 151.59, 149.49, 128.39, 127.92, 125.29, 120.96, 112.19, 110.61, 56.10, 56.08 ppm.

6-(3,4-Dimethoxyphenyl)isothiazolo[3,4-b]pyrazin-3-amine (21): To a solution of 3-amino-5-(3,4-dimethoxyphenyl)pyrazine-2-carbothioamide 20 (600 mg, 2.07 mmol) in methanol (5 mL) at 0 8C was added dropwise a 30% aqueous H$_2$O$_2$ solution (703 mL, 8.27 mmol). The mixture was stirred overnight at room temperature. After disappearance of the starting material the volatiles were evaporated under reduced pressure and the crude residue was purified by silica gel flash column chromatography (eluting with a gradient of dichloromethane/acetone in a ratio of 9:1 to 8:2) to yield the title compound (400 mg, 67%). ^{1}H NMR (300 MHz, DMSO): d = 8.95 (s, 1H), 8.24 (s, 2H), 7.89 (d, J=8.4 Hz, 1H), 7.82 (s, 1H), 7.13 (d, J=8.5 Hz, 1H), 3.90 (s, 3H), 3.86 ppm (s, 3H); HRMS m/z [M+H]$^+$ calcd for C$_{13}$H$_{12}$N$_4$O$_2$S$_1$: 289.0754, found: 289.0767

3-Bromo-6-(3,4-dimethoxyphenyl)isothiazolo[3,4-b]pyrazine (22): To a solution of CuBr$_2$ (170 mg, 0.76) and tert-butylnitrite (93 mg, 0.90 mmol) in dry acetonitrile (5 mL) under argon atmosphere at 0 8C was added 6-(3,4-dimethoxyphenyl)isothiazolo[3,4-b]pyrazin-3-amine 21 (200 mg, 0.67 mmol) and the mixture was stirred at 0 8C for 5 h. After disappearance of the starting material, volatiles were evaporated and the crude residue was purified by silica gel flash column chromatography (eluting with a mixture of dichloromethane/ethyl acetate in a ratio of 99:1) yielding the title compound (77 mg, 32%). ^{1}H NMR (300 MHz, CDCl$_3$): d = 9.27 (s, 1H), 7.97 (s, 1H), 7.79 (d, J=8.4 Hz, 1H), 7.01 (d, J=8.4 Hz, 1H), 4.02 (s, 3H), 3.98 ppm (s, 3H).

4-(6-(3,4-Dimethoxyphenyl)isothiazolo[3,4-b]pyrazin-3-yl)morpholine (23): To a solution of 3-bromo-6-(3,4-dimethoxyphenyl)isothiazolo[3,4-b]pyrazine 22 (77 mg, 0.22 mmol) in ethanol (5 mL) was added morpholine (57 mg, 0.66 mmol) and the reaction was stirred at reflux overnight. After disappearance of the starting material, volatiles were evaporated in vacuo and the crude residue was purified by silica gel flash column chromatography (eluting with a mixture of dichloromethane/methanol in a ratio of 98:2) to yield the title compound (48 mg, 64%). ^{1}H NMR (300 MHz, CDCl$_3$): d = 8.80 (s, 1H), 7.96 (d, J=2.0 Hz, 1H), 7.73 (dd, J=8.4, 2.0 Hz, 1H), 6.99 (d, J=8.5 Hz, 1H), 4.03 (s, 3H), 3.98 (s, 3H), 3.97–3.96 (m, 8H); ^{13}C NMR (75 MHz, CDCl$_3$): d = 173.06, 160.31, 154.08, 152.07, 150.02, 136.81, 129.26, 125.65, 121.33, 111.10, 110.81, 66.40, 56.48, 56.34, 50.05 ppm; HRMS m/z [M+H]$^+$ calcd for C$_{17}$H$_{18}$N$_4$O$_3$S$_1$: 359.1172, found: 359.1161.

4-Amino-2-(3,4-dimethoxyphenyl)pyrimidine-5-carbonitrile (25): A solution of 4-amino-2-chloropyrimidine-5-carbonitrile 24 (3.00 g, 19.50 mmol), tripotassium phosphate (8.28 g, 39 mmol) and 3,4-dimethoxyphenylboronic acid (3.67 g, 29.25 mmol) in dry dioxane (30 mL) was degassed and refilled with nitrogen gas two times.

Pd(OAc)$_2$ (219 mg, 0.98 mmol) and D-t-BPF (501 mg, 0.98 mmol) were added and the mixture was degassed and refilled with nitrogen gas two times and stirred at reflux overnight. After disappearance of the starting material, the mixture was allowed to cool to room temperature and the solid was filtered off and thoroughly washed with ethyl acetate. The filtrate was concentrated in vacuo and the crude residue was purified by silica gel flash column chromatography (eluting with a mixture of dichloromethane/ethyl acetate in a ratio of 95:5) to yield the title compound (2.76 g, 53%). ^{1}H NMR (300 MHz, DMSO): d = 8.68 (s, 1H), 7.97 (d, J=8.4 Hz, 1H), 7.91–7.80 (m, 3H), 7.09 (d, J=8.5 Hz, 1H), 3.84 (s, 3H), 3.83 ppm (s, 3H); ^{13}C NMR (126 MHz, DMSO): d = 164.65, 162.55, 161.47, 151.98, 148.55, 128.98, 122.15, 116.06, 111.33, 111.10, 86.80, 55.68, 55.49 ppm; HRMS m/z [M+H]$^+$ calcd for C$_{13}$H$_{12}$N$_4$O$_2$: 257.1033, found: 257.1038.

4-Amino-2-(3,4-dimethoxyphenyl)pyrimidine-5-carbothioamide (26): To a solution 4-amino-2-(3,4-dimethoxyphenyl)pyrimidine-5-carbonitrile 25 (2.00 g, 7.80 mmol) in ethanol (30 mL) was added Lawesson's reagent (6.31 g, 15.60 mmol). The mixture was held at reflux overnight. After disappearance of the starting material volatiles were evaporated in vacuo and the residue was dissolved in water and extracted three times with dichloromethane. The combined organic layers were evaporated under reduced pressure and the crude residue was purified by silica gel flash column chromatography (using a gradient of dichloromethane/acetone in a ratio of 85:15 to 75:15 as mobile phase) yielding the title compound (1.36 g, 60%). ^{1}H NMR (300 MHz, DMSO): d = 9.83 (s, 1H), 9.58 (s, 1H), 8.44 (s, 1H), 8.00–7.89 (m, 4H), 7.07 (d, J=8.5 Hz, 1H), 3.83 ppm (s, 6H); ^{13}C NMR (126 MHz, DMSO): d = 195.84, 163.00, 161.06, 153.48, 151.46, 148.56, 129.69, 121.53, 112.96, 111.36, 110.90, 55.68, 55.53 ppm.

6-(3,4-Dimethoxyphenyl)isothiazolo[3,4-d]pyrimidin-3-amine (27): To a solution of 4-amino-2-(3,4-dimethoxyphenyl)pyrimidine-5-carbothioamide 26 (500 mg, 1.72 mmol) in methanol (5 mL) at 0 8C was added dropwise a 30% aqueous H$_2$O$_2$ solution (585 mL, 6.89 mmol). The mixture was stirred overnight at room temperature. After disappearance of the starting material, the volatiles were evaporated in vacuo and the crude residue was purified by silica gel flash column chromatography (eluting with a gradient of dichloromethane/acetone 8:2) yielding the title compound (418 mg, 84%). ^{1}H NMR (300 MHz, DMSO): d = 9.38 (s, 1H), 8.87 (s, 2H), 8.09 (d, J=8.4 Hz, 1H), 8.00 (s, 1H), 7.09 (d, J=8.6 Hz, 1H), 3.87 (s, 3H), 3.84 ppm (s, 3H); ^{13}C NMR (126 MHz, DMSO): d = 178.21, 165.37, 163.19, 156.33, 151.90, 149.04, 130.51, 122.50, 111.75, 111.50, 108.97, 56.05, 55.91 ppm; HRMS m/z [M+H]$^+$ calcd for C$_{13}$H$_{12}$N$_4$O$_2$S$_1$: 289.0754, found: 289.0747.

3-Bromo-6-(3,4-dimethoxyphenyl)isothiazolo[3,4-d]pyrimidine (28): To a stirred solution of CuBr$_2$ (87 mg, 0.39) and tert-butylnitrite (46 mg, 0.45 mmol) in dry acetonitrile (10 mL) under argon atmosphere at 0 8C was added 6-(3,4-dimethoxyphenyl)isothiazolo[3,4-d]pyrimidin-3-amine 27 (100 mg, 0.35 mmol) and the mixture was stirred at room temperature overnight. After disappearance of the starting material, volatiles were evaporated and the crude residue was purified by silica gel flash column chromatography (eluting with a mixture of dichloromethane/acetone in a ratio of 95:5) yielding the title compound (60 mg, 49%). ^{1}H NMR (300 MHz, CDCl$_3$): d = 9.34 (s, 1H), 8.34 (d, J=8.0 Hz, 1H), 8.22 (s, 1H), 7.00 (d, J=8.3 Hz, 1H), 4.04 (s, 3H), 3.99 ppm (s, 3H); HRMS m/z [M+H]$^+$ calcd for C$_{13}$H$_{10}$Br$_1$N$_3$O$_2$S$_1$: 351.9750, found: 351.9746.

4-(6-(3,4-Dimethoxyphenyl)isothiazolo[3,4-d]pyrimidin-3-yl)morpholine (29): To a solution of 3-bromo-6-(3,4-dimethoxyphenyl)iso-

thiazolo[3,4-*d*]pyrimidine 28 (50 mg, 0.14 mmol) in ethanol (5 mL) was added morpholine (37 mg, 0.43 mmol). The reaction was stirred at reflux overnight. After disappearance of the starting ma- terial, volatiles were evaporated in vacuo and the crude residue was purified by silica gel flash column chromatography (eluting with a mixture of dichloromethane/methanol in a ratio of 95:5) to yield the title compound (33 mg, 65%). ^{1}H NMR (300 MHz, CDCl$_3$): δ = 9.33 (s, 1H), 8.27–8.21 (m, 1H), 8.20–8.15 (m, 1H), 7.02–6.91 (m, 1H), 4.04–3.92 (m, 10H), 3.69 ppm (d, *J* = 5.2 Hz, 4H); ^{13}C NMR (126 MHz, CDCl$_3$): δ = 164.64, 158.16, 153.06, 153.01, 149.38, 125.62, 123.05, 111.19, 111.07, 65.31, 56.20, 56.09, 50.89 ppm; HRMS *m/z* [*M* + H]$^+$ calcd for C$_{17}$H$_{18}$N$_4$O$_3$S$_1$: 359.1172, found: 359.1168.

3-Bromo-6-chloropyrazolo[1,5-*a*]pyrimidine (31): To a solution of 4-bromo-1*H*-pyrazol-3-amine 30 (1.0 g, 6.17 mmol) in methanol (18 mL) and acetic acid (12 mL) was added 2-chloromalonaldehyde (690 mg, 6.48 mmol), and the mixture was stirred at 70°C for 2 h. After disappearance of the starting material, the mixture was cooled to 0°C and the formed precipitate was filtered off and washed with methanol to yield the title compound (820 mg, 57%). ^{1}H NMR (300 MHz, DMSO): δ = 9.62 (d, *J* = 2.2 Hz, 1H), 8.69 (d, *J* = 2.2 Hz, 1H), 8.42 ppm (s, 1H); ^{13}C NMR (75 MHz, DMSO): δ = 150.27, 145.38, 143.30, 134.90, 117.44, 84.18 ppm; HRMS *m/z* [*M* + H]$^+$ calcd for C$_6$H$_3$Br$_1$Cl$_1$N$_3$: 231.9272, found: 231.9273.

6-Chloro-3-phenylpyrazolo[1,5-*a*]pyrimidine (32): To a solution of 3-bromo-6-chloropyrazolo[1,5-*a*]pyrimidine 31 (400 mg, 1.72 mmol) in dioxane (15 mL) and water (5 mL) were added phenyl boronic acid (254 g, 2.08 mmol), potassium carbonate (476 mg, 3.44 mmol), and Pd(PPh$_3$)$_4$ (20 mg, 0.02 mmol). The reaction mixture was de- gassed and refilled with nitrogen gas and stirred at 90°C over- night. After disappearance of the starting material, volatiles were evaporated and the crude residue was purified by silica gel flash column chromatography (using a mixture of heptane/acetone in a ratio of 90:10) to yield the title compound (220 mg, 56%). ^{1}H NMR (300 MHz, DMSO): δ = 9.60 (d, *J* = 2.3 Hz, 1H), 8.80 (s, 1H), 8.72 (d, *J* = 2.3 Hz, 1H), 8.14–8.07 (m, 2H), 7.50–7.41 (m, 2H), 7.33–7.22 ppm (m, 1H); HRMS *m/z* [*M* + H]$^+$ calcd for C$_{12}$H$_8$Cl$_1$N$_3$: 230.0479, found: 230.0471.

6-(3,4-Dimethoxyphenyl)-3-phenylpyrazolo[1,5-*a*]pyrimidine (33): To a solution of 6-chloro-3-phenylpyrazolo[1,5-*a*]pyrimidine 32 (100 mg, 0.44 mmol) in dioxane (4 mL) and water (1 mL) were added 3,4-dimethoxyphenyl boronic acid (96 mg, 0.53 mmol), po- tassium carbonate (121 mg, 0.88 mmol), and Pd(PPh$_3$)$_4$ (4 mg, 0.003 mmol). The reaction mixture was degassed and refilled with nitrogen gas and stirred at 90°C overnight. After disappearance of the starting material, volatiles were evaporated in vacuo and the crude residue was purified by silica gel flash column chromatogra- phy (using a mixture of dichloromethane/acetone in a ratio of

90:10) yielding the title compound (40 mg, 27%). ^{1}H NMR

(300 MHz, DMSO): δ = 9.51 (d, *J* = 2.3 Hz, 1H), 9.07 (d, *J* = 2.3 Hz, 1H), 8.78 (s, 1H), 8.22–8.15 (m, 2H), 7.50–7.40 (m, 4H), 7.30–7.23 (m, 1H), 7.10 (d, *J* = 8.4 Hz, 1H), 3.90 (s, 3H), 3.81 ppm (d, *J* = 7.7 Hz, 3H); ^{13}C NMR (75 MHz, DMSO): δ = 150.23, 149.84, 149.66, 143.45, 143.37, 132.68, 132.36, 129.14, 126.46, 126.32, 126.08, 122.11, 119.63, 112.80, 110.98, 109.34, 56.23, 56.11 ppm; HRMS *m/z* [*M* + H]$^+$ calcd for C$_{20}$H$_{17}$N$_3$O$_2$: 332.1393, found: 332.1403.

(*E*)-2-(5-Bromo-3-nitropyridin-2-yl)-*N,N*-dimethylethen-1-amine (35): To a solution of 5-bromo-2-methyl-3-nitropyridine 34 (1.00 g, 4.61 mmol) in dry DMF (10 mL) was added DMF-DMA (1.01 g, 9.22 mmol) dropwise. The mixture stirred at 90°C for 4 h, upon which a dark-red color formed. After disappearance of the starting

pound (1.23 g, 98%). The crude residue was used without further purification in the following reaction. HRMS *m/z* [*M* + H]$^+$ calcd for C$_9$H$_{10}$Br$_1$N$_3$O$_2$: 272.0030, found: 272.0032

6-Bromo-1*H*-pyrrolo[3,2-*b*]pyridine (36): A suspension of iron powder (1.13 g, 20.26 mmol) in glacial acetic acid (20 mL) was stirred at 0°C for 10 min. Subsequently, a solution of (*E*)-2-(5- bromo-3-nitropyridin-2-yl)-*N,N*-dimethylethen-1-amine 35 (1.00 g, 3.68 mmol) in glacial acetic acid (10 mL) was added dropwise and the mixture was stirred at room temperature for 3 h. After disap- pearance of the starting material, ethyl acetate was added to the mixture and it was filtrated using a paper filter. The filtered cake was washed thoroughly with ethyl acetate and the filtrate was evaporated in vacuo. The crude residue was purified by silica gel flash column chromatography (eluting with a mixture of dichloro- methane/ethyl acetate in a ratio of 90:10) to yield the title com- pound (660 mg, 91%). ^{1}H NMR (300 MHz, DMSO): δ = 11.46 (bs, 1H), 8.37 (d, *J* = 2.1 Hz, 1H), 8.03–8.00 (m, 1H), 7.69–7.66 (m, 1H), 6.60–6.57 ppm (m, 1H); HRMS *m/z* [*M* + H]$^+$ calcd for C$_7$H$_5$Br$_1$N$_2$: 196.9709, found: 196.9709.

6-Bromo-3-iodo-1*H*-pyrrolo[3,2-*b*]pyridine (37): To a solution of 6-bromo-1*H*-pyrrolo[3,2-*b*]pyridine 36 in dry THF (15 mL) was added *N*-iodosuccinimide at once and the mixture was stirred at room temperature for 3 h. After disappearance of the starting material, volatiles were evaporated and the crude residue was purified by silica gel flash column chromatography (eluting with a gradient of dichloromethane/ethyl acetate in a ratio of 99.5:0.5 to 99:1) yield- ing the title compound (400 mg, 37%). ^{1}H NMR (300 MHz, DMSO): δ = 8.43 (d, *J* = 2.0 Hz, 1H), 8.07 (d, *J* = 2.0 Hz, 1H), 7.85 ppm (s, 1H); ^{13}C NMR (75 MHz, DMSO): δ = 143.72, 134.62, 129.17, 121.50, 113.07 ppm; HRMS *m/z* [*M* + H]$^+$ calcd for C$_7$H$_4$Br$_1$I$_1$N$_2$: 322.8678, found: 322.8670

tert-Butyl 6-bromo-3-iodo-1*H*-pyrrolo[3,2-*b*]pyridine-1-carboxyl- ate (38): A mixture of 6-bromo-3-iodo-1*H*-pyrrolo[3,2-*b*]pyridine 37 (200 mg, 0.60 mmol), DMAP (8 mg, 0.06 mmol), TEA (80 mg, 0.8 mmol) and di-*tert*-butyl dicarbonate (158 mg, 0.72 mmol) was stirred in dry THF (6 mL) for 5 h at room temperature. After disap- pearance of the starting material, volatiles were evaporated in vacuo and the crude residue was purified using silica gel flash column chromatography (eluting with a mixture of heptane/ace- tone in a ratio of 9:1) to yield the title compound (240 mg, 95%). ^{1}H NMR (300 MHz, DMSO): δ = 8.66 (d, *J* = 2.0 Hz, 1H), 8.45 (d, *J* = 2.0 Hz, 1H), 8.20 (s, 1H), 1.63 ppm (s, 9H); HRMS *m/z* [*M* + H]$^+$ calcd for C$_8$H$_4$Br$_1$I$_1$N$_2$O$_2$: 366.8576, found: 366.8572.

6-Bromo-3-phenyl-1*H*-pyrrolo[3,2-*b*]pyridine (39): To a solution of *tert*-butyl 6-bromo-3-iodo-1*H*-pyrrolo[3,2-*b*]pyridine-1-carboxylate 38 (200 mg, 0.57 mmol) in dioxane (4 mL) and water (1 mL) were added phenylboronic acid (83 g, 0.68 mmol), potassium carbonate

(158 mg, 1.14 mmol), and Pd(PPh$_3$)$_4$ (7 mg, 0.006 mmol). The reac-

material, volatiles were evaporated in vacuo yielding the title com-

tion mixture was degassed and refilled with nitrogen gas and stirred at 90 °C overnight. After disappearance of the starting mate- rial, volatiles were evaporated in vacuo and the crude residue was purified by silica gel flash column chromatography (using a mix- ture of heptane/acetone in a ratio of 70:30) to yield the title com- pound (109 mg, 70%). ^{1}H NMR (300 MHz, DMSO): $d = 11.72$ (bs, 1H), 8.51 (d, $J = 2.1$ Hz, 1H), 8.25–8.18 (m, 3H), 8.08 (d, $J = 2.1$ Hz, 1H), 7.43–7.37 (m, 2H), 7.25–7.18 ppm (m, 1H); HRMS m/z $[M + H]^+$ calcd for $C_{13}H_9Br_1N_2$:273.0022, found: 273.0019

tert-Butyl 6-bromo-3-phenyl-1*H*-pyrrolo[3,2-*b*]pyridine-1-carbox-ylate (40): A mixture of 6-bromo-3-iodo-1*H*-pyrrolo[3,2-*b*]pyridine 39 (70 mg, 0.26 mmol), DMAP (3 mg, 0.03 mmol), TEA (35 mg, 0.35 mmol) and di-*tert*-butyl dicarbonate (68 mg, 0.31 mmol) were

140

stirred in dry THF (5 mL) for 5 h. After disappearance of the starting material, volatiles were evaporated and the crude residue was purified by silica gel flash column chromatography (eluting with a mixture of heptane/acetone in a ratio of 9:1) to yield the title compound (65 mg, 67%). ^{1}H NMR (300 MHz, DMSO): d = 8.72 (s, 1H), 8.54 (s, 1H), 8.43 (s, 1H), 8.25 (d, J = 7.5 Hz, 2H), 7.52–7.43 (m, 2H), 7.39–7.30 (m, 1H), 1.68 ppm (s, 9H); HRMS m/z [M + H]$^+$ calcd for C$_{14}$H$_9$Br$_1$N$_2$O$_2$: 316.9921, found: 316.9917.

tert-Butyl 6-(3,4-dimethoxyphenyl)-3-phenyl-1*H*-pyrrolo[3,2-*b*]pyridine-1-carboxylate (41): To a solution of *tert*-butyl 6-bromo-3-phenyl-1*H*-pyrrolo[3,2-*b*]pyridine-1-carboxylate 40 (65 mg, 0.17 mmol) in dioxane (4 mL) and water (1 mL) were added 3,4-dimethoxyphenylboronic acid (38 g, 0.21 mmol), potassium carbonate (47 mg, 0.34 mmol), and Pd(PPh$_3$)$_4$ (2 mg, 0.002 mmol). The reaction mixture was degassed and refilled with nitrogen gas and stirred at 90 °C overnight. The volatiles were evaporated in vacuo and the crude residue was purified by silica gel flash column chromatography (using a mixture of dichloromethane/ethyl acetate in a ratio of 90:10) to yield the title compound (11 mg, 15%). ^{1}H NMR (300 MHz, DMSO): d = 8.93 (d, J = 1.9 Hz, 1H), 8.54 (d, J = 1.7 Hz, 1H), 8.40 (s, 1H), 8.36–8.29 (m, 2H), 7.51–7.44 (m, 2H), 7.38–7.28 (m, 3H), 7.11 (d, J = 8.3 Hz, 1H), 3.88 (s, 3H), 3.83 (s, 3H), 1.70 ppm (s, 9H); ^{13}C NMR (75 MHz, DMSO): d = 149.50, 149.07, 148.77, 144.93, 144.22, 132.16, 131.74, 130.50, 129.15, 128.59, 127.31, 127.14, 126.00, 119.68, 119.62, 119.42, 112.61, 110.74, 85.10, 55.76, 55.73, 27.72 ppm.

6-(3,4-Dimethoxyphenyl)-3-phenyl-1*H*-pyrrolo[3,2-*b*]pyridine (42): To a solution of *tert*-butyl 6-(3,4-dimethoxyphenyl)-3-phenyl-1*H*-pyrrolo[3,2-*b*]pyridine-1-carboxylate 41 (11 mg, 0.026 mmol) in methanol (2 mL) was added a 4 n solution of HCl (2 mL) in dioxane and the mixture was stirred at 70 °C for 4 h. After disappearance of the starting material, volatiles were evaporated in vacuo and the crude residue was dissolved in water and washed three times with dichloromethane. Organic fractions were collected and concentrated in vacuo to yield the title compound (4 mg, 47%). ^{1}H NMR (300 MHz, DMSO): d = 12.97 (s, 1H), 8.84–8.78 (m, 1H), 8.70 (s, 1H), 8.53–8.44 (m, 1H), 7.92 (d, J = 7.4 Hz, 2H), 7.57–7.34 (m, 5H), 7.14 (d, J = 8.4 Hz, 1H), 3.91 (s, 3H), 3.84 ppm (s, 3H); ^{13}C NMR (75 MHz, DMSO): d = 149.54, 149.47, 135.55, 133.46, 132.76, 131.62, 129.91, 128.97, 128.61, 127.52, 127.09, 123.88, 119.92, 112.62, 112.42, 111.26, 55.98, 55.84 ppm; HRMS m/z [M + H]$^+$ calcd for C$_{21}$H$_{18}$N$_2$O$_2$: 331.1441, found: 331.1442.

5-(3,4-Dimethoxyphenyl)-3-fluoropicolinonitrile (44): To a solution 5-bromo-3-fluoropicolinonitrile 43 (5.00 g, 24.86 mmol) in dioxane (40 mL) and water (10 mL) were added 3,4-dimethoxyphenylboronic acid (5.432 g, 29.85 mmol), potassium carbonate (6.87 g, 49.72 mmol), and Pd(PPh$_3$)$_4$ (287 mg, 0.248 mmol). The reaction mixture was degassed and refilled with nitrogen gas and stirred at 90 °C overnight. After disappearance of the starting material, volatiles were evaporated in vacuo and the crude residue was purified by silica gel flash column chromatography (using a mixture of dichloromethane/ethyl acetate in a ratio of 99.5:0.5) to yield the title compound (5.54 g, 86%). ^{1}H NMR (300 MHz, DMSO): d = 9.05 (s, 1H), 8.58–8.42 (m, 1H), 7.54–7.47 (m, 2H), 7.13 (d, J = 8.4 Hz, 1H), 3.88 (s, 3H), 3.84 ppm (s, 3H); ^{13}C NMR (126 MHz, DMSO): d = 162.61, 160.50, 150.70, 149.43, 145.35, 141.96, 126.22, 121.78, 121.64, 120.65, 118.51, 113.97, 112.24, 110.94, 55.88, 55.75 ppm; HRMS m/z [M + H]$^+$ calcd for C$_{14}$H$_{11}$F$_1$N$_2$O$_2$: 259.0877, found:259.0881.

6-(3,4-Dimethoxyphenyl)-1*H*-pyrazolo[4,3-*b*]pyridin-3-amine (45): To a solution of 5-(3,4-dimethoxyphenyl)-3-fluoropicolinonitrile 44

(3.00 g, 11.61 mmol) in n-butanol (30 mL) was added hydrazine hydrate (2.91 g, 58.08 mmol) and the mixture was stirred at 121 °C overnight. After disappearance of the starting material, volatiles were evaporated in vacuo and the crude residue was purified by silica gel flash column chromatography (eluting with a mixture of dichloromethane/methanol in a ratio of 95:5) to yield the title compound (2.6 g, 83%). ^{1}H NMR (300 MHz, DMSO): d = 11.66 (bs, 1H), 8.59 (s, 1H), 7.84 (s, 1H), 7.38–7.24 (m, 2H), 7.08 (d, J = 8.4 Hz, 1H), 5.39 (bs, 2H), 3.88 (s, 3H), 3.82 ppm (s, 3H).

6-(3,4-Dimethoxyphenyl)-3-iodo-1*H*-pyrazolo[4,3-*b*]pyridine (46): A solution of 6-(3,4-dimethoxyphenyl)-1*H*-pyrazolo[4,3-*b*]pyridin-3-fluoropicolinonitrile 45 (1.00 g, 3.70 mmol) and *p*-toluenesulfonic acid (2.11 g, 11.1 mmol) in acetonitrile was stirred for 10 min. Subsequently a solution of sodium nitrite (640 mg, 9.30 mmol) and potassium Iodide (1.54 g, 9.30 mmol) in water (10 mL) was added dropwise over 30 min and the mixture was stirred at room temperature for 5 h. After disappearance of the starting material, volatiles were evaporated in vacuo and the crude residue was purified by silica gel flash column chromatography (eluting with a mixture of dichloromethane/methanol in a ratio of 95:5) to yield the title compound (400 mg, 28%). ^{1}H NMR (300 MHz, DMSO): d = 9.19–9.11 (m, 1H), 8.89–8.85 (m, 1H), 7.68–7.61 (m, 2H), 7.56 (s, 1H), 7.22–7.14 (m, J = 7.7 Hz, 2H), 3.96 (s, 3H), 3.89 ppm (s, 3H).

6-(3,4-Dimethoxyphenyl)-3-phenyl-1*H*-pyrazolo[4,3-*b*]pyridine (47): To a solution 6-(3,4-dimethoxyphenyl)-3-iodo-1*H*-pyrazolo[4,3-*b*]pyridine 46 (100 mg, 0.26 mmol) in dioxane (4 mL) and water (1 mL) were added 3,4-dimethoxyphenylboronic acid (38 mg, 0.31 mmol), potassium carbonate (72 mg, 0.52 mmol), and Pd(PPh$_3$)$_4$ (60 mg, 0.0052 mmol). The reaction mixture was stirred in a microwave at 120 °C for 1 h. After disappearance of the starting material, volatiles were evaporated in vacuo and the crude residue was purified by silica gel flash column chromatography (using a mixture of dichloromethane/methanol in a ratio of 98:2) to yield the title compound (20 mg, 23%). ^{1}H NMR (300 MHz, DMSO): d = 13.46 (s, 1H), 8.95 (s, 1H), 8.54 (d, J = 7.3 Hz, 2H), 8.20 (s, 1H), 7.60–7.33 (m, 5H), 7.12 (d, J = 8.4 Hz, 1H), 3.90 (s, 3H), 3.83 ppm (s, 3H); ^{13}C NMR (75 MHz, DMSO): d = 149.53, 149.33, 145.10, 141.99, 137.58, 134.53, 133.30, 132.87, 130.41, 128.70, 128.05, 126.47, 120.00, 115.41, 112.69, 111.52, 55.93, 55.87 ppm; HRMS m/z [M + H]$^+$ calcd for C$_{20}$H$_{17}$N$_3$O$_2$: 332.1393, found: 332.1396.

tert-Butyl thiophen-3-ylcarbamate (50): To a solution of thiophene-3-carboxylic acid 48 (2.00 g, 15.61 mmol) in dry dimethylformamide (25 mL) at 0 °C was added diphenylphosphoryl azide (4.30 g, 15.61 mmol) and the mixture was stirred at room temperature for 2 h. After disappearance of the starting material, *tert*-butanol was added (15 mL, 156.10 mmol) and the mixture was stirred at reflux for 17 h. After disappearance of the intermediate 49, the volatiles were evaporated and the crude residue was purified by silica gel flash column chromatography (using a mixture of heptane/acetone in a ratio of 9:1) to yield the title compound (1.91 g, 61%). ^{1}H NMR (300 MHz, DMSO): d = 9.62 (bs, 1H), 7.42–7.34 (m, 1H), 7.19–7.12 (m, 1H), 7.02–6.95 (m, 1H), 1.47 ppm (s, 9H); ^{13}C NMR (75 MHz, DMSO): d = 152.89, 137.48, 124.71, 121.26, 105.90, 28.25 ppm; HRMS m/z [M + H]$^+$ calcd for C$_5$H$_5$N$_1$O$_2$S$_1$: 144.0114, found: 144.0112.

3-Aminothiophene hydrochloride (51): *tert*-Butyl thiophen-3-ylcarbamate 50 (500 mg, 2.50 mmol) was dissolved in a 4 n solution of HCl in dioxane (10 mL) and the mixture was protected from light using aluminum foil and stirred at reflux for 3 h. After disappearance of the starting material, volatiles were evaporated and the crude residue (340 mg, 100%) was protected from light and used

as such without further purification in the following reaction. ^1H NMR (300 MHz, DMSO): $\delta = 10.46$ (bs, 2H), 7.76–7.63 (m, 1H), 7.63–7.51 (m, 1H), 7.15–7.10 ppm (m, 1H); ^{13}C NMR (75 MHz, DMSO): $\delta = 129.43$, 128.02, 123.32, 118.50 ppm; HRMS m/z $[M+H]^+$ calcd for $C_4H_5N_1S_1$: 100.0215, found: 100.0227.

Ethyl 3-amino-6-bromothieno[3,2-*b*]pyridine-2-carboxylate (54): To a solution of 5-bromo-3-nitropyridine-2-carbonitrile 53 (2.00 g, 21.93 mmol) and ethyl 2-mercaptoacetate (3.95 g, 32.89 mmol) in dimethylformamide (50 mL) was added potassium *tert*-butoxide (4.92, 43.86 mmol) portion wise. The mixture turned red and was stirred at room temperature for 3 h. After disappearance of the starting material the volatiles were evaporated in vacuo and the crude residue was purified by silica gel flash column chromatogra- phy (eluting with a mixture of heptane/ethyl acetate in a ratio of 80:20) to yield the title compound (4.24 g, 54%). ^1H NMR (300 MHz, DMSO): $\delta = 8.89$–8.60 (m, 2H), 6.90 (bs, 2H), 4.30 (q, $J = 7.0$ Hz, 2H), 1.31 ppm (t, $J = 6.8$ Hz, 3H); ^{13}C NMR (126 MHz, DMSO): $\delta = 164.47$, 147.92, 147.88, 145.40, 135.30, 134.49, 119.52, 98.47, 60.78, 14.85 ppm; HRMS m/z $[M+H]^+$ calcd for $C_{10}H_9Br_1N_2O_2S_1$: 300.9641, found: 300.9638.

Ethyl 3-amino-6-(3,4-dimethoxyphenyl)thieno[3,2-*b*]pyridine-2-carboxylate (55): To a solution ethyl 3-amino-6-bromothieno[3,2-*b*]pyridine-2-carboxylate 54 (3.50 g, 11.62 mmol) in dioxane (50 mL) were added 3,4-dimethoxyphenylboronic acid (2.55 g, 13.95 mmol), potassium phosphate (4.90 g, 23.24 mmol), and Pd(PPh₃)₄ (671 mg, 0.58 mmol). The reaction mixture was stirred at reflux for 2 days. After disappearance of the starting material, volatiles were evapo- rated in vacuo and the crude residue was purified by silica gel flash column chromatography (eluting with a mixture of heptane/ ethyl acetate in a ratio of 80:20) to yield the title compound (3.04 g, 76%). ^1H NMR (300 MHz, DMSO): $\delta = 9.00$ (d, $J = 2.0$ Hz, 1H), 8.66 (d, $J = 2.0$ Hz, 1H), 7.45–7.36 (m, 2H), 7.10 (d, $J = 8.1$ Hz, 1H), 6.89 (bs, 2H), 4.31 (q, $J = 7.1$ Hz, 2H), 3.89 (s, 3H), 3.82 (s, 3H), 1.32 ppm (t, $J = 7.1$ Hz, 3H). ^{13}C NMR (126 MHz, DMSO): $\delta = 164.11$, 147.57, 145.02, 134.92, 134.15, 133.21, 119.17, 118.62, 112.24, 110.49, 60.42, 55.69, 14.48 ppm; HRMS m/z $[M+H]^+$ calcd for

$C_{18}H_{18}N_2O_4S_1$: 359.1060, found: 359.1054.

Ethyl 3-bromo-6-(3,4-dimethoxyphenyl)thieno[3,2-*b*]pyridine-2-

carboxylate (56): To a stirred solution of CuBr₂ (1.72 g, 7.67) and *tert*-butyl nitrite (789 mg, 7.66 mmol) in dry acetonitrile (25 mL) under argon atmosphere at 0 °C was added ethyl 3-amino-6-(3,4-di-methoxyphenyl)thieno[3,2-*b*]pyridine-2-carboxylate 55 (2.5 g, 6.98 mmol) and the mixture was stirred at 0 °C for 6 h and then at room temperature overnight. After disappearance of the starting material, volatiles were evaporated in vacuo and the crude residue was purified by silica gel flash column chromatography (eluting with a mixture of heptane/ethyl acetate in a ratio of 70:30) yielding the title compound (1.38 g, 47%). ^1H NMR (300 MHz, DMSO): $\delta =$

9.20 (s, 1H), 8.88 (s, 1H), 7.48–7.35 (m, 2H), 7.12 (d, $J = 8.1$ Hz, 1H),

4.41 (q, $J = 7.0$ Hz, 2H), 3.89 (s, 3H), 3.83 (s, 3H), 1.37 ppm (t, $J = 7.0$ Hz, 3H); HRMS m/z $[M+H]^+$ calcd for $C_{18}H_{16}Br_1N_1O_4S_1$: 422.0056, found: 422.0052.

Ethyl 6-(3,4-dimethoxyphenyl)-3-phenylthieno[3,2-*b*]pyridine-2-carboxylate (57): To a solution ethyl 3-bromo-6-(3,4-dimethoxy-phenyl)thieno[3,2-*b*]pyridine-2-carboxylate 56 (1.00 g, 2.40 mmol) in dioxane (25 mL) were added phenylboronic acid (340 mg, 2.80 mmol), tripotassium phosphate (1.02 g, 4.80 mmol), and Pd(PPh₃)₄ (280 mg, 0.24 mmol). The reaction mixture was stirred at reflux overnight. After disappearance of the starting material, vola-

of heptane/acetone in a ratio of 80:20) yielding the title compound (422 mg, 42%). ^1H NMR (600 MHz, DMSO): $\delta = 9.08$ (d, $J = 2.1$ Hz, 1H), 8.87 (d, $J = 2.1$ Hz, 1H), 7.52–7.45 (m, 5H), 7.43 (d, $J = 2.0$ Hz, 1H), 7.40 (dd, $J = 8.3$, 2.1 Hz, 1H), 7.11 (d, $J = 8.4$ Hz, 1H), 4.21 (q, $J = 7.1$ Hz, 2H), 3.88 (s, 3H), 3.82 (s, 3H), 1.14 ppm (t, $J = 7.1$ Hz, 3H); ^{13}C NMR (151 MHz, DMSO): $\delta = 161.90$, 152.13, 149.46, 149.43, 147.58, 142.51, 134.65, 133.54, 133.33, 131.34, 130.60, 129.12, 128.12, 128.02, 127.45, 119.75, 112.43, 110.90, 61.49, 55.78, 55.70, 13.80 ppm; HRMS m/z $[M+H]^+$ calcd for $C_{24}H_{21}N_1O_4S_1$: 420.1264, found: 420.1261.

6-(3,4-Dimethoxyphenyl)-3-phenylthieno[3,2-*b*]pyridine-2-car-boxylic acid (58): To a solution of ethyl 6-(3,4-dimethoxyphenyl)-3-phenylthieno[3,2-*b*]pyridine-2-carboxylate 57 (200 mg, 0.48 mmol) in ethanol (10 mL) was added a solution of NaOH (192 mg, 4.8 mmol) in water (2 mL) and the mixture was stirred at room temperature for 4 h. After disappearance of the starting material, the mixture was neutralized using a 6 n HCl solution in water, upon which a precipitate formed. The precipitate was filtered off and washed with water to yield the title compound (168 mg, 89%). HRMS m/z $[M+H]^+$ calcd for $C_{22}H_{17}N_1O_4S_1$: 392.0951, found: 392.0941

6-(3,4-Dimethoxyphenyl)-3-phenylthieno[3,2-*b*]pyridine (59): To a solution of 6-(3,4-dimethoxyphenyl)-3-phenylthieno[3,2-*b*]pyri- dine-2-carboxylic acid 58 (100 mg, 0.25 mmol) in quinoline (1 mL) was added copper (11 mg, 0.18 mmol) and the reaction was stirred at 200 °C overnight. After disappearance of the starting material, the mixture was diluted with water and washed three times with dichloromethane. Organic phases were collected and concentrated in vacuo and the crude residue was purified by silica gel flash column chromatography (eluting with a mixture of heptane/ace- tone 80:20) to yield the title compound (42 mg, 48%). ^1H NMR (300 MHz, DMSO): $\delta = 9.10$ (d, $J = 2.1$ Hz, 1H), 8.84 (d, $J = 2.1$ Hz, 1H), 8.37 (s, 1H), 8.19–8.08 (m, 2H), 7.54–7.36 (m, 5H), 7.10 (d, $J = 8.4$ Hz, 1H), 3.89 (s, 3H), 3.82 ppm (s, 3H); ^{13}C NMR (75 MHz, DMSO): $\delta = 151.54$, 149.47, 149.15, 146.00, 135.21, 134.51, 134.32, 131.19, 129.70, 128.57, 128.50, 128.23, 127.70, 119.49, 112.50,

110.87, 55.80, 55.74 ppm; HRMS m/z $[M+H]^+$ calcd for $C_{21}H_{17}N_1O_2S_1$: 348.1053, found: 348.1053.

5-Chloro-3-nitro-*N*-phenylpyridin-2-amine (61): To a mixture of 2,5-dichloro-3-nitropyridine 60 (1.93 g, 10 mmol) and aniline (2.8 mL, 30 mmol) in 1,4-dioxane (100 mL) was added DIPEA (0.52 mL, 35 mmol) and the reaction was stirred at 80 °C overnight. After disappearance of the starting material, the reaction was cooled to room temperature and diluted with ethyl acetate, washed with water, dried over Na₂SO₄, and concentrated in vacuo. The crude residue was purified by silica gel flash column chroma- tography (eluting with a gradient of ethyl acetate/methanol in a ratio of 100:0 to 95:5) to yield the title compound (2.12 g) in 85%

yield. ^1H NMR (300 MHz, CDCl₃): $\delta = 10.05$ (s, 1H), 8.51 (d, $J = 2.5$ Hz,

tiles were evaporated in vacuo and the crude residue was purified by silica gel flash column chromatography (eluting with a mixture

1 H), 8.42 (d, $J=2.5$ Hz, 1 H), 7.65–7.56 (m, 2 H), 7.47–7.35 (m, 2 H), 7.28–7.16 ppm (m, 1 H).

5-Chloro-N^2-phenylpyridine-2,3-diamine (62): A mixture of 5-chloro-3-nitro-N-phenylpyridin-2-amine 61 (0.5 g, 2 mmol) and Raney nickel (0.1 g) in THF (20 mL) was degassed and filled with hydrogen gas. The reaction was allowed to stir at room tempera- ture for two h. After disappearance of the starting material the mixture was filtered, concentrated in vacuo and used in the follow- ing reaction without further purification.

6-Chloro-3-phenyl-3H-[1,2,3]triazolo[4,5-b]pyridine (63): To a so-lution of 5-chloro-N^2-phenylpyridine-2,3-diamine 62 in a mixture of glacial acetic acid (0.56 mL, 10 mmol), water (0.5 mL) and dichloro-

143

methane (0.5 mL) at 0°C was added sodium nitrite (0.18 g, 2.6 mmol) dropwise. After 20 min of stirring, the mixture was diluted with dichloromethane, washed with water and dried over Na_2SO_4. Organic phases were collected and concentrated in vacuo. The crude residue was purified by silica gel flash column chroma- tography (eluting with gradient of pentane/ethyl acetate in a ratio of 100:0 to 60:40) to yield the title compound (0.28 g, 62%). ^1H NMR (300 MHz, $CDCl_3$): d = 8.66 (d, J = 2.2 Hz, 1H), 8.39 (d, J = 2.2 Hz, 1 H), 8.26–8.19 (m, 2H), 7.63–7.54 (m, 2H), 7.50–7.43 ppm (m, 1H). ^{13}C NMR (75 MHz, $CDCl_3$): d = 149.95, 143.72, 138.23, 136.19, 129.61, 128.60, 128.16, 127.71, 121.36 ppm.

6-(3,4-Dimethoxyphenyl)-3-phenyl-3H-[1,2,3]triazolo[4,5-b]pyridine (64): To a solution of 6-chloro-3-phenyl-3H-[1,2,3]triazolo[4,5-b]pyridine 63 (120 mg, 0.52 mmol) in dimethylformamide (8 mL) and water (2 mL) were added 3,4-dimethoxyphenyl boronic acid (227 mg, 1.24 mmol), Cesium carbonate (542 mg, 1.61 mmol) and $Pd(PPh_3)_4$ (60 mg, 0.052 mmol). The reaction mixture was degassed and refilled with nitrogen gas and stirred at 100°C overnight. After disappearance of the starting material, volatiles were evaporated and the crude residue was dissolved in ethyl acetate and washed with water. Collected organic phases were dried over Na_2SO_4, con- centrated in vacuo and the crude residue was purified using silica gel flash column chromatography (eluting with a gradient of pen- tane/ethyl acetate in a ratio of 100:0 to 70:30) to yield the title compound (134 mg, 78%). ^1H NMR (300 MHz, $CDCl_3$): d = 8.96 (d, J = 2.1 Hz, 1H), 8.51 (d, J = 2.1 Hz, 1H), 8.36–8.28 (m, 2H), 7.66–7.56 (m, 2H), 7.52–7.43 (m, 1H), 7.20 (dd, J = 8.2, 2.1 Hz, 1H), 7.14 (d, J = 2.1 Hz, 1H), 7.01 (d, J = 8.3 Hz, 1H), 3.99 (s, 3H), 3.95 ppm (s, 3H); ^{13}C NMR (75 MHz, $CDCl_3$): d = 150.50, 149.85, 149.72, 144.63, 138.34, 136.65, 134.26, 130.16, 129.62, 128.34, 125.75, 121.41, 120.25, 112.11, 111.00, 56.21, 56.17 ppm; HRMS: $[M+H]^+$ calcd for $C_{19}H_{16}N_4O_2$: 333.1346; found, 333.1345.

5-Bromo-3-nitro-N-phenylpyridin-2-amine (66): To a solution of 5-bromo-2-chloro-3-nitropyridine 65 (2.37 g, 10 mmol) in NMP (5 mL) was added aniline (1.4 mL, 15 mmol) and DIPEA (5 mL, 30 mmol) and the mixture was stirred at 120°C for 1.5 h. After disappearance of the starting material, the reaction was allowed to cool to room temperature, diluted with water and washed with ethyl acetate. Organic phases were collected, washed with brine, dried over Na_2SO_4 and concentrated under reduced pressure. The crude resi- due was purified by silica gel flash column chromatography (elut- ing with a mixture of pentane/ethyl acetate in a ratio of 90:10) to yield the title compound (2.29 g, 78%). ^1H NMR (300 MHz, $CDCl_3$): d = 10.04 (s, 1H), 8.63 (s, 1H), 8.48 (d, J = 2.1 Hz, 1H), 7.59 (d, J = 8.0 Hz, 2H), 7.39 (t, J = 7.8 Hz, 2H), 7.27–7.13 ppm (m, 1H); ^{13}C NMR (126 MHz, DMSO): d = 155.29, 148.38, 138.04, 136.94, 129.23, 128.70, 124.59, 123.14, 106.20 ppm.

5-(3,4-Dimethoxyphenyl)-3-nitro-N-phenylpyridin-2-amine (67): To a solution of 5-bromo-3-nitro-N-phenylpyridin-2-amine 66 (600 mg, 2.0 mmol), in dioxane (16 mL) and water (4 mL) were added (3,4-dimethoxyphenyl)boronic acid (408 mg, 2.2 mmol), sodium carbonate (912 mg, 8.6 mmol) and $Pd(PPh_3)_4$ (120 mg, 0.1 mmol). The reaction mixture was degassed and refilled with ni- trogen gas and stirred at 80°C overnight. After disappearance of the starting material, volatiles were evaporated in vacuo and the crude residue was dissolved in ethyl acetate and washed with water. Collected organic phases were dried over Na_2SO_4, concen- trated in vacuo and the crude residue was purified using silica gel flash column chromatography (eluting with a mixture of pentane/ ethyl acetate in a ratio of 75:25) to yield the title compound (360 mg, 78%).

6-(3,4-Dimethoxyphenyl)-3-phenyl-3H-imidazo[4,5-b]pyridine (69): To a solution of 5-(3,4-dimethoxyphenyl)-3-nitro-N-phenylpyri- din-2-amine 68 (360 mg, 1 mmol) in glacial acetic acid (5 mL), was added zinc (2.2 g, 34 mmol) and the mixture was stirred at reflux for 3 h. After disappearance of the starting material, the reaction was allowed to cool to room temperature and filtrated through Celite, washed with acetic acid and concentrated in vacuo. The crude residue was subsequently suspended in triethyl orthofor- mate (10 mL) and stirred at 130°C for 2 h. After disappearance of the starting material the volatiles were evaporated in vacuo and the crude residue was dissolved in ethyl acetate, washed with water, saturated sodium bicarbonate and brine. Collected organic phases were dried over $MgSO_4$ and concentrated in vacuo. The crude residue was purified using silica gel flash column chromatog- raphy (eluting with a mixture of ethyl acetate/pentane in a ratio of 6:4) to give the title compound which was further purified by crys- tallization from methanol (116 mg, 35%). ^1H NMR (300 MHz, $CDCl_3$): d = 8.68 (d, J = 2.0 Hz, 1H), 8.38 (s, 1H), 8.29 (d, J = 2.1 Hz, 1H), 7.84–7.77 (m, 2H), 7.65–7.56 (m, 2H), 7.51–7.43 (m, 1H), 7.20 (dd, J = 8.2, 2.1 Hz, 1H), 7.15 (d, J = 2.1 Hz, 1H), 7.01 (d, J = 8.3 Hz, 1H), 3.98 (s, 3H), 3.95 ppm (s, 3H); ^{13}C NMR (75 MHz, $CDCl_3$): d = 149.77, 149.27, 146.24, 144.29, 143.76, 136.36, 133.16, 131.70, 130.01, 128.07, 126.43, 123.64, 120.08, 112.17, 111.21, 56.24 ppm; HRMS: $[M+H]^+$ calcd for $C_{20}H_{17}N_3O_2$, 392.1393; found, 392.1393.

7-Bromoquinazolin-4-ol (71): To a solution of methyl 2-amino-4-bromobenzoate 70 (1.00 g, 4.35 mmol) in triethyl orthoformate (20 mL) was added ammonium acetate (419 mg, 5.43 mmol) and the mixture was stirred at reflux overnight. After disappearance of the starting material the volatiles were evaporated in vacuo and the crude residue was dissolved in water. The formed precipitate was filtered off, yielding the title compound (600 mg, 60%).
^1H NMR (300 MHz, DMSO): d = 12.38 (bs, 1H), 8.14 (s, 1H), 8.03 (d, J = 8.5 Hz, 1H), 7.89 (d, J = 1.8 Hz, 1H), 7.69 ppm (dd, J = 8.5, 1.8 Hz, 1H).

7-Bromo-4-chloroquinazoline (72): 7-Bromoquinazolin-4-ol 71 (200 mg, 0.88 mmol) was suspended in phosphorus oxychloride (3,0 mL) and stirred at 125°C overnight. After disappearance of the starting material, the solvent was evaporated in vacuo and the crude residue was used as such without further purification in the following reaction.

4-(7-Bromoquinazolin-4-yl)morpholine (73): To a solution of crude residue containing 7-bromo-4-chloroquinazoline 72 in diox- ane was added morpholine (958 mL, 11 mmol) and the mixture was stirred at room temperature for 3 h. After disappearance of the starting material volatiles were evaporated in vacuo and the crude residue was purified by silica gel flash column chromatography (eluting with a mixture of dichloromethane/methanol 95:5) yield- ing the title compound (148 mg, 57%). ^1H NMR (300 MHz, DMSO): d = 8.83 (s, 1H), 8.15–8.03 (m, 2H), 7.82 (dd, J = 9.0, 1.9 Hz, 1H), 4.21–4.00 (m, 4H), 3.91–3.72 ppm (m, 5H).

4-(7-(3,4-Dimethoxyphenyl)quinazolin-4-yl)morpholine (74): To a solution of 4-(7-bromoquinazolin-4-yl)morpholine 73 (100 mg, 0.34 mmol) in dioxane (4 mL) and water (1 mL) were added 3,4-di- methoxyphenyl boronic acid (74 mg, 0.41 mmol), potassium car- bonate (94 mg, 0.68 mmol), and $Pd(PPh_3)_4$ (12 mg, 0.01 mmol). The reaction mixture was degassed, refilled with nitrogen and stirred at 90°C overnight. The volatiles were evaporated in vacuo and the crude residue was purified by silica gel flash column chromatogra- phy (eluting with a mixture of dichloromethane/methanol in a ratio of 99:1) yielding the title compound (90 mg, 75%). ^1H NMR (300 MHz, DMSO): d = 8.66 (s, 1H), 8.10–8.03 (m, 2H), 7.90–7.83 (m,

1H), 7.43–7.37 (m, 2H), 7.11 (d, $J = 8.9$ Hz, 1H), 3.90 (s, 3H), 3.83 (s, 3H), 3.81–3.73 ppm (m, 8H); ^{13}C NMR (75 MHz, DMSO): d = 163.68, 154.18, 152.06, 149.59, 149.38, 144.17, 131.28, 125.90, 124.57, 124.41, 119.72, 114.52, 112.38, 110.80, 66.17, 55.78, 55.75, 49.81 ppm; HRMS m/z $[M + H]^+$ calcd for $C_{20}H_{21}N_3O_3$: 352.16555, found 352.1660.

3-Amino-5-bromopyridine-2-carbonitrile (75): To a stirred solution of iron powder (4.900 g, 87.7 mmol) in 50 mL of acetic acid at room temperature, was added 5-bromo-3-nitropyridine-2-carboni- trile 53 (10 g„ 43.9 mmol) at once and the reaction was stirred for 3 h. After completion, ethyl acetate was added to the mixture and the precipitate was filtered off. The filtered cake was washed thoroughly with ethyl acetate and the filtrate was evaporated in vacuo. Crude was purified by silica gel flash column chromatography (eluting with dichloromethane) to yield the title compound (4.845 g 56%). ^{1}H NMR (300 MHz, DMSO): d = 8.08–7.66 (m, 1H), 7.55–7.26 (m, 1H), 6.58 ppm (bs, 2H); HRMS m/z $[M + H]^+$ calcd for $C_6H_4BrN_3$: 197.96618, found 197.9656.

3-Amino-5-(3,4-dimethoxyphenyl)picolinonitrile (76): To a solu- tion 3-amino-5-bromopyridine-2-carbonitrile 75 (1.0 g, 5.05 mmol) in dioxane (40 mL) and water (10 mL) were added 3,4-dimethoxy-phenylboronic acid (1.11 g, 6.06 mmol), potassium carbonate (1.38 g, 10.1 mmol), and Pd(PPh$_3$)$_4$ (58 mg, 0.05 mmol). The reaction

mixture was stirred at 90 8C overnight. The volatiles were evaporat-

ed and the crude residue was purified by silica gel flash column chromatography (eluting with a mixture of dichloromethane/ace-

tone in a ratio of 90:10) yielding the title compound (1.27 g, 98%).

^{1}H NMR (300 MHz, DMSO): d = 8.22 (d, $J = 1.9$ Hz, 1H), 7.42 (d, $J = 1.9$ Hz, 1H), 7.24–7.20 (m, 2H), 7.12–7.05 (m, 1H), 3.85 (s, 3H),

3.81 ppm (s, 3H); ^{13}C NMR (75 MHz, DMSO): d = 149.87, 149.34,

148.80, 139.62, 137.72, 128.63, 119.65, 117.34, 113.03, 112.34, 110.51, 55.76 ppm.

7-(3,4-Dimethoxyphenyl)pyrido[3,2-d]pyrimidin-4-amine (77): 3-Amino-5-(3,4-dimethoxyphenyl)picolinonitrile 76 (200 mg) was sus-pended in formamide (4 mL) and heated in a microwave for 10 min at 160 8C. The reaction was allowed to cool to room tem-perature and the formed precipitate was filtered off and washed with water to yield the title compound (164 mg, 74%). ^{1}H NMR (300 MHz, DMSO): d = 9.12 (d, $J = 2.1$ Hz, 1H), 8.45 (s, 1H), 8.30 (d, $J = 2.1$ Hz, 1H), 7.93 (bs, 2H), 7.50–7.39 (m, 2H), 7.10 (d, $J = 8.1$ Hz, 1H), 3.90 (s, 3H), 3.83 ppm (s, 3H); ^{13}C NMR (75 MHz, DMSO): d = 161.91, 156.56, 149.87, 149.51, 147.32, 144.88, 139.76, 131.01, 129.79, 128.67, 120.14, 112.39, 111.11, 55.88, 55.75 ppm; HRMS m/z $[M + H]^+$ calcd for $C_{15}H_{14}N_4O_2$: 283.1189, found: 383.1188.

7-(3,4-Dimethoxyphenyl)pyrido[3,2-d]pyrimidin-4-ol (78): 7-(3,4-Dimethoxyphenyl)pyrido[3,2-d]pyrimidin-4-amine 77 (120 mg, 0.43 mmol) was suspended in a 6 n HCl solution (5 mL) and stirred at reflux for 1 h. The reaction was allowed to cool to room temper-ature and the formed precipitate was filtered off to yield the title compound (85 mg, 66%). HRMS m/z $[M + H]^+$ calcd for $C_{15}H_{13}N_3O_3$:284.1030, found: 284.1029.

7-(3,4-Dimethoxyphenyl)-4-(1H-1,2,4-triazol-1-yl)pyrido[3,2-d]pyrimidine (79): A solution of phosphorus oxychloride (230 mg, 1.50 mmol), triazole (207 mg, 3.0 mmol) and DIPEA (116 mg, 0.90 mmol) in acetonitrile (5 mL) was stirred for 20 min at room temperature when 7-(3,4-dimethoxyphenyl)pyrido[3,2-d]pyrimidin- 4-

and concentrated in vacuo. The crude residue was used as such without further purification in the following reaction.

4-(7-(3,4-Dimethoxyphenyl)pyrido[3,2-d]pyrimidin-4-yl)morpho-line (80): To a solution of 7-(3,4-dimethoxyphenyl)-4-(1H-1,2,4-tria-zol-1-yl)pyrido[3,2-d]pyrimidine 79 (0.35 mmol) in dioxane (5 mL) was added morpholine (152 mg, 1.75 mmol) and the mixture was stirred at reflux for 1 h. After disappearance of the starting materi-al, the volatiles were evaporated in vacuo and the crude residue was purified by silica gel flash column chromatography (eluting with a mixture of dichloromethane/methanol in a ratio of 95:5) yielding the title compound (26 mg 25%). ^{1}H NMR (300 MHz, DMSO): d = 9.18 (d, $J = 2.3$ Hz, 1H), 8.56 (s, 1H), 8.36 (d, $J = 2.3$ Hz, 1H), 7.52–7.47 (m, 2H), 7.12 (d, $J = 9.0$ Hz, 1H), 4.49–4.39 (m, 4H), 3.90 (s, 3H), 3.83 (s, 3H), 3.81–3.76 ppm (m, 4H); ^{13}C NMR (75 MHz, DMSO): d = 158.58, 154.97, 149.99, 149.54, 147.24, 145.83, 138.64, 131.77, 131.35, 128.17, 120.06, 112.44, 110.92, 66.52, 55.86, 55.77, 47.80 ppm; HRMS m/z $[M + H]^+$ calcd for $C_{19}H_{20}N_4O_3$: 353.1608, 353.1601.

7-(3,4-Dimethoxyphenyl)pyrido[2,3-d]pyrimidin-4-amine (81): 2-Amino-6-(3,4-dimethoxyphenyl)nicotinonitrile 10 (400 mg) was sus-pended in formamide (4 mL) and heated in a microwave for 10 min at 160 8C. The reaction was allowed to cool to room tem-perature and the precipitate was filtered off and washed with

water to yield the title compound (200 mg, 46%). H NMR

(300 MHz, DMSO): d = 8.69 (d, $J = 8.6$ Hz, 1H), 8.52 (s, 1H), 8.15 (d, $J = 8.7$ Hz, 1H), 8.02 (bs, 1H), 7.93–7.83 (m, 2H), 7.13 (d, $J = 9.0$ Hz,

1H), 3.90 (s, 3H), 3.86 ppm (s, 3H); ^{13}C NMR (75 MHz, DMSO): d =

163.01, 161.23, 159.06, 158.68, 151.15, 149.14, 134.21, 130.56, 120.86, 117.87, 111.78, 110.56, 107.50, 55.75, 55.72 ppm; HRMS m/z

$[M + H]^+$ calcd for $C_{15}H_{14}N_4O_2$:283.1189, found: 283.1189.

ol 78 (85 mg, 0.30 mmol) was added and the mixture was stirred for 48 h at room temperature. After disappearance of the starting material, the precipitate was filtered off and the filtrate was washed with a 10% solution of HCl. Organic phases were collected

7-(3,4-Dimethoxyphenyl)pyrido[2,3-*d*]pyrimidin-4-ol (82): 7-(3,4-Dimethoxyphenyl)pyrido[2,3-*d*]pyrimidin-4-amine 81 (200 mg, 0.71 mmol) was suspended in a 6 n HCl solution (5 mL) and stirred at reflux for 2 h. The reaction was allowed to cool to room temper- ature and the precipitate was filtered off and washed with water to yield the title compound (120 mg, 60%). ^{1}H NMR (300 MHz, DMSO): d = 8.69 (s, 1H), 8.53 (d, J = 8.4 Hz, 1H), 8.21 (d, J = 8.4 Hz, 1H), 7.91–7.80 (m, 2H), 7.15 (d, J = 8.3 Hz, 1H), 3.89 (s, 3H), 3.86 ppm (s, 3H); ^{13}C NMR (75 MHz, DMSO): d = 161.38, 160.93, 151.50, 149.99, 149.18, 136.81, 132.19, 131.67, 131.55, 129.58, 128.99, 128.83, 121.09, 119.34, 111.94, 110.62, 55.83 ppm; HRMS m/z [M + H]$^+$ calcd for $C_{15}H_{13}N_3O_3$: 284.1030, found: 284.1025.

7-(3,4-Dimethoxyphenyl)-4-(1H-1,2,4-triazol-1-yl)pyrido[2,3-*d*]pyrimidine (83): A solution of phosphorus oxychloride (268 mg, 1.73 mmol), triazole (242 mg, 3.5 mmol) and DIPEA (136 mg, 1.05 mmol) in acetonitrile (5 mL) was stirred for 20 min at room temperature when 7-(3,4-dimethoxyphenyl)pyrido[3,2-*d*]pyrimidin- 4-ol 82 (100 mg, 0.35 mmol) was added. The mixture was stirred for 48 h at room temperature. After disappearance of the starting material, the precipitate was filtered of and the filtrate was washed with a 10% solution of HCl. Organic phases were collected and concentrated in vacuo. The crude residue was used as such in the following reaction.

4-(7-(3,4-Dimethoxyphenyl)pyrido[2,3-*d*]pyrimidin-4-yl)morpho- line (84): To a solution of 7-(3,4-dimethoxyphenyl)-4-(1H-1,2,4-tria- zol-1-yl)pyrido[2,3-*d*]pyrimidine 83 (0.35 mmol) in dioxane (5 mL) was added morpholine (152 mg, 1.75 mmol) and the mixture was stirred at reflux for 1 h. The volatiles were evaporated in vacuo and the crude residue was purified by silica gel flash column chroma- tography (eluting with a mixture of dichloromethane/methanol in a ratio of 95:5) yielding the title compound (20 mg, 19%). ^{1}H NMR

145

(300 MHz, DMSO): $\delta = 8.71$ (s, 1H), 8.43 (d, $J = 8.8$ Hz, 1H), 8.05 (d, $J = 8.7$ Hz, 1H), 7.92–7.80 (m, 2H), 7.13 (d, $J = 8.2$ Hz, 1H), 3.90 (s, 3H), 3.86 (s, 3H), 3.85–3.75 ppm (m, 8H); ^{13}C NMR (75 MHz, DMSO): $\delta = 163.99$, 160.90, 159.98, 157.06, 151.36, 149.19, 135.87, 130.21, 121.00, 117.33, 111.83, 110.49, 108.67, 66.13, 55.77, 55.72, 49.48 ppm; HRMS m/z $[M + H]^+$ calcd for $C_{19}H_{20}N_4O_3$: 353.1608, found: 353.1597.

3-Amino-5-(3,4-dimethoxyphenyl)pyrazine-2-carboxamide (85): To a solution of 3-amino-5-(3,4-dimethoxyphenyl)pyrazine-2-carbonitrile 19 (500 mg, 1.95 mmol) in concentrated formic acid (3 mL) was added concentrated sulfuric acid (140 mL). The mixture was heated in a microwave for 20 min at 100 °C. After disappearance of the starting material the mixture was allowed to cool and the formed bright yellow precipitate was filtered off and washed with water to yield the title compound (417 mg, 78%). ^{1}H NMR (300 MHz, CDCl$_3$): $\delta = 8.26$ (s, 1H), 7.63 (d, $J = 2.0$ Hz, 1H), 7.58 (dd, $J = 8.4$, 2.1 Hz, 1H), 6.97 (d, $J = 8.4$ Hz, 1H), 4.00 (s, 3H), 3.96 ppm (s, 3H); ^{13}C NMR (75 MHz, DMSO): $\delta = 168.73$, 154.58, 152.77, 150.98, 149.10, 128.35, 127.88, 123.66, 120.34, 111.83, 110.23, 55.73 ppm; HRMS m/z $[M + H]^+$ calcd for $C_{13}H_{14}N_4O_3$: 275.1139, found: 275.1164.

7-(3,4-Dimethoxyphenyl)pteridin-4(3H)-one (86): 3-Amino-5-(3,4-dimethoxyphenyl)pyrazine-2-carbonitrile 85 (400 mg, 1.56 mmol) was suspended in formamide (10 mL) and heated in a microwave at 160 °C for 20 min. The reaction was allowed to cool to room temperature, the precipitate was filtered off and washed with water to yield the title compound (315 mg, 71%). HRMS m/z $[M + H]^+$ calcd for $C_{14}H_{12}N_4O_3$: 285.0982, found: 285.0982.

4-Chloro-7-(3,4-dimethoxyphenyl)pteridine (87): To a solution of 7-(3,4-dimethoxyphenyl)pteridin-4(3H)-one 86 (300 mg, 1.05 mmol) in dry toluene were added DIPEA (407 mg, 3.15 mmol) and phosphorus oxychloride (483 mg, 3.15 mmol) and the mixture was stirred at reflux overnight. After disappearance of the starting material, the volatiles were evaporated and the crude residue was purified by silica gel flash column chromatography (eluting with a gradient of dichloromethane/ethyl acetate in a ratio of 97:3 to 95:5) yielding the title compound (179 mg, 55%). ^{1}H NMR (300 MHz, CDCl$_3$): $\delta = 9.50$ (s, 1H), 9.23 (s, 1H), 8.02 (d, $J = 2.1$ Hz, 1H), 7.86 (dd, $J = 8.5$, 2.1 Hz, 1H), 7.02 (d, $J = 8.5$ Hz, 1H), 4.02 (s, 3H), 3.98 ppm (s, 3H); HRMS m/z $[M + H]^+$ calcd for $C_{14}H_{11}Cl_1N_4O_2$: 303.0643, found: 303.0645.

4-(7-(3,4-Dimethoxyphenyl)pteridin-4-yl)morpholine (88): To a solution of 4-chloro-7-(3,4-dimethoxyphenyl)pteridine 87 (100 mg, 0.35 mmol) in dioxane (5 mL) was added morpholine (152 mg, 1.75 mmol) and the mixture was stirred at reflux for 4 h. After disappearance of the starting material, volatiles were evaporated and the crude residue was dissolved in water and washed with dichloromethane. The organic phases were collected and concentrated in vacuo to yield the title compound (120 mg, 97%). ^{1}H NMR (300 MHz, CDCl$_3$): $\delta = 9.11$ (s, 1H), 8.73 (s, 1H), 8.01 (d, $J = 2.1$ Hz, 1H), 7.78 (dd, $J = 8.5$, 2.1 Hz, 1H), 7.00 (d, $J = 8.5$ Hz, 1H), 4.58–4.43 (m, 4H), 4.02 (s, 3H), 3.97 (s, 3H), 3.92–3.86 ppm (m, 4H); ^{13}C NMR (75 MHz, CDCl$_3$): $\delta = 159.85$, 158.52, 155.88, 155.43, 152.32, 150.02, 138.60, 128.29, 126.40, 121.21, 111.09, 110.71, 67.33, 56.41, 56.23, 48.24 ppm; HRMS m/z $[M + H]^+$ calcd for $C_{18}H_{19}N_5O_3$: 354.1561, found: 354.1557.

GAK binding assay

K_d values for GAK were determined as previously described.[27] Briefly, the DNA-tagged GAK, an immobilized ligand on streptavidin-coated magnetic beads, and the test compound are combined. When binding occurs between GAK and a test compound, no binding can occur between GAK and the immobilized ligand. Upon washing, the compound-bound, DNA-tagged GAK is washed away. The beads carrying the ligands are then resuspended in elution buffer, and the remaining kinase concentration is measured by qPCR on the eluate. K_d values are determined using dose–response curves.

Abbreviations

AP: adaptor protein complex; Boc$_2$O: di-*tert*-butyldicarbonate; CCV: clathrin-coated vesicle; CHIKV: Chikungunya virus; DMF-DMA: *N*,*N*-dimethylformamide dimethyl acetal; DPPA: diphenyl phosphoryl azide; D-t-BPF: 1,1'-bis(di-*tert*-butylphosphino)ferrocene; EBOV: Ebola virus; DENV: Dengue virus; GAK: cyclin G-associated kinase; HCV: hepatitis C virus; K_d: dissociation constant; KO*t*Bu: potassium *tert*-butoxide; LR: Lawesson's reagent; LRRK2: leucine-rich repeat kinase 2; NIS: *N*-iodosuccinimide; *p*-TsOH: *para*-toluenesulfonic acid; *t*BuONO: *tert*-butyl nitrite; TGN: trans-Golgi network.

Conflict of interest

The authors declare no conflict of interest.

[1] Y. Kanaoka, S. H. Kimura, I. Okazaki, M. Ikeda, H. Nojima, *FEBS Lett.* 1997, *402*, 73– 80.
[2] B.-C. Park, Y.-I. Yim, X. Zhao, M. B. Olszewski, E. Eisenberg, L. E. Greene, *J. Cell Sci.* 2015, *128*, 3811–3821.
[3] H. Shimizu, I. Nagamori, N. Yabuta, H. Nojima, *J. Cell Sci.* 2009, *122*, 3145–3152.
[4] S. O. Dolly, M. D. Gurden, K. Drosopoulos, P. Clarke, J. de Bono, S. Kaye, P. Workman, S. Linardopoulos, *Br. J. Cancer* 2017, *117*, 954–964.
[5] C. R. M. Asquith, B.-T. Berger, J. Wan, J. M. Bennett, M. P. East, J. M. Elkins, O. Fedorov, P. H. Godoi, D. M. Hunter, S. Knapp, S. Mueller, C. I. Wells, H. S. Earp, T. M. Willson, W. J. Zuercher, *BioRxiv* 2018, 376772.
[6] M. Susa, E. Choy, X. Liu, J. Schwab, F. J. Hornicek, H. Mankin, Z. Duan, *Mol. Cancer Ther.* 2010, *9*, 3342–3350.
[7] D. A. Roosen, M. R. Cookson, *Mol. Neurodegener.* 2016, *11*, 73.
[8] C. X. Zhang, a. E. Y. Engqvist-Goldstein, S. Carreno, D. J. Owen, E. Smythe, D. G. Drubin, *Traffic* 2005, *6*, 1103 – 1113.
[9] V. I. Korolchuk, G. Banting, *Traffic* 2002, *3*, 428–439.
[10] E. Bekerman, G. Neveu, A. Shulla, J. Brannan, S. Y. Pu, S. Wang, F. Xiao, R. Barouch-Bentov, R. R. Bakken, R. Mateo, J. Govero, C. M. Nagamine, M. S. Diamond, S. De Jonghe, P. Herdewijn, J. M. Dye, G. Randall, S. Einav, *J. Clin. Invest.* 2017, *127*, 1338 –1352.
[11] S. Kametaka, K. Moriyama, P. V. Burgos, E. Eisenberg, L. E. Greene, R. Mattera, J. S. Bonifacino, *Mol. Biol. Cell* 2007, *18*, 2991–3001.
[12] D.-W. Lee, X. Zhao, F. Zhang, E. Eisenberg, L. E. Greene, *J. Cell Sci.* 2005, *118*, 4311–4321.

[13] F. Xiao, S. Wang, R. Barouch-Bentov, G. Neveu, S. Pu, M. Beer, S. Schor, S. Kumar, V. Nicolaescu, B. D. Lindenbach, G. Randall, S. Einav, *mBio* 2018, *9*, e02233-17.

[14] G. Neveu, A. Ziv-Av, R. Barouch-Bentov, E. Berkerman, J. Mulholland, S. Einav, *J. Virol.* 2015, *89*, 4387–4404.

[15] S.-Y. Pu, R. Wouters, S. Schor, J. Rozenski, R. Barouch-Bentov, L. I. Prugar, C. M. O'Brien, J. M. Brannan, J. M. Dye, P. Herdewijn, S. De Jonghe, S. Einav, *J. Med. Chem.* 2018, *61*, 6178–6192.

[16] S. Kovackova, L. Chang, E. Bekerman, G. Neveu, R. Barouch-Bentov, A. Chaikuad, C. Heroven, M. Š#la, S. De Jonghe, S. Knapp, S. Einav, P. Herdewijn, *J. Med. Chem.* 2015, *58*, 3393–3410.

[17] J. Li, S. Kovackova, S. Pu, J. Rozenski, S. De Jonghe, S. Einav, P. Herdewijn, *MedChemComm* 2015, *6*, 1666–1672.

[18] "Identifying and Representing Scaffolds", N. Brown in *Scaffold Hopping in Medicinal Chemistry* (Ed: N. Brown), Wiley-VCH, Weinheim, 2014, p. 3.

[19] R. Wouters, S.-Y. Pu, M. Froeyen, E. Lescrinier, S. Einav, P. Herdewijn, S. De Jonghe, *Eur. J. Med. Chem.* 2019, *163*, 256–265.

[20] P. Leonczak, L.-J. Gao, A. T. Ramadori, E. Lescrinier, J. Rozenski, S. De Jonghe, P. Herdewijn, *ChemMedChem* 2014, *9*, 2587–2601.

[21] M. R. Del Giudice, A. Borioni, C. Mustazza, F. Gatta, *J. Heterocycl. Chem.* 1994, *31*, 1503–1507.

[22] R. Saari, J.-C. Tçrm-, T. Nevalainen, *Bioorg. Med. Chem.* 2011, *19*, 939–950.

[23] T. Itoh, T. Mase, *Tetrahedron Lett.* 2005, *46*, 3573–3577.

[24] J. Lim, B. M. Taoka, S. Lee, A. Northrup, M. D. Altman, D. L. Sloman, M. G. Stanton, N. Noucti (Merck Sharp & Dohme Corp.), Int. PCT Pub. No. WO2011087999, July 21, 2011.

[25] G. W. Parshall, *J. Am. Chem. Soc.* 1974, *96*, 2360–2366.

[26] C. Ganser, E. Lauermann, A. Maderer, T. Stauder, J.-P. Kramb, S. Plutizki, T. Kindler, M. Moehler, G. Dannhardt, *J. Med. Chem.* 2012, *55*, 9531–9540.

[27] P. A. Procopiou, J. W. Barrett, N. P. Barton, M. Begg, D. Clapham, R. C. B. Copley, A. J. Ford, R. H. Graves, D. A. Hall, A. P. Hancock, A. P. Hill, H. Hobbs, S. T. Hodgson, C. Jumeaux, Y. M. L. Lacroix, A. H. Miah, K. M. L. Morriss, D. Needham, E. B. Sheriff, R. J. Slack, C. E. Smith, S. L. Sollis, H. Staton, *J. Med. Chem.* 2013, *56*, 1946–1960.

[28] E. Krasnokutskaya, N. Semenischeva, V. Filimonov, P. A. Knochel, *Synthesis* 2007, 81–84.

[29] R. C. Calhelha, M.-J. R. P. Queiroz, *Tetrahedron Lett.* 2010, *51*, 281–283.

[30] F. Dininno, M. L. Hammond, K. Dykstra, S. Kim, Q. Tan, K. Young, J. D. Hermes, H. Chen, S. Raeppel, M. Mannion, F. Gaudette, A. Vaisburg, J. Rahl, N. Georgopapadakou, N. Z. Zhou (Merck & Co. Inc., Methylgene Inc.), Int. PCT Pub. No. WO2008073142, June 19, 2008.

[31] L. H. Pettus, K. C. Sham, T. Andrew, S. Xu (Amgen Inc.), Int. PCT Pub. No. WO2009038784, March 26, 2009.

[32] M. T. Bilodeau, R. W. Hungate, A. M. Cunningham, T. J. Koester (Merck & Co. Inc.), Int. PCT Pub. No. WO1999016755, April 8, 1999.

[33] C. Li, Y. Shan, Y. Sun, R. Si, L. Liang, X. Pan, B. Wang, J. Zhang, *Eur. J. Med. Chem.* 2017, *141*, 506–518.

[34] A. Kung, Y.-C. Chen, M. Schimpl, F. Ni, J. Zhu, M. Turner, H. Molina, R. Overman, C. Zhang, *J. Am. Chem. Soc.* 2016, *138*, 10554–10560.

[35] Y. Loidreau, T. Besson, *Tetrahedron* 2011, *67*, 4852–4857.

[36] G. A. Roth, J. J. Tai, *J. Heterocycl. Chem.* 1996, *33*, 2051–2053.

[37] M. A. Fabian, W. H. Biggs, D. K. Treiber, C. E. Atteridge, M. D. Azimioara, M. G. Benedetti, T. A. Carter, P. Ciceri, P. T. Edeen, M. Floyd, J. M. Ford, M. Galvin, J. L. Gerlach, R. M. Grotzfeld, S. Herrgard, D. E. Insko, M. A. Insko, A. G. Lai, J.-M. L8lias, S. A. Mehta, Z. V. Milanov, A. M. Velasco, L. M. Wodicka, H. K. Patel, P. P. Zarrinkar, D. J. Lockhart, *Nat. Biotechnol.* 2005, *23*, 329–336.

Potent antiviral activity of novel multi-substituted 4-anilinoquin(az)olines

Sirle Saul[a], Szu-Yuan Pu[a], William J. Zuercher[b,c], Shirit Einav[a,*], Christopher R.M. Asquith[b,d,*]

[a] Department of Medicine, Division of Infectious Diseases and Geographic Medicine, and Department of Microbiology and Immunology, Stanford University School of Medicine, Stanford, CA 94305, USA
[b] Structural Genomics Consortium, UNC Eshelman School of Pharmacy, University of North Carolina at Chapel Hill, Chapel Hill, NC 27599, USA
[c] Lineberger Comprehensive Cancer Center, University of North Carolina at Chapel Hill, Chapel Hill, NC 27599, USA
[d] Department of Pharmacology, School of Medicine, University of North Carolina at Chapel Hill, Chapel Hill, NC 27599, USA

ARTICLE INFO

ABSTRACT

Screening a series of 4-anilinoquinolines and 4-anilinoquinazolines enabled identification of potent novel inhibitors of dengue virus (DENV). Preparation of focused 4-anilinoquinoline/quinazoline scaffold arrays led to the identification of a series of high potency 6-substituted bromine and iodine derivatives. The most potent compound 6-iodo-4-((3,4,5-trimethoxyphenyl)amino)quinoline-3-carbonitrile (**47**) inhibited DENV infection with an $EC_{50} = 79$ nM. Crucially, these compounds showed very limited toxicity with CC_{50} values > 10 µM in almost all cases. This new promising series provides an anchor point for further development to optimize compound properties.

In the past five decades there has been a dramatic increase in the global burden of the mosquito-borne dengue virus (DENV) infection. The geographical range of dengue infections, including those in the developed world, has been expanding due to climate change and rapid urbanization.[1] Consequently, ~400 million people are estimated to get infected with one or more of the 4 distinct DENV serotypes annually in over 128 endemic countries.[2,3] The majority of symptomatic individuals experience an uncomplicated dengue fever infection. However, 5–20% progress to a life-threatening disease, known as severe dengue, particularly upon a secondary infection with a heterologous DENV serotype.[4,5]

The development of an effective dengue vaccine has been hampered by the necessity to generate simultaneous protection against the 4 distinct DENV serotypes.[6,7] Moreover, since there are no approved antiviral therapies currently available, the management of dengue infections remains focused on the treatment of symptoms, rather than the underlying disease.[8] This results in continued morbidity and mortality.

In recent years, there has been a flurry of activity to identify novel DENV inhibitors,[9–24] but none of these compounds have yet entered clinical trials. These compounds include a number of kinase inhibitor scaffolds, such as the oxindole (sunitinib, JMX0395),[9,10] azaindole (**1**)[11] and isothiazolo[4,3-b]pyridine (**2–3**)[12,13] (Fig. 1).

To identify new chemical starting points to inhibit DENV, we looked to the chemically tractable 4-anilinoquin(az)oline scaffold. Our team recently reported erlotinib as a promising starting point with activity against DENV replication (Fig. 2).[9] There are a number of other quin(az)oline based inhibitors that have shown potent anti-DENV activity in the low nanomolar range, including RYL-634, **4** and **5** among others (Fig. 2).[9,22–26] These results focused our attention on exploring the possible anti-DENV activity of the quin(az)oline scaffold.

To further explore antiviral quin(az)oline activity, we probed the structure activity relationships (SAR) of the quinoline/quinazoline by profiling several focused arrays of compounds. We developed a series of hybrid molecules combining structural features of erlotinib and **2** to expand the SAR in the current literature and assess tractability of the scaffolds (Fig. 3).

We hence synthesized a series of compounds (**6–64**) to follow up on the initial results of erlotinib and **2** to explore the 4-anilinoquinazoline and 4-anilinoquinoline scaffolds through nucleophilic aromatic displacement of 4-chloroquin(az)olines (Scheme 1).[27–36] We were able to access products in good to excellent yields (34–83%) consistent with previous reports for literature and novel compounds.[27–37]

We tested the compounds for antiviral activity in human hepatoma (Huh7) cells infected with DENV2.[38–41] Their effect on overall infection was measured at 48 h post-infection via luciferase assays and the half-maximal effective concentration and the 90% effective concentrations (EC_{50} and EC_{90} values, respectively) were calculated. In parallel, we tested the effect of these compounds on cell viability via an AlamarBlue
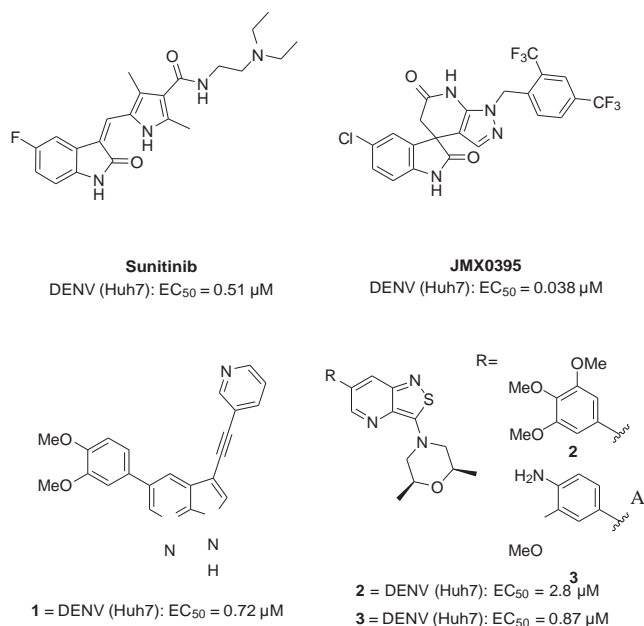
Fig. 1. A selection of previously reported inhibitors and associated activities on DENV (the data is all for serotype 2 for consistency). Huh7 = human hepatoma cells.
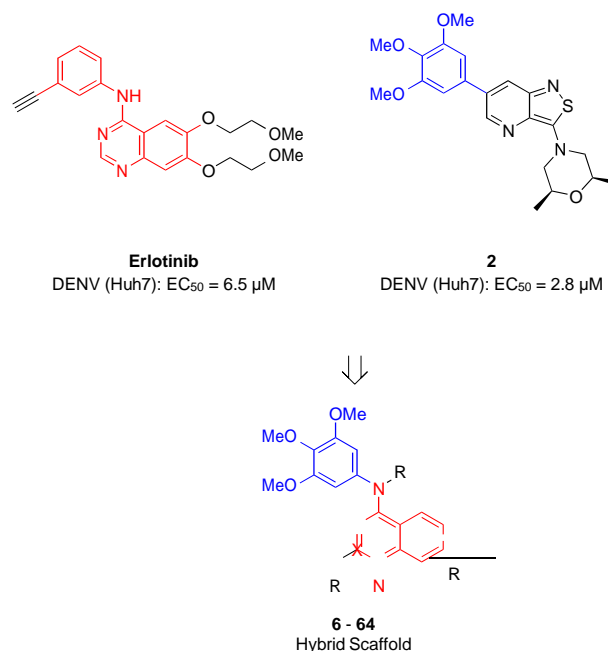
Fig. 3. Depiction of a hybrid series of trimethoxyanilinoquin(az)olines developed by combining erlotinib and **2**.

Scheme 1. General synthetic procedure.

Table 1

Screening results of SAR of trimethoxy quinazolines and anti-DENV activity.
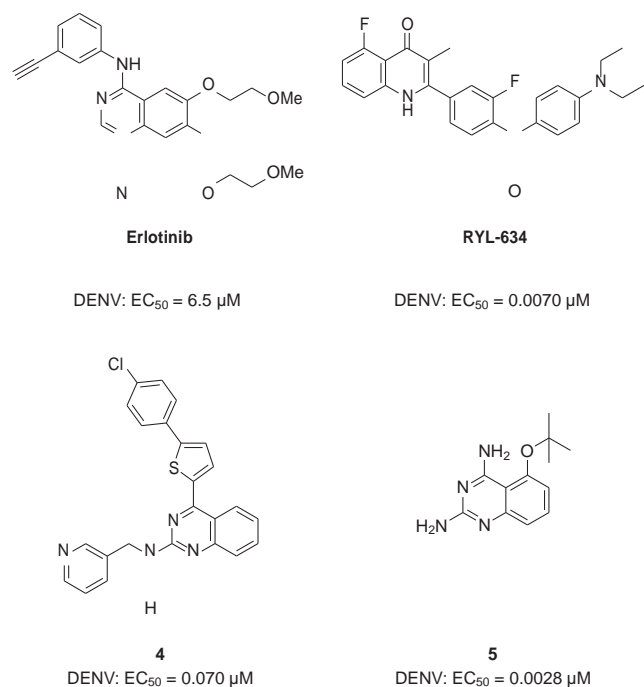
Fig. 2. Structures of quinazolines with anti-DENV activity.

Cmpd	R^1	R^2	DENV inhibition

assay in the DENV-infected Huh7 cells and measured the half-maximal cytotoxic concentration (CC$_{50}$) values.[42]

We first screened a series of trimethoxyanilinoquinazolines (**6–24**) (Table 1).[32] The unsubstituted trimethoxyanilinoquinazoline (**6**) showed a 2-fold increase in potency over erlotinib. However, further simple substitutions with a 6-methyl (**7**), 6-fluoro (**8**) or 6,7-difluoro (**9**) showed no activity or toxicity. Interestingly, the switch from 6-fluoro (**9**) to 6-chloro (**10**) led to a > 10-fold increase in activity and an almost 7-fold increase with respect to erlotinib. Similar activity values were

observed for compounds possessing 6-bromo (**11**) and 6-iodo (**12**). However, when there was an increase in size and electronegativity to 6-trifluoromethyl (**13**) the compound was inactive. Switching the halogen to the 7-postion (**14–18**) led to net decrease in activity. The 7-fluoro (**14**) was inactive and the 7-chloro (**15**) was equivalent to erlotinib and 6-fold less potent than the 6-chloro counterpart (**10**). The 7-bromo (**16**) and 7-iodo (**17**) were only 2- and 3-fold less potent respectively. In contrast, the 7-trifluoromethyl (**18**) was more active than **13**, its regioisomer at the 6-position, with equivalent activity to erlotinib. The 7-cyano (**19**) saw an increase in potency to almost 5-fold more than er-

lotinib with an $EC_{50} = 1.4$ µM. The 6-cyano (**20**) was 2-fold weaker,

			EC_{50}^{a} (µM)	CC_{50}^{b} (µM)
6	H	H	2.8	>10
7	Me	H	>10	>10
8	F	H	>10	>10
9	F	F	>10	>10
10	Cl	H	1.0	>10
11	Br	H	0.97	>10
12	I	H	1.0	>10
13	CF$_3$	H	>10	>10
14	H	F	>10	>10
15	H	Cl	6.1	>10
16	H	Br	2.0	>10
17	H	I	2.9	5.8
18	H	CF$_3$	5.1	>10
19	H	CN	1.4	>10
20	CN	H	3.7	>10
21	SO$_2$Me	H	>10	>10
22	OMe	H	>10	>10
23	OMe	OMe	6.6	>10
24	H	OMe	2.7	>10

a = infectivity assay in Huh7 cells mean average n = 2; b = cytotoxicity in Huh7 cells mean average n = 2.

Table 2

Screening results of SAR of trimethoxy quinolines and anti-DENV activity.
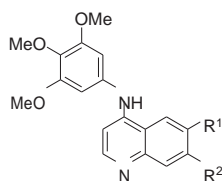
Cmpd	R^1	R^2	DENV inhibition	
			a	b
			EC_{50} (µM)	CC_{50} (µM)
25	H	H	0.82	> 10
26	F	H	0.52	> 10
27	F	F	1.0	5.5
28	Cl	H	0.52	> 10
29	Br	H	0.080	> 10
30	I	H	0.82	> 10
31	CF_3	H	0.59	> 10
32	CN	H	0.76	> 10
33	SO_2Me	H	0.84	> 10
34	^tBu	H	7.4	> 10
35	OMe	H	0.75	> 10
36	OMe	OMe	> 10	> 10
37	H	OMe	> 10	> 10
38	H	F	4.1	> 10
39	H	Cl	> 10	> 10
40	H	Br	8.4	> 10
41	H	I	3.6	> 10
42	H	CF_3	6.8	> 10
43	H	CN	3.3	> 10

a = infectivity assay in Huh7 cells mean average n = 2; b = cytotoxicity in Huh7 cells mean average n = 2.

Table 3

Screening results of SAR of trimethoxy 3-cyanoquinolines and anti-DENV activity.

Cmpd	R^1	R^2	DENV inhibition	
			EC_{50}^{a} (µM)	CC_{50}^{b} (µM)
44	H	H	> 10	> 10
45	Cl	H	1.3	> 10
46	Br	H	0.082	> 10
47	I	H	0.079	> 10
48	SO_2Me	H	> 10	> 10
49	OMe	H	3.1	> 10
50	OMe	OMe	5.5	> 10
51	H	OMe	> 10	> 10
52	H	Cl	> 10	> 10
53	H	Br	> 10	> 10
54	H	I	4.7	> 10

a = infectivity assay in Huh7 cells mean average n = 2; b = cytotoxicity in Huh7 cells mean average n = 2.

provement over erlotinib. The 7-cyano (**43**) yielded equipotent activity to **41** with an $EC_{50} = 3.3$ µM with an increased ligand efficiency.
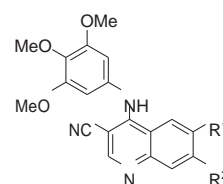
while the 6-methylsulfone (**21**) was inactive as was the corresponding 6-methoxy substitution (**22**). The 6,7-dimethoxy analog (**23**) had equivalent potency to erlotinib. Interestingly the 7-methoxy analog (**24**) showed a 2-fold increase in activity relative to erlotinib and **23**.

Even small changes to the central plane angle can have radical effects on the scaffold's biological properties. Consequently, we hypothesized that switching from the quinazoline to the quinoline core would more closely mimic the central plane angle present in **1** and lead to more potent activity. The change from quinoline to quinazoline was expected to increase the plane angle from nearly planar to around 50–60 degrees.[32] Our hypothesis proved to be valid as the unsubstituted trimethoxyanilinoquinoline (**25**) was 3-fold more potent than the corresponding quinoline (**6**) and 8-fold more potent than erlotinib (Table 2). The 6-fluoro analog (**26**) had equivalent potency to **25**. The 6,7-difluoro (**27**) was also equivalent but showed toxicity at higher concentrations ($CC_{50} = 5.5$ µM). The 6-chloro analog (**28**) was equivalent to the 6-fluoro (**26**), and the 6-bromo (**29**) exhibited a substantial increase in potency ($EC_{50} = 80$ nM), with a > 80-fold increase over erlotinib and 10-fold over the unsubstituted analog (**25**). The 6-bromo analog (**29**) demonstrated a local activity minimum as further substitution to increase the halogen size to 6-iodo (**30**) and 6-trifluoromethyl (**31**), along with the corresponding 6-cyano (**32**) and methylsulfone (**33**) all showed potency in the range 0.5–1 µM.

The incorporation of a slightly larger substituent, a 6-*tert*-butyl (**34**), led to an activity down to that of erlotinib. Switching to the 6-methoxy analog (**35**) recovered the potency loss with an almost 8-fold increase over erlotinib. Surprisingly, the 6,7-dimethoxy analog (**36**) showed no activity (n = 4 biological replicates) and neither did the 7-methoxy substitution (**37**). The other 7-position analogs (**38–43**) all demonstrated weaker activity. Variation of the halogen (**38–42**) resulted in no clear trend with the 7-iodo (**41**) the only compound with a 2-fold im-

To increase the plane angle to near orthogonality, we switched to the 3-cyanoquinoline (**44**–**54**) (Table 3).[32] The initial result was dis- appointing with the unsubstituted analog (**44**) having no observable activity up to the highest compound concentrations employed. Switching to the 6-chloro (**45**) yielded an analog with activity just above micromolar ($EC_{50} = 1.3$ µM). However, the 6-bromo (**46**) and 6- iodo (**47**) had activities equivalent to **29** and with a > 80-fold increase over erlotinib and 120-fold over the unsubstituted analog. Switching to the 6-methylsulfone (**48**) removed all activity. Some recovery of ac- tivity to $EC_{50} = 3.3$ µM was possible switching to the 6-methoxy (**49**). However, the 6,7-dimethoxy (**50**) showed a slight reduction in potency and the 7-methoxy (**51**) was inactive. Results were similar for the 7- chloro (**52**) and 7-bromo (**53**). Interestingly, there was some recovery with the 7-iodo (**54**) with an $EC_{50} = 4.7$ µM.
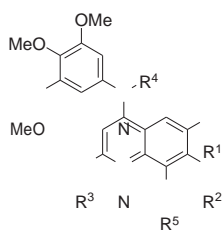
We sought to further understand the observed SAR between the quinazoline scaffold and the DENV inhibition profiles. This was achieved by synthesizing a series of derivatives with different electronic and steric profiles (**55**–**64**) (Table 4).[28,36] First, the direct 6-bromo analog (**55**) of **29** with a 2-methyl substitution was > 20-fold more potent than erlotinib but with an unexpected increase in toxicity ($CC_{50} = 2.5$ µM) with only a 10-fold selectivity index (CC_{50}/EC_{50}). Switching to the 6-methoxy (**56**), 6,7-dimethoxy (**57**), 7-methoxy (**58**) all yielded analogs with limited or no activity in addition to no toxicity. The 7-trifluoromethyl (**59**) was also inactive. However, moving the trifluoromethyl to the 6-position (**60**) yielded a compound that was 3- fold less potent than the 6-bromo (**55**), but with no toxicity and 7-fold more potency than erlotinib. Moving the methyl group to block the amino bridge (**61**) removed all activity. Switching the trifluoromethyl for a simple fluorine (**62**) decreased potency by over 2-fold. The 2- methyl group (**63**) was weakly active and the 8-methyl substitution (**64**) was inactive. These two results taken together suggest that the quinoline nitrogen is an important contributor to activity.

These results delineate the SAR of anti-DENV activity and the 4- anilinoquinoline/quinazoline scaffold. The 6-position bromine and io- dine analogs on the quinoline were by far the most potent series of analogs (**29**, **46**, **47** and **55**) (Fig. 4).

This body of work provides several exciting starting points for fur- ther optimization. The mechanism of the observed antiviral activity has

Table 4

Screening results of SAR of the trimethoxy quinoline core and anti-DENV activity.

Cmpd	R^1	R^2	*R^3*	R^4	R^5	DENV inhibition	
						^{a} (µM) EC$_{50}$	CC ^{b} (µM) $_{50}$
55	Br	H	Me	H	H	0.28	2.5
56	OMe	H	Me	H	H	10	>10
57	OMe	OMe	Me	H	H	10	>10
58	H	OMe	Me	H	H	>10	>10
59	H	CF$_3$	Me	H	H	>10	>10
60	CF$_3$	H	Me	H	H	0.91	>10
61	CF$_3$	H	H	Me	H	>10	>10
62	F	H	Me	H	H	2.3	>10
63	H	H	Me	H	H	8.0	>10
64	H	H	H	H	Me	>10	>10

a = infectivity assay in Huh7 cells mean average n = 2; b = cytotoxicity in Huh7 cells mean average n = 2.
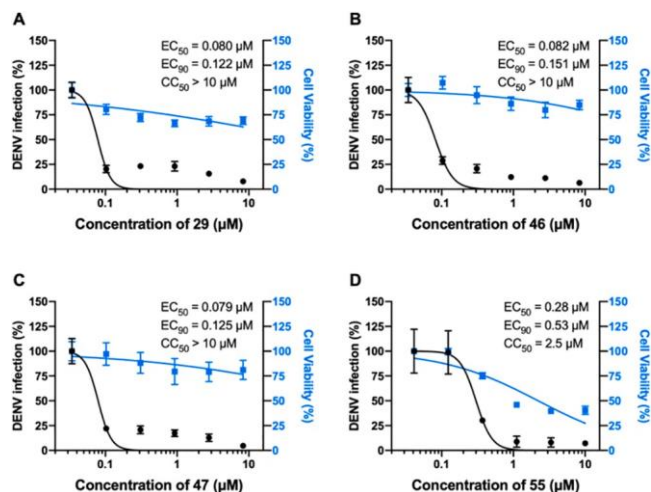

Fig. 4. Compounds **29**, **46**, **47** and **55** suppress DENV infection. Dose response of DENV infection (black) and cell viability (blue) to compounds **29** (A), **46** (B), **47** (C) and **55** (D) measured by luciferase and alamarBlue assays, respectively, 48 h after infection. Data are plotted relative to vehicle control. Shown are representative experiments from at least two conducted, each with 5 biological replicates; shown are means ± SD.

exclude a possibility that these compounds target a viral protein.

Erlotinib and **2** have both previously been reported to inhibit DENV replication.[9] The synthetic combination of these two molecules to form a series of trimethoxyquin(az)olines has defined a new series of DENV inhibitors. Several key results act as a signpost for further chemical optimization. The 6,7-dimethoxy-*N*-(3,4,5-trimethoxyphenyl)quinolin-4-amine analog **23** had equivalent potency to erlotinib showing that the glycol ether side chains are less important for activity. The 6-bromo-*N*-(3,4,5-trimethoxyphenyl)quinolin-4-amine analog **29** demonstrated a local minimum in the SAR, highlighting that a medium sized group was optimal in this position. The 6-bromo (**46**) and 6-iodo (**47**) 3-cyano-quinoline compounds supported this with activities equivalent to **29** and a > 80-fold increase over erlotinib and 120-fold over the un-substituted analog (**44**). This initial series of results are the first step in non-kinase ATP or non-ATP binding proteins.[43] Lastly, we cannot

yet to be defined and could be a combination of factors including kinases and other proteins. Some of these compounds are known to act as kinase inhibitors having been originally prepared as inhibitors targeting the ATP-binding site of human kinases including cyclin-G-associated kinase (GAK), serine/threonine-protein kinase 10 (STK10) and STE20-like serine/threonine-protein kinase (SLK).[32] It is possible that these kinases may be involved, but their ATP-binding sites may not be directly involved. Alternatively, other undefined proteins may participate in the mechanism of antiviral action. Indeed, compounds having structural features expected to impede interaction with a kinase hinge region (Table 4) also demonstrated antiviral activity. It is also possible that the observed phenotypes may originate from modulation of other,

defining a medicinal chemistry trajectory towards a series of optimized antiviral compounds with potential to treat DENV and possibly other viral agents.

Declaration of Competing Interest

The authors declare that they have no known competing financial interests or personal relationships that could have appeared to influence the work reported in this paper.

Acknowledgments

Appendix A. Supplementary data

Supplementary data to this article can be found online at https://doi.org/10.1016/j.bmcl.2020.127284.

References

1. Messina JP, Brady OJ, Golding N, et al. *Nat Microbiol.* 2019;4:1508.
2. Bhatt S, Gething PW, Brady OJ, et al. *Nature.* 2013;496:504.
3. Guzman MG, Gubler DJ, Izquierdo A, Martinez E, Halstead SB. *Nat Rev Dis Primers.* 2016;18:16055.
4. Machado CR, Machado ES, Rohloff RD, et al. *PLoS Negl Trop Dis.* 2013;7.
5. Chau TN, Anders KL, Lien le B. *PLoS Negl Trop Dis.* 2010;4.
6. Flipse J, Smit JM. *PLoS Negl Trop Dis.* 2015;9.
7. Yang, Y.; Meng, Y.; Halloran, M. E.; Longini, I. M. Jr. Clin Infect Dis 2018, 66, 178.
8. Stevens AJ, Gahan ME, Mahalingam S, Keller PA. *J Med Chem.* 2009;52:7911.
9. Bekerman E, Neveu G, Shulla A, et al. *J Clin Invest.* 2017;127:1338.
10. Xu J, Xie X, Chen H, Zou J, et al. *Bioorg Med Chem Lett.* 2020;30.
11. Verdonck S, Pu SY, Sorrell FJ, et al. *J Med Chem.* 2019;62:5810.
12. Pu SY, Wouters R, Schor S, et al. *J Med Chem.* 2018;61:6178.
13. Chen WC, Simanjuntak Y, Chu LW, et al. *J Med Chem.* 2020;63:1313.
14. Bardiot, D.; Koukni, M.; Smets, W.; Carlens, G.; McNaughton, M.; Kaptein, S.; Dallmeier, K.; Chaltin, P. Neyts, J.; Marchand, A. J Med Chem. 2018, 61, 8390.
15. Millies, B.; von Hammerstein, F.; Gellert, A.; Hammerschmidt, S.; Barthels, F.;

Göppel, U.; Immerheiser, M.; Elgner, F.; Jung, N.; Basic, M.; Kersten, C.; Kiefer, W.; Bodem, J.; Hildt, E.; Windbergs, M.; Hellmich, U. A.; Schirmeister, T. J Med Chem. 2019, 62, 11359.

16. Vincetti P, Caporuscio F, Kaptein S, et al. *J Med Chem.* 2015;58:4964.
17. Behnam MAM, Graf D, Bartenschlager R, Zlotos DP, Klein CD. *J Med Chem.* 2015;58:9354.
18. Nitsche C, Steuer C, Klein CD. *Bioorg Med Chem.* 2011;19:7318.
19. Saudi M, Zmurko J, Kaptein S, Rozenski J, Neyts J, Van Aerschot A. *Eur J Med Chem.* 2014;87:529.
20. Yokokawa F, Nilar S, Noble CG, et al. *J Med Chem.* 2016;59:3935.
21. Yang CC, Hu HS, Wu RH, et al. *Antimicrob Agents Chemother.* 2014;58:110.
22. Venkatesham A, Saudi M, Kaptein S, et al. *Eur J Med Chem.* 2017;126:101.
23. Yang Y, Cao L, Gao H, et al. *J Med Chem.* 2019;62:4056.
24. Wang QY, Patel SJ, Vangrevelinghe E, et al. *Antimicrob Agents Chemother.* 1823;2009:53.
25. Chao B, Tong XK, Tang W, et al. *J Med Chem.* 2012;55:3135.
26. Opsenica I, Burnett JC, Gussio R, et al. *J Med Chem.* 2011;54:1157.
27. Asquith CRM, Laitinen T, Bennett JM, et al. *Chem Med Chem.* 2018;13:48.
28. Asquith CRM, Berger BT, Wan J, et al. *J Med Chem.* 2019;62:2830.
29. Asquith CRM, Naegeli KM, East MP, et al. *J Med Chem.* 2019;62:4772.
30. Asquith CRM, Treiber DK, Zuercher WJ. *Bioorg Med Chem Lett.* 2019;29:1727.
31. Asquith CRM, Bennett JM, Su L, et al. *Molecules.* 2019;24:pii E4016.
32. Asquith CRM, Laitinen T, Bennett JM, et al. *ChemMedChem.* 2020;15:26.
33. Asquith CRM, Fleck N, Torrice CD. *Bioorg Med Chem Lett.* 2019;18:2695.
34. Asquith CRM, Maffuid KA, Laitinen T, et al. *ChemMedChem.* 2019;14:1693.
35. Asquith CRM, Tizzard G. *Molbank.* 2019;4:M1087.
36. Asquith, C. R. M.; Laitinen, T.; Wells, C. I.; Tizzard, G. J.; Zuercher, W. J. Molecules. 2020, 25, pii: E1697.
37. General procedure for the synthesis of 4-anilinoquin(az)olines: 4-chloroquin(az)oline derivative (1.0 eq.), aniline derivative (1.1 eq.), were suspended in ethanol (10 mL) and refluxed for 18 h. The crude mixture was purified by flash chromatography using EtOAc:hexane followed by 1-5 % methanol in EtOAc; After solvent removal under reduced pressure, the product was obtained as a free following solid or recrystallized from ethanol/water. Compounds 6-54 were synthesized as previous described32 and 60-61 as previously reported.28. 6-bromo-2-methyl-N-(3,4,5-trimethoxyphenyl)quinolin-4-amine (55) was obtained as a light yellow solid (149 mg, 0.370 mmol, 63%). m.p. > 250 °C; 1H NMR (400 MHz, DMSO-d6) δ 10.87 – 10.61 (m, 1H), 9.06 (d, J = 2.0 Hz, 1H), 8.28 – 7.87 (m, 2H), 6.82, (s, 1H), 6.78 (s, 2H), 3.80 (s, 6H), 3.72 (s, 3H), 2.63 (s, 3H). 13C NMR (100 MHz, DMSO-d6) δ 155.1, 153.6, 153.3, 137.6, 136.4, 136.1, 132.7 (s, 2C), 125.8, 122.1, 119.1, 117.6, 103.0 (s, 2C), 101.0, 60.2, 56.1 (s, 2C), 19.2. HRMS m/z [M+H]+ calcd for C19H20BrN2O3: 403.0657, found 403.0662, LC tR = 4.00 min, > 98% Purity. 6-methoxy-2-methyl-N-(3,4,5-trimethoxyphenyl)quinolin-4-amine (56) was obtained as a yellow solid (213 mg, 0.601 mmol, 83%). m.p. 135-137 °C; 1H NMR (400 MHz, DMSO-d6) δ 10.68 (s, 1H), 8.22 (d, J = 2.6 Hz, 1H), 8.05 (d, J = 9.2 Hz, 1H), 7.59 (dd, J = 9.2, 2.5 Hz, 1H), 6.80 (s, 2H), 6. 74 (s, 1H), 3.98 (s, 3H),), 3.81 (s, 6H), 3.72 (s, 3H), 2.61 (s, 3H). 13C NMR (100 MHz, DMSO-d6) δ 157.5, 153.5, 153.4, 152.2, 136.2, 133.5, 133.1 (s, 2C), 124.7, 121.3, 117.3, 103.2 (s, 2C), 103.0, 100.1, 60.2, 56.5, 56.1 (s, 2C), 19.5. HRMS m/z [M+H]+ calcd for C20H23N2O4: 355.1658, found 355.1655, LC tR = 3.84 min, > 98% Purity. 6,7-dimethoxy-2-methyl-N-(3,4,5-trimethoxyphenyl)quinolin-4-amine (57) was obtained as a light yellow solid (187 mg, 0.483 mmol, 72%). m.p. > 250 °C; 1H NMR (400 MHz, DMSO-d6) δ 10.49 (s, 1H), 8.11 (s, 1H), 7.48 (s, 1H), 6.77 (s, 2H), 6.65 (s, 1H), 3.98 (s, 3H), 3.94 (s, 3H), 3.81 (s, 6H), 3.72 (s, 3H), 2.57 (s, 3H). 13C NMR (100 MHz, DMSO-d6) δ 154.2, 153.5, 152.9, 151.2, 148.8, 136.1, 135.3, 133.2 (s, 2C), 110.2, 103.2 (s, 2C), 102.7, 99.6, 99.4, 60.2, 56.7, 56.1 (s, 2C), 56.0, 19.4. HRMS m/z [M+H]+ calcd for C21H25N2O5: 385.1763, found 385. 1762, LC tR = 3.82 min, > 98% Purity. 7-methoxy-2-methyl-N-(3,4,5-trimethoxyphenyl)quinolin-4-amine (58) was obtained as a colourless solid (194 mg, 0.504 mmol, 80%). m.p. > 350 °C; 1H NMR (400 MHz, DMSO-d6) δ 10.63 (s, 1H), 8.67 (d, J = 9.3 Hz, 1H), 7.48 (d, J = 2.5 Hz, 1H), 7.35 (dd, J = 9.3, 2.5 Hz, 1H), 6.77 (s,

2H), 6.65 (s, 1H), 3.94 (s, 3H), 3.80 (s, 6H), 3.72 (s, 3H), 2.59 (s, 3H). 13C NMR (100 MHz, DMSO-d6) δ 162.8, 154.1, 153.9, 153.5 (s, 2C), 140.8, 136.3, 133.0, 125.3, 117.2, 110.3, 103.3 (s, 2C), 99.8, 99.4, 60.2, 56.1 (s, 2C), 55.9, 19.6. HRMS m/z [M +H]+ calcd for C20H23N2O4: 355.1639, LC tR = 3.18 min, > 98% Purity. 2-methyl-7-(trifluoromethyl)-N-(3,4,5-trimethoxyphenyl)quinolin-4-amine (59) was obtained as a yellow solid (165 mg, 0.421 mmol, 69%). m.p. > 250 °C; 1H NMR (400 MHz, DMSO-d6) δ 11.01 (s, 1H), 9.01 (d, J = 8.8 Hz, 1H), 8.53 (d, J = 1.9 Hz, 1H), 8.06 (dd, J = 9.0, 1.8 Hz, 1H), 6.89 (s, 1H), 6.81 (s, 2H), 3.81 (s, 6H), 3.73 (s, 3H), 2.67 (s, 3H). 13C NMR (100 MHz, DMSO-d6) δ 155.1 (d, J = 212.2 Hz), 153.6 (s, 2C), 138.2, 136.5, 132.6, 132.5 (q, J = 32.2 Hz), 132.0, 125.7, 124.6, 122.0 – 121.6 (m), 118.4, 117.5 – 116.9 (m), 103.1 (s, 2C), 101.7, 60.2, 56.1 (s, 2C), 19.9. HRMS m/z [M+H]+ calcd for C20H20F3N2O3: 393.1426, found 393.1422, LC tR = 4.07 min, > 98% Purity. 6-fluoro-2-methyl-N-(3,4,5-trimethoxyphenyl) quinolin-4-amine (62) was obtained as a light yellow solid (179 mg, 0.523 mmol, 68%). m.p. > 250 °C; 1H NMR (400 MHz, DMSO-d6) δ 10.72 (s, 1H), 8.71 (dd, J = 10.5, 2.7 Hz, 1H), 8.21 (dd, J = 9.3, 5.1 Hz, 1H), 7.92 (ddd, J = 9.3, 8.0, 2.7 Hz, 1H), 6.80 (d, J = 6.2 Hz, 3H), 3.80 (s, 6H), 3.72 (s, 3H), 2.64 (s, 3H). 13C NMR (100 MHz, DMSO-d6) δ 159.5 (d, J = 244.9 Hz), 154.5, 153.9 (d, J = 3.8 Hz), 153.6 (s, 2C), 136.4, 135.6, 132.8, 122.8 (d, J = 17.2 Hz), 122.6, 117.2 (d, J = 9.5 Hz), 108.3 (d, J = 25.1 Hz), 103.1 (s, 2C), 100.4, 60.2, 56.1 (s, 2C), 19.7. HRMS m/z [M+H]+ calcd for C19H20FN2O3: 343.1458, found 343.1456, LC tR = 3.67 min, > 98% Purity. 2-methyl-N-(3,4,5-trimethoxyphenyl)quinolin-4-amine (63) was obtained as a colourless solid (200 mg, 0.616 mmol, 73%). m.p. > 250 °C; 1H NMR (400 MHz, DMSO-d6) δ 10.76 (s, 1H), 8.77 (dd, J = 8.6, 1.3 Hz, 1H), 8.11 (dd, J = 8.5, 1.2 Hz, 1H), 7.97 (ddd, J = 8.4, 7.0, 1.1 Hz, 1H), 7.72 (ddd, J = 8.3, 7.0, 1.2 Hz, 1H), 6.80 (s, 2H), 6.77 (s, 1H), 3.81 (s, 6H), 3.73 (s, 3H), 2.64 (s, 3H). 13C NMR (100 MHz, DMSO-d6) δ 154.6, 154.4, 153.6 (s, 2C), 138.5, 136.4, 133.5, 132.9, 126.4, 123.4, 119.8, 116.1, 103.2 (s, 2C), 100.3, 60.2, 56.1 (s, 2C), 19.8. HRMS m/z [M+H]+ calcd for C19H21N2O3: 325.1552, found 325.1551, LC tR = 3.59 min, > 98% Purity. 8-methyl-N-(3,4,5-trimethoxyphenyl)quinolin-4-amine (64) was obtained as a mustard solid (93.1 mg, 0.287 mmol, 34%). m.p. 130-132 °C; 1H NMR (400 MHz, DMSO-d6) δ 13.45 (s, 1H), 10.77 (s, 1H), 8.56 (d, J = 8.5 Hz, 1H), 8.39 (d, J = 6.9 Hz, 1H), 7.86 (d, J = 7.1 Hz, 1H), 7.68 (dd, J = 8.5, 7.1 Hz, 1H), 6.90 (d, J = 6.8 Hz, 1H), 6.80 (s, 2H), 3.75 (d, J = 31.4 Hz, 9H), 2.68 (s, 3H). 13C NMR (100 MHz, DMSO-d6) δ 155.4, 155.2, 153.7 (s, 2C), 136.5, 134.3, 134.2, 133.0, 126.6, 121.1, 117.2, 112.9, 103.2 (s, 2C), 100.6, 60.2, 56.2 (2, 2C), 17.8. HRMS m/z [M+H]+ calcd for C19H21N2O3: 325.1552, found 325.1550, LC tR = 3.60 min, > 98% Purity.

38. Virus construct. DENV2 (New Guinea C strain)[44,45] Renilla reporter plasmid used for in vitro assays was a gift from Pei-Yong Shi (The University of Texas Medical Branch).
39. Cells. Huh7 (Apath LLC) cells were grown in DMEM (Mediatech) supplemented with 10% FBS (Omega Scientific), nonessential amino acids, 1% L-glutamine, and 1% penicillin-streptomycin (ThermoFisher Scientific) and maintained in a humidified incubator with 5% CO2 at 37 °C.
40. Virus Production. DENV2 RNA was transcribed in vitro using mMessage/mMachine (Ambion) kits. DENV was produced by electroporating RNA into BHK-21 cells, harvesting supernatants on day 10 and titering via standard plaque assays on BHK-21 cells. In parallel, on day 2 post-electroporation, DENV-containing supernatant was used to inoculate C6/36 cells to amplify the virus.
41. Infection assays. Huh7 cells were infected with DENV in replicates (n = 5) at a multiplicity of infection (MOI) of 0.05. Overall infection was measured at 48 hours using a Renilla luciferase substrate.
42. Viability assays. Viability was assessed using AlamarBlue® reagent (Invitrogen) assay according to manufacturer's protocol. Fluorescence was detected at 560 nm on InfiniteM1000 plate reader.
43. Munoz L. *Nat Rev Drug Discov.* 2017;16:424.
44. Xie X, Gayen S, Kang C, Yuan Z, Shi P-Y. *J Virol.* 2013;87:4609.
45. Zou G, Xu HY, Qing M, Wang QY, Shi PY. *Antiviral Res.* 2011;91:11.

Repurposing of Kinase Inhibitors as Broad-Spectrum Antiviral Drugs

Stanford Schor[1,2] and Shirit Einav[1,2]

The high cost of drug development and the narrow spectrum of coverage typically provided by direct-acting antivirals limit the scalability of this antiviral approach. This review summarizes progress and challenges in the repurposing of approved kinase inhibitors as host-targeted broad-spectrum antiviral therapies.

Keywords: kinase inhibitors, antiviral drugs, repurposing, broad-spectrum antivirals

Introduction

There is an urgent need for antiviral strategies to combat hundreds of human disease-causing viruses. Currently approved antiviral drugs treat fewer than ten viral infections. A majority of these drugs are direct-acting antivirals (DAAs) that target proteins encoded by individual viruses. As such, this approach provides a narrow spectrum of coverage and therefore cannot address the large clinical need. The high average cost (over two billion dollars) and long timeline (8–12 years) to develop a new drug (Tufts center for the Study of Drug Development, 2014), further limit the scalability of the DAA approach to drug development, particularly with respect to emerging viruses. Lastly, the inability to provide adequate global health protection and national security preparedness against newly emerging viruses and the emergence of viral resistance further challenge conventional DAAs.

The host-targeted broad-spectrum antiviral strategy represents an attractive potential solution to overcome these limitations. Viruses are dependent on cellular proteins for each step of their life cycle. Targeting host proteins required by multiple viruses can thus provide a broad-spectrum coverage with a possible added benefit of a high genetic barrier to resistance. Moreover, a broad-spectrum therapeutic could be administered even before a viral threat has been accurately diagnosed, thereby increasing protection.

A particularly cost- and time-effective strategy for the development of broad-spectrum antivirals is to repurpose already approved drugs that target host functions required by multiple viruses. By lowering the development cost, this approach has the potential to increase drug access for patients. Moreover, it shortens the path to clinic by enabling utilization of available data (e.g., toxicity, pharmacokinetics, dosing, etc.). Lastly, it can promote preparedness for future outbreaks of newly emerging pathogens by facilitating off-label use of approved broad-spectrum antivirals against new viral indications.

Host kinase inhibitors represent one category of compounds with a great potential to be repurposed as broad-spectrum antivirals. Viruses hijack a large number of host kinases at distinct steps of their life cycle (Supekova et al., 2008; Li et al., 2009; Keating and Striker, 2012; Jiang et al., 2014). Some of these host kinases are broadly required and thus represent attractive targets for broad-spectrum therapy (Table 1 and Fig. 1). These findings, combined with the development and approval of a large number of kinase inhibitors for the treatment of cancer (Gross et al., 2015) and inflammatory conditions (Ott and Adams, 2011) have sparked efforts aimed to determine the therapeutic potential of such drugs to combat viral infections. In this review, we summarize recent efforts to determine the therapeutic potential and biological rationale of repurposing already approved kinase inhibitors as antivirals.

Targeting the NAK Family of Kinases

Targeting the NAK (Numb-associated kinases) family of Ser/Thr kinases by approved kinase inhibitors is one approach showing promise as a broad-spectrum antiviral strategy. We discovered a requirement for the host kinases adaptor protein 2 (AP2)-associated protein kinase 1 (AAK1) and cyclin G-associated kinase (GAK) in the regulation of intracellular viral trafficking during entry, assembly, and release of unrelated viruses (Neveu et al., 2012, 2015; Bekerman et al., 2017).

We recognized that the already approved anticancer drugs sunitinib and erlotinib potently inhibited AAK1 and GAK, respectively, and demonstrated activity against viruses from six viral families, including dengue (DENV) and Ebola viruses (EBOV) in cultured cells (Neveu et al., 2012, 2015; Bekerman et al., 2017). Sunitinib/erlotinib combinations protected against morbidity and mortality in murine models of dengue and Ebola infection (Bekerman et al., 2017). Moreover, we discovered that inhibition of AP-mediated

[1]Division of Infectious Diseases and Geographic Medicine, Department of Medicine, Stanford, California.

[2]Department of Microbiology and Immunology, Stanford University School of Medicine, Stanford, California.

1

Table 1. Classification, Antiviral Activity, and Mechanism of Action of Approved Kinase Inhibitors

Kinase family	Kinases	Inhibitors	EC50	In vitro	In vivo	Stages of viral lifecycle	Antiviral target validation (siRNA)	Molecular target validation	Mechanism of action	Refs.
NAK	AAK1 GAK	Sunitinib Erlotinib	0.12–12.9 mM 0.12–4.67 mM	Flaviviridae (HCV. DENV, WNV, ZIKV) Filoviridae (EBOV) Togaviridae (CHIKV) Arenaviridae (JUNV) Retroviridae (HIV) Paramyxoviridae (RSV)	DENV (mouse) EBOV(Mouse)	Entry Assembly Release	+	+	Inhibition of AP-mediated intracellular membrane trafficking	Bekerman et al. (2017) Neveu et al. (2012) Neveu et al. (2015)
ErbB	EGFR	Erlotinib Lapatinib Gefitinib	0.276–0.6 mM 0.18 mM 4.93 mM	Flaviviridae (HCV, DENV, WNV, ZIKV) Herpesviridae (HCMV) Poxviridae (Orthopoxvirus)	HCV (Mouse) HCMV (Guinea pig)	Entry	+	+	Inhibition of receptor-mediated endocytosis	Diao et al. (2012) Neveu et al. (2015) Langhammer et al. (2011) Lupberger et al. (2011) Schleiss et al. (2008)
MAPK/ERK	MEK1/2 ERK1/2	Trametinib Selumetinib	0.1–1 mM 1–10 mM	Coronaviridae (MERS, SARS)	ND	ND	ND	ND	ND	Kindrachuk et al. (2015)
Src	SRC FYN	Dasatinib Sarcatanib	12.2 mM* 4.7 mM*	Flaviviridae (DENV)	ND	RNA Replication Assembly	+	ND	Inhibition of actin motility	Chu and Yang (2007) de Wispelaere et al. (2013)
Abl	ABL1	Dasatinib Imatinib Nilotinib	12.2 mM* 9.8–17.7 mM –	Filoviridae (EBOV) Flaviviridae (DENV) Coronaviridae (MERS, SARS) Poxviridae (Vaccinia)	Vaccinia (Mouse)	Entry Release	+	ND	Inhibition of actin motility	Clark et al. (2016) Dyall et al. (2014) Garcia et al. (2012) Reeves et al. (2011)
CDK	CDK1 CDK2 CDK5 CDK4/6 CDK9	Palbociclib Dinaciclib PHA-690509 Alvocidib Seliciclib	0.016–0.02 mM 0.02–0.355 mM 0.9–1.72 mM 0.01–0.24 mM 0.024–0.04 mM	Retroviridae (HIV) Orthomyxoviridae (IAV) Flaviviridae (ZIKV) Herpesviridae (HCMV, HSV)	HSV-1 (Mouse)	ND	+	+	Inhibition of phosphorylation of viral proteins and reduction of host intracellular dNTPs	Badia et al. (2016) Chao et al. (2000) Guendel et al. (2010) Habran et al. (2005) Pauls et al. (2014a) Perwitasari et al. (2015) Schang et al. (2006) Xu et al. (2016) Yamamoto et al. (2014)
PI3K/Akt/mTor	mTor Akt	Everolimus Miltefosine Teriflunamide Leflunomide	1–10 mM >10 mM – –	Coronaviridae (MERS) Herpesviridae (HCMV) Polyomaviridae (BKV)	HCMV(Rat) BKV (Human)	ND	+	ND	Disabling of viral block of cell stress response and apoptosis	Kindrachuk et al. (2015) Jaw et al. (2017) Jung et al. (2013) Liacini et al. (2010) Waldman et al. (1999) Williams et al. (2005)

* = EC90.
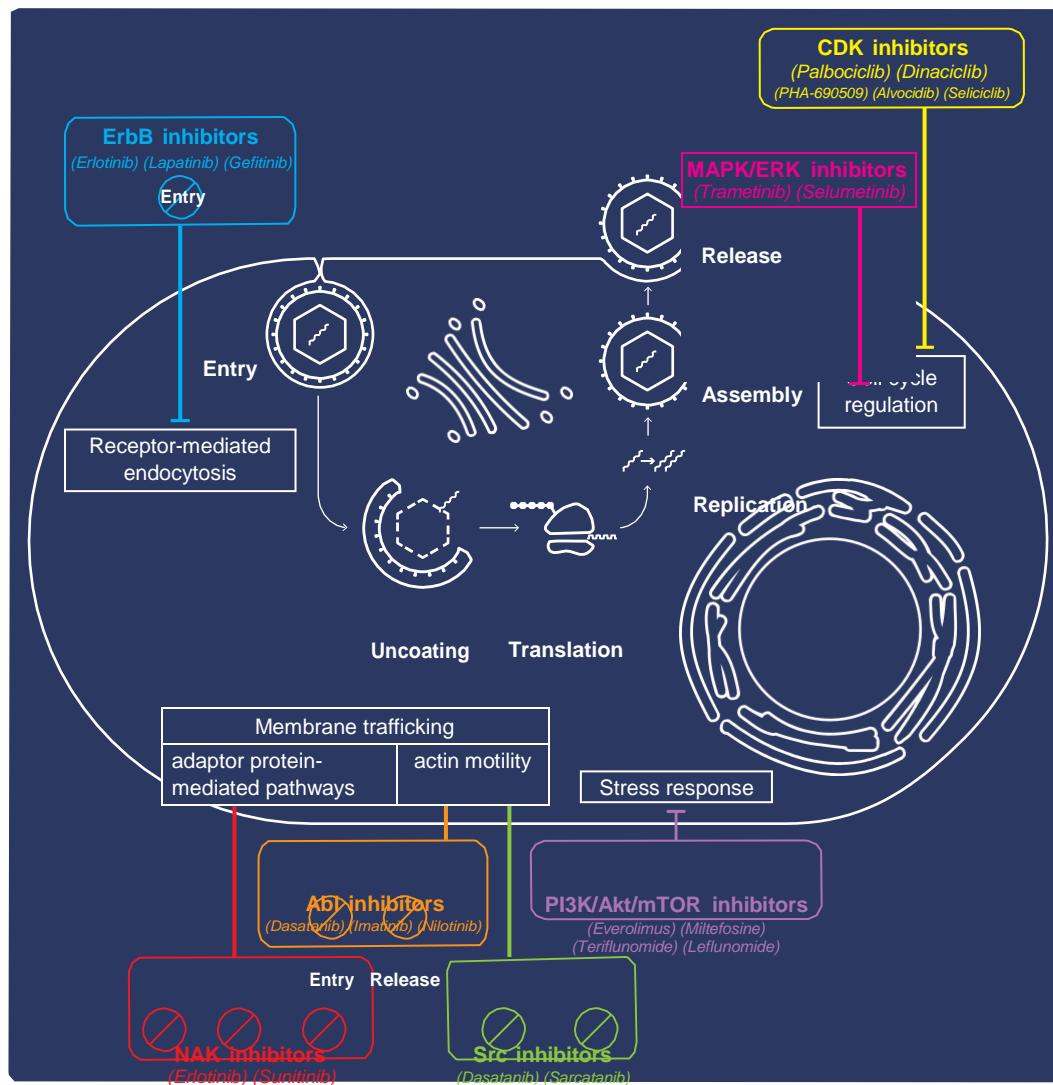
FIG. 1. Approved kinase inhibitors with broad-spectrum antiviral activity. Examples of classes of kinase inhibitors with broad-spectrum antiviral activity and the specific steps of the viral life cycle they target (if known) are denoted in *colored boxes*. Blunt *arrows* connect these compounds to the corresponding targeted cellular process thought to mediate their antiviral effect.

intracellular membrane trafficking regulated by AAK1 and GAK represents an important mechanism by which sunitinib and erlotinib inhibit viral infection *in vitro* and *in vivo* (Bekerman *et al.*, 2017). The safety and efficacy of sunitinib/erlotinib combinations will be evaluated in dengue patients in the future and potentially in patients with EBOV disease in future outbreaks (ClinicalTrials.gov NCT02380625).

Targeting the ErbB Family of Kinases

Epidermal growth factor receptor (EGFR), a member of the ErbB family of receptor tyrosine kinases, is another host factor broadly required by viruses (Zheng *et al.*, 2014). EGFR is utilized as an entry coreceptor by human cytomegalovirus (HCMV) (Wang *et al.*, 2003) and adeno-associated virus serotype 6 (AAV6) (Weller *et al.*, 2010). EGFR-mediated

signaling is implicated in the endocytosis of hepatitis C virus (HCV) and influenza A virus (IAV) (Eierhoff *et al.*, 2010; Lupberger *et al.*, 2011; Diao *et al.*, 2012; Neveu *et al.*, 2012,

2015; Zona *et al.*, 2013) and in postentry events, as in HCMV nuclear trafficking through regulation of F-actin dynamics (Wang *et al.*, 2005). IAV and other viruses hijack EGFR to evade host immune responses (Ueki *et al.*, 2013).

Altogether, these studies validate EGFR as a broad antiviral target. Indeed, erlotinib and gefitinib, approved anticancer drugs targeting EGFR, and lapatinib, an anticancer drug targeting EGFR and another member of the ERBb kinase family, ERBB2, demonstrated *in vitro* activity against a number of viruses, in- cluding HCV (Lupberger *et al.*, 2011; Diao *et al.*, 2012; Neveu *et al.*, 2015), HCMV (Schleiss *et al.*, 2008), and poxvirus (Langhammer *et al.*, 2011). Notably, erlotinib and gefitinib inhibited HCV and HCMV infections in a mouse and guinea pig model, respectively (Schleiss *et al.*, 2008; Lupberger *et al.*, 2011).

Targeting the MAPK/ERK Pathway

Several kinases in the MAPK/ERK (mitogen-activated pro- tein kinases/extracellular signal-regulated kinases) pathway are essential for viral replication. ERK1 and ERK2 phosphorylate

HIV-1 proteins and enhance viral infectivity (Yang and Ga-buzda, 1999). IAV activates this pathway and relies on it for effective virus production and export of the viral ribonucleo-protein complexes from the nucleus (Pleschka *et al.*, 2001). Activation of this pathway mediates EBOV entry into target cells and enhances cytokine production and cellular toxicity, thereby possibly contributing to disease pathogenesis (Kolo-koltsov *et al.*, 2009) (Zampieri *et al.*, 2007; Johnson *et al.*, 2014).

Moreover, infection with Middle East respiratory syn-drome coronavirus (MERS-CoV) activates this pathway and is inhibited by two anticancer compounds, trametinib, an Food and Drug Administration-approved MEK1/2 inhibitor, and selumetinib, an investigational (Phase III) MEK1/ERK1/2 inhibitor (Kindrachuk *et al.*, 2015). The broad-spectrum antiviral potential of these compounds in cultured cells and animal models remains to be established.

Targeting the Src and Abl Families of Kinases

The Src family of kinases (SFKs) is implicated in the life cycle of multiple viruses (Pagano *et al.*, 2013). The replication of viruses from the Flaviviridae family is dependent on the activation of various SFKs, such as Fyn, Lyn, c-Src, and Csk (DENV) (Chu and Yang, 2007; de Wispelaere *et al.*, 2013; Kumar *et al.*, 2016), c-Yes (West Nile Virus, WNV) (Hirsch *et al.*, 2005), and Csk (HCV) (Supekova *et al.*, 2008). The unrelated HIV-1 also activates SFKs to effectively replicate (Narute and Smithgall, 2012).

The approved drug dasatinib and the investigational (Phase III) compound saracatinib, with activity against SFKs, in-hibited DENV assembly *in vitro* (de Wispelaere *et al.*, 2013). This antiviral activity was initially attributed to inhibition of c-Src (Chu and Yang, 2007), yet the effect on assembly was subsequently shown to be non-Src mediated, whereas an in-dependent effect of the drug on DENV RNA replication was found to be Fyn-mediated (de Wispelaere *et al.*, 2013).

Another host kinase targeted by both dasatinib and sar-acatinib is c-Abl (cellular Abelson tyrosine kinase), a member of the Abl family of nonreceptor tyrosine kinases. C-Abl is implicated in the budding or release of poxviruses (Reeves *et al.*, 2011) and EBOV (Garcia *et al.*, 2012), the entry of coxsackievirus (Coyne and Bergelson, 2006) and poly-omavirus (Swimm *et al.*, 2010), and in DENV infection (Clark *et al.*, 2016). Imatinib and/or nilotinib, approved anticancer c-Abl inhibitors lacking anti-SFK activity, in-hibited replication of EBOV (Garcia *et al.*, 2012), DENV (Clark *et al.*, 2016), MERS-CoV and/or SARS-CoV (Dyall *et al.*, 2014) in cultured cells. While dasatinib also inhibited MERS-CoV and SARS-CoV, it remained uncertain which molecular target(s) (Abl only or Abl plus Src) mediated its activity against these viruses (Dyall *et al.*, 2014).

In a murine model of vaccinia virus, imatinib effectively reduced viral load, viral spread, and mortality (Reeves *et al.*, 2011). In contrast, dasatinib did not protect mice, but rather induced immunosuppression, raising a concern about its utility in controlling viral infections *in vivo*. It is thus im-portant to investigate the antiviral activity and safety of drugs targeting either Src and/or Abl kinases in animal models of other viral infections. Moreover, while inhibition of actin motility was proposed as a mechanism of antiviral action of Src and/or Abl inhibitors (Reeves *et al.*, 2011), additional mechanisms remain to be uncovered.

Targeting the Cyclin-Dependent Kinases

Numerous viruses regulate the host cell cycle by modifying the expression level and activity of members of the host cyclin-dependent kinases (CDKs) family (Schang, 2003). To promote its replication, adenovirus increases CDK2 phosphorylation, thereby forcing progression into late-G1/S-phase (Cheng *et al.*, 2013), whereas hepatitis B virus increases activity of the G_1-phase kinase CDK4 (Gearhart and Bouchard, 2010). CDK6 and CDK9 have both been validated as potential antiviral targets in HIV-1 infection (Nemeth *et al.*, 2011; Pauls *et al.*, 2014b), and CDK9 in herpes simplex virus type 1 (HSV-1) infection (Durand and Roizman, 2008).

Various CDK inhibitors with variable selectivity have demonstrated antiviral activity (Schang *et al.*, 2006). Palbo-ciclib, an approved CDK4/6 inhibitor suppressed HIV-1 re-verse transcription and HSV-1 replication *in vitro* (Pauls *et al.*, 2014a; Badia *et al.*, 2016). Moreover, four investigational CDK inhibitors, dinaciclib (CDK1/2/5/9 inhibitor, Phase III), seliciclib (CDK2/5 inhibitor, Phase II), alvocidib (CDK9 in-hibitor, Phase II), and PHA-690509 (CDK2 inhibitor, Phase I), inhibited multiple viruses, including HIV-1 (Chao *et al.*, 2000; Guendel *et al.*, 2010), IAV (Perwitasari *et al.*, 2015), and Zika in cultured cells (Xu *et al.*, 2016). Alvocidib and a novel CDK9 inhibitor, FIT-039, demonstrated broad *in vitro* activity against DNA viruses and efficacy in a murine model of HSV-1 (Ya-mamoto *et al.*, 2014). In addition to suppression of viral rep-lication, targeting CDKs in the context of oncogenic viral infections may also suppress viral persistence and/or trans-formation (Li *et al.*, 2003).

While grossly undertested, several studies have provided some insight about the potential mechanism of action (MOA) underlying the antiviral effect of CDK inhibitors. Inhibition of phosphorylation of viral proteins plays a role in the case of IAV and varicella zoster virus, (Habran *et al.*, 2005; Perwi-tasari *et al.*, 2015), whereas reduced intracellular dNTP availability and viral mRNA transcription through inhibition of a cellular protein phosphorylation is one mechanism by which palbociclib exerts its anti-HSV-1 and HIV-1 activities (Pauls *et al.*, 2014a; Badia *et al.*, 2016). A better under-standing of the MOA of these compounds in other viral in-fections remains an important area of investigation.

Targeting the PI3K/Akt/mTOR Pathway

Multiple viruses activate the phosphatidylinositol 3¢-kinase–Akt–mammalian target of rapamycin (PI3K/Akt/mTOR) pathway to support their replication and escape cellular stress responses (Buchkovich *et al.*, 2008). HCV (Mannová and Beretta, 2005), WNV (Shives *et al.*, 2014), and IAV (Ehrhardt *et al.*, 2006; Hale *et al.*, 2006) activate this pathway to promote distinct steps in their life cycle and control apoptosis. Although this pathway was shown to be activated in cells infected with MERS-CoV, everolimus, an mTor inhibitor approved to treat cancer and prevent transplant rejection, demonstrated only mild *in vitro* activity against MERS-CoV, and miltefosine, an approved AKT inhibitor, demonstrated no activity in this infection model (Kindrachuk *et al.*, 2015).

In contrast, leflunomide's active metabolite teriflunomide, which suppresses Akt phosphorylation and is approved for rheumatoid arthritis treatment, has shown potent anti-HCMV

activity both *in vitro* and in a rat model (Waldman *et al.*, 1999). Furthermore, treatment with leflunomide and the two approved immunosuppressant mTOR inhibitors everolimus and sirolimus, either individually or in combination, reduced BK viremia and disease progression in patients with BK virus nephropathy (Williams *et al.*, 2005; Jung *et al.*, 2013; Jaw *et al.*, 2017). Direct suppression of polyomavirus replication was proposed as one underlying MOA of this approach based on *in vitro* studies (Liacini *et al.*, 2010). These findings underscore the importance of further exploring the broad antiviral activity of inhibitors of this pathway.

Summary and Perspectives

While repurposing of approved drugs as host-targeted broad-spectrum antivirals offers several important advantages over development of new DAAs, it also raises concerns. One obvious concern when targeting host functions is toxicity. Nevertheless, the protective effect of sunitinib/erlotinib combinations in murine models of DENV and EBOV (Bekerman *et al.*, 2017) suggests that for some drugs it may be feasible to find a therapeutic window where the drug level is sufficient to inhibit viral replication with minimal cellular toxicity. Shortening the duration of therapy from months or years required to treat cancer to several days sufficient to treat most acute viral infections should further limit toxicity.

Emergence of viral resistance is another potential challenge of broad-spectrum antiviral drugs (de Wispelaere *et al.*, 2013; Haqqani and Tilton, 2013). Nevertheless, targeting host kinases that are not under the genetic control of viruses is more likely to have a higher barrier to resistance than classical DAAs. Moreover, simultaneous inhibition of several kinases or pathways by the same drug or drug combination could increase the effectiveness while minimizing viral resistance, as previously shown in cancer (Knight *et al.*, 2010). Indeed, while DENV overcame inhibition by a DAA with the emergence of a resistance mutation, it remained susceptible to sunitinib and erlotinib, supporting the higher genetic barrier of the host-targeted antiviral approach (Bekerman *et al.*, 2017).

Lastly, understanding the MOA is challenging since cellular kinase function in a complex network of interactions and their inhibitors are often not selective. For example, erlotinib's effect on HCV entry was first attributed solely to its effect on EGFR, its known cancer target (Lupberger *et al.*, 2011; Diao *et al.*, 2012). We later demonstrated that ectopic expression not only of EGFR, but also GAK, which is inhibited by erlotinib with a comparable potency to EGFR (Kd of 3.4 nM vs. 1 nM) (Karaman *et al.*, 2008), reversed erlotinib's anti-HCV effect (Neveu *et al.*, 2015).

Similarly, the anti-DENV effect of dasatinib was attributed to the inhibition of SFKs, particularly Fyn (Chu and Yang, 2007) (de Wispelaere *et al.*, 2013). Nevertheless, the finding that c-Abl, another dasatinib target, is essential for DENV infection (Clark *et al.*, 2016) suggests that c-Abl inhibition likely represents yet another mechanism through which dasatinib mediates its antiviral activity. These examples underscore the importance of validating not only the antiviral targets but also the molecular targets underlying the antiviral effect of such inhibitors.

In summary, these examples provide a proof-of-concept for the potential feasibility of repurposing of approved kinase inhibitors as host-targeted broad-spectrum antiviral therapies to combat viral infections. While not yet approved, compounds targeting other kinases, such as the phosphatidylinositol 4-kinase family and IkB kinase-a, have already demonstrated antiviral activity (Altan-Bonnet and Balla, 2012; Li *et al.*, 2013), suggesting that the repertoire of kinase inhibitor classes available for repurposing is likely to grow. Such approaches may find utility in combination with other strategies being developed to combat viruses.

Disclosure Statement

No competing financial interests exist.

References

Altan-Bonnet, N., and Balla, T. (2012). Phosphatidylinositol 4-kinases: hostages harnessed to build panviral replication platforms. Trends Biochem Sci 37, 293–302.

Badia, R., Angulo, G., Riveira-Munoz, E., Pujantell, M., Puig, T., Ramirez, C., Torres-Torronteras, J., Marti, R., Pauls, E., Clotet, B., *et al.* (2016). Inhibition of herpes simplex virus type 1 by the CDK6 inhibitor PD-0332991 (palbociclib) through the control of SAMHD1. J Antimicrob Chemother 71, 387–394.

Bekerman, E., Neveu, G., Shulla, A., Brannan, J., Pu, S.-Y., Wang, S., Xiao, F., Barouch-Bentov, R., Bakken, R.R., Mateo, R., *et al.* (2017). Anticancer kinase inhibitors impair intracellular viral trafficking and exert broad-spectrum antiviral effects. J Clin Invest 127, 1338–1352.

Buchkovich, N.J., Yu, Y., Zampieri, C.A., and Alwine, J.C. (2008). The TORrid affairs of viruses: effects of mammalian DNA viruses on the PI3K–Akt–mTOR signalling pathway. Nat Rev Microbiol 6, 266–275.

Chao, S.H., Fujinaga, K., Marion, J.E., Taube, R., Sausville, E.A., Senderowicz, A.M., Peterlin, B.M., and Price, D.H. (2000). Flavopiridol inhibits P-TEFb and blocks HIV-1 replication. J Biol Chem 275, 28345–28348.

Cheng, P.-H., Rao, X.-M., McMasters, K.M., and Zhou, H.S. (2013). Molecular basis for viral selective replication in cancer cells: activation of CDK2 by adenovirus-induced Cyclin E. PLoS One 8, e57340.

Chu, J.J., and Yang, P.L. (2007). c-Src protein kinase inhibitors block assembly and maturation of dengue virus. Proc Natl Acad Sci U S A 104, 3520–3525.

Clark, M.J., Miduturu, C., Schmidt, A.G., Zhu, X., Pitts, J.D., Wang, J., Potisopon, S., Zhang, J., Wojciechowski, A., Hann Chu, J.J., *et al.* (2016). GNF-2 inhibits dengue virus by targeting Abl kinases and the viral E protein. Cell Chem Biol 23, 443–452.

Coyne, C.B., and Bergelson, J.M. (2006). Virus-induced Abl and Fyn kinase signals permit coxsackievirus entry through epithelial tight junctions. Cell 124, 119–131.

de Wispelaere, M., LaCroix, A.J., and Yang, P.L. (2013). The small molecules AZD0530 and dasatinib inhibit dengue virus RNA replication via Fyn kinase. J Virol 87, 7367–7381.

Diao, J., Pantua, H., Ngu, H., Komuves, L., Diehl, L., Schaefer, G., and Kapadia, S.B. (2012). Hepatitis C virus induces epidermal growth factor receptor activation via CD81 binding for viral internalization and entry. J Virol 86, 10935–10949.

Durand, L.O., and Roizman, B. (2008). Role of cdk9 in the optimization of expression of the genes regulated by ICP22 of herpes simplex virus 1. J Virol 82, 10591–10599.

Dyall, J., Coleman, C.M., Hart, B.J., Venkataraman, T., Holbrook, M.R., Kindrachuk, J., Johnson, R.F., Olinger, G.G., Jr., Jahrling, P.B., Laidlaw, M., et al. (2014). Repurposing of clinically developed drugs for treatment of Middle East respiratory syndrome coronavirus infection. Antimicrob Agents Chemother 58, 4885–4893.

Ehrhardt, C., Marjuki, H., Wolff, T., Nurnberg, B., Planz, O., Pleschka, S., and Ludwig, S. (2006). Bivalent role of the phosphatidylinositol-3-kinase (PI3K) during influenza virus infection and host cell defence. Cell Microbiol 8, 1336–1348.

Eierhoff, T., Hrincius, E.R., Rescher, U., Ludwig, S., and Ehrhardt, C. (2010). The Epidermal Growth Factor Receptor (EGFR) Promotes uptake of Influenza A Viruses (IAV) into host cells. PLoS Pathog 6, e1001099.

Garcia, M., Cooper, A., Shi, W., Bornmann, W., Carrion, R., Kalman, D., and Nabel, G.J. (2012). Productive replication of Ebola virus is regulated by the c-Abl1 tyrosine kinase. Sci Transl Med 4, 123ra124.

Gearhart, T.L., and Bouchard, M.J. (2010). The hepatitis B virus X protein modulates hepatocyte proliferation pathways to stimulate viral replication. J Virol 84, 2675–2686.

Gross, S., Rahal, R., Stransky, N., Lengauer, C., and Hoeflich, K.P. (2015). Targeting cancer with kinase inhibitors. J Clin Invest 125, 1780–1789.

Guendel, I., Agbottah, E.T., Kehn-Hall, K., and Kashanchi, F. (2010). Inhibition of human immunodeficiency virus type-1 by cdk inhibitors. AIDS Res Ther 7, 7.

Habran, L., Bontems, S., Di Valentin, E., Sadzot-Delvaux, C., and Piette, J. (2005). Varicella-zoster virus IE63 protein phosphorylation by roscovitine-sensitive cyclin-dependent kinases modulates its cellular localization and activity. J Biol Chem 280, 29135–29143.

Hale, B.G., Jackson, D., Chen, Y.H., Lamb, R.A., and Randall, R.E. (2006). Influenza A virus NS1 protein binds p85beta and activates phosphatidylinositol-3-kinase signaling. Proc Natl Acad Sci U S A 103, 14194–14199.

Haqqani, A.A., and Tilton, J.C. (2013). Entry inhibitors and their use in the treatment of HIV-1 infection. Antiviral Res 98, 158–170.

Hirsch, A.J., Medigeshi, G.R., Meyers, H.L., DeFilippis, V., Früh, K., Briese, T., Lipkin, W.I., and Nelson, J.A. (2005). The Src family kinase c-yes is required for maturation of West Nile virus particles. J Virol 79, 11943–11951.

Jaw, J., Hill, P., and Goodman, D. (2017). Combination of leflunomide and everolimus for treatment of BK virus nephropathy. Nephrology 22, 326–329.

Jiang, W.-M., Zhang, X.-Y., Zhang, Y.-Z., Liu, L., and Lu, H.-Z. (2014). A high throughput RNAi screen reveals determinants of HIV-1 activity in host kinases. Int J Clin Exp Pathol 7, 2229–2237.

Johnson, J.C., Martinez, O., Honko, A.N., Hensley, L.E., Olinger, G.G., and Basler, C.F. (2014). Pyridinyl imidazole inhibitors of p38 MAP kinase impair viral entry and reduce cytokine induction by Zaire ebolavirus in human dendritic cells. Antiviral Res 107, 102–109.

Jung, Y.H., Moon, K.C., Ha, J.W., Kim, S.-J., Ha, I.-S., Cheong, H.I., and Kang, H.G. (2013). Leflunomide therapy

for BK virus allograft nephropathy after pediatric kidney transplantation. Pediatr Transplant 17, E50–E54.

Karaman, M.W., Herrgard, S., Treiber, D.K., Gallant, P., Atteridge, C.E., Campbell, B.T., Chan, K.W., Ciceri, P., Davis, M.I., Edeen, P.T., et al. (2008). A quantitative analysis of kinase inhibitor selectivity. Nat Biotech 26, 127–132.

Keating, J.A., and Striker, R. (2012). Phosphorylation events during viral infections provide potential therapeutic targets. Rev Med Virol 22, 166–181.

Kindrachuk, J., Ork, B., Hart, B.J., Mazur, S., Holbrook, M.R., Frieman, M.B., Traynor, D., Johnson, R.F., Dyall, J., Kuhn, J.H., et al. (2015). Antiviral potential of ERK/MAPK and PI3K/AKT/mTOR signaling modulation for middle east respiratory syndrome coronavirus infection as identified by temporal kinome analysis. Antimicrob Agents Chemother 59, 1088–1099.

Knight, Z.A., Lin, H., and Shokat, K.M. (2010). Targeting the cancer kinome through polypharmacology. Nat Rev Cancer 10, 130–137.

Kolokoltsov, A.A., Saeed, M.F., Freiberg, A.N., Holbrook, M.R., and Davey, R.A. (2009). Identification of novel cellular targets for therapeutic intervention against Ebola virus infection by siRNA screening. Drug Dev Res 70, 255–265.

Kumar, R., Agrawal, T., Khan, N.A., Nakayama, Y., and Medigeshi, G.R. (2016). Identification and characterization of the role of c-terminal Src kinase in dengue virus replication. Sci Rep 6, 30490.

Langhammer, S., Koban, R., Yue, C., and Ellerbrok, H. (2011). Inhibition of poxvirus spreading by the anti-tumor drug Gefitinib (Iressa). Antiviral Res 89, 64–70.

Li, J., Li, H., and Tsai, M.D. (2003). Direct binding of the N-terminus of HTLV-1 tax oncoprotein to cyclin-dependent kinase 4 is a dominant path to stimulate the kinase activity. Biochemistry 42, 6921–6928.

Li, Q., Brass, A., Ng, A., Hu, Z., Xavier, R., Liang, T.J., and Elledge, S. (2009). A genome-wide genetic screen for host factors required for hepatitis C virus propagation. Proc Natl Acad Sci U S A 106, 16410–16415.

Li, Q., Pene, V., Krishnamurthy, S., Cha, H., and Liang, T.J. (2013). Hepatitis C virus infection activates an innate pathway involving IKK-alpha in lipogenesis and viral assembly. Nat Med 19, 722–729.

Liacini, A., Seamone, M.E., Muruve, D.A., and Tibbles, L.A. (2010). Anti-BK virus mechanisms of sirolimus and leflunomide alone and in combination: toward a new therapy for BK virus infection. Transplantation 90, 1450–1457.

Lupberger, J., Zeisel, M., Xiao, F., Thumann, C., Fofana, I., Zona, L., Davis, C., Mee, C., Turek, M., Gorke, S., et al. (2011). EGFR and EphA2 are host factors for hepatitis C virus entry and possible targets for antiviral therapy. Nat Med 17, 589–595.

Mannová, P., and Beretta, L. (2005). Activation of the N-Ras–PI3K–Akt-mTOR pathway by hepatitis C virus: control of cell survival and viral replication. J Virol 79, 8742–8749.

Narute, P.S., and Smithgall, T.E. (2012). Nef alleles from all major HIV-1 clades activate Src-family kinases and enhance HIV-1 replication in an inhibitor-sensitive manner. PLoS One 7, e32561.

Nemeth, G., Varga, Z., Greff, Z., Bencze, G., Sipos, A., Szantai-Kis, C., Baska, F., Gyuris, A., Kelemenics, K., Szathmary, Z., et al. (2011). Novel, selective CDK9 inhibitors for the treatment of HIV infection. Curr Med Chem 18, 342–358.

Neveu, G., Barouch-Bentov, R., Ziv-Av, A., Gerber, D., Jacob, Y., and Einav, S. (2012). Identification and targeting of an interaction between a tyrosine motif within hepatitis C virus core protein and AP2M1 essential for viral assembly. PLoS Pathog 8, e1002845.

Neveu, G., Ziv-Av, A., Barouch-Bentov, R., Berkerman, E., Mulholland, J., and Einav, S. (2015). AP-2-associated protein kinase 1 and cyclin G-associated kinase regulate hepatitis C virus entry and are potential drug targets. J Virol 89, 4387–4404.

Ott, P.A., and Adams, S. (2011). Small-molecule protein kinase inhibitors and their effects on the immune system: implications for cancer treatment. Immunotherapy 3, 213–227.

Pagano, M.A., Tibaldi, E., Palu, G., and Brunati, A.M. (2013). Viral proteins and Src family kinases: mechanisms of pathogenicity from a ''liaison dangereuse.'' World J Virol 2, 71–78.

Pauls, E., Badia, R., Torres-Torronteras, J., Ruiz, A., Permanyer, M., Riveira-Munoz, E., Clotet, B., Marti, R., Ballana, E., and Este, J.A. (2014a). Palbociclib, a selective inhibitor of cyclin-dependent kinase4/6, blocks HIV-1 reverse transcription through the control of sterile alpha motif and HD domain-containing protein-1 (SAMHD1) activity. AIDS (London, England) 28, 2213–2222.

Pauls, E., Ruiz, A., Badia, R., Permanyer, M., Gubern, A., Riveira-Munoz, E., Torres-Torronteras, J., Alvarez, M., Mothe, B., Brander, C., et al. (2014b). Cell cycle control and HIV-1 susceptibility are linked by CDK6-dependent CDK2 phosphorylation of SAMHD1 in myeloid and lymphoid cells. J Immunol 193, 1988–1997.

Perwitasari, O., Yan, X., O'Donnell, J., Johnson, S., and Tripp, R.A. (2015). Repurposing kinase inhibitors as antiviral agents to control influenza A virus replication. Assay Drug Dev Technol 13, 638–649.

Pleschka, S., Wolff, T., Ehrhardt, C., Hobom, G., Planz, O., Rapp, U.R., and Ludwig, S. (2001). Influenza virus propagation is impaired by inhibition of the Raf/MEK/ERK signalling cascade. Nat Cell Biol 3, 301–305.

Reeves, P.M., Smith, S.K., Olson, V.A., Thorne, S.H., Bornmann, W., Damon, I.K., and Kalman, D. (2011). Variola and monkeypox viruses utilize conserved mechanisms of virion motility and release that depend on abl and SRC family tyrosine kinases. J Virol 85, 21–31.

Schang, L.M. (2003). The cell cycle, cyclin-dependent kinases, and viral infections: new horizons and unexpected connections. Prog Cell Cycle Res 5, 103–124.

Schang, L.M., St. Vincent, M.R., and Lacasse, J.J. (2006). Five years of progress on cyclin-dependent kinases and other cellular proteins as potential targets for antiviral drugs. Antiviral Chem Chemother 17, 293–320.

Schleiss, M., Eickhoff, J., Auerochs, S., Leis, M., Abele, S., Rechter, S., Choi, Y., Anderson, J., Scott, G., Rawlinson, W., et al. (2008). Protein kinase inhibitors of the quinazoline class exert anti-cytomegaloviral activity in vitro and in vivo. Antiviral Res 79, 49–61.

Shives, K.D., Beatman, E.L., Chamanian, M., O'Brien, C., Hobson-Peters, J., and Beckham, J.D. (2014). West nile virus-induced activation of mammalian target of rapamycin complex 1 supports viral growth and viral protein expression. J Virol 88, 9458–9471.

Supekova, L., Supek, F., Lee, J., Chen, S., Gray, N., Pezacki, J.P., Schlapbach, A., and Schultz, P.G. (2008). Identification of human kinases involved in hepatitis C virus replication by small interference RNA library screening. J Biol Chem 283, 29–36.

Swimm, A.I., Bornmann, W., Jiang, M., Imperiale, M.J., Lukacher, A.E., and Kalman, D. (2010). Abl family tyrosine kinases regulate sialylated ganglioside receptors for polyomavirus. J Virol 84, 4243–4251.

Tufts Center for the Study of Drug Development. (2014). Cost to develop and win 279 marketing approval for a new drug is $2.6 billion. [online] Available at: http://csdd.tufts.edu/news/complete_story/pr_tufts_csdd_2014_cost_study (accessed October 10, 2017).

Ueki, I.F., Min-Oo, G., Kalinowski, A., Ballon-Landa, E., Lanier, L.L., Nadel, J.A., and Koff, J.L. (2013). Respiratory virus–induced EGFR activation suppresses IRF1-dependent interferon ‖ and antiviral defense in airway epithelium. J Exp Med 210, 1929–1936.

Waldman, W.J., Knight, D.A., Blinder, L., Shen, J., Lurain, N.S., Miller, D.M., Sedmak, D.D., Williams, J.W., and Chong, A.S. (1999). Inhibition of cytomegalovirus in vitro and in vivo by the experimental immunosuppressive agent leflunomide. Intervirology 42, 412–418.

Wang, X., Huang, D.Y., Huong, S.-M., and Huang, E.-S. (2005). Integrin avb3 is a Coreceptor for Human Cytomegalovirus Infection. Nat Med 11, 515–521.

Wang, X., Huong, S.-M., Chiu, M.L., Raab-Traub, N., and Huang, E.-S. (2003). Epidermal growth factor receptor is a cellular receptor for human cytomegalovirus. Nature 424, 456–461.

Weller, M.L., Amornphimoltham, P., Schmidt, M., Wilson, P.A., Gutkind, J.S., and Chiorini, J.A. (2010). Epidermal growth factor receptor is a co-receptor for adeno-associated virus serotype 6. Nat Med 16, 662–664.

Williams, J.W., Javaid, B., Kadambi, P.V., Gillen, D., Harland, R., Thistlewaite, J.R., Garfinkel, M., Foster, P., Atwood, W., Millis, J.M., et al. (2005). Leflunomide for polyomavirus type BK nephropathy. N Engl J Med 352, 1157–1158.

Xu, M., Lee, E.M., Wen, Z., Cheng, Y., Huang, W.-K., Qian, X., Tcw, J., Kouznetsova, J., Ogden, S.C., Hammack, C., et al. (2016). Identification of small-molecule inhibitors of Zika virus infection and induced neural cell death via a drug repurposing screen. Nat Med 22, 1101–1107.

Yamamoto, M., Onogi, H., Kii, I., Yoshida, S., Iida, K., Sakai, H., Abe, M., Tsubota, T., Ito, N., Hosoya, T., et al. (2014). CDK9 inhibitor FIT-039 prevents replication of multiple DNA viruses. J Clin Invest 124, 3479–3488.

Yang, X., and Gabuzda, D. (1999). Regulation of human immunodeficiency virus type 1 infectivity by the ERK mitogen-activated protein kinase signaling pathway. J Virol 73, 3460–3466.

Zampieri, C.A., Fortin, J.-F., Nolan, G.P., and Nabel, G.J. (2007). The ERK Mitogen-activated protein kinase pathway contributes to Ebola virus glycoprotein-induced cytotoxicity. J Virol 81, 1230–1240.

Zheng, K., Kitazato, K., and Wang, Y. (2014). Viruses exploit the function of epidermal growth factor receptor. Rev Med Virol 24, 274–286.

Zona, L., Lupberger, J., Sidahmed-Adrar, N., Thumann, C., Harris, Helen J., Barnes, A., Florentin, J., Tawar, Rajiv G., Xiao, F., Turek, M., et al. (2013). HRas signal transduction promotes hepatitis C virus cell entry by triggering assembly of the host tetraspanin receptor complex. Cell Host Microbe 13, 302–313.

Address correspondence to:
Shirit Einav, MD
Department of Microbiology and Immunology
Stanford University School of Medicine
Stanford, CA 94305-5119

E-mail: seinav@stanford.edu

Combating Intracellular Pathogens with Repurposed Host-Targeted Drugs

Stanford Schor and Shirit Einav*

Department of Medicine, Division of Infectious Diseases and Geographic Medicine, and Department of Microbiology and Immunology, School of Medicine, Stanford University, 300 Pasteur Drive, Lane Building Rm L127, Stanford, California 94305, United States

ABSTRACT: There is a large, global unmet need for the development of countermeasures to combat intracellular pathogens. The development of novel antimicrobials is expensive and slow and typically focuses on selective inhibition of proteins encoded by a single pathogen, thereby providing a narrow spectrum of coverage. The repurposing of approved drugs targeting host functions required for microbial infections represents a promising alternative. This review summarizes progress and challenges in the repurposing of approved drugs as host-targeted broad-spectrum agents for the treatment of intracellular pathogens. These strategies include targeting both cellular factors required for infection by various viruses, intracellular bacteria, and/or protozoa as well as factors that modulate the host immune response to these microbial infections. The repurposed approach offers complementary means to develop therapeutics against existing and emerging intracellular microbial threats.

There is an urgent need for new strategies to combat hundreds of human disease-causing intracellular pathogens, including viruses, intracellular bacteria, and protozoa. Currently approved antiviral drugs treat fewer than ten viral infections. While antibacterial agents are more widely available, only a minority of them penetrate mammalian cells and achieve a therapeutic level in the appropriate intracellular compartment to treat intracellular bacterial infections.[1] The narrow spectrum of coverage of most antimicrobials that target microbial functions, particularly viruses, is another major limitation. Given the high average cost (over two billion dollars) and long timeline (8−12 years) to develop a new drug, the scalability of targeting microbes individually is limited. Lastly, resistance typically emerges rapidly when conventional drugs that target microbial functions are used as monotherapy.

An attractive solution to overcome these limitations is to repurpose already approved drugs that target host functions required for the lifecycle of intracellular pathogens as antimicrobial agents (Figure 1). Off-label use of approved drugs requires significantly less capital and time and diminishes the clinical risks, because such drugs were already rigorously tested (toxicity, pharmacokinetics, pharmacodynamics dosing, etc.) for their primary indication. Since some host functions are hijacked by various viruses, intracellular bacteria, and/or protozoa, they may represent targets for broad-spectrum antimicrobials. This approach can therefore increase the efficiency of antimicrobial development, improve drug access for patients, and facilitate readiness for future outbreaks of emerging pathogens. Additionally, host-targeted approaches may have the added benefit of a higher genetic barrier to the emergence of resistance.

One promising drug category for repurposing as antimicrobials is inhibitors of host kinases, such as those widely approved for the treatment of cancer and inflammatory conditions.[2] A large number of host kinases are co-opted by intracellular pathogens and thus represent attractive targets for broad-spectrum antimicrobial therapy.[3] Indeed, recent efforts have demonstrated the therapeutic potential of kinase inhibitors to combat various intracellular microbial infections. The anticancer epidermal growth factor receptor (EGFR) and/or ERBB2 kinase inhibitors gefitinib, erlotinib, and lapatinib demonstrate *in vitro* activity against a number of viruses including hepatitis C virus (HCV), human cytomegalovirus (HCMV), and poxvirus.[4,5] Gefitinib and lapatinib also inhibit HCV and HCMV infections in a mouse and guinea pig model, respectively,[4,5] and reduce replication of *Mycobacterium tuberculosis* (Mtb) in the lungs of infected mice.[6] The antiviral effect of these drugs is mediated in part by inhibition of signaling in the entry stage and/or in F-actin-mediated intracellular viral trafficking.[7,8] Enhanced antimicrobial immune effect via inhibition of EGFR/p38 mitogen associated protein kinase signaling plays a role in their anti-Mtb activity.[6]

Another class of approved kinase inhibitors demonstrating a broad antimicrobial coverage is the cellular Abelson tyrosine kinase (c-Abl) inhibitors, such as imatinib and nilotinib. These drugs inhibit replication of Ebola virus (EBOV), dengue virus (DENV), Middle Eastern respiratory syndrome coronavirus (MERS-CoV), and severe acute respiratory syndrome coronavirus (SARS-CoV) in cultured cells and reduce vaccinia virus load, spread, and overall mortality in a mouse model.[9−12] Moreover, imatinib treatment impairs entry and intracellular survival of Mtb and *Mycobacterium marinum* in infected macrophages and reduces the bacterial load and associated pathologies in mice infected with antibiotic-sensitive or resistant Mtb.[13] Notably, when coadministered with rifamycins, imatinib displays synergy, indicating its potential utility in combination anti-Mtb drug regimens.[13]

underlying the antimicrobial effect of c-Abl inhibitors remain to be validated. Moreover, while inhibition of actin motility is proposed as a mechanism of antiviral action of these drugs,[12]
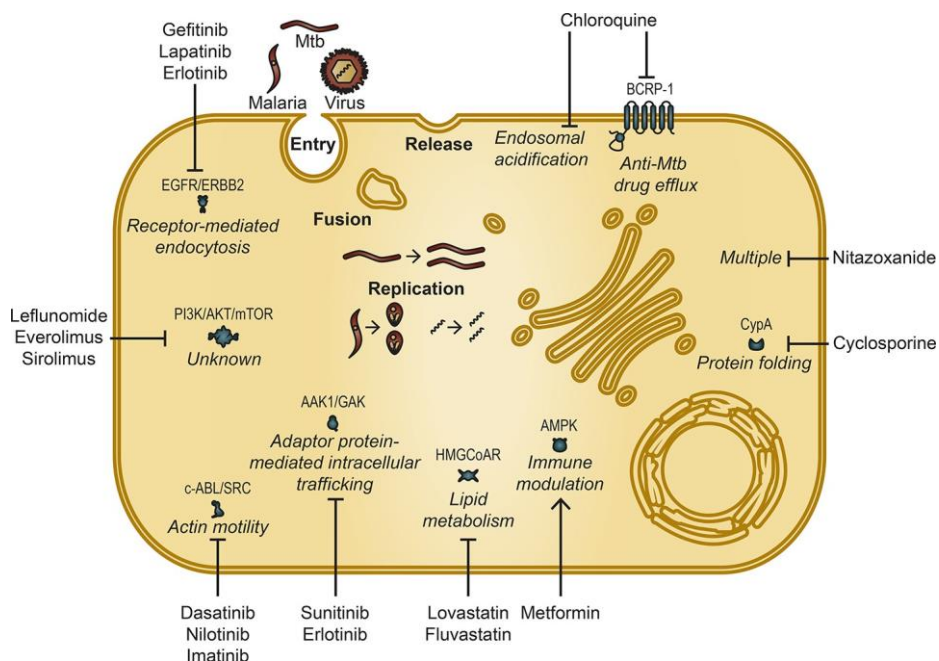
Figure 1. Approved host-targeted drugs can be repurposed as countermeasures against intracellular pathogens including viruses, intracellular bacteria such as Mtb, and protozoa such as malaria. Depicted are representative stages of the intracellular pathogen lifecycle that are often targeted by antimicrobials. Shown are examples of repurposed drugs and the relevant corresponding pathway and target protein(s), if known. Only targets that are validated as either antimicrobial and/or molecular targets underlying the antimicrobial effect are shown. CypA (Cyclophilin A). Blunt arrows represent inhibition, whereas pointed arrow represents activation.

the precise mechanism and mode of antibacterial action remain unknown.

The approved anticancer drugs sunitinib and erlotinib display potent activity against viruses from six viral families, including DENV and EBOV in cultured cells.[14] Combinations of these drugs reduce morbidity and mortality of dengue and Ebola infected mice and are advancing into clinical studies for dengue and possibly Ebola in future outbreaks (https://clinicaltrials.gov/ NCT02380625).[14] Inhibition of the cellular kinases adaptor protein 2 (AP2)-associated protein kinase 1 (AAK1) and cyclin G-associated kinase (GAK), regulators of adaptor protein-mediated intracellular viral trafficking, is an important mechanism of action (MOA) of this antiviral approach.[14]

Three approved immunosuppressive drugs that inhibit the phosphatidylinositol 3′-kinase–Akt–mammalian target of rapamycin (PI3K/AKT/mTOR) pathway, leflunomide, everolimus, and sirolimus, reduce viremia and nephropathy progression in patients infected with BK virus, a member of the polyomavirus family, when used individually or in combination.[15] Additionally, leflunomide demonstrates activity against HCMV both in vitro and in a rat model.[16] While direct suppression of viral replication is proposed as one underlying mechanism of this approach, the precise MOA and molecular targets remain unknown.

Inhibitors of cyclophilin, a host factor that facilitates protein folding, represent another class of drugs, beyond kinase inhibitors, that shows promise as antimicrobials. Cyclosporine, an immunosuppressant cyclophilin inhibitor, disrupts replication of multiple viruses, including HCV, DENV, other flaviviruses, and human immunodeficiency virus (HIV) in vitro.[17,18] Two experimental, nonimmunosuppressive cyclophilin inhibitors, alisporivir and SCY-635, also inhibit multiple RNA viruses in cultured cells, yet their effect in mouse models

is variable.[19] Alisporivir significantly reduced HCV viral load in chronically infected patients;[19] however, a clinical hold was placed on the Phase III trial due to toxicity. Cyclosporine also inhibits the erythrocytic stages of Plasmodium falciparum in vitro and rodent malaria in a mouse model.[20] Nevertheless, it remains unknown whether this effect results in part from inhibition of the host cyclophilin or solely the parasitic protein.

Another candidate for repurposing is nitazoxanide, a drug approved for the treatment of parasite-induced diarrhea. It inhibits replication of multiple viruses including HCV, flaviviruses, respiratory viruses, HIV, and hepatitis B virus (HBV) in cultured cells.[21] Nitazoxanide blocks maturation of the influenza hemagglutinin, but the target remains unknown. In the case of HCV, it is thought to activate protein kinase R leading to phosphorylation of eukaryotic initiation factor 2α, which then blocks viral replication.[21] In a phase II trial, nitazoxanide modestly reduced the time to resolution of symptoms of flu and is currently being evaluated in a phase III trial for this indication.[22] Whereas addition of nitazoxanide to peginterferon-ribavirin improved the sustained virologic response in HCV patients in a phase II trial, no such improvement was observed in a phase III trial in genotype 4 infected patients.[23] Additionally, nitazoxanide is effective against clinical Mtb isolates, including those that are resistant to standard antituberculosis drugs.[24] Disruption of membrane potential and pH homeostasis in Mtb is one proposed MOA.[24] A phase II clinical trial is currently ongoing to determine the efficacy of 14-day nitazoxanide treatment prior to initiation of standard antituberculosis therapy.

Metformin, a drug approved for the treatment of type 2 diabetes, inhibits the intracellular growth of Mtb (including drug resistant strains) and enhances the efficacy of approved anti-Mtb drugs in cell culture.[25] In a murine model, metformin mildly reduces Mtb load in target organs and improves lung

180

pathology when used individually or in combination drug treatment.[25] Notably, metformin demonstrated efficacy in decreasing disease severity and improving clinical outcome as an adjunct therapy in retrospective cohorts of tuberculosis patients with diabetes and also reduced the incidence of latent tuberculosis in diabetic patients.[25] Activation of the adenosine monophosphate−activated protein kinase (AMPK), which regulates cellular immune functions, is involved in mediating the antibacterial effect.[25] Beyond tuberculosis, a clinical study that aims to evaluate the size of HIV reservoirs upon addition of metformin to antiretroviral regimens is currently ongoing.

Statins, drugs that inhibit 3-hydroxy-3-methylglutaryl coenzyme A reductase (HMG-CoAR), represent another potential class for repurposing as host-targeted antimicrobials. Various statins inhibit replication of HCV and DENV *in vitro*.[26,27] Nevertheless, while several retrospective studies demonstrated that statins reduce relapse rates in patients infected with HCV when added to peginterferon-ribavirin, this effect was quite variable.[27] The mechanism of anti-HCV action of statins is mediated in part by their effect on lipid biosynthesis, as their antiviral activity in cells is reversed upon addition of mevalonate or geranylgeraniol, and resistance to these drugs coincides with an increase in HMG-CoAR level.[27] Due to their ability to restore endothelial stability, statins were also proposed as a strategy to treat infections associated with endothelial dysfunction. While no formal study has been conducted, it was reported that atorvastatin in combination with an angiotensin receptor blocker reduced mortality in 100 Ebola patients in Sierra Leone.[28]

The antimalarial and anti-inflammatory drug chloroquine also shows some promise as an antimicrobial agent. In a nonhuman primate dengue model, chloroquine reduces viremia, cytokine production, and organ damage.[29] However, when studied in dengue patients, it reduced pain and improved daily activity performance, yet it did not reduce disease duration or viremia.[30,31] In mice infected with Zika virus, chloroquine increases the life span and reduces vertical transmission and fetal brain infection.[32] Moreover, it reduces acute lung injury, morbidity, and mortality in a mouse model of avian influenza A H5N1.[33] The mechanism of antiviral activity of chloroquine is multifaceted and thought to involve alterations in the intracellular pH causing impaired fusion and cleavage of the prM protein during flaviviral release and/or inhibition of autophagy.[32,33] Chloroquine may also show utility as an add-on to antituberculosis regimens, as it enhances the intracellular killing of Mtb in human macrophages by inhibiting the BCRP-1 (breast cancer resistance protein-1)-mediated active efflux of the antituberculosis drugs isoniazid and pyrazinamide.[34]

Collectively, these data provide a proof-of-concept for the useful expansion of antimicrobial drug targets by focusing on host functions and for the therapeutic potential of repurposed drugs targeting these functions to combat intracellular pathogens. Further benefit is provided by the higher genetic barrier to resistance associated with many of these host-targeted approaches. Whereas emergence of resistance can complicate treatment with host-targeted approaches, as in the case of the chemokine receptor 5 antagonist maraviroc,[35] the time to resistance with other host-targeted approaches is longer and the level of resistance is lower relative to typical direct-acting antimicrobials monotherapy. This is exemplified by treatment of DENV with sunitinib/erlotinib combinations, Mtb with nitazoxanide, and HCV with cyclophilin inhib-

itors.[14,19,24] Targeting host proteins that are not under the genetic control of microbes and simultaneously inhibiting several host targets with the same drug or drug combination are thought to facilitate this increase in the resistance barrier of these approaches.

Nevertheless, repurposing of host-targeted drugs as antimicrobials faces its own challenges. Cellular proteins function in a complex network of interactions, and their inhibitors are often nonselective. Thus, the mechanism of antimicrobial action of host-targeted approaches often remains elusive, and the molecular targets underlying this effect are unvalidated. For example, erlotinib's effect on HCV infection was first attributed solely to its effect on EGFR, its cancer target, yet it was later demonstrated that inhibition of GAK, another target that is inhibited by erlotinib with a comparable potency to EGFR, also plays a role.[8,14] For other drugs, such as nitazoxanide and chloroquine, the MOA is even less clear and appears to be pathogen specific.[21,24,32−34]

Another challenge is that the antimicrobial effect observed *in vitro* often cannot be reproduced *in vivo*. For example, several multi kinase inhibitors, such as lestaurtinib, display *in vitro* activity against *Plasmodium falciparum* but no significant effect in malaria-infected mice.[36] Moreover, as exemplified by chloroquine for dengue treatment, a promising effect in animal models cannot guarantee an effect in patients.[29−31] Toxicity is another major concern. The Src- and c-Abl-inhibitor dasatinib demonstrates broad-spectrum antiviral activity in cultured cells, yet in a murine model of vaccinia virus, it induces immunosuppression rather than protection.[12,37] It is thus important to investigate the antimicrobial activity and safety of these drugs in animal models of other infections. Nevertheless, for some drugs, it may be feasible to find a therapeutic window where the drug level is sufficient to inhibit microbial replication with minimal cellular toxicity. Shifting from indications requiring long-term therapy (e.g., months to years for cancer) to a shorter duration sufficient to treat most acute infections should help limit toxicity. In contrast, the utility of some of these approaches for treating chronic infections requiring longer duration treatment may be more limited. This is exemplified by the unexpected occurrence of pancreatitis during the Phase III trial with alisporivir in chronically infected HCV patients. Nevertheless, drugs that are extensively used in humans, such as metformin and chloroquine, are more likely to be safe add-ons to standard regimens even for chronic infections.

In summary, these examples provide a proof-of-concept for the potential feasibility of repurposing approved drugs as host-targeted broad-spectrum therapies to combat intracellular microbial pathogens. To effectively meet the clinical needs posed by emerging intracellular pathogens, such approaches may find utility in combination with novel host-targeted approaches and microbial-targeted strategies.

■ AUTHOR INFORMATION

Corresponding Author
*E-mail: seinav@stanford.edu.
Notes
The authors declare no competing financial interest.

161

can Cancer Society (RSG-14-11 0-01-MPC), Stanford Bio-X, and Stanford SPARK program to S.E. The authors acknowledge all the contributions in the field that could not be included in the review.

■ REFERENCES

(1) McOrist, S. (2000) Obligate intracellular bacteria and antibiotic resistance. *Trends Microbiol. 8*, 483–486.

(2) Gross, S., Rahal, R., Stransky, N., Lengauer, C., and Hoeflich, K. P. (2015) Targeting cancer with kinase inhibitors. *J. Clin. Invest. 125*, 1780–1789.

(3) Keating, J. A., and Striker, R. (2012) Phosphorylation events during viral infections provide potential therapeutic targets. *Rev. Med. Virol. 22*, 166–181.

(4) Langhammer, S., Koban, R., Yue, C., and Ellerbrok, H. (2011) Inhibition of poxvirus spreading by the anti-tumor drug Gefitinib (Iressa). *Antiviral Res. 89*, 64–70.

(5) Schleiss, M., Eickhoff, J., Auerochs, S., Leis, M., Abele, S., Rechter, S., Choi, Y., Anderson, J., Scott, G., Rawlinson, W., Michel, D., Ensminger, S., Klebl, B., Stamminger, T., and Marschall, M. (2008) Protein kinase inhibitors of the quinazoline class exert anti-cytomegaloviral activity in vitro and in vivo. *Antiviral Res. 79*, 49–61.

(6) Stanley, S. A., Barczak, A. K., Silvis, M. R., Luo, S. S., Sogi, K., Vokes, M., Bray, M. A., Carpenter, A. E., Moore, C. B., Siddiqi, N., Rubin, E. J., and Hung, D. T. (2014) Identification of host-targeted small molecules that restrict intracellular Mycobacterium tuberculosis growth. *PLoS Pathog. 10*, e1003946.

(7) Wang, X., Huong, S. M., Chiu, M. L., Raab-Traub, N., and Huang, E. S. (2003) Epidermal growth factor receptor is a cellular receptor for human cytomegalovirus. *Nature 424*, 456–461.

(8) Lupberger, J., Zeisel, M., Xiao, F., Thumann, C., Fofana, I., Zona, L., Davis, C., Mee, C., Turek, M., Gorke, S., Royer, C., Fischer, B., Zahid, M., Lavillette, D., Fresquet, J., Cosset, F.-L., Rothenberg, S. M., Pietschmann, T., Patel, A., Pessaux, P., Doffol, M., Raffelsberger, W., Poch, O., McKeating, J., Brino, L., and Baumert, T. (2011) EGFR and EphA2 are host factors for hepatitis C virus entry and possible targets for antiviral therapy. *Nat. Med. 17*, 589–595.

(9) Garcia, M., Cooper, A., Shi, W., Bornmann, W., Carrion, R., Kalman, D., and Nabel, G. J. (2012) Productive replication of Ebola virus is regulated by the c-Abl1 tyrosine kinase. *Sci. Transl. Med. 4*, 123ra24.

(10) Dyall, J., Coleman, C. M., Hart, B. J., Venkataraman, T., Holbrook, M. R., Kindrachuk, J., Johnson, R. F., Olinger, G. G., Jahrling, P. B., Laidlaw, M., Johansen, L. M., Lear-Rooney, C. M., Glass, P. J., Hensley, L. E., and Frieman, M. B. (2014) Repurposing of clinically developed drugs for treatment of Middle East respiratory syndrome coronavirus infection. *Antimicrob. Agents Chemother. 58*, 4885–4893.

(11) Clark, M. J., Miduturu, C., Schmidt, A. G., Zhu, X., Pitts, J. D., Wang, J., Potisopon, S., Zhang, J., Wojciechowski, A., Hann Chu, J. J., Gray, N. S., and Yang, P. L. (2016) GNF-2 Inhibits Dengue Virus by Targeting Abl Kinases and the Viral E Protein. *Cell Chem. Biol. 23*, 443–452.

(12) Reeves, P. M., Smith, S. K., Olson, V. A., Thorne, S. H., Bornmann, W., Damon, I. K., and Kalman, D. (2011) Variola and monkeypox viruses utilize conserved mechanisms of virion motility and release that depend on abl and SRC family tyrosine kinases. *J. Virol 85*, 21–31.

(13) Napier, R. J., Rafi, W., Cheruvu, M., Powell, K. R., Zaunbrecher, M. A., Bornmann, W., Salgame, P., Shinnick, T. M., and Kalman, D. (2011) Imatinib-sensitive tyrosine kinases regulate mycobacterial pathogenesis and represent therapeutic targets against tuberculosis. *Cell Host Microbe 10*, 475–485.

(14) Bekerman, E., Neveu, G., Shulla, A., Brannan, J., Pu, S.-Y., Wang, S., Xiao, F., Barouch-Bentov, R., Bakken, R. R., Mateo, R., Govero, J., Nagamine, C. M., Diamond, M. S., De Jonghe, S., Herdewijn, P., Dye, J. M., Randall, G., and Einav, S. (2017) Anticancer kinase inhibitors impair intracellular viral trafficking and exert broad-spectrum antiviral effects. *J. Clin. Invest. 127*, 1338.

(15) Williams, J. W., Javaid, B., Kadambi, P. V., Gillen, D., Harland, R., Thistlewaite, J. R., Garfinkel, M., Foster, P., Atwood, W., Millis, J. M., Meehan, S. M., and Josephson, M. A. (2005) Leflunomide for polyomavirus type BK nephropathy. *N. Engl. J. Med. 352*, 1157–1158.

(16) Waldman, W. J., Knight, D. A., Blinder, L., Shen, J., Lurain, N. S., Miller, D. M., Sedmak, D. D., Williams, J. W., and Chong, A. S. (2000) Inhibition of cytomegalovirus in vitro and in vivo by the experimental immunosuppressive agent leflunomide. *Intervirology 42*, 412–418.

(17) Qing, M., Yang, F., Zhang, B., Zou, G., Robida, J. M., Yuan, Z., Tang, H., and Shi, P. Y. (2009) Cyclosporine inhibits flavivirus replication through blocking the interaction between host cyclophilins and viral NS5 protein. *Antimicrob. Agents Chemother. 53*, 3226–3235.

(18) Billich, A., Hammerschmid, F., Peichl, P., Wenger, R., Zenke, G., Quesniaux, V., and Rosenwirth, B. (1995) Mode of action of SDZ NIM 811, a nonimmunosuppressive cyclosporin A analog with activity against human immunodeficiency virus (HIV) type 1: interference with HIV protein-cyclophilin A interactions. *J. Virol 69*, 2451–2461.

(19) Lin, K., and Gallay, P. (2013) Curing a viral infection by targeting the host: the example of cyclophilin inhibitors. *Antiviral Res. 99*, 68–77.

(20) Murphy, J. R., Baqar, S., Baker, R. H., Roberts, E., Nickell, S. P., and Cole, G. A. (1988) Stage-selective inhibition of rodent malaria by cyclosporine. *Antimicrob. Agents Chemother. 32*, 462–466.

(21) Rossignol, J. F. (2014) Nitazoxanide: a first-in-class broad-spectrum antiviral agent. *Antiviral Res. 110*, 94–103.

(22) Haffizulla, J., Hartman, A., Hoppers, M., Resnick, H., Samudrala, S., Ginocchio, C., Bardin, M., Rossignol, J. F., and US Nitazoxanide Influenza Clinical Study Group (2014) Effect of nitazoxanide in adults and adolescents with acute uncomplicated influenza: a double-blind, randomised, placebo-controlled, phase 2b/3 trial. *Lancet Infect. Dis. 14*, 609–618.

(23) Kohla, M. A., El-Said, H., El-Fert, A., Ehsan, N., Ezzat, S., and Taha, H. (2016) Impact of nitazoxanide on sustained virologic response in Egyptian patients with chronic hepatitis C genotype 4: a double-blind placebo-controlled trial. *Eur. J. Gastroenterol. Hepatol. 28*, 42–47.

(24) Shigyo, K., Ocheretina, O., Merveille, Y. M., Johnson, W. D., Pape, J. W., Nathan, C. F., and Fitzgerald, D. W. (2013) Efficacy of nitazoxanide against clinical isolates of Mycobacterium tuberculosis. *Antimicrob. Agents Chemother. 57*, 2834–2837.

(25) Singhal, A., Jie, L., Kumar, P., Hong, G. S., Leow, M. K.-S., Paleja, B., Tsenova, L., Kurepina, N., Chen, J., Zolezzi, F., Kreiswirth, B., Poidinger, M., Chee, C., Kaplan, G., Wang, Y. T., and De Libero, G. (2014) Metformin as adjunct antituberculosis therapy. *Sci. Transl. Med. 6*, 263ra159–263ra160.

(26) Rothwell, C., Lebreton, A., Young Ng, C., Lim, J. Y., Liu, W., Vasudevan, S., Labow, M., Gu, F., and Gaither, L. A. (2009) Cholesterol biosynthesis modulation regulates dengue viral replication. *Virology 389*, 8–19.

(27) Simon, T. G., and Butt, A. A. (2015) Lipid dysregulation in hepatitis C virus, and impact of statin therapy upon clinical outcomes. *World J. Gastroenterol 21*, 8293–8303.

(28) Fedson, D. S., Jacobson, J. R., Rordam, O. M., and Opal, S. M. (2015) Treating the Host Response to Ebola Virus Disease with Generic Statins and Angiotensin Receptor Blockers. *mBio 6*, e00716-15.

(29) Farias, K. J., Machado, P. R., Muniz, J. A., Imbeloni, A. A., and da Fonseca, B. A. (2015) Antiviral activity of chloroquine against dengue virus type 2 replication in Aotus monkeys. *Viral Immunol. 28*, 161–169.

(30) Borges, M. C., Castro, L. A., and da Fonseca, B. A. L. (2013) Chloroquine use improves dengue-related symptoms. *Memorias do Instituto Oswaldo Cruz 108*, 596–599.

(31) Tricou, V., Minh, N. N., Van, T. P., Lee, S. J., Farrar, J., Wills, B., Tran, H. T., and Simmons, C. P. (2010) A Randomized

102

Controlled Trial of Chloroquine for the Treatment of Dengue in Vietnamese Adults. *PLoS Neglected Trop. Dis. 4*, e785.

(32) Shiryaev, S. A., Mesci, P., Pinto, A., Fernandes, I., Sheets, N., Shresta, S., Farhy, C., Huang, C.-T., Strongin, A. Y., Muotri, A. R., and Terskikh, A. V. (2017) Repurposing of the anti-malaria drug chloroquine for Zika Virus treatment and prophylaxis. *Sci. Rep. 7*, 15771.

(33) Yan, Y., Zou, Z., Sun, Y., Li, X., Xu, K. F., Wei, Y., Jin, N., and Jiang, C. (2013) Anti-malaria drug chloroquine is highly effective in treating avian influenza A H5N1 virus infection in an animal model. *Cell Res. 23*, 300–302.

(34) Matt, U., Selchow, P., Dal Molin, M., Strommer, S., Sharif, O., Schilcher, K., Andreoni, F., Stenzinger, A., Zinkernagel, A. S., Zeitlinger, M., Sander, P., and Nemeth, J. (2017) Chloroquine enhances the antimycobacterial activity of isoniazid and pyrazinamide by reversing inflammation-induced macrophage efflux. *Int. J. Antimicrob. Agents 50*, 55–62.

(35) Haqqani, A. A., and Tilton, J. C. (2013) Entry inhibitors and their use in the treatment of HIV-1 infection. *Antiviral Res. 98*, 158–170.

(36) Lotharius, J., Gamo-Benito, F. J., Angulo-Barturen, I., Clark, J., Connelly, M., Ferrer-Bazaga, S., Parkinson, T., Viswanath, P., Bandodkar, B., Rautela, N., Bharath, S., Duffy, S., Avery, V. M., Mohrle, J. J., Guy, R. K., and Wells, T. (2014) Repositioning: the fast track to new anti-malarial medicines? *Malar. J. 13*, 143.

(37) de Wispelaere, M., LaCroix, A. J., and Yang, P. L. (2013) The small molecules AZD0530 and dasatinib inhibit dengue virus RNA replication via Fyn kinase,. *J. Virol 87*, 7367–7381.

Old Drugs for a New Virus: Repurposed Approaches for Combating COVID-19
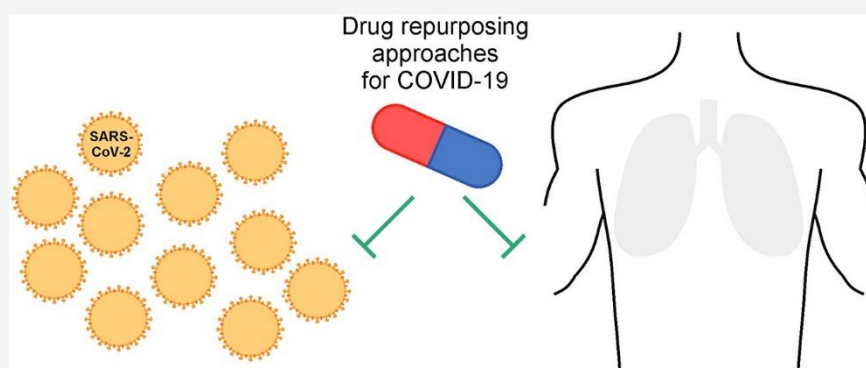
Sirle Saul and Shirit Einav*

Cite This: https://dx.doi.org/10.1021/acsinfecdis.0c00343

Read Online

ACCESS | Metrics & More | Article Recommendations

ABSTRACT: There is a large global unmet need for effective countermeasures to combat severe acute respiratory syndrome coronavirus 2 (SARS-CoV-2), the causative agent of coronavirus disease 2019 (COVID-19). The development of novel antiviral drugs is expensive and too slow to meet the immediate need. The repurposing of drugs that are approved or are under advanced clinical investigation provides a cost- and time-effective therapeutic solution. This review summarizes the major repurposed approaches that have been proposed or are already being studied in clinical trials for COVID-19. Among these approaches are drugs that aim to reduce SARS-CoV-2 replication by targeting either viral enzymatic functions or cellular factors required for the viral life cycle. Drugs that modulate the host immune response to SARS-CoV-2 infection by boosting it to enhance viral clearance or by suppressing it to prevent excessive inflammation and tissue injury represent another category. Lastly, we discuss means to discover repurposed drugs and the ongoing challenges associated with the off-label use of existing drugs in the context of the COVID-19 outbreak.

KEYWORDS: antiviral drugs, repurposing, COVID-19, SARS-CoV-2, small molecule inhibitors, anti-inflammatory drugs, direct acting antivirals, host-targeted approaches

The emergence of the novel, highly pathogenic severe acute respiratory syndrome coronavirus 2 (SARS-CoV-2), the causative agent of coronavirus disease 2019 (COVID-19), has evolved into a global pandemic. While the majority of infected individuals remain asymptomatic or experience a mild to moderate, self-limited illness, a fraction of the patients progresses to develop severe infection that is often complicated by respiratory failure, cardiac complications, and sometimes death.[1] Moreover, it appears that COVID-19 may be causing long-lasting lung and heart injury.[2,3] As of the 16th of July

2020, more than 13.9 million COVID-19 cases and over 590,000 deaths have been reported worldwide, and the pandemic has taken a huge toll on the health care system and global economy. Measures such as social distancing and home isolation provide a temporary solution to control viral spread; however, in the absence of an effective approved vaccine, the entire world population continues to be at risk for SARS-CoV-2 infection. Hence, there is an urgent need for

approaches to treat COVID-19 patients and prevent the short- and long-term complications associated with this disease.

As with other newly emerging viruses that have caused outbreaks within the past two decades, including the coronaviruses implicated in severe acute respiratory syndrome (SARS) and Middle East respiratory syndrome (MERS) as well as the unrelated Ebola (EBOV, filovirus) and Zika (ZIKV, flavivirus) viruses, no approved, clinically effective therapy is available for treating SARS-CoV-2. Since the development of[4]

new drugs typically takes 8 to 12 years, this approach cannot

provide an immediate solution in the context of such outbreaks. In contrast, repurposing already approved or investigational drugs can significantly accelerate the development and deployment of therapies for such emerging viral infections. Repurposing existing drugs that have already been shown to be safe in humans, albeit in a different disease model(s), reduces the clinical risk and facilitates a faster path into the clinic. Moreover, relying on existing human safety, pharmacology, and toxicology data reduces the substantial cost associated with the development of a new drug (over two billion dollars on average).[4]

Multiple repurposed drugs are currently being studied for COVID-19 in clinical trials, and many more are being investigated in preclinical models. One category of such drugs aims to reduce viral replication and can be classified into direct acting antivirals (DAAs) that target viral enzymes (primarily the viral proteases and polymerase) and host-targeted drugs that inhibit cellular functions required for viral replication. Inhibitors that modulate virus-induced inflamma- tion and tissue injury constitute another category. The major categories of repurposed approaches that are already being studied or have been proposed for COVID-19 treatment with representative examples are discussed below and illustrated in summary tables and figures.

REPURPOSED APPROACHES THAT PRIMARILY

INHIBIT VIRAL REPLICATION

Direct Acting Antivirals (DAAs). SARS-CoV-2 is an enveloped, positive-sense, single-stranded RNA virus whose replication and transcription are catalyzed by an RNA-dependent RNA polymerase (RdRp). The two SARS-CoV-2 proteases, papain like protease (PL[pro]) and the main protease (M[pro]), play a key role in replication and transcription via processing of the viral polyproteins.[5] As with other viral infections, due to their known biological functions and active enzymatic sites, the SARS-CoV-2 polymerase and proteases are intuitive therapeutic targets.

Polymerase Inhibitors. In the past decade, several chemically distinct nucleoside and nucleotide analogues that inhibit the polymerase of multiple unrelated RNA viruses have been developed. One example is remdesivir, an investigational nucleoside analogue originally developed as a therapy for EBOV disease. Remdesivir gets incorporated into nascent viral RNA chains and results in their premature termination.[6] While not previously approved, intravenous administration of remdesivir was found to be highly effective against EBOV disease in nonhuman primates (NHP).[6] Nevertheless, in a randomized controlled (PALM) clinical trial for Ebola (NCT03719586), mortality rates were higher with remdesivir treatment than with monocloncal antibodies.[7]

Remdesivir has previously demonstrated *in vitro* activity against SARS-CoV and MERS-CoV,[8] and it reduced disease severity, viral replication, and lung injury in mouse (SARS-CoV) and NHP (MERS-CoV) models.[8,9] Recently, remdesivir was shown to inhibit RNA synthesis by a purified recombinant SARS-CoV-2 RdRp[10] and to suppress SAR-CoV-2 infection in both Vero E6 (green monkey kidney) ($EC_{50} = 0.77$ μM) and Huh7 (human hepatoma) cells.[11] Moreover, remdesivir demonstrated potent inhibition of SARS-CoV-2 replication in human lung cells and primary human airway epithelial cultures ($EC_{50} = 0.01$ μM).[12] Therapeutic administration of remdesivir in mice infected with SARS-CoV encoding the RdRp of SARS-CoV-2 reduced viral load in the lungs and improved pulmonary function relative to the vehicle.[12] In an NHP SARS-CoV-2 infection model that causes lower respiratory tract disease, remdesivir treatment provided protection from respiratory signs and reduced pulmonary infiltrates on radiographs.[13] Viral titers in bronchoalveolar lavages, lung viral loads, and lung injury were significantly reduced in remdesivir-treated animals relative to controls.[13]

A remdesivir compassionate use study in 53 patients hospitalized for severe COVID-19 demonstrated clinical improvement in 68% of the patients;[14] however, no control arm was included in this study. In a double-blind, placebo-controlled, multicenter trial in patients with severe COVID-19, intravenous remdesivir treatment did not improve the time to clinical improvement; however, the study did not reach its target enrollment and was stopped.[15] In contrast, preliminary data from the double-blind, randomized, placebo-controlled adaptive COVID-19 treatment trial sponsored by the US National Institute of Health (NIH) (NCT04280705) involving 1059 hospitalized adult patients (538 assigned to remdesivir and 521, to placebo) with lower respiratory COVID-19 infection showed that a 10-day remdesivir treatment course shortened the median recovery time relative to the placebo from 15 to 11 days ($p < 0.001$) and reduced the estimates of mortality by 14 days from 11.9% to 7.1% with no increase in serious adverse events.[16] Moreover, a randomized, open-label, phase 3 trial involving 397 hospitalized patients with confirmed SARS-CoV-2 infection with oxygen require- ments (but not mechanically ventilated) demonstrated comparable efficacy of 5- and 10-day remdesivir treatment courses with clinical improvement of 2 points or more on the ordinal scale detected in 64% and 54% of patients, respectively. Collectively, these findings suggest that remdesivir is moderately effective and is generally safe and led to the recent emergency use approval of this drug for the treatment of COVID-19 by the US Food and Drug Administration (FDA).

The guanine analogue favipiravir, which is approved in Japan for the treatment of influenza A virus infection, is another example for a broad-spectrum polymerase inhibitor.[17] Favipir- avir moderately inhibits replication of several RNA viruses *in vitro*,[18] albeit with high EC_{50} values: 61.88 and 67 μM in the case of SARS-CoV-2 and EBOV, respectively.[11] High drug concentrations are therefore required to maintain levels above these EC_{50} values but appear to be effectively achieved and well tolerated. Moreover, by self-inhibiting its metabolism into an inactive oxidative metabolite, favipiravir increases the plasma parent/inactive metabolite ratio, thereby facilitating increased cellular uptake and compensating for the high EC_{50} values.[19] Indeed, favipiravir protected 100% of mice from an EBOV challenge[20] and was shown to prolong survival and reduce viral load in a retrospective EBOV study during the 2014−2015 outbreak.[21] In a prospective, randomized, multi-center study (ChiCTR200030254), favipiravir demonstrated no effect in critically ill COVID-19 patients; however, it improved clinical recovery at day 7 in moderate cases relative to Arbidol, a fusion inhibitor also used for influenza treatment (71.4% vs 55.9%, $p = 0.019$). In a clinical trial involving 80 patients in China (ChiCTR2000029600), the combination of favipiravir with interferon-α reduced SARS-CoV-2 clearance time relative to lopinavir/ritonavir plus interferon-α in the control arm (median of 4 vs 11 days).[22] Notably, while the adverse effects attributed to favipiravir treatment were mild and manageable,[23] caution is needed due to its teratogenic risk[18] and potential for drug−drug interactions.[19] Favipiravir is

B

165

currently being studied in several open label phase 2 clinical trials (NCT04358549, NCT04346628), and it has been recently approved for COVID-19 treatment in China and India.

A third investigational RdRp inhibitor, the adenosine analogue galidesivir, has also shown activity against a wide range of viruses (including coronaviruses) and protected NHP from Marburg virus (filovirus) infection.[24] Galidesivir has recently been shown to tightly bind to SARS-CoV-2 RdRp,[25] and its clinical safety and efficacy are currently being studied in a randomized, double-blind, placebo-controlled clinical COVID-19 trial (NCT03891420).

Viral Protease Inhibitors. Another attractive antiviral target is the viral main protease (M^{pro}). This chymotrypsin-like cysteine protease proteolytically cleaves protein precursors necessary for viral RNA replication and production of infectious viral particles.[26] Several protease inhibitors have been proposed and/or studied for the treatment of COVID-19. One example is the lopinavir/ritonavir combination, which is approved for the treatment of human immunodeficiency virus (HIV-1) infection. While treatment with these drugs individually has demonstrated moderate anti-SARS-CoV-2 activity in Vero E6 cells (EC$_{50}$ = 5.73 μM, lopinavir, and EC$_{50}$ = 8.63 μM, ritonavir),[27] their combination showed no benefit beyond supportive care in a randomized, controlled, open-label clinical trial in hospitalized patients with severe COVID-19.[28] The ability of the lopinavir/ritonavir combination to reduce SARS-CoV-2 load in the respiratory tract in patients with mild COVID-19 is currently being studied (NCT04307693). Nelfinavir, another oral protease inhibitor approved for HIV-1 treatment, showed antiviral activity against SARS-CoV[29] and SARS-CoV-2 (EC$_{50}$ = 0.77 μM, CC$_{50}$ > 20 μM) in Vero E6 expressing TMPRSS2 cells.[27]

A potentially more attractive repurposed option that also targets the viral protease is the organoselenium compound, ebselen. Ebselen mimics the action of glutathione peroxidase and thus has anti-inflammatory, antioxidant, and cytoprotective properties.[30] This compound has demonstrated no side effects when tested at high oral doses in humans in several phase 2/3 clinical studies for various indications including hearing loss,[31] diabetes,[32] and stroke.[33] Ebselen emerged as the top hit in a high-throughput activity screening assay of a library of 10,000 approved and investigational drugs, where it demonstrated the strongest inhibition of SARS-CoV-2 M^{pro} activity (IC$_{50}$ = 0.67 μM) and was shown to covalently bind to cysteine 145 within the catalytic dyad of the viral M^{pro}.[34] Moreover, it showed a moderate anti-SARS-CoV-2 activity in Vero cells, with an EC$_{50}$ of 4.67 μM,[34] which could likely be achieved with the previously tested oral dosing. Notably, since it is nonselective, the likelihood of the emergence of viral resistance to ebselen is predicted to be lower than to other protease inhibitors.

Host-Targeted Antiviral Approaches. Viruses replicate within the host cell while relying on cellular machineries for multiple distinct steps in their life cycle. Repurposing inhibitors that target cellular functions required for SARS-CoV-2 infection is thus an attractive approach that may have the added benefit of a higher genetic barrier to the emergence of resistance.[35]

Inhibitors of Cellular Proteases. Effective SARS-CoV-2 entry requires proteolytic processing for activation of the spike (S) glycoprotein by the cellular endosomal cysteine proteases cathepsin B and L (CatB/L) and the transmembrane serine protease 2 (TMPRSS2).[36] TMPRSS2 is also required for the

activation of the S protein of SARS-CoV and MERS-CoV[37,38] and was shown to be essential for viral spread and pathogenesis in animal models of these infections.[39] Pharmacological targeting of TMPRSS2 therefore represents an attractive approach to block the entry of coronaviruses.

Camostat mesylate is an oral serine protease inhibitor that has been clinically used in Japan for the treatment of pancreatitis.[40] Camostat was shown to reduce MERS-CoV, SARS-CoV, and SARS-CoV-2 entry in a lung epithelial cell line (Calu-3) and in primary human lung cells with no apparent cytotoxic effects.[36] In a mouse model, camostat was effective in protecting mice against death due to a lethal SARS-CoV infection, with a survival rate of ∼60% relative to vehicle-treated controls.[41] Several randomized, placebo-controlled clinical trials to determine the effect of camostat on COVID-19 infection have been initiated (NCT04353284, NCT04321096).

A closely related compound, nafamostat mesylate, is another safe serine protease inhibitor. It is approved in Japan as an anticoagulant and antipancreatitis agent. Nafamostat was previously shown to inhibit the TMPRSS2-dependent entry of MERS-CoV in Calu-3 cells,[42] and its activity against SARS-CoV-2 entry and overall infection was recently shown to be superior to that of camostat (EC$_{50}$ = 5 nM vs 87 nM, respectively).[43] A randomized, placebo-controlled clinical trial to assess the efficacy of intravenous nafamostat treatment in COVID-19 patients was recently initiated (NCT04352400).

Kinase Inhibitors. Viruses have been shown to hijack a large number of host kinases at distinct stages of their life cycle (reviewed in ref 44). Cellular kinase inhibitors approved as anticancer or anti-inflammatory drugs therefore represent another category of compounds with a great potential to be repurposed into antivirals. Beyond their effect on viral replication, many of these kinase inhibitors have also been shown to reduce inflammation and tissue injury, such as by suppressing the production of cytokines (interleukin 6 (IL-6), tumor necrosis factor α (TNF-α) and transforming growth factor β (TGF-β)) implicated in inflammation and lung fibrosis. These kinase inhibitors may thus potentially achieve a dual role in the treatment of COVID-19 patients.

Members of the Src family of kinases (SFKs) and the Abl family of nonreceptor tyrosine kinases have been implicated in the life cycle of multiple viruses (reviewed in refs 44 and 45). RNAi-mediated depletion of the Src family proteins Lyn and Fyn reduced MERS-CoV infection, suggesting these proteins may be required for coronavirus infection.[46] The approved anticancer drug dasatinib and the investigational (phase 3) compound saracatinib, with activity against both SFKs and c-Abl (cellular Abelson tyrosine kinase), have been shown to inhibit a broad-spectrum of viruses *in vitro*.[47,48] Dasatinib was found to inhibit SARS-CoV and MERS-CoV with EC$_{50}$'s of 2.1 and 5.4 μM in Vero E6 cells.[49] Saracatinib was shown to inhibit early stages of the MERS-CoV life cycle (EC$_{50}$ of 2.9 μM in Huh7 cells) and was synergistic when combined with gemcitabine, which also inhibits MERS-CoV replication.[46] The inhibition of actin motility was proposed as one mechanism of antiviral action of Src and/or Abl inhibitors in other viral infections;[50] however, the mechanism of antiviral action and the molecular targets (Abl only or Abl plus Src) that mediate the antiviral action of these drugs in coronavirus infections remain to be uncovered.

Similarly, imatinib and/or nilotinib, approved anticancer c-Abl inhibitors lacking anti-Src family kinase activity, also

inhibited the replication of coronaviruses[49] and other RNA viruses[51] in cultured cells. Nilotinib and imatinib inhibited SARS-CoV and/or MERS-CoV infections with an EC_{50} at a micromolar range (EC_{50}'s ~ 10−20 μM).[49] Imatinib was shown to inhibit the fusion of virions at the endosomal membrane by targeting Abl2 kinase,[52] and it was therefore proposed that it may inhibit the function, localization, or activity of TMPRSS2.[52] In a murine model of vaccinia virus, imatinib effectively reduced viral load, viral spread, and mortality. In contrast, dasatinib did not protect mice but rather induced immunosuppression, raising a concern about its utility in controlling viral infections *in vivo*.[50] The activity of these and other kinase inhibitors against SARS-CoV-2 is currently being studied in preclinical models. Moreover, several studies aimed at testing the safety and efficacy of imatinib in COVID-19 patients are ongoing.

Several kinases in the mitogen-activated protein kinase (MAPK)/extracellular signal-regulated kinase (ERK) pathway have been shown to be upregulated and essential for the replication of various viruses (reviewed in ref 44). Infection with MERS-CoV has been shown to activate this pathway and to be suppressed by two anticancer compounds, trametinib, an FDA-approved MEK1/2 inhibitor, and selumetinib, a recently approved MEK1/ERK1/2 inhibitor.[53] The anti-SARS-CoV-2 potential of these compounds is currently being studied in preclinical models.

A recent phosphoproteomics analysis revealed changes in the phosphorylation patterns of cellular and viral proteins during SARS-CoV-2 infection.[54] Among these alterations is the activation of the p38/MAPK signaling pathway, which mediates the response to stress stimuli and was previously shown to be similarly activated in cells infected with SARS-CoV and MERS-CoV.[53,55] Pharmacological inhibition of this pathway by either gilteritinib, an FDA approved anticancer inhibitor of AXL, or ralimetinib, a p38 inhibitor under phase 2 clinical trials for cancer, demonstrated potent anti-SARS-CoV-2 activity (EC_{50} = 0.807 μM and EC_{50} = 0.873 μM, respectively).[54] Prominent activation of PIKfyve (phosphatidylinositol 3-phosphate 5-kinase), a lipid kinase that regulates endosomal trafficking and endomembrane homeostasis, was also detected.[54] Apilimod, an investigational oral anti-inflammatory and anticancer (phase 2), safe drug that was developed to inhibit IL-12/23 and later found to target PIKfyve,[56] was shown to suppress the entry of SARS-CoV-2 pseudovirions[57] and overall replication (EC_{50} < 0.08 μM in Vero E6 cells; EC_{50} = 0.007 μM in A549 cells expressing ACE2).[54] The safety and efficacy of apilimod is being studied in a phase 2 randomized, double-blind, placebo-controlled trial in mild COVID-19 patients in an outpatient setting (NCT04446377). Lastly, SARS-CoV-2 infection was shown to promote the shutdown of mitotic kinases, resulting in cell cycle arrest.[54] Pharmacological inhibition of cyclin-dependent kinases by dinaciclib, an anticancer drug (phase 3), exhibited potent anti-SARS-CoV-2 activity (EC_{50} = 0.127 μM in Vero E6 cells; EC_{50} = 0.032 μM in A549 cells expressing ACE2).[54] However, serious hematological toxicities may limit the use of dinaciclib as an antiviral drug.[58]

mechanism that is relevant to the primary indication for which they are approved.

One such example is niclosamide, an FDA-approved drug used to treat tapeworm infection. Niclosamide has previously shown activity against various viruses including MERS-CoV and SARS-CoV with EC_{50} values of less than 0.1 μM in Vero cells.[59−61] It has recently emerged as a potent inhibitor of SARS-CoV-2 infection via high-throughput screening of a drug library (EC_{50} = 0.28 μM),[62] and it is currently being studied in animal models of SARS-CoV-2. While niclosamide exerts its antihelmintic effect by inhibiting oxidative phosphorylation and stimulating adenosine triphosphatase activity in the mitochondria,[63] it has been shown to regulate multiple signaling pathways and biological processes.[64] The precise mechanism of antiviral action of this multifunctional drug thus remains unknown. A clinical trial to investigate the efficacy of niclosamide in combination with diltiazem (a calcium channel blocker) for the treatment of mild COVID-19 in patients with comorbidities has been initiated (NCT04372082).

Other antiparasitic drugs demonstrating anti-SARS-CoV-2 activity are chloroquine and its less toxic derivative hydroxychloroquine.[65] Chloroquine and hydroxychloroquine are approved for the treatment of malaria and inflammatory diseases, such as lupus and rheumatoid arthritis. These drugs have shown activity against multiple viruses *in vitro* but did not improve virological or clinical outcome in human studies in other viral infections, such as dengue[66−68] and flu.[69] They are thought to exert their antiviral effect by preventing endosomal acidification required for virus/cell fusion and by blocking autophagosome−lysosome fusion.[70] Yet, additional mechanisms, such as interference with the glycosylation of angiotensin-converting enzyme 2 (ACE2), the cellular receptor[71] of coronaviruses, have also been proposed. Although chloroquine demonstrated *in vitro* activity against SARS-CoV and MERS-CoV at a concentration that can be achieved in serum by the approved oral dosing,[72,73] it did not effectively[74]

Host-Targeted Drugs with Complexed or Unclear Mechanism of Action (MOA). Among the approved drugs that exhibit anti-SARS-CoV-2 activity are agents for which the mechanism of antiviral action is complex and unclear. In general, these drugs have multifunctional activities, and their antiviral effect is unlikely to be mediated by the same

reduce viral replication in SARS-CoV infected mice.

Both drugs were recently shown to moderately inhibit SARS-CoV-2 replication in Vero E6 cells with variable EC_{50} values across different studies (0.72−7.36 μM, chloroquine; 4.5−12.96 μM, hydroxychloroquine).[11,75,76] On the basis of these *in vitro* data and their anti-inflammatory properties, the utility of hydroxychloroquine and chloroquine for the prevention and treatment of COVID-19 has been assessed in several studies (reviewed in 77). The majority of retrospective, observational studies in hospitalized COVID-19 patients have demonstrated no benefit with hydroxychloroquine treatment.[78] A reduction in COVID-19 associated mortality was detected in one study in hospitalized patients who received the drug early during their disease course, but only when controlling for COVID-19 risk factors.[79] Moreover, concerns have been raised about the safety of this approach and, specifically, its association with cardiac toxicity. Indeed, a clinical trial evaluating the safety and efficacy of chloroquine in patients with severe COVID-19 (NCT04323527) was terminated early due to prolongation of the QTc interval leading to increased cardiac toxicity and fatality rates.[80] As a result, prospective COVID-19 clinical trials with hydroxychloroquine and chloroquine have been terminated, and the emergency use authorization for these drugs has been revoked by the FDA.[81] The discussed repurposed approaches that primarily inhibit viral replication are illustrated in Table 1 and Figure 1.

Table 1. Repurposed Approaches That Inhibit Viral Replication[a]

		name	type	original indication	cell line	EC50	mouse model	NHP	target for antiviral activity	COVID-19 status
DAAs	viral polymerase inhibitors	remdesivir (GS-5734)	nucleoside analogue	investigational (Ebola)	Vero E6 / HAE	0.77 μM / 0.01 μM	SARS-CoV/RdRp of SARS-CoV-2 (reduced lung viral load)	SARS-CoV-2 (reduced viral load and lung injury)	RdRp	emergency use approval by US FDA
		favipiravir (T-705)	nucleoside analogue	influenza A virus (approved in Japan)	Vero E6	61.88 μM	ND	ND	RdRp	phase 2/3, approved in China and India
		galidesivir (BCX4430)	nucleoside analogue	investigational	ND	ND	ND	ND	RdRp	phase 1
	viral protease inhibitors	lopinavir (LPV) /ritonavir (RV)	protease inhibitor	HIV-1 infection	Vero E6	5.73 μM (LPV) 8.63 μM (RV)	ND	ND	Mpro	phase 2
		nelfinavir	protease inhibitor	HIV-1 infection	Vero E6	0.77 μM	ND	ND	Mpro	NI
		ebselen	organoselenium compound	investigational (arthritis, stroke etc)	Vero	4.67 μM	ND	ND	Mpro	NI
host-targeted antiviral approaches	cellular protease inhibtors	camostat mesylate (FOY-305)	serine protease inhibitor	pancreatitis (Japan)	Calu-3	0.087 μM	SARS-CoV (protects mice from death)	ND	TMPRSS2	phase 2/3
		nafamostat mesylate	serine protease inhibitor	anticoagulant and anti-pancreatitis agent (Japan)	Calu-3	0.005 μM	ND	ND	TMPRSS2	phase 2/3
	cellular kinase inhibitors	dasatinib	anticancer drug	leukemia	Vero E6	2.1 μM (SARS-CoV) 5.4 μM (MERS-CoV)	ND	ND	Src kinase + Abl kinase	NI
		saracatinib	investigational (phase 3)	Alzheimer's disease, cancer	Huh7	2.9 μM (MERS-CoV)	ND	ND	Src kinase + Abl kinase	NI
		imatinib (STI-571)	anticancer drug	leukemia	Vero E6	9.8 μM (SARS-CoV-2) 17.7 μM (MERS-CoV)	ND	ND	Abl kinase	phase 3
		nilotinib (AMN107)	anticancer drug	leukemia	Vero E6	μM range	ND	ND	Abl kinase	NI
		trametinib (GSK1120212)	anticancer drug	melanoma	ND	ND	ND	ND	MEK1/2 inhibition	NI
		selumetinib (AZD6244)	anticancer drug	neurofibromatosis type 1	ND	ND	ND	ND	MEK1/ERK1/1/2 inhibition	NI
		gilteritinib	anticancer drug	acute myeloid leukemia	Vero E6	0.807 μM	ND	ND	AXL kinase	NI
		ralimetinib (LY2228820)	investigantional (phase 2)	glioblastoma, ovarian cancer	Vero E6	0.873 μM	ND	ND	p38 MAPK	NI
		apilimod (STA-5326)	investigational (phase 2)	anti-inflammatory, anti-cancer	Vero E6 / A549-ACE2	< 0.08 μM / 0.007 μM	ND	ND	PIKfyve	phase 2
		dinaciclib (SCH-727965)	investigational (phase 3)	anti-cancer	Vero E6 / A549-ACE2	0.127 μM / 0.032 μM	ND	ND	cyclin-dependent kinase	NI
complexed or unclear MOA		niclosamide		tapeworm infection	Vero	0.28 μM	SARS-CoV-2 (being studied)	ND	ND	phase 3
		chloroquine (CQ)		malaria, inflammatory diseases	Vero E6	0.72 – 7.36 μM (CQ)	SARS-CoV (did not reduce viral replication)	ND	endosomal acidification, glycosylation of ACE2	phase 2/3
		hydroxychloroquine (HCQ)				4.5 – 12.96 μM (HCQ)	ND	ND		phase 3/4

[a]Known *in vitro* data for SARS-CoV-2 and *in vivo* data for SARS-CoV, MERS-CoV, and SARS-CoV-2 are included. Alternative names for drugs are mentioned. HAE, human airway epithelial cells; Vero, African green monkey kidney epithelial cells; Calu-3, human lung epithelial cells; Huh7, human hepatoma cells; A549-ACE2, human lung carcinoma cells expressing ACE2 receptor; RdRp, RNA-dependent RNA polymerase; Mpro, viral main protease; ND, not determined; NI, not initiated.

MODULATORS OF INFLAMMATION AND TISSUE INJURY

While the immune response induced by SARS-CoV-2 infection is protective, it also plays an important role in disease pathogenesis.[82] During the incubation period and early stages of COVID-19, the effective immune response facilitates viral clearance. However, when the response is insufficiently protective, SARS-CoV-2 replicates efficiently in tissues expressing ACE2, such as lungs, heart, and intestines, leading to massive tissue destruction, severe inflammation, vascular hyperpermeability, and ultimately, tissue fibrosis and long-term dysfunction. In the lungs, this excessive inflammatory response leads to acute respiratory distress syndrome (ARDS), which is often fatal,[83] or can result in an epidermal growth factor receptor (EGFR)-mediated pulmonary fibrosis, as observed in SARS-CoV infection.[84] Strategies that boost the innate immune response during the early stages of viral infection to enhance viral clearance and modulate the excessive inflammatory response to reduce tissue injury during the later stages of infection may both provide benefit. A number of repurposed approaches that aim to achieve these effects are currently being investigated.

Interferons (IFN) are one example. These soluble glycoproteins have strong antiviral, antiproliferative, and immunomodulatory effects. In an *ex vivo* model of human lung, SARS-CoV-2 largely failed to induce the expression of any IFNs (type I, II, or III),[85] indicating that the early innate immune response to this virus is impaired and supporting the use of exogenous IFN to stimulate innate immunity as a candidate therapeutic modality. Type I IFNs (IFN-I, e.g., IFN-α and IFN-β) have been approved for the treatment of chronic hepatitis B and C infections and have previously demonstrated *in vitro* activity and protection in various animal models of MERS-CoV[86] and SARS-CoV.[74] In a preliminary, uncontrolled study of patients infected with SARS-CoV, the use of type I IFN plus corticosteroids was associated with a faster resolution of radiographic lung abnormalities and improved oxygen saturation levels than treatment with corticosteroids alone.[87] SARS-CoV-2 appears to be more susceptible to IFN-α treatment *in vitro* than SARS-CoV.[88] In a retrospective study of 77 adults with moderate COVID-19, treatment with nebulized IFN-α2b reduced the duration of both detectable virus in the upper respiratory tract and elevated blood levels of inflammatory markers (IL-6 and C-reactive protein).[89] Several types and routes of administration of IFN-I are currently being studied in COVID-19 patients.

Perhaps a more attractive candidate approach for COVID-19 treatment is, however, type III IFNs (IFN-λ1−4). Although not approved yet, IFN-λ has been shown to be safe in large phase 1/2/3 trials (involving ∼3000 patients) for the treatment of hepatitis B, C, and D virus infections.[90] In
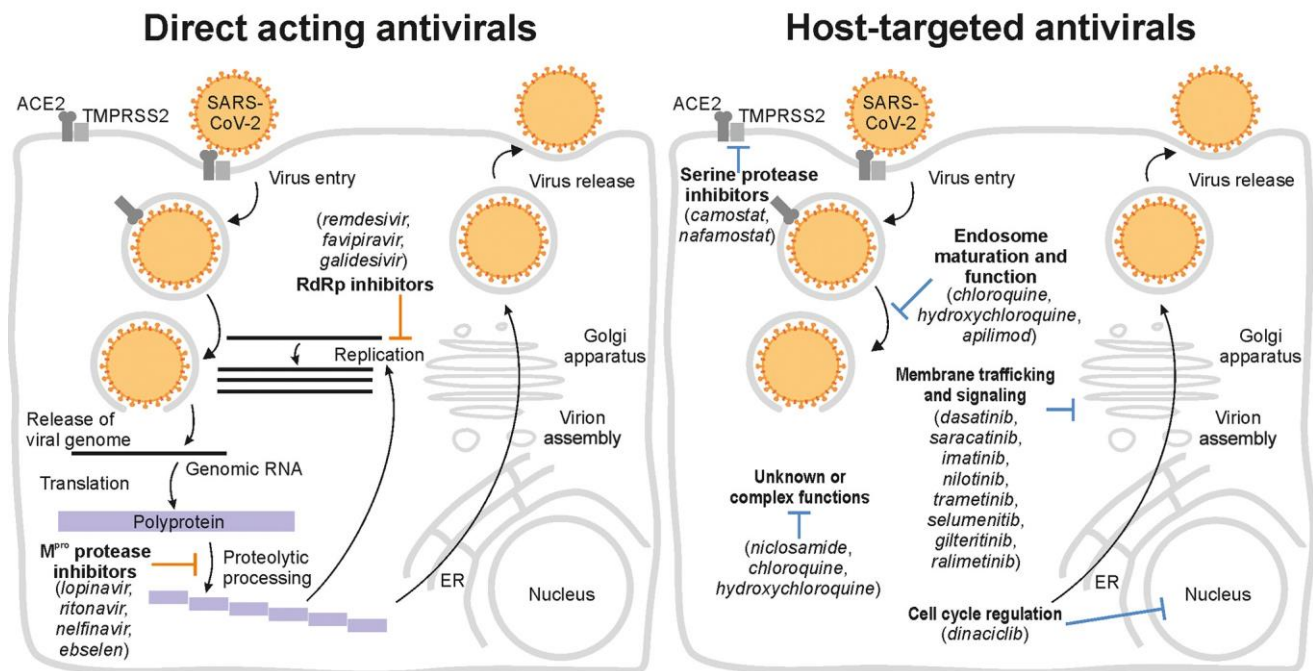
E

Figure 1. Repurposed drugs that primarily inhibit SARS-CoV-2 replication. The left panel depicts direct acting antivirals (DAAs) targeting SARS-CoV-2 enzymes (RNA-dependent RNA polymerase (RdRp) and viral main protease (M^pro)). The right panel illustrates host-targeted drugs that inhibit cellular functions required for viral replication. Each panel depicts specific stages of the viral life cycle, some of which are targeted by drugs. Examples of repurposed drugs are connected to the corresponding targeted proteins or pathways by blunt arrows.

contrast to IFN-α/β that signals through a ubiquitously expressed INF-α/β receptor (IFNAR), IFN-λ signals through the INF-λ receptor (IFNLR), whose expression is restricted to epithelial cells (including lung and gut) and a subset of immune cells (reviewed in ref 91). The administration of type III IFN at an early stage of COVID-19 could therefore result in an antiviral response that is localized to epithelial cells, thereby reducing side effects and inflammation associated with the systemic action of type I IFNs.[92] In a human airway epithelial cell culture model, IFN-λ3 and IFN-λ4 exhibited antiviral effects against MERS-CoV.[93] IFN-λ restricted SARS-CoV replication in the respiratory and gastrointestinal tracts in knockout mouse strains lacking receptors for type I IFN, type III IFN, or both.[94] Several phase 2 clinical randomized controlled trials to evaluate the safety and efficacy of pegylated INF-λ compared with the placebo in outpatients with uncomplicated COVID-19 (NCT04331899, NCT04344600), hospitalized patients with noncritical illness (NCT04388709), or both ambulatory and hospitalized patients (NCT04354259) are ongoing.

COVID-19 severity was found to positively correlate with the level of proinflammatory cytokines.[1] Increased serum expression levels of IL-2 and IL-6, in particular, appear to predict the severity and prognosis of patients with COVID-19.[95] Immunomodulatory agents that directly target these key cytokines may therefore help to reduce the inflammatory responses observed in severe cases.

Various approaches are currently being studied for their potential to reduce inflammation and/or tissue injury in moderate and severe forms of COVID-19. The benefit of using corticosteroids for the treatment of COVID-19 was initially debatable.[96,97] A systematic review and meta-analysis of the

safety and efficacy of corticosteroids revealed that their use in subjects with SARS-CoV-2, SARS-CoV, and MERS-CoV infections delayed viral clearance and did not convincingly improve survival.[98] Nevertheless, the preliminary results of the RECOVERY trial, a large randomized, controlled, open-label trial, have shown a benefit for dexamethasone treatment in severe COVID-19 patients. Specifically, up to a 10-day dexamethasone treatment course in 2104 patients reduced the 28-day mortality by one-third in patients on mechanical ventilation (29% vs 40.7%) and by one-fifth in patients requiring oxygen (21.5% vs 25%) relative to 4321 patients who received the standard of care, yet it had no effect in patients who did not require oxygen.[99] Additional phase 3 clinical trials testing various dosing regimens and formulations of corticosteroids in severe COVID-19 patients are currently ongoing.

Another class of anti-inflammatory agents that are being studied clinically are JAK inhibitors. Baricitinib is an oral JAK1/JAK2 inhibitor that has been shown to modulate innate and adaptive immune responses by inhibiting the production of inflammatory cytokines including TNF-α, IL-6, IL-17, and IFN-γ[100] and to profoundly reduce inflammation in animal models.[101] It is approved in over 65 countries for the treatment of rheumatoid arthritis. A small pilot study in 12 mild to moderate COVID-19 patients in Italy has suggested that baricitinib in combination with lopinavir/ritonavir may be safe for this study population and can improve clinical and laboratory parameters.[102] In a noncontrolled, retrospective cohort study of 15 patients with moderate to severe COVID-19, a short course of baricitinib in combination with hydroxychloroquine was tolerated and temporally associated with clinical improvement in 11 of 15 patients and recovery in 12 of 15 patients.[103] The safety and efficacy of baricitinib

F

Table 2. Repurposed Approaches Aimed at Modulating Inflammatory Responses and Reducing Tissue Injury[a]

	name	type	status	in vitro	mouse model	NHP	mechanism of action	COVID-19 status
innate immune response booster	IFN-I (e.g. IFN-α and INF-β)	glycoprotein (cytokine)	approved for chronic HBV and HCV	SARS-CoV-2 more susceptible to IFN-α treatment than SARS-CoV	SARS-CoV *(inhibits viral replication)*	MERS-CoV *(improves outcome)*	boosts innate immune response	phase 2/3
	IFN-III (IFN-λ1-4)	glycoprotein (cytokine)	investigational (phase 1/2/3)	IFN-λ3 and IFN-λ4 inhibit MERS-CoV	SARS-CoV *(inhibits viral replication)*	ND	boosts innate immune response	phase 2
anti-inflammatory, modulators of tissue injury	dexamethasone	corticosteroid	approved for inflammatory conditions	ND	ND	ND	inhibits inflammatory cytokine production	phase 3
	baricitinib	Janus kinase inhibitor	approved for rheumatoid arthritis	ND	ND	ND	inhibits inflammatory cytokine production	phase 3
	acalabrutinib	Bruton tyrosine kinase inhibitor	approved for lymphoid malignancies	ND	ND	ND	reduces the levels of inflammatory markers and cytokines	phase 2
	tofacitinib	Janus kinase inhibitor	approved for inflammatory diseases	ND	ND	ND	inhibits inflammatory cytokine production	phase 2
	tocilizumab	monoclonal antibody	approved for inflammatory diseases	ND	ND	ND	inhibits IL-6	phase 2/3
	sarilumab	monoclonal antibody	approved for rheumatoid arthritis	ND	ND	ND	inhibits IL-6	failed in phase 3, trial stopped
	ulinastatin	serine protease inhibitor	approved for acute pancreatitis and sepsis (Asia)	ND	ND	ND	inhibits IL-6, modulates RAS system	phase 1/2, recommended in China
	angiotensin 1-7	peptide	investigational	ND	ND	ND	modulates RAS system	phase 2/3
	nintedanib	multikinase inhibitor	approved for pulmonary fibrosis	ND	ND	ND	supresses lung fibrosis	phase 2

[a]Known *in vitro* and *in vivo* data for SARS-CoV, MERS-CoV, and SARS-CoV-2 are included. ND, not determined; IFN, interferon; RAS, renin angiotensin system; IL, interleukin.

individually and/or in combination drug regimens are currently being studied at a larger scale as part of the NIH's multicenter, adaptive, randomized blinded controlled trial for hospitalized COVID-19 patients (NCT04280705) and other trials (NCT04373044). Similarly, the effect of the early administration of tofacitinib, another oral JAK (JAK1/JAK3) inhibitor approved for various inflammatory diseases, on COVID-19 pneumonia, will also be investigated in a phase 2 study (NCT04332042).

Acalabrutinib is a covalent inhibitor of the Bruton tyrosine kinase (BTK), which mediates inflammation via regulation of macrophage signaling and activation. Acalabrutinib is approved in the United States (US) for the treatment of lymphoid malignancies.[104] Its off-label use for treating 19 patients hospitalized with severe COVID-19 was shown to reduce respiratory distress and levels of the inflammatory markers C-reactive protein and IL-6.[105] Additional, phase 2 clinical trials testing the efficacy and safety of acalabrutinib in patients hospitalized with COVID-19 are ongoing in the US (NCT04380688) and Europe (NCT04346199).

Various humanized monoclonal antibodies approved for the treatment of inflammatory diseases or cancer are also being tested for COVID-19 as repurposed candidates. In two retrospective studies, treatment with tocilizumab, an IL-6 receptor (IL-6R) inhibitor approved for rheumatoid arthritis, improved survival of severe COVID-19 patients; however, treatment prolonged their hospital stay and was associated with serious adverse events including transient respiratory worsening and bacterial infections.[106,107] Sarilumab, another IL-6R inhibitor, has recently failed in a US phase 3 trial involving 194 critically ill COVID-19 patients, and the trial has therefore been stopped.[108] The utility of these and other monoclonal antibodies that are currently being studied for COVID-19 treatment, such as bevacizumab that targets vascular endothelial growth factor A (VEGF-A) and nivolumab and camrelizumab that target the programmed cell death protein 1 (PD1), remains uncertain.

Ulinastatin is another anti-inflammatory agent that inhibits IL-6 but may provide additional benefits for severe COVID-19 patients, beyond those provided by IL-6 inhibition, and would likely be safer than the monoclonal antibodies targeting IL-6R.

This urinary serine protease inhibitor has demonstrated significant reduction in the levels of plasma pro-inflammatory cytokines in multiple clinical studies in various inflammatory conditions.[109] Notably, in an animal model of pancreatitis, it was also shown to activate the renin−angiotensin system (RAS) by upregulating the expression of ACE2 as well as the anti-inflammatory factor angiotensin 1−7 (Ang 1−7) and the Mas receptor.[110] This property makes ulinastatin a particularly attractive agent for COVID-19 treatment, since disease severity is thought to be linked in part to an imbalance in the RAS.[111]

The cell surface receptor ACE2 converts angiotensin II (Ang II) into Ang 1−7, which then binds to the Mas receptor to counteract the effects of Ang II on vasoconstriction, apoptosis, and inflammation.[112] An unopposed Ang II effect has been previously linked to increased pulmonary vascular permeability in animal models of ARDS.[113] It was previously shown that SARS-CoV infection and the viral spike protein reduce ACE2 expression and that injection of the spike-Fc protein (spike protein fused to the Fc portion of human IgG1) into mice causes acute lung failure, which could be attenuated by blocking the renin−angiotensin pathway.[113] By reducing ACE2 expression upon its entry into cells, SARS-CoV-2 may also facilitate such imbalance and enhancement of the Ang II effects, thereby contributing to ARDS and possibly myocarditis.[36,114,115] Ulinastatin may reverse this imbalance and reduce tissue injury by directly upregulating ACE2. Moreover, ulinastatin was shown to protect mice from lipopolysaccharide-induced acute lung injury and improve cardiac function in mice with diabetes by downregulating and reducing cytokine expression.[116,117] Collectively, ulinastatin thus has a potential to reduce inflammation and vasodilatation not only by restoring ACE2 and Ang 1−7 levels but also by reducing the activity of pro-inflammatory cytokines. Ulinastatin has been approved for the treatment of acute pancreatitis and sepsis in Asia[118] and, even more relevant, it was studied for the treatment of ARDS. In a meta-analysis of randomized controlled trials including over 2300 patients with ARDS, ulinastatin treatment reduced mortality and ventilator-associated pneumonia by nearly 50% and also reduced ICU and overall hospital stays.[119] On the basis of these findings and its favorable tolerability in patients, ulinastatin has been
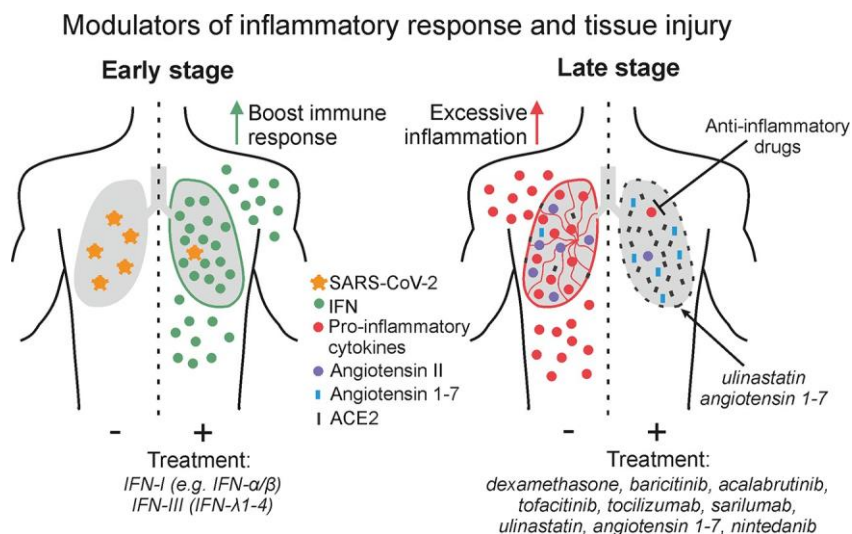
Figure 2. Repurposed drugs that modulate SARS-CoV-2-induced inflammatory responses and tissue injury. Drugs that boost innate immune responses could enhance viral clearance and provide protection during early stages of SARS-CoV-2 infection (left panel), whereas drugs that suppress inflammation by modulating the immune or renin−angiotensin system may reduce tissue injury (right panel).

recommended for the treatment of severe COVID-19 infection in China and a randomized, double-blind, placebo-controlled clinical trial to analyze its safety and efficacy for the treatment of COVID-19 has been initiated (NCT04393311). The utility of an Ang 1−7 peptide,[120] a different approach designed to reverse the RAS imbalance and reduce tissue injury, is also currently being clinically investigated in COVID-19 patients (NCT04332666).

Lastly, another category of agents being considered for its potential to reduce COVID-19-induced tissue damage are kinase inhibitors that suppress lung fibrosis. Several studies have suggested that the inhibition of epidermal growth factor receptor (EGFR) signaling may prevent the fibrotic response associated with various respiratory infections including SARS-CoV.[84] Several kinase inhibitors with anti-EGFR activity including gefitinib and erlotinib have been previously shown to inhibit the induction of fibrosis in various mouse models of tissue injury.[121] Nintedanib, a multikinase inhibitor with activity against fibroblast growth factor receptor (FGFR), platelet-derived growth factor receptor (PDGFR), and vascular endothelial growth factor receptor (VEGFR), which is approved for idiopathic pulmonary fibrosis, is currently being studied in patients with moderate to severe COVID-19 treatment for its potential effect to prevent pulmonary fibrosis (NCT04338802). The modulators of inflammation and tissue injury mentioned above are illustrated in Table 2 and Figure 2.

DISCUSSION

There is an urgent need for countermeasures to combat SARS-CoV-2 infection. It would take many months for a vaccine and much longer for a novel antiviral drug to be developed for effective prevention and treatment of this virus, respectively. Currently, the off-label use of drugs that are approved or are under advanced clinical investigation provides the main solution. Repurposing existing drugs requires significantly less capital and time and diminishes the clinical risks as such drugs have already been rigorously tested (toxicity, pharmacokinetics, pharmacodynamics, dosing, etc.) for their primary indication.

Since the majority of the antiviral drugs approved to date are DAAs that target viral proteins encoded by individual viruses, they typically provide a narrow spectrum of coverage and are therefore unlikely to be attractive candidates for repurposing. One example is provided by the HIV protease inhibitors, lopinavir/ritonavir. In contrast, existing antivirals that have already demonstrated broad-spectrum coverage, such as remdesivir, can facilitate readiness for future outbreaks of emerging pathogens and thus provide an immediate solution.

There are a number of strategies to identify antiviral candidates for repurposing among drugs that have already been approved or studied for other indications. One such approach is high-throughput screening of compound libraries for antiviral activity. Ebselen is one example of a compound that was discovered as having anti-SARS-CoV-2 activity using this approach.[34] The assembly of libraries that include a larger number of compounds that have already been approved or studied in humans, such as the REFRAME library,[122] has provided an important resource to support these efforts. Another approach is to identify existing drugs that target cellular factors known to be required for the life cycle of SARS-CoV-2. The discovery of camostat and nafamostat, inhibitors of cellular serine proteases, including TMPRSS2, exemplifies this strategy. Such host-targeted approaches may also have the added benefit of a higher genetic barrier to the emergence of resistance. At a larger scale, genomic and proteomic screens provide unbiased approaches for the discovery of proviral factors including druggable candidates. Mapping the interaction network of the individual SARS-CoV-2 proteins with the human proteome has recently revealed 66 druggable cellular factors that can be targeted by 69 compounds, many of which are either already approved or currently in clinical trials.[123] Moreover, phosphoproteomics analysis of SARS-COV-2-infected cells has revealed alterations in various cellular pathways during viral infection and facilitated discovery of small molecule inhibitors of these pathways as repurposing candidates.[54]

While repurposing of approved drugs as antivirals can offer an immediate solution, it also poses some challenges and raises important concerns. One challenge is that the antiviral effect

H

observed *in vitro* often cannot be reproduced *in vivo*. In the context of COVID-19, this was evident with lopinavir/ritonavir, which inhibited SARS-CoV-2 in cultured cells but did not show a benefit beyond standard care in patients when used by itself.[28] Furthermore, even a promising effect in animal models cannot guarantee effectiveness in patients, as exemplified by chloroquine for dengue treatment[66,68] and by remdesivir for EBOV disease treatment.[6,7]

Pharmacokinetic factors may contribute in part to the observed lack of correlation between preclinical and clinical models. Factors, such as achievable serum and particularly lung levels, have to be carefully evaluated when specific drugs are being considered for repurposing. For example, the pharmacokinetics of chloroquine and hydroxychloroquine is complex, and it is unclear whether the plasma level achieved with standard dosing is sufficient to effectively inhibit SARS-CoV-2 in patients.[76] Similarly, the plasma concentration of favipiravir in patients in the US has been shown to be 50% of that in Japanese patients, suggesting a possible ethnic or regional difference in its pharmacokinetics, which should be taken into account.[124] Toxicity is another major concern, particularly when targeting host functions. Importantly, drug safety in humans in one disease model cannot guarantee safety in another disease model. Chloroquine and hydroxychloroquine, for example, are generally safe when used to treat malaria and inflammatory diseases, yet in the context of SARS-CoV-2 infection, which affects the heart, they increase the risk of cardiac toxicity.[123] Nevertheless, for some drugs, it may be feasible to find a therapeutic window where the drug level is sufficient to inhibit viral replication with minimal cellular toxicity. Shortening the duration of therapy from months or years required to treat inflammatory diseases or cancer to several days or a few weeks sufficient to treat COVID-19 should further limit toxicity.

The emergence of viral resistance is another potential challenge of any antiviral strategy and particularly DAAs, such as those targeting the SARS-CoV-2 polymerase or protease. Although no phenotypic resistance to the currently used DAAs has been reported to date, there is already genotypic evidence for a high mutation rate in the SARS-CoV-2 RdRp sequence in patients.[125] While viral resistance can also limit treatment of host-targeted approaches,[47,126] in general, targeting cellular factors that are not under the genetic control of viruses is more likely to have a higher barrier to resistance than classical DAAs.[35,127]

Understanding the MOA of repurposed drugs is also often challenging. Cellular proteins function in a complex network of interactions, and their inhibitors are often not selective. The mechanism of antiviral action of host-targeted approaches therefore often remains elusive, and the molecular targets underlying this effect remain unvalidated. For example, erlotinib's effect on hepatitis C virus infection was first attributed solely to its effect on EGFR, its cancer target, yet it was later demonstrated that the inhibition of GAK, another cellular kinase that is inhibited by erlotinib with a comparable potency to EGFR, also plays a role.[127,128] For other drugs, such as chloroquine, the MOA is even less clear and appears to be pathogen specific.[69,129,130]

Access to drugs and cost pose additional challenges to repurposing existing drugs. The demand for specific drugs in the context of an outbreak can far exceed the available stockpiles. Indeed, early on, when used broadly for COVID-19, there was a significant shortage of hydroxychloroquine, which

limited its availability for patients with inflammatory diseases who rely on it for their chronic conditions. Similarly, in the face of the upscaled and expedited production, there is an insufficient number of remdesivir doses to meet the global need. The high cost associated with some of the studied repurposed candidates, such as tocilizumab, is another barrier for their wide use in the treatment of COVID-19 patients.

Lastly, there is an urgent need to effectively prioritize among the proposed repurposed approaches and to effectively study them in order to guide clinical practice. The unpredictable nature of outbreaks with respect to size, geographic location, and duration further complicates the design of clinical trials. Consequently, the design of many of the hundreds ongoing clinical trials is somewhat limited, for example, by lacking appropriate controls or by being underpowered to reveal a virological or clinical effect. Moreover, concerns about publication bias are being raised.[14,131,80] This brings up a global concern that, similarly to the 2014 EBOV disease outbreak in West Africa, many approaches will be studied, yet the cumulative knowledge gained will be somewhat limited. One solution to overcome this challenge is offered by the adaptive platform design; a study design approved by the FDA during the 2014 Ebola outbreak[132] (NCT02380625) that is currently being implemented in the clinical trial conducted by the US NIH (NCT04280705). Adapted from clinical studies in cancer,[133] this platform design facilitates the simultaneous investigation of multiple agents individually and in combinations. The interim analysis feature of this platform design enables the entry of new agents as they become available and the removal of failing agents.[132] The incorporation of response adaptive randomization changes the randomization ratio of assigning treatment regimens to gradually favor the arms that perform better.[132] The important advantage is that such a study is designed to determine not only whether specific drugs work or not but also, more importantly, which drugs work the best, thereby guiding clinical practice. The integration of the adaptive platform design with a "core protocol" that involves multiple investigative teams and can extend across multiple infectious disease outbreaks may provide an even better solution to address these challenges yet will require tremendous coordination.[134]

In summary, the discussed examples represent the broad range of repurposed approaches that are already being studied or proposed to combat COVID-19. While a number of these approaches are showing some promise, the clinical utility of the majority of them remains to be determined. Protection against SARS-CoV-2 is more likely to be achieved by a combination of approaches that inhibit viral replication with those that reduce inflammation and tissue injury.

▍ AUTHOR INFORMATION

Corresponding Author

Shirit Einav − *Department of Medicine, Division of Infectious Diseases and Geographic Medicine, and Department of Microbiology and Immunology, Stanford University School of Medicine, Stanford University, Stanford, California 94305, United States;* ⊙ orcid.org/0000-0001-6441-4171; Email: seinav@stanford.edu

Author

Sirle Saul − *Department of Medicine, Division of Infectious Diseases and Geographic Medicine, and Department of Microbiology and Immunology, Stanford University School of*

I

Medicine, Stanford University, Stanford, California 94305, United States

REFERENCES

(1) Huang, C., Wang, Y., Li, X., Ren, L., Zhao, J., Hu, Y., Zhang, L., Fan, G., Xu, J., Gu, X., Cheng, Z., Yu, T., Xia, J., Wei, Y., Wu, W., Xie, X., Yin, W., Li, H., Liu, M., Xiao, Y., Gao, H., Guo, L., Xie, J., Wang, G., Jiang, R., Gao, Z., Jin, Q., Wang, J., and Cao, B. (2020) Clinical Features of Patients Infected with 2019 Novel Coronavirus in Wuhan, China. *Lancet* 395 (10223), 497−506.

(2) Spagnolo, P., Balestro, E., Aliberti, S., Cocconcelli, E., Biondini, D., Casa, G. D., Sverzellati, N., and Maher, T. M. (2020) Pulmonary Fibrosis Secondary to COVID-19: A Call to Arms? *Lancet Respir. Med.*, DOI: 10.1016/S2213-2600(20)30222-8.

(3) Shi, S., Qin, M., Shen, B., Cai, Y., Liu, T., Yang, F., Gong, W., Liu, X., Liang, J., Zhao, Q., Huang, H., Yang, B., and Huang, C. (2020) Association of Cardiac Injury With Mortality in Hospitalized Patients With COVID-19 in Wuhan, China. *JAMA Cardiol.* 5, 802.

(4) DiMasi, J. A., Grabowski, H. G., and Hansen, R. W. (2016) Innovation in the Pharmaceutical Industry: New Estimates of R&D Costs. *J. Health Econ.* 47, 20−33.

(5) Krichel, B., Falke, S., Hilgenfeld, R., Redecke, L., and Uetrecht, C. (2020) Processing of the SARS-CoV Pp1a/Ab Nsp7−10 Region. *Biochem. J.* 477 (5), 1009−1019.

(6) Warren, T. K., Jordan, R., Lo, M. K., Ray, A. S., Mackman, R. L., Soloveva, V., Siegel, D., Perron, M., Bannister, R., Hui, H. C., Larson, N., Strickley, R., Wells, J., Stuthman, K. S., Van Tongeren, S. A., Garza, N. L., Donnelly, G., Shurtleff, A. C., Retterer, C. J., Gharaibeh, D., Zamani, R., Kenny, T., Eaton, B. P., Grimes, E., Welch, L. S., Gomba, L., Wilhelmsen, C. L., Nichols, D. K., Nuss, J. E., Nagle, E. R., Kugelman, J. R., Palacios, G., Doerffler, E., Neville, S., Carra, E., Clarke, M. O., Zhang, L., Lew, W., Ross, B., Wang, Q., Chun, K., Wolfe, L., Babusis, D., Park, Y., Stray, K. M., Trancheva, I., Feng, J. Y., Barauskas, O., Xu, Y., Wong, P., Braun, M. R., Flint, M., McMullan, L. K., Chen, S.-S., Fearns, R., Swaminathan, S., Mayers, D. L., Spiropoulou, C. F., Lee, W. A., Nichol, S. T., Cihlar, T., and Bavari, S. (2016) Therapeutic Efficacy of the Small Molecule GS-5734 against Ebola Virus in Rhesus Monkeys. *Nature* 531 (7594), 381−385.

(7) Mulangu, S., Dodd, L. E., Davey, R. T., Tshiani Mbaya, O., Proschan, M., Mukadi, D., Lusakibanza Manzo, M., Nzolo, D., Tshomba Oloma, A., Ibanda, A., Ali, R., Coulibaly, S., Levine, A. C., Grais, R., Diaz, J., Lane, H. C., and Muyembe-Tamfum, J.-J. (2019) A Randomized, Controlled Trial of Ebola Virus Disease Therapeutics. *N. Engl. J. Med.* 381 (24), 2293−2303.

(8) Sheahan, T. P., Sims, A. C., Graham, R. L., Menachery, V. D., Gralinski, L. E., Case, J. B., Leist, S. R., Pyrc, K., Feng, J. Y., Trantcheva, I., Bannister, R., Park, Y., Babusis, D., Clarke, M. O., Mackman, R. L., Spahn, J. E., Palmiotti, C. A., Siegel, D., Ray, A. S., Cihlar, T., Jordan, R., Denison, M. R., and Baric, R. S. (2017) Broad-Spectrum Antiviral GS-5734 Inhibits Both Epidemic and Zoonotic Coronaviruses. *Sci. Transl. Med.* 9 (396), No. eaal3653.

(9) de Wit, E., Feldmann, F., Cronin, J., Jordan, R., Okumura, A., Thomas, T., Scott, D., Cihlar, T., and Feldmann, H. (2020) Prophylactic and Therapeutic Remdesivir (GS-5734) Treatment in the Rhesus Macaque Model of MERS-CoV Infection. *Proc. Natl. Acad. Sci. U. S. A.* 117 (12), 6771.

(10) Gordon, C. J., Tchesnokov, E. P., Woolner, E., Perry, J. K., Feng, J. Y., Porter, D. P., and Gotte, M. (2020) Remdesivir Is a Direct-Acting Antiviral That Inhibits RNA-Dependent RNA Polymerase from Severe Acute Respiratory Syndrome Coronavirus 2 with High Potency. *J. Biol. Chem.* 295, 6785.

(11) Wang, M., Cao, R., Zhang, L., Yang, X., Liu, J., Xu, M., Shi, Z., Hu, Z., Zhong, W., and Xiao, G. (2020) Remdesivir and Chloroquine Effectively Inhibit the Recently Emerged Novel Coronavirus (2019-NCoV) in Vitro. *Cell Res.* 30 (3), 269−271.

(12) Sheahan, T. P., Sims, A. C., Zhou, S., Graham, R. L., Pruijssers, A. J., Agostini, M. L., Leist, S. R., Schafer, A., Dinnon, K. H., Stevens, L. J., Chappell, J. D., Lu, X., Hughes, T. M., George, A. S., Hill, C. S., Montgomery, S. A., Brown, A. J., Bluemling, G. R., Natchus, M. G., Saindane, M., Kolykhalov, A. A., Painter, G., Harcourt, J., Tamin, A., Thornburg, N. J., Swanstrom, R., Denison, M. R., and Baric, R. S. (2020) An Orally Bioavailable Broad-Spectrum Antiviral Inhibits SARS-CoV-2 in Human Airway Epithelial Cell Cultures and Multiple Coronaviruses in Mice. *Sci. Transl. Med.* 12 (541), No. eabb5883.

(13) Williamson, B. N., Feldmann, F., Schwarz, B., Meade-White, K., Porter, D. P., Schulz, J., van Doremalen, N., Leighton, I., Yinda, C. K., Perez-Perez, L., Okumura, A., Lovaglio, J., Hanley, P. W., Saturday, G., Bosio, C. M., Anzick, S., Barbian, K., Cihlar, T., Martens, C., Scott, D. P., Munster, V. J., and de Wit, E. (2020) Clinical Benefit of Remdesivir in Rhesus Macaques Infected with SARS-CoV-2. *bioRxiv*, DOI: 10.1101/2020.04.15.043166.

(14) Grein, J., Ohmagari, N., Shin, D., Diaz, G., Asperges, E., Castagna, A., Feldt, T., Green, G., Green, M. L., Lescure, F.-X., Nicastri, E., Oda, R., Yo, K., Quiros-Roldan, E., Studemeister, A., Redinski, J., Ahmed, S., Bernett, J., Chelliah, D., Chen, D., Chihara, S., Cohen, S. H., Cunningham, J., D'Arminio Monforte, A., Ismail, S., Kato, H., Lapadula, G., L'Her, E., Maeno, T., Majumder, S., Massari, M., Mora-Rillo, M., Mutoh, Y., Nguyen, D., Verweij, E., Zoufaly, A., Osinusi, A. O., DeZure, A., Zhao, Y., Zhong, L., Chokkalingam, A., Elboudwarej, E., Telep, L., Timbs, L., Henne, I., Sellers, S., Cao, H., Tan, S. K., Winterbourne, L., Desai, P., Mera, R., Gaggar, A., Myers, R. P., Brainard, D. M., Childs, R., and Flanigan, T. (2020) Compassionate Use of Remdesivir for Patients with Severe Covid-19. *N. Engl. J. Med.* 382, 2327.

(15) Wang, Y., Zhang, D., Du, G., Du, R., Zhao, J., Jin, Y., Fu, S., Gao, L., Cheng, Z., Lu, Q., Hu, Y., Luo, G., Wang, K., Lu, Y., Li, H., Wang, S., Ruan, S., Yang, C., Mei, C., Wang, Y., Ding, D., Wu, F., Tang, X., Ye, X., Ye, Y., Liu, B., Yang, J., Yin, W., Wang, A., Fan, G., Zhou, F., Liu, Z., Gu, X., Xu, J., Shang, L., Zhang, Y., Cao, L., Guo, T., Wan, Y., Qin, H., Jiang, Y., Jaki, T., Hayden, F. G., Horby, P. W., Cao, B., and Wang, C. (2020) Remdesivir in Adults with Severe COVID-19: A Randomised, Double-Blind, Placebo-Controlled, Multicentre Trial. *Lancet* 395 (10236), 1569−1578.

(16) Beigel, J. H., Tomashek, K. M., Dodd, L. E., Mehta, A. K., Zingman, B. S., Kalil, A. C., Hohmann, E., Chu, H. Y., Luetkemeyer, A., Kline, S., Lopez de Castilla, D., Finberg, R. W., Dierberg, K., Tapson, V., Hsieh, L., Patterson, T. F., Paredes, R., Sweeney, D. A., Short, W. R., Touloumi, G., Lye, D. C., Ohmagari, N., Oh, M., Ruiz-Palacios, G. M., Benfield, T., Fatkenheuer, G., Kortepeter, M. G., Atmar, R. L., Creech, C. B., Lundgren, J., Babiker, A. G., Pett, S., Neaton, J. D., Burgess, T. H., Bonnett, T., Green, M., Makowski, M., Osinusi, A., Nayak, S., and Lane, H. C. (2020) Remdesivir for the Treatment of Covid-19 □ Preliminary Report. *N. Engl. J. Med.*, DOI: 10.1056/NEJMoa2007764.

(17) De Clercq, E. (2015) Ebola Virus (EBOV) Infection: Therapeutic Strategies. *Biochem. Pharmacol.* 93 (1), 1−10.

(18) Furuta, Y., Komeno, T., and Nakamura, T. (2017) Favipiravir (T-705), a Broad Spectrum Inhibitor of Viral RNA Polymerase. *Proc. Jpn. Acad., Ser. B* 93 (7), 449−463.

J

(19) Du, Y.-X., and Chen, X.-P. (2020) Favipiravir: Pharmacokinetics and Concerns About Clinical Trials for 2019-NCoV Infection. *Clin. Pharmacol. Ther.* 108 (2), 242−247.

(20) Oestereich, L., Lüdtke, A., Wurr, S., Rieger, T., Muñoz-Fontela, C., and Günther, S. (2014) Successful Treatment of Advanced Ebola Virus Infection with T-705 (Favipiravir) in a Small Animal Model. *Antiviral Res.* 105, 17−21.

(21) Bai, C.-Q., Mu, J.-S., Kargbo, D., Song, Y.-B., Niu, W.-K., Nie, W.-M., Kanu, A., Liu, W.-W., Wang, Y.-P., Dafae, F., Yan, T., Hu, Y., Deng, Y.-Q., Lu, H.-J., Yang, F., Zhang, X.-G., Sun, Y., Cao, Y.-X., Su, H.-X., Sun, Y., Liu, W.-S., Wang, C.-Y., Qian, J., Liu, L., Wang, H., Tong, Y.-G., Liu, Z.-Y., Chen, Y.-S., Wang, H.-Q., Kargbo, B., Gao, G. F., and Jiang, J.-F. (2016) Clinical and Virological Characteristics of Ebola Virus Disease Patients Treated With Favipiravir (T-705)☐ Sierra Leone, 2014. *Clin. Infect. Dis.* 63 (10), 1288−1294.

(22) Cai, Q., Yang, M., Liu, D., Chen, J., Shu, D., Xia, J., Liao, X., Gu, Y., Cai, Q., Yang, Y., Shen, C., Li, X., Peng, L., Huang, D., Zhang, J., Zhang, S., Wang, F., Liu, J., Chen, L., Chen, S., Wang, Z., Zhang, Z., Cao, R., Zhong, W., Liu, Y., and Liu, L. (2020) Experimental Treatment with Favipiravir for COVID-19: An Open-Label Control Study. *Engineering*, DOI: 10.1016/j.eng.2020.03.007.

(23) Chen, C., Zhang, Y., Huang, J., Yin, P., Cheng, Z., Wu, J., Chen, S., Zhang, Y., Chen, B., Lu, M., Luo, Y., Ju, L., Zhang, J., and Wang, X. (2020) Favipiravir versus Arbidol for COVID-19: A Randomized Clinical Trial. *medRxiv*, DOI: 10.1101/2020.03.17.20037432.

(24) Warren, T. K., Wells, J., Panchal, R. G., Stuthman, K. S., Garza, N. L., Van Tongeren, S. A., Dong, L., Retterer, C. J., Eaton, B. P., Pegoraro, G., Honnold, S., Bantia, S., Kotian, P., Chen, X., Taubenheim, B. R., Welch, L. S., Minning, D. M., Babu, Y. S., Sheridan, W. P., and Bavari, S. (2014) Protection against Filovirus Diseases by a Novel Broad-Spectrum Nucleoside Analogue BCX4430. *Nature* 508 (7496), 402−405.

(25) Elfiky, A. A. (2020) Ribavirin, Remdesivir, Sofosbuvir, Galidesivir, and Tenofovir against SARS-CoV-2 RNA Dependent RNA Polymerase (RdRp): A Molecular Docking Study. *Life Sci.* 253, 117592.

(26) Hegyi, A., and Ziebuhr, J. (2002) Conservation of Substrate Specificities among Coronavirus Main Proteases. *J. Gen. Virol.* 83, 595−599.

(27) Ohashi, H., Watashi, K., Saso, W., Shionoya, K., Iwanami, S., Hirokawa, T., Shirai, T., Kanaya, S., Ito, Y., Kim, K. S., Nishioka, K., Ando, S., Ejima, K., Koizumi, Y., Tanaka, T., Aoki, S., Kuramochi, K., Suzuki, T., Maenaka, K., Matano, T., Muramatsu, M., Saijo, M., Aihara, K., Iwami, S., Takeda, M., McKeating, J. A., and Wakita, T. (2020) Multidrug Treatment with Nelfinavir and Cepharanthine against COVID-19. *bioRxiv*, DOI: 10.1101/2020.04.14.039925.

(28) Cao, B., Wang, Y., Wen, D., Liu, W., Wang, J., Fan, G., Ruan, L., Song, B., Cai, Y., Wei, M., Li, X., Xia, J., Chen, N., Xiang, J., Yu, T., Bai, T., Xie, X., Zhang, L., Li, C., Yuan, Y., Chen, H., Li, H., Huang, H., Tu, S., Gong, F., Liu, Y., Wei, Y., Dong, C., Zhou, F., Gu, X., Xu, J., Liu, Z., Zhang, Y., Li, H., Shang, L., Wang, K., Li, K., Zhou, X., Dong, X., Qu, Z., Lu, S., Hu, X., Ruan, S., Luo, S., Wu, J., Peng, L., Cheng, F., Pan, L., Zou, J., Jia, C., Wang, J., Liu, X., Wang, S., Wu, X., Ge, Q., He, J., Zhan, H., Qiu, F., Guo, L., Huang, C., Jaki, T., Hayden, F. G., Horby, P. W., Zhang, D., and Wang, C. (2020) A Trial of Lopinavir−Ritonavir in Adults Hospitalized with Severe Covid-19. *N. Engl. J. Med.* 382 (19), 1787−1799.

(29) Yamamoto, N., Yang, R., Yoshinaka, Y., Amari, S., Nakano, T., Cinatl, J., Rabenau, H., Doerr, H. W., Hunsmann, G., Otaka, A., Tamamura, H., Fujii, N., and Yamamoto, N. (2004) HIV Protease Inhibitor Nelfinavir Inhibits Replication of SARS-Associated Coronavirus. *Biochem. Biophys. Res. Commun.* 318 (3), 719−725.

(30) Azad, G. K., and Tomar, R. S. (2014) Ebselen, a Promising Antioxidant Drug: Mechanisms of Action and Targets of Biological Pathways. *Mol. Biol. Rep.* 41 (8), 4865−4879.

(31) Kil, J., Lobarinas, E., Spankovich, C., Griffiths, S. K., Antonelli, P. J., Lynch, E. D., and Le Prell, C. G. (2017) Safety and Efficacy of Ebselen for the Prevention of Noise-Induced Hearing Loss: A Randomised, Double-Blind, Placebo-Controlled, Phase 2 Trial. *Lancet* 390 (10098), 969−979.

(32) Beckman, J. A., Goldfine, A. B., Leopold, J. A., and Creager, M. A. (2016) Ebselen Does Not Improve Oxidative Stress and Vascular Function in Patients with Diabetes: A Randomized, Crossover Trial. *Am. J. Physiol.-Heart Circ. Physiol.* 311 (6), H1431−H1436.

(33) Yamaguchi, T., Sano, K., Takakura, K., Saito, I., Shinohara, Y., Asano, T., and Yasuhara, H. (1998) Ebselen in Acute Ischemic Stroke. *Stroke* 29 (1), 12−17.

(34) Jin, Z., Du, X., Xu, Y., Deng, Y., Liu, M., Zhao, Y., Zhang, B., Li, X., Zhang, L., Peng, C., Duan, Y., Yu, J., Wang, L., Yang, K., Liu, F., Jiang, R., Yang, X., You, T., Liu, X., Yang, X., Bai, F., Liu, H., Liu, X., Guddat, L. W., Xu, W., Xiao, G., Qin, C., Shi, Z., Jiang, H., Rao, Z., and Yang, H. (2020) Structure of Mpro from SARS-CoV-2 and Discovery of Its Inhibitors. *Nature* 582, 289.

(35) Bekerman, E., and Einav, S. (2015) Combating Emerging Viral Threats. *Science* 348 (6232), 282.

(36) Hoffmann, M., Kleine-Weber, H., Schroeder, S., Krüger, N., Herrler, T., Erichsen, S., Schiergens, T. S., Herrler, G., Wu, N.-H., Nitsche, A., Müller, M. A., Drosten, C., and Pöhlmann, S. (2020) SARS-CoV-2 Cell Entry Depends on ACE2 and TMPRSS2 and Is Blocked by a Clinically Proven Protease Inhibitor. *Cell* 181 (2), 271−280.E8.

(37) Matsuyama, S., Nagata, N., Shirato, K., Kawase, M., Takeda, M., and Taguchi, F. (2010) Efficient Activation of the Severe Acute Respiratory Syndrome Coronavirus Spike Protein by the Transmembrane Protease TMPRSS2. *J. Virol.* 84 (24), 12658.

(38) Shirato, K., Kawase, M., and Matsuyama, S. (2013) Middle East Respiratory Syndrome Coronavirus Infection Mediated by the Transmembrane Serine Protease TMPRSS2. *J. Virol.* 87 (23), 12552.

(39) Iwata-Yoshikawa, N., Okamura, T., Shimizu, Y., Hasegawa, H., Takeda, M., and Nagata, N. (2019) TMPRSS2 Contributes to Virus Spread and Immunopathology in the Airways of Murine Models after Coronavirus Infection. *J. Virol.* 93 (6), No. e01815-18.

(40) Gibo, J., Ito, T., Kawabe, K., Hisano, T., Inoue, M., Fujimori, N., Oono, T., Arita, Y., and Nawata, H. (2005) Camostat Mesilate Attenuates Pancreatic Fibrosis via Inhibition of Monocytes and Pancreatic Stellate Cells Activity. *Lab. Invest.* 85 (1), 75−89.

(41) Zhou, Y., Vedantham, P., Lu, K., Agudelo, J., Carrion, R., Nunneley, J. W., Barnard, D., Pöhlmann, S., McKerrow, J. H., Renslo, A. R., and Simmons, G. (2015) Protease Inhibitors Targeting Coronavirus and Filovirus Entry. *Antiviral Res.* 116, 76−84.

(42) Yamamoto, M., Matsuyama, S., Li, X., Takeda, M., Kawaguchi, Y., Inoue, J., and Matsuda, Z. (2016) Identification of Nafamostat as a Potent Inhibitor of Middle East Respiratory Syndrome Coronavirus S Protein-Mediated Membrane Fusion Using the Split-Protein-Based Cell-Cell Fusion Assay. *Antimicrob. Agents Chemother.* 60 (11), 6532.

(43) Hoffmann, M., Schroeder, S., Kleine-Weber, H., Müller, M. A., Drosten, C., and Pöhlmann, S. (2020) Nafamostat Mesylate Blocks Activation of SARS-CoV-2: New Treatment Option for COVID-19. *Antimicrob. Agents Chemother.*, DOI: 10.1128/AAC.00754-20.

(44) Schor, S., and Einav, S. (2018) Repurposing of Kinase Inhibitors as Broad-Spectrum Antiviral Drugs. *DNA Cell Biol.* 37 (2), 63−69.

(45) Pagano, M. A., Tibaldi, E., Palù, G., and Brunati, A. M. (2013) Viral Proteins and Src Family Kinases: Mechanisms of Pathogenicity from a "Liaison Dangereuse." *World J. Virol.* 2 (2), 71−78.

(46) Shin, S. J., Jung, E., Kim, M., Baric, S. R., and Go, Y. Y. (2018) Saracatinib Inhibits Middle East Respiratory Syndrome-Coronavirus Replication In Vitro. *Viruses* 10 (6), 283.

(47) de Wispelaere, M., LaCroix, A. J., and Yang, P. L. (2013) The Small Molecules AZD0530 and Dasatinib Inhibit Dengue Virus RNA Replication via Fyn Kinase. *J. Virol.* 87 (13), 7367.

(48) Chu, J. J. H., and Yang, P. L. (2007) C-Src Protein Kinase Inhibitors Block Assembly and Maturation of Dengue Virus. *Proc. Natl. Acad. Sci. U. S. A.* 104 (9), 3520.

(49) Dyall, J., Coleman, C. M., Hart, B. J., Venkataraman, T., Holbrook, M. R., Kindrachuk, J., Johnson, R. F., Olinger, G. G., Jahrling, P. B., Laidlaw, M., Johansen, L. M., Lear-Rooney, C. M.,

K

Glass, P. J., Hensley, L. E., and Frieman, M. B. (2014) Repurposing of Clinically Developed Drugs for Treatment of Middle East Respiratory Syndrome Coronavirus Infection. *Antimicrob. Agents Chemother. 58* (8), 4885.

(50) Reeves, P. M., Smith, S. K., Olson, V. A., Thorne, S. H., Bornmann, W., Damon, I. K., and Kalman, D. (2011) Variola and Monkeypox Viruses Utilize Conserved Mechanisms of Virion Motility and Release That Depend on Abl and Src Family Tyrosine Kinases. *J. Virol. 85* (1), 21.

(51) Clark, M. J., Miduturu, C., Schmidt, A. G., Zhu, X., Pitts, J. D., Wang, J., Potisopon, S., Zhang, J., Wojciechowski, A., Hann Chu, J. J., Gray, N. S., and Yang, P. L. (2016) GNF-2 Inhibits Dengue Virus by Targeting Abl Kinases and the Viral E Protein. *Cell Chem. Biol. 23* (4), 443−452.

(52) Coleman, C. M., Sisk, J. M., Mingo, R. M., Nelson, E. A., White, J. M., and Frieman, M. B. (2016) Abelson Kinase Inhibitors Are Potent Inhibitors of Severe Acute Respiratory Syndrome Coronavirus and Middle East Respiratory Syndrome Coronavirus Fusion. *J. Virol. 90* (19), 8924.

(53) Kindrachuk, J., Ork, B., Hart, B. J., Mazur, S., Holbrook, M. R., Frieman, M. B., Traynor, D., Johnson, R. F., Dyall, J., Kuhn, J. H., Olinger, G. G., Hensley, L. E., and Jahrling, P. B. (2015) Antiviral Potential of ERK/MAPK and PI3K/AKT/MTOR Signaling Modulation for Middle East Respiratory Syndrome Coronavirus Infection as Identified by Temporal Kinome Analysis. *Antimicrob. Agents Chemother. 59* (2), 1088.

(54) Bouhaddou, M., Memon, D., Meyer, B., White, K. M., Rezelj, V. V., Correa Marrero, M., Polacco, B. J., Melnyk, J. E., Ulferts, S., Kaake, R. M., Batra, J., Richards, A. L., Stevenson, E., Gordon, D. E., Rojc, A., Obernier, K., Fabius, J. M., Soucheray, M., Miorin, L., Moreno, E., Koh, C., Tran, Q. D., Hardy, A., Robinot, R., Vallet, T., Nilsson-Payant, B. E., Hernandez-Armenta, C., Dunham, A., Weigang, S., Knerr, J., Modak, M., Quintero, D., Zhou, Y., Dugourd, A., Valdeolivas, A., Patil, T., Li, Q., Hüttenhain, R., Cakir, M., Muralidharan, M., Kim, M., Jang, G., Tutuncuoglu, B., Hiatt, J., Guo, J. Z., Xu, J., Bouhaddou, S., Mathy, C. J. P., Gaulton, A., Manners, E. J., Felix, E., Shi, Y., Goff, M., Lim, J. K., McBride, T., O'Neal, M. C., Cai, Y., Chang, J. C. J., Broadhurst, D. J., Klippsten, S., De Wit, E., Leach, A. R., Kortemme, T., Shoichet, B., Ott, M., Saez-Rodriguez, J., tenOever, B. R., Mullins, R. D., Fischer, E. R., Kochs, G., Grosse, R., García-Sastre, A., Vignuzzi, M., Johnson, J. R., Shokat, K. M., Swaney, D. L., Beltrao, P., and Krogan, N. J. (2020) The Global Phosphorylation Landscape of SARS-CoV-2 Infection. *Cell*, DOI: 10.1016/j.cell.2020.06.034.

(55) Mizutani, T., Fukushi, S., Saijo, M., Kurane, I., and Morikawa, S. (2004) Phosphorylation of P38 MAPK and Its Downstream Targets in SARS Coronavirus-Infected Cells. *Biochem. Biophys. Res. Commun. 319* (4), 1228−1234.

(56) Cai, X., Xu, Y., Cheung, A. K., Tomlinson, R. C., Alcazar-Roman, A., Murphy, L., Billich, A., Zhang, B., Feng, Y., Klumpp, M., Rondeau, J.-M., Fazal, A. N., Wilson, C. J., Myer, V., Joberty, G., Bouwmeester, T., Labow, M. A., Finan, P. M., Porter, J. A., Ploegh, H. L., Baird, D., De Camilli, P., Tallarico, J. A., and Huang, Q. (2013) PIKfyve, a Class III PI Kinase, Is the Target of the Small Molecular IL-12/IL-23 Inhibitor Apilimod and a Player in Toll-like Receptor Signaling. *Chem. Biol. 20* (7), 912−921.

(57) Ou, X., Liu, Y., Lei, X., Li, P., Mi, D., Ren, L., Guo, L., Guo, R., Chen, T., Hu, J., Xiang, Z., Mu, Z., Chen, X., Chen, J., Hu, K., Jin, Q., Wang, J., and Qian, Z. (2020) Characterization of Spike Glycoprotein of SARS-CoV-2 on Virus Entry and Its Immune Cross-Reactivity with SARS-CoV. *Nat. Commun. 11* (1), 1620.

(58) Mita, M. M., Mita, A. C., Moseley, J. L., Poon, J., Small, K. A., Jou, Y.-M., Kirschmeier, P., Zhang, D., Zhu, Y., Statkevich, P., Sankhala, K. K., Sarantopoulos, J., Cleary, J. M., Chiriac, L. R., Rodig, S. J., Bannerji, R., and Shapiro, G. I. (2017) Phase 1 Safety, Pharmacokinetic and Pharmacodynamic Study of the Cyclin-Dependent Kinase Inhibitor Dinaciclib Administered Every Three Weeks in Patients with Advanced Malignancies. *Br. J. Cancer 117* (9), 1258−1268.

(59) Xu, J., Shi, P.-Y., Li, H., and Zhou, J. (2020) Broad Spectrum Antiviral Agent Niclosamide and Its Therapeutic Potential. *ACS Infect. Dis. 6* (5), 909−915.

(60) Wu, C.-J., Jan, J.-T., Chen, C.-M., Hsieh, H.-P., Hwang, D.-R., Liu, H.-W., Liu, C.-Y., Huang, H.-W., Chen, S.-C., Hong, C.-F., Lin, R.-K., Chao, Y.-S., and Hsu, J. T. A. (2004) Inhibition of Severe Acute Respiratory Syndrome Coronavirus Replication by Niclosamide. *Antimicrob. Agents Chemother. 48* (7), 2693.

(61) Gassen, N. C., Niemeyer, D., Muth, D., Corman, V. M., Martinelli, S., Gassen, A., Hafner, K., Papies, J., Mösbauer, K., Zellner, A., Zannas, A. S., Herrmann, A., Holsboer, F., Brack-Werner, R., Boshart, M., Müller-Myhsok, B., Drosten, C., Müller, M. A., and Rein, T. (2019) SKP2 Attenuates Autophagy through Beclin1-Ubiquitination and Its Inhibition Reduces MERS-Coronavirus Infection. *Nat. Commun. 10* (1), 5770.

(62) Jeon, S., Ko, M., Lee, J., Choi, I., Byun, S. Y., Park, S., Shum, D., and Kim, S. (2020) Identification of Antiviral Drug Candidates against SARS-CoV-2 from FDA-Approved Drugs. *Antimicrob. Agents Chemother. 64*, e00819-20.

(63) Frayha, G. J., Smyth, J. D., Gobert, J. G., and Savel, J. (1997) The Mechanisms of Action of Antiprotozoal and Anthelmintic Drugs in Man. *Gen. Pharmacol. 28* (2), 273−299.

(64) Chen, W., Mook, R. A., Premont, R. T., and Wang, J. (2018) Niclosamide: Beyond an Antihelminthic Drug. *Cell. Signalling 41*, 89−96.

(65) McChesney, E. W. (1983) Animal Toxicity and Pharmacokinetics of Hydroxychloroquine Sulfate. *Am. J. Med. 75* (1), 11−18.

(66) Farias, K. J. S., Machado, P. R. L., Muniz, J. A. P. C., Imbeloni, A. A., and da Fonseca, B. A. L. (2015) Antiviral Activity of Chloroquine Against Dengue Virus Type 2 Replication in Aotus Monkeys. *Viral Immunol. 28* (3), 161−169.

(67) Borges, M. C., Castro, L. A., and Fonseca, B. A. L. de. (2013) Chloroquine Use Improves Dengue-Related Symptoms. *Mem. Inst. Oswaldo Cruz 108* (5), 596−599.

(68) Tricou, V., Minh, N. N., Van, T. P., Lee, S. J., Farrar, J., Wills, B., Tran, H. T., and Simmons, C. P. (2010) A Randomized Controlled Trial of Chloroquine for the Treatment of Dengue in Vietnamese Adults. *PLoS Neglected Trop. Dis. 4* (8), No. e785.

(69) Yan, Y., Zou, Z., Sun, Y., Li, X., Xu, K.-F., Wei, Y., Jin, N., and Jiang, C. (2013) Anti-Malaria Drug Chloroquine Is Highly Effective in Treating Avian Influenza A H5N1 Virus Infection in an Animal Model. *Cell Res. 23* (2), 300−302.

(70) Mauthe, M., Orhon, I., Rocchi, C., Zhou, X., Luhr, M., Hijlkema, K.-J., Coppes, R. P., Engedal, N., Mari, M., and Reggiori, F. (2018) Chloroquine Inhibits Autophagic Flux by Decreasing Autophagosome-Lysosome Fusion. *Autophagy 14* (8), 1435−1455.

(71) Vincent, M. J., Bergeron, E., Benjannet, S., Erickson, B. R., Rollin, P. E., Ksiazek, T. G., Seidah, N. G., and Nichol, S. T. (2005) Chloroquine Is a Potent Inhibitor of SARS Coronavirus Infection and Spread. *Virol. J. 2* (1), 69.

(72) Keyaerts, E., Vijgen, L., Maes, P., Neyts, J., and Ranst, M. V. (2004) In Vitro Inhibition of Severe Acute Respiratory Syndrome Coronavirus by Chloroquine. *Biochem. Biophys. Res. Commun. 323* (1), 264−268.

(73) de Wilde, A. H., Jochmans, D., Posthuma, C. C., Zevenhoven-Dobbe, J. C., van Nieuwkoop, S., Bestebroer, T. M., van den Hoogen, B. G., Neyts, J., and Snijder, E. J. (2014) Screening of an FDA-Approved Compound Library Identifies Four Small-Molecule Inhibitors of Middle East Respiratory Syndrome Coronavirus Replication in Cell Culture. *Antimicrob. Agents Chemother. 58* (8), 4875.

(74) Barnard, D. L., Day, C. W., Bailey, K., Heiner, M., Montgomery, R., Lauridsen, L., Chan, P. K., and Sidwell, R. W. (2006) Evaluation of Immunomodulators, Interferons and Known in Vitro SARS-CoV Inhibitors for Inhibition of SARS-Cov Replication in BALB/c Mice. *Antivir. Chem. Chemother. 17* (5), 275−284.

(75) Liu, J., Cao, R., Xu, M., Wang, X., Zhang, H., Hu, H., Li, Y., Hu, Z., Zhong, W., and Wang, M. (2020) Hydroxychloroquine, a Less

Toxic Derivative of Chloroquine, Is Effective in Inhibiting SARS-CoV-2 Infection in Vitro. *Cell Discovery* 6 (1), 16.

(76) Yao, X., Ye, F., Zhang, M., Cui, C., Huang, B., Niu, P., Liu, X., Zhao, L., Dong, E., Song, C., Zhan, S., Lu, R., Li, H., Tan, W., and Liu, D. (2020) In Vitro Antiviral Activity and Projection of Optimized Dosing Design of Hydroxychloroquine for the Treatment of Severe Acute Respiratory Syndrome Coronavirus 2 (SARS-CoV-2). *Clin. Infect. Dis.*, No. ciaa237.

(77) Pastick, K. A., Okafor, E. C., Wang, F., Lofgren, S. M., Skipper, C. P., Nicol, M. R., Pullen, M. F., Rajasingham, R., McDonald, E. G., Lee, T. C., Schwartz, I. S., Kelly, L. E., Lother, S. A., Mitja, O., Letang, E., Abassi, M., and Boulware, D. R. (2020) Review: Hydroxychloroquine and Chloroquine for Treatment of SARS-CoV-2 (COVID-19). *Open Forum Infect. Dis.* 7, ofaa130.

(78) Geleris, J., Sun, Y., Platt, J., Zucker, J., Baldwin, M., Hripcsak, G., Labella, A., Manson, D. K., Kubin, C., Barr, R. G., Sobieszczyk, M. E., and Schluger, N. W. (2020) Observational Study of Hydroxychloroquine in Hospitalized Patients with Covid-19. *N. Engl. J. Med.* 382 (25), 2411−2418.

(79) Arshad, S., Kilgore, P., Chaudhry, Z. S., Jacobsen, G., Wang, D. D., Huitsing, K., Brar, I., Alangaden, G. J., Ramesh, M. S., McKinnon, J. E., O'Neill, W., Zervos, M., Nauriyal, V., Hamed, A. A., Nadeem, O., Swiderek, J., Godfrey, A., Jennings, J., Gardner-Gray, J., Ackerman, A. M., Lezotte, J., Ruhala, J., Fadel, R., Vahia, A., Gudipati, S., Parraga, T., Shallal, A., Maki, G., Tariq, Z., Suleyman, G., Yared, N., Herc, E., Williams, J., Lanfranco, O. A., Bhargava, P., and Reyes, K. (2020) Treatment with Hydroxychloroquine, Azithromycin, and Combination in Patients Hospitalized with COVID-19. *Int. J. Infect. Dis.* 97, 396−403.

(80) Borba, M. G. S., Val, F. F. A., Sampaio, V. S., Alexandre, M. A. A., Melo, G. C., Brito, M., Mourao, M. P. G., Brito-Sousa, J. D., Baía-Da-Silva, D., Guerra, M. V. F., Hajjar, L. A., Pinto, R. C., Balieiro, A. A. S., Pacheco, A. G. F., Santos, J. D. O., Jr, Naveca, F. G., Xavier, M. S., Siqueira, A. M., Schwarzbold, A., Croda, J., Nogueira, M. L., Romero, G. A. S., Bassat, Q., Fontes, C. J., Albuquerque, B. C., Daniel-Ribeiro, C.-T., Monteiro, W. M., Lacerda, M. V. G., and for the CloroCovid-19 Team (2020) Effect of High vs Low Doses of Chloroquine Diphosphate as Adjunctive Therapy for Patients Hospitalized With Severe Acute Respiratory Syndrome Coronavirus 2 (SARS-CoV-2) Infection: A Randomized Clinical Trial. *JAMA Netw. Open 3* (4), No. e208857.

(81) *Coronavirus (COVID-19) Update: FDA Revokes Emergency Use Authorization for Chloroquine and Hydroxychloroquine*, https://www.fda.gov/news-events/press-announcements/coronavirus-covid-19-update-fda-revokes-emergency-use-authorization-chloroquine-and.

(82) Tay, M. Z., Poh, C. M., Renia, L., MacAry, P. A., and Ng, L. F. P. (2020) The Trinity of COVID-19: Immunity, Inflammation and Intervention. *Nat. Rev. Immunol.* 20, 363.

(83) Shi, Y., Wang, Y., Shao, C., Huang, J., Gan, J., Huang, X., Bucci, E., Piacentini, M., Ippolito, G., and Melino, G. (2020) COVID-19 Infection: The Perspectives on Immune Responses. *Cell Death Differ.* 27 (5), 1451−1454.

(84) Venkataraman, T., Coleman, C. M., and Frieman, M. B. (2017) Overactive Epidermal Growth Factor Receptor Signaling Leads to Increased Fibrosis after Severe Acute Respiratory Syndrome Coronavirus Infection. *J. Virol.* 91 (12), No. e00182-17.

(85) Chu, H., Chan, J. F.-W., Wang, Y., Yuen, T. T.-T., Chai, Y., Hou, Y., Shuai, H., Yang, D., Hu, B., Huang, X., Zhang, X., Cai, J.-P., Zhou, J., Yuan, S., Kok, K.-H., To, K. K.-W., Chan, I. H.-Y., Zhang, A. J., Sit, K.-Y., Au, W.-K., and Yuen, K.-Y. (2020) Comparative Replication and Immune Activation Profiles of SARS-CoV-2 and SARS-CoV in Human Lungs: An Ex Vivo Study with Implications for the Pathogenesis of COVID-19. *Clin. Infect. Dis.*, No. ciaa410.

(86) Chan, J. F.-W., Yao, Y., Yeung, M.-L., Deng, W., Bao, L., Jia, L., Li, F., Xiao, C., Gao, H., Yu, P., Cai, J.-P., Chu, H., Zhou, J., Chen, H., Qin, C., and Yuen, K.-Y. (2015) Treatment With Lopinavir/Ritonavir or Interferon-B1b Improves Outcome of MERS-CoV Infection in a Nonhuman Primate Model of Common Marmoset. *J. Infect. Dis.* 212 (12), 1904−1913.

(87) Loutfy, M. R., Blatt, L. M., Siminovitch, K. A., Ward, S., Wolff, B., Lho, H., Pham, D. H., Deif, H., LaMere, E. A., Chang, M., Kain, K. C., Farcas, G. A., Ferguson, P., Latchford, M., Levy, G., Dennis, J. W., Lai, E. K. Y., and Fish, E. N. (2003) Interferon Alfacon-1 Plus Corticosteroids in Severe Acute Respiratory Syndrome A Preliminary Study. *JAMA* 290 (24), 3222−3228.

(88) Lokugamage, K. G., Schindewolf, C., and Menachery, V. D. (2020) SARS-CoV-2 Sensitive to Type I Interferon Pretreatment. *bioRxiv*, DOI: 10.1101/2020.03.07.982264.

(89) Zhou, Q., Chen, V., Shannon, C. P., Wei, X.-S., Xiang, X., Wang, X., Wang, Z.-H., Tebbutt, S. J., Kollmann, T. R., and Fish, E. N. (2020) Interferon-A2b Treatment for COVID-19. *Front. Immunol.* 11, 1061.

(90) Muir, A. J., Arora, S., Everson, G., Flisiak, R., George, J., Ghalib, R., Gordon, S. C., Gray, T., Greenbloom, S., Hassanein, T., Hillson, J., Horga, M. A., Jacobson, I. M., Jeffers, L., Kowdley, K. V., Lawitz, E., Lueth, S., Rodriguez-Torres, M., Rustgi, V., Shemanski, L., Shiffman, M. L., Srinivasan, S., Vargas, H. E., Vierling, J. M., Xu, D., Lopez-Talavera, J. C., and Zeuzem, S. (2014) A Randomized Phase 2b Study of Peginterferon Lambda-1a for the Treatment of Chronic HCV Infection. *J. Hepatol.* 61 (6), 1238−1246.

(91) Broggi, A., Granucci, F., and Zanoni, I. (2020) Type III Interferons: Balancing Tissue Tolerance and Resistance to Pathogen Invasion. *J. Exp. Med.* 217, No. e20190295.

(92) Prokunina-Olsson, L., Alphonse, N., Dickenson, R. E., Durbin, J. E., Glenn, J. S., Hartmann, R., Kotenko, S. V., Lazear, H. M., O'Brien, T. R., Odendall, C., Onabajo, O. O., Piontkivska, H., Santer, D. M., Reich, N. C., Wack, A., and Zanoni, I. (2020) COVID-19 and Emerging Viral Infections: The Case for Interferon Lambda. *J. Exp. Med.* 217, No. e20200653.

(93) Hamming, O. J., Terczynska-Dyla, E., Vieyres, G., Dijkman, R., Jørgensen, S. E., Akhtar, H., Siupka, P., Pietschmann, T., Thiel, V., and Hartmann, R. (2013) Interferon Lambda 4 Signals via the IFNλ Receptor to Regulate Antiviral Activity against HCV and Coronaviruses. *EMBO J.* 32 (23), 3055−3065.

(94) Mordstein, M., Neugebauer, E., Ditt, V., Jessen, B., Rieger, T., Falcone, V., Sorgeloos, F., Ehl, S., Mayer, D., Kochs, G., Schwemmle, M., Günther, S., Drosten, C., Michiels, T., and Staeheli, P. (2010) Lambda Interferon Renders Epithelial Cells of the Respiratory and Gastrointestinal Tracts Resistant to Viral Infections. *J. Virol.* 84 (11), 5670.

(95) Chen, L., Liu, H. G., Liu, W., Liu, J., Liu, K., Shang, J., Deng, Y., and Wei, S. (2020) [Analysis of Clinical Features of 29 Patients with 2019 Novel Coronavirus Pneumonia]. *Zhonghua Jie He He Hu Xi Za Zhi Zhonghua Jiehe He Huxi Zazhi Chin. J. Tuberc. Respir. Dis.* 43 (3), 203−208.

(96) Russell, C. D., Millar, J. E., and Baillie, J. K. (2020) Clinical Evidence Does Not Support Corticosteroid Treatment for 2019-NCoV Lung Injury. *Lancet* 395 (10223), 473−475.

(97) Shang, L., Zhao, J., Hu, Y., Du, R., and Cao, B. (2020) On the Use of Corticosteroids for 2019-NCoV Pneumonia. *Lancet* 395 (10225), 683−684.

(98) Li, H., Chen, C., Hu, F., Wang, J., Zhao, Q., Gale, R. P., and Liang, Y. (2020) Impact of Corticosteroid Therapy on Outcomes of Persons with SARS-CoV-2, SARS-CoV, or MERS-CoV Infection: A Systematic Review and Meta-Analysis. *Leukemia* 34 (6), 1503−1511.

(99) Horby, P., Lim, W. S., Emberson, J., Mafham, M., Bell, J., Linsell, L., Staplin, N., Brightling, C., Ustianowski, A., Elmahi, E., Prudon, B., Green, C., Felton, T., Chadwick, D., Rege, K., Fegan, C., Chappell, L. C., Faust, S. N., Jaki, T., Jeffery, K., Montgomery, A., Rowan, K., Juszczak, E., Baillie, J. K., Haynes, R., and Landray, M. J. (2020) Effect of Dexamethasone in Hospitalized Patients with COVID-19: Preliminary Report. *medRxiv*, DOI: 10.1101/2020.06.22.20137273.

(100) Kubo, S., Nakayamada, S., Sakata, K., Kitanaga, Y., Ma, X., Lee, S., Ishii, A., Yamagata, K., Nakano, K., and Tanaka, Y. (2018) Janus Kinase Inhibitor Baricitinib Modulates Human Innate and Adaptive Immune System. *Front. Immunol.* 9, 1510.

(101) Yaekura, A., Yoshida, K., Morii, K., Oketani, Y., Okumura, I., Kaneshiro, K., Shibanuma, N., Sakai, Y., and Hashiramoto, A. (2020) Chronotherapy Targeting Cytokine Secretion Attenuates Collagen-Induced Arthritis in Mice. *Int. Immunopharmacol. 84*, 106549.

(102) Cantini, F., Niccoli, L., Matarrese, D., Nicastri, E., Stobbione, P., and Goletti, D. (2020) Baricitinib Therapy in COVID-19: A Pilot Study on Safety and Clinical Impact. *J. Infect. 81*, P318−356.

(103) Titanji, B. K., Farley, M. M., Mehta, A., Connor-Schuler, R., Moanna, A., Cribbs, S. K., O'Shea, J., DeSilva, K., Chan, B., Edwards, A., Gavegnano, C., Schinazi, R. F., and Marconi, V. C. (2020) Use of Baricitinib in Patients with Moderate and Severe COVID-19. *Clin. Infect. Dis.*, No. ciaa879.

(104) Wang, M., Rule, S., Zinzani, P. L., Goy, A., Casasnovas, O., Smith, S. D., Damaj, G., Doorduijn, J., Lamy, T., Morschhauser, F., Panizo, C., Shah, B., Davies, A., Eek, R., Dupuis, J., Jacobsen, E., Kater, A. P., Le Gouill, S., Oberic, L., Robak, T., Covey, T., Dua, R., Hamdy, A., Huang, X., Izumi, R., Patel, P., Rothbaum, W., Slatter, J. G., and Jurczak, W. (2018) Acalabrutinib in Relapsed or Refractory Mantle Cell Lymphoma (ACE-LY-004): A Single-Arm, Multicentre, Phase 2 Trial. *Lancet 391* (10121), 659−667.

(105) Roschewski, M., Lionakis, M. S., Sharman, J. P., Roswarski, J., Goy, A., Monticelli, M. A., Roshon, M., Wrzesinski, S. H., Desai, J. V., Zarakas, M. A., Collen, J., Rose, K. M., Hamdy, A., Izumi, R., Wright, G. W., Chung, K. K., Baselga, J., Staudt, L. M., and Wilson, W. H. (2020) Inhibition of Bruton Tyrosine Kinase in Patients with Severe COVID-19. *Sci. Immunol. 5* (48), No. eabd0110.

(106) Somers, E. C., Eschenauer, G. A., Troost, J. P., Golob, J. L., Gandhi, T. N., Wang, L., Zhou, N., Petty, L. A., Baang, J. H., Dillman, N. O., Frame, D., Gregg, K. S., Kaul, D. R., Nagel, J., Patel, T. S., Zhou, S., Lauring, A. S., Hanauer, D. A., Martin, E., Sharma, P., Fung, C. M., and Pogue, J. M. (2020) Tocilizumab for Treatment of Mechanically Ventilated Patients with COVID-19. *Clin. Infect. Dis.*, No. ciaa954.

(107) Rossotti, R., Travi, G., Ughi, N., Corradin, M., Baiguera, C., Fumagalli, R., Bottiroli, M., Mondino, M., Merli, M., Bellone, A., Basile, A., Ruggeri, R., Colombo, F., Moreno, M., Pastori, S., Perno, C. F., Tarsia, P., Epis, O. M., and Puoti, M. (2020) SAFETY AND EFFICACY OF ANTI-IL6-RECEPTOR TOCILIZUMAB USE IN SEVERE AND CRITICAL PATIENTS AFFECTED BY CORONA-VIRUS DISEASE 2019: A COMPARATIVE ANALYSIS. *J. Infect.*, DOI: 10.1016/j.jinf.2020.07.008.

(108) *Sanofi and Regeneron provide update on Kevzara (sarilumab) Phase 3 U.S. Trial in COVID-19 patients*, https://www.sanofi.com/en/media-room/press-releases/2020/2020-07-02-22-30-00.

(109) Wang, H., Liu, B., Tang, Y., Chang, P., Yao, L., Huang, B., Lodato, R. F., and Liu, Z. (2019) Improvement of Sepsis Prognosis by Ulinastatin: A Systematic Review and Meta-Analysis of Randomized Controlled Trials. *Front. Pharmacol. 10*, 1370.

(110) Liu, R., Qi, H., Wang, J., Wang, Y., Cui, L., Wen, Y., and Yin, C. (2014) Ulinastatin Activates the Renin−Angiotensin System to Ameliorate the Pathophysiology of Severe Acute Pancreatitis. *J. Gastroenterol. Hepatol. 29* (6), 1328−1337.

(111) South, A. M., Tomlinson, L., Edmonston, D., Hiremath, S., and Sparks, M. A. (2020) Controversies of Renin−Angiotensin System Inhibition during the COVID-19 Pandemic. *Nat. Rev. Nephrol. 16* (6), 305−307.

(112) Simões e Silva, A., Silveira, K., Ferreira, A., and Teixeira, M. (2013) ACE2, Angiotensin-(1−7) and Mas Receptor Axis in Inflammation and Fibrosis. *Br. J. Pharmacol. 169* (3), 477−492.

(113) Kuba, K., Imai, Y., Rao, S., Gao, H., Guo, F., Guan, B., Huan, Y., Yang, P., Zhang, Y., Deng, W., Bao, L., Zhang, B., Liu, G., Wang, Z., Chappell, M., Liu, Y., Zheng, D., Leibbrandt, A., Wada, T., Slutsky, A. S., Liu, D., Qin, C., Jiang, C., and Penninger, J. M. (2005) A Crucial Role of Angiotensin Converting Enzyme 2 (ACE2) in SARS Coronavirus−Induced Lung Injury. *Nat. Med. 11* (8), 875−879.

(114) Xu, J., Zhao, S., Teng, T., Abdalla, E. A., Zhu, W., Xie, L., Wang, Y., and Guo, X. (2020) Systematic Comparison of Two Animal-to-Human Transmitted Human Coronaviruses: SARS-CoV-2 and SARS-CoV. *Viruses 12* (2), 244.

(115) Kassiri, Z., Zhong, J., Guo, D., Basu, R., Wang, X., Liu, P. P., Scholey, J. W., Penninger, J. M., and Oudit, G. Y. (2009) Loss of Angiotensin-Converting Enzyme 2 Accelerates Maladaptive Left Ventricular Remodeling in Response to Myocardial Infarction. *Circ.: Heart Failure 2* (5), 446−455.

(116) Ju, M., He, H., Chen, S., Liu, Y., Liu, Y., Pan, S., Zheng, Y., Xuan, L., Zhu, D., and Luo, Z. (2019) Ulinastatin Ameliorates LPS-induced Pulmonary Inflammation and Injury by Blocking the MAPK/NF-κB Signaling Pathways in Rats. *Mol. Med. Rep.*, 3347−3354.

(117) Wang, W.-K., Lu, Q.-H., Wang, X., Wang, B., Wang, J., Gong, H.-P., Wang, L., Li, H., and Du, Y.-M. (2017) Ulinastatin Attenuates Diabetes-Induced Cardiac Dysfunction by the Inhibition of Inflammation and Apoptosis. *Exp. Ther. Med. 14* (3), 2497−2504.

(118) He, G., Li, Q., Li, W., Ruan, Y., Xiong, X., Song, X., and Zeng, F. (2020) Effect of Ulinastatin on Interleukins and Pulmonary Function in Bypass Patients: A Meta-Analysis of Randomized Controlled Trials. *Herz 45*, 335.

(119) Zhang, X., Zhu, Z., Jiao, W., Liu, W., Liu, F., and Zhu, X. (2019) Ulinastatin Treatment for Acute Respiratory Distress Syndrome in China: A Meta-Analysis of Randomized Controlled Trials. *BMC Pulm. Med. 19* (1), 196.

(120) Khajah, M. A., Fateel, M. M., Ananthalakshmi, K. V., and Luqmani, Y. A. (2016) Anti-Inflammatory Action of Angiotensin 1−7 in Experimental Colitis. *PLoS One 11* (3), No. e0150861.

(121) Hardie, W. D., Davidson, C., Ikegami, M., Leikauf, G. D., Le Cras, T. D., Prestridge, A., Whitsett, J. A., and Korfhagen, T. R. (2008) EGF Receptor Tyrosine Kinase Inhibitors Diminish Trans-forming Growth Factor-α-Induced Pulmonary Fibrosis. *Am. J. Physiol.-Lung Cell. Mol. Physiol. 294* (6), L1217−L1225.

(122) Kim, Y.-J., Cubitt, B., Chen, E., Hull, M. V., Chatterjee, A. K., Cai, Y., Kuhn, J. H., and de la Torre, J. C. (2019) The ReFRAME Library as a Comprehensive Drug Repurposing Library to Identify Mammarenavirus Inhibitors. *Antiviral Res. 169*, 104558.

(123) Gordon, D. E., Jang, G. M., Bouhaddou, M., Xu, J., Obernier, K., White, K. M., O'Meara, M. J., Rezelj, V. V., Guo, J. Z., Swaney, D. L., Tummino, T. A., Huettenhain, R., Kaake, R. M., Richards, A. L., Tutuncuoglu, B., Foussard, H., Batra, J., Haas, K., Modak, M., Kim, M., Haas, P., Polacco, B. J., Braberg, H., Fabius, J. M., Eckhardt, M., Soucheray, M., Bennett, M. J., Cakir, M., McGregor, M. J., Li, Q., Meyer, B., Roesch, F., Vallet, T., Mac Kain, A., Miorin, L., Moreno, E., Naing, Z. Z. C., Zhou, Y., Peng, S., Shi, Y., Zhang, Z., Shen, W., Kirby, I. T., Melnyk, J. E., Chorba, J. S., Lou, K., Dai, S. A., Barrio-Hernandez, I., Memon, D., Hernandez-Armenta, C., Lyu, J., Mathy, C. J. P., Perica, T., Pilla, K. B., Ganesan, S. J., Saltzberg, D. J., Rakesh, R., Liu, X., Rosenthal, S. B., Calviello, L., Venkataramanan, S., Liboy-Lugo, J., Lin, Y., Huang, X.-P., Liu, Y., Wankowicz, S. A., Bohn, M., Safari, M., Ugur, F. S., Koh, C., Savar, N. S., Tran, Q. D., Shengjuler, D., Fletcher, S. J., O'Neal, M. C., Cai, Y., Chang, J. C. J., Broadhurst, D. J., Klippsten, S., Sharp, P. P., Wenzell, N. A., Kuzuoglu, D., Wang, H.-Y., Trenker, R., Young, J. M., Cavero, D. A., Hiatt, J., Roth, T. L., Rathore, U., Subramanian, A., Noack, J., Hubert, M., Stroud, R. M., Frankel, A. D., Rosenberg, O. S., Verba, K. A., Agard, D. A., Ott, M., Emerman, M., Jura, N., von Zastrow, M., Verdin, E., Ashworth, A., Schwartz, O., d'Enfert, C., Mukherjee, S., Jacobson, M., Malik, H. S., Fujimori, D. G., Ideker, T., Craik, C. S., Floor, S. N., Fraser, J. S., Gross, J. D., Sali, A., Roth, B. L., Ruggero, D., Taunton, J., Kortemme, T., Beltrao, P., Vignuzzi, M., García-Sastre, A., Shokat, K. M., Shoichet, B. K., and Krogan, N. J. (2020) A SARS-CoV-2 Protein Interaction Map Reveals Targets for Drug Repurposing. *Nature 583*, 459.

(124) Madelain, V., Nguyen, T. H. T., Olivo, A., de Lamballerie, X., Guedj, J., Taburet, A.-M., and Mentré, F. (2016) Ebola Virus Infection: Review of the Pharmacokinetic and Pharmacodynamic Properties of Drugs Considered for Testing in Human Efficacy Trials. *Clin. Pharmacokinet. 55* (8), 907−923.

(125) Pacchetti, M., Marini, B., Benedetti, F., Giudici, F., Mauro, E., Storici, P., Masciovecchio, C., Angeletti, S., Ciccozzi, M., Gallo, R. C., Zella, D., and Ippodrino, R. (2020) Emerging SARS-CoV-2 Mutation

N

Hot Spots Include a Novel RNA-Dependent-RNA Polymerase Variant. *J. Transl. Med. 18* (1), 179.

(126) Haqqani, A. A., and Tilton, J. C. (2013) Entry Inhibitors and Their Use in the Treatment of HIV-1 Infection. *Antiviral Res. 98* (2), 158−170.

(127) Bekerman, E., Neveu, G., Shulla, A., Brannan, J., Pu, S.-Y., Wang, S., Xiao, F., Barouch-Bentov, R., Bakken, R. R., Mateo, R., Govero, J., Nagamine, C. M., Diamond, M. S., De Jonghe, S., Herdewijn, P., Dye, J. M., Randall, G., and Einav, S. (2017) Anticancer Kinase Inhibitors Impair Intracellular Viral Trafficking and Exert Broad-Spectrum Antiviral Effects. *J. Clin. Invest. 127* (4), 1338−1352.

(128) Lupberger, J., Zeisel, M. B., Xiao, F., Thumann, C., Fofana, I., Zona, L., Davis, C., Mee, C. J., Turek, M., Gorke, S., Royer, C., Fischer, B., Zahid, M. N., Lavillette, D., Fresquet, J., Cosset, F.-L., Rothenberg, S. M., Pietschmann, T., Patel, A. H., Pessaux, P., Doffoel, M., Raffelsberger, W., Poch, O., McKeating, J. A., Brino, L., and Baumert, T. F. (2011) EGFR and EphA2 Are Host Factors for Hepatitis C Virus Entry and Possible Targets for Antiviral Therapy. *Nat. Med. 17* (5), 589−595.

(129) Shiryaev, S. A., Mesci, P., Pinto, A., Fernandes, I., Sheets, N., Shresta, S., Farhy, C., Huang, C.-T., Strongin, A. Y., Muotri, A. R., and Terskikh, A. V. (2017) Repurposing of the Anti-Malaria Drug Chloroquine for Zika Virus Treatment and Prophylaxis. *Sci. Rep. 7* (1), 15771.

(130) Matt, U., Selchow, P., Dal Molin, M., Strommer, S., Sharif, O., Schilcher, K., Andreoni, F., Stenzinger, A., Zinkernagel, A. S., Zeitlinger, M., Sander, P., and Nemeth, J. (2017) Chloroquine Enhances the Antimycobacterial Activity of Isoniazid and Pyrazinamide by Reversing Inflammation-Induced Macrophage Efflux. *Int. J. Antimicrob. Agents 50* (1), 55−62.

(131) Gautret, P., Lagier, J.-C., Parola, P., Hoang, V. T., Meddeb, L., Mailhe, M., Doudier, B., Courjon, J., Giordanengo, V., Vieira, V. E., Dupont, H. T., Honore, S., Colson, P., Chabriere, E., La Scola, B., Rolain, J.-M., Brouqui, P., and Raoult, D. (2020) Hydroxychloroquine and Azithromycin as a Treatment of COVID-19: Results of an Open-Label Non-Randomized Clinical Trial. *Int. J. Antimicrob. Agents 56*, 105949.

(132) Berry, S. M., Petzold, E. A., Dull, P., Thielman, N. M., Cunningham, C. K., Corey, G. R., McClain, M. T., Hoover, D. L., Russell, J., Griffiss, J. M., and Woods, C. W. (2016) A Response Adaptive Randomization Platform Trial for Efficient Evaluation of Ebola Virus Treatments: A Model for Pandemic Response. *Clin. Trials 13* (1), 22−30.

(133) Barker, A., Sigman, C., Kelloff, G., Hylton, N., Berry, D., and Esserman, L. (2009) I-SPY 2: An Adaptive Breast Cancer Trial Design in the Setting of Neoadjuvant Chemotherapy. *Clin. Pharmacol. Ther. 86* (1), 97−100.

(134) Dean, N. E., Gsell, P.-S., Brookmeyer, R., Crawford, F. W., Donnelly, C. A., Ellenberg, S. S., Fleming, T. R., Halloran, M. E., Horby, P., Jaki, T., Krause, P. R., Longini, I. M., Mulangu, S., Muyembe-Tamfum, J.-J., Nason, M. C., Smith, P. G., Wang, R., Henao-Restrepo, A. M., and De Gruttola, V. (2020) Creating a Framework for Conducting Randomized Clinical Trials during Disease Outbreaks. *N. Engl. J. Med. 382* (14), 1366−1369.

O

Contents lists available at ScienceDirect

Antiviral Research

Research paper

BIKE regulates dengue virus infection and is a cellular target for broad-spectrum antivirals

Szuyuan Pu [a,1], Stanford Schor [a,1], Marwah Karim [a], Sirle Saul [a], Makeda Robinson [a], Sathish Kumar [a], Laura I. Prugar [b], Danielle E. Dorosky [b], Jennifer Brannan [b], John M. Dye [b], Shirit Einav [a,*]

[a] Department of Medicine, Division of Infectious Diseases and Geographic Medicine, Department of Microbiology and Immunology, Stanford University, CA, USA
[b] US Army Medical Research Institute of Infectious Diseases, Viral Immunology Branch, Fort Detrick, Maryland, USA

ABSTRACT

Global health is threatened by emerging viruses, many of which lack approved therapies and effective vaccines, including dengue, Ebola, and Venezuelan equine encephalitis. We previously reported that AAK1 and GAK, two of the four members of the understudied Numb-associated kinases (NAK) family, control intracellular trafficking of RNA viruses. Nevertheless, the role of BIKE and STK16 in viral infection remained unknown. Here, we reveal a requirement for BIKE, but not STK-16, in dengue virus (DENV) infection. BIKE mediates both early (post-internalization) and late (assembly/egress) stages in the DENV life cycle, and this effect is mediated in part by phosphorylation of a threonine 156 (T156) residue in the μ subunit of the adaptor protein (AP) 2 complex. Pharmacological compounds with potent anti-BIKE activity, including the investigational anticancer drug 5Z-7-oxozeaenol and more selective inhibitors, suppress DENV infection both *in vitro* and *ex vivo*. BIKE overexpression reverses the antiviral activity, validating that the mechanism of antiviral action is, at least in part, mediated by BIKE. Lastly, 5Z-7-oxozeaenol exhibits antiviral activity against viruses from three unrelated RNA viral families with a high genetic barrier to resistance. These findings reveal regulation of poorly understood stages of the DENV life cycle via BIKE signaling and establish a proof-of-principle that pharmacological inhibition of BIKE can be potentially used as a broad-spectrum strategy against acute emerging viral infections.

1. Introduction

Dengue virus (DENV) infection is a global health threat, estimated to infect ~390 million people annually (Bhatt et al., 2013; Messina et al., 2019). The geographical range of dengue, including in the developed world, has been expanding due to climate change and rapid urbanization (Messina et al., 2019). DENV is an enveloped, positive single-stranded RNA virus whose 10.7 kb genome encodes a single polyprotein that is proteolytically cleaved into individual proteins (Diamond and Pierson, 2015). The DENV nonstructural (NS) proteins form the viral replication machinery, whereas the capsid, pre-membrane (prM), and envelope (E) proteins form virions. DENV enters cells via clathrin-mediated endocytosis (Diamond and Pierson, 2015). The current model of infectious DENV production suggests that viral particles assemble in ER sites where the E protein is present (Welsch et al., 2009).

They become infectious once processed in the *trans*-Golgi network (TGN) and exit the cell via the secretory pathway (Kudelko et al., 2012). Nevertheless, a comprehensive understanding of the mechanisms that govern viral particle trafficking during DENV entry and assembly/egress is still lacking.

The Numb-Associated Kinases (NAK) family of Ser/Thr kinases is composed of AAK1 (adaptor-associated kinase 1), GAK (G-cyclin associated kinase), BIKE (BMP2-inducible kinase), and STK16 (serine/threonine kinase 16). This is a diverse family of kinases with only limited homology in the kinase domain and low homology in other protein regions (Sorrell et al., 2016). Several NAKs have been shown to regulate intracellular membrane trafficking (Sato et al., 2009; Sorensen and Conner, 2008). AAK1 and GAK phosphorylate the μ subunits of the endocytic adaptor protein (AP) complex 2 (AP2M1) and the secretory AP complex 1 (AP1M1), thereby stimulating their binding to cellular

cargo (Conner and Schmid, 2002). STK16, the most distantly related member of the family, regulates secretion in the constitutive secretory pathway at the TGN (In et al., 2014; López-Coral et al., 2018). BIKE, whose structure is closely related to AAK1, was identified as an accessory protein on a subset of clathrin-coated vesicles (CCVs) and was shown to bind the endocytic adaptor Numb and to phosphorylate a synthetic AP2M1 peptide (Kearns et al., 2001; Krieger et al., 2013; Sorrell et al., 2016). However, the biological relevance of AP2M1 phosphorylation by BIKE remained unclear and the functions of BIKE signaling are largely unknown.

We have previously reported that AAK1 and GAK regulate intracellular trafficking of hepatitis C virus (HCV) and DENV during viral entry and assembly/egress in part by phosphorylating AP1M1 and AP2M1 (Bekerman et al., 2017; Neveu et al., 2015; 2012; Xiao et al., 2018). Moreover, we have demonstrated that AAK1 and GAK are required for infections with several other RNA viral families and are the molecular targets underlying the broad-spectrum antiviral effect of various repurposed and novel kinase inhibitors that we have been developing (Bekerman et al., 2017; Pu et al., 2018; Verdonck et al., 2019). The role of the remaining members of the NAK family, BIKE and STK16, in DENV infection remained unknown.

Here, we demonstrate that BIKE, but not STK16, is required for two temporally distinct stages of the DENV life cycle and show that this effect is mediated in part by phosphorylation of a threonine 156 (T156) AP2M1 residue. Moreover, we demonstrate that pharmacological compounds with potent anti-BIKE activity inhibit DENV infection both *in vitro* and *ex vivo*, exhibit broad-spectrum antiviral activity with a high genetic barrier to resistance, and their mechanism of antiviral action is, at least in part, mediated by BIKE.

2. Materials and methods

2.1. Cell lines

Huh7, Huh7.5 (Apath LLC), T-REx-293, 293T BHK-21 (ATCC), U-87 MG (ATCC) and Vero (ATCC) cells were grown in Dulbecco's modified Eagle's medium (DMEM) (Mediatech) supplemented with 10% fetal bovine serum (Omega Scientific), 1% l-glutamine, and 1% penicillin-streptomycin (Gibco), with or without nonessential amino acids, and maintained in a humidified incubator with 5% $CO2$ at 37 °C. Cells were tested negative for mycoplasma by the MycoAlert mycoplasma detection kit (Lonza, Morristown, NJ).

2.2. Plasmids and virus constructs

DENV2 (New Guinea C strain) TSV01 Renilla reporter plasmid (pACYC NGC FL) was a gift from Pei-Yong Shi (University of Texas Medical Branch, Galveston, Texas, USA) (Zou et al., 2011) and DENV 16681 plasmid (pD2IC-30P-NBX) was a gift from Claire Huang (Centers for Disease Control and Prevention, Public Health Service, US Department of Health and Human Services, Fort Collins, Colorado, USA) (Huang et al., 2010). pCMV-DV2Rep was a gift from Andrew Yueh (Institute of Biotechnology and Pharmaceutical Research, Taipei, Taiwan) (Yang et al., 2013). The plasmid encoding VEEV TC-83 with a nanoluciferase reporter (VEEV TC-83-Cap-NLuc-Tav, hereafter VEEV-TC-83-nLuc) was a gift from Dr. William B. Klimstra (Department of Immunology, University of Pittsburgh) (Sun et al., 2014). The plasmid encoding the kinase domain of BIKE with N-terminal TEV (tobacco etch virus)-cleavable His_6 tags was a gift from Dr. Stefan Knapp at the University of Oxford (Sorrell et al., 2016). The plasmids encoding WT and T156A AP2M1 mutant were previously reported (Bekerman et al., 2017).

2.3. Compounds

5z-7-oxozeaenol was purchased from Cayman Chemical. ML336 was

purchased from AOBIOUS. Compound 25A and 34A were synthesized by the Zuercher laboratory (UNC) (Agajanian et al., 2019). Compounds' structure was defined by NMR and mass spectroscopy. ≥ 95% purity was confirmed by HPLC.

2.4. Western blotting and antibodies

Cells were lysed in M-Per protein extraction reagent (Thermo Fisher Scientific). For detection of phospho-AP2M1, cells were pretreated with 100 nM calyculin A (Cell Signaling), a PP1 and PP2a phosphatase inhibitor, for 30 min prior to lysis. Clarified protein lysates were run on 4%−12% Bis-Tris gels (Invitrogen), transferred onto PVDF membranes (Bio-Rad). Blots were blocked and blotted with anti-BIKE (Santa Cruz biotechnology, catalog sc-134284), anti-AP2M1 (Abcam, catalog ab75995), anti-GLuc (New England BioLabs, catalog E8023S), anti-−phospho-AP2M1 (T156) (Cell Signaling, catalog 3843S), and anti-β-actin (Sigma-Aldrich, catalog A3854) antibodies. Signal was detected with HRP-conjugated secondary antibodies. Band intensity was quantified with ImageJ software (NIH).

2.5. RNA interfering

siGENOME Human BMP2K (55589) siRNA SMART Pool (GAA-CAUAGACCUGAUAUAU, GGACUGUGCUGUUAAUUCA, GGAACUAU-GUACUUUGUGA, CGAUGUGCAUUGAAGCGAA) and siGENOME Non-Targeting siRNA Pool #1 (D-001206-13-05) (UAGCGACUAAACACAU-CAA, UAAGGCUAUGAAGAGAUAC, AUGUAUUGGCCUGUAUUAG, AUGAACGUGAAUUGCUCAA) were purchased from Dharmacon. siRNAs (1 pmole) were transfected into Huh7 cells using RNAiMax (ThermoFisher Scientific) 72 h before infection.

2.6. Generation of BIKE KO cell lines

CRISPR guide RNA (gRNA) sequences were designed using the CRISPR design tool (http://chopchop.cbu.uib.no/). BIKE (GGTGGCGGCCGACCGCGAAC) sgRNA was synthesized and cloned into the pX458 gRNA plasmid (a gift from Dr. Feng Zhang, Addgene plasmid # 48138), as described (Ran et al., 2013). Single clonal knockout of Huh7 cells were obtained using the PX458 vector that expresses Cas9 and sgRNA against BIKE. Green fluorescent protein (GFP) positive single cells were sorted at 24 h post-transfection using a BD InFlux Cell Sorter into 96-well plates and screened for knockout via western blot, as described (Ran et al., 2013).

2.7. Protein expression and purification

Plasmid encoding N-terminally His_6-tagged BIKE domain was electroporated into Rosetta strain BL21 *E. coli* cells using Gene Pulser Xcell™ Electroporation Systems (Bio-Rad) with 1800V. Protein expression was induced with 0.5 mM IPTG at 20 °C overnight. Cells were then harvested and resuspended in lysis buffer composed of 50 mM HEPES (pH 7.5), 500 mM NaCl, 5 mM imidazole, 5% glycerol, and 0.5 mM TCEP [tris-(2-carboxyethyl)phosphine]. Following sonication and spinning at 48,400×*g* at 4 °C for 60 min the supernatant was harvested. BIKE was purified via Ni-affinity followed by TEV protease digestion to remove the HIS_6 tag. BIKE was further purified by size-exclusion chromatography via Superdex S75 10/60 column on AKTA pure (GE Lifesciences). Protein was concentrated via 10 kDa Amicon centrifugal filters (Merck) and suspended in storage buffer composed of 10 mM HEPES (pH 7.5), 300 mM NaCl, 5% glycerol, and 0.5 mM TCEP at -80 °C.

2.8. Virus production

DENV RNA was transcribed *in vitro* from pACYC-DENV2-NGC plasmid by mMessage/mMachine (Ambion) kits and electroporated into BHK-21 cells. EBOV (Kikwit isolate) was grown in Vero E6 cells.

VEEV-TC-83-nLuc RNA was transcribed *in vitro* from cDNA plasmid templates linearized with MluI via MegaScript Sp6 kit (Invitrogen #AM1330) and electroporated into BHK-21 cells. Supernatants were collected, clarified and stored at -80 ˚C until further use. Virus stock titers were determined via standard plaque assay on BHK-21 (DENV, VEEV) or Vero E6 (EBOV) cells, and titers were expressed as PFU/ml.

2.9. Infection assays

Huh7, T-Rex-293, and MDDC cells were infected with DENV in replicates (n = 3–10) at an MOI of 0.01 or 0.05. Overall infection was measured at 48 or 72 h using a *Renilla* luciferase substrate or a standard plaque assay. Huh7 cells were infected with EBOV at an MOI of 1 under biosafety level 4 conditions. 48 h postinfection, supernatants were collected and stored at -80 ˚C. Cells were formalin-fixed for 24 h prior to removal from biosafety level 4. Infected cells were detected using an EBOV glycoprotein-specific monoclonal antibody (KZ52) and quantitated by automated fluorescence microscopy using an Operetta High Content Imaging System and the Harmony software package (PerkinElmer). U-87 MG cells were infected with VEEV-TC83-nLuc in 8 replicates at MOI of 0.01. Overall infection was measured at 18 hpi via a nanoluciferase assay using a luciferin solution obtained from the hydrolysis of its O-acetylated precursor, hikarazine-103 (prepared by Dr. Yves Janin, Institut Pasteur, France) as a substrate (Coutant et al., 2019a; 2019b).

2.10. Viability assays

Viability was assessed using alamarBlue reagent (Invitrogen) or CellTiter-Glo reagent (Promega) assay according to manufacturer's protocol. Fluorescence was detected at 560 nm on an InfiniteM1000 plate reader and luminescence on an InfiniteM1000 plate reader (Tecan) or a SpectraMax 340 PC.

2.11. Entry assays

Huh7 cells were infected with luciferase reporter DENV2. 2 h postinfection, cells were lysed in Trizol, RNA was extracted and the intracellular viral RNA level was measured by qRT-PCR. Alternatively, *Renilla* luciferase activity was measured at 6 h postinfection on InfiniteM1000 plate reader (Tecan).

2.12. DENV RNA replication

As described (Bekerman et al., 2017; Wu et al., 2015; Yang et al., 2013), Huh7 cells were co-transfected with a reporter DNA-launched DENV2 replicon (pCMV-DV2Rep) that contains a minimal cytomegalovirus (CMVmin) promoter regulated by an upstream tetracycline response elements and a TET-ON plasmid (Wu et al., 2015; Yang et al., 2013). Eighteen hours posttransfection, viral RNA transcription was induced by doxycycline and shut down by changing to doxycycline-free medium 24 h later, which allowed us to shorten the exposure to doxycycline. Replication was monitored by luciferase activity.

2.13. Extra- and intracellular infectivity

Extracellular infectivity was measured in culture supernatants derived from 24-well plates transfected with 200 ng of DENV RNA for 48 h and used to infect naive cells for 48 h. Intracellular DENV infectivity was measured by inoculation of naive cells with lysates of transfected cells subjected to 3 rounds of free-thawing in ethanol-dry ice and clarified at 5000 *g*, as previously described (Bekerman et al., 2017). Luciferase or standard plaque assay were used to quantify infectious virus.

2.14. Pharmacological inhibition

Cells were treated with the inhibitors or DMSO at the time of inoculation. The inhibitors were left for the duration of the assay. Viral infection was measured via luciferase (DENV, VEEV) or plaque (DENV, EBOV) assays.

2.15. Gain-of-function assays

Doxycycline-inducible cell lines were established to overexpress BIKE via the Flp-In™ recombination system (ThermoFisher). T-REx-293 cells with a pFRT/lacZeo site and pcDNA™6/TR were co-transfected with puromycin-resistant vector encoding Flp-In™ recombination target site and pOG44 plasmid containing Flp recombinase followed by puromycin selection. To overexpress BIKE in the doxycycline-inducible T-REx-293 cell lines, 1 μM of doxycycline was added to the medium and incubated for 8 h. Cells were then infected with DENV (MOI = 0.05) and when relevant, treated with the compounds, followed by 72 h incubation prior to luciferase and viability assays. WT or T156A AP2M1, BIKE, or empty vector controls were transfected into Huh7 cells. 24 h posttransfection, cells were infected with luciferase reporter DENV (MOI = 0.05) and incubated for 48 h prior to luciferase and viability assays.

2.16. Resistance studies

VEEV (TC-83) was used to inoculate U-87 MG cells at MOI of 0.1 and passaged every 24 h by transferring of an equal volume of viral supernatant to naive cells under increasing drug selection (2.5–5 μM, passages 1–3; 5–10 μM, passages 4–7; 10–15 μM, passages 8–10). Upon completion of 10 passages, virus titer from the resulting supernatants was measured by plaque assays. ML336 resistance mutation in NSP2 at passage 10 was confirmed by purification and reverse transcription of viral RNA from cell supernatants, as described in the RNA extraction and quantification section. NSP2 region was amplified with iProof high-fidelity PCR kit (Bio-Rad) using the following primers: (forward: GATGTGGAYYTGAGACCAGCYTCAGCATGGAC; reverse: AGTCAANACTTCACAGAAAGCCCATGTTGTTCTCATCAA (N = any base, Y = C or T)) and sequenced (Sequetech Corp.).

2.17. Quantification and statistical analysis

All data were analyzed with GraphPad Prism software. Fifty percent effective concentrations (EC$_{50}$) were measured by fitting of data to a 3-parameter logistic curve. *P* values were calculated by 1- or 2-way ANOVA with either Dunnett's or Tukey's multiple comparisons tests as specified in each figure legend.

3. **Results**

3.1. BIKE but not STK16 is required for DENV infection

To probe the functional relevance, we first monitored DENV infection in human hepatoma (Huh7) cells upon depletion of BIKE and STK16 by small interfering RNAs (ON-TARGETplus SMARTpool siRNAs [Dharmacon]) (Fig. 1A). siBIKE, but not siSTK16, reduced infection with DENV2 (NGC strain) expressing a luciferase reporter gene (Zou et al., 2011) by ~65% relative to non-targeting (NT) control, as measured via luciferase assays at 48 h postinfection, with no apparent cytotoxic effect (Fig. 1B and C). A much greater effect was measured upon BIKE depletion via plaque assays with 2 and 1.5 log reduction of DENV titers in cells infected with an MOI of 0.01 or 0.05, respectively (Fig. 1D), with no cytotoxicity (Fig. 1E). siBIKE similarly suppressed DENV infection in a BIKE-depleted doxycycline-inducible T-REx-293 cell line (Torres et al., 2009). Induction of BIKE expression only partially restored the bulk cellular level of BIKE, yet it completely reversed the effect of siBIKE, largely excluding off-target effects as the cause of the observed
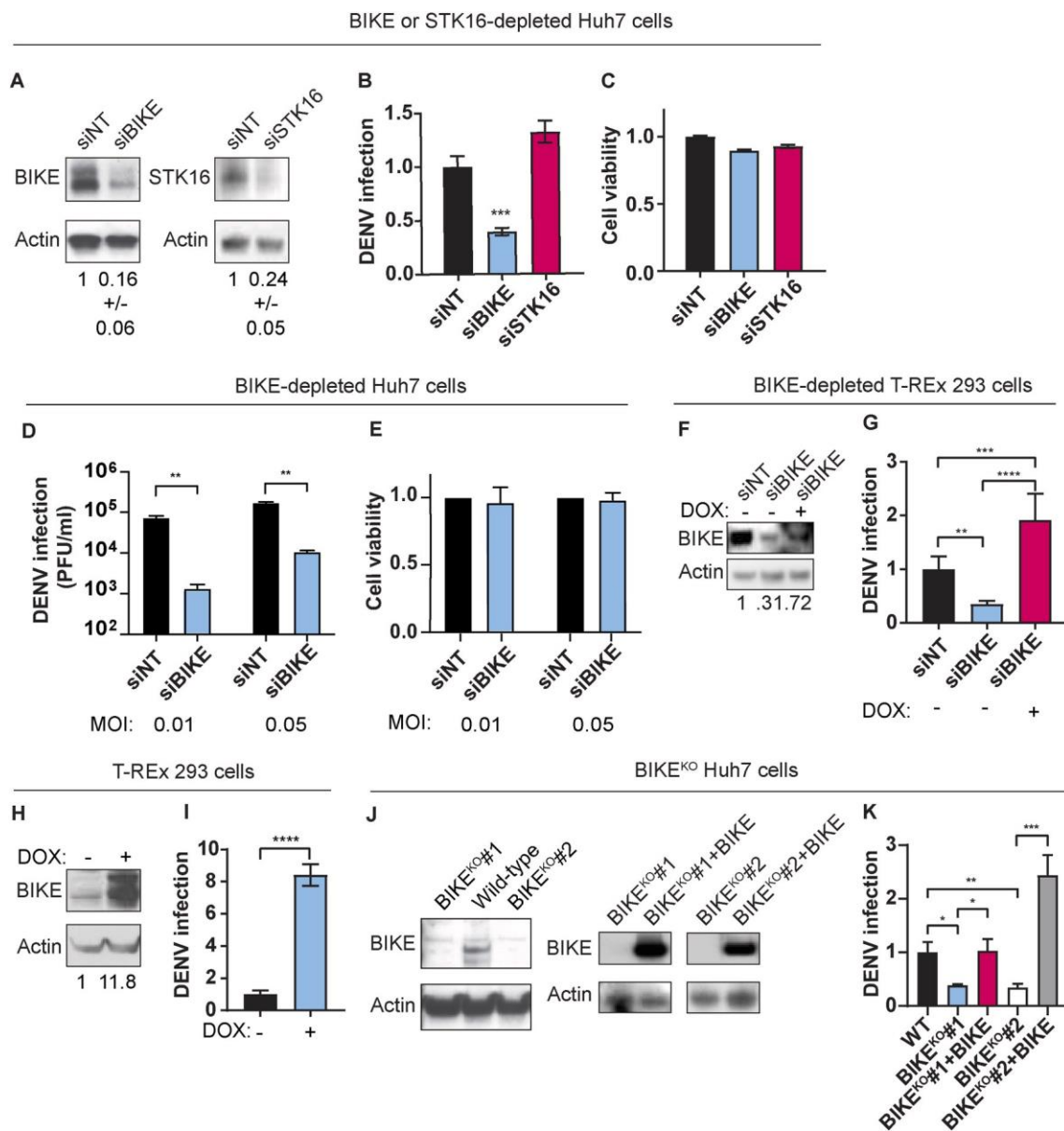
Fig. 1. BIKE is required for DENV infection**(A, F)** Confirmation of gene expression knockdown via Western blot in Huh7 (**A**) and Dox-inducible BIKE-overexpressing T-REx-293 cells (**F**) transfected with the indicated siRNAs and in these cells upon DOX induction (**F**). Representative membranes are shown. Numbers represent means±SD of protein-to-actin ratio relative to NT control from 3 membranes

(B-G) Infection (**B, D, G**) and cellular viability (**C, E**) measured at 48 h post-inoculation of the indicated cells with luciferase reporter DENV2 via luciferase (MOI = 0.05) (**B, G**) or plaque assays (MOI = 0.01, 0.05) (**D**) and alamarBlue assays (**C, E**), respectively. (**H, I**) BIKE protein (**H**) and DENV2 infection measured in the stable Dox-inducible BIKE-overexpressing T-REx-293 cell line via luciferase assays 48 h post-inoculation (MOI = 0.05) (**I**) in the presence or absence of DOX. (**J, K**) BIKE protein by Western blot (**J**) and DENV2 infection measured via luciferase assays 48 h postinoculation (MOI = 0.05) (**K**) of Huh7 cell lines deleted for BIKE via CRISPR/Cas9 and in these cells upon complementation with BIKE-FLAG (BIKE). Samples in the two right panels in H were run on the same gel from which several lanes were cut out. Shown are means±SD of results of representative experiments out of two (**E, G, I**) or three (**B, C**) conducted each with five replicates. *, P < 0.05; **, P < 0.01; ***, P < 0.001; ****, P < 0.0001 relative to corresponding controls by one-way ANOVA with Dunnett's (**B, C**) or Tukey's (**G, K**) post-hoc tests or two-tailed unpaired student t-test **(D, E, I)**.

phenotype, and suggesting that the local level of active BIKE achieved by overexpression is sufficient to drive its function in DENV infection (Fig. 1F and G). Moreover, induction of BIKE expression in the wild type (WT) T-REx-293 cell line increased DENV infection by ~8 fold relative to non-induced cells, supporting the requirement of BIKE for DENV infection (Fig. 1H and I). To confirm the role of BIKE in DENV infection, we generated two isogenic BIKE-knockout (BIKE^KO) Huh7 cell lines (Fig. 1J). BIKE deletion reduced DENV infection by 3.5−4 fold relative to WT cells (Fig. 1K). Moreover, ectopic expression of BIKE in the BIKE^KO

cells completely restored or even increased DENV infection, confirming that the observed phenotype resulted from BIKE deletion (Fig. 1J and K). Taken together, these loss-of-function and gain-of-function studies indicate that BIKE is required for DENV infection.

3.2. BIKE is required for both early and late stages of the DENV life cycle

We next monitored distinct stages in the DENV life cycle in Huh7 cells depleted or deleted of BIKE. We first determined the effect of BIKE depletion on early stages of the DENV life cycle via luciferase assays 6 h

following infection with the luciferase reporter DENV2 (Zou et al., 2011). siBIKE reduced DENV infection by ~50% relative to NT control in this assay (Figs. 1A and 2A). Consistent with these findings, BIKE deletion reduced DENV infection at 6 h by over 70% in the BIKE^KO cell lines (Figs. 1J and 2A). Treatment with a translation inhibitor (cycloheximide), but not a DENV RNA replication inhibitor (SDM25N (Van Cleef et al., 2013)) suppressed viral infection at 6 h postinfection, indicating that this assay monitors DENV entry through translation (data not shown), thereby excluding a role for BIKE in DENV RNA replication. To further pinpoint the specific stage, we thus measured DENV

internalization via RT-PCR at 2 h post DENV inoculation. BIKE deletion had no effect on DENV internalization (Fig. 2B). To probe for a potential role in viral translation, next we monitored translation and RNA replication by luciferase assays at 24 and 72 h following induction of DENV subgenomic replicon (pCMV-DV2Rep) expression in Huh7 cells (Fig. 2C) (Yang et al., 2013). Neither DENV translation nor DENV RNA replication were affected by BIKE depletion (Fig. 2C). To assess for an effect in later stages of the viral life cycle, we transfected full length DENV RNA into Huh7 cells, obtained clarified cell lysates and culture supernatants at 48 h, and used these to inoculate naïve cells followed by luciferase or
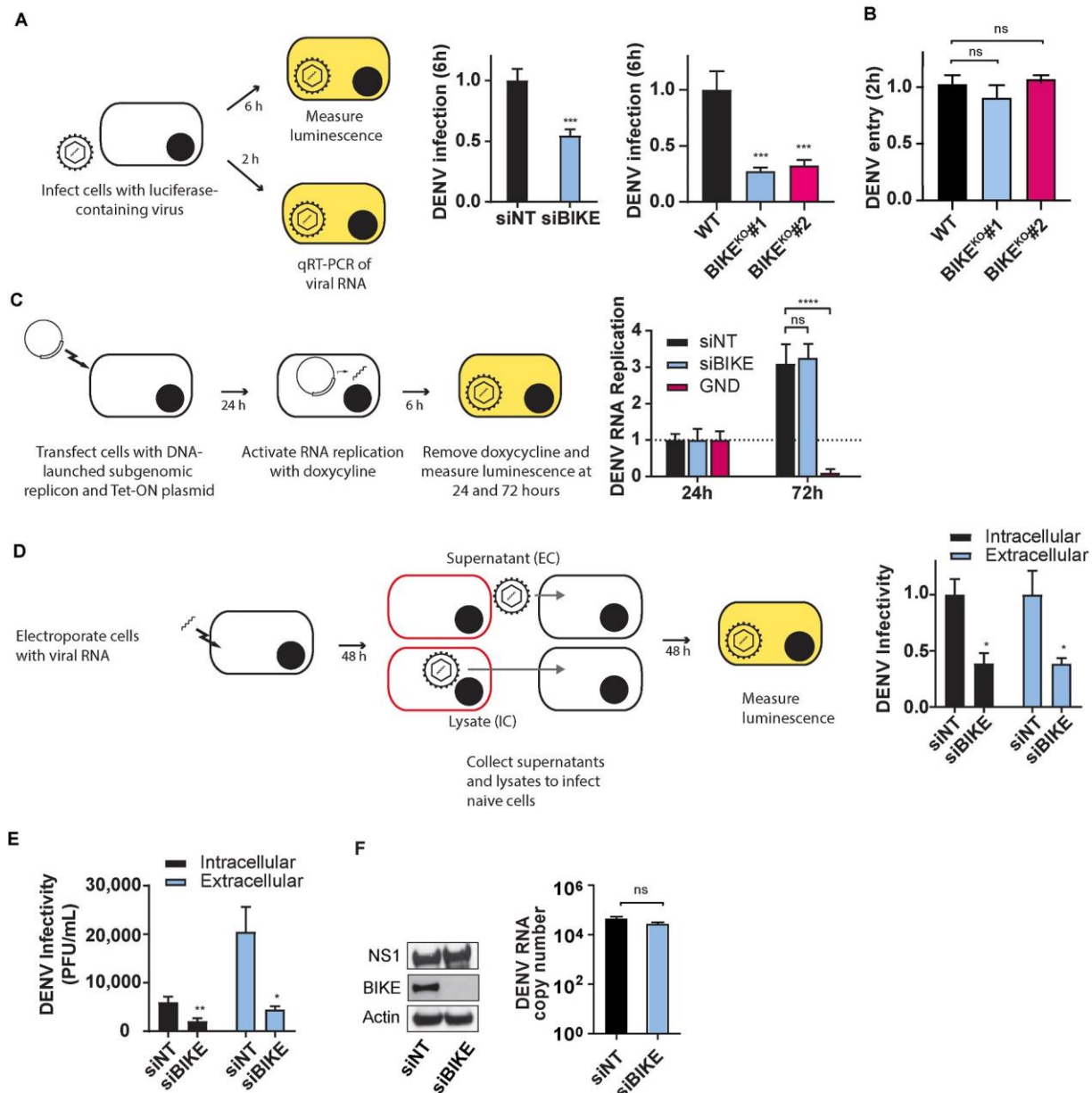

Fig. 2. BIKE is required for an early (postinternalization) and late (assembly/egress) stages of the DENV life cycle.
(**A**) Early stages monitored by luciferase activity at 6 h postinoculation of Huh7 cells depleted (left) or deleted (right) for BIKE with luciferase reporter DENV2 (MOI = 5). (**B**) DENV entry measured in BIKE deleted cells via RT-PCR assays 2 h following viral inoculation. (**C**) DENV RNA replication monitored by luciferase activity at 24 and 72 h following co-transfection of Huh7 cells with a Tet-inducible DNA-launched DENV replicon along with TET-ON plasmid and induction by doxycycline for 24 h (GND is a replication-incompetent DENV). Data are normalized to signal at 24 h postinduction. (**D**) DENV infectivity measured via luciferase or plaque assays (**E**) by inoculating naïve cells with lysates (intracellular) and supernatants (extracellular) derived from Huh7 cells transfected with *in vitro* transcribed DENV2 RNA 48 h post-transfection. (**F**) Intracellular levels of NS1 expression and DENV RNA copy number in BIKE depleted and control cells via Western blot and qRT-PCR assays. Shown are means±SD of results of representative experiments out of three conducted each with four replicates. *, P < 0.05; **, P < 0.01; ***, P < 0.001; ****, P < 0.0001 relative to NT or WT controls by (one-way (**A, B, D, E**) or two-way (**C**) ANOVA with Dunnett's post-hoc test or two-tailed unpaired student t-test (**F**). ns; non-significant, PFU; plaque-forming units.

plaque assays at 48 h. A 2.5−4 fold reduction in both intra- and extracellular infectivity was observed in BIKE depleted versus control cells, suggesting a defect in DENV assembly and egress (Fig. 2D and E). The level of intracellular NS1 and DENV RNA in cell lysates derived from the BIKE-depleted DENV RNA transfected cells was comparable to NT controls, further excluding a role for BIKE in DENV translation and RNA replication (Fig. 2F). Our attempts to monitor RNA replication and infectious virus production in the BIKE^KO cell lines were limited by low efficiency of DENV RNA transfection into these cells. These results implicate BIKE in the DENV life cycle via regulation of two temporally distinct steps, an early post-internalization and pre-translation step and infectious virus production.

3.3. BIKE mediates its role in DENV infection in part via AP2M1 phosphorylation at T156

We have previously shown that AP2M1 is required for DENV entry and infectious virus production (Bekerman et al., 2017; Neveu et al., 2015, 2012; Xiao et al., 2018). While recombinant BIKE (rBIKE) was described to phosphorylate a synthetic AP2M1 peptide (Sorrell et al., 2016), the role of AP2M1 as a functional BIKE substrate was not established. To confirm AP2M1 phosphorylation, rBIKE (Fig. 3A) was incubated for 1 h with ATP and an AP2M1 peptide harboring T156, a residue previously shown to be modified by AAK1 (Ricotta et al., 2002) and GAK (Tabara et al., 2011), followed by Electrospray Ionisation Mass Spectrometry (ESI-MS). A 79.9 Da shift from a molecular weight of 1903 Da, corresponding to the unphosphorylated AP2M1 peptide, to 1982.9 Da was detected, indicating the addition of a single phosphate group by rBIKE (Fig. 3B). To confirm these findings, we measured the level of phospho-AP2M1 upon BIKE depletion. A significant reduction in the phospho-AP2M1, but not total AP2M1 level, was observed in Huh7 cells depleted for BIKE or treated with 10 μM of 5Z-7-oxozeaenol, a pan-NAK inhibitor, relative to NT control (Fig. 3C), confirming that BIKE phosphorylates endogenous, full length AP2M1 in cultured cells. To determine if AP2M1 is a mediator of BIKE activity in DENV infection, we conducted gain-of-function assays. Ectopic expression of WT but not T156A AP2M1 mutant or control vector reversed the antiviral effect of siBIKE (Fig. 3D and E). These results indicate that AP2M1 T156 phosphorylation by BIKE is functionally relevant and represents a mechanism through which BIKE regulates DENV infection.

3.4. A selective AAK1/BIKE inhibitor suppresses DENV infection and AP2M1 phosphorylation in vitro

To determine whether a similar effect on DENV infection to that achieved genetically can be achieved pharmacologically and further validate BIKE as an antiviral target, we treated DENV-infected cells with NAK inhibitors. Compound 25A is a highly selective, potent anti-BIKE and anti-AAK1 kinase inhibitor (dissociation constants (kD) of 68 nM and 71 nM, respectively) that was developed as a chemical probe (Agajanian et al., 2019) (Fig. 4A). We measured a dose-dependent inhibition of DENV2 infection in Huh7 cells following a 2-day treatment with compound 25A with half-maximal effective concentration (EC$_{50}$) of 1.34 μM by luciferase assays and half-maximal cellular cytotoxicity (CC$_{50}$) greater than 10 μM by alamarBlue assays in the same samples (Fig. 4B). In contrast, compound 34A, designed as an inactive 25A derivative, demonstrated no antiviral activity (Fig. 4B). To confirm that 25A inhibits phosphorylation of the AAK1 and GAK ligand AP2M1, we measured levels of phospho-AP2M1 upon drug treatment. A ~10-fold reduction in the phospho-AP2M1 to total AP2M1 ratio was measured in Huh7 cells upon treatment with compound 25A but not 34A (Fig. 4C), confirming that the antiviral activity is correlated with functional inhibition of BIKE and AAK1.

3.5. 5Z-7-oxozeaenol inhibits viral infection in vitro and its mechanism of antiviral action is in part mediated by BIKE

5Z-7-oxozeaenol is a natural product acting as an ATP-competitive irreversible inhibitor of ERK2 (IC$_{50}$ = 80 nM), TAK1 (IC$_{50}$ = 8 nM) and VEGF-R2 (IC$_{50}$ = 52 nM) (Fig. 5A) (Ninomiya-Tsuji et al., 2003; Wu et al., 2013). 5Z-7-oxozeaenol potently binds BIKE, GAK, and AAK1 at 3.8, 10, and 13% of control, respectively, at 10 μM via a publicly available KINOMEscan (DiscoverX, Harvard Medical School LINCS Dataset (ID:20211)). We measured a dose-dependent inhibition of DENV2 infection in Huh7 cells following a 2-day drug treatment with 5Z-7-oxozeaenol with an EC$_{50}$ of 2.47 μM and a CC$_{50}$ of 10 μM and a dramatic reduction in AP2M1 phosphorylation (Fig. 5B and C). Next, we conducted gain-of-function assays, to determine whether inhibition of BIKE is a mechanism underlying the anti-DENV effect of this drug. Following doxycycline-mediated induction of BIKE expression, T-REx 293 cells were infected with a luciferase reporter DENV and treated with 5Z-7-oxozeaenol for 72 h prior to luciferase and viability assays. DENV infection was partially restored by BIKE expression upon doxycycline induction in 5Z-7-oxozeaenol treated BIKE-inducible T-REx-293 cells
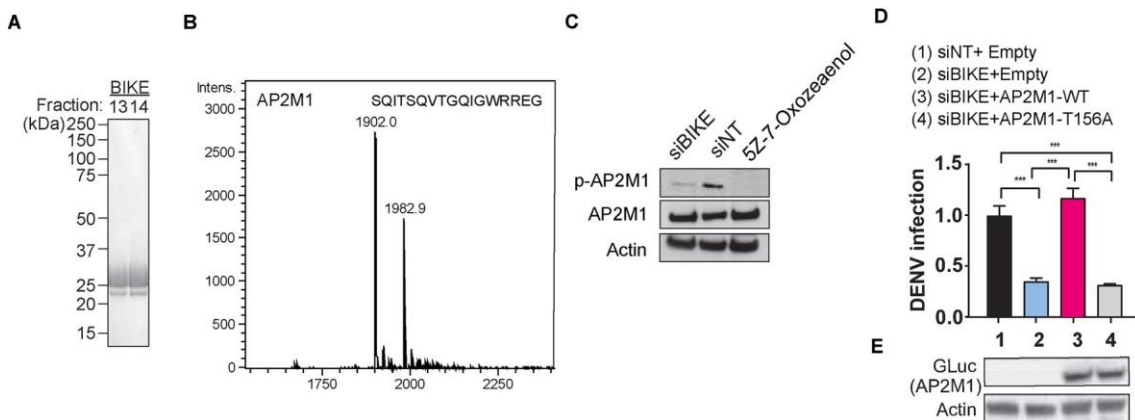

Fig. 3. BIKE mediates DENV infection in part through phosphorylation of AP2M1 at T156
(A) rBIKE by gel filtration following expression in bacterial cells. Representative fractions are shown. Molecular weight markers are indicated on the left (kDa). (**B**) Mass spectrum of the synthetic AP2M1 peptide following incubation with rBIKE and ATP. (**C**) Effect of the indicated siRNAs or treatment with 10 μM of 5Z-7-oxozeaenol on AP2M1 phosphorylation in Huh7 cells measured by Western blotting. (**D**) Infection measured at 48 h after inoculation (MOI = 0.05) of the indicated cells with luciferase reporter DENV2 via luciferase assays. (**E**) AP2M1-GLuc expression in Huh7 cells transfected with the indicated siRNAs.***, P < 0.001 by one-way ANOVA with Tukey's post-hoc tests.
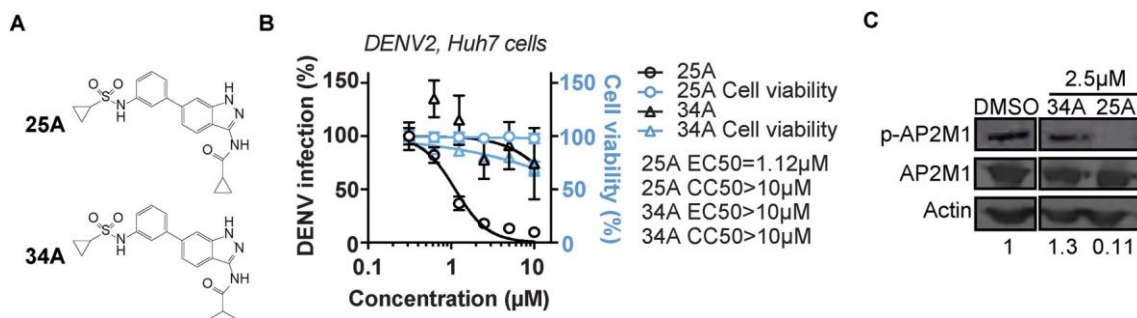
Fig. 4. A selective BIKE/AAK1 inhibitor inhibits DENV infection and its mechanism of antiviral action is in part mediated by BIKE
(A) Chemical structures of 25A and 34A. (**B**) Dose response of DENV infection (blue) and cellular viability (black) to the indicated compounds measured in Huh7 cells. (**C**) Effect of 1-h treatment with 25A or 34A at the indicated concentrations on AP2 phosphorylation in Huh7 cells measured by Western blotting. Numbers indicate the ratio of phospho-AP2 (pAP2) to total AP2. Samples were run on the same gel, from which several lanes were cut out. Data in all panels are representative of 2 or more independent experiments. Individual experiments in B had 8–10 biological replicates, means ± SD are shown.
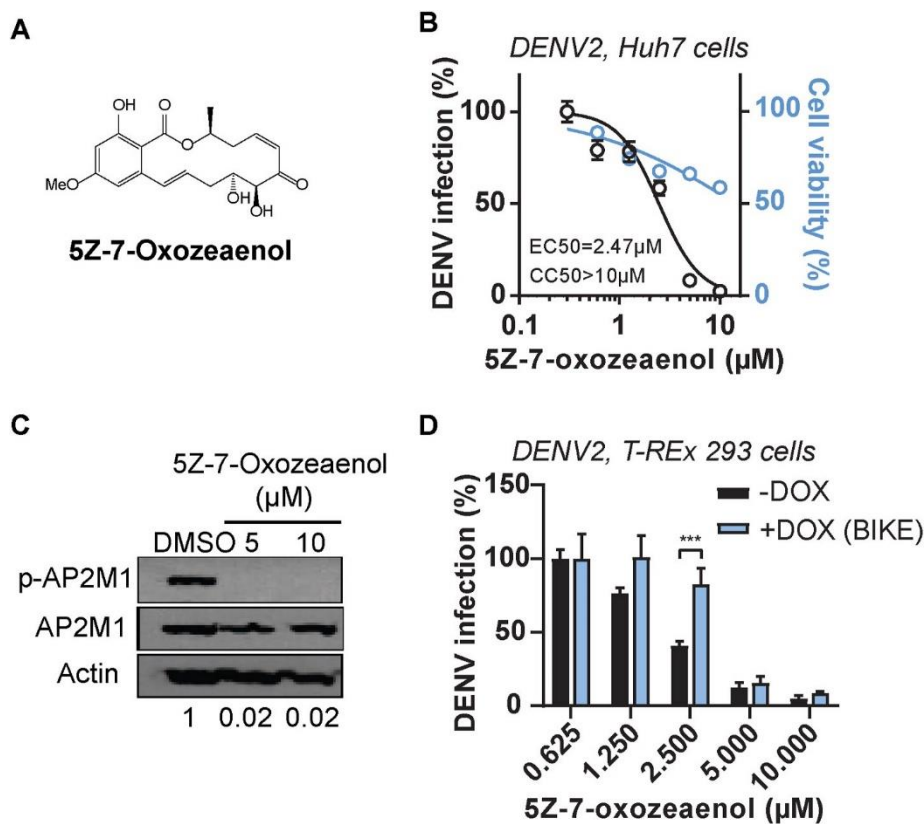

Fig. 5. 5Z-7-oxozeaenol inhibits DENV infection and its mechanism of antiviral action is in part mediated by BIKE

(A) Chemical structure of 5Z-7-oxozeaenol. (**B**) Dose response of DENV infection (blue) and cellular viability (black) to the indicated compounds measured in Huh7 cells. (**C**) Effect of 1-h treatment with 5Z-7-oxozeaenol at the indicated concentrations on AP2 phosphorylation in Huh7 cells measured by Western blotting. Numbers indicate the ratio of phospho-AP2 (pAP2) to total AP2. (**D**) DENV infec- tion normalized to cellular viability in T-REx 293 cells induced with doxycycline to express BIKE or uninduced cells 48 h postinfection with a luciferase reporter DENV and treatment with 5Z-7-oxozeaenol.

***, $P < 0.001$ relative to uninduced controls at the same concentration by two-way ANOVA with Tukey's post hoc test. Data in all panels are repre- sentative of 2 or more independent experiments. In- dividual experiments in B and D had 8–10 biological replicates, means ± SD are shown.

(Figs. 5D and 1E). These results pharmacologically validate BIKE as a regulator of DENV infection and as a molecular target that mediates the antiviral effect of these compounds.

3.6. 5Z-7-oxozeaenol inhibits DENV infection ex vivo and demonstrates a broad-spectrum antiviral potential

To further evaluate the therapeutic potential of 5Z-7-oxozeaenol, we studied its antiviral effect in primary human monocyte derived dendritic cells (MDDC); an established *ex vivo* model system for DENV (Rodri- guez-Madoz et al., 2010). We measured a dose-dependent inhibition of DENV infection following a 3-day drug treatment with an EC_{50} of 0.54 μM by luciferase assays and a CC_{50} of 5.49 μM by alamarBlue assays (Fig. 6A). Lastly, we investigated whether members of unrelated viral families, Ebola virus (EBOV), a filovirus, and Venezuelan equine

encephalitis virus (VEEV), an alphavirus are also susceptible to 5Z-7-oxozeaenol treatment. 5Z-7-oxozeaenol treatment resulted in a dose-dependent reduction in authentic EBOV infection in Huh7 with EC_{50} value of 4.09 μM and no apparent cellular toxicity within the concentration range tested (Fig. 6B). Similarly, 5Z-7-oxozeaenol treat- ment inhibited infection of U-87 MG (human astrocytes) with TC-83 (a live-attenuated vaccine VEEV strain) in a dose-dependent manner, as measured by luciferase assays 18 h postinfection with a nano-luciferase reporter virus, with EC_{50} value of 2.6 μM and CC_{50} greater than 20 μM (Fig. 6C).

3.7. 5Z-7-oxozeaenol has a high genetic barrier to resistance

To determine whether viruses can escape treatment with 5Z-7-oxo- zeaenol, we chose to focus on VEEV (TC-83) since it has the shortest
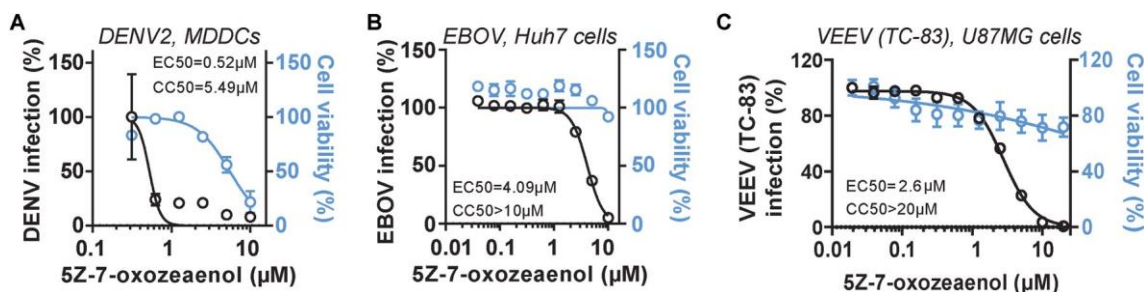
Fig. 6. 5Z-7-oxozeaenol inhibits DENV infection in MDDCs as well as EBOV and VEEV (TC-83).
(**A**) Dose response of DENV infection (MOI = 0.05) (blue) and cellular viability (black) to 5Z-7-oxozeaenol measured in human primary MDDCs via luciferase and alamarBlue assays, respectively. (**B**) Dose response of EBOV infection (MOI = 1) (blue) and cellular viability (black) to 5Z-7-oxozeaenol measured in Huh7 cells under biosafety level 4 containment 48 h postinfection (MOI = 1) via plaque assay and CellTiter-Glo luminescent cell viability assay, respectively. (**C**) Dose response of VEEV (TC-83) infection (MOI = 0.1) (blue) and cellular viability (black) to 5Z-7-oxozeaenol measured in U-87 MG cells via luciferase and alamarBlue assays, respectively. Data in all panels are representative of 2 or more independent experiments. Individual experiments had 5 biological replicates, means ± SD are shown. Shown in A is a representative experiment with cells from a single donor, of two experiments conducted with cells derived from two donors.

life cycle among the viruses tested. VEEV was passaged in the presence of 5Z-7-oxozeaenol or the VEEV nonstructural 2p (ns2P) protein inhibitor ML336 (Chung et al. (2010)) at increasing concentrations (2.5–15 μM) corresponding to values between EC_{50} and EC_{90} in U-87 MG cells. Infectious virus output was quantified over several passages by plaque assays. By passage 3, VEEV overcame inhibition by ML336. In contrast, VEEV remained suppressed for 10 passages under the 5Z-7-oxozeaenol treatment without any phenotypic resistance (Fig. 7A). Moreover, virus from culture supernatants obtained at passage 10 under 5Z-7-oxo- zeaenol or DMSO treatment remained susceptible to 5Z-7-oxozeaenol. In contrast, virus obtained at passage 10 under ML336 treatment lost its susceptibility to ML336, with the emergence of a previously character- ized resistance mutation in NSP2 (Y102C in VEEV TC-83), whereas virus obtained at the same passage under DMSO treatment remained sus- ceptible to ML336 (Fig. 7B and C). These results point to 5Z-7-oxozeae- nol as a potential broad-spectrum antiviral strategy with a higher relative barrier to resistance than a direct-acting antiviral.

4. Discussion

We have previously demonstrated regulation of intracellular traf- ficking of various RNA viruses via AAK1- and GAK-mediated phos- phorylation of AP complexes and validated these kinases as targets for broad-spectrum antivirals (Bekerman et al., 2017; Neveu et al., 2015; Pu et al., 2018; Verdonck et al., 2019; Xiao et al., 2018). Yet, the roles of BIKE in healthy and disease states are largely unknown. By integrating molecular virology, genetic, and pharmacological approaches, we reveal a requirement for BIKE in DENV infection and demonstrate that AP2M1 is a substrate that is involved in mediating BIKE's role. Moreover, we provide a proof of concept that pharmacological inhibition of BIKE can be potentially used as a broad-spectrum strategy against acute emerging RNA viral infections, and we validate BIKE as a molecular target mediating this antiviral activity. These findings provide insights into the virus-host determinants that regulate DENV infection and have potential implications for the design of antiviral strategies.

BIKE was previously implicated in osteoblast differentiation, myopia, and cancer (Buraschi et al., 2012; Kearns et al., 2001; Liu et al.,
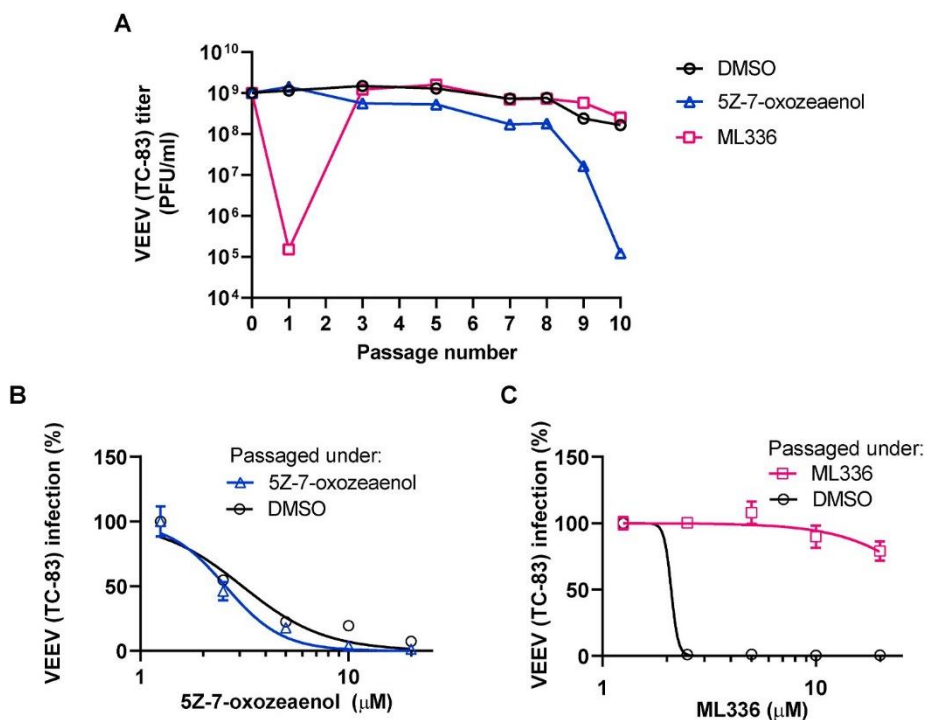

Fig. 7. 5Z-7-oxozeaenol has a high genetic barrier to resistance.
(**A**) VEEV (TC-83) used to infect U-87 MG cells and passaged every 24 h by inoculation of naive cells with equal volumes of viral supernatants under DMSO treatment or selection with 5Z-7-oxozeaenol or ML336 (VEEV ns2P inhibitor) increasing from 2.5 to 15 μM over 10 passages. Viral titers were measured by plaque assays. (**B and C**) Dose response to 5Z-7-oxozeaenol (B) and ML336 (C) of VEEV harvested after 10 passages in U-87 MG cells in the presence of 5Z-7-oxozeaenol (B) and ML336 (C), via luciferase assays. Retained susceptibility to 5Z-7-oxo- zeaenol and loss of susceptibility to ML336 are shown. Data are representative of at least 2 experi- ments. Shown are means ± SD. Individual experi- ments in A and B/C had 2 and 3 biological replicates, respectively.

2009; Mercado-Matos et al., 2018). It was also shown to be required for HIV infection via a genome-wide RNAi screen (Zhou et al., 2008), however, the substrates that mediate this effect, the relevant stage of the viral life cycle, and BIKE's role in other viral infections have not been studied. We provide evidence that BIKE mediates at least two temporally distinct stages in the DENV life cycle: an early postinternalization but pretranslation stage (such as trafficking from the plasma membrane to early endosomes, uncoating, or viral RNA trafficking to sites of RNA replication) and a later, assembly/egress stage. Like AAK1 and GAK, BIKE therefore represents a regulator of viral infection and a candidate druggable target for antiviral treatment. We predict that a lower dynamic range and partial overlap in substrates of the various NAKs (e.g. AP2M1) account for the relatively modest effect of BIKE depletion or deletion measured on DENV infection via luciferase assays. Indeed, a dramatic effect was measured in BIKE depleted cells via plaque assays and upon treatment with NAK inhibitors. The requirement for BIKE by unrelated RNA viral families suggests that it may be a target for broad-spectrum antivirals.

To date, no functionally proven substrates of BIKE have been discovered. While BIKE was shown to bind Numb and to phosphorylate a synthetic AP2M1 peptide, neither of these endocytic adaptors were shown to be biologically relevant BIKE substrates (Kearns et al., 2001; Krieger et al., 2013; Sorrell et al., 2016). We show that AP2M1 phosphorylation on T156 is biologically relevant via two cell-based assays and that it is involved in mediating BIKE's role in DENV infection. Since we have previously shown that AP2M1 is required for early and late steps in the DENV life cycle (Bekerman et al., 2017; Neveu et al., 2015, 2012), our current findings suggest that BIKE mediates its role in these steps in part via AP2M1 phosphorylation. We, however, cannot exclude the possibility that additional BIKE substrates exist and are involved in mediating BIKE's role in viral infections.

We show that 5Z-7-oxozeaenol, a potent, albeit non-selective inhibitor of NAKs, and 25A, a highly selective BIKE and AAK1 inhibitor, restrict DENV infection *in vitro*. The IC_{50} or K_D values of 5Z-7-oxozeaenol and 25A for BIKE inhibition or binding are 3.8 nM and ~70 nM, respectively, whereas their EC_{50} values for DENV infection are 0.52–2.47 μM. Such ~100–500-fold differences between IC_{50} values measured *in vitro* and EC_{50} values measured via cell-based assays are typical for kinase inhibitors and are often attributed to the absence of ATP competition in the *in vitro* assay, to differences in the fraction of substrate that is consumed under the given assay conditions, to the relative concentration and cellular distribution of the kinase, and to the intracellular bioavailability (determined by the rates of entry to the cells and/or active pumping out of the cells) of the compounds (Bekerman et al., 2017; Knight and Shokat, 2005). We hypothesize that optimization of the compounds via structure-activity relationship analysis will improve their potency as antiviral agents. Dendritic cells represent the primary target of DENV in humans and better model human physiology and disease than immortalized cell lines (Schmid et al., 2014). Our finding that 5Z-7-oxozeaenol treatment exhibits antiviral efficacy in MDDCs with minimal toxicity to host cells therefore further supports the biological relevance of this approach.

We provide evidence that modulation of NAK activity is an important mode of antiviral action of these compounds in DENV infection. Due to lack of affinity of 25A to 5Z-7-oxozeaenol's cancer targets, the activity of 25A confirms that BIKE and AAK1 are relevant antiviral targets. PDGFR, the only other target significantly bound by 25A via KINOME scan (Agajanian et al., 2019), has no apparent role in DENV infection (Bekerman et al., 2017). Furthermore, we characterized the mechanism by which pharmacological inhibitors of NAKs mediate their anti-DENV effect. We establish that the antiviral activity of 5Z-7-oxozeaenol and 25A correlates with reduced phospho-AP2M1 levels and is mechanistically explained in part by a block in AP2M1 phosphorylation. These findings also present phosphorylated AP2M1 as a useful pharmacodynamic biomarker. Our gain-of-function assays support inhibition of BIKE activity as an important mode of antiviral action of 5Z-7-oxozeaenol.

Nevertheless, we cannot exclude the possibility that other targets of 5Z-7-oxozeaenol are involved in mediating this antiviral effect.

Most antivirals inhibit viral enzymes and are thus limited by a narrow-spectrum of coverage and a rapid emergence of drug resistance (Bekerman and Einav, 2015). We predicted that since BIKE is a cellular target and was previously found to be essential for HIV replication, compounds with anti-BIKE activity may have broad-spectrum activity beyond Flaviviridae. Indeed, we reveal activity against the filovirus, EBOV and the alphavirus, VEEV (TC-83). Targeting cellular BIKE subnetworks may thus provide a path for broad-spectrum antivirals. Furthermore, targeting of cellular proteins that are not under the genetic control of viruses is more likely to have a higher barrier to resistance than classical direct-acting antivirals. This is exemplified by our current data and prior data with sunitinib/erlotinib combinations (Bekerman et al., 2017). Although we predict that the genetic barrier to resistance of 5Z-7-oxozeaenol is high, it may be possible to select for resistance over longer-term passage under different conditions or in a different, chronic infection model. The strategies used by viruses to overcome drug-mediated inhibition are similar to those used by cancer cells. Simultaneous inhibition of several kinases or targeting of several pathways by the same drug or drug combination may thus prove attractive in combating viral pathogens, as reported in cancer (Knight et al., 2010). The "polypharmacology" provided by a drug such as 5Z-7-oxozeaenol could therefore increase the effectiveness while minimizing viral resistance.

Covalent kinase inhibitors are widely used in cancer treatment (Barf and Kaptein, 2012), yet their potential in treating viral infections has not been explored. We provide a proof of concept that covalent kinase inhibitors may have utility in combating acute viral infections, an attractive indication requiring a shorter duration of treatment. Notably, E6201, a closely related 5Z-7-oxozeaenol derivative, is undergoing clinical development for cancer, proposing a repurposing potential (Barf and Kaptein, 2012; Tibes et al., 2018).

Taken together, these results validate virus-host interactions required for DENV entry and assembly/release and reveal a novel druggable cellular target with implications for the design of host- targeted, broad-spectrum antiviral strategies with a high barrier to resistance.

Acknowledgements

References

Agajanian, M.J., Walker, M.P., Axtman, A.D., Ruela-de-Sousa, R.R., Serafin, D.S., Rabinowitz, A.D., Graham, D.M., Ryan, M.B., Tamir, T., Nakamichi, Y., Gammons, M.V., Bennett, J.M., Couñago, R.M., Drewry, D.H., Elkins, J.M., Gileadi, C., Gileadi, O., Godoi, P.H., Kapadia, N., Müller, S., Santiago, A.S., Sorrell, F. J., Wells, C.I., Fedorov, O., Willson, T.M., Zuercher, W.J., Major, M.B., 2019. WNT activates the AAK1 kinase to promote clathrin-mediated endocytosis of LRP6 and establish a negative feedback loop. Cell Rep. 26, 79–93 e8.

Barf, T., Kaptein, A., 2012. Irreversible protein kinase inhibitors: balancing the benefits and risks. J. Med. Chem.

Bekerman, E., Einav, S., 2015. Infectious disease. Combating emerging viral threats. Science 348, 282–283.

Bekerman, E., Neveu, G., Shulla, A., Brannan, J., Pu, S.-Y., Wang, S., Xiao, F., Barouch-Bentov, R., Bakken, R.R., Mateo, R., Govero, J., Nagamine, C.M., Diamond, M.S., De Jonghe, S., Herdewijn, P., Dye, J.M., Randall, G., Einav, S., 2017. Anticancer kinase inhibitors impair intracellular viral trafficking and exert broad-spectrum antiviral effects. J. Clin. Invest. 127, 1338–1352.

Bhatt, S., Gething, P.W., Brady, O.J., Messina, J.P., Farlow, A.W., Moyes, C.L., Drake, J. M., Brownstein, J.S., Hoen, A.G., Sankoh, O., Myers, M.F., George, D.B., Jaenisch, T., Wint, G.R., Simmons, C.P., Scott, T.W., Farrar, J.J., Hay, S.I., 2013. The global distribution and burden of dengue. Nature 496, 504–507.

Buraschi, S., Neill, T., Owens, R.T., Iniguez, L.A., Purkins, G., Vadigepalli, R., Evans, B., Schaefer, L., Peiper, S.C., Wang, Z.-X., Iozzo, R.V., 2012. Decorin protein core affects the global gene expression profile of the tumor microenvironment in a triple-negative orthotopic breast carcinoma xenograft model. PLoS One.

Chung, D., Schroeder, C.E., Sotsky, J., Yao, T., Roy, S., Smith, R.A., Tower, N.A., Noah, J. W., McKellip, S., Sosa, M., Rasmussen, L., White, E.L., Aube, J., Golden, J.E., 2010. ML336: development of quinazolinone-based inhibitors against Venezuelan equine encephalitis virus (VEEV). In: Probe Reports from the NIH Molecular Libraries Program. National Center for Biotechnology Information (US)).

Conner, S.D., Schmid, S.L., 2002. Identification of an adaptor-associated kinase, AAK1, as a regulator of clathrin-mediated endocytosis. J. Cell Biol. 156, 921–929.

Coutant, E.P., Gagnot, G., Hervin, V., Baatallah, R., Goyard, S., Jacob, Y., Rose, T., Janin, Y., 2019a. Bioluminescence profiling of NanoKAZ/NanoLuc luciferase using a chemical library of coelenterazine analogues. Chem. Eur J.

Coutant, E.P., Goyard, S., Hervin, V., Gagnot, G., Baatallah, R., Jacob, Y., Rose, T., Janin, Y.L., 2019b. Gram-scale synthesis of luciferins derived from coelenterazine and original insights into their bioluminescence properties. Org. Biomol. Chem. 17, 3709–3713.

Diamond, M.S., Pierson, T.C., 2015. Molecular insight into dengue virus pathogenesis and its implications for disease control. Cell 162, 488–492.

Huang, C.Y.-H., Butrapet, S., Moss, K.J., Childers, T., Erb, S.M., Calvert, A.E., Silengo, S. J., Kinney, R.M., Blair, C.D., Roehrig, J.T., 2010. The dengue virus type 2 envelope protein fusion peptide is essential for membrane fusion. Virology 396, 305–315.

In, J.G., Striz, A.C., Bernad, A., Tuma, P.L., 2014. Serine/threonine kinase 16 and MAL2 regulate constitutive secretion of soluble cargo in hepatic cells. Biochem. J.

Kearns, A.E., Donohue, M.M., Sanyal, B., Demay, M.B., 2001. Cloning and characterization of a novel protein kinase that impairs osteoblast differentiation in vitro. J. Biol. Chem. 276, 42213–42218.

Knight, Z.A., Shokat, K.M., 2005. Features of selective kinase inhibitors. Chem. Biol.

Knight, Z.A., Lin, H., Shokat, K.M., 2010. Targeting the cancer kinome through polypharmacology. Nat. Rev. Canc. 10, 130–137.

Krieger, J.R., Taylor, P., Gajadhar, A.S., Guha, A., Moran, M.F., McGlade, C.J., 2013. Identification and selected reaction monitoring (SRM) quantification of endocytosis factors associated with Numb. Mol. Cell. Proteomics 12, 499–514.

Kudelko, M., Brault, J.-B., Kwok, K., Li, M.Y., Pardigon, N., Peiris, J.S.M., Bruzzone, R., Després, P., Nal, B., Wang, P.G., 2012. Class II ADP-ribosylation factors are required for efficient secretion of dengue viruses. J. Biol. Chem. 287, 767–777.

Liu, H.-P., Lin, Y.-J., Lin, W.-Y., Wan, L., Sheu, J.J.-C., Lin, H.-J., Tsai, Y., Tsai, C.-H., Tsai, F.-J., 2009. A novel genetic variant of BMP2K contributes to high myopia. J. Clin. Lab. Anal. 23, 362–367.

López-Coral, A., Striz, A.C., Tuma, P.L., 2018. A serine/threonine kinase 16-based phospho-proteomics screen identifies wd repeat protein-1 as A regulator of constitutive secretion. Sci. Rep. 8, 13049.

Mercado-Matos, J., Janusis, J., Zhu, S., Chen, S.S., Shaw, L.M., 2018. Identification of a novel invasion-promoting region in insulin receptor substrate 2. Mol. Cell Biol. 38.

Messina, J.P., Brady, O.J., Golding, N., Kraemer, M.U.G., Wint, G.R.W., Ray, S.E., Pigott, D.M., Shearer, F.M., Johnson, K., Earl, L., Marczak, L.B., Shirude, S., Davis Weaver, N., Gilbert, M., Velayudhan, R., Jones, P., Jaenisch, T., Scott, T.W., Reiner Jr., R.C., Hay, S.I., 2019. The current and future global distribution and population at risk of dengue. Nat Microbiol.

Neveu, G., Barouch-Bentov, R., Ziv-Av, A., Gerber, D., Jacob, Y., Einav, S., 2012. Identification and targeting of an interaction between a tyrosine motif within hepatitis C virus core protein and AP2M1 essential for viral assembly. PLoS Pathog. 8, e1002845.

Neveu, G., Ziv-Av, A., Barouch-Bentov, R., Berkerman, E., Mulholland, J., Einav, S., 2015. AP-2-associated protein kinase 1 and cyclin G-associated kinase regulate hepatitis C virus entry and are potential drug targets. J. Virol. 89, 4387–4404.

Ninomiya-Tsuji, J., Kajino, T., Ono, K., Ohtomo, T., Matsumoto, M., Shiina, M., Mihara, M., Tsuchiya, M., Matsumoto, K., 2003. A resorcylic acid lactone, 5Z-7-oxozeaenol, prevents inflammation by inhibiting the catalytic activity of TAK1 MAPK kinase kinase. J. Biol. Chem. 278, 18485–18490.

Pu, S.-Y., Wouters, R., Schor, S., Rozenski, J., Barouch-Bentov, R., Prugar, L.I., O'Brien, C.M., Brannan, J.M., Dye, J.M., Herdewijn, P., De Jonghe, S., Einav, S., 2018. Optimization of isothiazolo[4,3- b]pyridine-based inhibitors of cyclin G associated kinase (GAK) with broad-spectrum antiviral activity. J. Med. Chem. 61, 6178–6192.

Ricotta, D., Conner, S.D., Schmid, S.L., von Figura, K., Honing, S., 2002. Phosphorylation of the AP2 mu subunit by AAK1 mediates high affinity binding to membrane protein sorting signals. J. Cell Biol. 156, 791–795.

Rodriguez-Madoz, J.R., Bernal-Rubio, D., Kaminski, D., Boyd, K., Fernandez-Sesma, A., 2010. Dengue virus inhibits the production of type I interferon in primary human dendritic cells. J. Virol. 84, 4845–4850.

Sato, J., Shimizu, H., Kasama, T., Yabuta, N., Nojima, H., 2009. GAK, a regulator of clathrin-mediated membrane trafficking, localizes not only in the cytoplasm but also in the nucleus. Gene Cell. 14, 627–641.

Schmid, M.A., Diamond, M.S., Harris, E., 2014. Dendritic cells in dengue virus infection: targets of virus replication and mediators of immunity. Front. Immunol. 5, 647.

Sorensen, E.B., Conner, S.D., 2008. AAK1 regulates Numb function at an early step in clathrin-mediated endocytosis. Traffic 9, 1791–1800.

Sorrell, F.J., Szklarz, M., Abdul Azeez, K.R., Elkins, J.M., Knapp, S., 2016. Family-wide structural analysis of human numb-associated protein kinases. Structure 24, 401–411.

Sun, C., Gardner, C.L., Watson, A.M., Ryman, K.D., Klimstra, W.B., 2014. Stable, high-level expression of reporter proteins from improved alphavirus expression vectors to track replication and dissemination during encephalitic and arthritogenic disease. J. Virol. 88, 2035–2046.

Tabara, H., Naito, Y., Ito, A., Katsuma, A., Sakurai, M.A., Ohno, S., Shimizu, H., Yabuta, N., Nojima, H., 2011. Neonatal lethality in knockout mice expressing the kinase-dead form of the gefitinib target GAK is caused by pulmonary dysfunction. PloS One 6, e26034.

Tibes, R., Borad, M.J., Dutcus, C.E., Reyderman, L., Feit, K., Eisen, A., Verbel, D.A., Von Hoff, D.D., 2018. Safety, pharmacokinetics, and preliminary efficacy of E6201 in patients with advanced solid tumours, including melanoma: results of a phase 1 study. Br. J. Canc. 118, 1580–1585.

Torres, J.Z., Miller, J.J., Jackson, P.K., 2009. High-throughput generation of tagged stable cell lines for proteomic analysis. Proteomics 9, 2888–2891.

Van Cleef, K.W., Overheul, G.J., Thomassen, M.C., Kaptein, S.J., Davidson, A.D., Jacobs, M., Neyts, J., van Kuppeveld, F.J., van Rij, R.P., 2013. Identification of a new dengue virus inhibitor that targets the viral NS4B protein and restricts genomic RNA replication. Antivir. Res. 99, 165–171.

Verdonck, S., Pu, S.-Y., Sorrell, F.J., Elkins, J.M., Froeyen, M., Gao, L.-J., Prugar, L.I., Dorosky, D.E., Brannan, J.M., Barouch-Bentov, R., Others, 2019. Synthesis and structure-activity relationships of 3, 5-disubstituted-pyrrolo [2, 3-b] pyridines as inhibitors of adaptor associated kinase 1 (AAK1) with antiviral activity. J. Med. Chem.

Welsch, S., Miller, S., Romero-Brey, I., Merz, A., Bleck, C.K.E., Walther, P., Fuller, S.D., Antony, C., Krijnse-Locker, J., Bartenschlager, R., 2009. Composition and three-dimensional architecture of the dengue virus replication and assembly sites. Cell Host & Microbe.

Wu, J., Powell, F., Larsen, N.A., Lai, Z., Byth, K.F., Read, J., Gu, R.-F., Roth, M., Toader, D., Saeh, J.C., Chen, H., 2013. Mechanism and in vitro pharmacology of TAK1 inhibition by (5Z)-7-Oxozeaenol. ACS Chem. Biol. 8, 643–650.

Wu, R.H., Tsai, M.H., Chao, D.Y., Yueh, A., 2015. Scanning mutagenesis studies reveal a potential intramolecular interaction within the C-terminal half of dengue virus NS2A involved in viral RNA replication and virus assembly and secretion. J. Virol. 89, 4281–4295.

Xiao, F., Wang, S., Barouch-Bentov, R., Neveu, G., Pu, S., Beer, M., Schor, S., Kumar, S., Nicolaescu, V., Lindenbach, B.D., Randall, G., Einav, S., 2018. Interactions between the Hepatitis C Virus Nonstructural 2 Protein and Host Adaptor Proteins 1 and 4 Orchestrate Virus Release (mBio).

Yang, C.-C., Tsai, M.-H., Hu, H.-S., Pu, S.-Y., Wu, R.-H., Wu, S.-H., Lin, H.-M., Song, J.-S., Chao, Y.-S., Yueh, A., 2013. Characterization of an efficient dengue virus replicon for development of assays of discovery of small molecules against dengue virus. Antivir. Res. 98, 228–241.

Zhou, H., Xu, M., Huang, Q., Gates, A.T., Zhang, X.D., Castle, J.C., Stec, E., Ferrer, M., Strulovici, B., Hazuda, D.J., Espeseth, A.S., 2008. Genome-scale RNAi screen for host factors required for HIV replication. Cell Host Microbe 4, 495–504.

Zou, G., Xu, H.Y., Qing, M., Wang, Q.Y., Shi, P.Y., 2011. Development and characterization of a stable luciferase dengue virus for high-throughput screening. Antivir. Res. 91, 11–19.